

SYNTHESIS OF POLYMER NETWORKS AS OPTIMIZED ALIGNMENT MEDIA FOR NMR SPECTROSCOPY

Zur Erlangung des akademischen Grades eines
DOKTORS DER NATURWISSENSCHAFTEN

(Dr. rer. nat.)

von der KIT-Fakultät für Chemie und Biowissenschaften
des Karlsruher Instituts für Technologie (KIT)

genehmigte

DISSERTATION

von

M.Sc. Diego Estupiñán Méndez

aus Bogotá, Kolumbien

1. Referent: Prof. Dr. Christopher Barner-Kowollik

2. Referent: Priv.-Doz. Dr. Pavel Levkin

Tag der mündlichen Prüfung: 25. Juli 2019

To my family

*“You know more than you think you know,
just as you know less than you want to know”*

Lord Henry Wotton, in Oscar Wilde's *The Picture of Dorian Gray*

Die vorliegende Arbeit wurde von April 2016 bis Juni 2019 unter Anleitung von Associate Prof. Dr. Leonie Barner und Prof. Dr. Christopher Barner-Kowollik am Karlsruher Institut für Technologie (KIT) angefertigt.

Hiermit erkläre ich, dass die vorliegende Arbeit im Rahmen der Betreuung durch Associate Prof. Dr. Leonie Barner und Prof. Dr. Christopher Barner-Kowollik selbstständig von mir verfasst wurde und keine anderen als die angegebenen Quellen und Hilfsmittel verwendet wurden. Die wörtlich oder inhaltlich übernommenen Stellen wurden als solche kenntlich gemacht und die Regeln zur Sicherung der guten wissenschaftlichen Praxis des Karlsruher Instituts für Technologie (KIT) in der jeweils gültigen Fassung wurden beachtet. Die elektronische Version dieser Arbeit stimmt mit der schriftlichen Version überein. Außerdem ist die Abgabe und Archivierung der Primärdaten gemäß Abs. A (6) der Regeln zur Sicherung guter wissenschaftlicher Praxis des KIT beim Institut gesichert. Des Weiteren erkläre ich, dass diesem Promotionsverfahren gingen keine anderen Promotionsverfahren voran und ich bin in keinen weiteren Promotionsverfahren Kandidat.

Karlsruhe, den 11.06.2019

Diego Estupiñán Méndez

Abstract

One of the most powerful spectroscopic methods employed for the structural elucidation of (bio)molecules is nuclear magnetic resonance (NMR) spectroscopy. Recently, anisotropic NMR techniques have been developed, which permit the spatial characterization of analytes. Nevertheless, this information is only available if the molecules of interest are partially aligned with respect to the magnetic field. The methods currently used for the alignment of analytes present several limitations that hinder their wide application. Hence, the present work investigates the synthesis of polymer networks as optimized alignment media for anisotropic NMR analyses.

First, conventional free-radical copolymerization techniques were employed to obtain crosslinked polystyrene (PS) networks, which were shaped into sticks and used as initial model system. The influence of the amount of crosslinker (divinylbenzene) on the mechanical properties and on the alignment characteristics of the sticks was determined. An increase in the degree of crosslinking translates into a higher alignment strength, at the expense of a decreased mechanical flexibility. However, it is highly desirable to have a flexible gel – robust against mechanical failure – and at the same time, to preserve good alignment properties. Thus, the addition of plasticizers during the synthesis of the networks was systematically investigated. These additives rendered the sticks softer and more flexible in comparison to the samples without plasticizer. Therefore, breaking of the gels upon swelling and deformation was diminished, and the reusability of the sticks was enhanced by making them stable against several cycles of swelling and deswelling. On the other hand, with these flexible samples it was possible to precisely adjust the alignment strength by mechanically compressing the gel. Notwithstanding, the amount of additive needed to effectively avoid cracking and breaking upon swelling is relatively high (at least 17.5% v/v). Thus, it cannot be ruled out that the particular NMR resonances of the plasticizer will eventually interfere with the signals stemming from the analyte. Moreover, it is plausible that the amount of additive inside the gel decreases after several swelling/deswelling cycles, eventually losing its plasticizing effect. Therefore, the possibility of using different styrene derivatives was investigated in order to produce intrinsically softer sticks. Preliminary experiments demonstrated that PS gels prepared from styrenic monomers with long alkyl chains in *para* position display diminished formation of cracks

upon swelling. Nevertheless, the sticks obtained by this approach were very brittle, hence further studies are necessary to optimize their mechanical properties for future application as NMR alignment media.

The second step in the optimization of the current alignment media was the introduction of functionality into the networks. Two novel functional PS-based systems were developed, one including chiral moieties and the second one with paramagnetic binding tags. For the chiral sticks, (+)- and (-)-menthol-styrene monomers were synthesized and their copolymerization behavior with styrene was studied. Crosslinked sticks containing low (5 mol%) and high (25 mol%) amounts of each enantiomer were prepared and characterized. These chiral alignment media allowed the unambiguous enantiodifferentiation of optically active analytes. The corresponding anisotropic NMR experiments revealed a markedly different behavior of the stereocenters of the analyte when analyzed inside the (+)- or (-)-sticks, but the specific interactions between polymer chains and analyte cannot be unraveled. For the second functional system, a phenanthroline derivative of styrene was utilized as comonomer. The phenanthroline units incorporated into the PS networks (0.8 mol%) are good ligands for lanthanide ions, which in turn influence the alignment of analytes via paramagnetic interactions. Europium was selected as model lanthanide because it forms a strongly red fluorescent complex with phenanthroline, giving a visual cue for the successful functionalization of the gels.

In the last part of the current thesis, the synthesis of topologically homogeneous polymer networks as potential alignment media was investigated. As general approach, well-defined telechelic PS strands were prepared by reversible addition-fragmentation transfer (RAFT) polymerization, and later on crosslinked using click chemistry protocols. Initially, the UV-induced nitrile imine-mediated tetrazole-ene cycloaddition (NITEC) was explored as crosslinking methodology. This reaction takes place between a tetrazole and an activated ene under UV irradiation, generating a strongly fluorescent pyrazoline adduct. A custom RAFT agent was designed for this purpose and utilized to obtain α,ω -tetrazole-functionalized PS chains. The conversion kinetics of these end-capped PS chains during NITEC addition can be monitored by fluorescence spectroscopy. On the one hand, step-growth polymers obtained by reaction with bismaleimides showed concomitant increase in the fluorescence emission with increasing reaction conversion. Moreover, by reacting the tetrazole-PS strands with a trifunctional maleimide linker, fluorescent networks were obtained. A critical advantage of this approach is the appearance of one fluorescent unit for each link formed. Hence, the number of crosslinks in the network was readily quantified via fluorescence

emission readouts. This method represents the first example in the literature for the direct quantification of crosslinking degree during network formation. Nonetheless, limitations concerning light penetration depth prevented the application of this methodology for the synthesis of cylindrical PS sticks. To circumvent this issue, Michael-type thiol-ene protocols as alternative crosslinking methodology were investigated. Again, RAFT polymerization techniques were employed to obtain well-defined polystyrene strands of different length, which were subsequently aminolyzed to yield α,ω -thiol-functional polystyrene. These telechelic chains were crosslinked under basic conditions using a tetrafunctional acrylate, thus affording end-linked PS networks with tunable mesh size. As expected, changing the average mesh size has an effect in the swelling behavior of the networks. Thiol-ene gels exhibited higher swelling ratios when the molecular weight of the precursor polymers was increased. In addition, networks obtained from mixed strands of different molecular weight were prepared and characterized. These mixed networks exhibited macroscopic properties analogous to networks prepared from single strands with the same average molecular weight. However, introducing heterogeneity deliberately yields a significantly different internal microstructure. Finally, the performance of the thiol-ene networks (single and mixed) as optimized alignment media was compared with free-radical-based networks of similar crosslinking degree.

In summary, the present doctoral thesis addresses the development of polymer gels as alignment media with improved mechanical, functional, and alignment properties. Furthermore, investigations on the controlled synthesis of networks were carried out, introducing alternative network characterization methods such as fluorescence spectroscopy. In this way, the effect of the internal structure of the gel on its alignment behavior can be assessed. The work herein presented paves the way for the rational design of optimized polymer-based alignment media, in order to widen the application of NMR spectroscopy in anisotropic media as standard analytical technique.

Zusammenfassung

Eine der leistungsstärksten spektroskopischen Methoden zur Strukturaufklärung von (Bio-) Molekülen ist die Kernspinresonanzspektroskopie (engl. NMR). Kürzlich wurden anisotrope NMR-Techniken entwickelt, die auch die dreidimensionale Charakterisierung von Analyten erlauben. Derartige räumliche Informationen sind jedoch nur verfügbar, wenn sich ein Teil der zu untersuchenden Moleküle entlang des Magnetfeldes ausrichtet. Die gegenwärtig verwendeten Methoden zur Ausrichtung von Analyten sind durch vielfältige Limitierungen geprägt, was ihre breite Anwendung verhindert. Deshalb ist das Thema der vorliegenden Arbeit die Synthese von Polymernetzwerken als optimierte Orientierungsmedien für anisotrope NMR-Analysen.

Mithilfe konventioneller radikalischer Copolymerisationstechniken wurden zunächst vernetzte Polystyrol (PS) -Netzwerke hergestellt, die in Form von Stäbchen als anfängliches Modellsystem verwendet wurden. Zu Beginn wurde der Einfluss des Anteils an Vernetzer (Divinylbenzol) auf die mechanischen Eigenschaften, sowie die Ausrichtungseigenschaften der Stäbchen bestimmt. Dabei zeigte sich, dass eine Erhöhung des Vernetzungsgrades zu einer erhöhten Ausrichtung führt, allerdings wird die mechanische Flexibilität dadurch herabgesetzt. Erstrebenswert ist jedoch ein flexibles Gel, das bei mechanischer Beanspruchung robust bleibt und gleichzeitig gute Ausrichtungseigenschaften besitzt. Daher wurde der Zusatz von Weichmachern während der Netzwerksynthese systematisch untersucht. Diese Zusätze verleihen den Stäbchen weichere und flexiblere Eigenschaften, wodurch die Gefahr des Gelbruchs beim Quellen und Verformen verringert wird. Diese erhöhte Stabilität gewährte eine häufigere Wiederverwendbarkeit der Stäbchen über mehrere Quell- und Entquellzyklen. Darüber hinaus ermöglichten diese flexiblen Proben die Ausrichtung des Analyten durch mechanisches Zusammendrücken des Gels zusätzlich stark anzupassen. Dennoch ist die benötigte Menge an Additiv relativ hoch (mindestens 17,5% v/v), um das Reißen und Brechen beim Quellvorgang wirksam zu vermeiden. Somit ist nicht auszuschließen, dass die jeweiligen NMR-Resonanzen des Weichmachers letztendlich die vom Analyten stammenden Signale stören. Darüber hinaus ist zu vermuten, dass die Menge an Additiv im Gel nach mehreren Quell- / Entquellzyklen abnimmt, wodurch es seine flexiblen Eigenschaften verliert. Daher wurde die Verwendung verschiedener Styrolderivate zur direkten Herstellung weicherer Stäbchen untersucht. Vorversuche zeigten, dass PS-

Gele, die aus Styrolmonomeren mit langen Alkylketten in *para*-Position hergestellt wurden, eine verminderte Rissbildung während des Quellens der Proben zeigen. Dennoch waren die mit diesem Ansatz erhaltene Stäbchen sehr spröde, weshalb weitere Untersuchungen erforderlich sind, um ihre mechanische Eigenschaften zu optimieren und ihre zukünftige Anwendung als NMR-Ausrichtungsmedium zu garantieren.

Eine Alternative zur Optimierung der aktuellen Ausrichtmedien stellt die Einführung von funktionellen Gruppen in die Netzwerke dar. Dazu wurden zwei neuartige funktionalisierte PS-basierte Systeme entwickelt; eines mit chiralen Gruppen, das zweite mit paramagnetischen Bindungstaschen. Für die chiralen Stäbchen wurden sowohl (+) - als auch (-) - Menthol-Styrol-Monomere synthetisiert und deren Copolymerisationsverhalten mit Styrol untersucht. Vernetzte Stäbchen, die geringe (5 mol-%) und hohe (25 mol-%) Mengen jedes Enantiomers enthielten, wurden hergestellt und charakterisiert. Diese chiralen Ausrichtungsmedien ermöglichen die eindeutige Unterscheidung der Enantiomeren von optisch aktiven Analyten. Die anisotropen NMR-Experimente zeigen ein markant unterschiedliches Verhalten der Stereozentren des jeweiligen Analyten innerhalb der (+) - oder (-) - Stäbchen, doch die spezifischen Wechselwirkungen zwischen Polymerketten und Analyt können nicht eindeutig belegt werden. Für das zweite funktionelle System wurde ein Phenantrolinderivat des Styrols als Comonomer verwendet. Die in die PS-Netzwerke eingebauten Phenanthrolineinheiten (0,8 mol-%) sind gute Liganden für Lanthanoidionen, die wiederum die Ausrichtung der Analyten über paramagnetische Wechselwirkungen beeinflussen. Europium wurde als Model-Lanthanoid ausgewählt, da es mit Phenanthrolin einen stark rot fluoreszierenden Komplex bildet, der einen visuellen Anhaltspunkt für die erfolgreiche Funktionalisierung der Gele liefert.

Im letzten Teil dieser Arbeit wurde die Synthese topologisch homogener Polymernetzwerke als potentielle Orientierungsmedien untersucht. Für diesen Ansatz wurden wohl-definierte telechele PS-Stränge durch reversible Additions-Fragmentierungs-Transfer-Polymerisation (RAFT-Polymerisation) hergestellt und später gemäß Click-Chemie-Protokollen vernetzt. Zunächst wurde die UV-induzierte Nitrilimin-vermittelte Tetrazol-En-Cycloaddition (NITEC) als Vernetzungsmethode untersucht. Diese Reaktion findet unter UV-Bestrahlung zwischen einem Tetrazol und einem aktivierten En statt und erzeugt ein stark fluoreszierendes Pyrazolin-Addukt. Zu diesem Zweck wurde ein spezielles RAFT-Agens entwickelt, um damit α,ω -Tetrazol-funktionalisierte PS-Ketten herzustellen. Die Umsatzkinetik dieser endständig funktionalisierten PS-Ketten konnte während der NITEC-Addition mittels Fluoreszenzspektroskopie überwacht werden. Einerseits zeigten

Stufenwachstumspolymere, die durch eine solche NITEC-Addition mit Bismaleimiden erhalten wurden, eine zum Reaktionsumsatz korrelierende Zunahme der Fluoreszenzemission. Durch die Umsetzung der Tetrazol-PS-Stränge mit trifunktionellen Maleimid-Linkern konnten schließlich fluoreszierende Netzwerke erhalten werden. Dieser neue Ansatz ist herausragend, da jede gebildete Verbindung als eine fluoreszierende Einheit erscheint. Somit konnte die genaue Anzahl der Vernetzungen im Netzwerk leicht über Fluoreszenzmissionsmessungen quantifiziert werden. Diese Methode ist das erste literaturbekannte Beispiel für die direkte Quantifizierung des Vernetzungsgrades während der Netzwerkbildung. Aufgrund der Einschränkungen hinsichtlich der Lichtdurchdringungstiefe konnte diese Methode jedoch nicht erfolgreich für die Synthese zylindrischer PS-Stäbchen angewendet werden. Um dieses Problem zu umgehen, wurden Thiol-En-Michael-Addition-Protokolle als alternative Vernetzungsmethode untersucht. Wiederum wurden wohl-definierte Polystyrolstränge unterschiedlicher Länge mittels RAFT-Polymerisationstechniken erhalten, die anschließend zu α,ω -thiol-funktionalisiertem Polystyrol aminolysiert wurden. Diese telechelen Ketten wurden im Basischen mithilfe eines tetrafunktionellen Acrylats vernetzt, wodurch endverknüpfte PS-Netzwerke mit einstellbarer Maschengröße erhalten wurden. Erwartungsgemäß wirkt sich eine Änderung der durchschnittlichen Maschengröße auf das Quellverhalten der Netze aus. So zeigten Thiol-En-Gele höhere Quellraten bei höheren Molekulargewichten der Vorläuferpolymere. Zusätzlich wurden Netzwerke aus gemischten Strängen mit unterschiedlichem Molekulargewicht hergestellt und charakterisiert. Die makroskopischen Eigenschaften dieser gemischten Netzwerke ähnelten stark den Netzwerken, die aus Einzelsträngen mit demselben durchschnittlichen Molekulargewicht hergestellt wurden. Die Mikrostruktur dieser gezielt heterogenen Netzwerke unterscheidet sich hingegen stark. Die Eignung dieser Thiol-En-Netzwerke (homo- und heterogen) als optimierte Ausrichtungsmedien wurde mit den radikalbasierten Netzwerken mit ähnlichem Vernetzungsgrad verglichen.

Zusammenfassend behandelt die vorliegende Promotionsschrift die Entwicklung von Polymergelen als Orientierungsmedien mit verbesserten mechanischen, funktionellen und ausrichtenden Eigenschaften. Darüber hinaus wurden Untersuchungen zur kontrollierten Synthese von Netzwerken durchgeführt und alternative Methoden zur Netzwerkcharakterisierung wie die Fluoreszenzspektroskopie vorgestellt. Auf diese Weise kann der Einfluss der inneren Struktur des Gels auf sein Ausrichtungsverhalten beurteilt werden. Die hier vorgestellte Arbeit ebnet den Weg für das rationale Design optimierter polymerbasierter Ausrichtungsmedien, um die Anwendung der NMR-Spektroskopie in anisotropen Medien als Standardanalysetechnik zu erweitern.

Publications Arising from this Thesis

1a. Counting the Clicks in Fluorescent Polymer Networks

D. Estupiñán, C. Barner-Kowollik, L. Barner, *Angew. Chem. Int. Ed.* **2018**, *57*, 5925.

1b. Bestimmung der Verknüpfungspunkte in fluoreszenten Polymernetzwerke

D. Estupiñán, C. Barner-Kowollik, L. Barner, *Angew. Chem.* **2018**, *130*, 6028.

2. Self-Reporting Fluorescent Step-Growth RAFT Polymers Based on Nitrile Imine-Mediated Tetrazole-ene Cycloaddition Chemistry

D. Estupiñán, T. Gegenhuber, J. P. Blinco, C. Barner-Kowollik, L. Barner, *ACS Macro Lett.* **2017**, *6*, 229.

Table of Contents

Abstract.....	i
Zusammenfassung.....	iv
List of publications.....	vii
Table of contents.....	viii
1. Introduction.....	1
2. Theory and background.....	6
2.1. Free-radical polymerization.....	6
2.1.1. Free-radical copolymerization.....	10
2.2. Reversible-deactivation radical polymerization.....	12
2.3. Chain-addition vs. step-growth polymerization.....	22
2.4. Photochemistry.....	26
2.4.1. Fundamentals.....	27
2.4.2. Photochemical polymer modification.....	30
2.5. Polymer networks.....	34
2.5.1. Fundamentals.....	35
2.5.2. Synthesis.....	38
2.5.3. Characterization methods.....	40
2.5.4. Applications.....	43
2.6. Nuclear magnetic resonance spectroscopy.....	44
2.6.1. Fundamentals.....	44
2.6.2. NMR analysis of polymers.....	48
2.6.3. Anisotropic NMR.....	49
3. Synthesis of optimized polymer-based alignment media.....	54
3.1. Polystyrene sticks via free radical polymerization.....	55

3.1.1. PS sticks with tunable alignment strength.....	57
3.1.2. PS sticks with optimized mechanical properties.....	61
3.1.3. Shape optimization of PS sticks.....	70
3.2. Functional polystyrene sticks.....	72
3.2.1. PS gels with chiral units.....	74
3.2.1.1. Enantiodifferentiation in chiral PS gels.....	82
3.2.2. Lanthanide-functionalized PS gels.....	89
3.3. Summary and outlook.....	92
4. Towards homogeneous alignment media.....	97
4.1. NITEC chemistry applied to step-growth polymers.....	98
4.1.1. Monomer design.....	100
4.1.2. UV-induced step-growth polymerization.....	104
4.1.2.1. Calibration curve.....	106
4.1.2.2. Kinetics via fluorescence spectroscopy.....	110
4.1.3. RAFT and step-growth polymerization.....	113
4.2. Network formation via NITEC.....	118
4.2.1. Conditions for network formation.....	120
4.2.2. Characterization via fluorescence spectroscopy.....	129
4.2.2.1. Aminolysis of RAFT polymers.....	132
4.2.2.2. Effect of aminolysis on fluorescence.....	138
4.2.2.3. Calibration curve.....	143
4.2.3. Quantification of crosslinking density.....	145
4.2.4. Upscale experiments.....	153
4.3. Network formation via thiol-ene chemistry.....	156
4.3.1. Thiol end-capped PS chains.....	157
4.3.2. Crosslinking of thiol-PS chains.....	160
4.3.3. Conversion of thiol groups.....	164
4.3.4. Thiol-ene vs. free-radical networks.....	166

4.3.5. Thiol-ene-based gels as alignment media.....	174
4.4. Summary and outlook.....	177
5. Concluding remarks.....	183
6. Experimental section.....	191
6.1. Materials.....	191
6.2. Analytical methods and instrumentation.....	192
6.3. Experimental procedures.....	196
7. References.....	228
8. Appendix.....	242
8.1. Synthesis of optimized polymer-based alignment media.....	242
8.2. NITEC chemistry applied to step-growth polymers.....	248
8.3. Network formation via NITEC.....	251
8.4. Network formation via thiol-ene chemistry.....	257
8.5. List of abbreviations.....	259
8.6. List of figures, schemes, and tables.....	263
Complete list of publications and conference contributions.....	287
Curriculum Vitae.....	289
Acknowledgments.....	291

CHAPTER 1:

INTRODUCTION

Identification and structural determination of (bio)organic compounds is nowadays routinely accomplished by means of spectroscopic analysis. One of the most important analytical techniques is nuclear magnetic resonance (NMR) spectroscopy. With this method it is possible to establish the constitution of a given molecule (i.e. analyte) by direct evaluation of classical NMR observables like chemical shifts (δ), scalar couplings (J -coupling), and nuclear Overhauser effect (NOE) interactions.^{1,2} Nevertheless, the evaluation of these standard NMR parameters provide only limited information on the full spatial characteristics of the analyte. For instance, information about conformation or relative stereochemistry is not readily available from classical NMR experiments in solution. In an isotropic solution, molecules are constantly moving without any spatial restriction. Therefore, interactions like quadrupolar and dipolar couplings are averaged, hence impossible to be observed directly.² However, if the molecules are partially aligned in the measuring medium, an incomplete averaging of their anisotropic interactions takes place, allowing their direct measurement. Residual Dipolar Couplings (RDCs) are anisotropic parameters that provide access to long-range structural determination, including angles and distances between atoms.² More specifically, angular information relative to an external reference can be acquired and assigned to the geometrical orientation between different fragments of the analyte.^{1,3} In this way, distant parts of a molecule can be correlated through anisotropic NMR interactions, giving access to the conformation and configuration of a molecule,⁴ or enabling enantiomeric determination.^{5,6} Such output of information is rarely achieved by any other analytical technique alone.

Typically, the alignment of molecules can be achieved through three general methods. One strategy is the inclusion of anisotropic paramagnetic ions.⁷ However, this technique is almost exclusively applicable to biomolecules, as line broadening limits its use for small molecules.¹ The second and most common type of alignment media are liquid crystals. These media consist of solutions of a “liquid crystal builder”, either

INTRODUCTION

inorganic as graphene oxide,⁸ or polymeric like poly(γ -benzyl-L-glutamate) (PBLG), polyisocyanates and polyacetylenes.² However, these liquid crystalline systems present narrow solvent compatibility and a limiting concentration at which the liquid crystalline phase is formed. This issue predetermines the alignment degree of the analyte (normally very strong), thus hampering the interpretation of the spectra.^{1,9} Notwithstanding, current developments report the use of doped ionic liquid crystals as weakly alignment media for polar analytes.¹⁰ The third method to induce alignment is the use of mechanically strained polymer gels.⁹ In this case, crosslinked polymers are allowed to swell inside a cylindrical chamber (e.g. NMR tubes), and subjected to anisotropic deformation by compression or stretching. The analyte molecules interact with the strained polymer chains of the gel, thus reducing their isotropic motion and reaching a partially aligned state.^{1,2} The main advantages of the polymer-based alignment media are their wider compatibility with both polar and non-polar solvents,¹¹ and – more important – the possibility of tuning the degree of alignment either by crosslinking density^{9,12} or mechanically strain.¹³

Although the potential applicability of polymer gels as alignment media is remarkable, there are still several drawbacks to overcome. On the one hand, the limited availability of adequate gel/solvent pairs restricts their implementation only to analytes compatible with a specific system. For each polymer used as alignment medium, optimal swelling is attained solely at certain solvent polarities and crosslinking degrees.¹⁴ Examples of polymer alignment media compatible with a range of solvent polarities or even with mixtures of solvents are scarce.¹¹ On the other hand, detailed structural characterization of a polymer gel is a very challenging task, and even the simplest topological heterogeneities are difficult to quantify.^{15,16} This prevents the development of relationships between gel structure and alignment properties, as well as the establishment of models which predict the behavior of an analyte inside a gel. Moreover, the most common method to produce polymer networks, namely free-radical crosslinking copolymerization, generates a high degree of heterogeneity in the microstructure of the gel.¹⁶ Such defects result in a broad distribution of meshes (instead of a single mesh size) and other connectivity imperfections, which could negatively impact the resolution of the NMR signals (e.g. broad linewidth).

The aim of the current work is to obtain and characterize highly defined polymeric networks with optimized properties as alignment media and, ultimately, to understand the phenomena related to the alignment process. By controlling the network synthesis conditions and developing alternative network characterization methods, structure-property relationships can be derived in order to improve the performance of the

currently available polymer-based alignment matrices. To the best of our knowledge, no controlled polymerization/crosslinking strategy has been investigated to date for the synthesis of homogeneous alignment media for anisotropic NMR studies. The present doctoral thesis is divided in three general research areas. The first one involves the optimization of the existing heterogeneous alignment media obtained by conventional free-radical polymerization (Chapter 3.1). The synthesis parameters of crosslinked polystyrene (PS) gels were systematically studied to achieve optimal mechanical and alignment properties in a reproducible fashion. In this way, the gel robustness and alignment strength scalability was improved (Figure 1.1, left panel). Second, the functionalization of heterogeneous free-radical-based networks with selected groups – i.e. chiral moieties and lanthanide-binding tags – was investigated (Chapter 3.2). Thus, novel PS-based alignment media with enhanced performance in terms of enantiodiscrimination and paramagnetic ion complexation were developed (Figure 1.1, left panel). The third research topic was devoted to the synthesis of homogeneous polymer networks. In order to obtain gels with precise topologies, modern polymer synthesis techniques and orthogonal crosslinking reactions are required.^{17,18} Thus, well-defined end-functional PS strands were prepared via reversible-deactivation radical polymerization techniques, in particular reversible addition-fragmentation chain transfer (RAFT) polymerization.¹⁹ Subsequently, the individual polymer chains were crosslinked via click reactions, namely nitrile imine-mediated tetrazole-ene cycloaddition (NITEC),¹⁷ and thiol-ene protocols^{17,18} (Figure 1.1, right panel). In the former case, fluorescent step-growth polymers and end-linked networks with variable and – remarkably – directly quantifiable crosslinking degree were developed (Chapters 4.1 and 4.2). In the latter case, PS networks of tunable mesh size and controllable structural heterogeneity were obtained (Figure 1.1, right panel). Furthermore, the swelling and alignment behavior of the homogeneous thiol-ene gels was assessed and compared with the state-of-the-art free-radical-based gels, highlighting the advantages and limitations of the controlled network synthesis approach (Chapter 4.3). In summary, by controlling the parameters involved in the synthesis of the gels, and establishing alternative characterization methods, a direct correlation between network structure and alignment performance can be rationalized. This will pave the way for the development of the next generation of polymer-based alignment media for anisotropic NMR spectroscopy.

INTRODUCTION

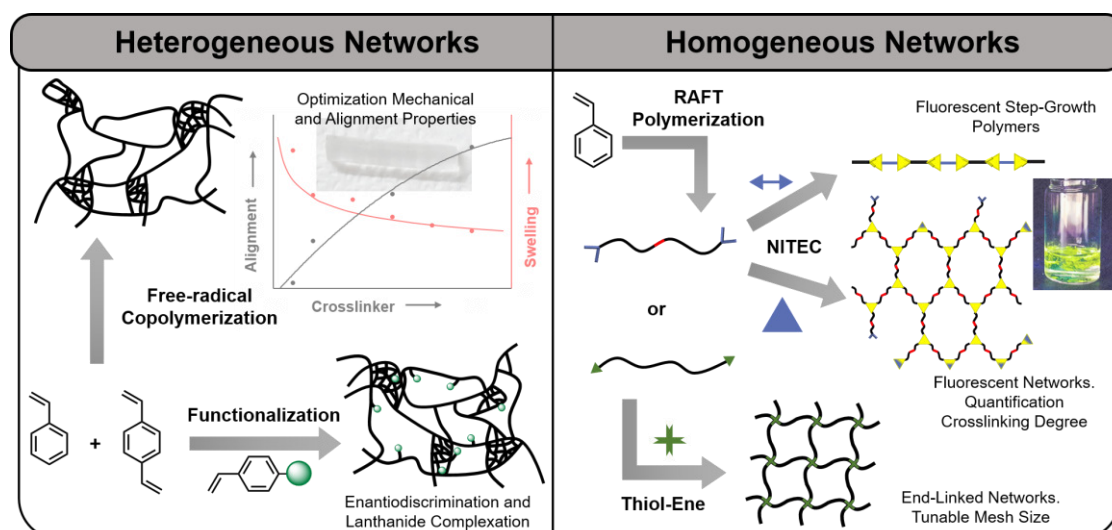


Figure 1.1. Schematic representation of the projects presented in the current thesis. Heterogeneous PS networks were prepared via free-radical polymerization, their mechanical properties and functionalization features were optimized for their application as alignment media (left panel). Homogeneous networks were obtained by RAFT polymerization followed by crosslinking via NITEC or thiol-ene protocols (right panel).

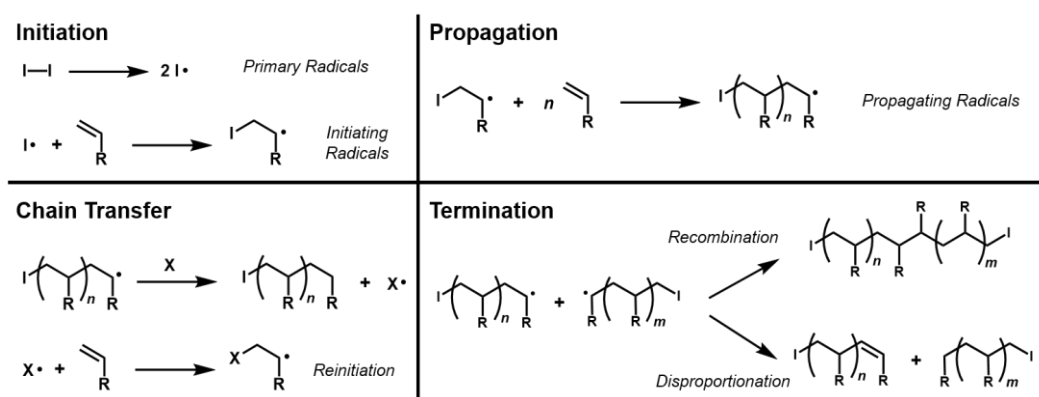
CHAPTER 2:

THEORY AND BACKGROUND

In the following sections, a theoretical background of the topics covered in the current thesis will be presented. First, the fundamentals of radical polymerization are briefly described, including controlled radical polymerization techniques and a comparison with step-growth polymerization. Subsequently, an overview of photochemistry and its application in polymer chemistry as ligation method is given, followed by the main features of polymer networks and gels. Finally, an introduction to the basic theory of NMR spectroscopy, its application to polymer networks, and recent anisotropic NMR methods, is outlined.

2.1. Free-Radical Polymerization

Polymers are long-chain macromolecules of high molecular weight (typically in the range of 10^4 – 10^6 g·mol⁻¹),²⁰ formed by successive reaction of small building blocks termed monomers, in a process known as polymerization. From the several polymerization methods available nowadays, the most industrially relevant is free-radical polymerization (FRP).²¹ Kinetically, this method can be described by four main steps: initiation, propagation, chain transfer and termination (Scheme 2.1).



Scheme 2.1. Generally accepted mechanism of free-radical polymerization (FRP) of vinyl C=C–R monomers, where I represents an initiator and X a chain transfer species.

THEORY AND BACKGROUND

During the initiation step, primary radicals are generated, which are responsible for starting the polymerization process. The procedures for initiating radical polymerizations are manifold, including thermal, photochemical, and redox methodologies, among others. The most common initiation system comprises the decomposition of an initiator molecule (I-I in Scheme 2.1, top left) into free radicals either by heat, irradiation with light or oxidation-reduction reactions.^{20,21} The subsequent addition of these primary radicals to the vinyl double bond of the monomer yields the initiating radicals.²¹ Alternative procedures for the initiation of radical polymerization encompass thermal self-initiation of the monomer, initiation by ionizing radiation, electrolysis, plasma polymerization, and sonication.²⁰

In the propagation step, the previously formed initiating radicals grow by successive addition of new monomer molecules, increasing the chain-length of the polymer. As depicted in Scheme 2.1 (top right), each monomer addition creates a new propagating radical, in a process driven by the exothermic conversion of the π bond of the monomer into a σ bond in the polymer. A highly negative change in the enthalpy of the system is thus needed for the propagation to take place, since the organization of monomers into a polymeric chain occurs with a negative change in entropy. The net change in the free energy during propagation ΔG_p can be written as follows,

$$\Delta G_p = \Delta H_p - T\Delta S_p \quad (\text{Eq. 2.1})$$

where ΔH_p and ΔS_p represent the change in the enthalpy and entropy in the propagation step, respectively, at a given temperature T . Therefore, there is a maximum temperature at which the polymerization can be carried out: the so-called ceiling temperature T_c . Above this critical temperature, ΔG_p becomes positive and the depropagation reaction becomes spontaneous.²¹ The addition of new monomer units to the growing macroradical can occur in a head-to-tail (H-T) or head-to-head (H-H) fashion, as depicted in Scheme 2.2. Although steric and electronic effects greatly favor the head-to-tail propagation placement, under certain conditions H-H polymers with unexpected properties can be deliberately prepared.²²



Scheme 2.2. Head-to-tail (H-T) vs. head-to-head (H-H) addition of monomers during propagation.

The kinetics of the propagation process (conversion of monomer M) can be described by Equation 2.2, in which k_p^i is the propagation rate coefficient of a

THEORY AND BACKGROUND

macroradical P_i^* with chain-length i . It has been demonstrated that propagation rate is chain-length dependent.²³

$$-\frac{d[M]}{dt} = \sum_i k_p^i [P_i^*][M] \quad (\text{Eq. 2.2})$$

Moreover, the propagation reaction is chemically controlled, which means k_p is independent of monomer conversion. Only in a very viscous system (for monomer conversions $\geq 80\%$), propagation becomes diffusion controlled.²³

Due to their intrinsic high reactivity, propagating radicals can react also with other non-radical species X, in a process known as chain transfer (refer to Scheme 2.1, bottom left). This reaction produces a dead polymer chain and a new radical X^\bullet , eventually also capable of reinitiating a new propagating chain. X can be any element present in the polymerization system, namely initiator, monomer, polymer, solvent, impurities or a deliberately added chain transfer agent. Chain transfer during polymerization causes a net reduction of the propagating chain length (lower molecular weight). In addition, branching, back-biting or even crosslinking events occur if chain transfer to the polymer strands themselves takes place. On the other hand, the effect that chain transfer exerts on the polymerization rate depends mainly on the rate of reinitiation by species X^\bullet . Only when reinitiation is much slower than k_p , an overall decrease in the polymerization rate is observed (retardation or even degenerative chain transfer). Chain transfer effects might be used advantageously in industrial processes by deliberately diminishing the molecular weight of a polymer, hence reducing the viscosity of the medium and improving heat transfer.²³

The last fundamental step of the free-radical polymerization is termination, a process in which the existing radicals annihilate each other in a bimolecular reaction. Termination can occur either by recombination, i.e. coupling of two different radical centers, or by disproportionation, which involves hydrogen abstraction to form a saturated and an unsaturated polymer chain (see Scheme 2.1, bottom right). Depending on the monomer used, either recombination or disproportionation – or a mixture of both – takes place during termination. In any case, termination results in dead polymer chains, i.e. chains with no propagating radical that permit them to further grow. The magnitude of the termination rate coefficient (k_t) strongly depends on many different factors including the medium viscosity, the chain length of the terminating macroradicals, temperature, pressure and monomer conversion.²³ Since the corresponding rate coefficients are very high ($k_t \approx 10^7\text{--}10^9 \text{ M}^{-1}\cdot\text{s}^{-1}$),²¹ termination is diffusion controlled.²⁴

THEORY AND BACKGROUND

Taking into account the effect of each individual step in the mechanism of free-radical polymerization, a simple expression for the rate of polymerization R_p can be derived. Nevertheless, the following approximations²³ are needed: i) The propagation and termination rate coefficients, k_p and k_t respectively, are independent of chain-length and monomer conversion. ii) Monomer disappearance due to initiation is very small in comparison to propagation, which allows the rate of polymerization being approximately equal to the rate of propagation. iii) A steady-state is rapidly reached in which the concentration of radicals does not change, or in other words, the rates of initiation and termination are equal. iv) All reactions are irreversible. Using approximations (i) and (ii), a simplified version of Equation 2.2 is obtained, which describes the rate of polymerization,

$$-\frac{d[M]}{dt} = R_p = k_p[P^*][M] \quad (\text{Eq. 2.3})$$

By approximation (iii) it follows that

$$R_i = R_t, \quad 2fk_d[I] = 2k_t[P^*][P^*] \quad (\text{Eq. 2.4})$$

where f is the initiator efficiency, k_d the rate coefficient of initiator decomposition and $[I]$ the initiator concentration. The right side of Equation 2.4 represents the rate of termination with k_t being the rate coefficient of termination of a pair of macroradicals (P^*). Importantly, the method of termination (recombination or disproportionation) has no influence on the rate of polymerization, but strongly affects the molecular weight distribution of the final polymer.²³ Combining Equations 2.3 and 2.4 yields the final expression for the rate of polymerization:

$$R_p = k_p[M] \left(\frac{fk_d[I]}{k_t} \right)^{1/2} \quad (\text{Eq. 2.5})$$

On the other hand, the rate of chain transfer can be described by Equation 2.6,

$$R_{tr} = k_{tr}[P^*][X] \quad (\text{Eq. 2.6})$$

with $[X]$ and $[P^*]$ as the concentration of transfer agent and propagating radical, respectively. As already mentioned before, the transfer species X could be either solvent S , initiator I , monomer M , polymer P or added transfer agent T . The chain transfer rate coefficient can be then individually defined as C_x for the different molecules in the following manner:

$$C_S = \frac{k_{tr}^S}{k_p} \quad C_I = \frac{k_{tr}^I}{k_p} \quad C_M = \frac{k_{tr}^M}{k_p} \quad C_P = \frac{k_{tr}^P}{k_p} \quad C_T = \frac{k_{tr}^T}{k_p} \quad (\text{Eq. 2.7})$$

THEORY AND BACKGROUND

The degree of polymerization DP_n , defined as the average number of monomer units per polymer chain, can be understood as the rate of polymerization R_p divided by the rate of all chain-stopping events, i.e. termination R_t and chain transfer R_{tr} :

$$DP_n = \frac{R_p}{R_t + R_{tr}} \quad (\text{Eq. 2.8})$$

Using Equations 2.3, 2.4, 2.6, 2.7, and 2.8, the following expression can be derived,

$$\frac{1}{DP_n} = \frac{k_t R_p}{k_p^2 [M]^2} + C_M + C_S \frac{[S]}{[M]} + C_I \frac{[I]}{[M]} + C_P \frac{[P]}{[M]} + C_T \frac{[T]}{[M]} \quad (\text{Eq. 2.9})$$

commonly known as the general form of the Mayo Equation. It correlates the number average degree of polymerization with the rate of polymerization and the different transfer constants.

2.1.1. Free-Radical Copolymerization

When two different monomers, M_1 and M_2 , are polymerized simultaneously the process is termed copolymerization. The obtained copolymer contains overall amounts of each monomer that depend on their relative concentrations and reactivities.²⁰ The organization of these monomers into the polymer chain permits the classification of copolymers in three basic structures: statistical, alternating and block copolymers (Figure 2.1).

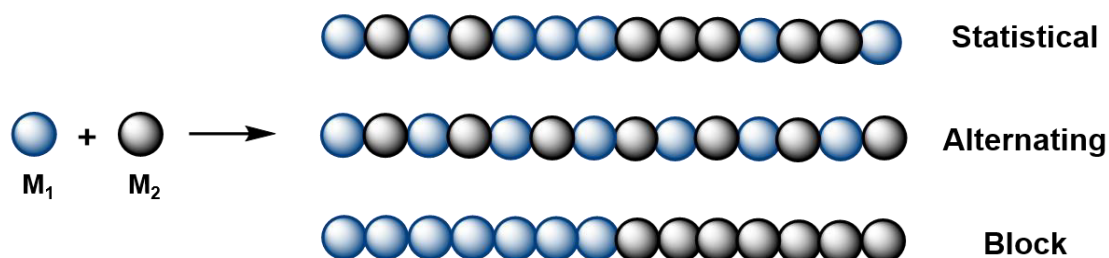


Figure 2.1. Possible structures obtained by copolymerization of two different monomers M_1 and M_2 .

In statistical copolymers, the distribution of monomers along the chain follows known statistical laws (Markovian statistics), while in alternating copolymers both comonomer units are arranged one next to the other in a regular alternating fashion. In contrast, a block copolymer consists of long uninterrupted clusters of one monomer followed by the second one. The nature of the different distributions lies in the kinetic elemental steps taking place between the components of the copolymerization (monomers and propagating species), and it can be numerically estimated by the so-called reactivity ratios.²⁵

THEORY AND BACKGROUND

According to the terminal model of copolymerization, only the identity of the monomer at the propagating end is responsible for the copolymerization behavior (macroradical P_1^* or P_2^*), irrespective of the chain composition preceding it. With this approximation, only the self-propagation (reaction with the same monomer) or cross-propagation (reaction with the opposite monomer) is considered. Thus, analogous to Equation 2.3, the ratio of monomer disappearance (incorporation into the copolymer) can be written as follows:

$$-\frac{d[M_1]}{dt} = k_{11}[P_1^*][M_1] + k_{21}[P_2^*][M_1] \quad (\text{Eq. 2.10})$$

$$-\frac{d[M_2]}{dt} = k_{22}[P_2^*][M_2] + k_{12}[P_1^*][M_2] \quad (\text{Eq. 2.11})$$

Hence, the copolymer composition can be defined as:²⁶

$$\frac{d[M_1]}{d[M_2]} = \frac{k_{11}[P_1^*][M_1] + k_{21}[P_2^*][M_1]}{k_{22}[P_2^*][M_2] + k_{12}[P_1^*][M_2]} \quad (\text{Eq. 2.12})$$

Using the steady-state approximation (Equation 2.13) and defining the following r parameters (Equation 2.14),

$$k_{12}[P_1^*][M_2] = k_{21}[P_2^*][M_1] \quad (\text{Eq. 2.13})$$

$$r_1 = \frac{k_{11}}{k_{12}} \quad r_2 = \frac{k_{22}}{k_{21}} \quad (\text{Eq. 2.14})$$

Equation 2.12 can be rearranged to

$$\frac{d[M_1]}{d[M_2]} = \frac{[M_1](r_1[M_1] + [M_2])}{[M_2]([M_1] + r_2[M_2])} \quad (\text{Eq. 2.15})$$

which is known as the instantaneous copolymer composition equation. It correlates the composition of the copolymer with the monomer feed concentrations $[M_1]$ and $[M_2]$, and the monomer reactivity ratios r_1 and r_2 (valid only for low monomer conversions $< 5\%$). This equation can also be expressed in terms of the molar fractions of monomers M_1 and M_2 in the feed (f_1 and f_2), and in the copolymer (F_1 and F_2), respectively:

$$f_1 = 1 - f_2 = \frac{[M_1]}{[M_1] + [M_2]}, \quad F_1 = 1 - F_2 = \frac{d[M_1]}{d[M_1] + d[M_2]} \quad (\text{Eq. 2.16})$$

$$F_1 = \frac{r_1 f_1^2 + f_1 f_2}{r_1 f_1^2 + 2f_1 f_2 + r_2 f_2^2} \quad (\text{Eq. 2.17})$$

As already mentioned before, the copolymerization behavior can be numerically characterized by the values of the monomer reactivity ratios. Three different cases are feasible:

$$r_1 \cdot r_2 = 1 \quad r_1 \cdot r_2 = 0 \quad r_1 > 1, r_2 > 1 \quad (\text{Eq. 2.18})$$

THEORY AND BACKGROUND

The first possibility, $r_1 \cdot r_2 = 1$, represents an ideal copolymerization, meaning that both propagating species P_1^* or P_2^* have the same preference for adding either monomer. Hence, M_1 and M_2 are incorporated in a statistical arrangement. In the special case where $r_1 = r_2 = 1$, the resulting copolymer is called random or Bernoullian copolymer. If one of the monomers is more reactive than the other towards both macroradicals (i.e. $r_1 > 1$, $r_2 < 1$ or vice versa), the copolymer will contain a larger proportion of the more reactive monomer in random placement.^{20,25} The second case is encountered when $r_1 \cdot r_2 = 0$, characteristic of an alternating copolymer. In this particular case, both of the macroradicals adds preferentially the opposite monomer, generating a regular $\dots M_1 M_2 M_1 M_2 M_1 M_2 \dots$ alternating structure. The behavior of most copolymerizations lies between the extremes of ideal and alternating, with a tendency towards alternation when the product $r_1 \cdot r_2$ approaches from unity to zero.²⁰ The last scenario ($r_1 > 1$, $r_2 > 1$) represents the case of a block copolymer structure. This kind of behavior is rarely encountered in free-radical polymerization.

The terminal model has been extensively applied in copolymerization kinetics during decades. However, the results derived from it fail to completely describe all copolymerization systems.^{27,28} Theoretical studies suggest that the assumptions taken in the terminal model lack of physical meaning,^{27,28} since significant penultimate unit effects are known to operate.^{29,30} Additional effects such as polarity, depropagation, complex formation, and partitioning have also a strong influence in the copolymerization kinetics and should be taken into account.^{27,28} Therefore, alternative theories like explicit and implicit penultimate models, radical and monomer complexes, or the Bootstrap model have been developed. Nevertheless, the terminal model is still adequate for descriptive purposes, since no adjustable parameters are required to fit the experimental data.

2.2. Reversible-Deactivation Radical Polymerization

As described above, the mechanism of free-radical polymerization follows a series of complex elemental steps. The stochastic nature of the individual events taking place simultaneously during FRP affect the structure of the final product. The complexity of the transfer and termination reactions, for example, limit the lifetime of the propagating radicals and cause poor control in the molecular weight distribution and end groups of the obtained polymer, as schematically depicted in Figure 2.2. Transfer to polymer, either intramolecular (back-biting) or intermolecular, induces branching formation, while transfer to solvent or monomer promotes chain-braking and introduces

undesired end groups. Moreover, the possibility of termination via recombination changes drastically the size distribution of the final macromolecule. In the case of copolymerizations carried out by FRP, the lack of the necessary control over the microstructure of the final polymer hinders the production of specific macromolecular architectures.

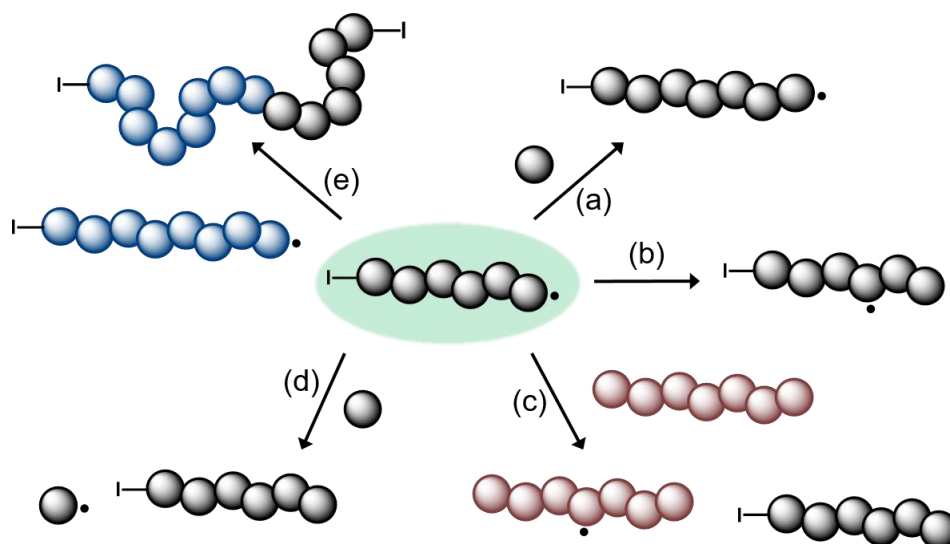


Figure 2.2. During FRP macroradicals propagate (a), but are also susceptible to chain-breaking scenarios such as back-biting transfer (b), intermolecular transfer to polymer (c), transfer to monomer (d), termination by recombination (e), and others. These events heavily influence molecular weight distribution, branching, and end-group fidelity of the final polymer.

In order to overcome these issues, modifications to the conventional radical polymerization procedure have been introduced during the last few decades. Since the late 1990's a boost in academic and industrial research on the so-called reversible-deactivation radical polymerization (RDRP) can be observed. Previously known as “controlled radical polymerization” or “living radical polymerization”, RDRP methods are based on a reversible deactivation of the growing chains. The macroradicals are driven to a dormant state in order to extend the period of chain growth. The rate of chain growth becomes basically the same for all chains, provided that i) initiation is fast and quantitative, ii) the concentration of radicals is low relative to the concentration of chains, and iii) the interconversion between dormant and active states is fast compared to propagation.³¹ It is important to mention that although chain-breaking events like transfer or termination occur considerably less than in FRP, these cannot be completely suppressed by RDRP.

Several different RDRP methods are currently in use, differing in the intrinsic mechanism of activation and deactivation of the propagating radicals. The three most

THEORY AND BACKGROUND

prominent are Nitroxide-Mediated Polymerization (NMP),^{32,33} Atom Transfer Radical Polymerization (ATRP)³⁴ and Reversible Addition-Fragmentation Chain Transfer (RAFT) polymerization.^{19,33} All of these three methods provide access to narrowly-dispersed end-functional linear polymers – as well as more complex architectures like blocks, stars, and others – without compromising the convenience and scope of radical polymerization.

Nitroxides are well known as radical scavenger molecules, due to their stable unpaired electron, delocalized between the nitrogen and oxygen atoms.³⁵ This property allows nitroxides to “trap” carbon-centered radicals by formation of alkoxyamines. In NMP protocols, nitroxides are used to reversibly bind the propagating radical, acting as deactivating groups (Figure 2.3A). Typical values for the deactivation are in the range of $k_{\text{act}}/k_{\text{deact}} \sim 10^{-11}$ M for styrene at 120 °C,³⁶ meaning that the dormant state predominates during the polymerization process. TEMPO (2,2,6,6-tetramethyl-1-piperidynyl-*N*-oxyl) was the first molecule used to mediate the controlled radical polymerization of styrene. Since then, a plethora of nitroxides (some of them exemplified in Figure 2.3B) have been successfully applied in NMP of many different monomers.³⁷

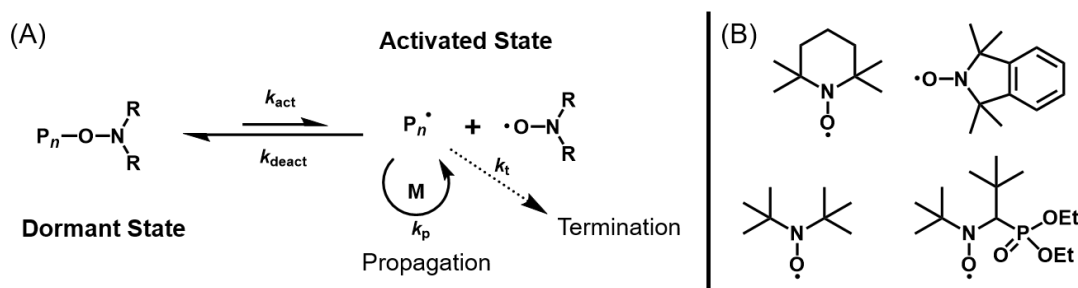
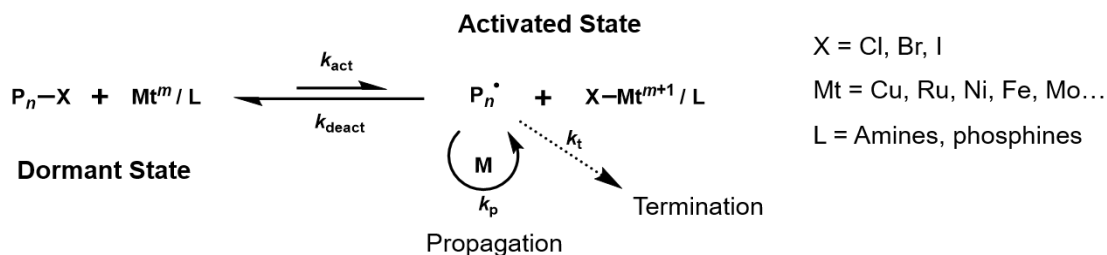


Figure 2.3. (A) Simplified mechanism of nitroxide-mediated polymerization, showing the equilibrium between dormant alkoxyamines and activated propagating radicals. (B) Structures of nitroxides typically employed in NMP.

In atom transfer radical polymerization ATRP, the concentration of radicals is limited by deactivation via reversible atom (Cl, Br, I) or even group (e.g. SCN) transfer, catalyzed by transition metal complexes. The control in the polymerization is achieved by the equilibrium between propagating radicals and the dormant state, normally alkyl halides/macromolecular species.³⁴ As depicted in Scheme 2.3, the dormant species (P_n-X) reacts with the transition metal complex activator (Mt^m/L , where Mt represents the metal center in the lower oxidation state m , and L the ligand). The redox equilibrium generates propagating macroradicals (P_n^\bullet) and halides of the transition metal complex ($X-Mt^{m+1}/L$) in higher oxidation state. ATRP is a catalytic process where the redox pair

THEORY AND BACKGROUND

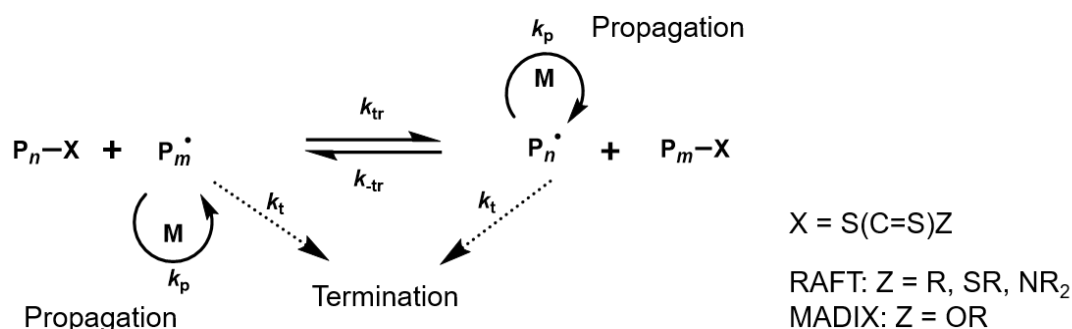
$\text{Cu}^{\text{I}}/\text{L}$ and $\text{X-Cu}^{\text{II}}/\text{L}$ has been the most used system. However, different transition metal complexes, including Ru, Fe, Mo, Os, and others, have found application as catalysts.³⁴



Scheme 2.3. Fundamental mechanism of atom transfer radical polymerization, ATRP.

Compared to NMP, ATRP offers a wider application scope in terms of catalyst and ligand chemistries, monomer classes, temperature ranges and accessible initiators. Such features make ATRP more attractive for the synthesis of new polymeric materials, not to mention its versatility for building complex polymer architectures with high precision. Nonetheless, the use of metal and ligand species limits its widespread industrial application.²¹ Therefore, a great deal of investigation has been devoted to tackle this and other issues to further develop ATRP chemistries. Recent advances encompass the use of activators regenerated by electron transfer (ARGET), initiators for continuous activator regeneration (ICAR), and novel methodologies like photochemical ATRP, metal-free ATRP, electrochemical and mechanochemical ATRP.³⁸

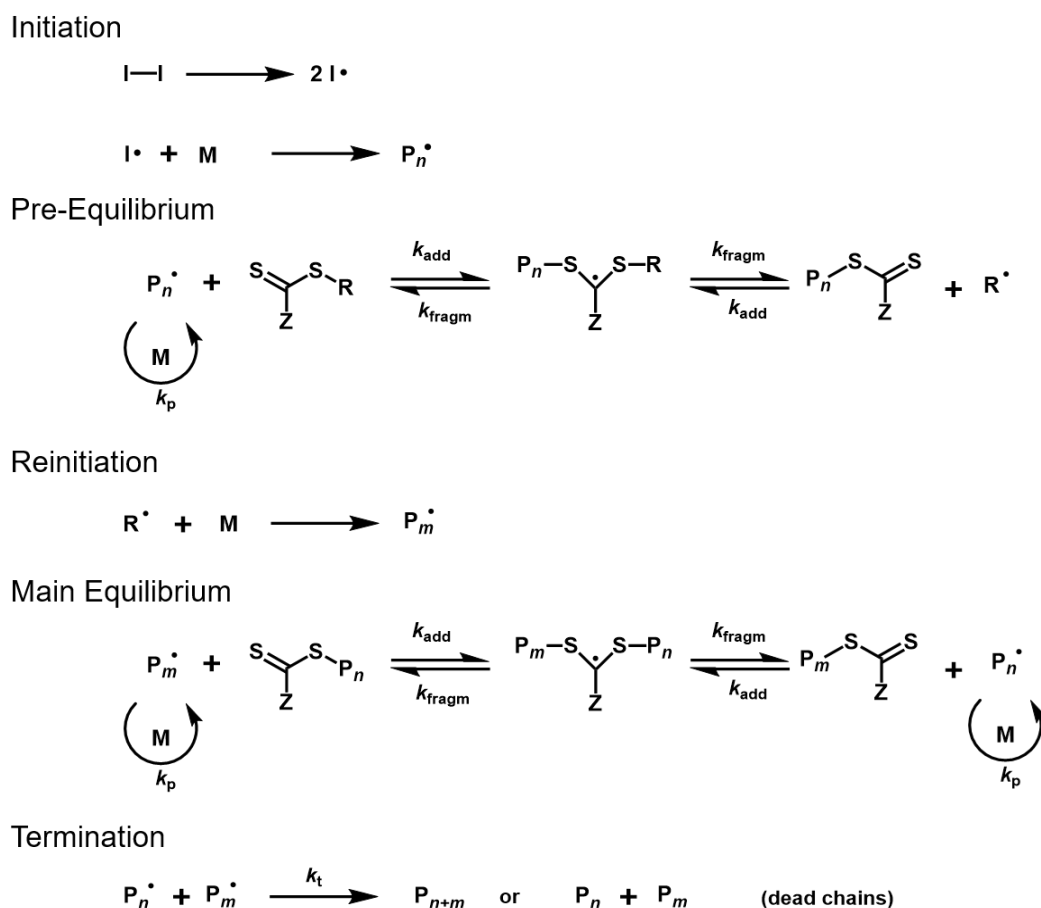
Contrary to NMP and ATRP, in the reversible addition-fragmentation chain transfer (RAFT) polymerization, the deactivation of radicals follows a degenerative transfer mechanism (Scheme 2.4). Here, radical activity is transferred from one polymer chain to another with no net reduction in radical concentration or significant energy variation.³¹



Scheme 2.4. General mechanism of degenerative transfer radical polymerization.

THEORY AND BACKGROUND

RAFT is the most important example of degenerative transfer polymerization, in which dithioesters, xanthates, trithiocarbonates or dithiocarbamates are used as chain transfer agents (CTA). Reactions performed with xanthates are also known as MADIX, macromolecular design by interchange of xanthates.³⁹ The basic components needed for RAFT polymerization are: a source of radicals (initiator), monomer, RAFT agent (CTA) and, sometimes, a solvent. The corresponding mechanism of the RAFT process is shown in Scheme 2.5. The generation, propagation and termination of radicals in the RAFT mechanism does not differ from the conventional free-radical polymerization (refer to Scheme 2.1). Therefore, once the steady state is reached, the presence of a CTA in the polymerization medium does not affect the rate of polymerization, provided that fragmentation and subsequent reinitiation by R^\bullet are not rate determining.⁴⁰



Scheme 2.5. The mechanism of RAFT polymerization consists in five different steps, namely initiation, pre-equilibrium, reinitiation, main equilibrium (degenerative transfer), and termination.

A small amount of radicals (originated from initiator decomposition) are needed to start the process. These initiator radicals generate propagating macroradicals (P_n^\bullet) by successive monomer addition. Eventually the macroradicals undergo addition to the

CTA forming a radical intermediate (stabilized by the Z group), that can fragment back to the original species or release a new radical centered in the leaving group (R•). The judicious choice of the R group is crucial for the success of the RAFT process. R should be stable enough to be released as a radical, but at the same time, reactive enough to effectively reinitiate the polymerization, forming new macroradicals (P_m•). Ideally, the majority of the polymer chains are initiated by the R• radicals. The actual propagation and chain growth takes place in the main equilibrium, i.e. the degenerative transfer stage. In this permanent addition/fragmentation equilibrium, all chains grow steadily at similar rate (given that $k_p < k_{add}/k_{fragm}$). In this step, control over the molecular weight in the polymerization is achieved with some (few) termination events taking place simultaneously, provided that the rate of addition of the propagating radical to the CTA is larger than the rate of termination. It is important to mention that in RAFT polymerization, the number of chains that undergo bimolecular termination directly corresponds to the number of radicals initially introduced in the system.¹⁹ Therefore, the theoretical fraction of living chains L , assuming no side reactions, can be calculated from the following equation

$$L = \frac{[CTA]_0}{[CTA]_0 + 2f[I]_0(1 - e^{-k_d t})\left(1 - \frac{f_c}{2}\right)} \quad (\text{Eq. 2.19})$$

where $[CTA]_0$ and $[I]_0$ are the initial concentrations of RAFT agent and initiator, respectively, f is the initiator efficiency, k_d the initiator decomposition rate coefficient, and f_c the coupling factor ($f_c = 1$ means 100% termination by recombination, $f_c = 0$ means 100% termination by disproportionation).¹⁹

Typically, $L \geq 0.95$ in a well-designed RAFT polymerization experiment.⁴⁰ In this case, the fraction of chains stemming from the initiator is negligible, so $L \sim 1$ by discarding the initiator term in the denominator of Equation 2.19. The actual fraction of living chains can be then estimated by the degree of polymerization and the concentration of CTA⁴⁰

$$L = \frac{(\bar{M}_n - m_{CTA})[CTA]_0}{([M]_0 - [M]_t)m_M} \quad (\text{Eq. 2.20})$$

with \bar{M}_n the number average molecular weight, m_{CTA} the molar mass of the transfer agent, m_M the molar mass of the monomer and $[CTA]_0$, $[M]_0$ and $[M]_t$ the concentrations of transfer agent and monomer at time 0 and time t , respectively. From this equation, the theoretical number average molecular weight of a well-designed RAFT polymerization is obtained ($L \sim 1$):

$$\bar{M}_n = \frac{([M]_0 - [M]_t)m_M}{[CTA]_0} + m_{CTA} \quad (\text{Eq. 2.21})$$

THEORY AND BACKGROUND

The monomer consumption after certain time t can be alternatively described by the fractional monomer conversion p :

$$([M]_0 - [M]_t) = p[M]_0 \quad (\text{Eq. 2.22})$$

Combining Equations 2.21 and 2.22 results in the general expression for the theoretical molecular weight of a RAFT polymerization:

$$\bar{M}_n = \frac{p[M]_0 m_M}{[CTA]_0} + m_{CTA} \quad (\text{Eq. 2.23})$$

Nevertheless, if the fraction of initiator-derived chains is significant, a more general expression for calculating the molecular weight should be used:

$$\bar{M}_n = \frac{p[M]_0 m_M}{[CTA]_0 + 2f[I]_0(1 - e^{-k_d t})\left(1 - \frac{f\epsilon}{2}\right)} + m_{CTA} \quad (\text{Eq. 2.24})$$

From Equation 2.23 it can be inferred that a plot of \bar{M}_n vs. conversion should be linear. A positive deviation from this line indicates incomplete usage of the RAFT agent, a phenomenon also known as hybrid behavior.⁴⁰ The hybrid effect can be originated in a low transfer constant k_{add} to the initial RAFT agent in the pre-equilibrium (see Scheme 2.5), translating in a high initial molecular weight that slowly approaches to the \bar{M}_n calculated by Equation 2.23 as polymerization proceeds. On the other hand, a negative deviation from the values predicted from Equation 2.23 hints to other sources of polymer chains being significant, including initiator-stemming chains (Equation 2.24).⁴¹

RAFT polymerization techniques can be applied to a wide range of monomers. Both “more-activated” monomers (MAMs), including butadiene, styrene, (meth)acrylates, (meth)acrylamides, acrylonitriles, and “less-activated” monomers (LAMs), such as vinyl acetate, *N*-vinylpyrrolidone, and *N*-vinylcarbazole, can be polymerized in a controlled fashion by RAFT protocols, provided that a suitable RAFT agent is chosen. Depending on the monomer class, the choice of the R and Z groups of the RAFT agent becomes crucial: R should be a similar or better leaving group than the propagating radical (e.g. for a tertiary propagating radical, R should be a tertiary leaving group); Z on the other hand should stabilize the radical intermediate just enough that addition is preferred to propagation (to minimize the hybrid effect), but without causing inhibition of the polymerization.⁴⁰ Guidelines of which kind of Z and R groups perform well with the different kinds of monomers abound in the specialized literature.^{19,33,39,41-43} Figure 2.4 shows several Z and R groups commonly employed for RAFT polymerization. For the Z groups displayed, the rate of addition to the RAFT agent decreases from left to right, while the rate of fragmentation increases. For the R

THEORY AND BACKGROUND

groups, both addition and fragmentation rate decreases from left to right, implying that MAMs are better polymerized utilizing Z and R groups placed on the left of the figure, while RAFT agents with Z and R groups located on the figure right side should be chosen for LAMs.

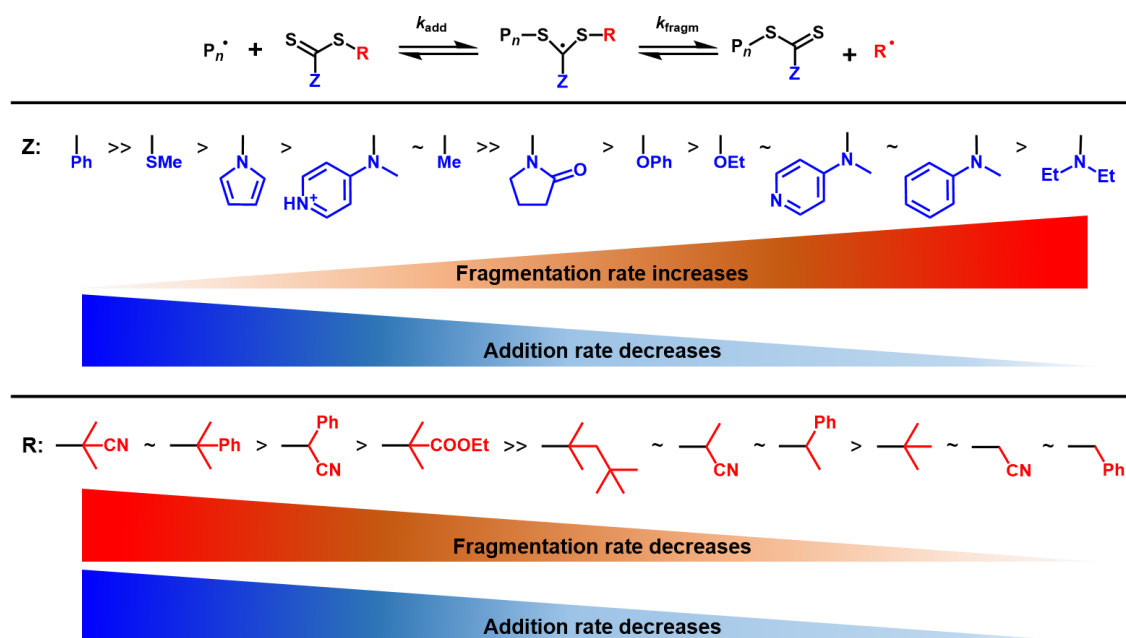
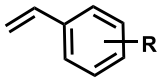
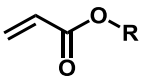
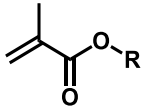
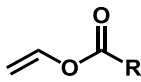
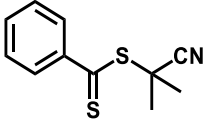
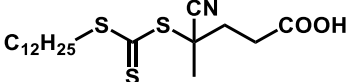
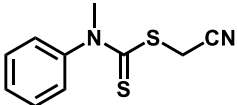
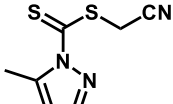
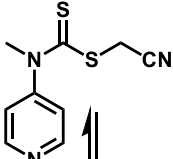
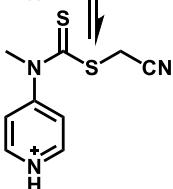


Figure 2.4. Addition and fragmentation reactions in a RAFT polymerization pre-equilibrium, and selection of available Z and R groups. Figure adapted from Ref 42.

A small selection of RAFT agents and their compatibility with the different kinds of monomers^{19,44,45} is summarized in Table 2.1. Dithiobenzoates and trithiocarbonates (first two structures in Table 2.1, respectively) are among the most popular RAFT agents for polymerization of MAMs. Dithiocarbamates on the contrary, are more suited for polymerization of LAMs (third structure in Table 2.1). Recent developments have led to very versatile “universal” RAFT agents (fourth structure in Table 2.1), which perform well in the polymerization of both LAMs and MAMs (except methacrylates).¹⁹ Another approach is the use of “switchable” RAFT agents, for example, the pH responsive *N*-(4-pyridinyl)-dithiocarbamate depicted in the last two entries of Table 2.1. The neutral adduct of this CTA controls well the polymerization of vinyl acetate, and after protonation with *p*-toluenesulfonic acid, excellent control over the polymerization of butyl acrylate was observed.⁴⁴ A more comprehensive list of available RAFT agents, their compatibility with different monomers and synthesis methods can be found in recent reviews.⁴¹⁻⁴³

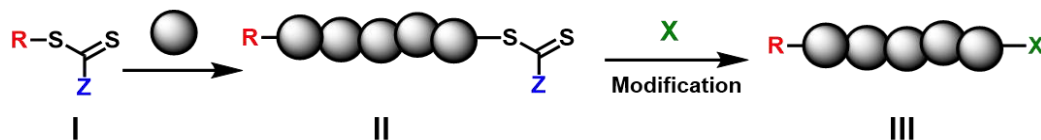
THEORY AND BACKGROUND

Table 2.1. Selection of RAFT agents and their compatibility with different monomer classes. MAMs: styrenes, acrylates, methacrylates; LAMs: vinyl esters. (+: compatible, -: incompatible).

RAFT Agent	MAMs			LAMs
				
	++	+	+++	-
	+++	++	+++	-
	-	-	-	+++
	++	+++	-	++
	-	+	-	+++
	++	+++	+	-

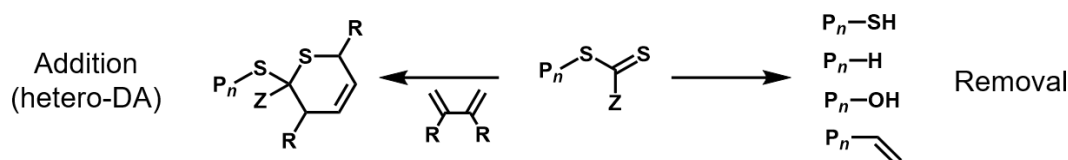
The versatility of the RAFT process is not only exhibited in the polymerization of different monomer classes, the access to complex polymer architectures like blocks, stars, and comb polymers, or the possibility of surface functionalization. RAFT protocols also offer a unique tool for precise polymer functionalization and end-group modification. As schematically depicted in Scheme 2.6, there are three different possibilities to functionalize a polymer via RAFT: introduction of a functional R group, a functional Z group or chemical postmodification of the thiocarbonylthio moiety.⁴⁶ Polymer functionalization via R group is frequently encountered in the literature. Recent examples include functionalization with carboxyl⁴⁷ and hydroxyl groups,⁴⁸ allyl moieties,⁴⁹ alkynes,⁵⁰ azides,⁵¹ pentafluorophenyl esters,⁵² ferrocenyl⁵³ and norbornenyl groups,⁵⁴ tetrazoles and photo-enols,⁵⁵ phenacyl sulfides,⁵⁶ maleimides⁵⁷ and dibromomaleimides,⁵⁸ and several fluorescent markers⁵⁹ such as pyrene, naphthalene, anthracene, phenanthroline, and rhodamine B, among others. Functional groups that

would interfere with the RAFT polymerization like thiols and primary amines, can be present in masked form, i.e. disulfides⁶⁰ for the former, and phthalimides⁶¹ or *tert*-butyl carbamates for the latter.⁶² Many of the functional groups mentioned above can be also introduced by the Z, yielding homo- and heterotelechelic polymers.⁶³



Scheme 2.6. Functionalization approaches of polymers via RAFT. The monomer units are inserted between the R and the thiocarbonylthio groups of the CTA (I), giving an R-group end-functional polymer (II). Eventually, Z can bear also a functional group in (II), or it can be removed via postmodification to afford telechelic polymers (III). Scheme adapted from Ref 46.

On the other hand, the thiocarbonylthio moiety incorporated at the end of the polymer chain can be subjected to various postmodification reactions (refer to Scheme 2.6, structure III). Among the different RAFT end-group transformations reported in the literature, the [4+2] cycloaddition of activated dienes to the thiocarbonylthio group via hetero-Diels–Alder reaction (Scheme 2.7, left), either via thermal^{48,64} or photoinduced^{65,66} protocols can be highlighted. Alternatively, the thiocarbonylthio scaffold can be cleaved and thus transformed to different functional groups (Scheme 2.7, right). For example, the use of strong nucleophiles such as primary amines (aminolysis),⁶⁷⁻⁶⁹ or reducing agents like sodium borohydride,^{70,71} affords thiol end-functional polymers. Radical-induced reduction⁷² or UV photocleavage,⁷³ replace the thiocarbonylthio group with a hydrogen atom. Oxidation with hydrogen peroxide generates hydroxyl-terminated polymers,⁷⁴ and thermolysis under inert atmosphere yields unsaturated terminal groups.^{61,75}



Scheme 2.7. End-group postmodification of RAFT polymers either by [2+4] hetero-Diels–Alder cycloaddition to the thiocarbonylthio group (left), or by its removal via various methodologies (right).

The unique characteristics of RDRP methods (NMP, ARTP, RAFT and others) make them excellent candidates for the production of highly defined specialty polymer-based materials. However, the industrial application of RDRP into commercially

THEORY AND BACKGROUND

available products is currently still quite limited.⁷⁶ Issues such as cost-effectiveness of controlling agents, residual by-products, chemical instability or lack of environmentally-friendly protocols hinder the upscale of RDPD methods from laboratory experiments to large industrial processes.²¹ Nevertheless, emerging technologies including high-throughput combinatorial methodologies⁷⁷ have the potential to accelerate experimental design and characterization methods for the development of future industrially relevant RDRP products.

2.3. Chain-Addition vs. Step-Growth Polymerization

In Section 2.1 the fundamentals of free-radical polymerization were described. FRP belongs to the group of chain-addition polymerizations, in which propagating species with a reactive center (radical, cation or anion) add successively monomer units in a chain reaction (refer to Scheme 2.1). Contrarily, step-growth polymerizations – sometimes also called polycondensations – do not present a reactive propagating center. In step-growth polymers, macromolecular formation is achieved by stepwise reaction of complementary functional groups present in the monomers, i.e. monomers react with each other to form dimers, then trimers, tetramers, etc., until high molecular weight polymers are obtained near the end of the process (Figure 2.5).

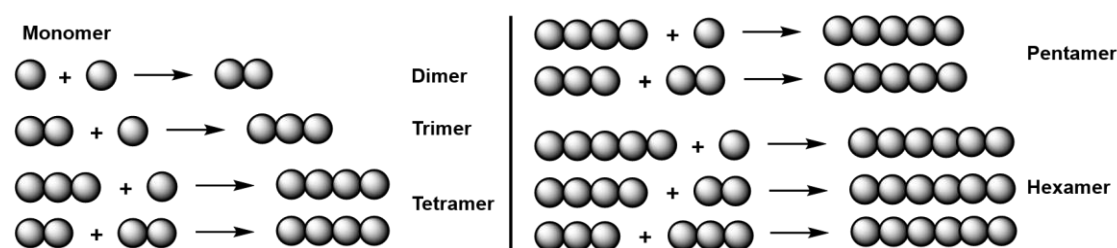


Figure 2.5. Stepwise growing of monomers into dimers, trimers, tetramers... characteristic of polycondensations.

The kinetics of polymerization of a step-growth process is substantially different from the kinetics of chain-addition mechanisms. In radical polymerization, propagation constants are high – $k_p \approx 10^2\text{--}10^4 \text{ M}^{-1}\cdot\text{s}^{-1}$, depending on the monomer²³ – and, as already mentioned, k_p is independent of monomer conversion (up to $p \leq 80\%$ where it becomes diffusion controlled). As a consequence, very rapid chain growth and relatively constant degree of polymerization is observed, depending only on the rate of polymerization and the rate of chain-stopping events (refer to Equation 2.8). For living polymerizations, i.e. when termination events are suppressed, there is a linear increase

in the molecular weight of the polymer with increasing monomer conversion (e.g. Equation 2.23). A very different situation is encountered in step-growth polymerizations, where monomer disappears faster and molecular weight increases throughout the course of the reaction (Figure 2.6). Hence, high molecular weight polymer is only obtained at very high conversions ($p > 98\%$).²⁰

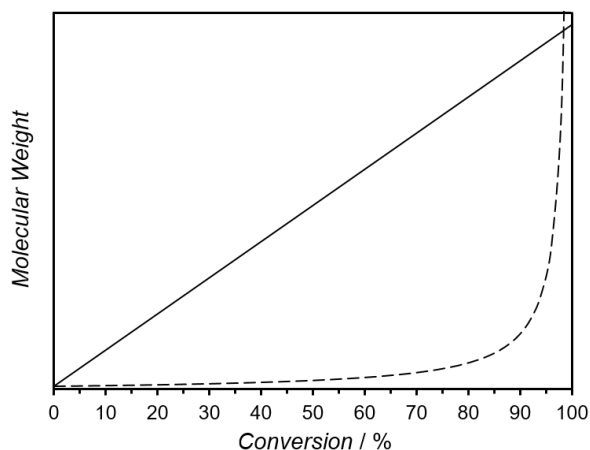
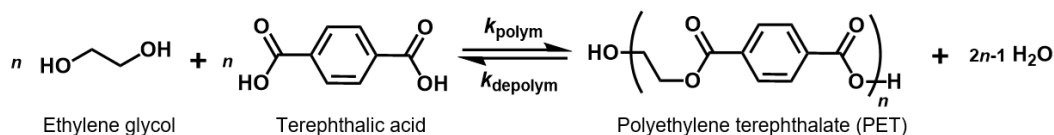


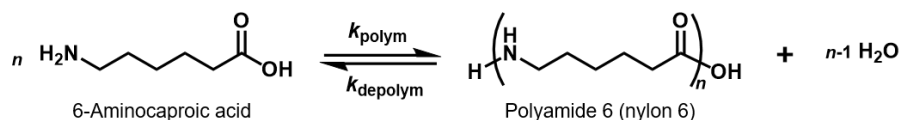
Figure 2.6. Comparison of molecular weight evolution in living (or controlled) chain-addition polymerization (solid line), and step-growth polymerization (dashed line).

Step-growth polymerizations can be classified in two different groups, depending on the monomer functionality. The reaction can take place between two monomers with complementary functional groups (AA–BB monomers), or both functional groups can be present in the same molecule (AB monomers). Examples of noteworthy step polymers within these two classes are depicted in Scheme 2.8. It is important to mention that condensation reactions are in equilibrium with their respective hydrolysis products. Therefore, to push the equilibrium to high conversions, the removal of the small molecules produced (normally water or alcohols) is necessary.

I. AA–BB monomers



II. AB monomers



Scheme 2.8. Step-growth polymerization of (I) AA–BB monomers, in this case a diol and a diacid to produce a polyester, and (II) AB monomers, here an amino acid that forms a polyamide (nylon).

THEORY AND BACKGROUND

The original investigations on step-growth polymerizations were led by Wallace Carothers, who first derived the relationship between degree of polymerization and extent of the reaction (conversion) in polycondensations.⁷⁸ The degree of polymerization DP_n in step polymers can be defined as the initial number of monomers N_0 divided the total number of molecules present after certain reaction time N_t :

$$DP_n = \frac{N_0}{N_t} = \frac{[M]_0}{[M]_t} \quad (\text{Eq. 2.25})$$

By rearranging Equation 2.22 and substituting it in Equation 2.25, the well-known Carothers relationship is obtained (Equation 2.26). Here p is the fractional monomer conversion, i.e. the fraction of functional groups that have reacted at time t :

$$DP_n = \frac{1}{1-p} \quad (\text{Eq. 2.26})$$

If we consider the condensation of AB monomers,



then the fraction of A (or B) groups that have reacted to form an n -mer is p^{n-1} , and the fraction of unreacted A (or B) groups is $1-p$. Thus the molar fraction of n -meres x_n present at time t would be:

$$x_n = \frac{N_n}{N_t} = (1-p)p^{n-1} \quad (\text{Eq. 2.28})$$

From Equations 2.25 and 2.26 it follows that $N_t = N_0(1-p)$, hence:

$$N_n = N_t(1-p)p^{n-1} = N_0(1-p)^2p^{n-1} \quad (\text{Eq. 2.29})$$

The weight fraction of n -meres present at time t (the weight of all n -meres divided by the weight of all units) is defined as,

$$w_n = \frac{nN_n m_0}{N_0 m_0} \quad (\text{Eq. 2.30})$$

where m_0 represents the mass of one monomer unit. Substitution of Equation 2.29 in Equation 2.30 gives the weight fraction distribution:

$$w_n = n(1-p)^2p^{n-1} \quad (\text{Eq. 2.31})$$

An alternative definition of the degree of polymerization can be thus derived from Equation 2.28, as the sum of all molar fractions times n :

$$DP_n = \sum_n n x_n = \sum_n n p^{n-1} (1-p) \quad (\text{Eq. 2.32})$$

Using the series convergence for $p < 1$,

$$\sum_n n p^{n-1} = \frac{1}{(1-p)^2} \quad (\text{Eq. 2.33})$$

we arrive to the Carothers relationship (Equation 2.26). In a similar way, the sum of all n -mere weight fractions (Equation 2.31) gives the weight degree of polymerization:

$$DP_w = \sum_n n w_n = \sum_n n^2 p^{n-1} (1-p)^2 \quad (\text{Eq. 2.34})$$

For which the following convergent series can be used,

$$\sum_n n^2 p^{n-1} = \frac{(1+p)}{(1-p)^3} \quad (\text{Eq. 2.35})$$

thus,

$$DP_w = \frac{(1+p)}{(1-p)} \quad (\text{Eq. 2.36})$$

Using Equations 2.26 and 2.36 the expressions for number average molecular weight, \bar{M}_n , and weight average molecular weight, \bar{M}_w , in step-growth polymerizations are obtained (m_0 mass of monomer):

$$\bar{M}_n = m_0 \frac{1}{(1-p)} \quad \bar{M}_w = m_0 \frac{(1+p)}{(1-p)} \quad (\text{Eq. 2.37})$$

The previous equations also hold true for AA–BB monomers, taking into account that the molecular weight of the repetition unit is the mean of the molar mass of both components,

$$m_0 = \frac{m_{AA} + m_{BB}}{2} \quad (\text{Eq. 2.38})$$

and that a perfect stoichiometry between A and B units must exist. In the case of a non-stoichiometric mixture of functional groups, an imbalance parameter r is introduced (ratio AA/BB),²⁰ which is always equal or less than unity:

$$DP_n = \frac{1+r}{1+r-2rp} \quad (\text{Eq. 2.39})$$

For a perfect stoichiometric ratio between AA and BB, $r = 1$ and Equation 2.39 reduces to the normal Carothers relationship.

For radical polymerizations (chain-addition mechanism) at low conversion, with termination events by disproportionation or chain transfer (no recombination), the expressions for number- and weight-fractions, N_n and w_n respectively, are the same as for step-growth polymerization (Equations 2.29 and 2.31). The same equivalence is encountered for the number- and weight-average degree of polymerization (Equations 2.26 and 2.36), except that in radical polymerization the conversion is defined as the probability that a radical active center continues propagation instead of termination.²⁰

$$p = \frac{R_p}{R_p + R_t + R_{tr}} \quad (\text{Eq. 2.40})$$

THEORY AND BACKGROUND

Conversely, if termination by recombination is predominant and no transfer reactions take place, then the following equations apply:

$$N_n = (n - 1)(1 - p)^2 p^{n-2} \quad (\text{Eq. 2.41})$$

$$w_n = \frac{1}{2} n(1 - p)^3 (n - 1) p^{n-2} \quad (\text{Eq. 2.42})$$

$$DP_n = \frac{2}{1-p} \quad DP_w = \frac{(2+p)}{(1-p)} \quad (\text{Eq. 2.43})$$

For both chain-addition and step-growth polymerizations, the broadness of the molecular weight distribution is defined by the ratio DP_w/DP_n , commonly known as dispersity index (\mathcal{D})

$$\mathcal{D}_X = \frac{DP_w}{DP_n} \quad \mathcal{D}_M = \frac{\bar{M}_w}{\bar{M}_n} \quad (\text{Eq. 2.44})$$

(in most of the cases $\mathcal{D}_X = \mathcal{D}_M$). A perfectly narrow molecular weight distribution is characterized by $\mathcal{D} = 1$. From Equation 2.37 it follows that:

$$\mathcal{D} = \frac{\bar{M}_w}{\bar{M}_n} = 1 + p \quad (\text{Eq. 2.45})$$

Therefore, for step-growth polymers the breadth of the size distribution increases with conversion until the limiting value of $\mathcal{D} = 2$ (for $p = 1$). Contrarily, radical chain polymerizations at high conversions exhibit broad distributions (dispersity values of 2–5), and even broader if branching by transfer to polymer takes place ($\mathcal{D} = 20\text{--}50$).²⁰ A different situation arises in living polymerizations and RDRP protocols, where \mathcal{D} values are typically very close to unity.

2.4. Photochemistry

Photochemical transformations have been happening on Earth since its very beginnings, when electromagnetic radiation from the early Sun was the only available source of energy.⁷⁹ Solar radiant energy is of utmost importance for life on Earth, since it initiates and regulates various photobiological phenomena such as photosynthesis, phototaxis, photomorphogenesis, visual phototransduction, mutagenic response, etc.⁸⁰ Furthermore, photochemical reactions play nowadays a prominent role in the development of novel responsive materials for state-of-the-art technological applications.^{17,81-83} However, photochemistry developed relatively recently as a branch of science. Its systematic study flourished in the nineteenth century after the pioneering work of H. Trommsdorff on the photochemistry of Santonin (a sesquiterpene lactone), followed up by the Italian chemists Sestini and Canizzaro.⁸⁴ The latter introduced light-

induced reactions to G. Ciamician and P. Silber, who in the early 1900's conducted a great body of photochemical work, essentially initiating the modern investigation of organic photochemistry.^{85,86} At the same time, the physical foundations of the interaction of light and matter were laid by the revolutionary theories of J. Maxwell, M. Planck, and A. Einstein. Maxwell's theory of electromagnetism⁸⁷ of 1865 states that light travels in space as an oscillating electric field (wave). Later in 1901 Planck postulates the quantization of energy,⁸⁸ from which Einstein deduced the particle nature of light.^{89,90}

2.4.1. Fundamentals

In the modern sense, photochemistry comprises such reactions initiated by electronically excited molecules.⁹¹ In other words, a chemical transformation is provoked by the electronic excitation of a molecule, due to photon absorption. The rate of light absorption is given by the Lambert-Beer law,

$$A = \log_{10} \frac{I_0}{I} = \varepsilon_\nu C d \quad (\text{Eq. 2.46})$$

where I_0 and I represent the incident and transmitted light intensities, respectively, ε_ν is the molar extinction coefficient (as function of frequency ν), C is the concentration of the sample, and d the optical path length. The logarithm of I_0/I is commonly known as absorbance A . Alternatively, the Lambert-Beer law can be expressed in terms of the transmittance T :

$$T = 10^{-A} = 10^{-\varepsilon_\nu C d} \quad (\text{Eq. 2.47})$$

However, molecules possess discrete electronic configurations, dictated by the atomic energy quantization. Thus, a molecule can only absorb photons with specific energies (frequencies), determined by the Bohr's relation,

$$\Delta E = h\nu \quad (\text{Eq. 2.48})$$

with Planck's constant $h = 6.626 \times 10^{-34}$ J·s. Light absorption is then restricted to the energy difference between the ground state of a molecule (lowest energy level) and any of its excited (higher) states.

Additionally, the atoms in a molecule have several vibrational and rotational modes whose energy is also quantized. Nevertheless, electronic excitation occurs on shorter time-scales as molecular vibration.⁹² The Franck-Codon approximation states that electronic transitions take place without change in the positions of the nuclei within the molecule. Hence, a transition to the most probable electronic-vibrational level combination is not far from the pure electronic transition. On the other hand, the

THEORY AND BACKGROUND

electronic excitation energies in a molecule can be estimated from its molecular orbitals (MOs), obtained from a linear combination of the atomic orbitals (AOs) of the constituent atoms.⁹¹ Depending on the in-phase and out-of-phase combination of the AOs, the resulting MOs are governed by their symmetry (σ or π) and their nodal properties (bonding or antibonding, the latter denoted by an asterisk). Some molecules present also non-bonding (n) orbitals which are normally pure atomic orbitals not taking part in the construction of MOs. Electronic transitions are then possible between the different MOs, provided that photons of sufficient energy are absorbed (Figure 2.7). For instance, $\sigma \rightarrow \sigma^*$ transitions require more energy than $\pi \rightarrow \pi^*$ (or $n \rightarrow \pi^*$) transitions, the former appearing in the far UV region and the latter in the visible range.

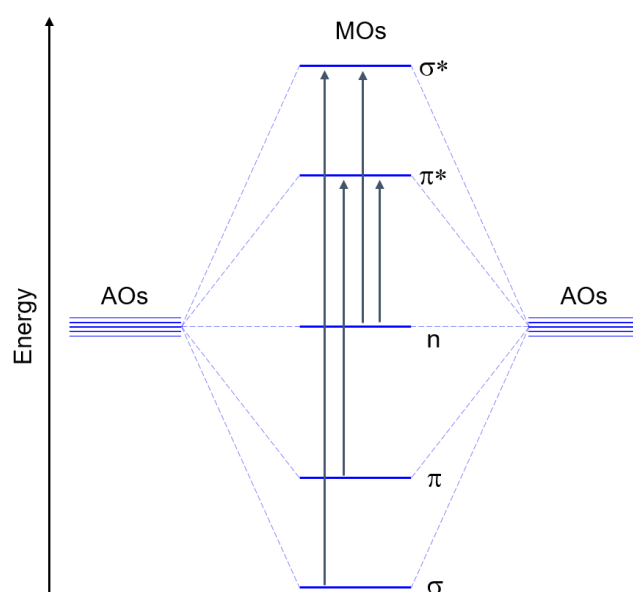


Figure 2.7. Combination of atomic orbitals (AOs) to form bonding (σ , π) and antibonding (π^* , σ^*) molecular orbitals (MOs), as well as non-bonding (n) orbitals. The possible electronic transitions are shown as vertical arrows and can be classified with the labels of the involved orbitals (e.g. $\sigma \rightarrow \sigma^*$ or $n \rightarrow \pi^*$ transitions). Figure adapted from Ref 91.

When no details on the symmetry properties is known or needed, it is useful to represent the electronic states in terms of their multiplicity. There exist Singlet (S) and Triplet (T) states, labeled with increasing cardinal numbers from the ground state (S_0) to the different excited states (S_1 , S_2 , S_3 ... T_1 , T_2 ...). Due to electron pairing in the bonding MOs of the ground state, only one singlet state is possible (S_0). Upon excitation, this restriction does not apply anymore and it is possible to have both singlet (spin paired) and triplet (spin parallel) states.⁹¹ A schematic representation of the energy organization of the different states was proposed by A. Jablonski,⁹³ where

singlet levels are depicted as horizontal lines in order of increasing energy, and triplet levels are shifted in space but maintaining the same energy organization. An energy reference value of zero is assigned to the ground state S_0 . The vibrational states corresponding to each electronic state are depicted as thin horizontal lines. This visual representation of the energy states is called Jablonski diagram (Figure 2.8).

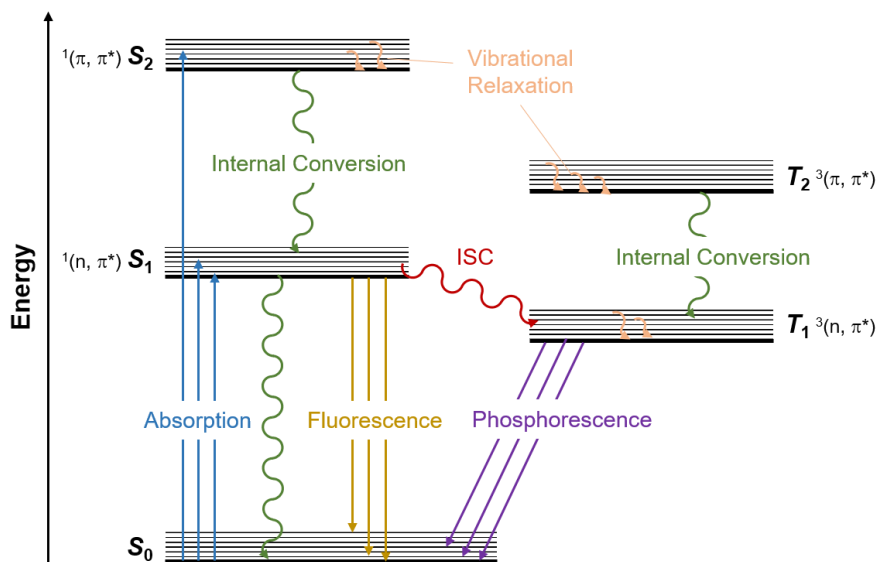


Figure 2.8. Jablonski diagram displaying singlet ground (S_0) and singlet or triplet excited (S_1 , S_2 , T_1 , T_2) electronic states, with their respective vibrational states. Different radiative (straight arrows) or non-radiative (wavy arrows) photophysical processes can take place upon photon absorption. Figure adapted from Ref 92.

Once a molecule is excited to a higher electronic state it will eventually relax back to the ground state. There are several photophysical pathways in which the excess of energy can be released, depending on both the intrinsic properties of the molecule and external interaction with other species. Two classes of processes can be distinguished, involving either release of radiation (straight arrows in the Jablonski diagram), or heat (wavy arrows). The last class is also known as non-radiative transitions, which might involve vibrational relaxation from higher vibrational levels, or internal conversion of electronic energy into lower levels of vibrational energy of the same multiplicity (see Figure 2.8). A non-radiative transition from a singlet (S_1) to a triplet (T_1) state is termed intersystem crossing (ISC). On the other hand, there exist radiative transitions either from the singlet excited state to the ground state ($S_1 \rightarrow S_0$) termed fluorescence, or from the triplet to the ground state ($T_1 \rightarrow S_0$) called phosphorescence (feasible only after ISC). However, phosphorescence is a spin-restricted process, appearing as a delayed emission. Under certain conditions, a molecule in the T_1 state can be excited to higher

THEORY AND BACKGROUND

triplet states by absorption of certain radiation, in a process named triplet–triplet absorption, from which the system relaxes back to T_1 via internal conversion.⁹¹ Bimolecular collisions with other molecules can also cause non-radiative relaxation, competing with fluorescence transitions, what is commonly known as quenching. Electronic energy transfer (Equation 2.49) is another bimolecular deactivation process, in which a molecule in an excited state (energy donor) transfer its energy radiationless to a different molecule (energy acceptor), either via singlet–singlet or triplet–triplet transfer:



The energy acceptor can then undergo various photophysical and photochemical processes, depending on its particular electronic characteristics.

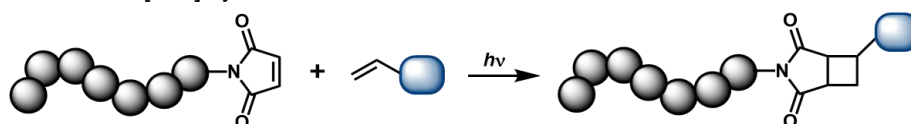
The photochemical properties of a molecule depend on the different radiative and non-radiative relaxation pathways it can undergo upon excitation. After photon absorption, the excess of energy can dissipate in form of radiation or heat instead of triggering a photochemical reaction, diminishing its quantum yield. In addition, the reactivity of an excited molecule might be very different whether it is in the singlet or the triplet state. Therefore, a clear knowledge of the photophysical processes that an excited molecule can experience is important to understand a particular photochemical reaction. In general, photoreactions can be unimolecular (involving only the excited molecule, e.g. dissociation, isomerization) or bimolecular, where a second reaction partner (usually unexcited) is required.⁹¹

2.4.2. Photochemical Polymer Modification

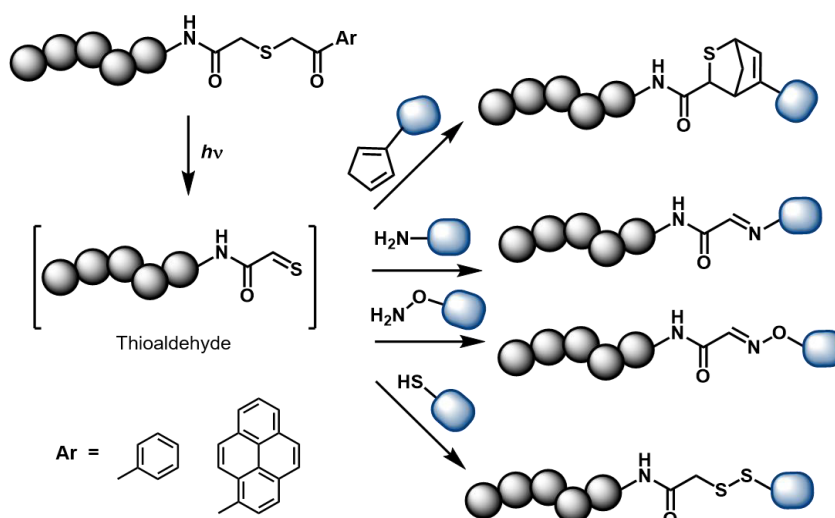
The variety of uni- and bimolecular reactions carried out photochemically is manifold. Some examples include dissociations, isomerizations and rearrangements, photoredox processes, photodimerizations, cycloadditions, chemiluminescence, etc. In the field of polymer chemistry, photoreactions are often encountered in photoinitiating systems,⁹⁴⁻⁹⁶ as external stimulus to initiate or facilitate RDRP processes,⁹⁷ and in various methodologies for polymer functionalization, degradation or polymer–polymer ligation.⁹⁸ Several application fields profit from the benefits of photochemical reactions in polymer science. For example, well-established technologies such as electrical and optical materials, dental fillings, membranes, adhesives, and coatings,⁹⁹ as well as emerging applications such as direct laser writing (DLW),¹⁰⁰⁻¹⁰² surface patterning,¹⁰³⁻¹⁰⁶ or tissue engineering,¹⁰⁷⁻¹⁰⁹ are inconceivable without the use of photopolymerization or photoconjugation approaches. Recent examples of photochemical modification of polymers encompass photoinitiated radical thiol-ene reactions,^{102,110,111} photoinduced

[2+2] cycloaddition (including alkene-enone conjugation,¹¹² Paterno–Büchi reaction,¹¹³ photodimerization of coumarin¹¹⁴ or styrylpyrene^{115,116} derivatives), [4+4] anthracene dimerization,^{104,117} nucleophilic addition^{118,119} or [4+2] hetero-Diels–Alder reaction^{56,118} on photogenerated thioaldehydes, [4+2] Diels–Alder reaction on photocaged dienes (photo-enol),¹²⁰⁻¹²² and 1,3-dipolar cycloaddition on photoactivated azirines,¹²³ among other strategies (see Scheme 2.9).

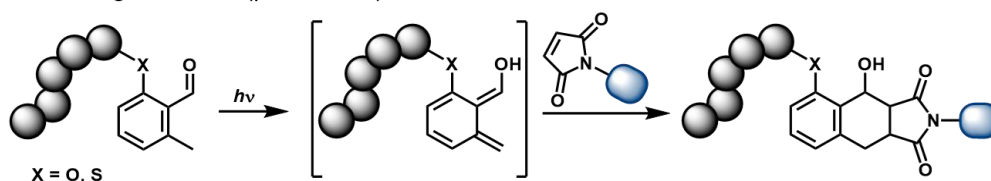
Alkene-enone [2+2] cycloaddition



Phenacyl and pyrenacyl sulfide



Photocaged dienes (photo-enol)

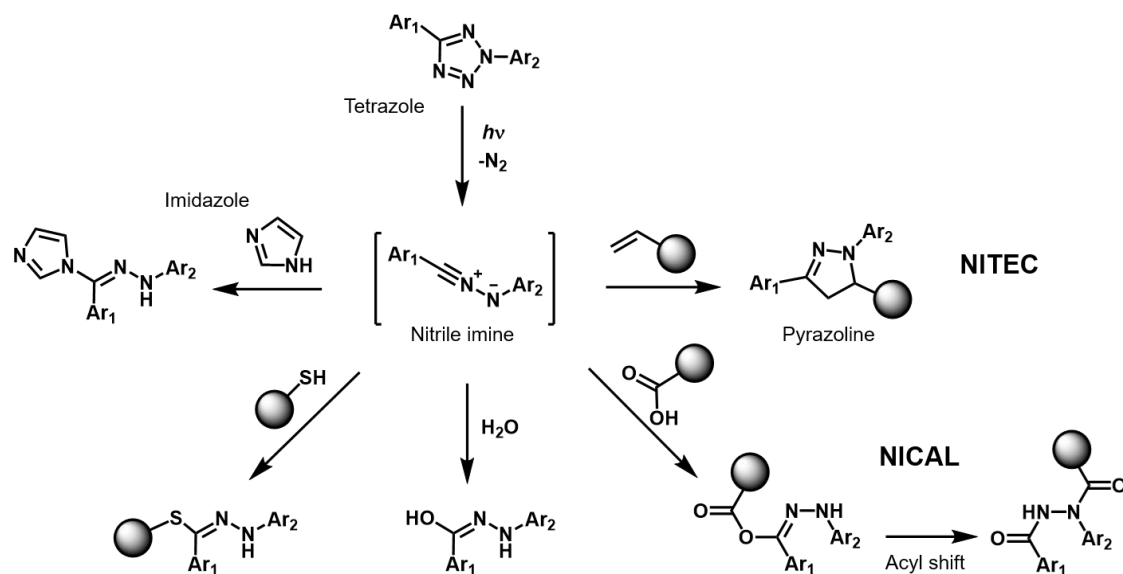


Scheme 2.9. Selection of photoreactions currently used in polymer modification: UV-induced alkene-enone [2+2] cycloaddition¹¹² (UV light), photogeneration of thioaldehydes from phenacyl¹¹⁹ (UV light) or pyrenacyl¹¹⁸ (visible light) sulfides, and Diels–Alder [4+2] cycloaddition of photo-enols¹²⁰⁻¹²² (UV light X = O, visible light X = S).

Another important class of photoreactive moieties are aryltetrazoles. As originally reported by Huisgen,¹²⁴ tetrazoles decompose upon irradiation (nitrogen gas is released),^{125,126} generating a very reactive nitrile imine dipole.¹²⁷ Once formed, this reactive intermediate readily undergoes 1,3-dipolar cycloaddition with activated alkene dipolarophiles,¹²⁸ yielding a fluorescent five-member pyrazoline ring (see

THEORY AND BACKGROUND

Scheme 2.10). hence, this photoinitiated 1,3-dipolar reaction has been coined as nitrile imine-mediated tetrazole-ene cycloaddition (NITEC). The pro-fluorescent characteristics of the NITEC reaction, along with the relatively mild conditions required and high yields obtained, positioned it as a very convenient strategy for bio-conjugation and labeling.¹²⁹⁻¹³¹ Furthermore, its potential for polymer modification¹³²⁻¹³⁶ and functionalization of surfaces or materials¹³⁷⁻¹⁴³ has been developed within the group of Barner-Kowollik in the last few years.



Scheme 2.10. Light-induced degradation of diaryltetrazoles yields a nitrile imine intermediate, which readily reacts with activated alkenes (NITEC), carboxylic acids (NICAL), water, thiols, and imidazole.

Initially, the NITEC process was regarded as a bio-orthogonal reaction by Lin and co-workers.^{130,131,144} Nevertheless, the nitrile imine intermediate was later found to be susceptible to nucleophilic attack (see Scheme 2.10). A variety of nucleophiles have been reported to react with nitrile imines including thiols,^{145,146} water,^{144,147} imidazole,¹⁴⁷ and carboxylic acids.¹⁴⁸ The conjugation with carboxylic acids, also called nitrile imine-mediated carboxylic acid ligation (NICAL), has been recently used by Barner-Kowollik and coworkers as a strategy for polymer chain folding^{149,150} and synthesis of photoreactive polymer nanoparticles.¹⁵¹

Importantly, the photochemical behavior of the tetrazole is strongly influenced by its aryl substituents (Ar₁ and Ar₂ in Scheme 2.10). Variation of the *N*-substituent Ar₂ specially affects the wavelength range in which the nitrile imine formation takes place (Figure 2.9). An unsubstituted phenyl ring in Ar₂ requires UV light (250–300 nm) for the tetrazole activation.^{128,132} Substitution of the phenyl ring with a methoxy substituent in *para* position shifts the activation wavelength to 320 nm,¹³³⁻¹³⁵ while a *p*-dimethylamino

THEORY AND BACKGROUND

group allows activation at 365 nm.^{152,153} Similarly, naphthalene and coumarin tetrazole derivatives can be also activated at 365 nm.¹⁵⁴ Further conjugation of the aromatic system in Ar₂ red-shifts the activation wavelength, thus a terthiophene-substituted tetrazole (Ar₁ = 2-thiophenyl) requires light of 405 nm for activation¹⁵⁵ and pyrene-tetrazole species can react at visible light (410–420 nm).^{136,156} Nonetheless, sole extension of the conjugated system does not ensure a red-shift of the activation wavelength, as reported for biphenyl,¹⁵⁶ styryl,¹⁵² aryl-1,3-butadiene and aryl-acetylene derivatives.¹⁵⁴ Theoretical calculations on the NITEC system reveal that λ -dependent reactivity patterns does not necessarily follow the maximum absorption wavelength.¹⁵⁶

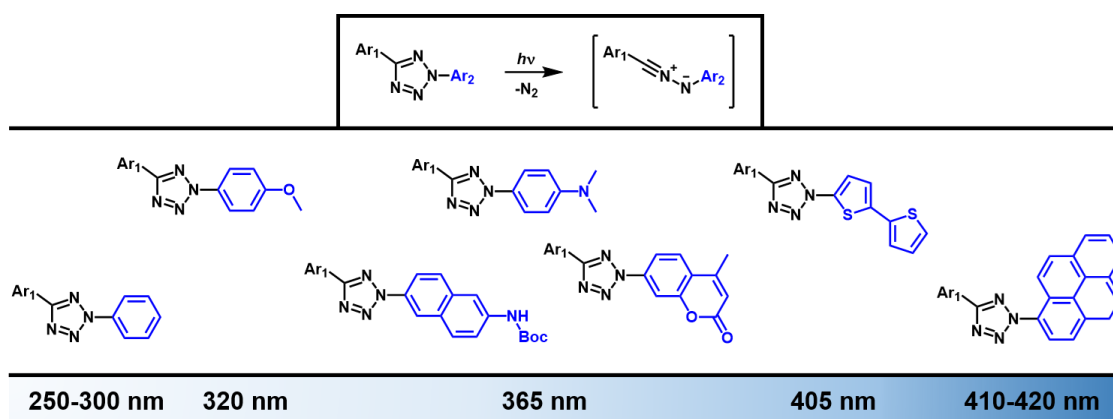


Figure 2.9. *N*-Substitution of aryltetrazoles changes the activation wavelength necessary for nitrile imine formation.

In this respect, Barner-Kowollik and coworkers have pioneered the use of tunable laser technologies for the quantitative analysis of photoreactivity patterns in a wavelength-dependent fashion.^{115,116,157-159} By plotting photoreaction yields vs. irradiation wavelength (at constant photon count) the so-called action plots are obtained, from which information on the ideal trigger wavelength for a given photochemical process can be retrieved. Hence, using action plot technology it has been demonstrated that maximum conversion is not achieved at the maximum absorption wavelength of the starting material, as reported for the NITEC reaction¹⁵⁹ and other photoinitiated processes ([2+2] cycloadditions,^{115,116} dissociation of radical photoinitiators^{157,158}). Furthermore, DFT calculations revealed that adequate photoactivation of the aryltetrazole and subsequent nitrile imine formation requires a fast ISC (refer to Figure 2.8), favored when the energy gap between the excited single state S₁ and a triplet state is low.^{156,159}

As a final remark, the gap between the activation wavelengths of the different structures can be exploited as a method for independently trigger NITEC reactions in a

THEORY AND BACKGROUND

λ -orthogonal fashion. For example, the one pot reaction of *p*-methoxyphenyl and pyrene tetrazoles (refer to Figure 2.9) with alkenes, can be orthogonally addressed by irradiation with UV (320 nm) and blue (410–420 nm) light, respectively.¹⁶⁰ The same principle has been applied for other λ -orthogonal systems, for example photo-enol vs. tetrazole ligation¹⁶¹⁻¹⁶³ or thiol-ene vs. NITEC reaction.¹⁶⁴

2.5. Polymer Networks

The term macromolecular architecture is used to describe the potential structural variety in polymer systems, deviating from continuous linear strands. Depending on their basic chain connectivity, polymers can be classified in linear, branched, cyclic, and crosslinked architectures, and combinations thereof (Figure 2.10). Indeed, these different topologies provide access to unprecedented properties and functions,¹⁶⁵ necessary for the development of new polymeric materials.

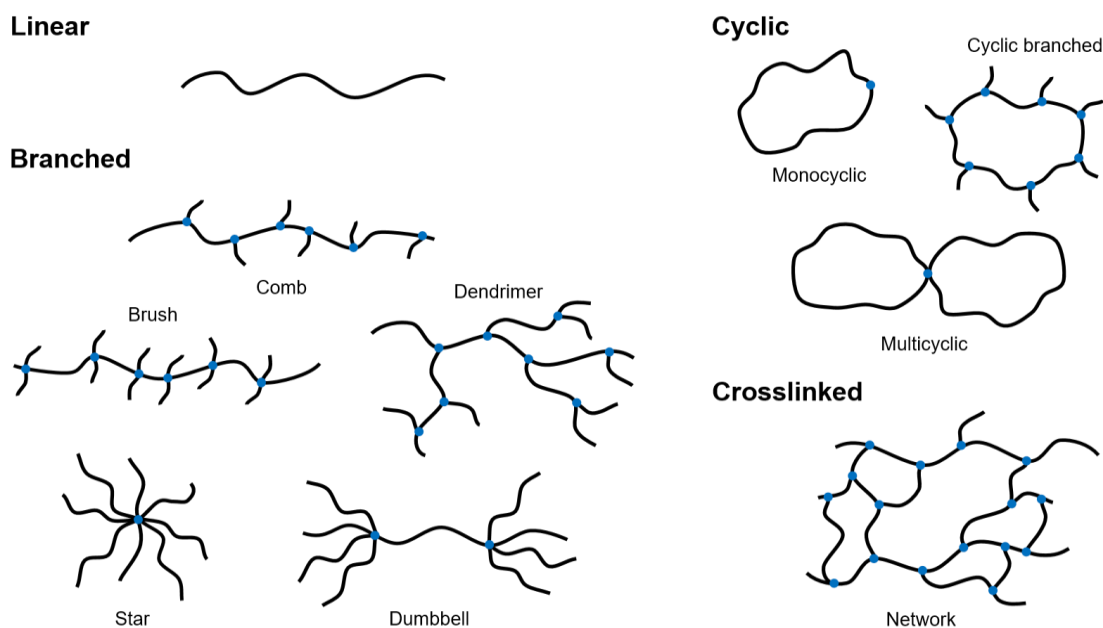


Figure 2.10. Structural representation of some polymer architectures. Depending on the connectivity of the constituting chains, polymers can be classified as linear, branched, cyclic or crosslinked topologies.

In crosslinked architectures, different polymer chains are bound one to another forming a single three-dimensional macromolecular entity called network. According to the IUPAC definition,¹⁶⁶ a network is a “highly ramified structure in which essentially each constitutional unit is connected to each other constitutional unit and to the macroscopic phase boundary by many paths through the structure”. A swollen network,

i.e. a network in which the whole volume between the crosslinked chains is expanded by a fluid, is known as gel.¹⁶⁶ In the next sections the fundamentals of polymer networks, their synthesis, characterization methods, and selected applications are reviewed.

2.5.1. Fundamentals

As stated above, polymer networks are three-dimensional structures consisting of crosslinked chains. This particular characteristic distinguishes networks from other macromolecular architectures, giving them unique rubberlike properties, such as elastic deformation and resistance to dissolution.¹⁶⁷ Solvent molecules penetrate and occupy the spaces between the joint strands, causing swelling of the structure. Therefore, a gel can be considered as a combination of a solid-like and a liquid-like material.

Several models have been proposed for the statistical understanding of the mechanical behavior of swollen networks, yielding expressions for the relationship between structure and elastic properties. The principal structural parameter of a network that influences its mechanical behavior is the number of crosslinks or junctions interconnecting the chains. In an elastically active junction of functionality f , three or more chains emerge ($f \geq 3$) which, ideally, end in another active junction. Such chains are hence called elastically active chains. With these definitions, the degree of crosslinking of a network can be understood as the concentration of elastically active chains ν_c (Equation 2.50), the mean molecular weight M_c of the active chains between each junction (Equation 2.51), the crosslinking density μ_c , i.e. the amount of crosslinks per unit volume (Equation 2.52), or the cycle rank density ξ_c (Equation 2.53), defined as the number of independent circuits in the system¹⁶⁷ (Figure 2.11).

$$\nu_c = \frac{\nu_{el}}{V_0} \quad (\text{Eq. 2.50})$$

$$M_c = \rho \frac{V_0 N_A}{\nu_{el}} \quad (\text{Eq. 2.51})$$

$$\mu_c = \frac{\mu_{el}}{V_0} \quad (\text{Eq. 2.52})$$

$$\xi_c = \frac{\xi}{V_0} \quad (\text{Eq. 2.53})$$

$$\xi = \nu_{el} - \mu_{el} + 1 \quad (\text{Eq. 2.54})$$

Here ν_{el} represents the number of elastically active chains, V_0 the volume of the dry network, ρ is the density of the polymer, N_A the Avogadro's constant, μ_{el} the number of active junctions (crosslinks), and ξ the cycle rank (Equation 2.54).

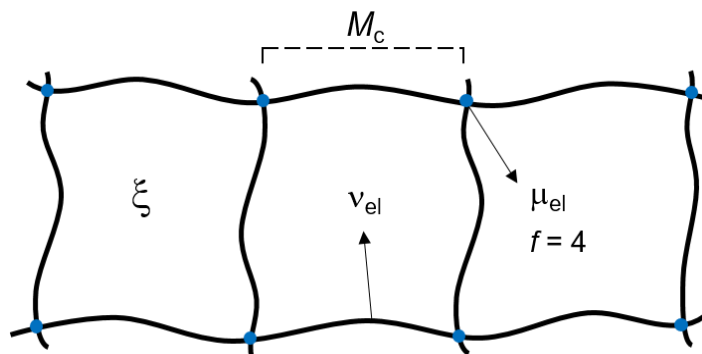


Figure 2.11. Schematic representation of an ideal network with $v_{el} = 10$ elastically active chains (each one of molecular weight M_c), $\mu_{el} = 8$ active junctions with functionality $f = 4$, and $\zeta = 3$ cycles. Figure adapted from Ref 167.

The two main statistical theories of rubber elasticity used for the description of networks are the affine model and the phantom model, the former proposed by Kuhn, Wall, and Flory,^{168,169} the latter developed by James and Guth.¹⁷⁰ The affine model works with the assumption that the chains in the network deform independently and in the same way as the whole sample. The crosslinks are thus considered to be fixed to an elastic non-fluctuating background, which deforms affinely.¹⁷¹ Conversely, the phantom model allows free motion (fluctuation) of the crosslinks about their average positions. The magnitude of the fluctuations determines how strong the network deformation couples to single chain deformation. Hence, through the surface chains the macroscopic deformation is transmitted to the bulk of the network.¹⁷¹

Both of these classical theories consider that the macroscopic behavior of the network is derived from the statistical properties of its individual chains. The affine and phantom models thus represent upper and lower limiting cases, respectively, of the properties of a network, failing to accurately describe the behavior of real systems.¹⁶⁷ In real networks, inter-chain interactions like entanglements and other steric constraints contribute to the net elastic behavior. Therefore, more advanced theories such as constrained junction fluctuation model, diffused-constraint model, tube and slip-tube models, have been proposed to bridge the two unconstrained affine and phantom classical models.^{167,171}

Figure 2.11 depicts an idealized representation of a polymer network, in which all chains are connected to different junction points at both ends. This implies that every constituting chain is elastically active in a perfect network.¹⁶⁶ Perfect networks are thus macro- and microscopically homogeneous, particularly characterized by identical chain lengths between junctions, identical segment and crosslinking densities, and constant

functionality f throughout the network (regular meshes).¹⁷² Nonetheless, the contrary is observed in real (non-ideal) systems, where normally a broad distribution of chain lengths, functionality, and crosslinks – broad mesh size distribution – is obtained along the network. Additional topological defects such as dangling ends, loops, and entanglements are also present in real imperfect networks (Figure 2.12), decreasing their structural order and affecting their mechanical properties.^{15,16,173,174}

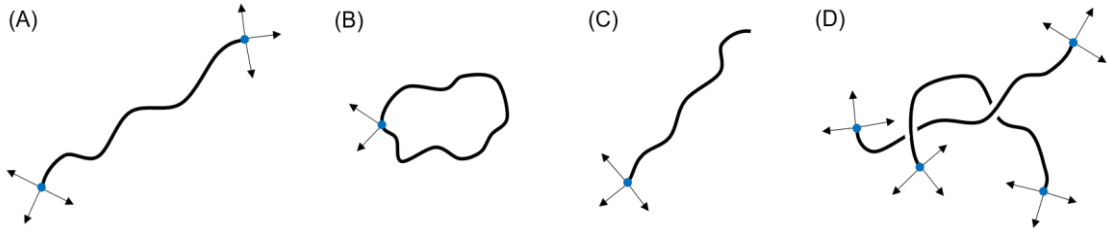


Figure 2.12. The concentration of elastically active chains (A) in real networks decreases by the presence of structural defects like loops (B), dangling ends (C), and entanglements (D).

As already mentioned, solvent addition to a network generates a swollen gel by diffusion of the solvent molecules into the polymeric matrix. In this way, the volume of the gel increases continuously until an equilibrium state is reached. The maximum equilibrium swelling that can be attained by a gel is determined by its crosslinking degree and the specific polymer–solvent interactions. Therefore, the equilibrium swelling ratio becomes a characteristic property of a swollen gel in a given solvent:

$$Q_m = \frac{m_{\text{swollen}}}{m_{\text{dry}}} \quad (\text{Eq. 2.55})$$

$$Q = \frac{(Q_m - 1)\bar{v}_1 + \bar{v}_2}{\bar{v}_2} \quad (\text{Eq. 2.56})$$

Here Q_m represents the mass swelling ratio, Q the volumetric swelling ratio, \bar{v}_1 is the specific volume of the solvent, and \bar{v}_2 the specific volume of the polymer. The theoretical extent of swelling for an ideal network can be predicted by the following form of the Flory–Rehner equation, where chain ends within the network have been neglected,¹⁷⁵

$$v_c = \frac{V_1}{M_c \bar{v}_2} = \frac{-[\ln(1-v_2) + v_2 + \chi_{12}v_2^2]}{(v_2^{1/3} - 2v_2/f)} \quad (\text{Eq. 2.57})$$

with v_c and M_c as defined in Equations 2.52 and 2.53, respectively, V_1 the molar volume of solvent, χ_{12} the Flory–Huggins interaction parameter (solvent-polymer interactions), and v_2 the volume fraction of polymer in the swollen mass. The relationship between the swelling ratio Q and v_2 is given by:

THEORY AND BACKGROUND

$$Q = \frac{1}{\nu_2} \quad (\text{Eq. 2.58})$$

Therefore, provided that ν_2 is known, the ideal mass swelling ratio Q_m can be obtained by replacing into Equation 2.56:

$$\nu_2 = \frac{\bar{\nu}_2}{(Q_m - 1)\bar{\nu}_1 + \bar{\nu}_2} \quad (\text{Eq. 2.59})$$

2.5.2. Synthesis

The junction points that hold together a network can be of chemical or physical nature. Physical networks are composed of temporarily crosslinked chains, interacting via hydrogen bonding, ion complexation, chain entanglements, traces of crystallinity, π - π stacking, dipole interactions, multiple helices, etc. The number of physical crosslinks present at a given time depends on external conditions such as pressure and temperature.¹⁷⁶ The transient characteristics of the physical crosslinks commonly impart reversibility to the network formation in response to external stimuli, conferring self-healing and shape-memory properties to the obtained materials.¹⁷⁷ A typical example of a thermoreversible physical network is gelatin, composed of junction crosslinked zones of collagen triple helices.¹⁷⁶ Upon thermal denaturation in water, the collagen helix structures adopt a random coil conformation, making the system soluble. More recent examples include gels formed by host-guest complexation,¹⁷⁸⁻¹⁸⁰ hydrogen bonding,¹⁸¹ electrostatic interactions,¹⁸² and metal coordination,¹⁸²⁻¹⁸⁴ among others.

Conversely, chemical networks are formed by permanent covalent crosslinks. Two different approaches can be distinguished in the synthesis of chemical networks, depending on the crosslinking process. Statistically crosslinked networks are achieved by simultaneous polymerization and crosslinking of mono- and multifunctional monomers – either by step-growth or chain-addition polymerization protocols – or after crosslinking of randomly functionalized polymer chains (Figure 2.13A). On the other hand, end-linked networks are obtained by connecting the end-groups of pre-existing polymer chains with complementarily functionalized multi-arm linkers (Figure 2.13B).

The different approaches employed for the formation of polymer networks have a strong influence on the topology (and properties) of the final material. Step-growth polymer networks present heterogeneous internal structure, determined by the onset of crosslinking (curing). Excessively slow or fast crosslinking can be detrimental for the final properties of the material.²⁰ However, many industrially relevant thermoset materials are obtained by step-growth crosslinking, like unsaturated polyesters, alkyds, polyurethanes, melamines, phenolic resins, epoxy resins, polysiloxanes, etc.^{20,172}

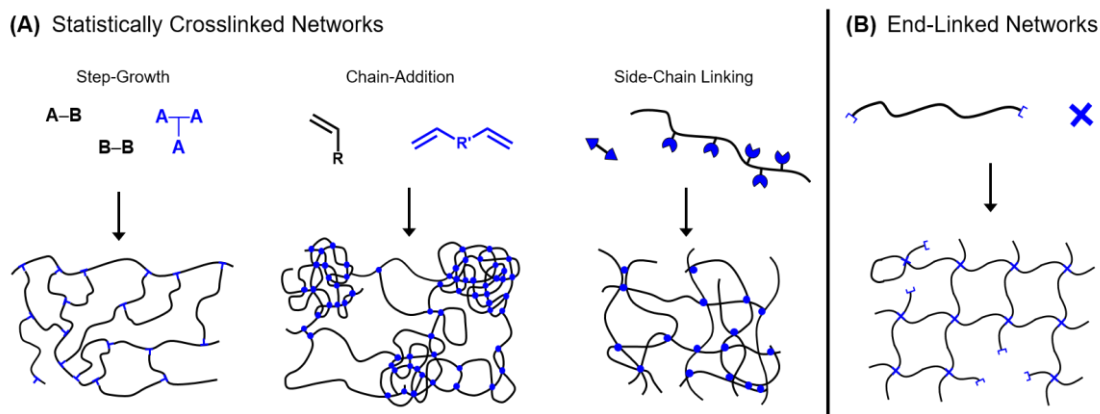


Figure 2.13. Synthesis of statistically crosslinked networks (A) by chain or step copolymerization, or by ligation of randomly functionalized polymer strands. Contrarily, end-linked networks (B) are obtained from end-group reaction of telechelic polymer precursors.

Networks obtained via free-radical copolymerization of vinyl monomers and crosslinkers exhibit a markedly heterogeneous structure, derived from the inherent random characteristics of this polymerization method. As discussed previously in Sections 2.1 and 2.3, termination and transfer events in FRP are responsible for broad molecular weight distribution of the primary chains. Furthermore, high molecular weight polymers are formed already in early stages of the reaction, existing in a very dilute regime (low monomer conversion). High dilution prevents polymer overlapping and favors internal crosslinking, generating nano- and microgels. These (soluble) microgel structures are eventually interconnected by longer chains as the reaction proceeds, until macroscopic gelation is reached.¹⁸⁵ The consequences of such gelation mechanism are inhomogeneous crosslink distribution, broad mesh size distribution, and connectivity defects (loops, dangling ends). Nonetheless, FRP represents one of the simplest methods to obtain polymer networks and gels for a plethora of applications, e.g. UV curable materials,¹⁸⁶ porous materials,¹⁸⁷ biomedical materials,¹⁸⁸ stimuli-responsive materials,^{189,190} and many others.

An additional level of structural control in networks is achieved when pre-existing polymer chains are allowed to crosslink.^{191,192} Vulcanization and other related technologies are prominent examples of this approach.¹⁹³ Recently, λ -orthogonal photopolymerization/photocrosslinking procedures have been developed, allowing spatial adjustment of the mechanical properties of the obtained networks.¹⁹⁴ Moreover, living anionic and controlled RDRP methodologies enable the synthesis of polymer precursors with narrow molecular weight distributions and defined functional groups.¹⁹⁵

THEORY AND BACKGROUND

The interconnection of these strands via randomly positioned junctions along the chain affords more regular network structures.^{122,196}

On the other hand, the end-linking of well-defined polymer precursors allows a regular distribution of the crosslinking points in the network (homogeneous M_c), hence a more uniform mesh size distribution.¹⁹⁷ Topological defects such as loops and dangling ends cannot be completely avoided during the formation of end-linked networks. However, the occurrence of primary loops can be reduced by ligation of complementary star-shaped macromonomers¹⁹⁸ or by semibatch monomer addition strategies.¹⁷⁴ In order to reduce the incidence of dangling ends, complete functional group conversion should be aimed. In this respect, highly efficient ligation reactions – (photo)click chemistry^{17,18,199} – can be employed as end-linking methods. Thiol-based chemistry (including photoinduced radical thiol-ene,^{200,201} thermal Michael-type thiol-ene,^{175,202} and *para*-fluoro-thiol reaction²⁰³) is one of the most common methods for end-linking of networks. Equally important for end-linked network formation are the azide-alkyne^{51,174,204} and Diels–Alder²⁰⁵⁻²⁰⁷ cycloadditions, along with modern photochemical ligation techniques like NITEC reactions,^{55,208} photo-enol chemistry,⁵⁵ and UV-induced photodimerizations.^{117,209} It is important to mention that by means of Diels–Alder cycloadditions, light-induced dimerizations, and other dynamic covalent reactions like phenyl boronate ester complexation, disulfide bond formation, imine and acylhydrazone formation,^{210,211} reversible chemical networks can be afforded.

Recent advances in the synthesis of polymer gels have led to the development of interpenetrating networks (IPN)²¹² and double networks (DN).²¹³ These kind of structures benefit from the distinct properties of their single components merged in one material, enhancing their mechanical properties and performance. For instance, a mixture of rigid tightly and ductile loosely crosslinked FRP-based networks, yields an extremely tough DN.²¹⁴ Further combinations of the crosslinking methods described previously, both physical and chemical, have been used to prepare DN with exciting properties. For instance, hydrogen bonding + double helix formation,²¹⁵ electrostatic + metal coordination,¹⁸² FRP + crystallite sites crosslinking,²¹⁶ and statistical + end-linking^{217,218} strategies, among others, have been reported in the recent literature for the synthesis of double networks.

2.5.3. Characterization Methods

It is feasible to acquire information about the microscopic structure of a gel by analysis of its macroscopic behavior. The interpretation of experimental macroscopic properties in terms of the different statistical models of rubber elasticity (refer to

Section 2.5.1) permits the phenomenological characterization of polymer networks. For instance, as mentioned above, by measuring the equilibrium swelling of a polymer gel in a given solvent, the (ideal) crosslinking degree can be retrieved from the Flory–Rehner relationship, Equations 2.57 and 2.59. From these equations it can be seen that, qualitatively, the swelling and crosslinking degrees are inversely proportional. However, obtaining accurate quantitative values from swelling experiments is inevitably hindered by the intrinsic approximations and parameters of the chosen theoretical model.²¹⁹

Hence, the most widespread approach for characterizing polymer networks relies on the analysis of their mechanical properties. The network response to deformation forces (stress and strain) is nowadays routinely investigated by rheology measurements. For example, rheological dynamic mechanical analyses enable the determination of the onset of gelation, defined as the intersection of the frequency (ω) dependent storage modulus $G'(\omega)$ and loss modulus $G''(\omega)$ curves,²²⁰ as represented schematically in Figure 2.14. A viscous regime predominates at the beginning of the reaction, which becomes elastic (sharp increase in storage modulus) as the extent of crosslinking increases. Gelation occurs at the point when $G' = G''$, independent of frequency and temperature.¹⁷⁶

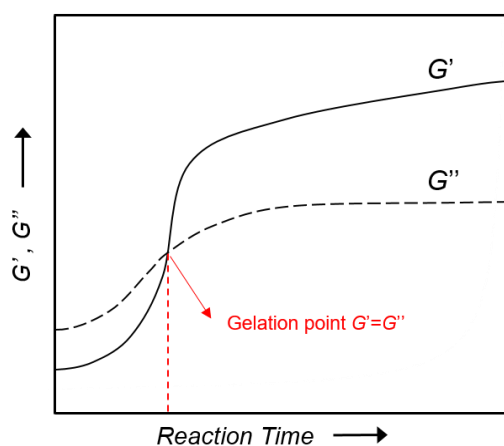


Figure 2.14. The onset of gelation for a crosslinking polymerization can be determined by rheology as the crossing point (red dashed line) between storage and loss moduli (G' and G'' , respectively).

Furthermore, the storage modulus G' provides information on the elastic behavior of the polymer network. From the classical affine and phantom network theories, a relationship between the elastic modulus G' and the degree of crosslinking can be derived,¹⁶⁷

THEORY AND BACKGROUND

$$G'_{\text{aff}} = kTv_c \quad G'_{\text{ph}} = kT\xi_c \quad (\text{Eq. 2.60})$$

where k represents the Boltzmann constant, T the absolute temperature, and v_c and ξ_c are defined as in Equations 2.50 and 2.53. However, actual stress–strain experiments on real networks differ from the predictions based on the affine and phantom models. A more general expression of Equation 2.60 can be written as

$$G' = \left(1 - \frac{2h}{f}\right) kTv_{\text{eff}} \quad (\text{Eq. 2.61})$$

with the constant h varying between zero (affine limit) and unity (phantom limit),²²¹ f the functionality of the junctions, and v_{eff} the effective concentration of elastically active chains.¹⁵ However, the presence of topological defects in the network architecture (refer to Figure 2.12) strongly affects its elastic behavior, giving rise to deviations of the experimental v_{eff} values from the expected theoretical ones. On the one hand, trapped entanglements (Figure 2.12D) influence the elastic modulus in a similar way as chemical crosslinks.²²¹ On the other hand, loops and dangling ends (Figure 2.12B and 2.12C, respectively) do not contribute to the overall network elasticity,²²² leading to overestimation of theoretical G' values.

In the last few years, Johnson and collaborators have studied methods to quantify²²³ and control¹⁷⁴ the number of cyclic defects (loops) in end-linked polymer networks. Their strategy (isotopic labeling, selective disassembly, mass spectrometric analysis), allowed them to correlate the effect of loops on G' , and develop a modified phantom model to account for these topological defects.¹⁵ Nonetheless, this protocol fails to distinguish the effect of entanglements and dangling chains on the elastic properties. In this regard, spectroscopic methods could be used to determine the incidence of dangling ends, provided that the concentration of unreacted groups is higher than the detection limit of the selected spectroscopic technique. For example, real-time Fourier-transform infrared spectroscopy (RT-FTIR) has been used to monitor the extent of conversion of thiol and alkene moieties in a photoinduced thiol-ene end-linking network formation.²²⁴ Another widely used spectroscopic method for the analysis of polymers is NMR spectroscopy. The scope of this technique regarding the determination of crosslinking densities in polymer networks will be described in Section 2.6.2.

From the previous discussion, it is evident that a comprehensive characterization of the structural features of a network is not trivial. The interpretation of macroscopic observables such as swelling and viscoelasticity rely on the classical network theories, which do not include the effects exerted by structural defects. Moreover, the influence

of such heterogeneities on the mechanical properties strongly depends on the length scale of their experimental determination.²²⁵ On the other hand, the quantitative assessment of even the simplest defects in networks (loops),^{174,223} requires challenging synthetic strategies that limit their further application. Therefore, network characterization demands a combination of the information retrieved from rheology, spectroscopy, mass spectrometry, theoretical simulations, and other techniques, in order to gain a better understanding of the internal structure of polymeric gel systems.

2.5.4. Applications

The mechanical attributes exhibited by polymer networks stem from several factors such as monomer type, synthesis method (e.g. step-growth, chain addition, end-linking, physical interactions, double or interpenetrating networks), crosslinking density, topological homogeneity, swelling extent, etc. The interplay between these factors confer polymer networks a vast range of elastic characteristics ($G' \approx 10^2$ – 10^7 Pa).^{15,226} The very different rubberlike properties, along with an intrinsic insoluble nature, make polymer networks excellent materials for an immense variety of applications.

Hydrogels are hydrophilic polymer networks capable of absorbing large amounts of water (from 10–20% until thousands of times their dry weight).²²⁷ Their water compatibility and remarkable swelling behavior have positioned hydrogels as suitable biomedical and healthcare materials. Historically, they have been used as soft contact lenses, diapers (superabsorbents), medical implants, cell culture substrates, and drug delivery systems.^{188,227,228} Recent advances in self-healing and stimuli-responsive hydrogels have led to the development of (bio)sensing materials,²²⁹ artificial muscles,²³⁰ tissue engineering and regenerative medicine,^{227,231} microfluidic devices,²³² coatings for Li-ion batteries,²³³ and separation²³⁴ or actuator²³⁵ technology.

Emerging applications of polymer networks in the field of materials science include flame retardants,²³⁶ smart adhesives,^{237,238} and photo-healable materials.²³⁹ As mentioned before in Section 2.4.2, photochemistry equips network synthesis with an exceptional spatio-temporal control.¹⁷ Accordingly, the unique characteristics of photochemical network formation have permitted, among others, the production of advanced biomedical devices¹⁰⁷⁻¹⁰⁹ and the development of 3D printing technology.²⁴⁰ Critically, three-dimensional printed networks offer a wide range of tunable properties such as thermo-responsiveness,¹⁰⁰ selective degradation^{101,102} and functionalization,²⁴¹ and electric conductivity,²⁴² particularly important for the manufacture of novel functional network-based materials.

THEORY AND BACKGROUND

The application of polymer gels for anisotropic NMR experiments^{1,2} has flourished during the last few decades. In the early 2000's, R. Tycko et al. demonstrated that mechanically stretched hydrophilic polymer gels are able to induce the partial alignment of biomolecules,^{243,244} thus allowing the determination of anisotropic NMR observables, a topic that will be covered in more detail in Section 2.6.3. The versatility in the synthesis of chemical networks have permitted the development of tunable polymer-based alignment media. Hydrophobic systems like polystyrene gels can be used as alignment media for apolar solvents,⁹ while for polar solvents polyacrylonitrile or poly(2-hydroxyethyl methacrylate) gels can be employed.^{12,14} Poly(ethylene oxide) gels, on the other hand, offer a wider range of solvent compatibility.¹¹ In every case, the degree of alignment can be scaled by changing the network crosslinking density or the mechanical strain applied to the gel.^{9,11-14} Furthermore, physical gels have also been utilized as NMR alignment media, for example gelatin swollen in water.²⁴⁵ This particular gel presents chiral cages (stemming from the collagen triple helix crosslinks), which enabled enantiodifferentiation of optically active analytes like L- and D-alanine.

2.6. Nuclear Magnetic Resonance Spectroscopy

As indicated before in the introductory chapter of this thesis, NMR spectroscopy is nowadays one of the most important analytical techniques for the characterization of (bio)organic molecules. The structure of many different hydrocarbon-based compounds (including polymers) can be elucidated using currently available NMR methodologies. Depending on the level of structural detail required, solid or liquid state high resolution NMR methods can be applied. In this way, NMR experiments provide access to both qualitative and quantitative information. In the following subsections a brief introduction to basic solution NMR theory is given, along with some applications of liquid state NMR in the field of polymer networks. Finally, the fundamentals of anisotropic NMR techniques are outlined.

2.6.1. Fundamentals

The nucleus of an atom is characterized by a nuclear spin quantum number (I), a fundamental property that depends on the number of protons and neutrons present in the nucleus. For example, ^{12}C , and ^{16}O nuclei are characterized by $I = 0$ (no spin), while ^1H , ^3H , ^{13}C , and ^{15}N exhibit $I = 1/2$, and ^2H , and ^{14}N nuclei present a spin value of $I = 1$.²⁴⁶ In general, an overall non-zero nuclear spin implies a non-zero magnetic moment μ ,

$$\mu = \hbar\gamma I \quad (\text{Eq. 2.62})$$

THEORY AND BACKGROUND

where \hbar is the reduced Planck constant, and γ is the gyromagnetic ratio, a fundamental constant for each nucleus. Nuclei with spin $I = \frac{1}{2}$ have a spherical charge distribution, hence a uniform dipolar magnetic moment. Conversely, $I = 1$ nuclei are characterized by non-spherical quadrupolar magnetic moments.

In the absence of an external magnetic field, the orientation of the different μ in a sample is random (same energy). However, when the sample is placed in a magnetic field B_0 , the magnetic moments μ of the sample assume $2I + 1$ different orientations, also called angular states.²⁴⁶ Thus, for a spin value of $I = \frac{1}{2}$, there are $2I + 1 = 2$ different angular states, N_0 and N_1 (Figure 2.15A). Similarly, for $I = 1$, three different angular states are possible. The angular states present different energies and therefore, an energy gap between them. This can be expressed by the following equation,

$$\Delta E = \gamma \hbar B_0 \quad (\text{Eq. 2.63})$$

from which it is evident that ΔE is proportional to B_0 . The population of this two levels follows a Boltzmann distribution, therefore a small bias towards the lower energy state ($N_0 > N_1$) is observed. This excess of population causes a net spin magnetization M_0 along the external magnetic field. However, the angular level splitting is not static, but exhibit a conical precession movement around the direction of B_0 (Figure 2.15B).

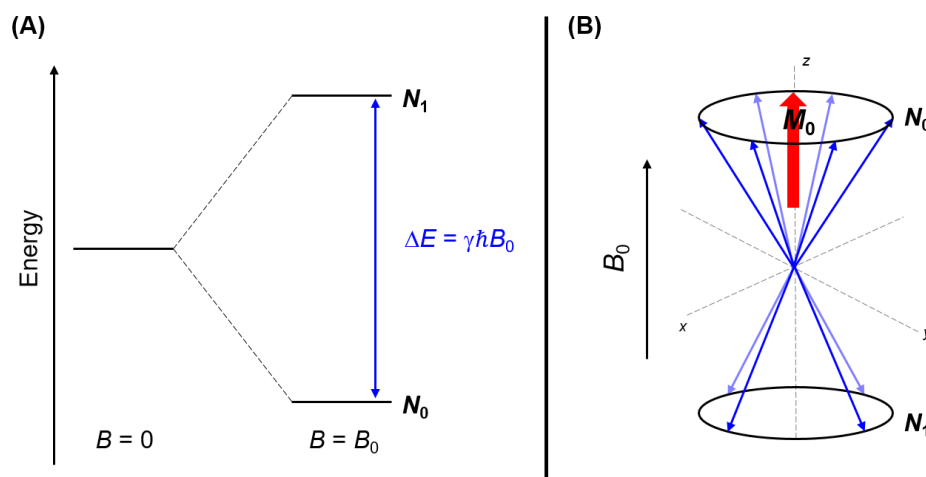


Figure 2.15. (A) Splitting of nuclear level energies for $I = \frac{1}{2}$ in an external magnetic field of magnitude B_0 , parallel to the z -axis. (B) Precession cone of the nuclear levels around the direction of B_0 . The higher population of N_0 confers the system an overall macroscopic magnetization M_0 . Figure adapted from Ref 246.

THEORY AND BACKGROUND

When a weak magnetic pulse B_1 , oscillating in the radiofrequency range (ν_{rf}), is applied perpendicular to the direction of B_0 (Figure 2.16A), it displaces the bulk magnetization vector M_0 into the x - y plane (Figure 2.16B). The absorption of this radiofrequency (rf) is then detected as a magnetic resonance signal by the receiver. Eventually, the energy gained is released to the environment and the system returns to the initial equilibrium state via relaxation processes (Figure 2.16C).

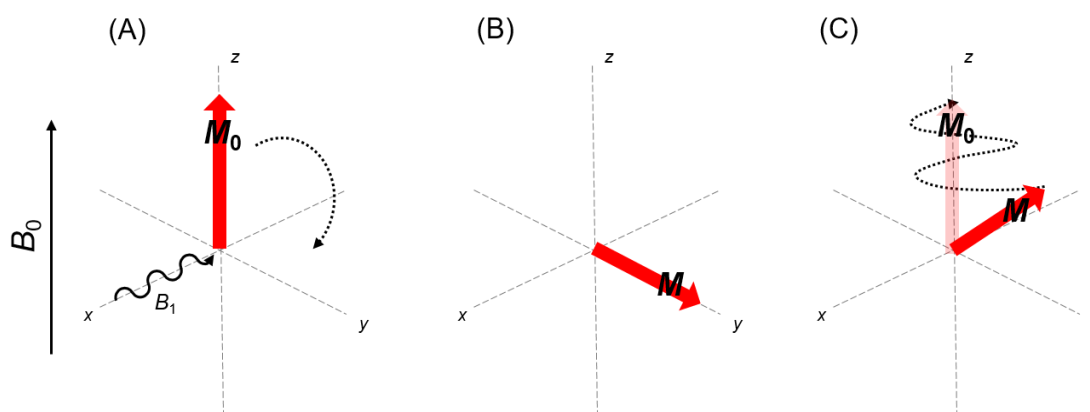


Figure 2.16. (A) Deflection of the macroscopic magnetization vector M_0 into the horizontal plane by applying a perpendicular rf oscillating field B_1 . (B) The generated in-plane magnetization M is detected as a signal. (C) Relaxation of M returns the system to the initial lower energy state M_0 . Figure adapted from Ref 246.

Two different relaxation mechanisms take place in order to return the system to its initial equilibrium state. A longitudinal relaxation, or spin-lattice relaxation, proceeds in the direction of the external magnetic field with certain relaxation time T_1 . On the other hand, the transverse relaxation, also known as spin-spin relaxation, proceeds perpendicular to the external field. The time required to complete the transverse relaxation is denoted by T_2 . Both relaxation times T_1 and T_2 are described by exponential decays that depend on the particular characteristics of each system, including the γ values of the nuclei at resonance and their chemical environment. Typically, T_2 relaxation times are shorter or equal to T_1 ($T_2 \leq T_1$). Both relaxation processes exert a strong influence in the obtained resonance signals. For instance, protons in non-viscous media, exhibit T_2 relaxation times long enough to yield narrow signals, and T_1 relaxation times that enable the correlation between signal intensity and amount of protons.²⁴⁶ However, this is not necessarily valid for other nuclei.

According to Equation 2.63, in an external field of constant strength B_0 , only one signal is expected after resonance rf absorption. However, B_0 affects not only the nucleus, but also the electron cloud surrounding it. The circulating electrons generate

a secondary magnetic field opposed to B_0 , an effect known as electron shielding.²⁴⁷ Consequently, the effective resonance frequency of the shielded nuclei is lower than expected for B_0 . The shielding extent depends on the actual electron density around the nucleus, which is in turn determined by its specific chemical environment. Therefore, the shielding of a particular nucleus should be compared with a reference compound, typically the highly shielded nuclei of tetramethylsilane (TMS). The difference between the absorption frequency of a particular proton and the absorption frequency of the reference (defined as zero), is called chemical shift (δ).²⁴⁷

$$\delta = \frac{B_{ref} - B_{sample}}{B_{ref}} \times 10^6 (\text{ppm}) \quad (\text{Eq. 2.64})$$

Hence, δ (expressed in ppm) is a parameter dictated solely by the individual nuclear absorptions and not by the magnetic field strength used for the measurement.²⁴⁷ In this way, the analysis of structural differences and chemical environments within a molecule is granted.

A further phenomenon encountered in solution NMR experiments is the spin coupling, also known as scalar J -coupling. The interaction of neighboring (normally up to three bonds apart) nuclear spins through their respective bonding electrons causes splitting of the resonance signals.²⁴⁶ Thus, initially singlet signals split into multiplets, whose multiplicity depends on the number of neighboring coupled nuclei n , according to $2nI + 1$ (I is the spin number). For instance, for nuclei with spin $I = \frac{1}{2}$, coupling with 1, 2 or 3 neighboring nuclei generates a doublet, a triplet or a quartet, respectively. The effectiveness of the coupling interaction is given by the spin coupling constant J (in Hz), which is independent of the external magnetic field.²⁴⁷ The third classical interaction present in solution NMR experiments is the so-called nuclear Overhauser effect (NOE). This relaxation phenomenon enables the analysis of nuclei in close spatial proximity (up to 5 Å for ^1H nuclei),²⁴⁶ even if they are not coupled through bonding electrons.

The most relevant nuclei for the NMR analysis of organic molecules in solution are by far ^1H and ^{13}C . Nevertheless, additional nuclei like ^{15}N , ^{19}F , ^{29}Si , and ^{31}P have gained importance thanks to recent advances in high resolution NMR techniques. Moreover, multidimensional (2D, 3D, 4D...) NMR experiments offer the possibility to resolve overlapping signals and facilitate the assignment of chemical shifts. Therefore, NMR spectroscopy is nowadays regarded as a powerful analytical method that provides access to detailed structural information.

THEORY AND BACKGROUND

2.6.2. NMR Analysis of Polymers

Spectroscopic analysis via NMR stands out as a very versatile technique for the characterization of polymers and polymerization processes. Contrarily to small molecules, polymers present slow Brownian rotation in solution (relative to the timescale of the NMR experiment). Moreover, the high concentration of protons present in a very similar chemical environment in the polymer leads to strong signal overlapping. Therefore, the ^1H NMR spectra of macromolecules always exhibit broader signals than their monomeric counterparts. This aspect enables monitoring the conversion kinetics of polymerizations, e.g. by comparison of the narrow vinyl proton signals of a monomer and the newly formed broad aliphatic proton signals of the corresponding polymer. In the same manner, the determination of the copolymerization behavior of a pair of monomers and their reactivity ratios r_1 and r_2 (refer to Section 2.1.1), can be achieved by NMR spectroscopy.²⁴⁸

Another important highlight of NMR spectroscopy applied to polymer systems is end-group analysis for the determination of molecular weights. The degree of polymerization DP_n of an end-functional macromolecule can be calculated via NMR, provided that the signals of polymer and end-group do not overlap, and that the integration is reliable. Additionally, this method provides useful information on end-group fidelity in RDRP protocols, and functionalization yields in post-modification reactions^{247,248} (refer to Sections 2.2 and 2.4.2, respectively).

On the other hand, NMR spectroscopy has been widely employed to determine the stereoregularity (tacticity) of a polymer. Stereoregularity plays a major role in the physical properties of a polymeric material, since it is the key factor determining crystallinity.²⁴⁹ The pendant groups of a polymer strand can be present in the same configuration (isotactic), in an alternating regular configuration (syndiotactic), or can be randomly organized along the chain (atactic).^{247,248} The different chiral sequences in the polymer backbone give rise to specific patterns in the ^1H - and ^{13}C -NMR signals, which can be interpreted in terms of the tacticity of the polymer sample.²⁴⁷⁻²⁴⁹ Additional information about polymer structure and connectivity can be retrieved by means of two-dimensional NMR techniques. Currently available 2D NMR experiments like COSY, HMQC, HMBC, TOCSY, NOESY, and others, are useful for the determination of atom connectivity, neighboring nuclei, couplings, bond orders, spatial relationships, etc.²⁴⁷ Moreover, DOSY experiments permit the resolution of the NMR signals of a polymer mixture, according to the diffusion coefficients of their single components.

Furthermore, relaxation studies, i.e. analysis of the characteristic T_1 and T_2 relaxation times, provide access to information about segmental motion in polymer samples.²⁴⁹ Since molecular motion has a strong effect on the NMR signal linewidth, relaxation studies have found broad application in the investigation of crosslinking density in polymer gels.^{250,251} T_1 relaxation times are not greatly affected by crosslinking or molecular weight, due to their sensitivity to short range molecular motion. Conversely, T_2 times are influenced by long range cooperative motion of the polymer chains, thus strongly dependent on entanglements and crosslinks.²⁵⁰ The chain segments adjacent to junctions experience the highest decrease in mobility, hence T_2 decreases in close proximity to crosslink points.²⁵¹ Therefore, investigation of T_2 decay times in crosslinked polymer melts (above the glass transition temperature T_g), provide a straightforward method to characterize entanglement and crosslinking densities.²⁵⁰ However, the high temperatures needed can influence the crosslinking rate and induce thermal degradation of the sample. Studies on swollen gels below T_g have been reported as well, but artifacts due to mechanical strain upon swelling (T_2 is orientation dependent) cannot be ruled out.²⁵¹ Alternatively, analysis of ^{13}C relaxation times in solid state NMR experiments can be used to overcome this issue and retrieve information of crosslinking density. Nevertheless, the very large linewidths obtained by this methodology can make difficult the interpretation of the spectra.²⁵¹

2.6.3. Anisotropic NMR

The structural characteristics of a given compound (atom connectivity, configuration, conformation) can be determined by evaluation of its classical NMR resonance parameters in solution, namely chemical shift δ , J -coupling, and NOE enhancement. Nonetheless, these standard NMR parameters are restricted to short-range interactions between nuclei.¹ Therefore, the correlation of distant parts of a molecule through space (apart from distance information up to 5 Å retrieved from NOE), is normally not feasible by classical solution-NMR analysis. In an isotropic solution, the Brownian motion of the analyte averages any orientation-dependent (anisotropic) interaction that might take place within different parts of the molecule. The most prominent anisotropic parameters are dipolar and quadrupolar couplings, which contain relevant spatial information (angles and distances between atoms). On the other hand, in solid state NMR the analyte molecules are “frozen”, thus exhibiting very large anisotropic interactions and broad linewidths which hamper the interpretation of spectra. Consequently, the access to the spatial features of a molecule, without losing chemical shift information, requires an intermediate condition between isotropic solution and solid state. This problem was addressed by the introduction of alignment media, a

THEORY AND BACKGROUND

matrix that enables a preferred orientation of samples in the magnetic field. Reaching partial alignment of a sample is important in order to average significantly (but not completely) the anisotropic dipolar couplings, so that their magnitude lies below the scalar J -couplings (from $\sim 10^3$ Hz fully anisotropic to $\sim 10^0$ Hz range after isotropic averaging).² In this way, the spatial information on the analyte is still available, without compromising chemical shift resolution.

As a result, the so-called residual dipolar couplings (RDCs) correspond to the anisotropic dipolar interactions D , which remain measurable after partial average. The dipolar coupling D_{ij} between two (hetero)nuclear spins i and j , is determined by the gyromagnetic ratios γ_i and γ_j , the distance between both nuclei r_{ij} , and the angle θ_{ij} between vector r and the external magnetic field B_0 (see Equation 2.65 and Figure 2.17).^{1,2,252}

$$D_{ij} = -\frac{\hbar\gamma_i\gamma_j\mu_0}{16\pi^2} \left\langle \frac{1}{r_{ij}^3} (3\cos^2\theta_{ij} - 1) \right\rangle \quad (\text{Eq. 2.65})$$

Here μ_0 represents the vacuum permeability and the angular brackets indicate average of all orientations over time.

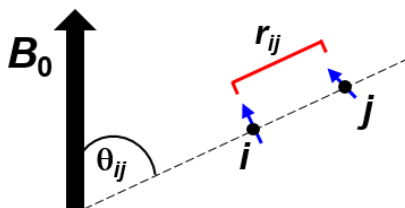


Figure 2.17. Schematic representation of dipolar coupling interaction between two spins (i and j) in an external magnetic field B_0 . Figure adapted from Ref 252.

It can be inferred from Equation 2.65 that RDCs contain both angular (θ_{ij}) and distance (r_{ij}) information between nuclei interacting in space, not restricted to bonding or neighboring groups. In the special case where nuclei i and j are directly attached, r_{ij} represents the bond length.² For rigid compounds, the time average of θ_{ij} and r_{ij} remains constant throughout all equivalent parts of the molecule. Therefore, if the distance r_{ij} is known, the magnitude of the RDCs depend only on the angle θ_{ij} (refer to Equation 2.65). Contrarily, in flexible compounds θ_{ij} and r_{ij} values are also averaged respect to the internal motion, in addition to the averaging from the tumble Brownian motion. The effect exerted by this further degree of freedom can create problems in the interpretation of RDC data for flexible molecules.²

THEORY AND BACKGROUND

There are several strategies to achieve partial alignment of a molecule respect to the external magnetic field. Proteins can be aligned by means of paramagnetic metal ions with anisotropic magnetic susceptibility (attached either naturally,²⁵³ or synthetically⁷ to the biomolecule). However, the excessive line broadening of the nuclear resonances neighboring the metal center hinders the application of this technique for small molecules.¹

The second approach comprises the use of liquid crystalline (LC) phases to induce molecular orientation. Nematic liquid crystals (a class of thermotropic LC phases that form at a certain temperature range), were originally employed as alignment media.²⁵⁴ Nonetheless, this kind of systems introduce a very strong degree of alignment, only meaningful when used for small symmetric molecules. However, the currently used LC alignment media is based in two-component lyotropic liquid crystals, which consist in a “liquid crystal builder” and a solvent. In contrast to thermotropic liquid crystals, lyotropic LC phases are formed at a certain concentration range. This property allows increasing the degree of ordering in such alignment media by incremental LC builder concentration. However, a minimum builder concentration is always required, below which the LC phase disrupts.² For most of the waterborne lyotropic crystals presently used, this critical concentration is low enough to permit the weak alignment of hydrophilic analytes.¹ Examples of such lyotropic liquid crystals include phospholipid bicelles,²⁵⁵ bacteriophages,²⁵⁶ and graphene oxide,⁸ in water or water-solvent mixtures. Moreover, helical polypeptides,²⁵⁷ polyarylacetylenes,⁶ and polyisocyanopeptides²⁵⁸ have recently found application as LC alignment media compatible with apolar organic solvents. Some of those even permit the enantiodiscrimination of optically active compounds via RDC analysis.^{6,257}

An alternative strategy to achieve partial alignment of an analyte is the use of strained polymer gels. By this approach, anisotropy is generated mechanically by compressing or stretching the gel, a feature that allows wider scalability in the alignment strength.^{13,252} Typically, a dry polymer network of cylindrical shape is swollen inside an NMR tube. When the gel reaches the walls of the tube, further swelling is only possible in the longitudinal direction, generating stretching uniaxial anisotropic strain.² Alternatively, gel swelling can be restricted by a plunger (e.g. in a Shigemi tube), generating compression uniaxial strain.²⁴⁴ Any compound present within the gel would tend to align in the strain direction, independent of the strength of the external magnetic field. Furthermore, there is a plethora of available crosslinked polymers that can be used as alignment media in combination with solvents of different polarity. For example, polystyrene,⁹ perdeuterated polystyrene,²⁵⁹ poly(methyl methacrylate),²⁶⁰ and

THEORY AND BACKGROUND

polydimethylsiloxane,²⁶¹ gels have been used as alignment media in apolar organic solvents, polyacrylonitrile,¹² poly(2-hydroxyethyl methacrylate),¹⁴ and poly(vinyl acetate)²⁶² gels can be employed for polar solvents, polyacrylamide²⁶³ and gelatin²⁴⁵ for water, and poly(ethylene oxide) is a nearly universally compatible alignment medium.¹¹ The flexibility of polymer networks in terms of synthesis procedures, tunable degree of crosslinking, and solvent affinity have positioned them as very versatile alignment media. Nevertheless, the principal drawback of polymer-based alignment media lies in their poor reusability, since analyte diffusion and swelling equilibration is often time consuming and can lead to mechanical failure of the gel. Furthermore, from a theoretical point of view there exist to date no solid models to describe structure-property relationships of analytes inside a polymer network, although some attempts to simulate the preferred orientation of a molecule in gel-based media by molecular dynamics were recently reported.^{264,265} From a synthetic point of view, crosslinked gels are typically obtained by irradiation of polymer strands or by free-radical polymerization of vinyl monomers, methodologies that introduce structural heterogeneity, as already mentioned in Section 2.5.2. The defects present in the network microstructure can be detrimental for the resolution of the NMR signals (broad linewidth).

CHAPTER 3:

SYNTHESIS OF OPTIMIZED POLYMER-BASED ALIGNMENT MEDIA

Presently, NMR spectroscopy in anisotropic media stands as a powerful tool for structure elucidation of biologic compounds and natural products.^{1-3,252} Apart from the short-ranged spatial information retrieved from NOE interactions,²⁴⁶ unequivocal three-dimensional structural characterization of a molecule is normally not feasible by conventional isotropic NMR experiments. However, anisotropic interactions such as residual dipolar couplings (RDCs), contain information that enables the determination of conformation, configuration,⁴ enantiomeric arrangement,^{5,6} and other spatial features of an analyte. Remarkably, analysis of RDCs in combination with computer-assisted structure elucidation algorithms and DFT calculations have proven a level of spatial resolution comparable to crystallographic data.²⁶⁶ Nevertheless, access to anisotropic information by NMR is only granted if isotropic molecular tumbling is restricted. Reduced tumbling motion can be achieved when molecules are analyzed inside an alignment medium, as outlined in Section 2.6.3. From the currently available alignment media, polymer gels stand out for their synthetic versatility, wide solvent compatibility and tunable alignment strength.^{9,13} Critically, tuning the alignment degree by applying mechanical strain is advantageous because, in principle, different measurements can be performed on the same sample without changing the alignment medium. Notwithstanding, this would require a robust polymer gel that resists several deformation cycles without losing its stability or alignment properties. Moreover, the possibility of functionalizing polymer gels, incorporating selected groups that impart

Unless otherwise indicated, D. Estupiñán designed and performed all experiments. Anisotropic NMR measurements and corresponding data evaluation were carried out by P. Tzvetkova. Rheology measurements were conducted by L. Arens. Optimization of synthesis conditions for compounds **28–31** was performed by M. Dobrowolska, under the supervision of D. Estupiñán. Monomer **36** and precursor [Eu(dbm)₃(H₂O)₂] were prepared, characterized, and kindly provided by H. Rothfuss and N. Knöfel. L. Barner motivated and supervised the project, in collaboration with B. Luy.

SYNTHESIS OF POLYMER-BASED ALIGNMENT MEDIA

additional performance to the alignment media, has not been exploited so far. According to this, in the present chapter the preparation of free-radical-generated polystyrene (PS) networks is discussed, aiming to optimize the performance, mechanical features, and alignment properties of the existing polymer-based alignment media. Section 3.1 describes the synthesis conditions of PS gels and the strategies employed to modify their alignment strength without compromising mechanical stability. The use of plasticizers, in particular bis(2-ethylhexyl) adipate, was found to reduce mechanical failure and improve the reusability, as well as the alignment scalability of the gels. In addition, the possibility of using styrene derivatives for the network synthesis, to avoid the use of plasticizers, was also explored. Further on in Section 3.2, the inclusion of functional groups in the network backbone to impart additional properties, i.e. enantiodiscrimination and paramagnetic ion complexation, was investigated. Thus, (+)- and (-)-menthol moieties were successfully incorporated into the PS networks, creating chiral orientating media, which allowed the enantiomeric differentiation of optically active analytes. On the other hand, a phenanthroline ligand for the complexation of europium ions was attached to the network backbone, affording fluorescent lanthanide-functionalized PS gels.

3.1. Polystyrene Sticks via Free-Radical Polymerization

The concept of strain induced alignment in swollen elastomers was introduced by Deloche and Samulski already in the early 1980's.²⁶⁷ However, only after the pioneering work of Tycko^{243,244} and Grzesiek²⁶⁸ in 2000, this technique became a popular method for structural elucidation via NMR analysis of anisotropic parameters. The partial alignment of analytes inside a polymer matrix can be simplistically understood as the result of specific interactions between solute and polymer chains (steric occlusion, π - π interactions, hydrogen bonding, etc.).^{265,266} Polymer gels, swollen in an adequate solvent, have isotropic organization of crosslinked polymeric chains. These chains, however, acquire a preferred orientation by subjecting the gel to mechanical strain, either parallel to the stretching direction or perpendicular to the compressing direction, as depicted schematically in Figure 3.1. Concomitantly, the tumble motion of the analyte molecules interacting with the network strands is restricted at the polymer surface, thus inducing their overall alignment when strain is applied (see Figure 3.1).

SYNTHESIS OF POLYMER-BASED ALIGNMENT MEDIA

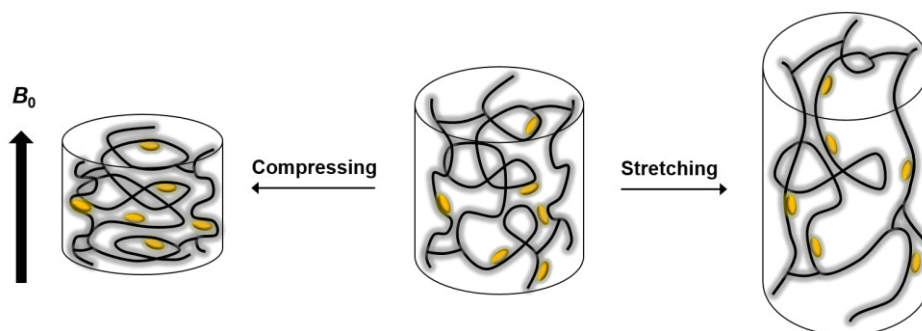


Figure 3.1. Upon mechanical strain, network strands (black) orient anisotropically by stretching (right) or compressing (left) the gel. Initially isotropic analyte molecules (yellow), interacting with the polymer surface, adopt the same orientation of the gel strands, thus partially aligning in respect to the external magnetic field B_0 .

Importantly, the degree of alignment – i.e. the effective number of molecules ordered in a particular direction – depends on the strength of the mechanical strain, applied either by extensive¹³ or compressive^{244,269} forces. Alternatively, the degree of alignment can be tuned with changes in the crosslinking density of the gel.^{9,260,262} Higher crosslinking degrees in the network structure indicate lower average molecular weight M_c of the active chains between junctions (refer to Section 2.5.1). Plausibly, the shorter chains present less mobility and limited conformational freedom (hence arranging more anisotropically), causing a stronger alignment degree of the solute molecules.

A common way to determine the alignment strength of an orientating medium is to measure the quadrupolar splitting ($\Delta\nu_Q$) values of a deuterated solvent. Deuterium (^2H) has a nuclear spin $I = 1$ and hence a non-spherical charge distribution, in contrast to protons (^1H) and other nuclei with spin $I = \frac{1}{2}$ (refer to Section 2.6.1). Spherical charge distributions for $I = \frac{1}{2}$ nuclei generate a symmetrical magnetic dipole, while $I \geq 1$ nuclei (for instance, deuterium) exhibit non-symmetric quadrupole moments.²⁴⁶ The characteristic resonance frequency of deuterium in isotropic solution splits into two signals when the ^2H nuclei are placed inside an anisotropic media (Figure 3.2). Needless to say, the magnitude of the $\Delta\nu_Q$ splitting depends on the degree of alignment.

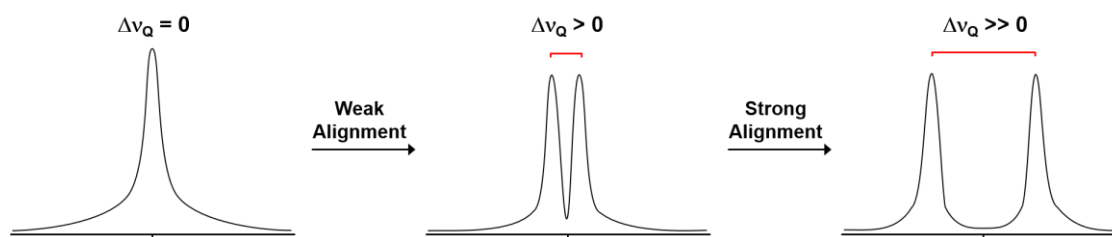


Figure 3.2. Representation of deuterium quadrupolar splittings ($\Delta\nu_Q$) for the determination of alignment strength in ^2H NMR spectra. In isotropic media $\Delta\nu_Q = 0$, while in anisotropic media $\Delta\nu_Q > 0$.

SYNTHESIS OF POLYMER-BASED ALIGNMENT MEDIA

3.1.1. PS Sticks with Tunable Alignment Strength

The investigations on tunable alignment strength were commenced using PS gels as model system, produced by conventional free-radical copolymerization of styrene and divinylbenzene (DVB) as crosslinker, following previous literature reports.^{9,270} Monomer and crosslinker (0.2 mol% DVB respect to styrene) were copolymerized in bulk at 80 °C, using azobisisobutyronitrile (AIBN, 0.1 mol% respect to styrene) as radical initiator. Commercially available borosilicate glass NMR tubes of 3 mm outer diameter (internal diameter ca. 2.2 mm), sealed with rubber septa, were used as reaction chambers (refer to Figure 8.1 in Appendix 8.1). Since no solvent is employed for the polymerization and the reaction is carried out until full monomer conversion, solid PS networks of cylindrical shape are obtained (Figure 3.3A). With this setup, translucent dry PS sticks of 2.2 mm diameter are directly recovered after polymerization, by simply breaking the glass mold used as reactor. The detailed synthetic procedures can be found in the experimental section of this thesis (Chapter 6). When the dry cylindrical sticks are allowed to freely swell in an excess of chloroform, a volume increase in all directions is observed. However, restricted swelling, e.g. inside conventional 5 mm outer diameter NMR tubes, affords gels uniaxially stretched in the longitudinal direction (Figure 3.3B).

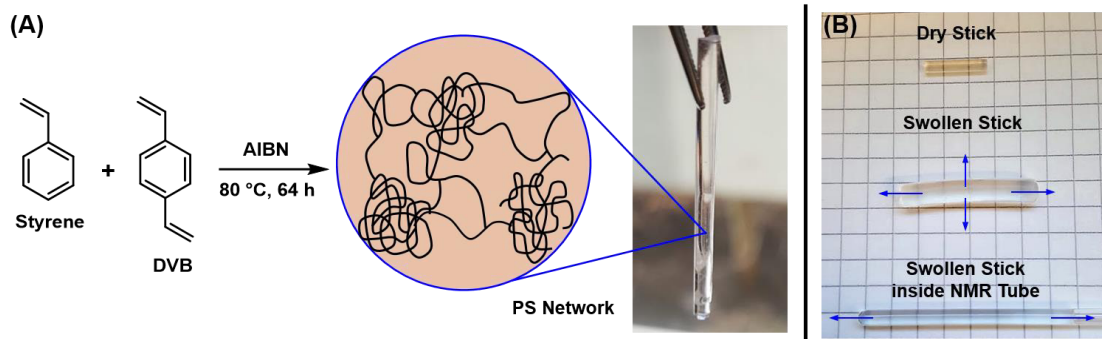


Figure 3.3. (A) Synthetic pathway for free-radical-based PS network sticks. (B) Free swelling of the dry PS sticks leads to volume increase in all directions, while swelling inside NMR tubes restrict the volume increase in the longitudinal direction (stretching).

The restricted swelling of the PS gels inside NMR tubes, as depicted in Figure 3.4A, affords an anisotropic environment by stretching forces (see Figure 3.1). Clearly, effective extensive strain is obtained only if the swollen diameter of the gel is larger than the inner diameter of the NMR tube (ca. 4.0 mm for regular 5 mm outer diameter tubes). Hence, the initial dimensions of the dry stick and its degree of swelling predetermine the maximum uniaxial stretching attained with a particular gel sample.

SYNTHESIS OF POLYMER-BASED ALIGNMENT MEDIA

Consequently, sticks of different diameters are needed to attain different stretching degrees. More advantageous is the adjustment of the extensive strain applied on one single gel sample. This can be achieved in a specially designed stretching apparatus,¹³ as depicted in Figure 3.4B. Such device operates under the same principle as a conventional NMR tube, but it incorporates a flexible perfluorinated elastomer tube that holds the gel sample. By stretching the elastomer tube, the polymer gel inside expands at the same ratio, with the advantage that it can be conveniently fixed in a desired stretched position using specially designed screws.¹³ Alternatively, polymer gels can be compressed to induce anisotropy (refer to Figure 3.1). Compressive strain has been achieved by swelling the sticks inside a Shigemi tube and locking the plunger at a desired position with tape.²⁶⁹ Similarly, in a compressing apparatus (Figure 3.4C) the gel is pushed into NMR tubes by a plunger, whose position can be adjusted at will with a screw. It is important to mention that, in compression experiments, the swollen diameter of the gel should be smaller than the diameter of the NMR tube. Only in this way the gel can expand radially until it reaches the walls of the tube. Once full equilibrium swelling is reached, either under extensive or compressive strain, the PS gels can be directly used as alignment media for anisotropic NMR experiments. In the present thesis, deuterated chloroform (CDCl_3) was used as solvent, unless otherwise stated. For the eventual characterization of analyte molecules, these can be first dissolved in CDCl_3 and the resulting solution is used to swell the gel.

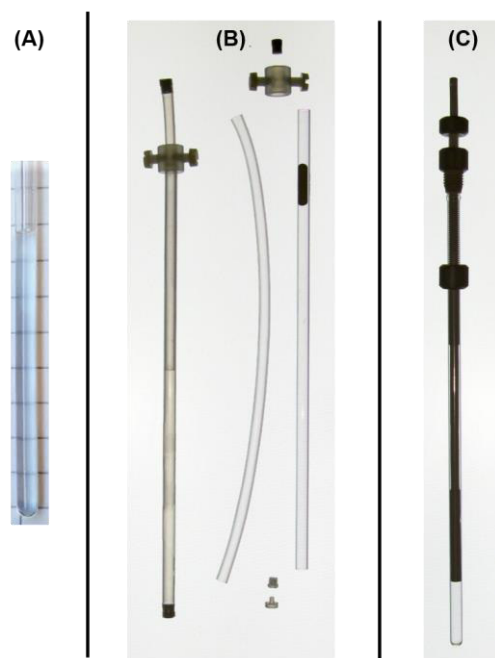


Figure 3.4. (A) Stretched gel in a conventional 5 mm NMR tube. (B) Stretching apparatus. (C) Compressing apparatus.

SYNTHESIS OF POLYMER-BASED ALIGNMENT MEDIA

^1H NMR characterization of the PS gel (Figure 3.5A) display the expected resonance signals of the aliphatic polymer backbone (Al.), between 1.0–2.5 ppm, and the signals of the aromatic side groups (1, 2, and 3) in the range of 6.1–7.7 ppm, particularly broad due to crosslinking (refer to Section 2.6.2). The resonance signals 4 and 5, assigned to residual monomer (two doublets centered at 5.3 and 5.8 ppm), are very weak, indicating near to quantitative styrene conversion. On the other hand, ^2H NMR analyses permit the characterization of the alignment properties of the gel (refer to Figure 3.2). The quadrupolar splitting of the CDCl_3 signal ($\Delta\nu_Q$, measured in Hz), typical of anisotropic media, is determined in ^2H NMR spectra. A collection of ^2H spectra can be recorded in the vertical direction of the gel, thus scanning the quadrupolar splittings along the gel length. This allows a two-dimensional space mapping of $\Delta\nu_Q$ values for the whole length of the PS stick (Figure 3.5B). The projection of single ^2H spectra permits the determination of $\Delta\nu_Q$ values at different positions in the stick (Figure 3.5C). Therefore, this method serves as a probe for macroscopic homogeneity of the alignment medium, since non-uniform swelling, cracks, trapped air bubbles, and other discontinuities in the gel prevent a regular distribution of $\Delta\nu_Q$ values – thus alignment strength – throughout the sample (compare with Figure 3.7 and with Figure 8.2B in Appendix 8.1). The deviations at the top and the bottom of 2D spectrum in Figure 3.5B correspond to the edges of the gel, which twists when it reaches the borders of the NMR tube. Shimming drifts at these positions are responsible for the bending observed in the 2D projection.

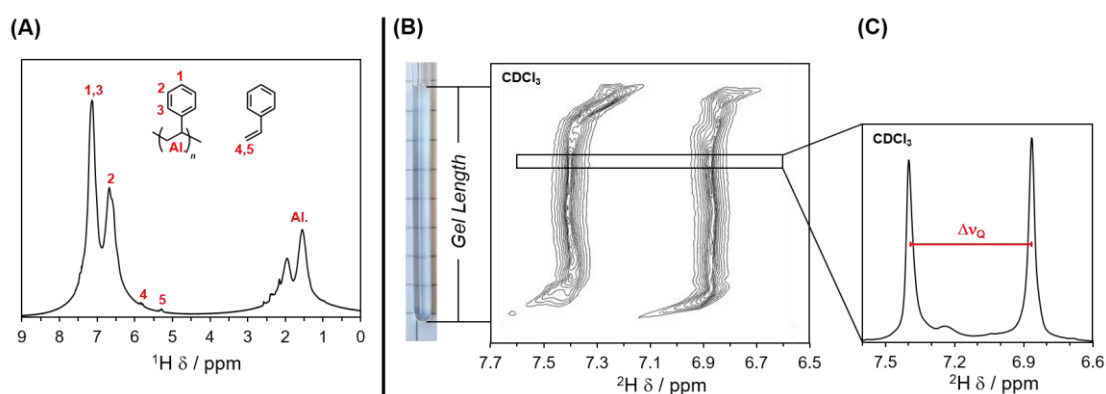


Figure 3.5. (A) ^1H NMR spectrum of crosslinked PS stick swollen in CDCl_3 . (B) 2D projection of ^2H quadrupolar splittings ($\Delta\nu_Q$) of the CDCl_3 resonance signal, determined along the vertical direction of the stick (single $\Delta\nu_Q$ slice depicted in the ^2H NMR spectrum in C).

Next, the effect of the crosslinking degree on the alignment properties of the PS gels was investigated. PS sticks with different amounts of crosslinker (0.1–1.0 mol%

SYNTHESIS OF POLYMER-BASED ALIGNMENT MEDIA

DVB, refer to the experimental section) were prepared, following the same procedure as described before. The alignment strength of the networks (CDCl_3 $\Delta\nu_Q$, measured in compressing apparatus) increases with higher crosslinking degrees, by simply augmenting the initial concentration of DVB used for the gel synthesis (Table 3.1).

Table 3.1. Swelling, thermal, and alignment properties of PS networks prepared with different amounts of crosslinker (DVB).

Sample ^a	DVB	Q_m ^b	T_g	$^2\text{H } \Delta\nu_Q$ ^c
1	0.1 mol%	15.8 ± 0.3	101 °C	3 Hz
2	0.2 mol%	10.7 ± 0.1	94 °C	27 Hz
3	0.4 mol%	10.2 ± 0.5	95 °C	n.d
4	0.6 mol%	8.2 ± 0.1	95 °C	54 Hz
5	0.8 mol%	7.2 ± 0.3	95 °C	n.d
6	1.0 mol%	6.6 ± 0.3	98 °C	81 Hz

^a Styrene + DVB + 0.1 mol% AIBN. 80 °C, 64 h.

^b Mass swelling ratio, calculated from Eq. 2.55 after free swelling of the sticks in CHCl_3 for 24 h. Standard deviation determined from three independent replicas.

^c CDCl_3 quadrupolar splitting from samples in compressing apparatus (except gel 4 in 5 mm NMR tube). Samples pre-swollen in acetone. $\Delta\nu_Q$ values could not be determined for networks 3 and 5 due to excessive cracking and signal broadening.

Importantly, the variation of the degree of alignment is crucial for the application of the gels in anisotropic NMR techniques. Depending on the analyte, very small $\Delta\nu_Q$ might not retrieve the desired spatial information, while very large $\Delta\nu_Q$ values could hinder the interpretation of the spectra. In this respect, a wide $\Delta\nu_Q$ range (3–81 Hz) was achieved for the different PS sticks within a 10-fold variation in the amount of crosslinker, confirming the observations reported in literature.⁹ Notwithstanding, changing the amount of DVB not only affects the quadrupolar splittings but, at the same time, it has a profound impact on the mechanical characteristics of the gels. Increasing the crosslinking density promotes the formation of rigid gels, with concomitant decrease in their degree of swelling (see Figure 3.6 and Table 3.1). Experimentally, the swelling extent was determined as the mass swelling ratio Q_m (refer to Equation 2.55 in Section 2.5.1). The corresponding theoretical Q_m values of the PS gels in chloroform were calculated according to the Flory–Rehner swelling theory. As described previously in Section 2.5.1, Equations 2.55, 2.57, and 2.59 can be used to determine Q_m for the polystyrene-chloroform system at different crosslinking degrees (the amount of DVB determines the average molecular weight between crosslinks M_c , refer to Appendix 8.1). The experimental Q_m data show a positive deviation from the theoretical

SYNTHESIS OF POLYMER-BASED ALIGNMENT MEDIA

values predicted from the Flory–Rehner equation (Figure 3.6), probably accounting for the intrinsic microstructural heterogeneity of the free-radical-generated networks (refer to Section 2.5.2).

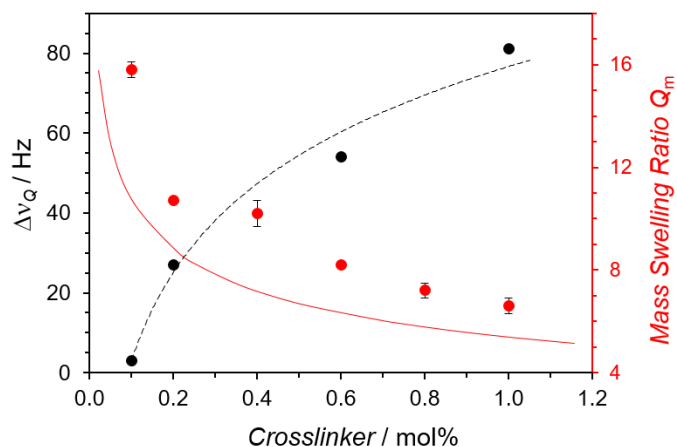


Figure 3.6. Quadrupolar splitting $\Delta\nu_Q$ of the CDCl_3 resonance signal (black), and equilibrium mass swelling ratio Q_m (red) of PS gels prepared with different amounts of DVB. Dashed black line is a guide for the eye, red solid line represents Q_m predicted from Flory–Rehner equation.

Contrarily, the thermal properties of the networks, in particular the glass transition temperature (T_g), was found to be mainly independent of the amount of DVB (see Table 3.1). This kind of thermal behavior was expected, since it has been reported that slightly crosslinked PS networks ($< 5\%$)²⁷¹ exhibit constant T_g values close to pure high molecular weight polystyrene ($T_g \approx 100\text{ }^\circ\text{C}$).²⁷²

3.1.2. PS Sticks with Optimized Mechanical Properties

As mentioned above, the mechanical characteristics of the gels depend on their crosslinking degree, changing from soft and flexible to brittle and fragile networks with increasing amounts of DVB. Indeed, the determination of quadrupolar splittings in chloroform-swollen PS gels with $\text{DVB} \geq 0.2\text{ mol}\%$ proved to be very challenging (Figure 3.7). Highly crosslinked gels break easily when they swell in CDCl_3 and mechanical strain is applied, hindering their application as alignment media. This was observed in compressing and stretching apparatuses, as well as in 5 mm NMR tubes without additional strain. Possibly, the very fast rate of swelling of PS gels in chloroform and the high vapor pressure of this solvent, in addition to the rigidity of highly crosslinked networks, promote their mechanical failure.

SYNTHESIS OF POLYMER-BASED ALIGNMENT MEDIA

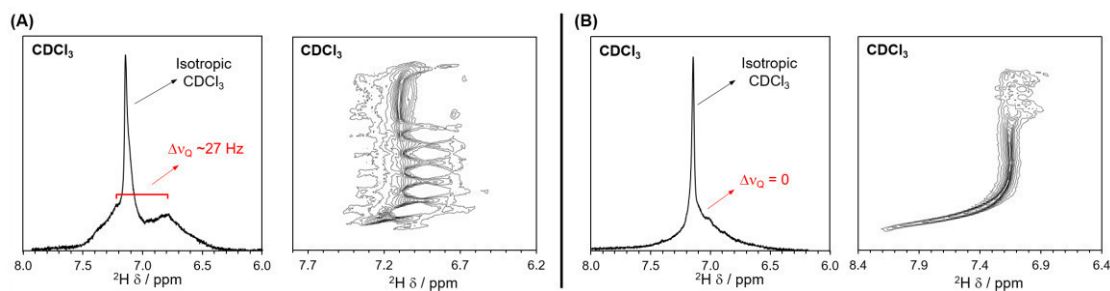


Figure 3.7. CDCl_3 ^2H NMR spectrum (left) and 2D projection of quadrupolar splittings $\Delta\nu_Q$ (right), determined in (A) stick **2** (0.2 mol% DVB, $\Delta\nu_Q \sim 27$ Hz), and (B) stick **3** (0.4 mol% DVB), for which no $\Delta\nu_Q$ could be determined. Cracking and breaking of the gels hinders $\Delta\nu_Q$ determination. The sharp resonance signal in the ^2H NMR spectra corresponds to isotropic CDCl_3 ($\Delta\nu_Q = 0$).

Attempts to pre-swell the networks in a different (less good) solvent like methanol or hexane, followed by swelling in chloroform, did not improve the mechanical stability of the system. Nonetheless, pre-swelling the gels with acetone gave acceptable results and permitted the determination of $\Delta\nu_Q$ values for some gels (see Table 3.1). Notwithstanding, this is not a viable approach for applications in which a second co-solvent might interfere or interact with the analyte (e.g. conformational studies). An additional complication arises from the long equilibration times necessary to achieve full equilibrium swelling of the PS gels in chloroform. Initially weak and broad CDCl_3 splitting signals become narrow only after complete equilibrium between swelling and strain forces in the gel is reached. For the tested PS samples in chloroform, around six weeks were necessary to yield constant lineshapes for the quadrupolar splittings (refer to Figure 8.2A in Appendix 8.1). This excessively long equilibration time promotes evaporation of the solvent, hence further cracking of the gel samples (see Figure 8.2B in Appendix 8.1). To overcome these issues, a robust and flexible gel is required, capable of sustaining macroscopic integrity after being subjected to swelling changes, strain forces and long equilibration times. In this respect, we explored the possibility of adding plasticizers to the copolymerization mixture in order to obtain soft and flexible PS gels at concentrations of DVB > 0.2 mol% (details of the synthesis can be found in the experimental section). It is well known in literature that the addition of diluents (plasticizers) to polymers decreases their glass transition temperature.²⁷¹ Therefore, the effect of three diluents, namely toluene, *N,N*-dimethylformamide (DMF), and bis(2-ethylhexyl) adipate on the properties of PS networks was systematically studied (Table 3.2).

SYNTHESIS OF POLYMER-BASED ALIGNMENT MEDIA

Table 3.2. Swelling ratio and crack formation of PS sticks prepared with different amounts of plasticizers: Toluene, *N,N*-dimethylformamide, and bis(2-ethylhexyl) adipate.

Sample ^a	Toluene	DMF	Adipate	Q_m ^b	Cracks ^c
3	-	-	-	10.2 ± 0.5	Yes
7	1% v/v	-	-	10.1 ± 0.2	Yes
8	5% v/v	-	-	10.1 ± 0.3	Yes
9	10% v/v	-	-	9.5 ± 0.2	Yes
10	20% v/v	-	-	10.4 ± 0.3	No ^d
11	-	5% v/v	-	10.5 ± 0.1	Yes
12	-	10% v/v	-	9.8 ± 0.2	Yes
13	-	15% v/v	-	10.5 ± 0.2	No
14	-	17.5% v/v	-	10.6 ± 0.3	No ^d
15	-	20% v/v	-	11.4 ± 0.2	No ^d
16	-	-	5% v/v	10.5 ± 0.2	Yes
17	-	-	10% v/v	9.9 ± 0.1	Yes
18	-	-	12% v/v	9.6 ± 0.2	Yes
19	-	-	15% v/v	9.4 ± 0.2	Yes
20	-	-	17.5% v/v	9.2 ± 0.2	No
21	-	-	20% v/v	8.6 ± 0.7	No

^a Styrene + 0.4 mol% DVB + 0.1 mol% AIBN + additive. 80 °C, 64 h.

^b Mass swelling ratio, calculated from Eq. 2.55 after free swelling of the sticks in CHCl₃ for 24 h. Standard deviation determined from three independent replicas.

^c Cracks determined visually after fast free swelling of the sticks (ca. 10 mm length) in 5 mL CHCl₃.

^d Obtained sticks were too soft, sticky, and difficult to handle.

An intermediate crosslinking density of 0.4 mol% DVB was chosen in order to reach a relatively high quadrupolar splitting (see Figure 3.6) that can be scaled by mechanical strain, without having too brittle sticks. The T_g of the different samples was obtained from differential scanning calorimetry (DSC), measured on the dry sticks directly after polymerization. On the other hand, the mass swelling ratio Q_m was determined after free-swelling the sticks in chloroform for 24 h. After this swelling period it was observed that the swollen gels presented cracks in their structure. However, increasing amounts of additives rendered the sticks softer and prevented the formation of cracks upon swelling (see Figure 3.8A). Nonetheless, an excessive amount of diluent generated sticky samples that adhere to the glass walls of the reactor, thus becoming very difficult to handle (e.g. networks **10**, **14**, and **15** in Table 3.2).

SYNTHESIS OF POLYMER-BASED ALIGNMENT MEDIA

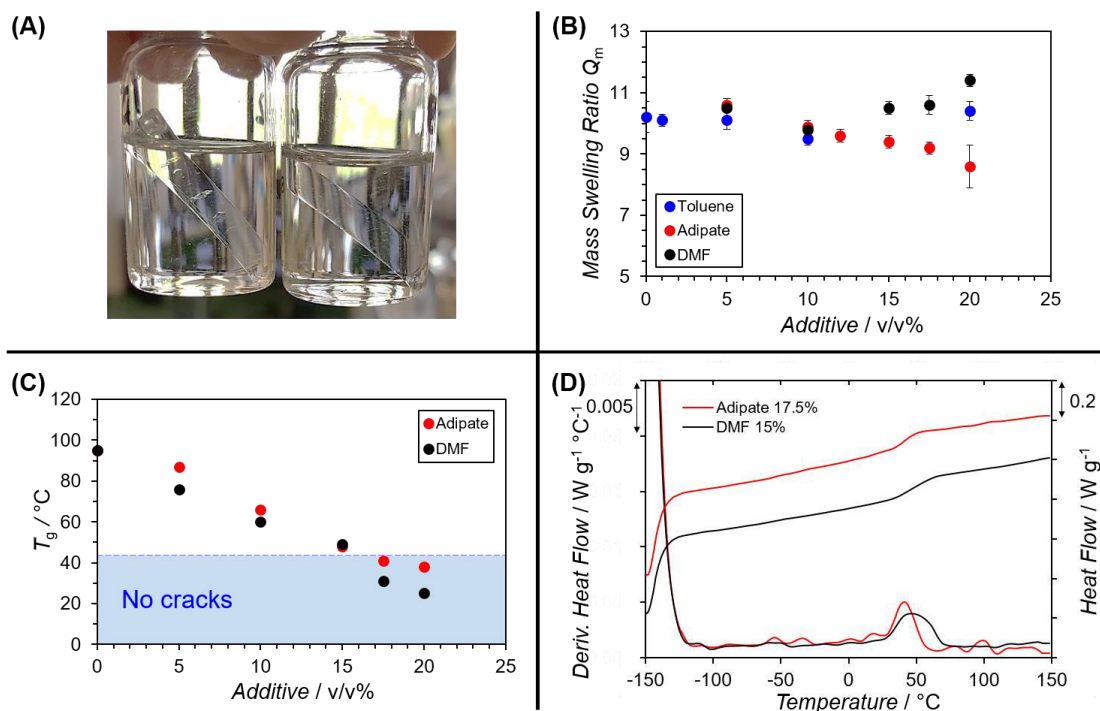


Figure 3.8. (A) PS sticks develop cracks upon free swelling in chloroform (left), which can be avoided by the use of plasticizers (right). (B) Variation of mass swelling ratio Q_m with increasing amounts of additives, toluene (blue), adipate (red), and DMF (black). (C) Decrease of T_g with increasing amounts of additives. No cracks were observed for samples with $T_g \leq 42$ °C. (D) Comparison of heat flow curves (right axis) and their corresponding first derivate (left axis) for networks **13** (black, DMF 15% v/v) and **20** (red, adipate 17.5% v/v), revealing broader transition temperature for **13**.

Furthermore, these additives exert different effects on the swelling behavior of the gels. The addition of adipate causes a decrease in the degree of swelling, while higher swelling ratios are obtained with DMF. Contrarily, networks prepared with toluene present a relatively constant mass swelling ratio (see Figure 3.8B and Table 3.2). However, due to the relatively high evaporation rate of toluene, its plasticizing properties and effect over the mechanical features of the gels did not remain constant over time. Therefore, DMF and adipate (substances with low vapor pressure) were selected for further experiments. Determination of the glass transition temperature for the different DMF- and adipate-containing samples, confirmed the expected decrease in T_g with increasing amounts of additive (plasticizing effect). Additionally, DSC analyses revealed that T_g values below 42 °C are needed to avoid the formation of cracks upon free swelling (Figure 3.8C). The only exception was found for network **13** (DMF 15% v/v, $T_g = 49$ °C), which did not present cracks. Comparison of the derivate of the heat flow curves for samples **13** and **20** (adipate 17.5% v/v, $T_g = 41$ °C)

SYNTHESIS OF POLYMER-BASED ALIGNMENT MEDIA

shows that **13** has a broad transition temperature, encompassing the range $T_g \leq 42$ °C in which cracks are not formed (Figure 3.8D).

According to these results, the minimum amount of plasticizer needed to avoid cracking upon swelling was reached for networks **13** (DMF 15% v/v) and **20** (adipate 17.5% v/v). Due to the lower toxicity and virtually negligible vapor pressure of the adipate in comparison to DMF, sample **20** was chosen for further mechanical characterization. For the determination of the mechanical characteristics of the networks, rheology measurements were performed on disks swollen in toluene. For the synthesis of the PS disks, the same experimental procedure as for the PS sticks was adopted, changing solely the reactor size to afford dry samples of ca. 17 mm diameter and 4 mm height (refer to the experimental section in Chapter 6). The rheological characterization (frequency sweep) was performed on fully swollen disks, after punching a sample of 25 mm diameter. It is important to mention that very slow swelling was necessary for samples with DVB > 0.1 mol% (without plasticizer) to avoid cracking and breaking of the disks (see Figure 3.9A and Figure 8.3 in Appendix 8.1). Figure 3.9B shows a comparison between the storage (G') and loss (G'') moduli for networks **1**, **3**, and **20** (DVB 0.1%, 0.4%, and 0.4% plus plasticizer, respectively). Rheology data for the individual samples can be found in Figure 8.4 in Appendix 8.1.

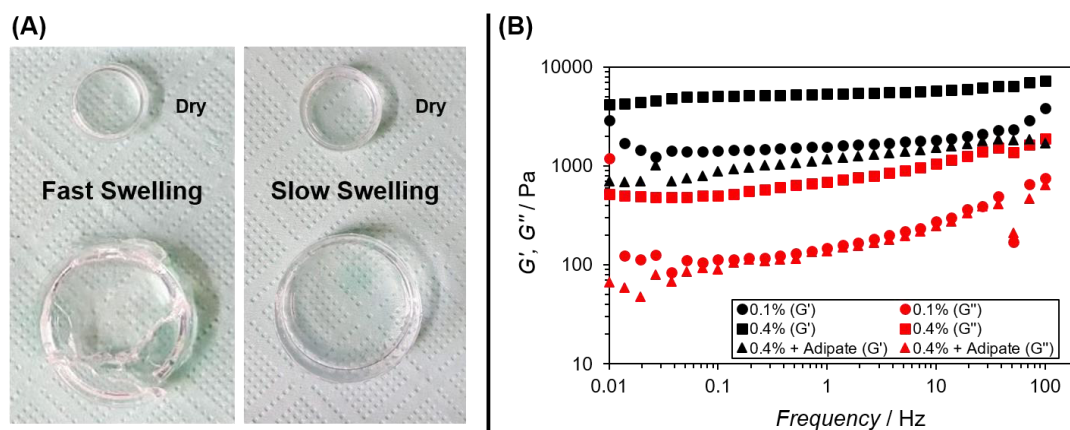


Figure 3.9. (A) Comparison of fast free swelling (left) and slow swelling (right) procedures for PS disks **3** (DVB 0.4 mol%) in toluene. (B) Frequency sweep curves displaying storage (G' , black) and loss (G'' , red) moduli for samples **1** (DVB 0.1 mol%, dots), **3** (DVB 0.4 mol%, squares), and **20** (DVB 0.4 mol% + 17.5% v/v adipate, triangles) fully swollen in toluene.

The storage modulus curves in Figure 3.9B determined for the different PS disks display G' values typical for soft elastic materials. Increasing the crosslinking density from 0.1 mol% (**1**, circles) to 0.4 mol% (**3**, squares), causes a change in the storage modulus of the gels from ca. 1 kPa to ca. 4 kPa, respectively, confirming that higher

SYNTHESIS OF POLYMER-BASED ALIGNMENT MEDIA

crosslinking degrees generate more rigid networks. However, adding adipate render networks **20** (triangles) similarly soft to sample **1** ($G' \sim 1$ kPa), but keeping a crosslinking density of 0.4 mol% DVB. In this way, soft and flexible gels with high crosslinking degree (i.e. high alignment strength) could be obtained.

The strain-induced scalability of the alignment strength achieved with sample **20** was subsequently tested in compression experiments. Dry sticks of ca. 25 mm length were allowed to swell in CDCl_3 inside a compressing apparatus, fixing the plunger position to the stick size until radial equilibrium swelling under compression was reached. Afterwards, the compressive strain was released in small steps (around 1 mm release) until full relaxation of the gel was reached (Figure 3.10A).

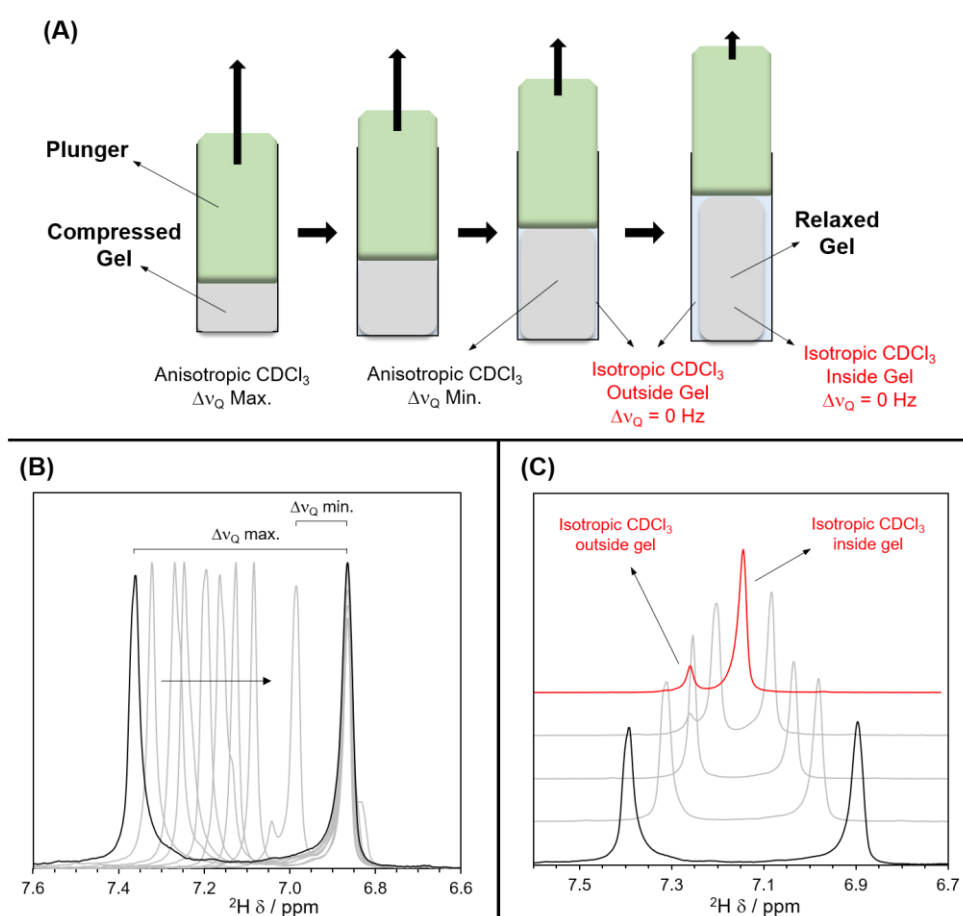


Figure 3.10. (A) Schematic representation of a fully compressed PS gel that is allowed to relax in small decompression steps. (B) Variation of CDCl_3 quadrupolar splitting in network **20** (DVB 0.4 mol%, 17.5% v/v adipate). Fully compressed state is depicted in black ($\Delta\nu_Q$ max.) and intermediate steps in grey. ^2H δ values were artificially fixed at 6.85 ppm (right signal) to facilitate comparison. (C) Variation of CDCl_3 $\Delta\nu_Q$ in network **20** between fully compressed (black) and fully relaxed (red) samples. In the relaxed state, two isotropic CDCl_3 signals can be seen, corresponding to the solvent inside ($\delta = 7.14$ ppm) and outside the gel ($\delta = 7.26$ ppm).

SYNTHESIS OF POLYMER-BASED ALIGNMENT MEDIA

The $\Delta\nu_Q$ values for each decompression stage were thus determined, as depicted in Figure 3.10B. This process permitted the variation of the quadrupolar splitting of CDCl_3 between 49 Hz ($\Delta\nu_Q$ max) and 11 Hz ($\Delta\nu_Q$ min), before the full relaxed state was reached. It can be seen from Figure 3.10C that without compression strain, the isotropic state is obtained ($\Delta\nu_Q = 0$ Hz) in which no splitting of the chloroform signal is observed. Instead, two different isotropic CDCl_3 signals are obtained, one corresponding to the solvent inside the gel (7.14 ppm), and the other assigned to free solvent between the gel and the glass walls (7.26 ppm). The different chemical shifts of the CDCl_3 signal arises from the different chemical environment inside and outside the gel. The high electronic density of the styrene residues in the gel exerts certain shielding effect on the solvent, shifting its resonance signal to high field, in comparison to the free solvent molecules. Remarkably, no mechanical failure or crack formation in the sticks was observed along the duration of the experiment, yielding well-resolved sharp and narrow signals in the NMR spectra. These results represent a critical improvement on the performance of adipate-containing PS gels, in terms of mechanical stability and tunable alignment strength.

Although the addition of plasticizers offers the possibility to obtain soft but robust gels, there are some drawbacks associated with this strategy. First, the amount of additive required to avoid gel cracking is relatively high (around 16 wt.% DMF or 18 wt.% adipate). This implies a significant change in the solvent polarity for the DMF system, and in the case of the adipate, the appearance of the characteristic resonance signals of the plasticizer, which might eventually interfere with the signals of the analyte (compare Figure 3.5A and Figure 3.11).

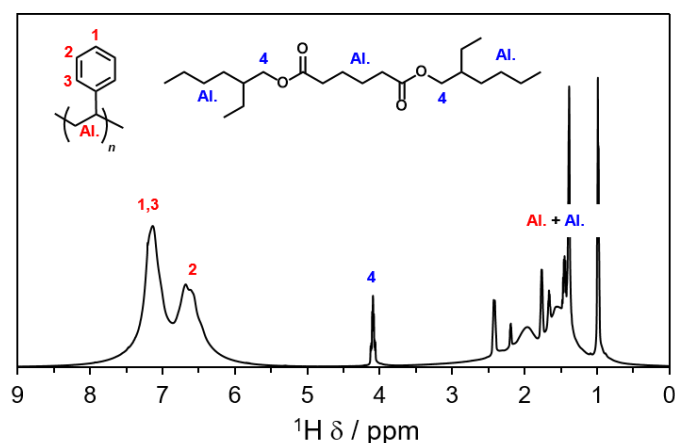


Figure 3.11. ^1H NMR spectrum of PS network **20** (DVB 0.4 mol% + 17.5% v/v adipate) showing the characteristic signals of PS (red) and plasticizer (blue).

SYNTHESIS OF POLYMER-BASED ALIGNMENT MEDIA

Moreover, the plasticizer could be eventually washed out after several swelling steps with fresh solvent, potentially compromising the reusability of the gels. Even though sticks **20** were subjected to five swelling/deswelling cycles in chloroform, after which no crack formation was observed, a long-term decrease in the mechanical stability of the gels cannot be ruled out.

To avoid the implementation of plasticizers, substitution of the aromatic ring of the styrene monomer was investigated as strategy to lower the T_g of 0.4 mol% DVB crosslinked networks. As reported in literature,²⁷³ ring substituents in *meta* position tend to decrease the T_g of the obtained polymers in comparison to unsubstituted PS. Contrarily, *ortho*-substituted polymers have higher glass transition temperature than PS, while *para*-substitution have little effect on the T_g .²⁷³ However, if *n*-alkyl chains are present in the *para* position, a decrease in the glass transition temperature is observed, which depends on the length of the alkyl substituent.²⁷⁴ Furthermore, halogen substituents tend to increase the T_g , except for polymers of 2-fluorostyrene, which show lower T_g than PS.^{273,275} According to this, DVB-crosslinked sticks were prepared from the following commercially available monomers: 2-fluorostyrene, 3-methylstyrene, 4-methoxystyrene, and 4-ethoxystyrene (see experimental section in Chapter 6), and their swelling and thermal characteristics were determined (Table 3.3). Unfortunately, in all four cases studied the formation of cracks in the networks upon swelling could not be avoided. As reported in Table 3.3, the largest reduction of the T_g was obtained for sample **24**, prepared from 4-methoxystyrene ($T_g = 62$ °C). Evidently, the glass transition temperature of these networks still lays above the limit of 42 °C, determined previously for the samples with plasticizers.

Table 3.3. Swelling and thermal properties of networks prepared with different styrene derivatives.

Sample ^a	Monomer	Q_m ^b	T_g	Cracks ^c
22	2-Fluorostyrene	9.5 ± 0.3	85 °C	Yes
23	3-Methylstyrene	12.1 ± 0.3	74 °C	Yes
24	4-Methoxystyrene	11.3 ± 0.2	62 °C	Yes
25	4-Ethoxystyrene	12.4 ± 0.3	92 °C	Yes

^a Monomer + 0.4 mol% DVB + 0.1 mol% AIBN. 80 °C, 64 h.

^b Mass swelling ratio, calculated from Eq. 2.55 after free swelling of the sticks in CHCl₃ for 24 h. Standard deviation determined from three independent replicas.

^c Cracks determined visually after fast free swelling of the sticks in 5 mL CHCl₃.

SYNTHESIS OF POLYMER-BASED ALIGNMENT MEDIA

Therefore, styrene derivatives with long alkyl chains in *para* position²⁷⁴ were prepared, in order to afford stronger reductions of the glass transition temperature of the corresponding gels. The synthesis of monomers containing *n*-pentyl (**26**) and *n*-dodecyl (**27**) groups, was carried out via Steglich esterification of 4-vinylbenzoic acid and primary alcohols (1-pentanol or 1-dodecanol, refer to the experimental section in Chapter 6). *N,N*-Dicyclohexylcarbodiimide (DCC) and 4-(dimethylamino)pyridine (DMAP) were used as coupling agent and catalyst, respectively. In this way, compounds **26** and **27** were obtained in 45–70% isolated yield after purification by column chromatography (Scheme 3.1).



Scheme 3.1. Synthesis route for styrene derivatives **26** and **27**, functionalized with *n*-pentyl and *n*-dodecyl residues, respectively.

Afterwards, crosslinked networks were prepared by copolymerization of **26** or **27** with styrene (in different proportions) and 0.4 mol% DVB, under the same reaction conditions as for pure PS gels (see experimental section). Figure 3.12 displays the variation of the T_g and Q_m of networks prepared with increasing amounts of functional comonomers pentyl-styrene **26** and dodecyl-styrene **27**.

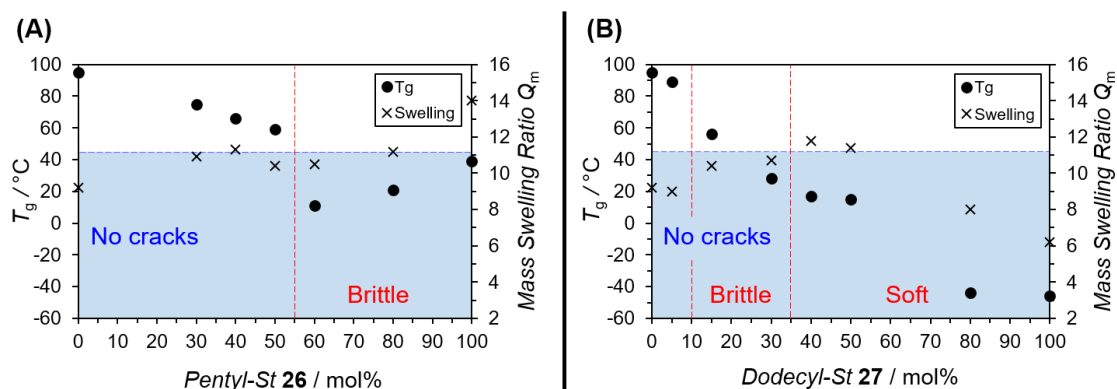


Figure 3.12. Variation of T_g (dots, left axis) and mass swelling ratio (crosses, right axis) of 0.4 mol% DVB crosslinked networks prepared from styrene and different amounts of (A) pentyl-styrene **26**, and (B) dodecyl-styrene **27**. No cracks observed upon swelling for samples with $T_g \leq 42$ °C. Networks prepared with > 55 mol% **26** (or 10–35 mol% **27**) were too brittle in the dry state. Samples obtained from > 35 mol% **27** were very soft and difficult to handle.

SYNTHESIS OF POLYMER-BASED ALIGNMENT MEDIA

It can be seen from Figure 3.12 that the inclusion of *n*-alkyl-substituted styrene moieties into the network enables a stronger decrease in the glass transition temperature reaching values of 11 °C with pentyl-styrene **26** and -46 °C with dodecyl-styrene **27**. Additionally, the T_g can be roughly adjusted over a broad range by changing the feed ratio of comonomer (**26** or **27**) to styrene. Nevertheless, it was not feasible to obtain sticks with optimal mechanical features from these experiments. In the case of the pentyl-styrene networks, more than 55 mol% of **26** was needed to have a $T_g < 42$ °C, and therefore no cracks upon swelling. However, such amount of comonomer render very brittle networks in the solid state (before swelling) which broke easily when recovered from the reactor mold. Similarly brittle and fragile were dodecyl-styrene networks prepared with 10–35 mol% **27**. Probably, the strong van der Waals interactions²⁷⁶ between the *n*-alkyl residues present in the network are responsible for this behavior. Further increments of dodecyl-styrene comonomer **27** generate networks with very low T_g . These gels were very soft and sticky even without any swelling (see Figure 3.12), making difficult their isolation after synthesis, since they tend to adhere to the glass walls of the reactor.

A possible way to overcome these issues would be to copolymerize one of the commercially available styrene derivatives (for instance 3-methylstyrene) with low amounts of **27** (< 10 mol%). This would probably lead to networks with $T_g < 42$ °C, without making predominant the van der Waals associations. Alternatively, the synthesis of styrene derivatives with shorter alkyl chains (*n*-propyl, *n*-butyl) and their copolymerization with styrene could be studied.

3.1.3. Shape Optimization of PS Sticks

Apart from the systematic variation of crosslinking degree and amount of plasticizers (or *n*-alkyl comonomers), a further synthetic parameter that can be optimized is the outer diameter of the PS sticks. This parameter is particularly important in compression experiments, because the diameter of the fully swollen gel, before compression, should be lower than the inner diameter of the NMR tube, so that the gel can expand radially when compressive strain is applied. The adjustment of the swollen diameter of the stick, its degree of crosslinking, and the compressive force applied to it, could permit the formation of a layer of isotropic solvent molecules between the walls of the NMR tube and the anisotropic gel (e.g. third structure in Figure 3.10A). Such fine tuning is desirable for the determination of isotropic and anisotropic properties of a molecule in one single NMR experiment.¹⁴ Therefore, polytetrafluoroethylene (PTFE, Teflon®) tubing of different diameters was used as reaction mold for the synthesis of crosslinked sticks (refer to the experimental section in Chapter 6 and Figure 8.1 in

SYNTHESIS OF POLYMER-BASED ALIGNMENT MEDIA

Appendix 8.1). Teflon[®] is a renowned non-adhesive inert material, resistant to chemical attack and to a wide temperature range. In addition, PTFE tubing of various diameters is readily available from commercial sources. Thus, the synthesis of 0.4 mol% DVB crosslinked samples **17** (adipate 10% v/v), **19** (adipate 15% v/v), and **20** (adipate 17.5% v/v) was carried out in PTFE tubes of 1.5 mm and 1.6 mm internal diameter, and their properties compared with glass-cast counterparts (Table 3.4).

Table 3.4. Swelling and thermal properties of networks prepared in different mold reactors.

Sample ^a	Reactor	Adipate	Q _m ^b	T _g
17	2.2 mm I.D. glass NMR tube	10% v/v	9.9 ± 0.1	66 °C
17-1.6T	1.6 mm I.D. PTFE tube	10% v/v	10.5 ± 0.2	61 °C
19	2.2 mm I.D. glass NMR tube	15% v/v	9.4 ± 0.2	49 °C
19-1.6T	1.6 mm I.D. PTFE tube	15% v/v	10.6 ± 0.2	45 °C
20	2.2 mm I.D. glass NMR tube	17.5% v/v	9.2 ± 0.2	41 °C
20-1.5T	1.5 mm I.D. PTFE tube	17.5% v/v	10.4 ± 0.2	35 °C
20-1.6T	1.6 mm I.D. PTFE tube	17.5% v/v	10.7 ± 0.7	34 °C

^a Styrene + 0.4 mol% DVB + 0.1 mol% AIBN. 80 °C, 64 h. Reactions in glass NMR tubes or in Teflon[®] tubes (marked with T) of 1.5 mm or 1.6 mm internal diameter (I.D.).

^b Mass swelling ratio, calculated from Eq. 2.55 after free swelling of the sticks in CHCl₃ for 24 h. Standard deviation determined from three independent replicas.

The data in Table 3.4 reveal that the material used as reactor mold has an influence in the swelling and thermal properties of the obtained PS networks. Samples prepared from the same precursor solution, but cast from PTFE tubes, exhibited higher degree of swelling and slightly lower T_g values than gels cast from glass NMR tubes. The decrease in the T_g particularly suggests a plasticizing effect taking place in PTFE-cast networks. In fact, the presence of non-crosslinked material washed out from the sticks produced in Teflon[®] tubes, was evidenced in the vials used for swelling after evaporation of the solvent. Plausibly, the non-crosslinked polymers act as diluents in the networks, causing the plasticizer effect observed in PTFE molds. Conversely, such solid residues were not observed when glass-cast gels were swollen. A possible explanation for the incomplete crosslinking observed in Teflon[®] tubes lies in the considerably higher oxygen permeability of PTFE at elevated temperatures (as reported by the manufacturer²⁷⁷), in comparison to borosilicate glass. It is noteworthy to mention that the use of glass reactors also generates networks with smoother surfaces than those obtained from PTFE molds, as observed before in the literature.²⁴⁴ Therefore, such issues were surmounted by performing the polymerization in soda lime

SYNTHESIS OF POLYMER-BASED ALIGNMENT MEDIA

glass capillaries, available in different diameters from commercial manufacturers (1.2 mm and 1.5 mm internal diameter). It can be seen from Table 3.5 that, when the reactor material is kept constant, the only parameter that varies significantly is the diameter of the sticks.

Table 3.5. Swelling and thermal properties of networks prepared in glass reactors of different diameter.

Sample ^a	Reactor	D. Dry ^b	D. Swollen ^c	Q _m ^d	T _g
20	2.2 mm I.D. glass NMR tube	2.2 mm	3.8 mm	9.2 ± 0.2	41 °C
20-1.2G	1.2 mm I.D. glass capillary	1.2 mm	2.1 mm	9.4 ± 0.1	39 °C
20-1.5G	1.5 mm I.D. glass capillary	1.5 mm	2.6 mm	9.4 ± 0.2	39 °C

^a Styrene + 0.4 mol% DVB + 0.1 mol% AIBN + 17.5% v/v adipate. 80 °C, 64 h. Reactions in glass NMR tubes or capillaries (marked with G) of 1.2 mm or 1.5 mm internal diameter (I.D.).

^b Diameter of dry sticks as obtained after polymerization.

^c Diameter of fully swollen sticks after free swelling in CHCl₃ for 24 h.

^d Mass swelling ratio, calculated from Eq. 2.55 after free swelling of the sticks in CHCl₃ for 24 h. Standard deviation determined from three independent replicas.

These results demonstrate the versatility of the crosslinking procedure described in the present section for the preparation of PS sticks as alignment media. The swelling, mechanical, and alignment characteristics of the networks can be tuned in a reproducible fashion by facile adjustment of the initial reaction parameters: (co)monomer concentration, crosslinker amount, presence of plasticizers, and reactor geometry.

3.2. Functional Polystyrene Sticks

In Section 3.1.2 it was demonstrated that copolymerization crosslinking of *n*-alkyl derivatives of styrene (e.g. compounds **26** and **27** in Scheme 3.1) yields networks with different swelling and thermal properties than their pure PS counterparts. This approach was further exploited to introduce different functionalization in the PS-based networks, namely chiral moieties and paramagnetic binding tags.

Generally speaking, chiral alignment media are well known in the recent literature, in particular liquid crystalline (LC) phases.^{2,252,278} Typical examples of optically active liquid crystals with enantiodiscriminating properties encompass cholesteric phases,²⁷⁹ and lyotropic helical homopolypeptides such as poly(γ -benzyl-L-glutamate) (PBLG),²⁸⁰ poly(γ -ethyl-L-glutamate) (PELG),²⁸¹ and poly(ϵ -carbobenzyloxy-

SYNTHESIS OF POLYMER-BASED ALIGNMENT MEDIA

L-lysine) (PCBLL),²⁸² along with their corresponding D-isomers (PBDG, PEDG, PCBDL).^{252,278} These synthetic polypeptide LC phases can be depicted as parallel rods formed by a chiral helix backbone, with achiral glutamate/lysine ester residues pointing out of the rod plane.²⁸¹ More recently, polypeptide LC phases with a helically chiral backbone and chiral ester residues have been reported,²⁸³ as well as LC systems capable of thermoreversible helix inversion.²⁸⁴ Alternatively, enantiodifferentiating liquid crystals can consist of an intrinsically achiral backbone that folds into a helix by introducing chiral elements in the backbone, as is the case for polyarylacetylenes.^{6,285} In contrast to the abundant chiral LC phases, enantiodifferentiating gel-based alignment media are rarely encountered in the literature. The most prominent examples are natural gelatin²⁴⁵ and collagen,²⁸⁶ networks suitable for the analysis of water soluble enantiomers. It has been suggested that the triple helix collagen crosslink junctions of gelatin (refer to Section 2.5.2) permit enantiospecific alignment, analogous to the helical polypeptides PBLG, PELG, and PCBLL described above.²⁷⁸ On the other side, almost no synthetic polymer networks capable of enantiodifferentiation have been developed to date, with the exception of polyacrylamide-based chiral gels, able to swell in DMSO and aqueous media.²⁸⁷ Examples of chiral polymer-based alignment media compatible with apolar solvents are seldom encountered. An elegant approach however is the crosslinking of PBLG polymers to obtain a gel. Such kind of systems combine the chiral properties of liquid crystals with the scalability of gels, and can swell in chloroform, dichloromethane, benzene, dioxane and tetrahydrofurane.²⁵⁷

On the other hand, paramagnetic metal ions with anisotropic magnetic susceptibilities have been extensively used to induce alignment in biomolecular systems.^{7,253} Indeed, molecules with significant magnetic susceptibility tend to partially align at high magnetic fields, since the energy of interaction of the induced magnetic dipoles with the external magnetic field is orientation depending.²⁸⁸ Paramagnetic metalloproteins are characterized by very high molecular magnetic anisotropy (due to the metal ion contribution), hence prone to orient in high magnetic fields to an extent comparable to alignment media.²⁸⁹ If sufficient metal ions are present (usually stoichiometric amounts),⁷ molecular motion in solution is reduced, enabling extraction of RDCs. The incorporation of lanthanide ions (e.g. Ce³⁺, Tb³⁺, Er³⁺, Yb³⁺) into the binding groups of the metalloproteins has been used to induce different macromolecular orientations (since each Ln³⁺ has a particular magnetic susceptibility tensor), helping in the determination of protein structure.²⁸⁹ Additionally, lanthanide labeling has been used for structural determination in protein systems through paramagnetic phenomena, such as pseudocontact shifts and paramagnetic relaxation

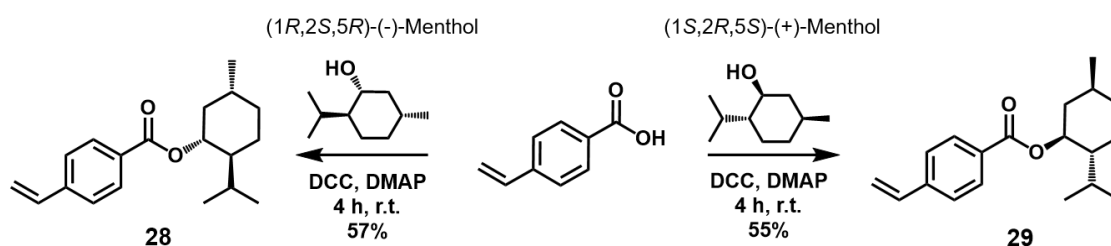
SYNTHESIS OF POLYMER-BASED ALIGNMENT MEDIA

enhancement.²⁹⁰ The site-specific attachment of lanthanide ions within the protein permits the determination of spatial information, because the paramagnetism causes changes in the chemical shifts and signal intensities of the nuclear spins located close to the metal center (up to 40 Å apart).²⁹⁰ However, this strategy has been to date exclusively applied within the analyte molecule itself. The possibility of incorporate lanthanide ions into polymer-based alignment media to study alignment has not been explored so far.

Taking this into account, the targeted functionalization of PS-based alignment media with chiral elements and lanthanide binding tags was investigated. The corresponding results are presented in the following subsections.

3.2.1. PS Gels with Chiral Units

In order to achieve enantiodiscriminating PS gels, the introduction of chiral units – in particular menthol moieties – into the polymer strands was investigated. As reported by Teraguchi et al., menthol-functionalized macroporous PS monoliths showed optical resolution ability via enantioselective adsorption of chiral analytes into the monolith pores.²⁹¹ The possibility of preparing PS alignment media by this strategy was thus explored. First, the synthesis of menthol-styrene derivatives was carried out adapting the procedure described in Ref 291. Since both enantiomers of menthol are commercially available, it was possible to obtain (-)- and (+)-menthol-styrene monomers **28** and **29**, respectively, after Steglich esterification of menthol and 4-vinylbenzoic acid (Scheme 3.2). After purification by column chromatography, monomers **28** and **29** were obtained in 55–57% isolated yield (refer to the experimental section in Chapter 6).



Scheme 3.2. Synthesis route for monomers (-)-menthol-styrene **28** and (+)-menthol-styrene **29**.

Subsequently, **28** and **29** were used as comonomers in the synthesis of DVB crosslinked PS sticks. Optimization of the synthesis conditions allowed the production of alignment media with 5 mol% and 25 mol% of chiral monomer (respect to styrene), at crosslinking density of 0.2 mol% DVB (see experimental section). Hence, mirror

SYNTHESIS OF POLYMER-BASED ALIGNMENT MEDIA

networks prepared from (-)- and (+)-menthol-styrene, as well as (\pm)-racemic networks prepared with equivalent amounts of **28** and **29**, could be synthesized (Table 3.6).

Table 3.6. Swelling and thermal properties of chiral PS networks, prepared with different amounts of (-)- and (+)-menthol-styrene derivatives.

Sample ^a	Ratio St : Mt*	Mt*	Q _m ^b	T _g
30	75 : 25	28 (-)	15.0 \pm 0.2	77 °C
31	75 : 25	29 (+)	14.8 \pm 0.2	78 °C
32	75 : 25	28 + 29 (racemic)	14.9 \pm 0.2	76 °C
33	95 : 5	28 (-)	13.4 \pm 0.1	96 °C
34	95 : 5	29 (+)	13.6 \pm 0.2	95 °C
35	95 : 5	28 + 29 (racemic)	13.3 \pm 0.2	96 °C
2	100 : 0	-	10.7 \pm 0.1	94 °C

^a Styrene (St) + menthol-styrene (Mt*) + 0.2 mol% DVB + 0.1 mol% AIBN. 80 °C, 64 h.

^b Mass swelling ratio, calculated from Eq. 2.55 after free swelling of the sticks in CHCl₃ for 24 h. Standard deviation determined from three independent replicas.

It can be seen from the data in Table 3.6 that networks prepared with equal amounts of opposite enantiomers (or a racemic mixture of both), exhibit the same swelling and thermal behavior (compare samples **30–32** and samples **33–35**). The chirality of the comonomer has no influence on the macroscopic properties of the final network. The $\Delta\nu_Q$ values obtained for the different gels are also independent of the chirality of the menthol derivative used for the synthesis, as exemplified in Figure 3.13 for samples **33–35**.

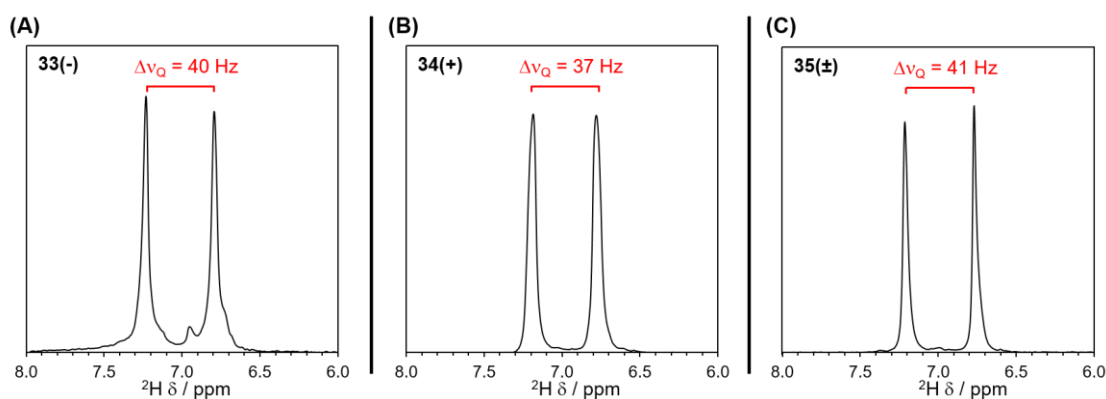


Figure 3.13. CDCl₃ ²H NMR spectra depicting the quadrupolar splittings $\Delta\nu_Q$ obtained in (A) sample **33** (5% (-)-M* **28**, $\Delta\nu_Q = 40$ Hz), (B) sample **34** (5% (+)-M* **29**, $\Delta\nu_Q = 37$ Hz), and (C) sample **35** (5% racemic mixture **28** + **29**, $\Delta\nu_Q = 41$ Hz).

SYNTHESIS OF POLYMER-BASED ALIGNMENT MEDIA

However, the relative amounts of menthol in the PS network does affect the mechanical and thermal characteristics of the gels. An increase in the degree of swelling and a decrease in the T_g was observed for networks prepared with increasing amounts of chiral monomer (see Table 3.6). Furthermore, rheology measurements performed on samples with 25 mol% and 5 mol% (-)-menthol, **30** and **33**, respectively (disks swollen in toluene), showed a significant decrease in the storage modulus after introduction of monomer **28** ($G' \sim 0.2$ KPa), in comparison to plain PS networks **2** ($G' \sim 3$ kPa). Even when low amounts of menthol (5 mol%) were used in the copolymerization, the resulting chiral networks were very soft materials when swollen (Figure 3.14), an advantageous feature since the formation of cracks is diminished (although not completely avoided) without the need for plasticizers. The smaller G' values agree with the higher swelling ratios observed for samples **30** and **33** in comparison to PS gels **2** at the same crosslinking degree (see Table 3.6).

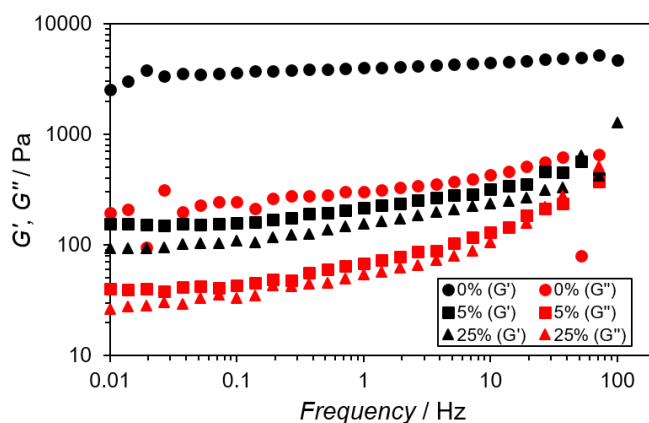


Figure 3.14. Frequency sweep curves displaying storage (G' , black) and loss (G'' , red) moduli for gels **2** (0 mol% **28**, dots), **33** (5 mol% **28**, squares), and **30** (25 mol% **28**, triangles). Measurements were performed on disks fully swollen in toluene.

On the other hand, the preparation of crosslinked gels with > 50 mol% of menthol-styrene required the use of higher amounts of DVB (e.g. 0.6 mol% DVB for 52 mol% **28**, see experimental section). Using this amount of crosslinker, rigid and brittle networks that broke easily even before swelling were obtained. Therefore, it was not possible to obtain 0.2 mol% DVB crosslinked PS gels with menthol contents higher than 25 mol%. In fact, the preparation of monoliths made of 100% chiral monomer was reported with DVB > 23 mol%,²⁹¹ conditions not suitable for NMR alignment media.

In order to gain insights into the microstructure of linear copolymers of styrene and (-)-menthol-styrene **28** (without crosslinking), the comonomer reactivity ratios (r_1 and r_2) were determined, according to the terminal model of copolymerization (refer to

SYNTHESIS OF POLYMER-BASED ALIGNMENT MEDIA

Section 2.1.1). Adapting previously reported experimental protocols,²⁹² polymerizations were carried out in bulk, at feed compositions of 10–95 mol% styrene (St), using diglyme as internal standard (details can be found in the experimental section in Chapter 6). ¹H NMR spectroscopy was used to determine monomer conversion for the different samples, since the resonance signals corresponding to both monomers and the internal standard are well resolved (refer to Figure 8.5 in Appendix 8.1).

For the determination of reactivity ratios it is important that monomer conversion is kept low, in order to avoid compositional drift.²⁵ Herein, conversions were determined by analysis of the reaction mixture before and directly after polymerization. The intensities of resonance signals 2, 5, and 6 from monomer **28** and signals 5, and 6 from styrene, relative to signal 1 from diglyme, were compared before and after reaction, as exemplified in Figure 3.15.

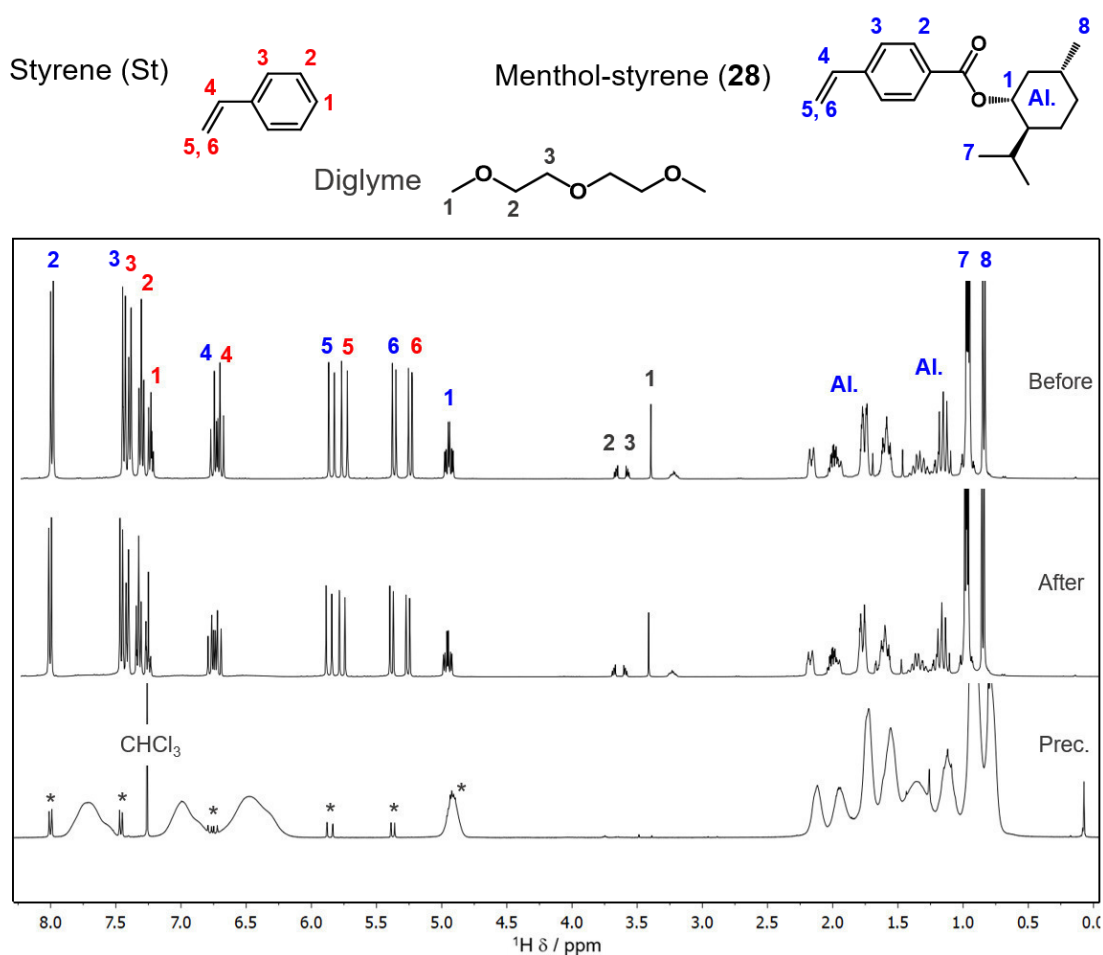


Figure 3.15. ¹H NMR spectra in CDCl₃ of 50% St–**28** reaction mixture before (top) and after (middle) polymerization, and resulting copolymer after precipitation in cold methanol (bottom). Signals of the residual monomer **28** in the precipitated polymer are marked with asterisks.

SYNTHESIS OF POLYMER-BASED ALIGNMENT MEDIA

After the reaction mixture was quenched in ice bath, the polymers were precipitated in cold methanol to remove the excess of monomer, and the copolymer composition was determined via ^1H NMR measurements. The NMR spectra of the purified polymers confirms the effective removal of styrene. However, it was not possible to completely remove the excess of monomer **28** by successive precipitations in methanol (see bottom spectrum in Figure 3.15). Nevertheless, this did not prevent the determination of copolymer compositions, since the integrals of the well-resolved signals of residual monomer (denoted by an asterisk m^*) could be included in the calculations. As depicted in Figure 3.16, the resonance signals of the copolymers in the aromatic region can be assigned to each of the constituting monomers. Taking into account the relative number of equivalent protons, the integral areas of the signals **1**, **2**, and **3** from polystyrene, and **1**, **2**, and **3** from poly(menthol-styrene), can be used to estimate the number of each monomer unit in the copolymer.

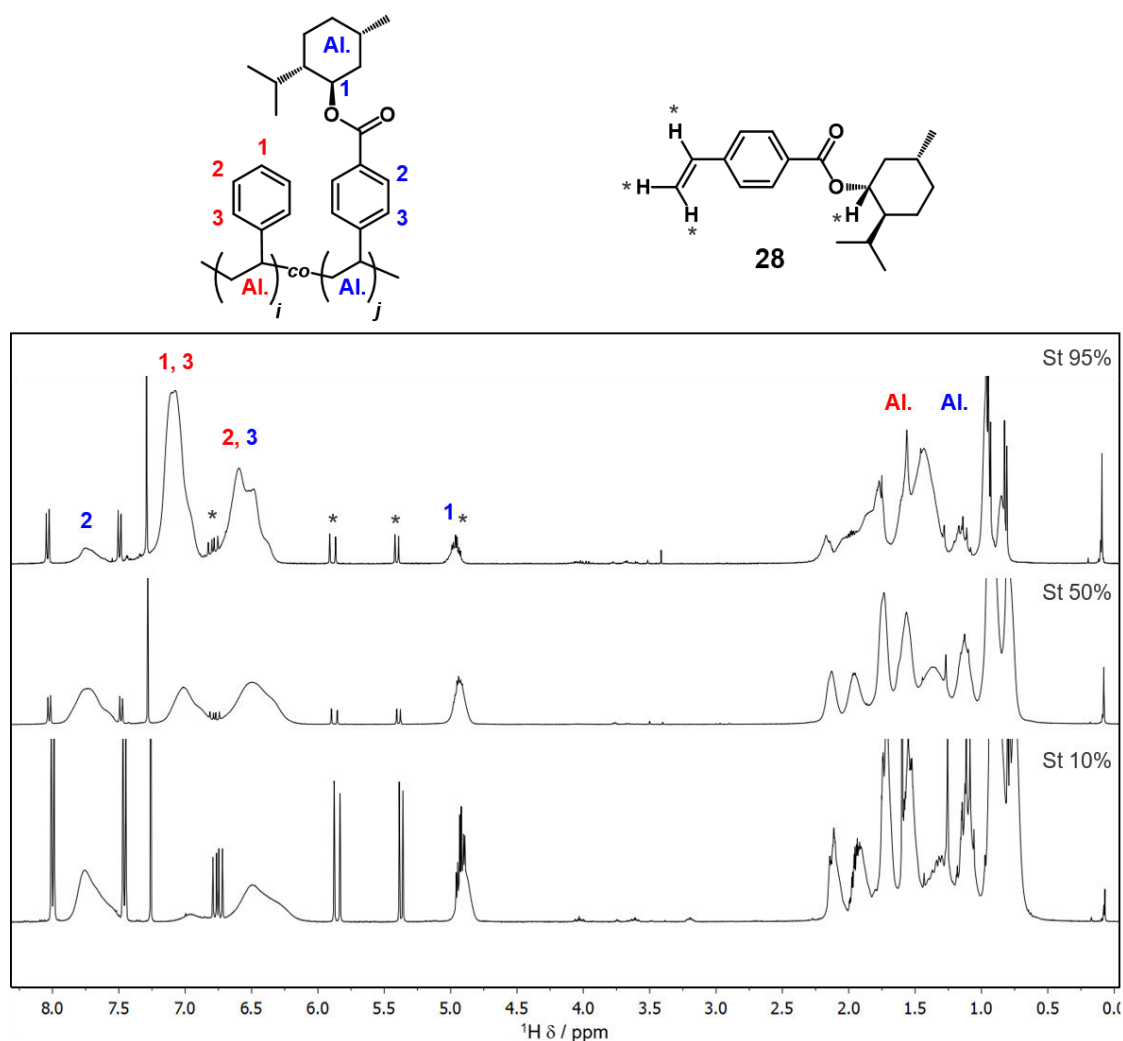


Figure 3.16. ^1H NMR spectra in CDCl_3 of some copolymers (10%, 50%, and 95% St) after precipitation in cold methanol. Signals of the residual monomer **28** used in the calculations are denoted by an asterisk (m^*).

SYNTHESIS OF POLYMER-BASED ALIGNMENT MEDIA

Thus, the following relationships were used: Equations 3.1 and 3.2 for menthol-styrene (**28**) units and Equations 3.3 and 3.4 for styrene (St) units.

$$\%(28) = 100 \frac{\text{Area } 2/2}{(\text{Area } 2/2) + (\text{Area } 1,3/3)} \quad (\text{Eq. 3.1})$$

$$\%(28) = 100 \frac{(\text{Area } 1-m^*)}{(\text{Area } 1-m^*) + (\text{Area } 1,3/3)} \quad (\text{Eq. 3.2})$$

$$\%(St) = 100 \frac{\text{Area } 1,3/3}{(\text{Area } 2/2) + (\text{Area } 1,3/3)} \quad (\text{Eq. 3.3})$$

$$\%(St) = 100 \frac{(\text{Area } 2,3 - \text{Area } 2-m^*)/2}{((\text{Area } 2,3 - \text{Area } 2-m^*)/2) + (\text{Area } 2/2)} \quad (\text{Eq. 3.4})$$

The corresponding values for initial monomer feed, monomer conversion and copolymer composition, as determined by ¹H NMR, are summarized in Table 3.7.

Table 3.7. Initial feed and conversion of monomers **28** and styrene (St), as well as the corresponding copolymer composition.

Entry	Feed				Conversion ^a		Composition ^b	
	28 _{theo} (%)	St _{theo} (%)	28 _{exp} (%)	St _{exp} (%)	28 (%)	St (%)	28 (%)	St (%)
1	5	95	5.6	94.4	3.1	5.2	11.8	88.2
2	10	90	10.2	89.8	4.2	12.1	20.2	79.8
3	15	85	15.2	84.8	5.2	12.4	28.0	72.0
4	25	75	24.5	75.5	2.7	9.4	40.0	60.0
5	50	50	49.1	50.9	9.2	14.7	61.4	38.6
6	75	25	74.8	25.2	30.0	24.8	80.0	20.0
7	90	10	89.7	10.3	10.2	12.7	91.3	8.7

^a Determined by ¹H NMR using diglyme as internal standard.

^b Determined by ¹H NMR after precipitation of the copolymers in cold methanol.

The columns in Table 3.7 highlighted in blue (initial monomer feed of styrene and **28**) and green (composition of styrene and **28** in the copolymer), were used for the determination of the reactivity ratios. The data evaluation was carried out according to the Fineman-Ross, Fineman-Ross inverted, Kelen-Tüdös, and Mayo-Lewis methods. The corresponding values employed for the calculations are given in Table 3.8.

SYNTHESIS OF POLYMER-BASED ALIGNMENT MEDIA

Table 3.8. Data used to determine reactivity ratios.

Entry	x^a	y^b	$F = x^2/y^c$	$G = [x(y-1)]/y$	y/x^2	$(y-1)/x$	$\eta = G/(\alpha+F)^c$	$\zeta = F/(\alpha+F)^c$
1	16.71	7.47	37.34	14.47	0.03	0.39	0.36	0.94
2	8.82	3.95	19.70	6.59	0.05	0.33	0.30	0.90
3	5.60	2.57	12.17	3.42	0.08	0.28	0.24	0.84
4	3.07	1.50	6.30	1.02	0.16	0.16	0.12	0.74
5	1.04	0.63	1.71	-0.61	0.58	-0.36	-0.15	0.43
6	0.34	0.25	0.45	-1.01	2.21	-2.23	-0.37	0.17
7	0.11	0.09	0.14	-1.09	7.26	-7.92	-0.45	0.06

^a $x = [\text{St}]/[\mathbf{28}]$ from comonomer feed (Table 3.7).

^b $y = [\text{St}]/[\mathbf{28}]$ from copolymer composition (Table 3.7).

^c $\alpha = (F_{\max} \cdot F_{\min})^{1/2} = 2.27$

The Fineman-Ross and Fineman-Ross inverted methods employ a linearization of the feed and composition data (parameters x and y in Table 3.8) according to Equations 3.5 and 3.6, respectively. Linear fits of the data retrieved from these equations are used to determine r_1 and r_2 values (Figure 3.17).

$$\frac{x(y-1)}{y} = r_1 \frac{x^2}{y} - r_2 \quad (\text{Eq. 3.5})$$

$$\frac{(y-1)}{x} = -r_2 \frac{y}{x^2} + r_1 \quad (\text{Eq. 3.6})$$

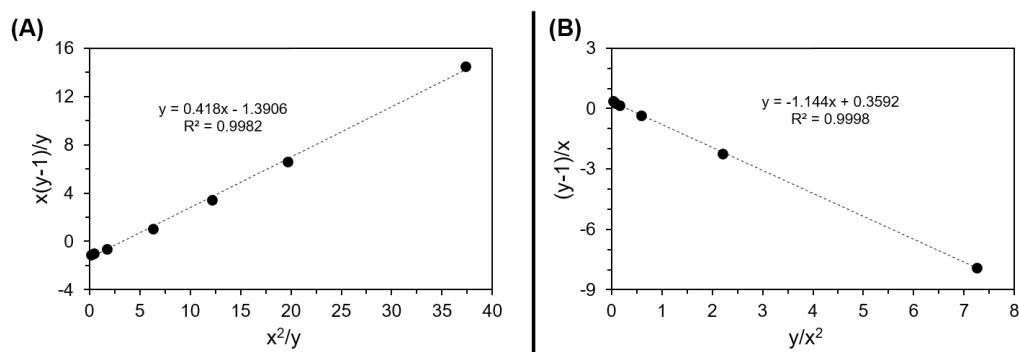


Figure 3.17. Fineman-Ross (A) and Fineman-Ross inverted (B) methods for the determination of reactivity ratios. From the slope and intercept of the linear fits, values of $r_1 = 0.42$, $r_2 = 1.39$ (Fineman-Ross) and $r_1 = 0.36$, $r_2 = 1.14$ (Fineman-Ross inverted) are obtained.

The Kelen-Tüdös method introduces the parameter $\alpha = (F_{\max} \cdot F_{\min})^{1/2}$ where F_{\max} and F_{\min} are the maximum and minimum values of x^2/y from the Fineman-Ross method (see Table 3.8). Linearization according to Equation 3.7 permits the determination of r_1 and r_2 (Figure 3.18).

SYNTHESIS OF POLYMER-BASED ALIGNMENT MEDIA

$$\frac{G}{(\alpha+F)} = \left(r_1 + \frac{r_2}{\alpha}\right) \left(\frac{F}{\alpha+F}\right) - \frac{r_2}{\alpha} \quad (\text{Eq. 3.7})$$

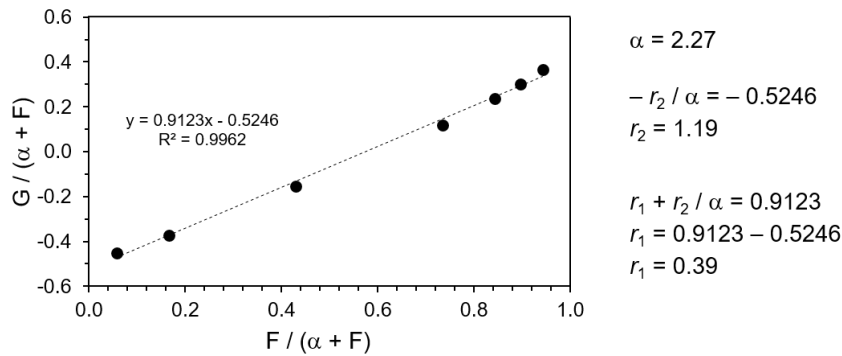


Figure 3.18. Kelen-Tüdös method for the determination of reactivity ratios: $r_1 = 0.39$, $r_2 = 1.19$.

Finally, the Mayo-Lewis method uses the instantaneous copolymer composition equation (Equation 2.17 in Section 2.1.1), derived from the kinetics of monomer disappearance. The relationship between molar fraction of styrene in the copolymer (F_1) and molar fraction of styrene in the comonomer feed (f_1) is given in Equation 3.8. The reactivity ratios r_1 and r_2 can be then retrieved by non-linear least-squares fit of the Mayo-Lewis plot (Figure 3.19).

$$F_1 = \frac{r_1 f_1^2 + f_1(1-f_1)}{r_1 f_1^2 + 2f_1(1-f_1) + r_2(1-f_1)^2} \quad (\text{Eq. 3.8})$$

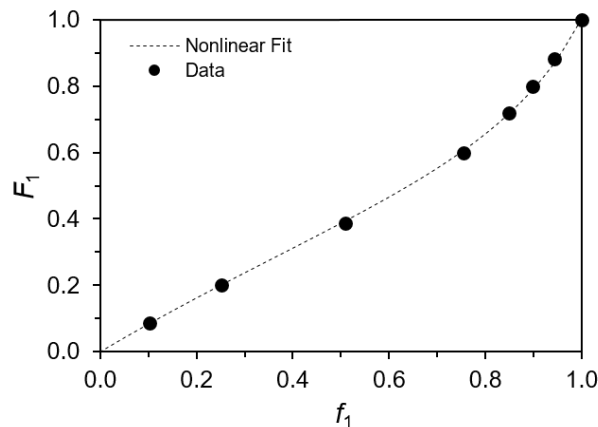


Figure 3.19. Mayo-Lewis method for the determination of reactivity ratios. Non-linear least-squares fit of the Mayo-Lewis plot gives $r_1 = 0.36$, $r_2 = 1.16$.

A summary of the reactivity ratios obtained by the different methods, and their corresponding products $r_1 \cdot r_2$, is given in Table 3.9. The application of the different fits provided r_1 values between 0.36–0.42, and r_2 values in the range 1.14–1.39. For all the methods employed, values of $r_1 < 1$ and $r_2 > 1$ (thus $r_2 > r_1$) were obtained. This

SYNTHESIS OF POLYMER-BASED ALIGNMENT MEDIA

behavior indicates a higher reactivity of monomer **28** in comparison to styrene towards both propagating species. Consequently, the corresponding copolymers would exhibit higher proportions of the menthol-functional monomer at the beginning of the chain, with more styrene segments added at later stages of the polymerization (after depletion of **28**). The product $r_1 \cdot r_2 \approx 0.46$ suggests a deviation from the ideal copolymerization behavior, meaning that a pure statistical arrangement of styrene and menthol-styrene is unlikely to form.²⁰

Table 3.9. Comonomer reactivity ratios r_1 and r_2 for the copolymerization of styrene (St) and **28**.

Method	r_1 (St)	r_2 (28)	$r_1 \cdot r_2$
Fineman-Ross	0.42	1.39	0.58
Fineman-Ross Inverted	0.36	1.14	0.41
Kelen-Tüdös	0.39	1.19	0.46
Mayo-Lewis	0.36	1.16	0.42

As discussed in Section 2.1.1, the terminal model of copolymerization consider that the terminal unit at the propagating chain has sole influence on its reactivity. Since only the self-propagation and cross-propagation constants are taken into account, any contribution of side reactions, polarity and substituent effects are neglected. Although the terminal model of free-radical copolymerization has been extensively used to determine copolymerization kinetics, in the last decade it has been recognized that the assumptions taken in the terminal model lead to inaccurate data.^{27,28} When, for example, penultimate units effects are operative, the results obtained from the terminal model lack physical validity.^{29,30} In such cases the implementation of explicit penultimate models,^{28,293,294} radical and monomer complexes, or monomer partition (Bootstrap model)^{27,28} becomes necessary. Notwithstanding, the terminal model reactivity ratios are suitable for descriptive purposes, quite useful as adjustable engineering parameters.²⁹⁴

3.2.1.1. Enantiodifferentiation in Chiral PS Gels

The functionalization of PS networks with chiral moieties inevitably introduces additional resonance signals stemming from the menthol residues. However, the extraction of RDCs for optically active molecules is not hindered, provided that there is not strong signal overlapping between polymer and analyte (see Figure 8.6 in Appendix 8.1). Two different pairs of chiral molecules were analyzed via NMR

SYNTHESIS OF POLYMER-BASED ALIGNMENT MEDIA

spectroscopy in anisotropic CDCl_3 swollen gels **30–32** ($\Delta\nu_Q \sim 51$ Hz) using a stretching apparatus: On the one hand, both enantiomers of isopinocampheol, (+)- and (-)-IPC (Figure 3.20A), and on the other hand, the diastereomer pair altenuene and isoaltenuene (Figure 3.20B).

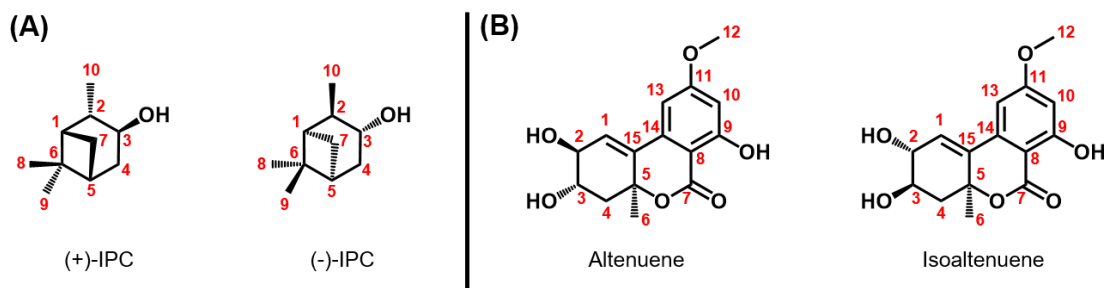


Figure 3.20. Molecular structures of the model chiral analytes: (A) (+)- vs (-)-IPC (isopinocampheol), (B) Altenuene vs isoaltenuene.

As initial approach, the anisotropic behavior of (+)-IPC and (-)-IPC in the chiral PS gels was investigated. Isopinocampheol is considered the golden standard for enantiomeric differentiation via RDC analysis due to its well-known structure (see Figure 3.20A).

The common method to extract RDC values involves, first, the determination of the scalar J -couplings of the molecule in isotropic solution, and second, the total couplings T as obtained in anisotropic media. The difference between T and J yields the residual dipolar couplings.² For the present experiments, one-bond heteronuclear carbon–proton couplings (obtained from two-dimensional P.E.HSQC techniques²⁹⁵) were employed for RDC determination, as exemplified in Figure 3.21 for (+)-IPC in PS gel **31**. This molecule was first analyzed in isotropic medium to extract the J -couplings of each C–H signal. In Figure 3.21A, the $^1J(\text{C},\text{H})$ values for the signals C4–H4a and C4–H4s (highlighted in blue) are 126.89 Hz and 126.63 Hz, respectively. Afterwards, analysis of (+)-IPC in anisotropic PS gel **31** (Figure 3.21B) yielded the total couplings $T = ^1J(\text{C},\text{H}) + D(\text{C},\text{H})$ 128.36 Hz and 129.49 Hz, for signals C4–H4a and C4–H4s, respectively. The difference between the values in anisotropic and isotropic media retrieves the following RDC values: 1.47 Hz for C4–H4a and 2.86 Hz for C4–H4s.

SYNTHESIS OF POLYMER-BASED ALIGNMENT MEDIA

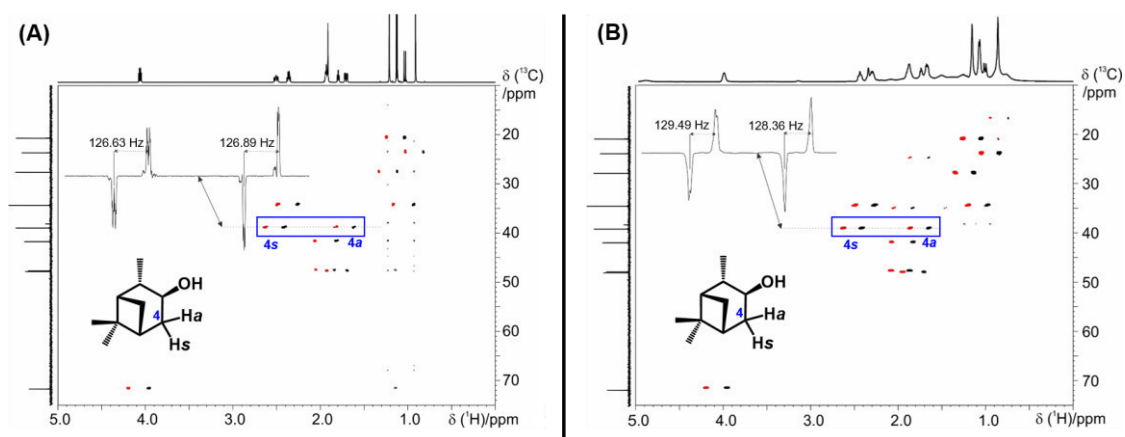


Figure 3.21. (A) P.E.HSQC spectrum of (+)-IPC in isotropic CDCl_3 solution. $^1J(\text{C},\text{H})$ values of signals C4–H4a (126.89 Hz) and C4–H4s (126.63 Hz), highlighted in blue, are given. (B) P.E.HSQC spectrum of (+)-IPC inside swollen gel **31**. The total couplings are obtained in this case, C4–H4a (128.36 Hz) and C4–H4s (129.49 Hz). The difference between T and J couplings yields the RDCs for C4–H4a (1.47 Hz) and C4–H4s (2.86 Hz).

For the enantiodiscrimination experiments, the RDCs of the enantiomer (+)-IPC were determined separately in networks **30** and **31** ((-)- and (+)-gels, respectively), and the obtained values were compared. The difference between both RDC sets (Δ_{RDC}) was subsequently used to assess any enantiodiscrimination taking place for this molecule, as represented schematically in Figure 3.22A.

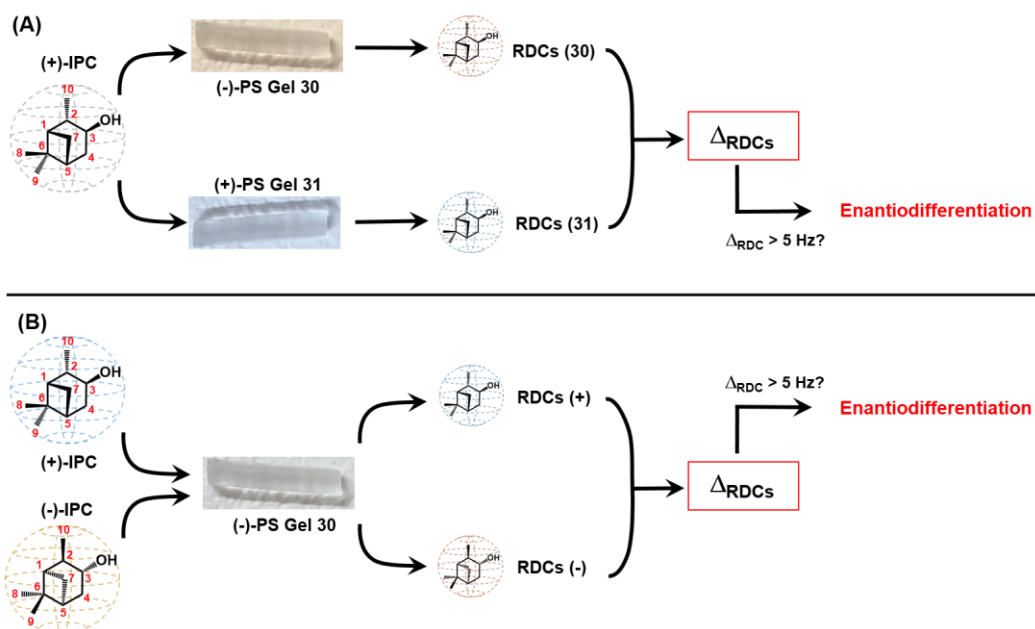


Figure 3.22. (A) Determination of RDCs of (+)-IPC in mirror gels **30** and **31**. The difference between these RDC values (Δ_{RDC}) is used to evaluate enantiodifferentiation. (B) Determination of RDCs of enantiomers (+)-IPC and (-)-IPC in PS gel **30**. The corresponding Δ_{RDC} values are used to evaluate enantiodifferentiation.

SYNTHESIS OF POLYMER-BASED ALIGNMENT MEDIA

In a second experiment, both enantiomers (+)- and (-)-IPC were measured independently in the same alignment media ((-)-gel **30**), and the corresponding Δ_{RDC} values were again calculated (Figure 3.22B). Importantly, to unequivocally quantify enantiodiscrimination, a significant difference in the measured RDCs values is required ($\Delta_{\text{RDC}} \geq 5$ Hz). Lower differences might be biased by experimental artifacts such as shimming drifts or shape inhomogeneities in the gel, thus making impossible to unambiguously ascribe the Δ_{RDC} values to chiral interactions. The results of the experiments depicted in Figure 3.22 are summarized in Table 3.10.

Close inspection of this dataset reveals that, in both cases, there is almost no difference in the RDCs of (+)- and (-)-IPC in the chiral media **30** and **31** ($\Delta_{\text{RDC}} < 1.5$ Hz). The only remarkable exception was observed for the C–H coupling in position 5 (refer to Figure 3.20A), highlighted in red in Table 3.10. From the first experiment (Figure 3.22A), it can be seen that the C5–H5 dipolar coupling of (+)-IPC in (-)-PS gel **30** (RDC = 17.27 Hz), strongly differs from the dipolar coupling determined in (+)-PS gel **31** (RDC = 2.65 Hz). This results in a significant difference between the RDC values ($\Delta_{\text{RDC}} = 14.6$ Hz), clearly indicating that the interaction of the (+)-IPC with the alignment medium is influenced by the chirality of the menthol-PS gel employed.

Table 3.10. RDCs of (+)- and (-)-IPC in chiral PS alignment media **30** and **31**.

Analyte	(+)-IPC	(+)-IPC	Δ_{RDC} (Hz)	(+)-IPC	(-)-IPC	Δ_{RDC} (Hz)
	30 (-)	31 (+)		30 (-)	30 (-)	
Assignment ^a	RDC (Hz)	RDC (Hz)		RDC (Hz)	RDC (Hz)	
C10–H10	-2.29	-2.31	0.02	-2.29	-2.73	0.44
C9–H9	-2.19	-2.26	0.07	-2.19	-2.55	0.36
C8–H8	2.38	2.64	-0.26	2.38	3.10	-0.72
C7–H7_a	-4.53	-3.82	-0.71	-4.53	-4.81	0.28
C7–H7_s	-4.87	-3.28	-1.59	-4.87	-4.39	-0.48
C5–H5	17.27	2.65	14.62	17.27	5.63	11.64
C4–H4_a	1.07	1.47	-0.40	1.07	1.84	-0.77
C4–H4_s	3.04	2.86	0.18	3.04	3.43	-0.39
C3–H3	5.70	6.05	-0.35	5.70	7.21	-1.51
C2–H2	2.76	2.63	0.13	2.76	2.81	-0.05
C1–H1	-1.66	-2.98	1.32	-1.66	-3.71	2.05

^a Atom labels from Figure 3.20A. RDCs determined from directly bonded C–H atoms. Carbon atoms bonded to two different protons (*anti* and *syn* protons) are labeled *a* and *s*, respectively.

SYNTHESIS OF POLYMER-BASED ALIGNMENT MEDIA

Similarly, from the second set of experiments (see Figure 3.22B) it can be observed that, in the same gel (here (-)-menthol-PS **30**), the C5–H5 dipolar coupling of (+)-IPC (RDC = 17.27 Hz) is significantly different than the coupling of (-)-IPC (RDC = 5.63 Hz). Hence, different enantiomers interact differently with the chiral medium, allowing their enantiodiscrimination. However, the difference in RDCs obtained from the second experiment ($\Delta_{\text{RDC}} = 11.6$ Hz) is less pronounced than in the first case. In fact, all RDCs of (-)-IPC determined in the (-)-menthol-PS gel **30** were systematically higher than the RDCs of (+)-IPC in the (+)-menthol-PS gel **31**, in a 0.18–2.98 Hz range (see Table 3.10). A plausible explanation for this inconsistent behavior might lie in small inhomogeneities in the macroscopic shape of the polymer sticks **30** and **31**, or slightly different amounts of (-)- and (+)-menthol units, respectively, present inside the mirror gels. From the current dataset, it is not possible to elucidate the specific interaction mechanism acting between enantiomer and chiral gel, which finally leads to enantiodifferentiation. Notwithstanding, the feasibility of discriminate the enantiomers of IPC in chiral PS networks via RDC analysis was demonstrated for the first time.

The enantiodifferentiating performance of the novel chiral PS media was then compared with the state-of-the-art crosslinked PBLG gels. In the PBLG system reported in literature, different signals can be used to distinguish both IPC enantiomers (C2–H2, C3–H3, C4–H4s, C7–H7a, and C7–H7s).²⁵⁷ Conversely, the chiral PS media herein presented only allows differentiating the signal C5–H5 (see Figure 3.20A), suggesting completely different chiral interactions taking place between analyte and alignment media for the PBLG and PS gels. In any case, the helical PBLG system offers a much lower resolution (only up to 7 Hz Δ_{RDC})²⁵⁷ in comparison to the 12–15 Hz achieved by PS networks **30** and **31**. As discussed before, higher differences in the RDCs diminish the risk of data misinterpretation due to artifacts arising from the experimental conditions. Moreover, the preparation of PBLG gels has the disadvantage of being time consuming. Their synthesis involves first, the polymerization of γ -benzyl-L-glutamate, then crosslinking for at least 20 days, lastly followed by a swelling equilibration time of 1–2 months.²⁵⁷ In contrast, the chiral PS gels require a relatively straightforward synthesis of monomers,²⁹¹ followed by facile free-radical polymerization/crosslinking.

Next, the enantiodiscrimination properties of the chiral PS networks **30–32** were further evaluated using the diastereomers altenuene and isoaltenuene (refer to Figure 3.20B). Following the same procedure as for the IPC system, the RDCs for both analytes were determined via P.E.HSQC measurements,²⁹⁵ as exemplified in Figure 3.23.

SYNTHESIS OF POLYMER-BASED ALIGNMENT MEDIA

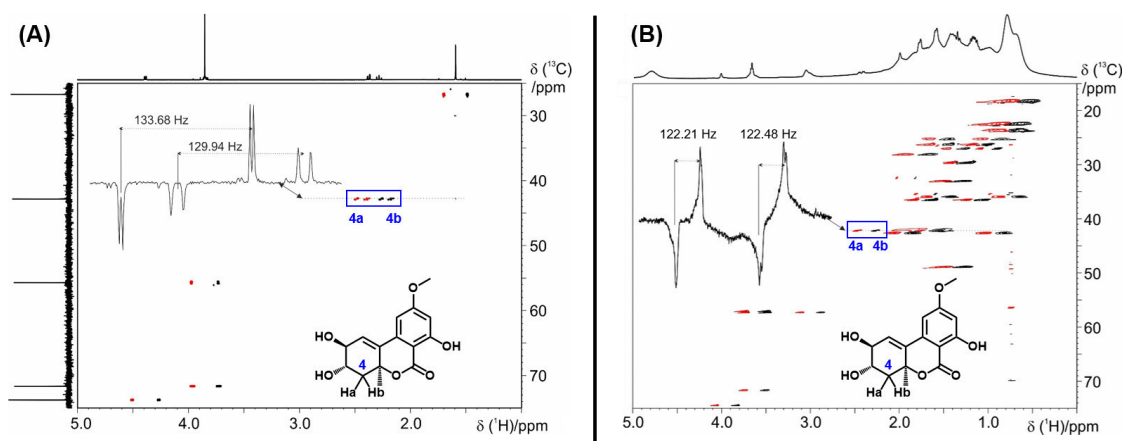


Figure 3.23. (A) P.E.HSQC spectrum of altenuene in isotropic CDCl_3 solution. $^1J(\text{C},\text{H})$ values of signals C4–H4a (133.68 Hz) and C4–H4b (129.94 Hz), highlighted in blue, are given. (B) P.E.HSQC spectrum of altenuene inside swollen gel **31**. The total couplings are obtained in this case, C4–H4a (122.21 Hz) and C4–H4b (122.48 Hz). The difference between T and J couplings yields the RDCs for C4–H4a (-11.47 Hz) and C4–H4b (-7.46 Hz).

In this case, both analytes (altenuene and isoaltenuene) were examined separately, first in (-)-menthol-PS networks **30** (Figure 3.24A), and then in (+)-menthol-PS networks **31** (Figure 3.24B).

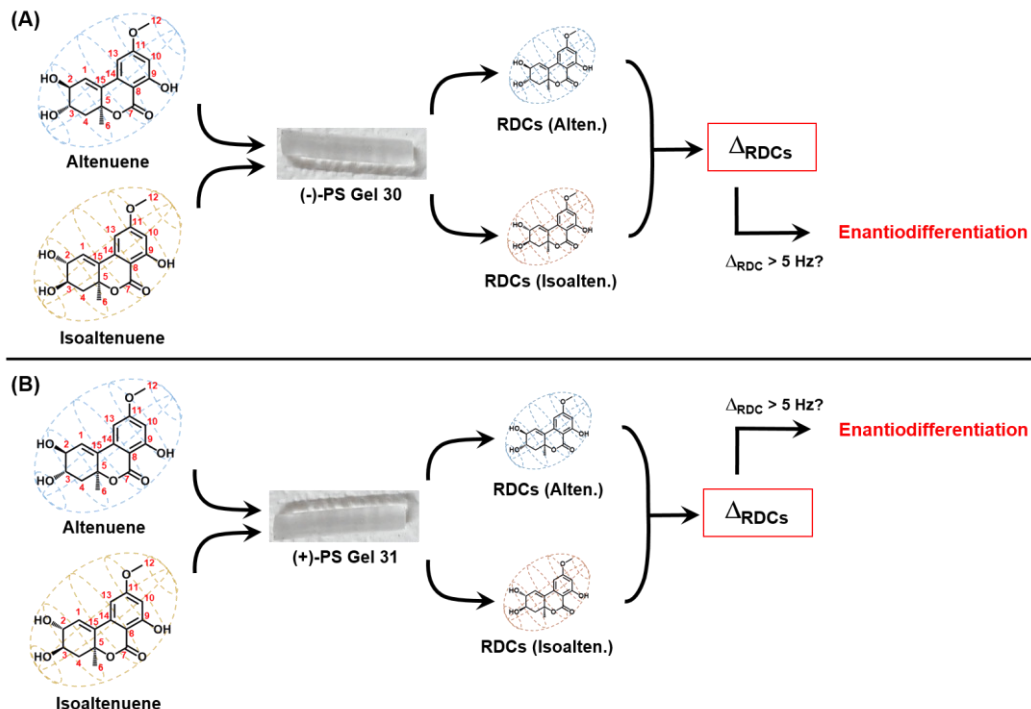


Figure 3.24. (A) Determination of RDCs of the diastereomers altenuene and isoaltenuene in (-)-PS gel **30**. The difference between these RDC values (Δ_{RDC}) is used to evaluate enantiodifferentiation. (B) Determination of RDCs of altenuene and isoaltenuene in (+)-PS gel **31**. The corresponding Δ_{RDC} values are used to evaluate enantiodifferentiation.

SYNTHESIS OF POLYMER-BASED ALIGNMENT MEDIA

Analogous to the IPC system, the corresponding RDC and Δ_{RDC} values for the (iso)altenuene pair were compared in order to assess the possibility of isomeric differentiation in the chiral PS media (Table 3.11). A very good resolution (up to 15 Hz Δ_{RDC}) was also obtained in this case and, contrarily to IPC, not only one but several signals of altenuene and isoaltenuene could be differentiated, highlighted in red in Table 3.11. In the case of (-)-gels **30**, the couplings C13–H13, C4–H4a, C4–H4b, and C2–H2 of isoaltenuene and altenuene exhibited noteworthy Δ_{RDC} values between 8.9–15.5 ppm. On the other hand, in (+)-gels **31** the (iso)altenuene pair showed the highest RDC difference for signals C4–H4b, C3–H3, C2–H2, and C1–H1 (Δ_{RDC} 5.7–14.7 Hz). The fact that different signals are distinguished depending on which of the mirror gels (**30** or **31**) is used, hints to specific spatial interactions between the menthol units in the networks and each of the diastereomeric analytes.

Table 3.11. RDCs of altenuene and isoaltenuene in chiral PS alignment media **30** and **31**.

Analyte Network Assignment ^a	Isoalten.	Alten.	Δ_{RDC} (Hz)	Isoalten.	Alten.	Δ_{RDC} (Hz)
	30 (-)	30 (-)		31 (+)	31 (+)	
C13–H13	-5.86	-15.43	9.57	-6.85	-10.90	4.06
C12–H12	2.51	2.45	0.06	2.40	2.83	-0.43
C10–H10	-3.57	-0.63	-2.95	-2.47	-3.69	1.22
C6–H6	-3.75	-6.46	2.71	-4.14	-5.58	1.44
C4–H4a	-5.60	-14.49	8.89	-7.68	-11.47	3.79
C4–H4b	6.49	-9.00	15.49	7.22	-7.46	14.68
C3–H3	6.98	2.71	4.28	7.72	1.38	6.34
C2–H2	9.58	-3.55	13.14	11.68	-2.63	14.31
C1–H1	-8.17	-8.63	0.46	-10.36	-4.66	-5.70

^a Atom labels from Figure 3.20B. RDCs determined from directly bonded C–H atoms. Carbon atom C4 is bonded to two different protons, here labeled a and b.

These pair of diastereomers have a more planar structure, compared to the rather globular IPC, plausibly explaining why (iso)altenuene interacts differently than IPC with the PS-based chiral media. As reported in Table 3.11, the highest difference was obtained when altenuene and isoaltenuene were analyzed independently in gels of the same chirality (either **30** or **31**). A comparison of the RDCs of the same diastereomer (e.g. isoaltenuene) in mirror or in racemic gels, did not show such exceptionally high Δ_{RDC} values (see Tables 8.1 and 8.2 in Appendix 8.1). Critically, the specific

SYNTHESIS OF POLYMER-BASED ALIGNMENT MEDIA

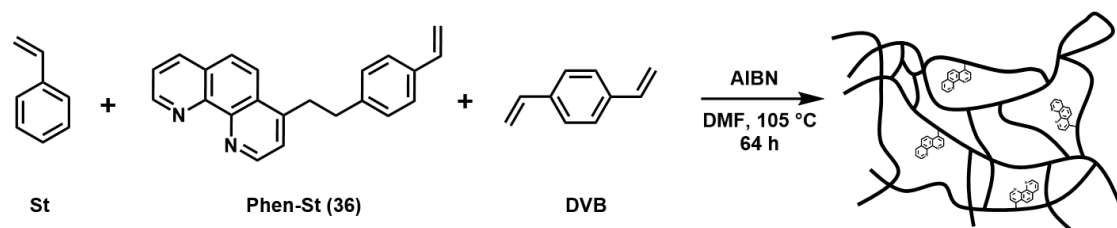
diastereotopic interactions interplaying between chiral PS and chiral analyte, ultimately leading to enantiodifferentiation, cannot be unraveled by these experiments. Nonetheless, the powerful enantiodifferentiating ability achieved by functionalization of PS gels with chiral elements was demonstrated. Although the application of these chiral PS-based alignment media alone does not permit the determination of absolute stereochemical configuration, it will facilitate the structural elucidation of unknown analytes in combination with complementary NMR techniques. Further experiments with networks **33–35** are currently ongoing, in order to evaluate how the amount of chiral moieties in the gel affects the enantiodiscriminating properties.

3.2.2. Lanthanide-Functionalized PS Gels

Paramagnetic metal ions, such as lanthanides, induce the partial orientation of molecules with high magnetic anisotropy in strong magnetic fields.^{7,289} Additionally, lanthanide ions can be used for the determination of distances and relative positions within a molecule. The nuclear spins located nearby the metal center experience paramagnetic relaxation enhancement and pseudocontact shifts, observed as line broadening and signal shift, respectively, in NMR spectra. These phenomena operate through space, giving long range (up to 40 Å) structural information.²⁹⁰ However, the application of paramagnetic phenomena in polymer-based alignment media has not yet been studied. Polymer gels with incorporated lanthanide ions could help to disclose spatial polymer-analyte interactions and provide information on the actual alignment process taking place upon mechanical strain. Therefore, the use of conventional free-radical polymerization methods to prepare PS gels functionalized with lanthanide binding tags was investigated.

Recently, Rothfuss et al. developed a phenanthroline-based approach for the complexation of metal ions into polymers.²⁹⁶ They proved that 1,10-phenanthroline ligands can be incorporated into PS chains via NMP, yielding polymers capable of lanthanide ion complexation (i.e. Eu^{3+} and Tb^{3+}). The resulting materials exhibited strong fluorescence emission, stemming from the phenanthroline-lanthanide complexes. Based on the reported phenanthroline-styrene system,²⁹⁶ the conditions for free-radical copolymerization of styrene, monomer **36**, and DVB were investigated, with the aim of obtaining crosslinked PS networks functionalized with phenanthroline ligands (Scheme 3.3).

SYNTHESIS OF POLYMER-BASED ALIGNMENT MEDIA



Scheme 3.3. Synthesis of PS networks functionalized with 1,10-phenanthroline units by free-radical copolymerization of styrene, phenanthroline-styrene **36**, and DVB.

Contrarily to the chiral monomers **28** and **29**, phenanthroline-styrene **36** is a solid compound insoluble in styrene. Therefore, bulk copolymerization was not feasible for this system, for which DMF was selected as solvent²⁹⁶ (refer to the experimental section in Chapter 6). Optimization of the relative amounts of solvent and monomer **36** respect to styrene, at 0.4 mol% DVB crosslinking, was necessary to afford phenanthroline-functional sticks with adequate physical characteristics (Table 3.12). Inclusion of **36** into the networks promotes the formation of hard and brittle sticks. Thus, a maximum amount of 1.0 mol% of **36** (respect to styrene) could be incorporated into the gels without making them too brittle, for which a DMF content of 14% v/v was required. In order to reduce the solvent percentage to 10% v/v, 0.8 mol% of **36** was employed, improving the handling of the dry networks after synthesis. Further decrease in the amount of comonomer **36**, to reduce the percentage of DMF, led to very brittle and easily breakable networks, which could not be characterized (see Table 3.12). In this respect, the diluent (DMF) plays the dual role of solubilizing monomer **36** and acting as plasticizer.

Table 3.12. Swelling and thermal properties of phenanthroline-functional PS networks, prepared with different amounts of monomer **36** and diluent (DMF).

Sample ^a	Ratio St : 36	DMF	Q_m ^b	T_g
37	99.0 : 1.0	14% v/v	9.9 ± 0.1	52 °C
38	99.2 : 0.8	10% v/v	10.1 ± 0.4	57 °C
39 ^c	99.6 : 0.4	5% v/v	n.d	n.d

^a Styrene (St) + phenanthroline-styrene (**36**) + 0.4 mol% DVB + 0.1 mol% AIBN + DMF. 105 °C, 64 h.

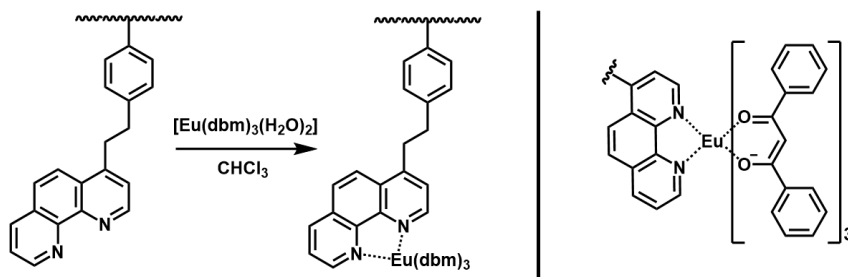
^b Mass swelling ratio, calculated from Eq. 2.55 after free swelling of the sticks in CHCl_3 for 24 h. Standard deviation determined from three independent replicas.

^c Networks were very brittle and broke easily. Their swelling and thermal behavior could not be determined.

Taking this into account, networks **38** were used as model compound for further lanthanide complexation experiments. As previously demonstrated by Rothfuss et al.²⁹⁶

SYNTHESIS OF POLYMER-BASED ALIGNMENT MEDIA

1,10-phenanthroline moieties attached to PS chains readily react with the europium complex precursor $[\text{Eu}(\text{dbm})_3(\text{H}_2\text{O})_2]$, dbm = dibenzoylmethane. The high affinity of the phenanthroline ligands for europium allows the facile displacement of coordination water molecules in the precursor, as depicted in Scheme 3.4.



Scheme 3.4. Complexation of europium ions by phenanthroline ligands present in polystyrene chains.

Due to the strong enhancement of the fluorescence of lanthanide complexes by 1,10-phenanthroline ligands,^{296,297} europium functionalized PS networks would display fluorescence emission properties. This feature allows a straightforward determination of network functionalization by visually inspecting their fluorescence emission. Hence, metal complexation was carried out by swelling dry phen-PS networks **38** in a solution of europium precursor $[\text{Eu}(\text{dbm})_3(\text{H}_2\text{O})_2]$ in chloroform for 24 h (see experimental section). A 1.5-fold excess of europium ions respect to the theoretical amount of phenanthroline units in the network was employed. After coordination of $[\text{Eu}(\text{dbm})_3]^{3+}$ ions to the phenanthroline units in the network took place, the samples were washed with fresh CHCl_3 for further 24 h (three times) in order to remove unbound metal complexes (Figure 3.25). As negative control, plain PS networks **12** were used (refer to Table 3.2). The swelling and thermal characteristics of the resulting gels can be found in Table 3.13.

Table 3.13. Swelling and thermal properties of europium-coordinated PS networks.

Sample	Ratio St : 36	Eu Complex ^a	Q_m^b	T_g
38	99.0 : 0.8	No	10.1 ± 0.4	57 °C
38-Eu	99.2 : 0.8	Yes	11.6 ± 0.1	58 °C
12	100: 0	Yes	9.8 ± 0.2	60 °C

^a Networks swollen in solution of $[\text{Eu}(\text{dbm})_3(\text{H}_2\text{O})_2]$ in CHCl_3 for 24 h and washed with fresh CHCl_3 for 24 h (x3).

^b Mass swelling ratio, calculated from Eq. 2.55 after free swelling of the sticks in CHCl_3 for 24 h. Standard deviation determined from three independent replicas.

SYNTHESIS OF POLYMER-BASED ALIGNMENT MEDIA

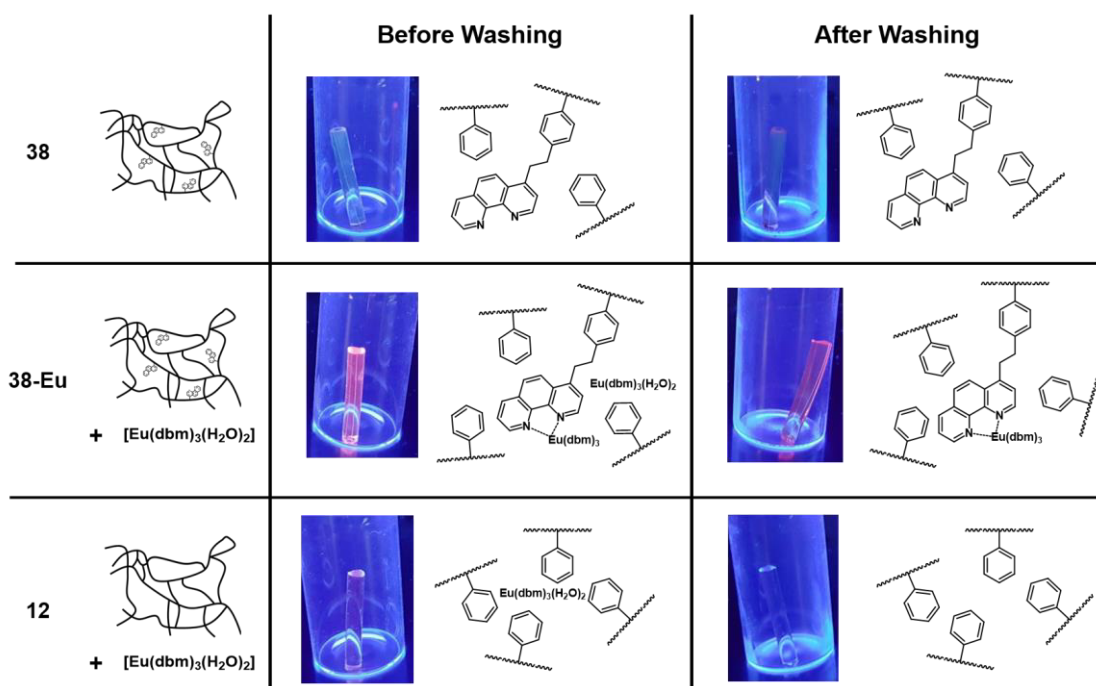


Figure 3.25. Functionalization of PS networks with lanthanide ions. Phenanthroline-PS networks **38** were swollen in a CHCl₃ solution of [Eu(dbm)₃(H₂O)₂] to afford europium-coordinated gels **38-Eu**, characterized by strong red fluorescence emission. After washing the samples to remove excess of lanthanide precursor, the fluorescence emission of **38-Eu** does not disappear, as it is the case for the negative control **12** (plain PS gels).

After several washing cycles, non-functionalized PS networks **12** were not able to retain the adsorbed europium complex, which was simply washed out of the gels. Conversely, the strong red fluorescence emission of networks **38-Eu** remains after washing, corroborating the effective coordination of Eu³⁺ ions to the phenanthroline-containing PS networks **38**. These results demonstrate the feasibility of the herein proposed synthesis route to obtain lanthanide-functionalized polymer gels. The corresponding application of networks **38** and **38-Eu** as alignment media in anisotropic NMR experiments is currently ongoing.

3.3. Summary and Outlook

In summary, the systematic study of the conditions involved in the synthesis of free-radical-based PS networks permitted the optimization of their mechanical properties for their application as alignment media. The alignment strength of the gels (measured as CDCl₃ quadrupolar splitting), could be modified within a range of $\Delta\nu_Q = 3\text{--}81$ Hz, by simply changing their crosslinking degree from 0.1–1.0 mol% DVB. Nevertheless, crosslinking densities > 0.2 mol% DVB rendered the networks brittle and

SYNTHESIS OF POLYMER-BASED ALIGNMENT MEDIA

easily breakable (formation of cracks upon swelling). To diminish their mechanical failure, the addition of plasticizers was investigated. In general, when the T_g of the gels was reduced to at least 42 °C, the incidence of cracks was avoided (plasticizing effect). In this way, flexible but robust gels with optimal mechanical characteristics could be obtained by addition of 17.5% v/v of bis(2-ethylhexyl) adipate as plasticizer (at 0.4 mol% DVB crosslinking). These gels exhibited excellent strain-induced alignment properties without suffering mechanical failure. When fully compressed, a maximum alignment strength of $\Delta\nu_Q = 49$ Hz was afforded, which could be adjusted at will by small decompression steps, until a minimum of $\Delta\nu_Q = 11$ Hz was reached. The fully relaxed isotropic state of the gel ($\Delta\nu_Q = 0$) was attained by further decompression, without any crack formation during the whole experiment. Additional studies are currently ongoing in order to assess the reusability of these adipate-containing gels. Ultimately, it is envisioned that analyte molecules could be pumped into the gel, adequately analyzed by strain-tuning of the alignment strength to a desired $\Delta\nu_Q$ value, and then pumped out of the networks. These analysis cycles could be then repeated several times with different analytes, without changing the alignment medium.

Nonetheless, the long-term stability of the gels containing plasticizers cannot be guaranteed because, eventually, the additives could be washed out of the networks after several swelling cycles. Consequently, the possibility of employing styrene derivatives for the network synthesis to modulate their mechanical and thermal behavior, was explored. First, commercially available monomers (2-fluorostyrene, 3-methylstyrene, 4-methoxystyrene, and 4-ethoxystyrene) were used for the preparation of PS networks. However, the lowest T_g that could be afforded by this approach was 62 °C, still too high to avoid cracking of the samples. Then, pentyl- and dodecyl-styrene derivatives were synthesized and employed as monomers for network formation. A stronger decrease in the T_g was afforded for the alkyl-networks, which could be roughly modulated by copolymerization with styrene at different ratios. However, relatively high amounts of alkyl-monomer were needed to reach T_g values < 42 °C (more than 55 mol% pentyl- or 15 mol% dodecyl-styrene). Although the formation of cracks upon swelling was avoided, these networks were fragile and brittle in the dry state, probably due to strong van der Waals interactions between the alkyl residues. Therefore, further studies are needed in order to afford networks with optimum mechanical characteristics using styrene derivatives. The use of shorter alkyl-chain (*n*-butyl or *n*-propyl) derivatives and their copolymerization with the commercially available monomers mentioned above will be topic of future investigations.

SYNTHESIS OF POLYMER-BASED ALIGNMENT MEDIA

Furthermore, the functionalization of PS networks with chiral units was achieved. Gels with (-)- and (+)-menthol moieties (5 mol% and 25 mol% menthol units respect to styrene) could be obtained by free-radical copolymerization crosslinking of styrene, DVB and (-)- or (+)-menthol-styrene derivatives. Determination of the copolymerization reactivity ratios between styrene ($r_1 \approx 0.38$) and menthol-styrene ($r_2 \approx 1.22$) suggested a higher reactivity of the menthol monomer towards both propagating species, according to the terminal model of copolymerization. Plausibly, more menthol units are incorporated at the beginning of the polymer chain, adding gradually more styrene segments as the polymerization proceeds. The product $r_1 \cdot r_2 \approx 0.46$ hints to a non-ideal copolymerization behavior, implying that the arrangement of the comonomers in the gel is not completely random. Afterwards, the enantiodifferentiation ability of the 25 mol% menthol-PS gels was tested with two pairs of optically active model compounds. On the one hand, the enantiomer pair (-)-IPC and (+)-IPC (golden standard for enantiodifferentiation via RDC) exhibited only few different RDCs when analyzed either in the (-)-menthol-PS gels or in the (+)-menthol-PS gels. However, the resolution obtained with the novel chiral PS gels (up to 15 Hz Δ_{RDC}) was higher than the state-of-the-art crosslinked PBLG media (up to 7 Hz Δ_{RDC}).²⁵⁷ On the other hand, the diastereomer pair altenuene and isoaltenuene showed markedly different behavior when analyzed in the (-)- and (+)-menthol gels, again with a remarkable high resolution (ca. 15 Hz Δ_{RDC}). Although the specific interactions between chiral analyte and chiral PS media are not yet understood, these results serve as proof of principle for PS gels with enantiodifferentiating properties, achieved by functionalization with chiral units (in this case menthol moieties). The influence of the amount of menthol units on the enantiodiscriminating properties of the gels is currently under investigation, using the 5 mol% menthol-PS networks.

Finally, the functionalization of the PS gels with lanthanide binding tags was demonstrated. 1,10-phenanthroline ligands (0.8 mol% respect to styrene) could be successfully incorporated into the network strands by conventional free-radical copolymerization, using 10% v/v DMF as solubilizing and plasticizing agent. Then, facile europium complexation was afforded by swelling the gels in a $[\text{Eu}(\text{dbm})_3(\text{H}_2\text{O})_2]$ precursor solution, yielding red fluorescent $\text{Eu}(\text{dbm})_3$ -containing PS networks. After extensive washing, the fluorescence emission of the Eu-PS gels do not disappear, giving a visual cue for effective lanthanide coordination. Since paramagnetic metal ions are commonly used for protein alignment,^{7,253,289} it will be interesting to evaluate the effect of the europium in the alignment properties of the novel gels. Moreover, it is expected that the paramagnetic relaxation enhancement and pseudocontact shifts,²⁹⁰

SYNTHESIS OF POLYMER-BASED ALIGNMENT MEDIA

exerted on analyte molecules inside the Eu-PS gels, will provide clues to understand the alignment process. Depending on the results of the preliminary anisotropic NMR experiments, the local concentration of europium ions will be adjusted to avoid excessive line broadening, thus loss of information. Afterwards, the identity of the lanthanide ion (Ln^{3+}) will be varied in order to modulate the paramagnetic effects.²⁹⁰ Additionally, the functionalization of the PS gels with alternative spinlabel paramagnetic systems (e.g. nitroxide radicals) will be subject of future investigations.

CHAPTER 4:

TOWARDS HOMOGENEOUS ALIGNMENT MEDIA

In the previous chapter, the synthesis of polymer-based alignment media was investigated, improving the performance of the state-of-the-art gels for anisotropic NMR spectroscopy. However, conventional free-radical crosslinking copolymerization methods employed for the synthesis of the gels inevitably introduce a high degree of heterogeneity in the network internal structure.¹⁶ As outlined before in Section 2.5.2, free-radical-based gels exhibit inhomogeneous distribution of meshes and connectivity defects such as loops, dangling ends and entanglements. Such heterogeneities might have adverse effects in the resolution of the resonance signals in NMR spectra recorded in the polymer gels. Moreover, the structural characterization of this kind of networks is limited to their macroscopic properties, retrieved from classical swelling and rheology techniques (refer to Section 2.5.3). If only classical characterization methods are employed, a detailed picture of the local imperfections of the gel remains elusive.^{15,225} Consequently, incomplete knowledge of the network microstructure prevents the development of models that describe the behavior of analytes inside polymeric alignment media.

Taking this into account, the preparation of homogeneous networks as potential alignment media was investigated. End-linking of well-defined polystyrene precursors (obtained by RAFT polymerization) was explored as synthesis strategy to obtain gels

Parts of the present chapter were adapted with permission from Ref 298: D. Estupiñán, T. Gegenhuber, J. P. Blinco, C. Barner-Kowollik, L. Barner, *ACS Macro Lett.* **2017**, *6*, 229. Copyright 2017, American Chemical Society (Section 4.1); and with permission from John Wiley and Sons from Ref 299: D. Estupiñán, C. Barner-Kowollik, L. Barner, *Angew. Chem. Int. Ed.* **2018**, *57*, 5925 (Section 4.2). Unless otherwise stated, D. Estupiñán designed and performed all experiments. Acquisition of mass spectrometry data presented in Section 4.2 was conducted by J. Steinkönig. NMR relaxometry measurements were performed by C. Pfeifer. Compounds **41** and **68** were kindly provided by K. Hildebrandt and F. Cavalli, respectively. General project supervision and fruitful scientific discussions were done by L. Barner and C. Barner-Kowollik.

TOWARDS HOMOGENEOUS ALIGNMENT MEDIA

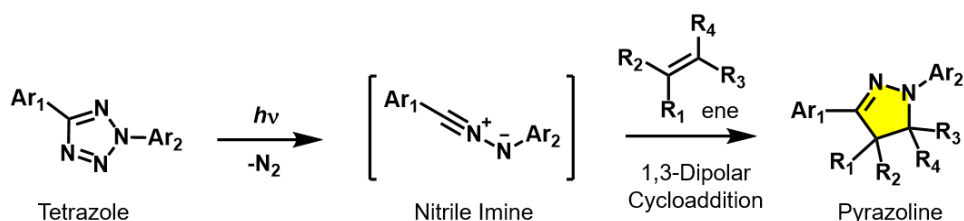
with reduced structural heterogeneity (refer to Section 2.5.2). The UV-induced NITEC reaction (Section 2.4.2) was first selected as end-linking method due to its high efficiency and pro-fluorescent behavior.^{55,208} Importantly, the fluorescence emission of the NITEC product was exploited as alternative characterization method for polymer systems. In Section 4.1 it was demonstrated that conversion in step-growth polymers prepared via NITEC protocols can be monitored by fluorescence spectroscopy.²⁹⁸ The scope of this methodology was then expanded to crosslinked systems, as discussed in Section 4.2. The formation of intrinsically fluorescent networks was hence achieved, which were subsequently degraded^{174,223} to enable their spectroscopical analysis in solution. Critically, this strategy represents the first example of direct quantification of the crosslinking density of a polymer network, using simple fluorescence emission readouts.²⁹⁹ Although a high level of control and characterization was achieved with the NITEC networks, it was not possible to scale up this procedure to produce cylindrical sticks, necessary for the application as alignment media (refer to Chapter 3). Therefore, Michael-type thiol-ene chemistry¹⁷⁵ was utilized as ligation mechanism, as described in Section 4.3. This approach permitted the reaction of α,ω -thiol-functional polystyrene chains with tetrafunctional acrylates, yielding insoluble end-linked networks. Thiol-ene gels with different mesh sizes were thus obtained, by employing PS precursors of different chain lengths. Furthermore, when PS chains of disparate molecular weight were mixed and used as precursors, heterogeneity could be deliberately introduced into the microstructure of the networks. Subsequently, the different networks were characterized by swelling experiments and NMR relaxometry, and compared with free-radical-based gels of similar crosslinking degrees. As final remark, thiol-ene gels prepared from single and mixed molecular weight PS precursors were shaped into sticks in order to assess their applicability as alignment media. Anisotropic NMR experiments on these end-linked networks and their free-radical counterparts are currently ongoing.

4.1. NITEC Chemistry Applied to Step-Growth Polymers

The importance of photochemistry in polymer science was highlighted previously in Section 2.4.2. Among the myriad of photoreactions available, the so-called nitrile imine-mediated tetrazole-ene cycloaddition (NITEC) reaction has gained recent interest for polymer and surface modification.¹³²⁻¹⁴³ The facile functionalization of materials via NITEC chemistry lies in the high reactivity of the nitrile imine dipole generated after irradiation of aryltetrazoles with UV light (refer to Scheme 2.10). If this intermediate is

TOWARDS HOMOGENEOUS ALIGNMENT MEDIA

formed in the presence of activated enes, rapid 1,3-dipolar cycloaddition at ambient temperature takes place, producing a fluorescent five-member pyrazoline ring (Scheme 4.1).



Scheme 4.1. Formation of pyrazolines through UV-induced nitrile imine-mediated tetrazole-ene cycloaddition (NITEC) reaction.

Probably the most attractive feature of this process is the pro-fluorescent behavior associated to the NITEC reaction. Starting from non-fluorescent tetrazole and alkene precursors, a strongly fluorescent pyrazoline adduct is obtained. Therefore, this photoreaction has been employed as a self-reporting modification strategy for many different macromolecular systems such as biomolecules,^{130,144} cellulose,^{105,137,142} step-growth polymers,¹³³ polymeric^{129,134,141,143,151,300} as well as inorganic³⁰¹ nanoparticles, polymerosomes,³⁰² molecular adhesives,³⁰³ and polymer gels,^{55,164,208,304} among others. In this way, inspection of the fluorescence emission of the material after reaction serves as visual cue for effective functionalization. Nonetheless, the application of this pro-fluorescent approach for quantification purposes was so far not reported in literature. Hence, the formation of step-growth polymers via NITEC was selected as model system to investigate the quantification potential achieved with this process.

There is only a limited number of reports on photochemical step-growth polymerization procedures in the recent literature.³⁰⁵⁻³⁰⁷ In fact, the formation of pure photoinduced step-growth polymers using photo-enol^{308,309} and NITEC¹³³ chemistries has been pioneered in the group of Barner-Kowollik. In the present work, a bifunctional tetrazole was reacted with a bifunctional maleimide in a NITEC process to obtain AA–BB step-growth polymers. Hence, each repeat unit in the polymer is composed of a fluorescent pyrazoline moiety (Figure 4.1), enabling the determination of monomer conversion via fluorescence spectroscopy.

TOWARDS HOMOGENEOUS ALIGNMENT MEDIA

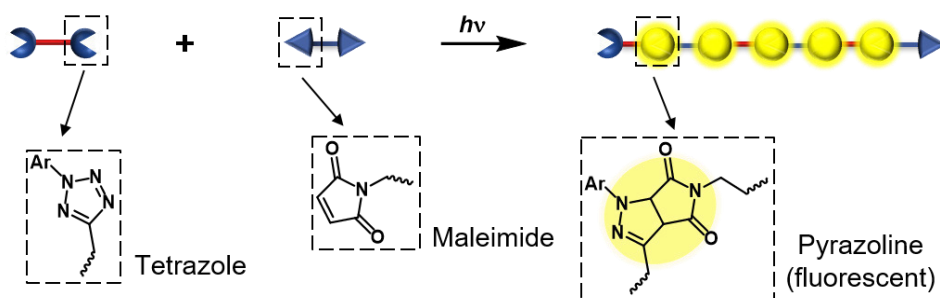
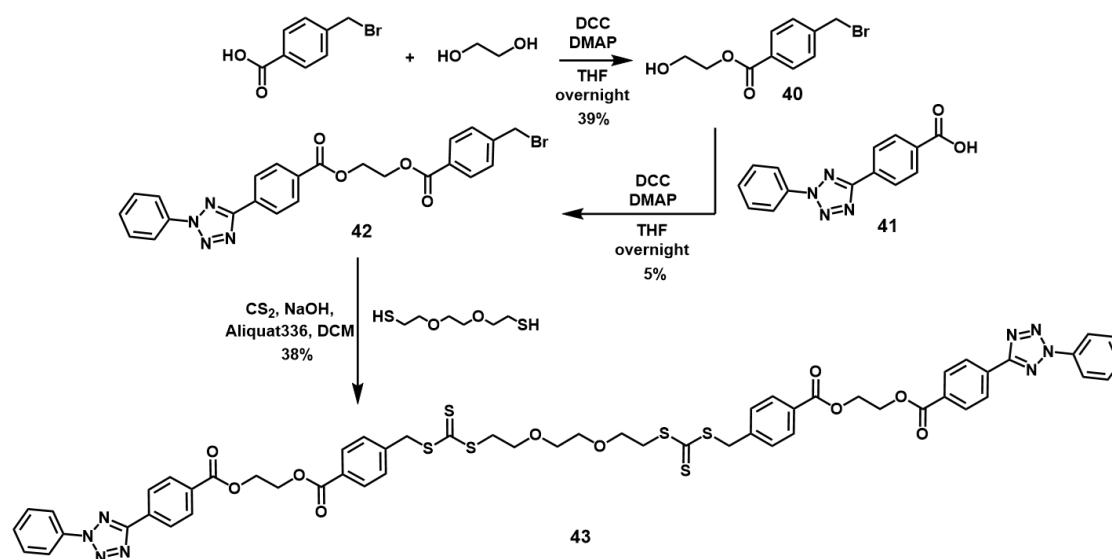


Figure 4.1. NITEC approach to fluorescent AA-BB step-growth polymers by reaction of a bifunctional tetrazole and a bifunctional maleimide.

4.1.1. Monomer Design

A symmetrical tetrazole-containing trithiocarbonate-based RAFT agent **43** was specially designed as initial monomer, adapting previous literature procedures.^{55,310} The synthesis route is depicted in Scheme 4.2. Compound **40** was first prepared and attached to tetrazole derivative **41** via Steglich esterification protocols, to obtain the bromide precursor **42**. Afterwards, **42** was reacted with a bifunctional thiol and carbon disulfide CS_2 (in the presence of the phase-transfer catalyst Aliquat336), to yield the bifunctional tetrazole-RAFT agent **43**. Details of the experimental procedures can be found in Chapter 6.



Scheme 4.2. Synthesis route for the bifunctional tetrazole-chain transfer agent **43**.

Afterwards, the step-growth polymerization of AA-BB monomers **43** and the commercially available 4,4'-methylenebis(*N*-phenylmaleimide) **44** (Figure 4.2A), was carried out at ambient temperature under UV irradiation ($\lambda_{\text{max}} = 320 \text{ nm}$), in a custom-

TOWARDS HOMOGENEOUS ALIGNMENT MEDIA

built photoreactor (refer to Figure 8.8 in Appendix 8.2). Crude samples were taken after certain amounts of time and directly analyzed without further purification. The resulting polymers **45** were analyzed by size-exclusion chromatography (SEC). The presence of starting compounds (**43** and **44**) was observed along with high molecular weight material, which increases with longer irradiation times (Figure 4.2B). Nevertheless, the SEC traces also show the appearance of signals at lower molecular weight than precursor **43**, probably indicating that polymer degradation is taking place. Possibly, the trithiocarbonate groups stemming from monomer **43** are susceptible to decomposition after long UV irradiation,³¹¹ which would hinder the formation of high molecular weight step-growth polymers. A fluorescent material was indeed obtained after irradiation. However, there is not a linear increase in the fluorescence emission of the polymers with reaction time (Figure 4.2C), suggesting that changes in the structure of the fluorophore are taking place after long UV irradiation.

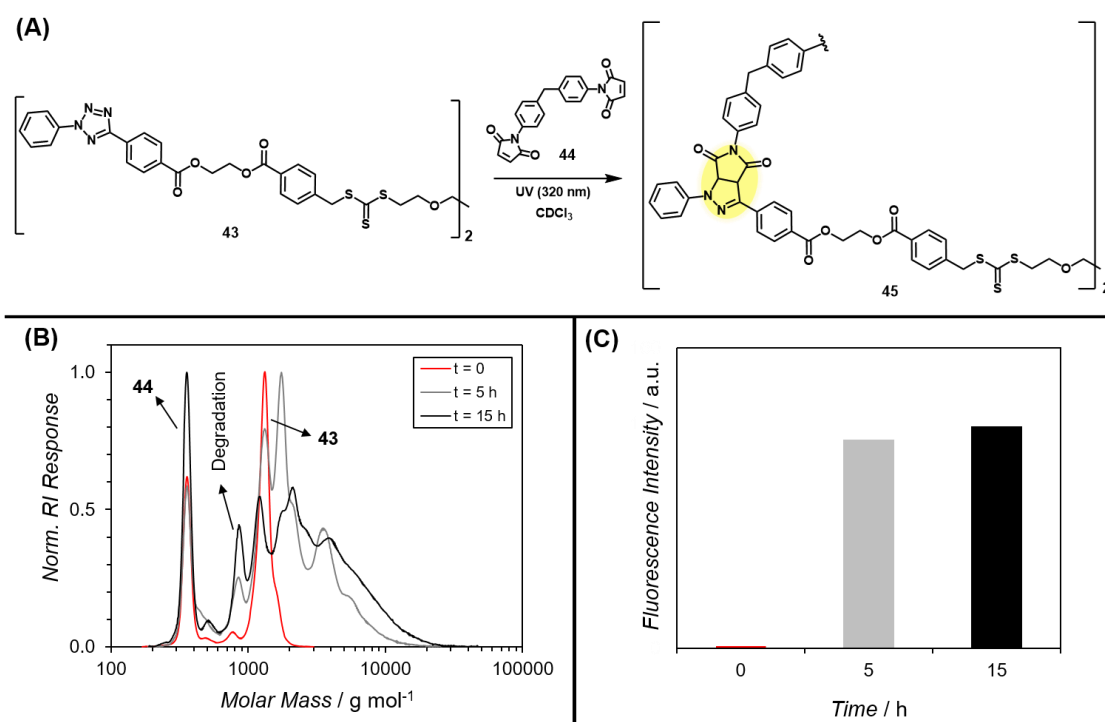
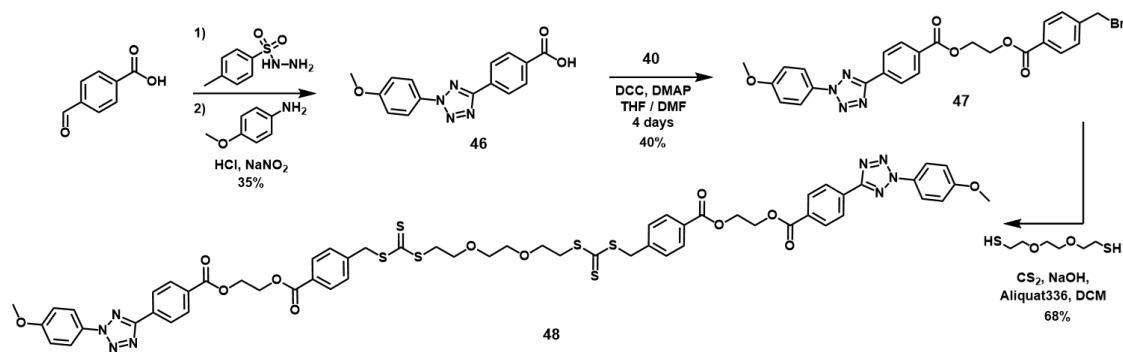


Figure 4.2. (A) Synthesis of fluorescent step-growth polymers **45** from AA–BB monomers **43** and **44**, under UV irradiation. (B) SEC traces of crude samples obtained after 0 h (red), 5 h (grey), and 15 h (black) irradiation. Signals of starting monomers **43** and **44** are marked by arrows, as well as signals corresponding to degradation products. (C) Fluorescence emission ($\lambda_{\text{max}} = 494 \text{ nm}$) of crude samples **45** after 0 h (red), 5 h (grey), and 15 h (black) irradiation.

Taking this into account, a more reactive tetrazole moiety was chosen in order to increase the formation of high molecular weight material, and diminish the extent of

TOWARDS HOMOGENEOUS ALIGNMENT MEDIA

trithiocarbonate and fluorophore degradation. As shown in Figure 2.9 in Chapter 2, substitution of the aromatic ring of the tetrazole changes the wavelength necessary to activate the NITEC process. Therefore, a methoxyphenyl-tetrazole derivative **46** was chosen and used as precursor for the synthesis of the bifunctional tetrazole-RAFT agent **48** (Scheme 4.3). The detailed experimental protocols and characterization by spectroscopic methods can be found in Chapter 6.



Scheme 4.3. Synthesis route for methoxy-tetrazole **46** and corresponding bifunctional tetrazole-chain transfer agent **48**.

Small molecule studies with monofunctional *N*-methylmaleimide revealed that the methoxy-tetrazole **46** not only reacts faster than unsubstituted tetrazole **41** at 320 nm (5% vs. 1% yield, respectively, after 15 min irradiation), but also the formation of side products is decreased (Figures 4.3 and 4.4).

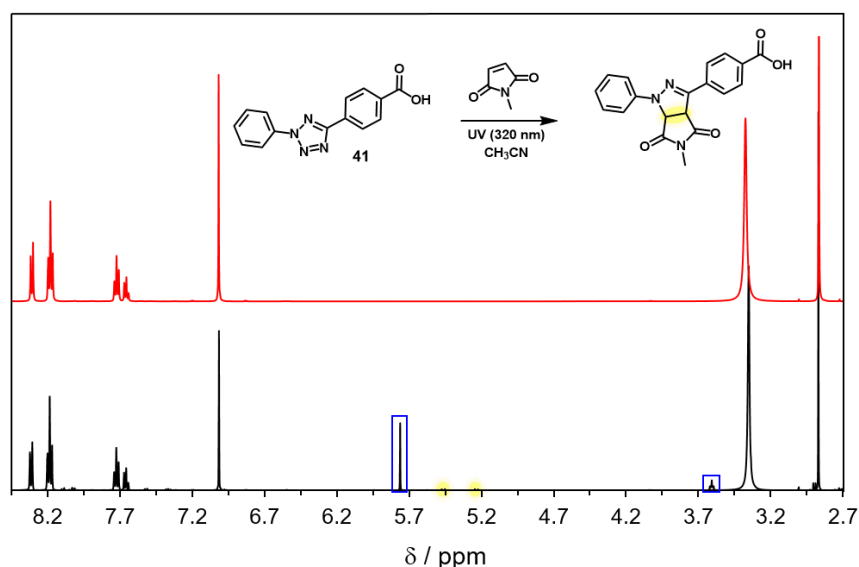


Figure 4.3. ¹H NMR spectra in DMSO-*d*₆ of crude NITEC reaction between tetrazole **41** and *N*-methylmaleimide after 0 min (red) and 15 min (black) irradiation at 320 nm. Resonance signals marked in blue correspond to side products, while signals in yellow correspond to the expected pyrazoline protons (1% yield).

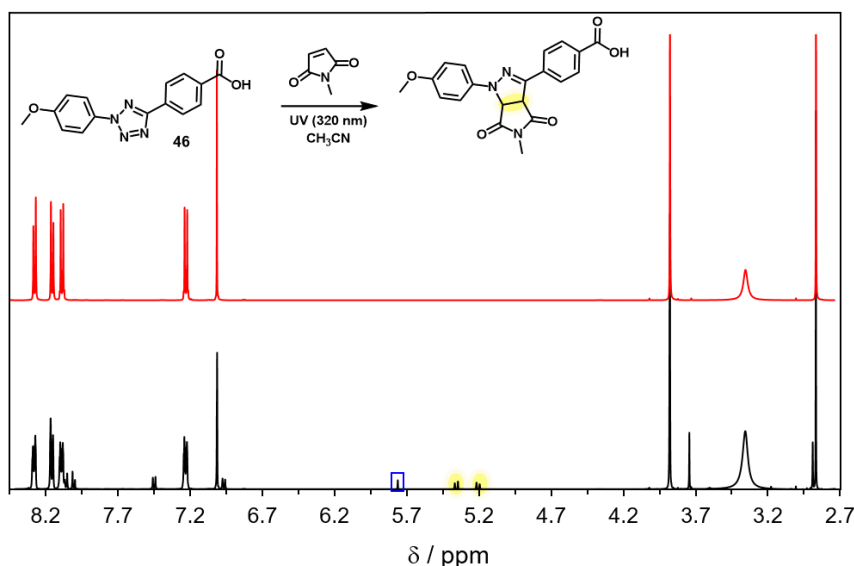


Figure 4.4. ^1H NMR spectra in $\text{DMSO-}d_6$ of crude NITEC reaction between tetrazole **46** and *N*-methylmaleimide after 0 min (red) and 15 min (black) irradiation at 320 nm. Resonance signals marked in blue correspond to side products, while signals in yellow correspond to the expected pyrazoline protons (5% yield).

Moreover, comparison of the UV absorption spectra of RAFT compounds **43** and **48** shows a bathochromic shift of the absorption maximum of the methoxy-tetrazole RAFT agent in comparison to the unsubstituted one, affording a better overlap of the absorption spectrum of **48** with the emission maximum of the UV lamp used for the photopolymerization (Figure 4.5). Although it has been demonstrated that reactivity patterns do not necessarily coincide with the wavelength of maximum absorption,^{115,116,157-159} in the present case the photoactivation of **48** at 320 nm was favored over compound **43**.

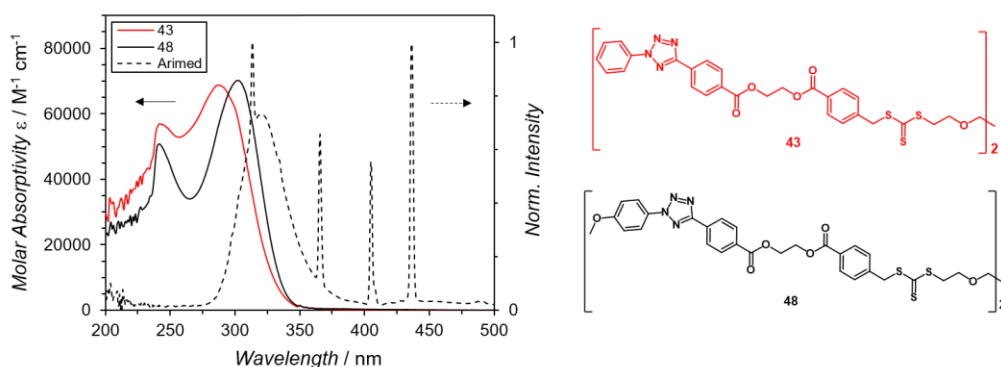


Figure 4.5. Left axis: UV-vis absorption spectra of monomers **43** (red) and **48** (black), showing a bathochromic shift in the absorption maximum for the methoxy-substituted derivative **48**. Right axis: Emission spectrum of the UV lamp (Arimed B6, $\lambda_{\text{max}} = 320 \pm 30$ nm) used as irradiation source (dashed black line).

TOWARDS HOMOGENEOUS ALIGNMENT MEDIA

4.1.2. UV-Induced Step-Growth Polymerization

The UV-induced polymerization of AA–BB monomers **48** and **44** (performed in CDCl₃ or THF-*d*₆, refer to the experimental section in Chapter 6) was carried out, yielding fluorescent step-growth macromolecules **49**. Characterization by ¹H NMR spectroscopy (Figure 4.6) shows that the initially sharp resonance signals of the monomers decrease in intensity with longer irradiation times and give rise to new broad resonance signals, corresponding to the polymer. In particular, the integration area of signals **2** and **3** of the polymer was compared to the integration area of monomer signal **1** (**48**), to determine the conversion (Equations 4.1 and 4.2). Similarly, the yield of the pyrazoline product can be determined using the area of the characteristic proton signals **4** and **5** respect to signal **1** (Equations 4.3 and 4.4).

$$\text{Conv. (\%)} = 100 \frac{\text{Area 2}}{\text{Area 2} + \text{Area 1}} \quad (\text{Eq. 4.1})$$

$$\text{Conv. (\%)} = 100 \frac{\text{Area 3}}{\text{Area 3} + \text{Area 1}} \quad (\text{Eq. 4.2})$$

$$\text{Yield (\%)} = 100 \frac{2(\text{Area 4})}{2(\text{Area 4}) + \text{Area 1}} \quad (\text{Eq. 4.3})$$

$$\text{Yield (\%)} = 100 \frac{2(\text{Area 5})}{2(\text{Area 5}) + \text{Area 1}} \quad (\text{Eq. 4.4})$$

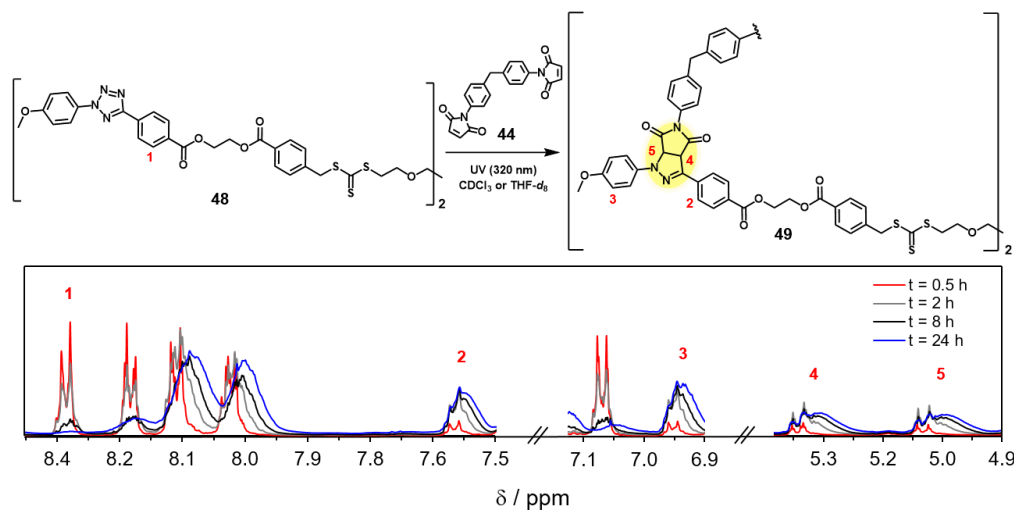


Figure 4.6. Synthesis of step-growth polymers **49** from monomers **48** and **44** under UV irradiation, $\lambda = 320$ nm. The ¹H NMR resonance signals of monomer (**1**) and polymer (**2**, **3**, **4**, and **5**) can be used to determine monomer conversion and polymer yield. Adapted with permission from Ref 298. Copyright 2017, American Chemical Society.

Complete signal assignment can be found in Figure 8.9 in Appendix 8.2. The numerical values retrieved from Equations 4.1 and 4.2, and from Equations 4.3 and 4.4,

TOWARDS HOMOGENEOUS ALIGNMENT MEDIA

were averaged to determine conversion and yield, respectively, at different irradiation times. Excellent agreement was observed for the calculated values of RAFT agent conversion and poly(pyrazoline) yield in CDCl_3 (Figure 4.7A), suggesting that formation of side products does not play a significant role on the photopolymerization. The kinetic plot of the polymerization process displays an initial sharp increase in the conversion of **48** up to 6 h irradiation, after which a slower increase is observed, reaching a maximum plateau of ca. 90% (Figure 4.7B). Consequently, the concentration of RAFT monomer at every irradiation time $[\mathbf{48}]_t$ can be calculated from the conversion at time t and the initial concentration $[\mathbf{48}]_i$. Monomer concentration constantly decreases in the course of the reaction, as depicted in Figure 4.7C. By plotting the inverse of monomer concentration $[\mathbf{48}]^{-1}$ at different irradiation times, a linear correlation is obtained, indicating pseudo-second order kinetics of the reaction rate (Figure 4.7D). The slope of the linear regression gives a rate constant $k = 0.0096 \text{ mM}^{-1} \cdot \text{h}^{-1}$.

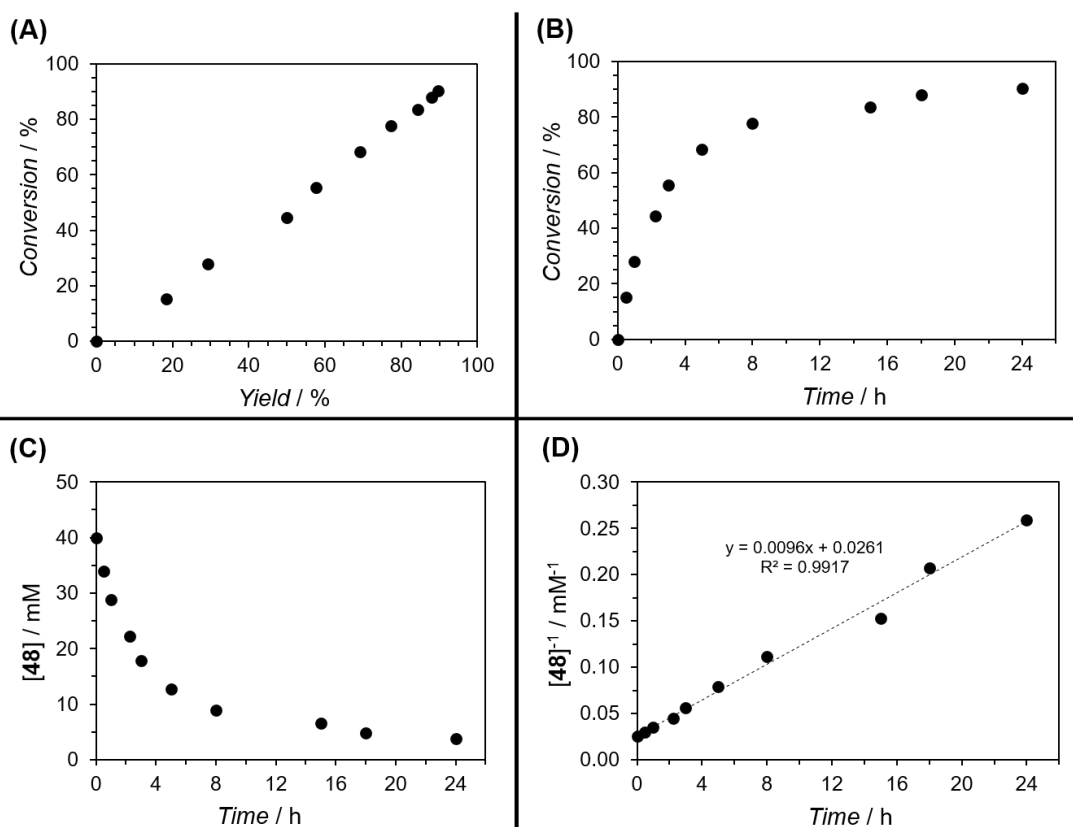


Figure 4.7. (A) Correlation of conversion of **48** and yield of poly(pyrazoline) **49** in CDCl_3 , calculated by NMR using Equations 4.1–4.4. (B) Kinetic plot displaying conversion of monomer **48** with increasing irradiation time. (C) Decrease in the concentration of **48** during the course of the reaction. (D) Plot of the inverse of monomer concentration ($1 / [\mathbf{48}]$) against reaction time, showing a linear relationship.

TOWARDS HOMOGENEOUS ALIGNMENT MEDIA

Analysis of polymers **49** by SEC (UV detector at $\lambda = 300$ nm) showed the decrease of the signals corresponding to the starting compounds (**48** and **44**) with increasing irradiation time. Concomitantly, typical molecular weight distributions corresponding to step-growth polymers were obtained, displaying signals for dimers, trimers, tetramers, etc. These signals decrease in intensity with longer irradiation times, giving rise to broader distributions as the reaction proceeds (Figure 4.8A). No strong signals corresponding to polymer degradation were observed in the SEC traces during the duration of the experiment (compare with Figure 4.2B). The UV-vis absorption spectra of polymers **49** display the formation of a broad absorption band (355–470 nm) not present in the starting material, typical of pyrazoline adducts, along with an additional absorbance at 260 nm (Figure 4.8B). Furthermore, polymers **49** exhibit broad fluorescence emission spectra (from 470 to 670 nm, excitation wavelength 459 nm), corroborating the pro-fluorescent behavior of the NITEC reaction (Figure 4.8C).

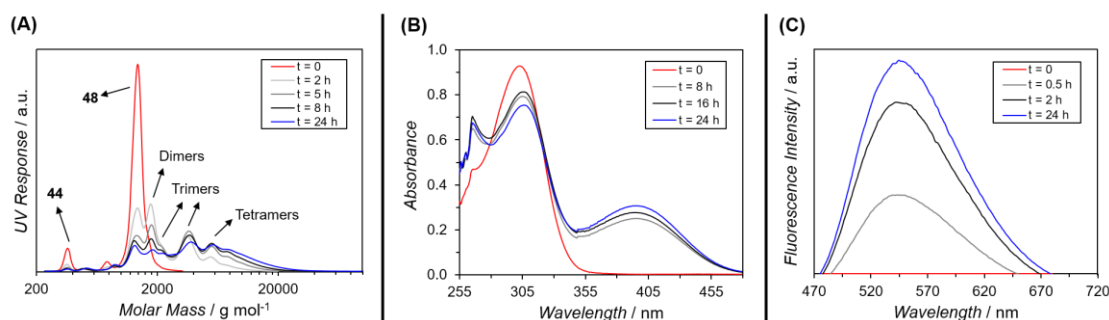


Figure 4.8. (A) SEC traces of step-growth polymers **49** obtained after different irradiation times. Signals of starting materials **44** and **48** are marked by arrows, as well as signals corresponding to dimers, trimers and tetramers. (B) UV-vis absorption spectra of samples **49** after different irradiation times. Broad absorption bands centered at 400 nm are characteristic of the poly(pyrazoline) products. (C) Fluorescence intensity of samples **49** after different irradiation times. The maximum emission increases as polymerization proceeds. Adapted with permission from Ref 298. Copyright 2017, American Chemical Society.

4.1.2.1. Calibration Curve

In order to quantitatively utilize the fluorescence emission properties of the poly(pyrazolines) **49**, a calibration curve that correlates fluorescence intensity and concentration of pyrazoline is required. Hence, small molecule studies with monofunctional tetrazole **46** and *N*-phenylmaleimide **50** were carried out (Figure 4.9). Both compounds were mixed in DMF and irradiated at 320 nm for certain time, and the crude products were analyzed via NMR and fluorescence spectroscopy. To determine the conversion of tetrazole **46**, the absolute areas of the well resolved resonance

TOWARDS HOMOGENEOUS ALIGNMENT MEDIA

signals **4** and **8** (pyrazoline product **51**) were compared with signal **1** of the tetrazole **46** (Equation 4.5). Alternatively, the resonance signals **11** (tetrazole) and **12** (pyrazoline) can be employed (Equation 4.6).

$$\text{Conv.} = 100 \frac{\text{Area } 4}{\text{Area } 4 + \text{Area } 1} \text{ or } 100 \frac{\text{Area } 8}{\text{Area } 8 + \text{Area } 1} \quad (\text{Eq. 4.5})$$

$$\text{Conv.} = 100 \frac{\text{Area } 12}{\text{Area } 12 + \text{Area } 11} \quad (\text{Eq. 4.6})$$

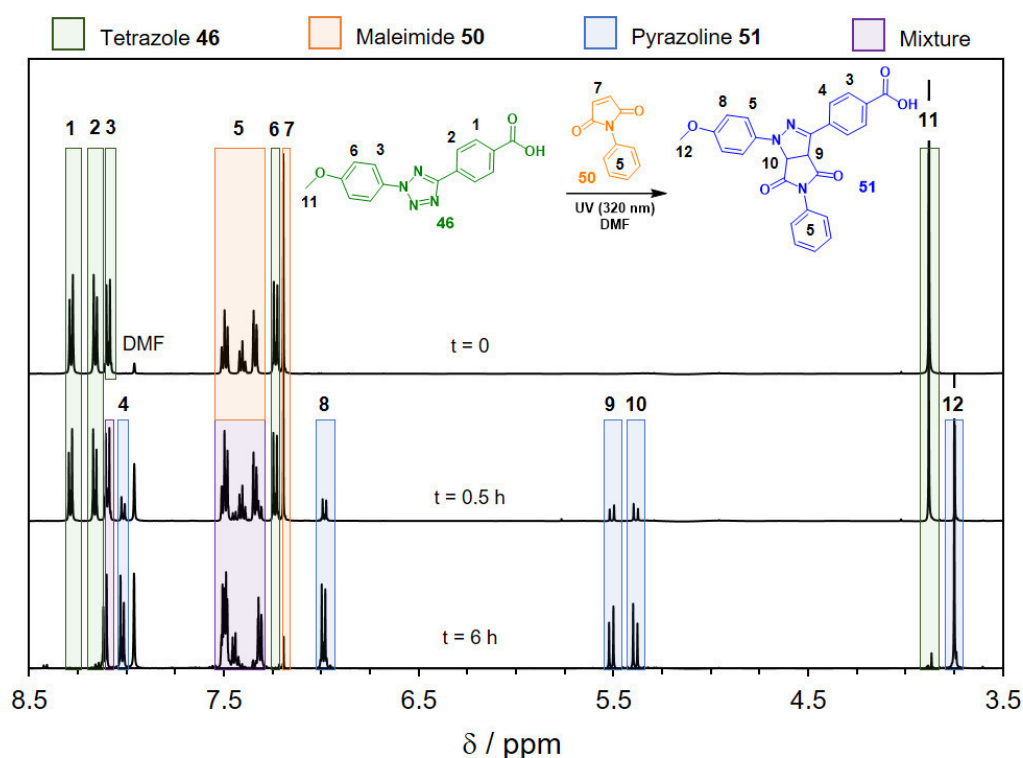


Figure 4.9. ^1H NMR spectra in $\text{DMSO-}d_6$ of crude pyrazoline standards **51** obtained after irradiation of tetrazole **46** and maleimide **50** for 0 h, 0.5 h, and 6 h at 320 nm. Adapted with permission from Ref 298. Copyright 2017, American Chemical Society.

Likewise, the yield of the pyrazoline adduct **51** was calculated using the areas of the resonance signals **9** and **10**, in comparison to signal **1** (Equation 4.7). The obtained values of conversion and yield were then averaged, giving similar numerical values (no influence of side products).

$$\text{Yield} = 100 \frac{2(\text{Area } 9)}{2(\text{Area } 9) + \text{Area } 1} \text{ or } 100 \frac{2(\text{Area } 10)}{2(\text{Area } 10) + \text{Area } 1} \quad (\text{Eq. 4.7})$$

Next, the fluorescence emission of each crude product (in DMF) was recorded, showing concomitant increase in the emission intensity with higher conversion, as shown exemplarily in Figure 4.10A. The concentration of pyrazoline **51** in the sample was calculated as follows,

TOWARDS HOMOGENEOUS ALIGNMENT MEDIA

$$[\text{pyrazoline } 51] = \frac{(\text{yield})[\text{tetrazole } 46]_i}{100} \quad (\text{Eq. 4.8})$$

from the initial concentration of tetrazole **46** and the pyrazoline yield, as determined from Equations 4.5–4.7. In this way a calibration curve for the correlation of fluorescence intensity and concentration of pyrazoline adduct **51** was constructed (Figure 4.10B).

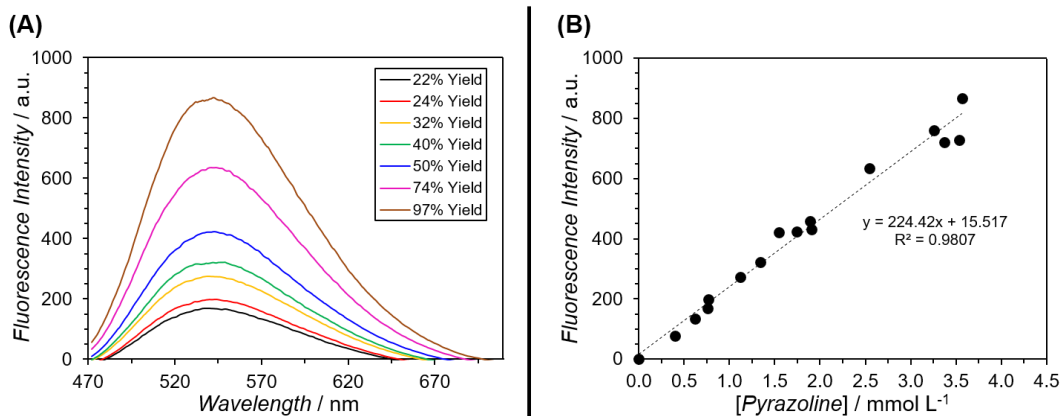
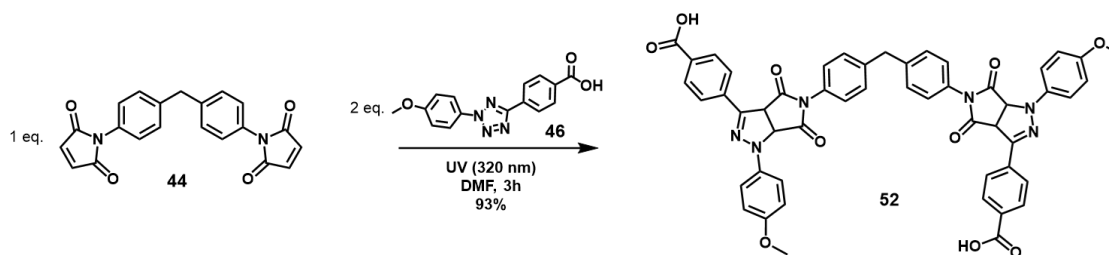


Figure 4.10. (A) Fluorescence emission spectra of crude standards **51** in DMF. (B) Calibration curve for the correlation of fluorescence intensity and pyrazoline concentration. Adapted with permission from Ref 298. Copyright 2017, American Chemical Society.

The main advantage of this procedure is that crude samples can be directly analyzed by fluorescence spectroscopy, without the need for any intermediate purification protocol. The implementation of the calibration curve from Figure 4.10B was first carried out on a small molecule control. Bifunctional maleimide **44** was reacted with two equivalents of tetrazole **46** under UV irradiation, as depicted in Scheme 4.4.



Scheme 4.4. NITEC reaction between bismaleimide **44** and tetrazole **46** to obtain pyrazoline **52**.

The yield of the obtained pyrazoline product **52** was determined via NMR spectroscopy (Figure 4.11), as well as fluorescence measurements (Figure 4.12) using the calibration curve in Figure 4.10B to estimate the amount of pyrazoline in the sample. Equivalent values for the pyrazoline concentration in the crude mixture were retrieved

TOWARDS HOMOGENEOUS ALIGNMENT MEDIA

from both techniques (NMR = 3.3 mM, fluorescence = 3.5 mM), validating the applicability of the calibration curve for the determination of conversion in NITEC systems via fluorescence measurements.

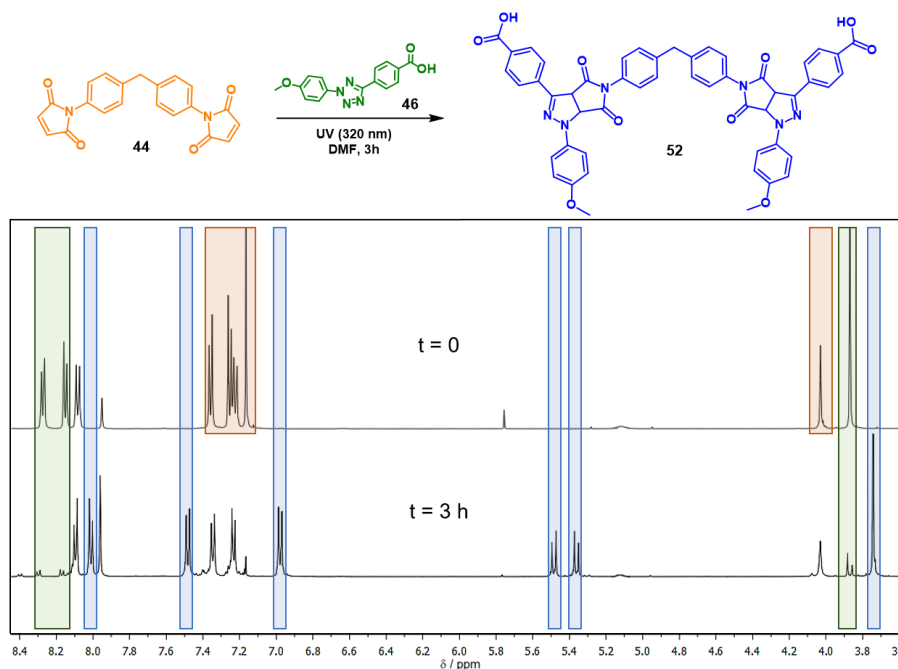


Figure 4.11. ¹H NMR spectra in DMSO-d₆ of initial mixture of **44** and **46** at t = 0, and crude sample **52** obtained after 3 h irradiation (93% yield = 3.3 mM pyrazoline).

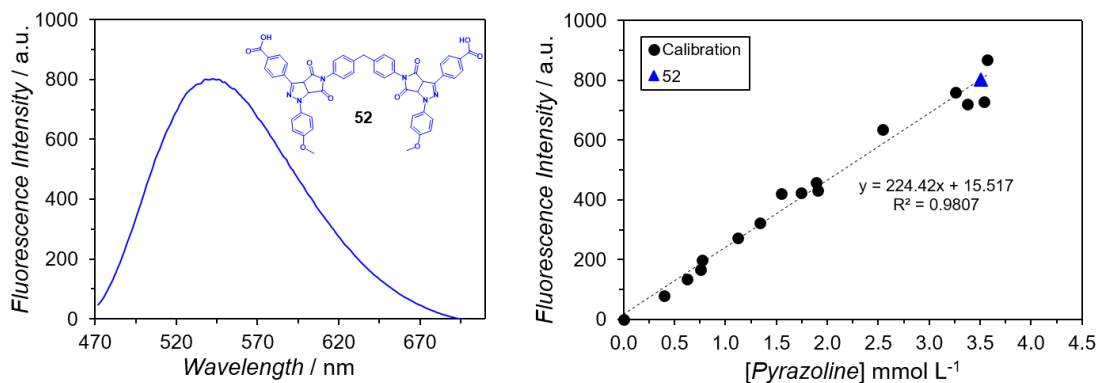


Figure 4.12. Fluorescence emission spectrum of crude sample **52** obtained after 3 h irradiation (left). Interpolation in the calibration curve (right) gives a concentration of 3.5 mM pyrazoline.

Additionally, control experiments performed with **46** and different nucleophiles were conducted. From Scheme 2.10 in Chapter 2, it can be observed that tetrazoles also react with nucleophiles under irradiation with light, generating in some cases fluorescent products.¹⁴⁴⁻¹⁵¹ Therefore, it was necessary to evaluate the influence of possible nucleophilic addition by-products on the fluorescence emission properties of

TOWARDS HOMOGENEOUS ALIGNMENT MEDIA

the pyrazoline standards (Figure 4.13), using the same experimental conditions as for the preparation of the calibration curve (refer to the experimental section). These experiments reveal that only tetrazole self-reaction (Control 1) and thiol addition (Control 4) produce fluorescent adducts – though less intense than pyrazoline **51** – under the applied experimental conditions. Notwithstanding, such addition products do not contribute to the overall fluorescence intensity when a maleimide is present in the reaction mixture (compare Control 2, Control 5, and Control 6). Therefore, the robustness of the calibration curve for the determination of pyrazoline concentration via fluorescence spectroscopy was further demonstrated.

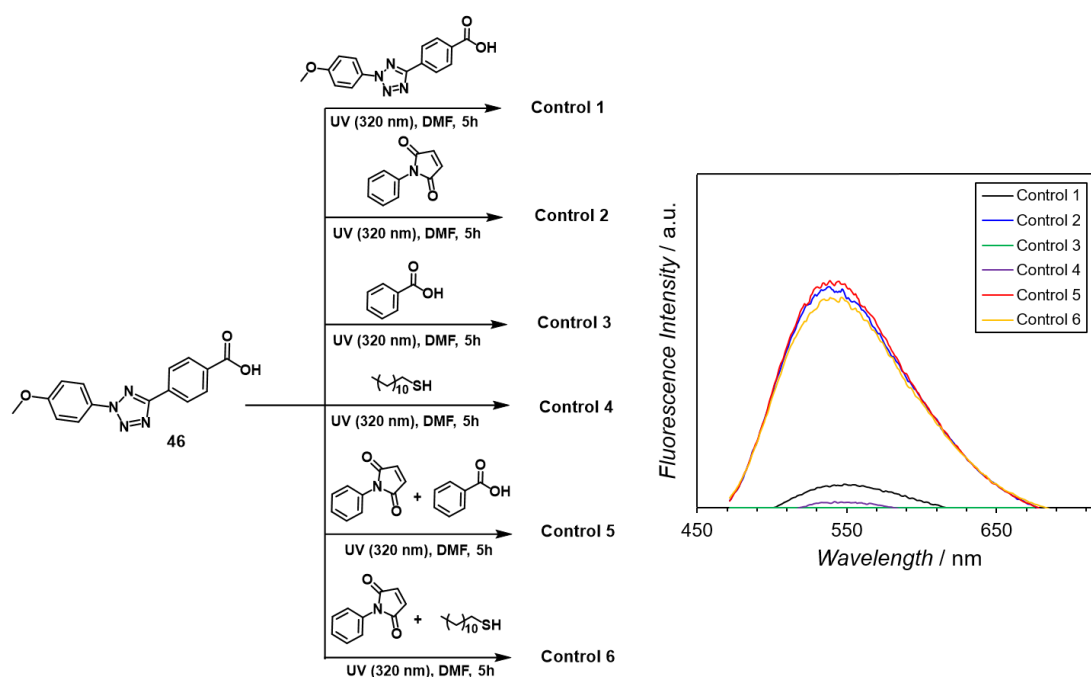


Figure 4.13. Control experiments performed with **46** and different nucleophiles. Fluorescence emission intensity of each adduct (in DMF) was recorded and compared with the expected emission of the pyrazoline standard (Control 2). Adapted with permission from Ref 298. Copyright 2017, American Chemical Society.

4.1.2.2. Kinetics via Fluorescence Spectroscopy

The calibration curve in Figure 4.10B was used to determine the concentration of pyrazoline – thus the conversion of tetrazole – for the step-growth polymers **49** in CDCl_3 (Figure 4.14). By determining the fluorescence emission of the different crude samples (without purification), a very good agreement with the values obtained from NMR spectroscopy (refer to Figure 4.7B) was observed. These results prove that fluorescence measurements represent a simple yet powerful tool to access polymerization kinetics in NITEC-based systems.

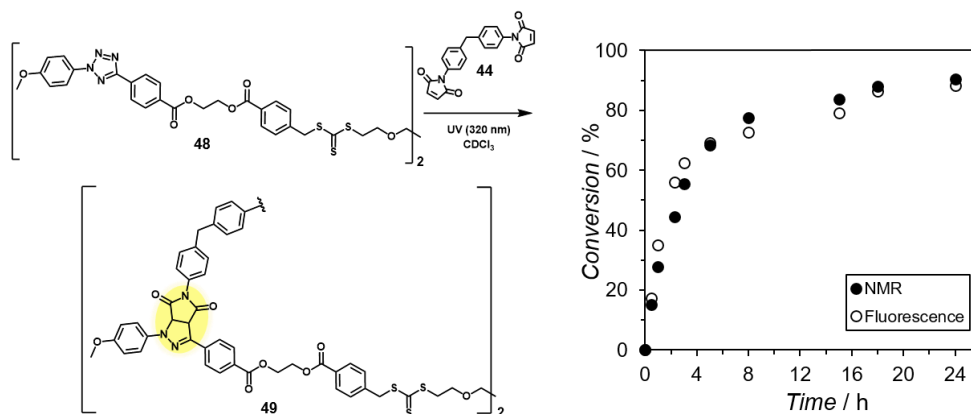


Figure 4.14. Conversion of monomer **48** in CDCl_3 with increasing irradiation time determined via NMR (solid symbols) and fluorescence spectroscopy (open symbols).

Nonetheless, quantification of the conversion in step-growth polymerization **49**, performed in $\text{THF-}d_6$, did not show the same good agreement between NMR and fluorescence as in CDCl_3 . The fluorescence intensity of samples obtained at long irradiation times (> 12 h) displayed lower values than expected (Figure 4.15A). A possible explanation to this phenomenon lies in the aromatization of the pyrazoline ring (fluorophore), yielding a pyrazole moiety. This aromatic adduct is not fluorescent, hence the quantification of conversion by fluorescence is unavoidably underestimated. However, the extent of aromatization in $\text{THF-}d_6$ could be determined by NMR spectroscopy in both small molecule (see Figure 8.10 in Appendix 8.2) and polymer systems (Figure 4.15B).

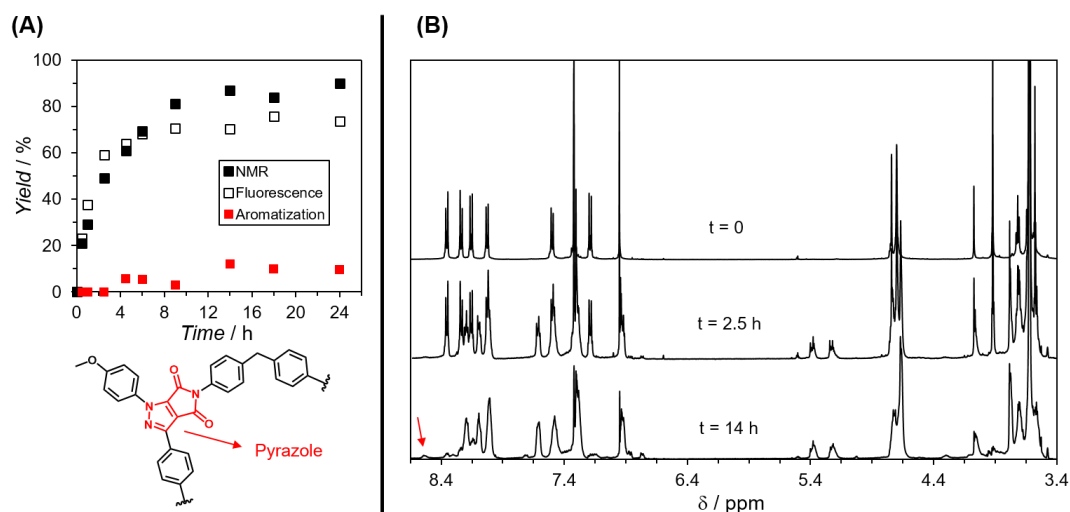


Figure 4.15. (A) Yield of pyrazoline in polymers **49**, determined by NMR spectroscopy (black solid symbols) and fluorescence spectroscopy (open symbols). Red solid symbols represent the percentage of aromatization, calculated by integration of the NMR resonance signals around 8.5 ppm. (B) Exemplary NMR spectra in $\text{THF-}d_6$ of samples **49** after 0 h, 2.5 h, and 14 h irradiation.

TOWARDS HOMOGENEOUS ALIGNMENT MEDIA

Thus, applying the percentage of aromatization as correction factor, again very good agreement was found between conversion determined by NMR and fluorescence spectroscopy in THF- d_8 (Figure 4.16A). Additionally, it can be observed from the plot in Figure 4.16A that the solvent has no strong influence in the kinetics of step-growth polymerization of monomers **48** and **44**. Next, the evolution of the molecular weight of polymers **49** (determined via SEC analysis) was evaluated and compared to the theoretical model developed by Carothers (refer to Equation 2.37 in Section 2.3). Figure 4.16B displays the experimental plot of weight average molecular weight, \bar{M}_w , vs. monomer conversion, along with the theoretical Carothers plot:

$$\bar{M}_w = m_0 \frac{(1+p)}{(1-p)} \quad (\text{Eq. 4.9})$$

with p the fractional monomer conversion and m_0 half of the mass of the repeating unit (see Figure 8.11 in Appendix 8.2).

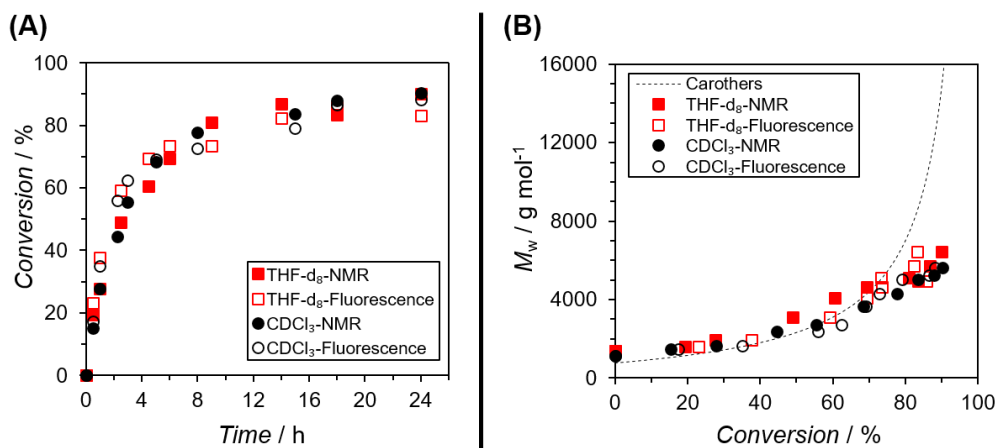


Figure 4.16. (A) Conversion kinetics for the step-growth polymers **49**, determined by NMR (solid symbols) and fluorescence spectroscopy (open symbols) in $CDCl_3$ (black dots) and THF- d_8 (red squares). (B) Corresponding plot of weight average molecular weight vs. conversion. Dashed line represents the theoretical Carothers curve. Adapted with permission from Ref 298. Copyright 2017, American Chemical Society.

The Carothers plot in Figure 4.16B shows good agreement of experimental and theoretical values for up to 75% conversion. High molecular weight polymers, as predicted by Equation 4.9, could not be obtained at higher monomer conversions. This inconsistency could not be explained solely by uncertainties in the determination of \bar{M}_w values via SEC (calibration with PS standards). A non-strictly equimolar mixture of the AA–BB monomers **48** and **44** (see Equation 2.39 in Section 2.3) is more likely to be responsible for the lower molecular weight obtained for polymers **49**, in respect to the theoretical values predicted from Equation 4.9. Therefore, polymerizations were carried

out using different molar ratios of both monomers (from 1.05 : 1 to 1 : 1.05 mol ratio **48** : **44**). It can be seen from Figures 4.17A and 4.17B that the different molar ratios have little effect in the conversion, but strongly affect the molecular weight of the final step-growth polymers. A slight excess of monomer **48** (1.05 and 1.01 equivalents) promotes a substantial increase in the \bar{M}_w for conversions > 80%, reaching better agreement with the Carothers curve. Conversely, increasing the amount of monomer **44** does not have an impact in the molecular weight of the resulting polymers (see Figure 4.17B). These observations indicate that small amounts of impurities are present in monomer **48**, probably stemming from the synthesis and purification protocol. The SEC traces in Figure 4.17C, corresponding to molar ratio 1.01 : 1 **48** : **44**, show the formation of polymers with broad molecular weight distributions, in which dimers, trimers and tetramers are almost not present at long irradiation times (compare with Figure 4.8A).

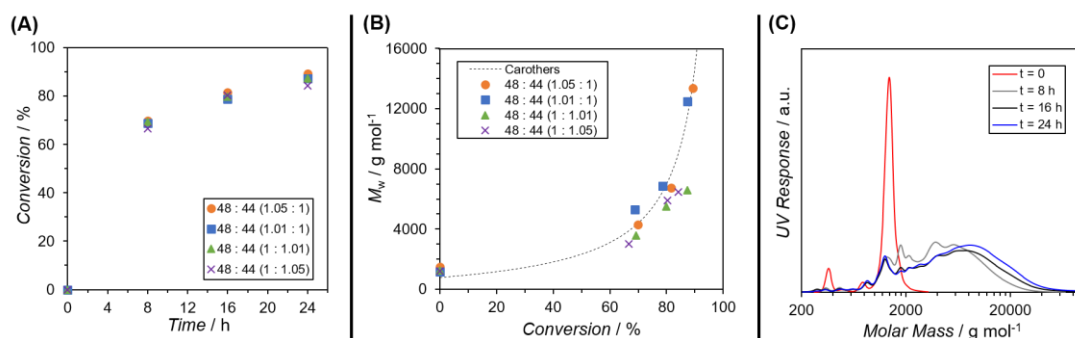


Figure 4.17. (A) Conversion vs. reaction time for step-growth polymers prepared with different ratios of monomers **48** and **44** (determined by NMR spectroscopy) in CDCl₃. (B) Corresponding \bar{M}_w vs. conversion plot. Dashed line represents the Carothers curve. (C) SEC traces of polymers prepared from 1.01 : 1 ratio **48** : **44** after 0 h, 8 h, 16 h, and 24 h irradiation. Adapted with permission from Ref 298. Copyright 2017, American Chemical Society.

4.1.3. RAFT and Step-Growth Polymerization

So far, compound **48** was used as bifunctional tetrazole monomer in AA–BB photoinduced NITEC step-growth polymerization protocols. However, due to the trithiocarbonate moieties present in the structure of **48**, this molecule can be also employed for the reversible-deactivation radical polymerization of styrene, more specifically via RAFT methodologies (refer to Section 2.2). Literature reports⁵⁵ show the feasibility of obtaining well-defined styrenic polymers with RAFT agents analogous to **48**. In this work α,ω -tetrazole-functional PS chains of two different molecular weights, **53** and **54** ($\bar{M}_w = 2100 \text{ g}\cdot\text{mol}^{-1}$ and $4000 \text{ g}\cdot\text{mol}^{-1}$, respectively), were obtained by RAFT

TOWARDS HOMOGENEOUS ALIGNMENT MEDIA

polymerization of styrene and **48** (Figure 4.18A). The corresponding SEC traces are displayed in Figure 4.18B, characterized by narrow molecular weight distributions ($\bar{D} = 1.15$ and 1.21, respectively). Details of the RAFT polymerization procedure can be found in the experimental section.

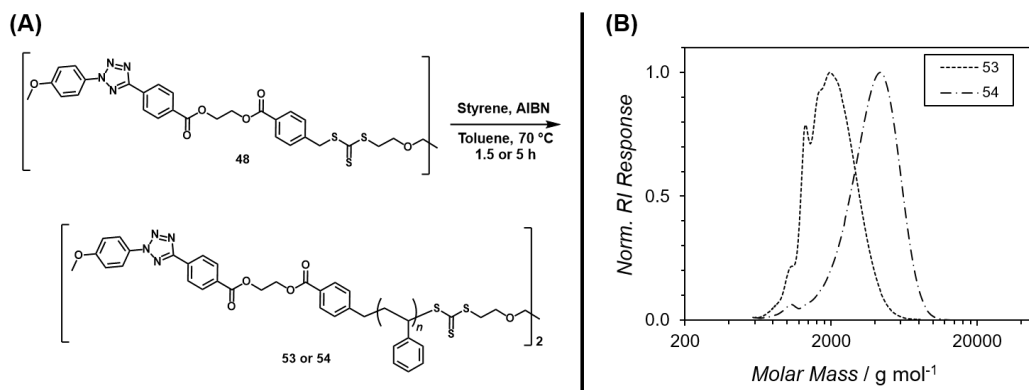


Figure 4.18. (A) RAFT polymerization of styrene mediated by **48** to yield bifunctional tetrazole-PS **53** and **54**. (B) SEC traces (RI detector) of PS strands **53** and **54**. Adapted with permission from Ref 298. Copyright 2017, American Chemical Society.

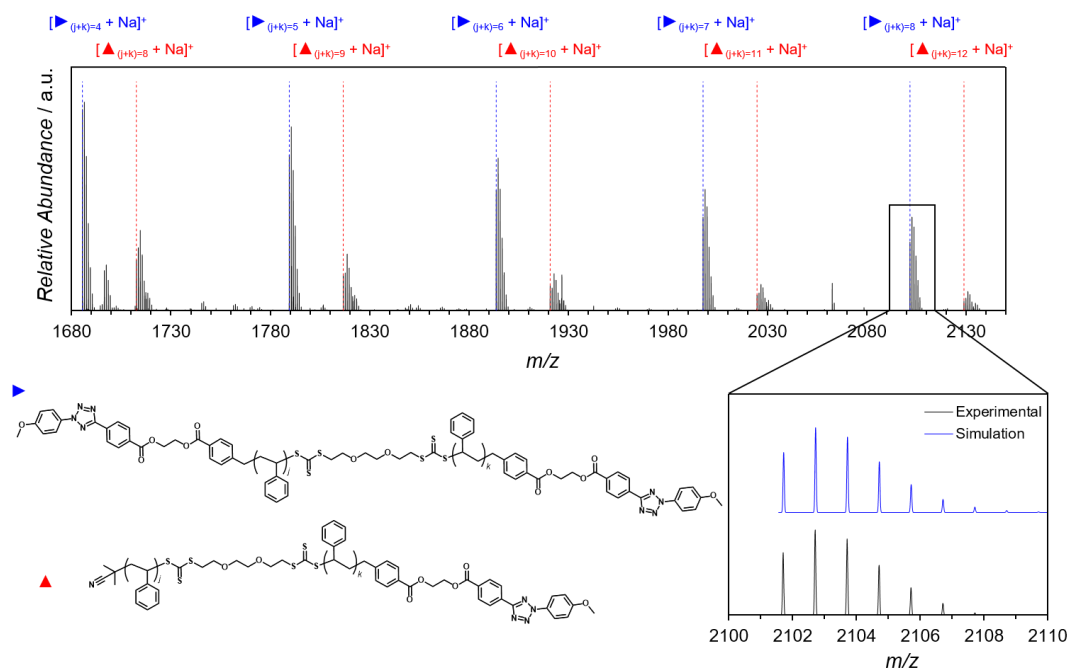


Figure 4.19. ESI-MS spectrum (positive mode) of bifunctional tetrazole-PS **53**, showing typical mass and isotopic pattern for the expected structure \blacktriangleright (simulated pattern depicted in blue in the inset). A secondary PS structure corresponding to AIBN-initiated polymer (\blacktriangle), inherent to the RAFT process, was also found.

TOWARDS HOMOGENEOUS ALIGNMENT MEDIA

In addition, electrospray ionization mass spectrometry (ESI-MS) analyses confirmed the good end group fidelity of the obtained bifunctional tetrazole-PS chains (Figure 4.19). Signals corresponding to the expected tetrazole end-capped polymer were found, along with characteristic peaks for AIBN-initiated chains. As depicted in Scheme 2.5 (Section 2.2), the initiation mechanism of RAFT polymerizations require the input of small amounts of radical initiators. Although the presence of initiator-capped chains in RAFT polymerization processes is unavoidable, their incidence can be minimized in well-designed polymerizations.^{19,40} By keeping the ratio of initiator to RAFT agent low (typically 0.1 mol%), more than 95% of the chains are initiated by the R• group stemming from the chain transfer agent (refer to Section 2.2).

The α,ω -tetrazole-functional polymers **53** and **54** were then used as bifunctional precursors for the NITEC step-growth polymerization with bismaleimide **44** in THF- d_8 , affording the fluorescent poly(pyrazolines) **55** and **56**, respectively, as shown in Figure 4.20A. The corresponding SEC traces of samples taken at different irradiation times are depicted in Figures 4.20B and 4.20C. In both cases, the signals of the starting materials decrease with longer irradiation times, becoming gradually broad as the reaction proceeds.

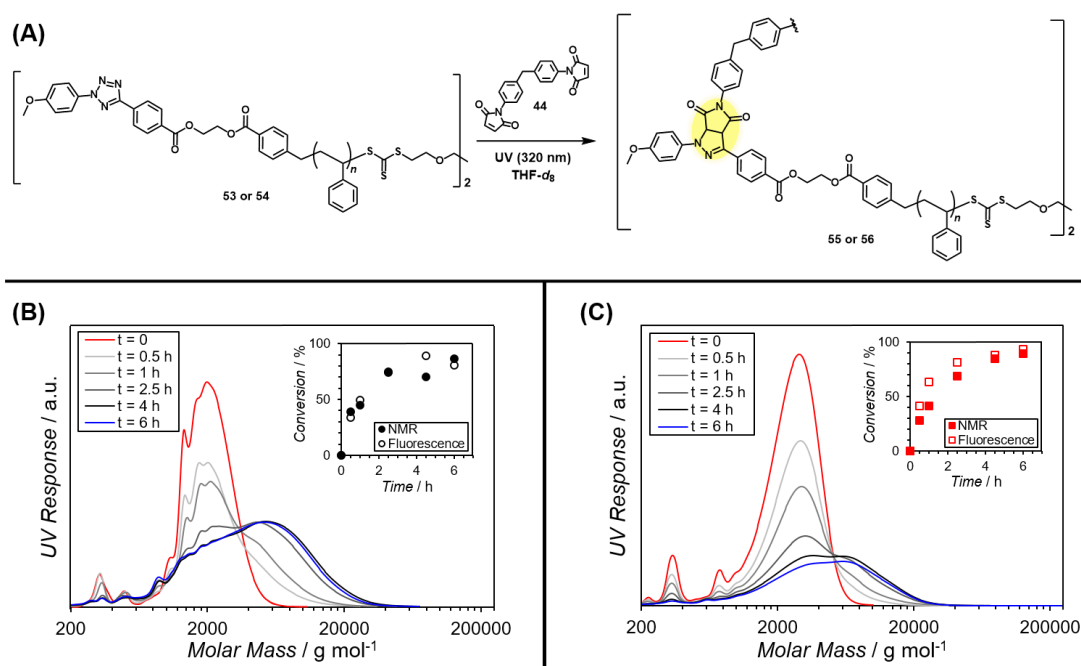


Figure 4.20. (A) Step-growth polymerization of PS samples **53** or **54** with bismaleimide **44** to yield poly(pyrazolines) **55** and **56**, respectively. (C) SEC traces (UV detector) of NITEC step-growth polymers **55** at different irradiation times. (D) Corresponding SEC traces of polymers **56**. Insets display conversion determined by NMR (solid symbols) and fluorescence (open symbols) spectroscopy. Adapted with permission from Ref 298. Copyright 2017, American Chemical Society.

TOWARDS HOMOGENEOUS ALIGNMENT MEDIA

It can be seen that the molecular weight distributions of polymers **55** and **56** do not change significantly between 4 h and 6 h irradiation, suggesting that the NITEC ligation under the studied conditions finishes before 4 h. The conversion kinetics using PS precursors **53** and **54** are shown in the insets of Figures 4.20B and 4.20C, respectively. Both NMR and fluorescence spectroscopy were utilized for the determination of conversion. As observed before for polymers **49** in THF, aromatization of the pyrazoline fluorophore takes place at long irradiation times. Conversion values retrieved from NMR and fluorescence spectroscopy showed equivalent results only after the fluorescence values were corrected with the extent of aromatization (refer to Figure 4.21 and Figure 8.12 in Appendix 8.2).

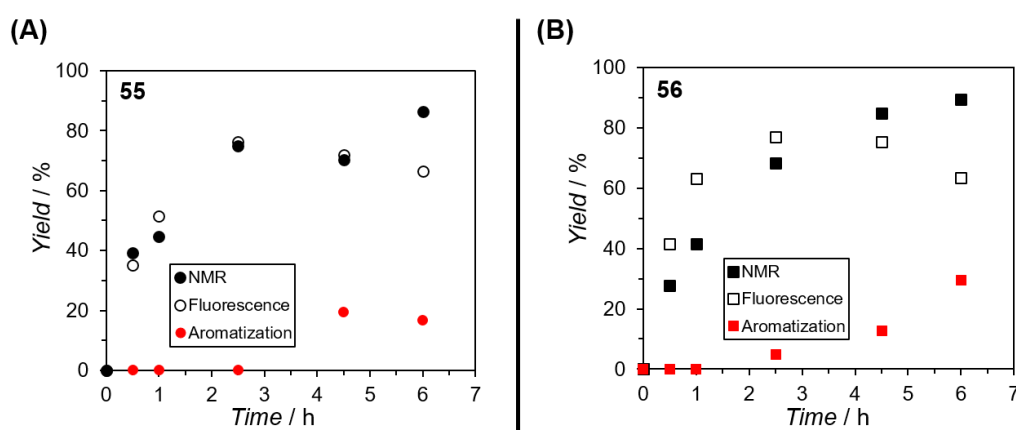


Figure 4.21. Yield of pyrazoline adducts in polymers **55** (A) and **56** (B), determined by NMR (black solid symbols) and fluorescence (open symbols) spectroscopy. The yield of the aromatization by-product is represented in each case by red solid symbols.

A maximum conversion of around 90% was reached already after 4 h reaction, in agreement with the evolution of molecular weight determined by SEC. Moreover, the ligation kinetics of **55** and **56** were found to be chiefly independent of the molecular weight of the PS starting material (either **53** or **54**), as shown in Figure 4.22A. From Figure 4.22B, a kinetic rate constant $k = 0.0461 \text{ mM}^{-1} \cdot \text{h}^{-1}$ can be extracted from the slope of the linear regression. In comparison to the step-growth polymers **49** (derived from RAFT agent **48**), the NITEC ligation of PS precursors **53/54** is accelerated by a factor of six (compare Figures 4.7D and 4.22B). The reason for this behavior possibly lies in the lower initial concentration of precursors **53/54** compared to **48** (ca. $20 \text{ mmol} \cdot \text{L}^{-1}$ vs. $40 \text{ mmol} \cdot \text{L}^{-1}$, respectively), facilitating the penetration of UV light into the solution.

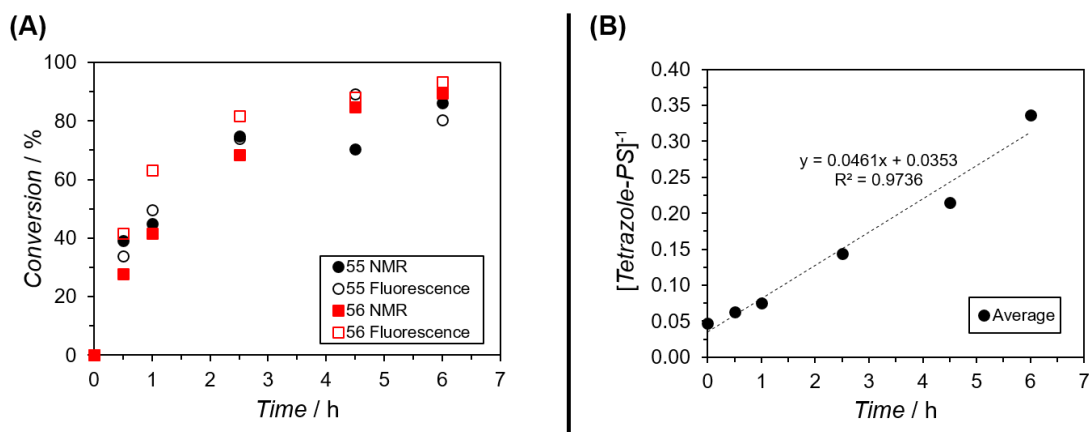


Figure 4.22. (A) Conversion vs. reaction time for step-growth polymers **55** (black) and **56** (red), determined by NMR (solid symbols) and fluorescence (open symbols) spectroscopy. (B) Plot of the inverse of precursor concentration (average of **53** and **54** determined by NMR spectroscopy) against reaction time.

At the same time, the lower initial concentration promotes an acceleration of the onset of aromatization, which reach values close to 30% already after 6 h irradiation (see Figures 4.21 and 4.23A). This phenomenon greatly impacts the fluorescence emission properties of the obtained materials, which can even disappear if excessively long irradiation is applied beyond the completion of the NITEC reaction (see Figure 8.13 in Appendix 8.2). The onset of aromatization for polymers **56** (prepared from PS precursor **54** and bismaleimide **44** at 1 : 1 ratio) could be also observed in the UV-vis absorption spectra of samples taken at different irradiation times. Figure 4.23B shows that the broad absorption band (355–470 nm) characteristic of the poly(pyrazoline) product, decreases in intensity as aromatization takes place. At the same time, the absorption band at 260 nm becomes more intense with increasing extent of aromatization.

As final remark, the molecular weight of polymers **56** (1 : 1 ratio **54** : **44**) at different conversions was compared to the theoretical Carothers plot (Figure 4.23C). The experimental data fits the theoretical curve only at low conversions. Above 40% conversion, the obtained molar masses are significantly lower than predicted by the Carothers equation. Possibly, the dispersity in the molecular weight of **54**, in addition to the presence of some initiator-capped end polymer chains (see Figure 4.19) has high impact in the stoichiometric balance of reactive groups, necessary to reach higher molecular weights. As depicted in Figure 4.23C, slightly higher molar masses were obtained when an initial molar ratio 1.01 : 1 (**54** : **44**) was employed.

TOWARDS HOMOGENEOUS ALIGNMENT MEDIA

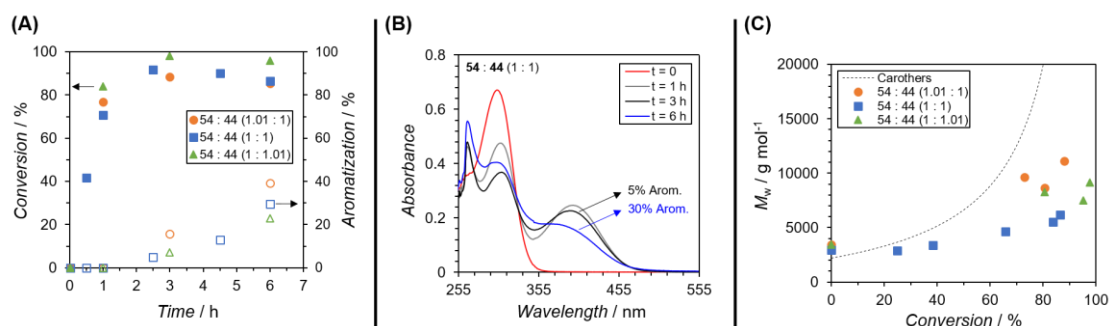


Figure 4.23. (A) Left axis: Conversion vs. reaction time for step-growth polymers **56**, prepared with different molar ratios of precursors **54** and **44** (solid symbols). The open symbols (right axis) represent the extent of aromatization of the different samples with irradiation time. (B) UV-vis absorption spectra of **56** (1 : 1 ratio **54** : **44**) at different irradiation times. (C) Plot of weight average molecular weight vs. conversion for polymers **56** prepared with different **54** : **44** molar ratios. Dashed line represents the theoretical Carothers curve. Adapted with permission from Ref 298. Copyright 2017, American Chemical Society.

The results presented in this section demonstrate the application of fluorescence spectroscopy as quantitative characterization method for NITEC-based systems. Once a calibration curve that relates the fluorescence intensity with the concentration of pyrazoline was provided, calculation of extent of polymerization in AA–BB step-growth NITEC polymers via fluorescence spectroscopy was possible. This technique grants conversion values similar to those retrieved from NMR analyses, in a facile and rapid fashion. Such characteristics make fluorescence analyses an advantageous tool for systems in which NMR signals overlap and integration might be equivocal. Nevertheless, it is important to determine the onset of aromatization, a phenomenon that can seriously impact the fluorescence emission properties of the sample, thus the quantification potential of the NITEC approach. Additionally, a novel tetrazole-bifunctional chain transfer agent **48** was developed, combining two orthogonal reaction pathways in the same molecule: photoreactive tetrazole end groups and trithiocarbonate moieties (with adequate R and Z groups), able to control the radical polymerization of styrene. In this way, well-defined α,ω -tetrazole-capped PS chains of different molecular weights could be obtained and further ligated with bismaleimides in a photopolymerization process.

4.2. Network Formation via NITEC

In the previous section it was demonstrated how NITEC chemistry can be used as a powerful tool to access quantitative information on the kinetics of step-growth

TOWARDS HOMOGENEOUS ALIGNMENT MEDIA

polymerizations. The formation of one fluorescent unit for each ligation point (refer to Figure 4.1) offers the unique possibility to monitor conversion in macromolecular systems by simple fluorescence readouts. It was thus desirable to extend the scope of this strategy to crosslinked networks, using the fluorescence arising from each junction point as an estimation for crosslinking density (Figure 4.24).

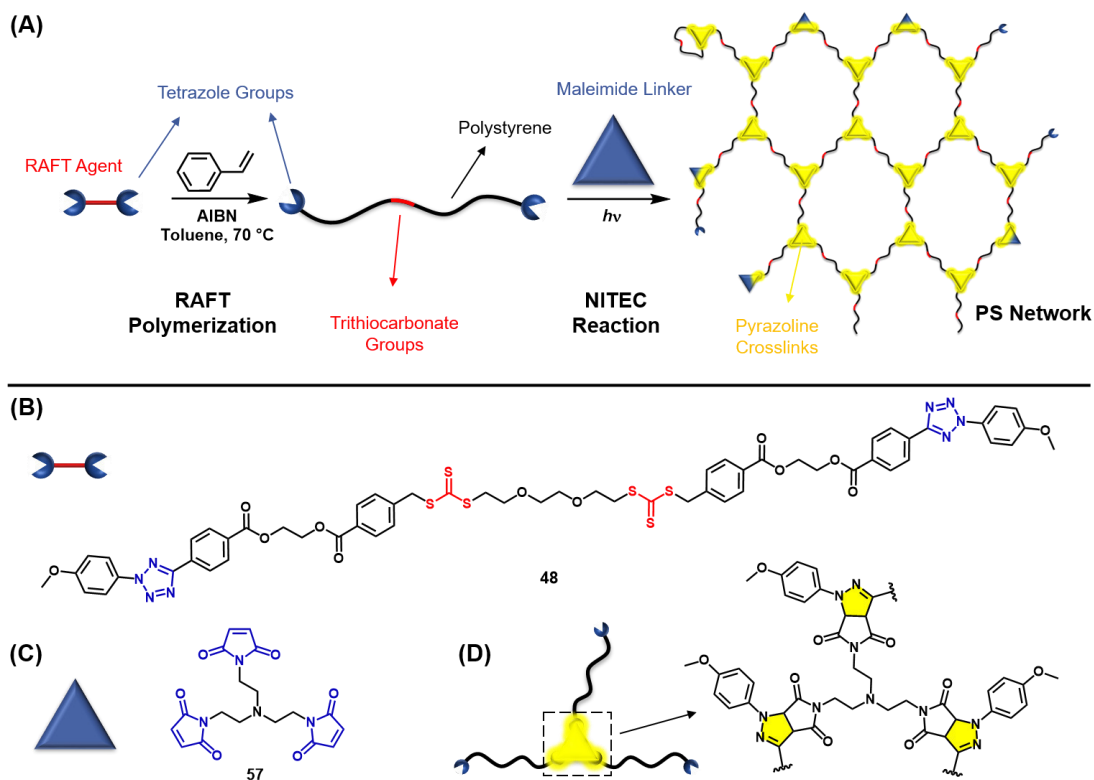


Figure 4.24. (A) General reaction scheme of network formation. Well-defined end-capped tetrazole PS chains are obtained via RAFT polymerization and subsequently end-linked with a trifunctional maleimide via NITEC chemistry. (B) Structure of tetrazole-RAFT agent **48**. (C) Structure of trimaleimide linker **57**. (D) Structure of fluorescent pyrazoline crosslink motifs obtained after NITEC ligation. Adapted with permission from John Wiley and Sons, Ref 299.

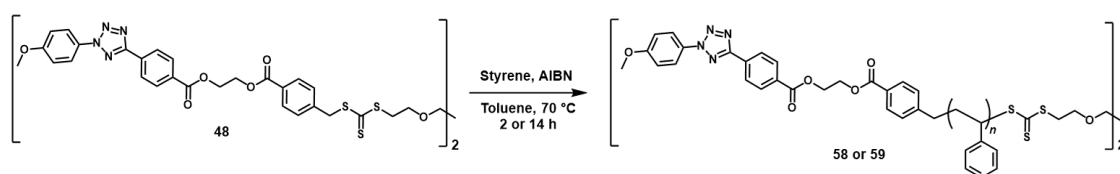
Employing a two-step synthesis approach (RAFT polymerization of styrene followed by UV-induced crosslinking, see Figure 4.24A), higher level of structural homogeneity is expected for the obtained PS networks, in comparison to the free-radical-based gels introduced in Chapter 3. On the one hand, the RAFT polymerization strategy affords well-defined telechelic linear PS precursors of tunable chain length (refer to Figure 8.14 in Appendix 8.3), which directly determine the average mesh size of the corresponding networks. On the other hand, the UV-induced NITEC end-linking of the PS precursors allows a temporal control on the extent of crosslinking, which depends solely on how long the sample is irradiated. Moreover, the intrinsic

TOWARDS HOMOGENEOUS ALIGNMENT MEDIA

fluorescence of the obtained NITEC networks provides a unique analytical tool for crosslinking determination, in analogy to the step-growth polymers presented in Section 4.1.

4.2.1. Conditions for Network Formation

First, tetrazole end-capped PS strands were prepared via RAFT polymerization of styrene, mediated by CTA **48** (Scheme 4.5). Analogous to the RAFT polymers presented in the previous section (refer to Figure 4.18), PS precursors (**58** and **59**) of two different molecular weights ($\bar{M}_n = 2800 \text{ g}\cdot\text{mol}^{-1}$ the former and $\bar{M}_n = 7200 \text{ g}\cdot\text{mol}^{-1}$ the latter, determined by SEC) were afforded, exhibiting narrow molecular weight distributions ($\mathcal{D} = 1.15$ and 1.11 , respectively, refer to Figure 4.39B).



Scheme 4.5. RAFT polymerization of styrene mediated by bifunctional-tetrazole CTA **48**.

End group fidelity was investigated by ^1H NMR spectroscopy (Figures 4.25 and 4.26). The characteristic resonances of polystyrene, at 1.2–2.0 ppm (aliphatic backbone, **h**) and 6.2–7.1 ppm (aromatic side chains, **i**) are present in the spectra, in combination with the signals stemming from the tetrazole-chain transfer agent **48**, between 7.8–8.4 ppm (aromatic protons **e**, **d**, **c**, and **g**), between 4.6–4.8 ppm and 3.4–3.8 ppm (aliphatic linkers, **f**, **j** and **k**), and the characteristic singlet at 3.9 ppm, corresponding to the methoxy group of the tetrazole, **a**. Integration of the signals stemming from the tetrazole units and the styrene backbone permits estimation of the degree of polymerization (refer to Section 2.6.2). In this way, number average molecular weights $\bar{M}_n = 2700 \text{ g}\cdot\text{mol}^{-1}$ for PS **58** and $\bar{M}_n = 7300 \text{ g}\cdot\text{mol}^{-1}$ for PS **59**, were calculated via ^1H NMR analysis.

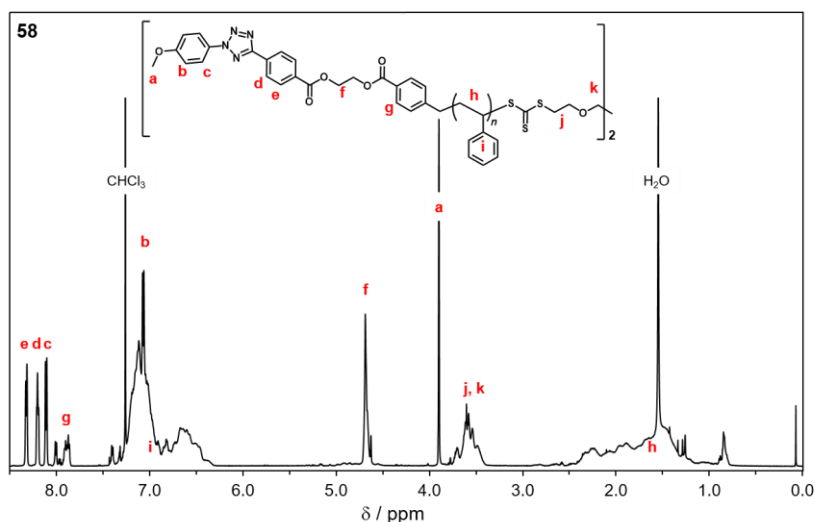


Figure 4.25. ¹H NMR spectrum in CDCl₃ of RAFT PS **58**. Ratio of repeat unit resonance integrals (i, 7.2–6.3 ppm) to end group resonance integrals (a, 3.9–3.8 ppm; e, 8.4–8.3 ppm) results in $\bar{M}_{n(\text{NMR})} = 2700 \text{ g}\cdot\text{mol}^{-1}$. Adapted with permission from John Wiley and Sons, Ref 299.

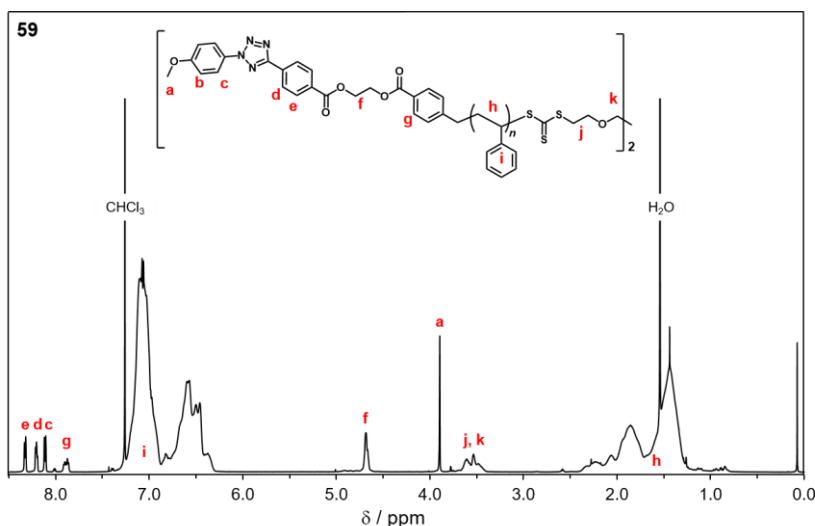


Figure 4.26. ¹H NMR spectrum in CDCl₃ of RAFT PS **59**. Ratio of repeat unit resonance integrals (i, 7.2–6.3 ppm) to end group resonance integrals (a, 3.9–3.8 ppm; e, 8.4–8.3 ppm) results in $\bar{M}_{n(\text{NMR})} = 7300 \text{ g}\cdot\text{mol}^{-1}$. Adapted with permission from John Wiley and Sons, Ref 299.

The formation of α,ω -tetrazole-capped PS chains was further confirmed by SEC-ESI-MS analysis. Analogous to the RAFT polymers presented in the previous section (see Figure 4.19), sample **59** displays the characteristic m/z distribution patterns of the expected bifunctional tetrazole PS, along with a small fraction of AIBN-initiated chains (Figure 4.27).

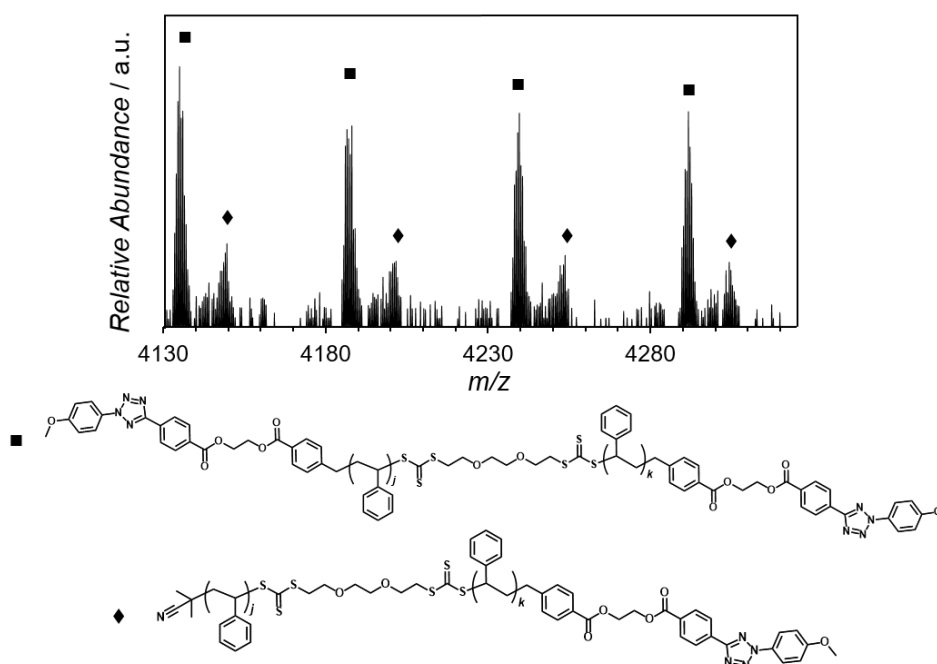


Figure 4.27. SEC-ESI-MS spectrum (negative mode) of RAFT PS **59** showing typical mass and isotopic pattern for the expected structure ■. Secondary PS structure ◆ (AIBN-initiated polymer) was also found. The spectrum was recorded at the maximum of the molar mass distribution (retention time 15.9 min in SEC chromatogram). Adapted with permission from John Wiley and Sons, Ref 299.

Table 4.1. Structure assignment for the peaks in the MS spectrum in Figure 4.27.

Structure	n	m/z (exp)	m/z (theo)	$\Delta m/z$
$[\blacksquare+21]^{2-}$	$j + k = 65$	4132.0366	4132.0488	0.0122
$[\blacklozenge+21]^{2-}$	$j + k = 69$	4145.5869	4145.6231	0.0362

Afterwards, the conditions for network formation were investigated employing the long styrene polymers **59** and the commercially available trimaleimide linker **57** (see Figure 4.24C) as precursors. Initially, the same reaction conditions as for step-growth polymers **49** (described in Section 4.1) were utilized. Both reagents were mixed and dissolved in CDCl_3 (keeping an equimolar ratio of tetrazole and maleimide groups), at $40 \text{ mmol}\cdot\text{L}^{-1}$ starting concentration of **59**. Under such conditions, up to 48 h irradiation at 320 nm – using the photoreactor setup described in Figure 8.8, Appendix 8.2 – were needed to obtain appreciable amounts of crosslinked material (Figure 4.28). Nevertheless, it is well known in literature that the initial concentration of network precursors greatly affects the structure and final properties of the obtained gels. This also holds true for networks prepared from end-linking methods, for which lower initial

TOWARDS HOMOGENEOUS ALIGNMENT MEDIA

concentrations of precursors favor internal cyclization (primary and secondary loops).^{175,223}

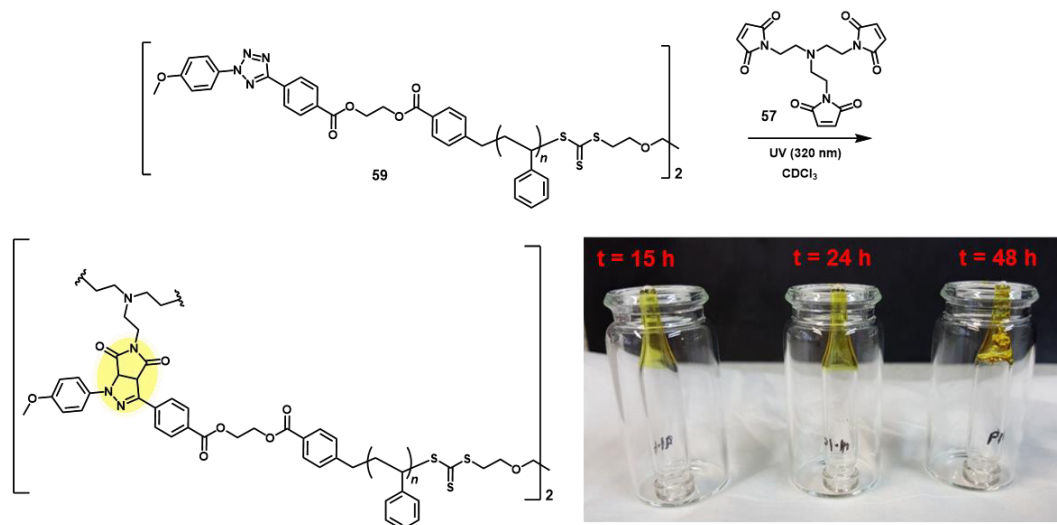


Figure 4.28. NITEC network formation from PS precursor **59** and crosslinker **57**, irradiated 15 h, 24 h, and 48 h at 320 nm.

Taking this into account, the initial concentration of **59** was increased to $65 \text{ mmol}\cdot\text{L}^{-1}$ (ca. $470 \text{ mg}\cdot\text{mL}^{-1}$), at which the solubility limit of crosslinker **57** in chloroform was reached. Under these conditions, irradiation times up to 64 h (320 nm) were needed to obtain insoluble networks. When the effect of the molecular weight of the PS precursor was studied, it was found that PS strands **58** dissolved at the same starting molar concentration as before ($65 \text{ mmol}\cdot\text{L}^{-1}$, ca. $180 \text{ mg}\cdot\text{mL}^{-1}$) did not produce any insoluble material. Conversely, if the mass concentration was kept constant ($470 \text{ mg}\cdot\text{mL}^{-1}$, ca. $168 \text{ mmol}\cdot\text{L}^{-1}$ **58**), more insoluble material was obtained, though qualitatively less than for the long chain precursor **59** (Figure 4.29). Notwithstanding, the more concentrated the precursor solution, the less effective is the penetration of light into the center of the vial, so the bulk of the solution becomes virtually unreachable to the irradiation source.

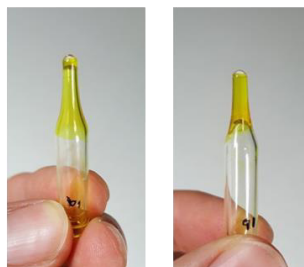
TOWARDS HOMOGENEOUS ALIGNMENT MEDIA

PS **58** $\bar{M}_n = 2800 \text{ g}\cdot\text{mol}^{-1}$
 $65 \text{ mmol}\cdot\text{L}^{-1} \approx 182 \text{ mg}\cdot\text{mL}^{-1}$



PS **59** $\bar{M}_n = 7200 \text{ g}\cdot\text{mol}^{-1}$
 $65 \text{ mmol}\cdot\text{L}^{-1} \approx 470 \text{ mg}\cdot\text{mL}^{-1}$

PS **58** $\bar{M}_n = 2800 \text{ g}\cdot\text{mol}^{-1}$
 $168 \text{ mmol}\cdot\text{L}^{-1} \approx 470 \text{ mg}\cdot\text{mL}^{-1}$



PS **59** $\bar{M}_n = 7200 \text{ g}\cdot\text{mol}^{-1}$
 $65 \text{ mmol}\cdot\text{L}^{-1} \approx 470 \text{ mg}\cdot\text{mL}^{-1}$

Figure 4.29. Comparison of network formation at different initial concentrations of PS precursors **58** and **59**. Samples were irradiated at 320 nm for 64 h.

In order to overcome this issue, the reaction vessel was changed from conical vials to glass slides (precursor solution pressed between two slides). This setup has the advantage that larger areas can be irradiated with minimal decrease in the light penetration. Additionally, the solvent was changed to DMF due to the better solubility of **57** in this solvent (details of the experimental procedure can be found in Chapter 6). In both cases (vials and slides), solids presenting strong fluorescence emission were obtained (Figure 4.30), corroborating that fluorescence can be used as visual cue for network formation in NITEC-based systems.^{55,208,304}

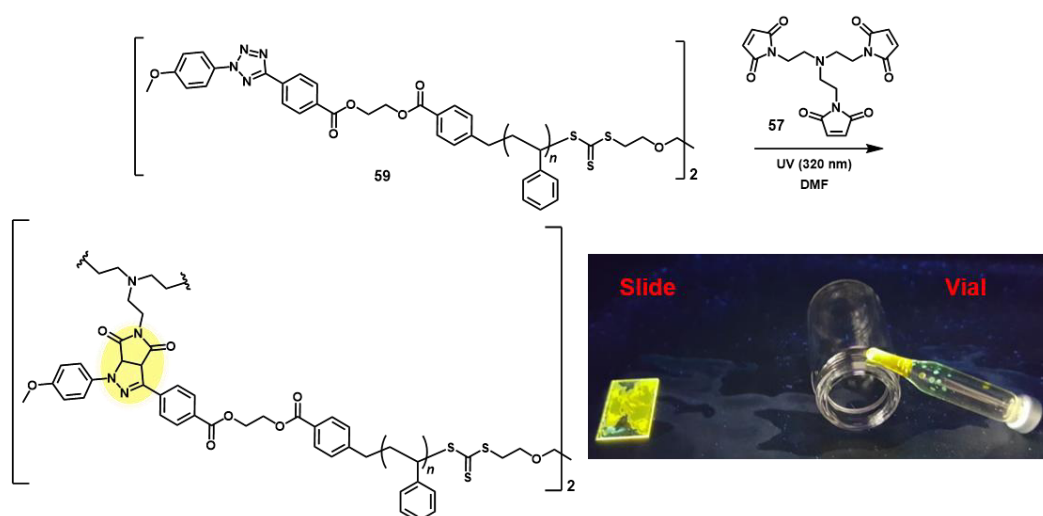


Figure 4.30. NITEC network formation from PS precursor **59** and crosslinker **57**, irradiated 48 h at 320 nm, either inside glass vials or between two glass slides.

TOWARDS HOMOGENEOUS ALIGNMENT MEDIA

The crude solid obtained after irradiation was washed several times with chloroform and THF to extract soluble material. All fractions from washing were collected and the solvent evaporated to recover the soluble fraction. Similarly, the crosslinked material that did not dissolve was dried and the relative amounts of soluble and insoluble fraction were determined by gravimetry (Table 4.2). The experimental data reveals that the amount of insoluble material increases with longer reaction times, up to 24 h irradiation, after which it decreases again. This phenomenon might be explained by UV degradation of the trithiocarbonate moieties after long irradiation times,³¹¹ as reported in the previous section for step-growth polymers **45**.

Table 4.2. Soluble and insoluble fractions of NITEC networks prepared from tetrazole-PS **59** and trimaleimide **57**, irradiated at 320 nm.

Entry ^a	Irradiation Time	Soluble Fraction	Insoluble Fraction
1	0 h	100 wt.%	0 wt.%
2	15 h	62 wt.%	38 wt.%
3	24 h	59 wt.%	41 wt.%
4	39 h	63 wt.%	37 wt.%
5	48 h	72 wt.%	28 wt.%
6	48 h	88 wt.%	12 wt.%

^a [59]₀ = 710 mg·mL⁻¹ in DMF. Glass slides used in entries 1–5, conical vial in entry 6.

Figure 4.31A displays the SEC traces of the soluble fractions at different irradiation times. It can be observed that broad molecular weight distributions are obtained, accounting for polymer–polymer ligation. Moreover, signals of lower molecular weight than the starting material become important at longer irradiation times, corroborating the possible scenario of UV degradation of the trithiocarbonate moieties. On the other hand, it is evident from entries 5 and 6 in Table 4.2 that performing the reaction in glass slides yields more insoluble material than in conical vials, at constant irradiation time. The SEC traces of the soluble fraction obtained in these two reaction vessels after 48 h irradiation were also compared (Figure 4.31B). It was found that in the vials not only more insoluble fraction is obtained, but the molecular weight distribution is broader than for the glass slides. It can be inferred from these observations that the network formation in conical vials is not efficient, since it affords mostly macromolecular ligation (soluble step-growth polymers) instead of crosslinking.

TOWARDS HOMOGENEOUS ALIGNMENT MEDIA

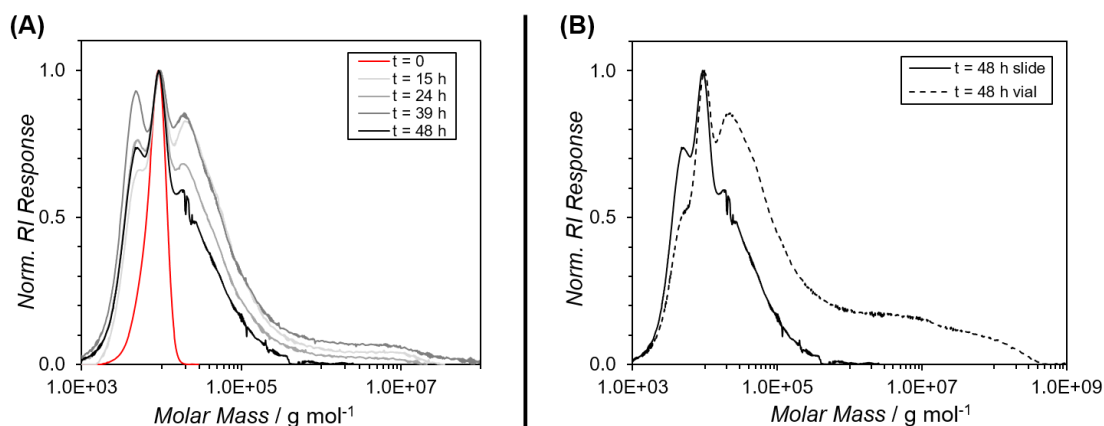


Figure 4.31. (A) SEC traces of soluble fractions obtained from the NITEC reaction of **59** and **57** (in glass slides), after several irradiation times. (B) Comparison of SEC traces of soluble fractions after 48 h irradiation, obtained in glass slides (solid line) and conical vials (dashed line).

Although optimization of the reaction vessel increased the formation of insoluble material, long irradiation times (up to 24 h) are still required. This can have a detrimental impact on the fluorescence emission properties of the networks, e.g. aromatization of the pyrazoline fluorophore as observed for the step-growth polymers in Section 4.1. Such phenomena would obviously hinder the accurate determination of crosslinking density via fluorescence spectroscopy. Therefore, the irradiation setup was modified in order to decrease reaction time without compromising network yield (compare Figure 8.8 in Appendix 8.2 and Figure 8.15 in Appendix 8.3).

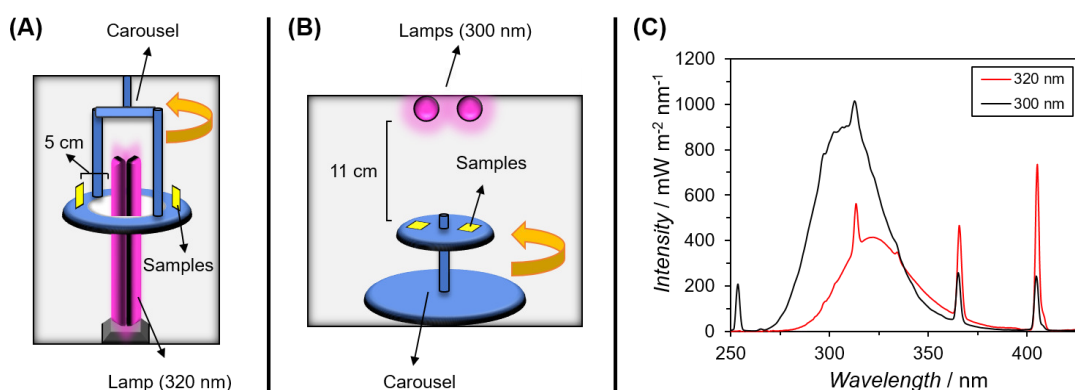


Figure 4.32. Schematic representation of the photoreactors used for network formation. (A) One lamp ($\lambda_{\text{max}} = 320$ nm) in the middle and samples revolving around it at 5 cm distance. (B) Two lamps ($\lambda_{\text{max}} = 300$ nm) irradiating the samples from the top, at 11 cm distance. (C) Comparison of the absolute light intensity reaching the samples in each of the photoreactors: 320 nm (red line) and 300 nm (black line).

TOWARDS HOMOGENEOUS ALIGNMENT MEDIA

Instead of using one single lamp with λ_{\max} 320 nm (Figure 4.32A), a photoreactor having two lamps emitting at λ_{\max} 300 nm was utilized (Figure 4.32B). In this way, the actual irradiation dose reaching the sample (between 200–400 nm) was increased from 2.1 to 4.6 mW·cm⁻² (Figure 4.32C). With this optimized setup, the precursor solutions (PS strands **58** or **59**, 710 mg·mL⁻¹ in DMF; trimaleimide **57**, 1 : 1 mol ratio tetrazole : maleimide) were placed between glass slides (Figure 4.33A) and irradiated 0–8 h at 300 nm (Figure 4.33B).

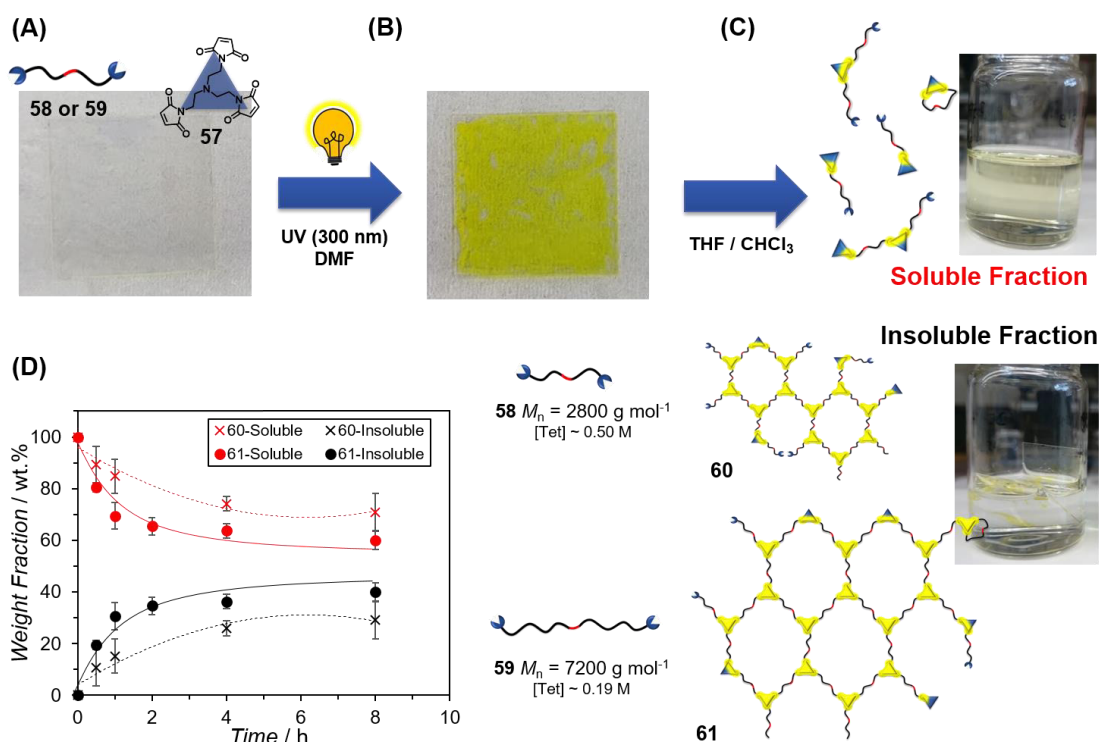


Figure 4.33. (A) PS precursors **58** or **59** and trimaleimide **57** were mixed in DMF and sandwiched between two glass slides. Initial concentration of tetrazole groups is ca. 0.50 M for **58** and ca. 0.19 M for **59**. (B) Irradiation at 300 nm produces yellow solids. (C) From the crude solid, soluble and insoluble fractions are isolated by extensive washing with THF and chloroform. Insoluble networks **60** (from short PS **58**) and **61** (from long PS **59**) are thus obtained. (D) Evolution of soluble (red) and insoluble (black) fractions of networks **60** (crosses) and **61** (dots), at different irradiation times. Error bars represent standard deviation from three independent replicas. Solid and dashed lines are guides for the eye. Adapted with permission from John Wiley and Sons, Ref 299.

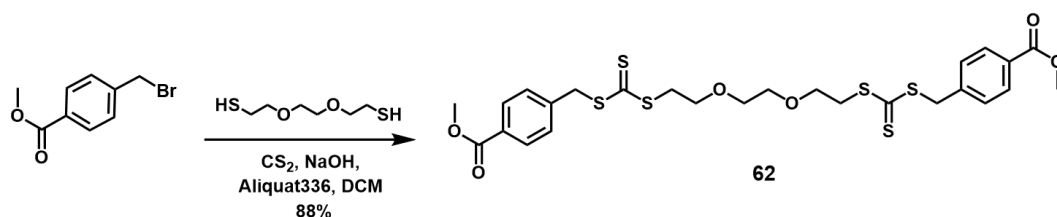
Afterwards, the crude yellow solid was immersed in THF and washed several times with fresh solvent to separate the soluble and insoluble fractions (Figure 4.33C). Insoluble networks **60** and **61** (stemming from the short and long PS precursors **58** and **59**, respectively) were thus obtained. The weight percentage of soluble and insoluble fractions of samples **60** and **61** was determined by gravimetry. Figure 4.33D depicts

TOWARDS HOMOGENEOUS ALIGNMENT MEDIA

the corresponding kinetic evolution of the different fractions with increasing irradiation time. It can be seen that longer irradiation promotes the decrease of the percentage of soluble fraction, with a concomitant increase in the insoluble fraction. This is a good indication that crosslinking takes place only under UV irradiation, since no insoluble material was formed at $t = 0$. Furthermore, the process can be stopped at will by simply removing the irradiation source, achieving excellent temporal control over the crosslinking process.

From the kinetic plot in Figure 4.33D it can be highlighted that for every irradiation time employed, lower amounts of insoluble network **60** (derived from short PS precursor **58**) are obtained, in comparison to networks **61**. This observation concurs with the preliminary experiments performed in conical vials (refer to Figure 4.29). Probably, the higher molar concentration of reactive groups in the short polymer **58**, compared to the long one **59** at the same mass concentration ($[\text{tetrazole}]_i \approx 0.50 \text{ M}$ vs. 0.19 M , respectively), accounts for this behavior. Furthermore, a maximum amount of 40 wt.% of insoluble fraction was obtained for network **61** already after 8 h irradiation at 300 nm. Conversely, using the 320 nm lamp setup, more than 15 h were necessary to obtain comparable values (see Table 4.2).

In order to quantitatively assess the effect of the UV irradiation on the trithiocarbonate groups,³¹¹ a model chain transfer agent **62** – analogous to compound **48** but without tetrazole groups – was synthesized (Scheme 4.6). Following the same reaction route as for **48**, the non-functional CTA **62** was obtained in 88% isolated yield (refer to the experimental section in Chapter 6).



Scheme 4.6. Synthesis of trithiocarbonate-based symmetrical RAFT agent **62**.

Afterwards, **62** was mixed with trimaleimide **57** in DMF ($[\text{62}]_i = 0.11 \text{ M}$), the solution placed between glass slides and irradiated at 300 nm for 0–16 h, mimicking the experimental conditions employed for network formation. The different samples were then analyzed by ¹H NMR spectroscopy to determine the extent of trithiocarbonate degradation (Figure 4.34A). Comparing the characteristic resonances of the protons **d** and **e** next to the trithiocarbonate groups with the signals of the aromatic

moiety **a**, **b**, and **c** at different irradiation times, a numerical estimation of trithiocarbonate degradation could be obtained (Figure 4.34B).

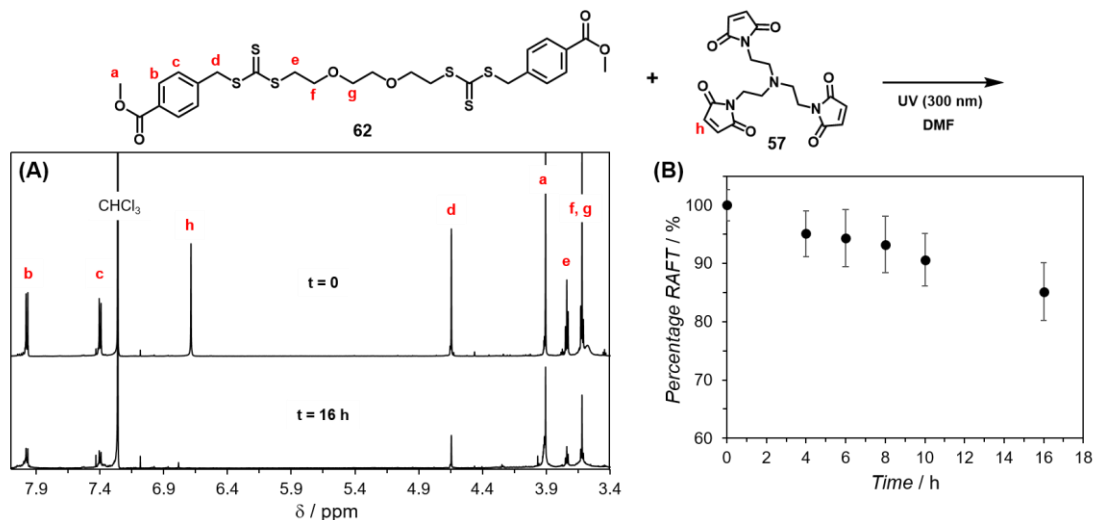


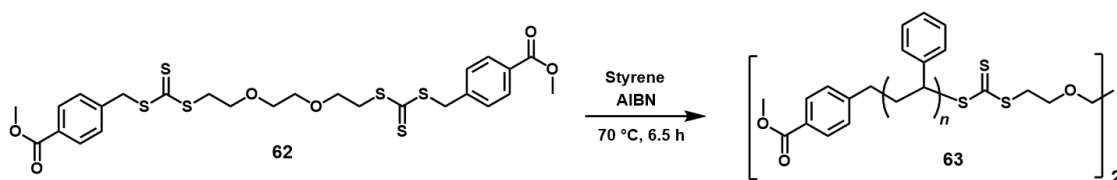
Figure 4.34. (A) ¹H NMR spectra in CDCl₃ of mixtures of **62** and **57**, irradiated at 300 nm for different times. Ratios of resonance signals d/b, d/c, e/b, e/c, d/a, and e/a, were used to determine degradation of trithiocarbonate groups. (B) Plot of percentage of trithiocarbonate groups vs. irradiation time. Ratios from NMR signals were averaged (error bars represent standard deviation) and normalized to 100% for $t = 0$. Adapted with permission from John Wiley and Sons, Ref 299.

It was found that ca. 95% of the initial amount of trithiocarbonate groups remain intact after 8 h UV irradiation under the studied conditions. However, this value decreases to 90% after 10 h and 85% after 16 h, confirming that long irradiation times are deleterious for the integrity of the CTA. In this respect, a maximum of 8 h irradiation was adopted for the network formation, in order to have appreciable amounts of insoluble material and minimize the impact of trithiocarbonate degradation.

4.2.2. Characterization via Fluorescence Spectroscopy

Once the synthesis conditions for network formation were standardized, the evaluation of the fluorescence emission of the different network samples was investigated. As first approach, direct measurement of fluorescence in the solid state was attempted. For this purpose, a calibration curve that correlates fluorescence intensity and amount of pyrazoline in a solid PS matrix was required. Therefore, the model RAFT agent **62** was used to obtain PS strands **63** ($\bar{M}_w = 4600 \text{ g} \cdot \text{mol}^{-1}$, $\mathcal{D} = 1.15$), that resemble the photoactive precursors **58** and **59** without tetrazole moieties (Scheme 4.7). Details of the polymerization procedure can be found in the experimental section in Chapter 6.

TOWARDS HOMOGENEOUS ALIGNMENT MEDIA



Scheme 4.7. Synthesis of PS strands **63** via RAFT polymerization mediated by CTA **62**.

Subsequently, PS **63** was dissolved in the pyrazoline standard solutions **51** already introduced in Section 4.1 (see Figures 4.9 and 4.10), at a concentration of $300 \text{ mg}\cdot\text{mL}^{-1}$ (in THF). Then, the polymer-pyrazoline mixtures were casted onto glass slides via spin coating, obtaining relatively homogeneous films of fluorescent polymer-fluorophore blend (Figure 4.35A). The films were directly analyzed by fluorescence spectroscopy in the solid state, using a cuvette with a special inset holder for glass slides (Figure 4.35B). In this way, a calibration curve for fluorescence emission in the solid films was obtained, since the amount of pyrazoline **51** in the original solution is known. Even though the dispersity of the points is relatively high, a fairly good linear relationship was found for the measurements in solid state (see Figure 4.35B).

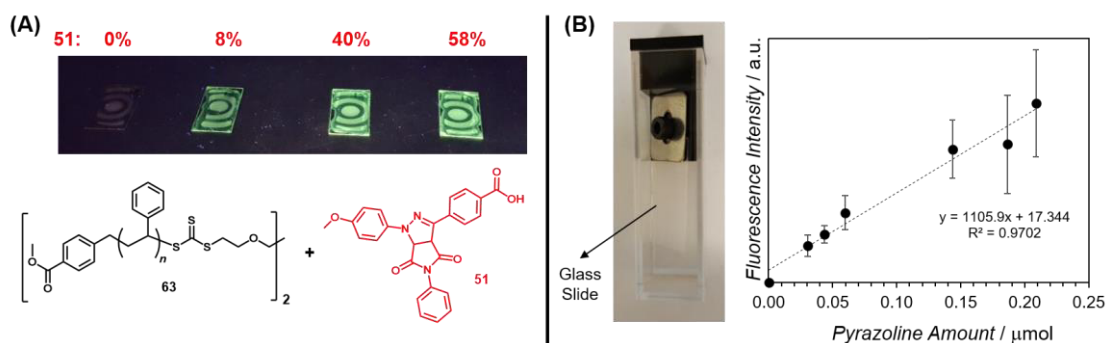


Figure 4.35. (A) Solutions of RAFT-PS **63** and pyrazoline standards **51** in THF were casted onto glass slides by spin coating, obtaining homogeneous fluorescent films. (B) Fluorescence cuvette with special holder for glass slides. The films were thus analyzed in the solid state to construct a calibration curve. Error bars represent standard deviation from eight independent samples.

The calibration curve for solid films was thus validated using a step-growth polymer system as test sample. Tetrazole-functional PS **59** was irradiated with bismaleimide **44** for different times to obtain fluorescent ligated macromolecules in solution, similar to the ones reported in Section 4.1 (Figure 4.36A).

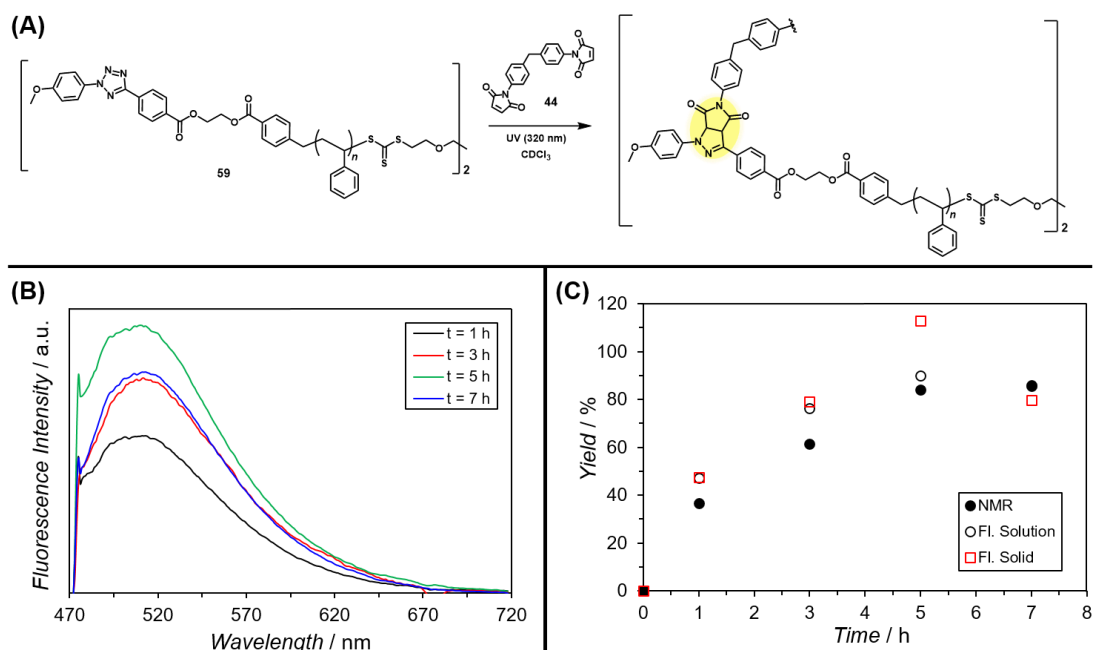


Figure 4.36. (A) Preparation of step-growth polymers from tetrazole-functional PS **59** and bismaleimide **44** in solution, at 320 nm irradiation for 0–7 h. (B) The different samples were dissolved in THF, casted onto glass slides by spin coating and fluorescence intensity measured in the solid state. (C) The yield of poly(pyrazoline) was calculated either by NMR (solid black dots), fluorescence in solution (open black dots), or fluorescence in solid state (open red squares), giving similar results.

The different soluble samples were then spin coated onto glass slides, following the same procedure as for the calibration curve in Figure 4.35. This procedure yielded homogeneous films that were directly analyzed in the solid state via fluorescence spectroscopy (Figure 4.36B). The yield of poly(pyrazoline) for the different samples was then determined using the calibration curve in Figure 4.35B, and the results compared with the values extracted from NMR spectroscopy and conventional fluorescence measurements in solution. Fairly good agreement was obtained for the yield of pyrazoline in the step-growth polymers using the different techniques, demonstrating the applicability of spin coated films as calibration curve in the solid state (Figure 4.36C). Nonetheless, in order to obtain accurate and reproducible results from this technique, thin and very homogeneous films are required. Taking into account that the insoluble samples **60** and **61**, obtained after solvent washing, are rather rough and inhomogeneous (Figure 4.37), it was not possible to apply the spin coating method to quantitatively analyze their fluorescence emission.

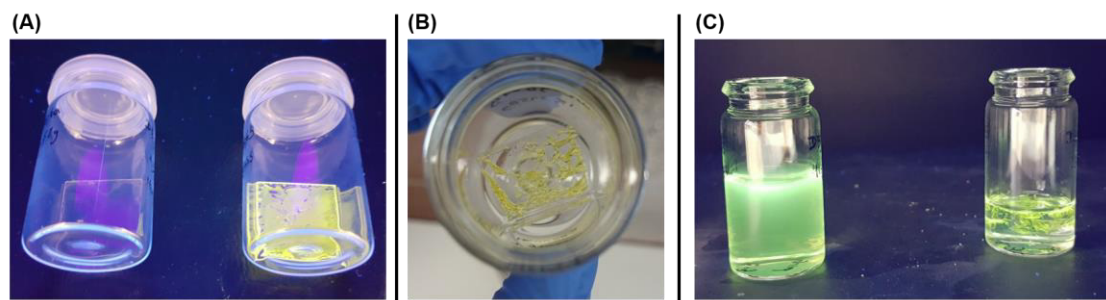


Figure 4.37. (A) Photographs of samples **61** after $t = 0$ (left) and $t = 8$ h irradiation at 300 nm. (B) Insoluble fraction of **61** ($t = 8$ h) remaining in the glass slide after extensive washing with solvents. (C) Both soluble (left) and insoluble (right) fractions of **61** exhibit strong fluorescence emission.

4.2.2.1. Aminolysis of RAFT Polymers

The fluorescence intensity of the networks could not be directly analyzed in the solid state for quantitative purposes. Therefore, the possibility of degrading the networks into soluble systems,^{174,223} without affecting their fluorophore groups, was investigated. For instance, aminolysis of the trithiocarbonate groups stemming from the RAFT agent (refer to Section 2.2) was explored as degradation strategy. The experimental conditions for the aminolysis were adapted from previous literature reports⁶⁹ and, as first approach, optimized for the model RAFT polystyrene **63**.

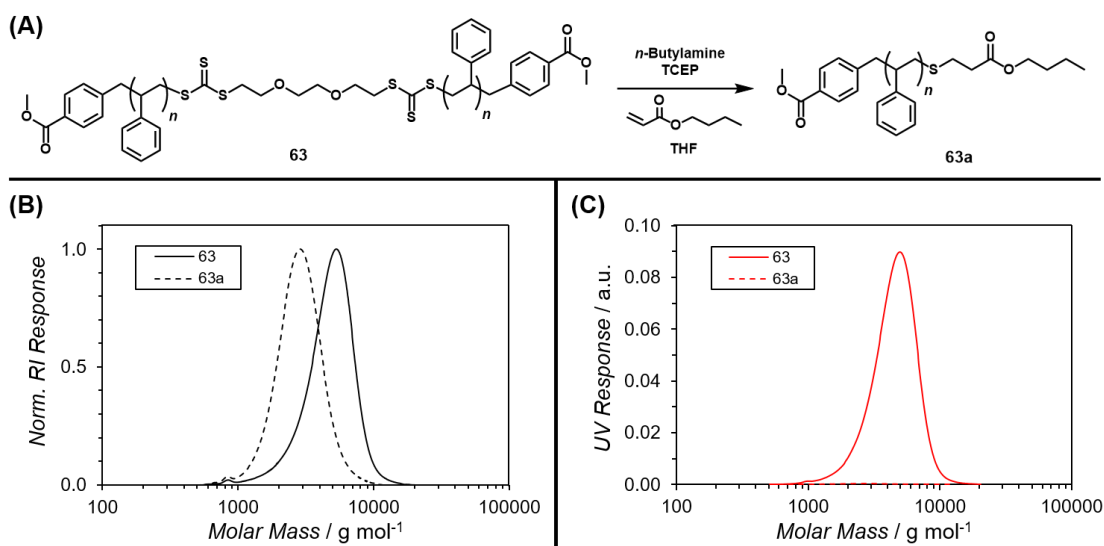


Figure 4.38. (A) One-pot aminolysis/Michael addition of RAFT polymer **63** to produce butyl acrylate-capped chains **63a**. (B) SEC traces (RI detector) of polymer samples before (**63**, solid line) and after (**63a**, dashed line) aminolysis. (C) SEC traces (UV detector at 320 nm) of **63** (solid line) and **63a** (dashed line), showing strong decrease in the signal intensity after aminolysis.

TOWARDS HOMOGENEOUS ALIGNMENT MEDIA

This one-pot protocol involves trithiocarbonate aminolysis with *n*-butylamine (in the presence of reducing agent tris(2-carboxyethyl)phosphine TCEP), followed by Michael addition of the obtained thiol to butyl acrylate (Figure 4.38A). As a result, colorless polymer samples **63a** of roughly half the molecular weight of their parent yellow precursors **63** were afforded (refer to the experimental section). The SEC traces in Figure 4.38B clearly show the reduction in the molar mass after the aminolysis procedure. Furthermore, SEC analysis with UV detection (Figure 4.38C) displays a significant reduction in the signal intensity after aminolysis, corroborating the loss of the trithiocarbonate groups.

Similarly, the optimized aminolysis protocol was tested on the bifunctional tetrazole PS precursors **58** and **59** (Figure 4.39A). An excess of *n*-butylamine is employed for the cleavage of the trithiocarbonate groups present in the polymer chains, affording an intermediate thiol-capped polymer. The input of a reducing agent (TCEP) is necessary in this step to avoid disulfide formation and other oxidation reactions of the free –SH moieties.⁶⁹ Subsequently, the free thiol moieties are treated with an excess of butyl acrylate, promoting their Michael-type thiol-ene reaction. The excess of amine from the first step serves as catalyst for the Michael addition in the second step. The intermediate small molecule side products obtained in this one-pot reaction are conveniently removed from the mixture by precipitation of the polymers in cold methanol.

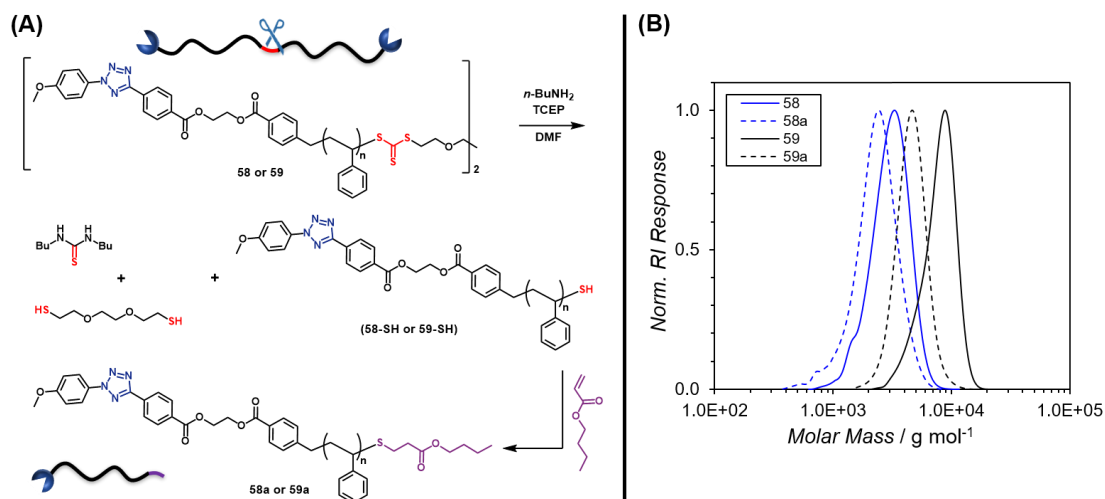


Figure 4.39. (A) Aminolysis of RAFT tetrazole-PS precursors **58** or **59**. Treatment with *n*-butylamine in the presence of TCEP generates thiol-capped polymers **58-SH** or **59-SH** which react in situ with butyl acrylate in a Michael-type addition. Polymer strands **58a** or **59a**, with half the molecular weight of their parent polymers, are thus obtained. (B) SEC traces of PS samples before (**58** and **59**, solid blue and black lines, respectively) and after aminolysis (**58a** and **59a**, dashed blue and black lines, respectively). Adapted with permission from John Wiley and Sons, Ref 299.

TOWARDS HOMOGENEOUS ALIGNMENT MEDIA

Complete trithiocarbonate cleavage was confirmed by analysis of the SEC traces, showing the expected reduction in the molar mass (Figure 4.39B). Additionally, NMR spectroscopy was used to characterize the aminolyzed polymers (Figure 4.40). The resonance signals **j** and **k** corresponding to the aliphatic linker (3.4–3.8 ppm) disappear after aminolysis, and new resonances **l** (4.0 ppm) and **m** (0.9–1.0 ppm), stemming from the butyl acrylate residues, are introduced.

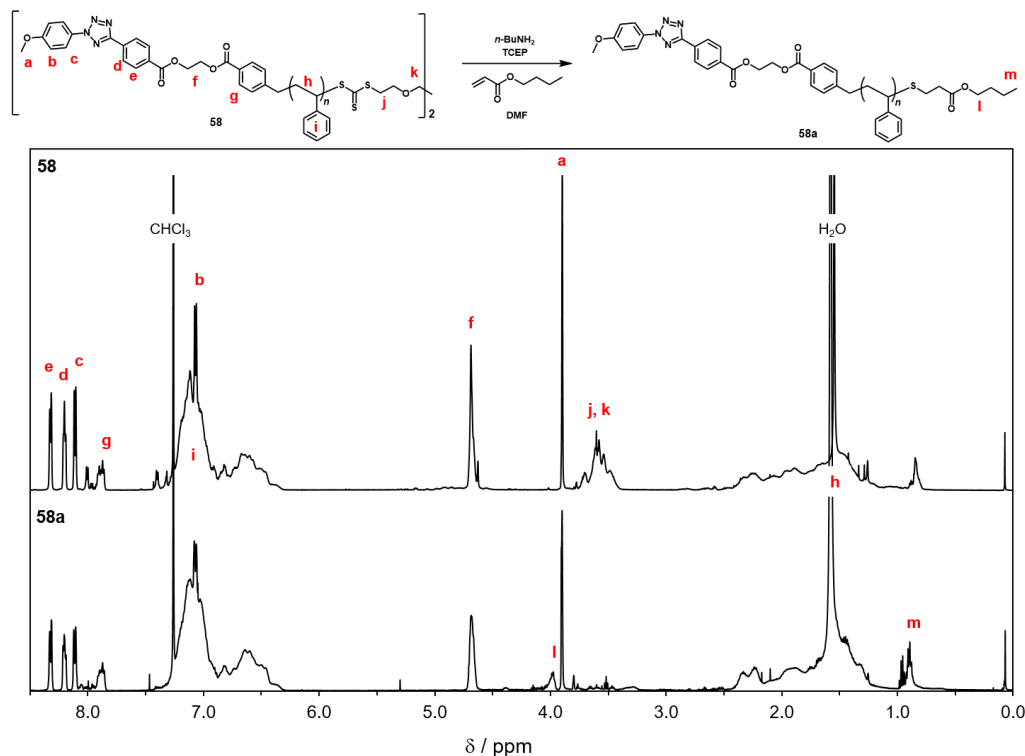


Figure 4.40. ¹H NMR spectra in CDCl₃ of RAFT PS before and after aminolysis, **58** and **58a**, respectively. Disappearance of resonance signals **j** and **k**, and appearance of new signals **l** and **m** confirm the structure of the expected product. Adapted with permission from John Wiley and Sons, Ref 299.

Furthermore, SEC-ESI-MS analysis of the aminolysis product confirmed the effective trithiocarbonate degradation. The spectrum in Figure 4.41 displays the *m/z* distribution pattern for the expected polymer structure ■, containing the end groups ascribed to the thiol-Michael addition to butyl acrylate. In addition, a secondary dithiocarbamate-capped polymer structure ♦ was found, suggesting that under the employed experimental conditions, not all the trithiocarbonate groups are fully degraded to thiols (see Figure 4.41 and Table 4.3).

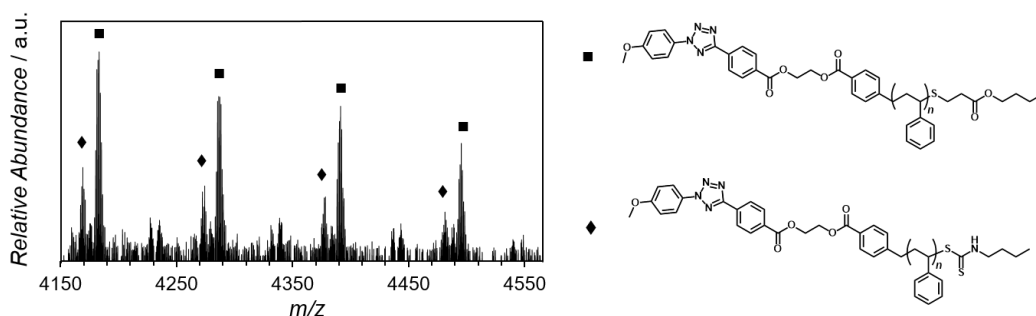


Figure 4.41. SEC-ESI-MS spectrum (negative mode) of aminolysis product **59a** showing typical mass and isotopic pattern for the expected structure **■**. Secondary structure **◆**, corresponding to incomplete aminolysis, was also found. The spectrum was recorded at the maximum of the molar mass distribution (retention time 17.1 min in SEC chromatogram). Reprinted with permission from John Wiley and Sons, Ref 299.

Table 4.3. Structure assignment for the peaks in the MS spectrum in Figure 4.41.

Structure	<i>n</i>	<i>m/z</i> (exp)	<i>m/z</i> (theo)	Δ <i>m/z</i>
■ +I ⁻	33	4179.1768	4179.1856	0.0088
◆ +I ⁻	33	4166.1016	4166.1475	0.0459

Having characterized the degradation of linear precursors **58** and **59** via aminolysis, the same experimental conditions were applied for the disassembly of networks **60** and **61**. Effectively, the initially insoluble networks could be transformed to soluble material after aminolysis. SEC analysis of the soluble and insoluble fractions of network **61**, after aminolysis, display broad molecular weight distributions (Figure 4.42).

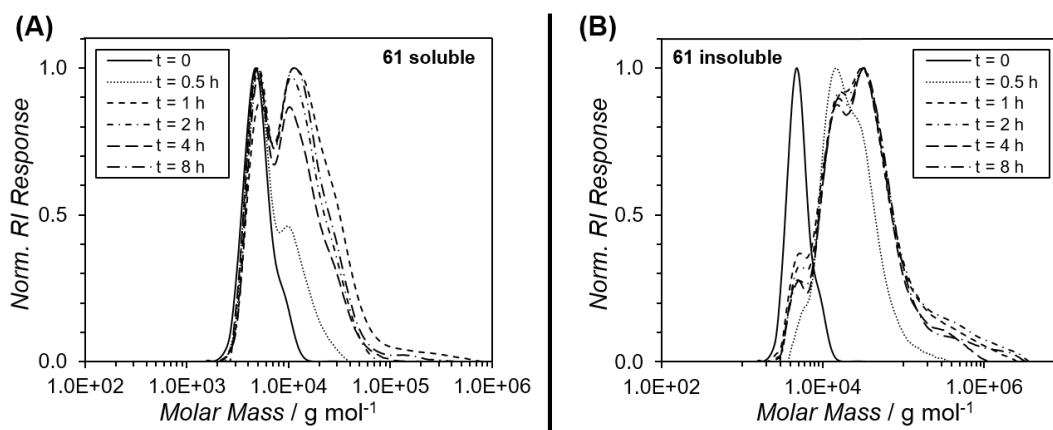


Figure 4.42. Comparison of SEC traces, after aminolysis, of (A) samples **61**, soluble fraction, and (B) samples **61**, insoluble fraction, at different irradiation times. Adapted with permission from John Wiley and Sons, Ref 299.

TOWARDS HOMOGENEOUS ALIGNMENT MEDIA

The soluble fractions of networks **61** show bimodal molecular weight distributions, with higher average molar masses than the corresponding soluble fraction at $t = 0$ after aminolysis (Figure 4.42A). Similarly, the molecular weight distributions of the insoluble fractions (Figure 4.42B) after aminolysis show the presence of high molecular weight material. In every case, the insoluble fractions present macromolecular species of higher molecular weight than their soluble fraction counterparts (refer to Figure 8.16 in Appendix 8.3) Such observations indicate an incomplete trithiocarbonate degradation after applying the aminolysis procedure, from which possibly soluble dimers, trimers, and higher structures are present (see Figure 4.54A).

Critically, the number of fluorescent pyrazoline moieties initially present in the networks remains constant after the aminolysis procedure. In principle, the resulting soluble network fragments can be readily analyzed via fluorescence spectroscopy in solution, enabling the determination of the amount of pyrazoline units (crosslinks) originally connecting the PS chains in networks **60** and **61** (Figure 4.43). Even if the exact structure of the soluble network fragments after aminolysis is not known, this does not prevent the quantification of the pyrazoline groups via fluorescence spectroscopy. The dimers, trimers, and higher structures obtained after aminolysis can be treated as fluorescent step-growth polymers, like the ones previously investigated in Section 4.1. Therefore, access to the crosslinking densities of the networks is granted, as long as completely soluble fragments are obtained after aminolysis.

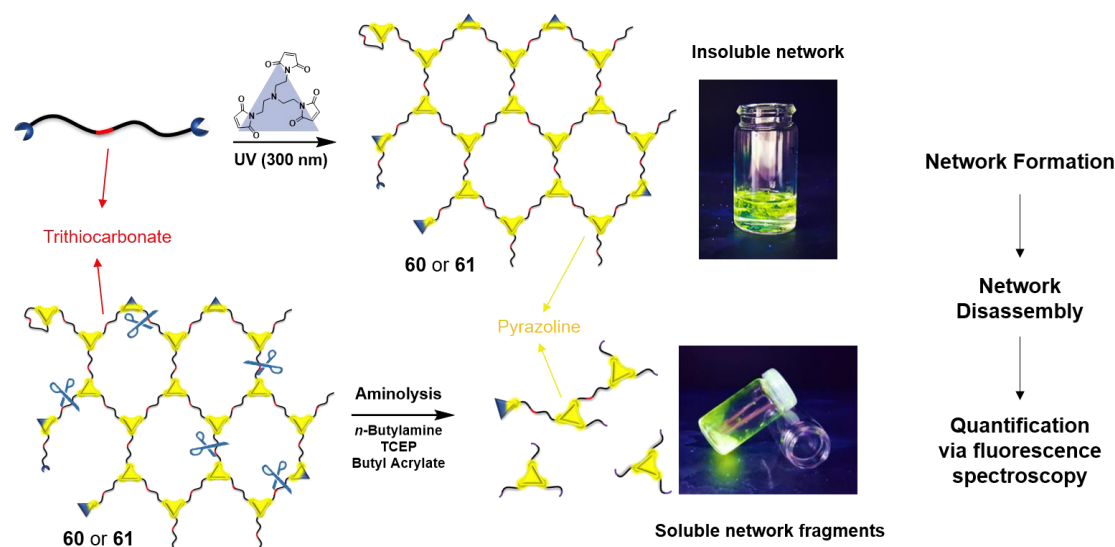


Figure 4.43. Aminolysis of insoluble networks **60** and **61** to produce soluble network fragments. These can be analyzed by fluorescence spectroscopy in solution to retrieve the original number of pyrazoline groups. Adapted with permission from John Wiley and Sons, Ref 299.

TOWARDS HOMOGENEOUS ALIGNMENT MEDIA

However, a plausible scenario that can take place during aminolysis is thiol addition to unreacted maleimide units stemming from linker **57**. The thiol-ene reaction with maleimides is known in the literature to occur very fast at room temperature, even without the addition of base catalysts.³¹² Thus, this process was investigated on linear polymers **59**, exchanging butyl acrylate by **57** as coupling partner during aminolysis (Figure 4.44A).

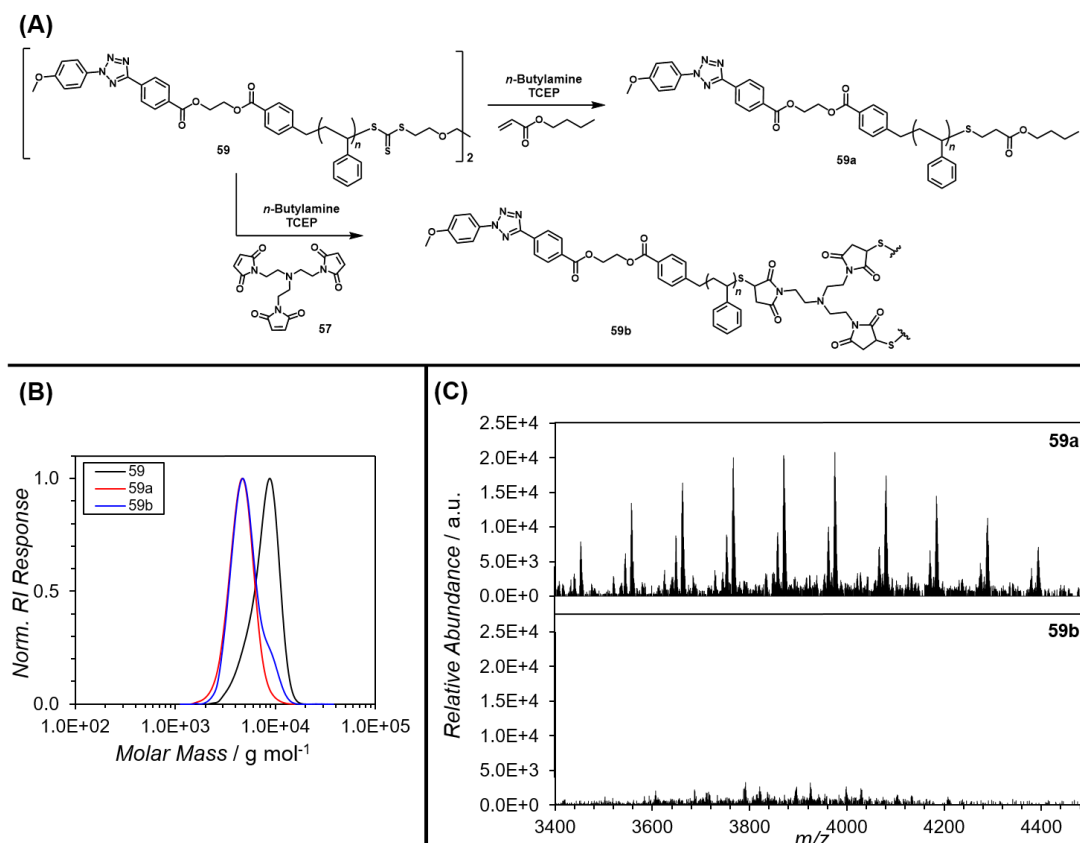


Figure 4.44. (A) Aminolysis of RAFT tetrazole-PS **59** followed by Michael addition to butyl acrylate to yield **59a**, or trimaleimide **57**, producing adduct **59b**. (B) SEC traces of PS samples before aminolysis (**59**, black line), and after coupling with butyl acrylate (**59a**, red line) or trimaleimide (**59b**, blue line). (C) SEC-ESI-MS spectra of adducts **59a** (top) and **59b** (bottom). Adapted with permission from John Wiley and Sons, Ref 299.

Figure 4.44B displays the SEC traces of the parent polymer **59**, the aminolysis product coupled to butyl acrylate **59a**, and the aminolyzed sample **59b** coupled to trimaleimide **57**. The molecular weight distributions of **59a** and **59b** mostly coincide, with the exception of a small shoulder at high molar mass present in the SEC curve of **59b**. Possibly, this shoulder comes from double and triple Michael addition to the three available maleimide groups in **57**. ESI-MS characterization of both aminolysis adducts **59a** and **59b** shows stronger ionization of sample **59a** (Figure 4.44C), with the

TOWARDS HOMOGENEOUS ALIGNMENT MEDIA

characteristic peaks of the expected product (see Figure 4.41 and Table 4.3). On the other hand, analysis of the m/z peak distribution of **59b** reveal the presence of the expected Michael addition product, along with unreacted thiol (Figure 4.45). Due to the poor ionization of the maleimide-addition adducts in **59b**, double and triple Michael addition products could not be found in the MS spectrum.

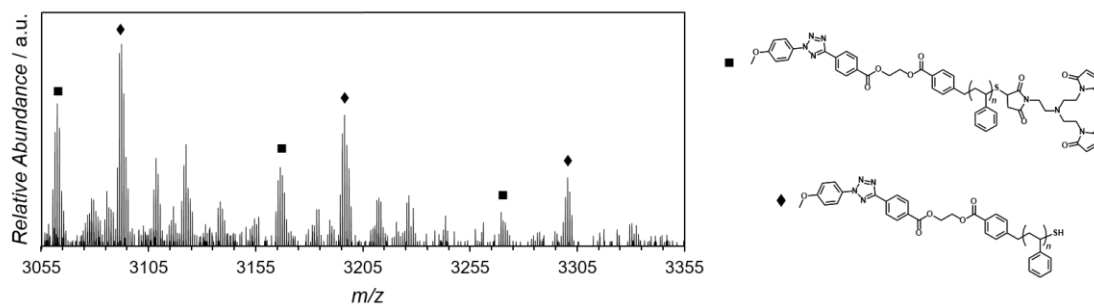


Figure 4.45. SEC-ESI-MS spectrum (negative mode) of aminolysis product **59b** showing typical mass and isotopic pattern for the expected structure ■. Secondary structure ◆, corresponding to thiol-capped polymer, was also found. The spectrum was recorded at 18.9 min retention time in the SEC chromatogram.

Table 4.4. Structure assignment for the peaks in the MS spectrum in Figure 4.45.

Structure	n	m/z (exp)	m/z (theo)	$\Delta m/z$
[■ – H] ⁻	21	3060.3170	3060.5605	0.2435
[◆ – H] ⁻	25	3090.3602	3090.6883	0.3281

In fact, it is important that the extent of Michael addition to trimaleimide during network aminolysis is kept as low as possible. Control experiments on networks produced with an excess of **57** (1 : 3 and 1 : 5 mol ratio tetrazole : maleimide) showed faster formation of insoluble fraction than for the standard 1 : 1 ratio (see Figure 8.17 in Appendix 8.3). However, the insoluble fraction of such networks could not be degraded by aminolysis to a fully soluble material. Probably, the excess of trimaleimide offers the possibility of multiple Michael addition of **59-SH** generated in situ, yielding crosslinked material that cannot be further disassembled.

4.2.2.2. Effect of Aminolysis on Fluorescence

The effect of the aminolysis/Michael addition procedure on the structure of the pyrazoline fluorophore was carefully evaluated. First, control experiments with the small molecule model **51** (refer to Figure 4.9) were performed. As described before in Section 4.1, the concentration of pyrazoline in DMF solution can be estimated by NMR

TOWARDS HOMOGENEOUS ALIGNMENT MEDIA

and correlated to the fluorescence emission of the crude samples. As expected, a linear relationship between fluorescence intensity and concentration of **51** was observed (Figure 4.46). Then, the standard solutions of **51** were subjected to the same aminolysis/Michael addition protocol as for networks **60** and **61**, and their fluorescence intensity was again recorded. Surprisingly, a systematic two-fold increase in the fluorescence emission for the samples after aminolysis was obtained, in comparison to the samples before aminolysis. As depicted in Figure 4.46, the linear behavior between emission intensity and pyrazoline concentration is still maintained, but the slope of the curve is larger after treating the samples with TCEP, *n*-butylamine, and butyl acrylate.

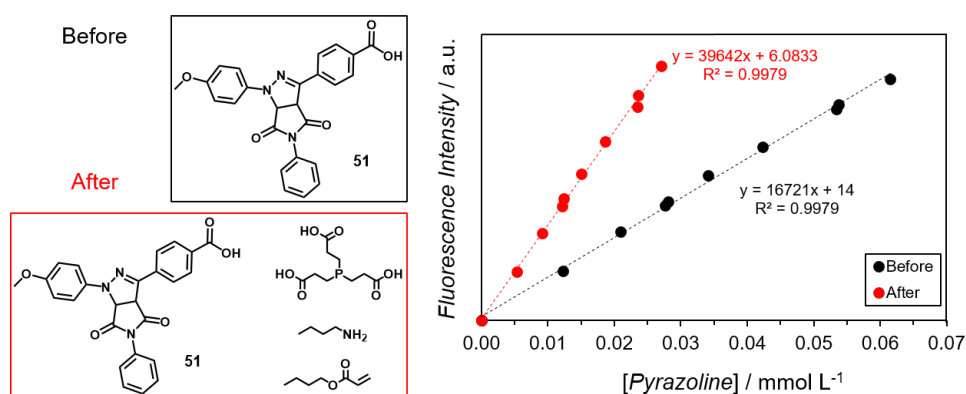


Figure 4.46. Correlation of fluorescence intensity and concentration of pyrazoline **51** before (black) and after (red) aminolysis. Adapted with permission from John Wiley and Sons, Ref 299.

In order to gain insights into this strong variation in the fluorescence emission, the structure of the fluorophore after applying the aminolysis protocol (Figure 4.47A) was analyzed by spectroscopic methods. ¹H NMR spectroscopy (Figure 4.47B) reveals a small shift on the resonances of the fluorophore in the aromatic region (signals 1 and 2 at 8.1 and 8.0 ppm, respectively). After aminolysis these resonance signals move slightly to higher fields (**1'** and **2'**). A similar shift was observed for signal 7 (5.5 ppm), characteristic of the pyrazoline ring, which changes slightly its chemical shift to **7'** after aminolysis (full spectra can be found in Figure 8.18 in Appendix 8.3). Such changes suggest that the *n*-butylamine might open the succinimide ring in **51** via nucleophilic attack, producing structure **51'** (see Figure 4.47A). ESI-MS analysis confirmed the identity of the proposed structure **51'** (Figure 4.47C), and revealed that the initial structure **51** is quantitatively converted to the open pyrazoline adduct.

TOWARDS HOMOGENEOUS ALIGNMENT MEDIA

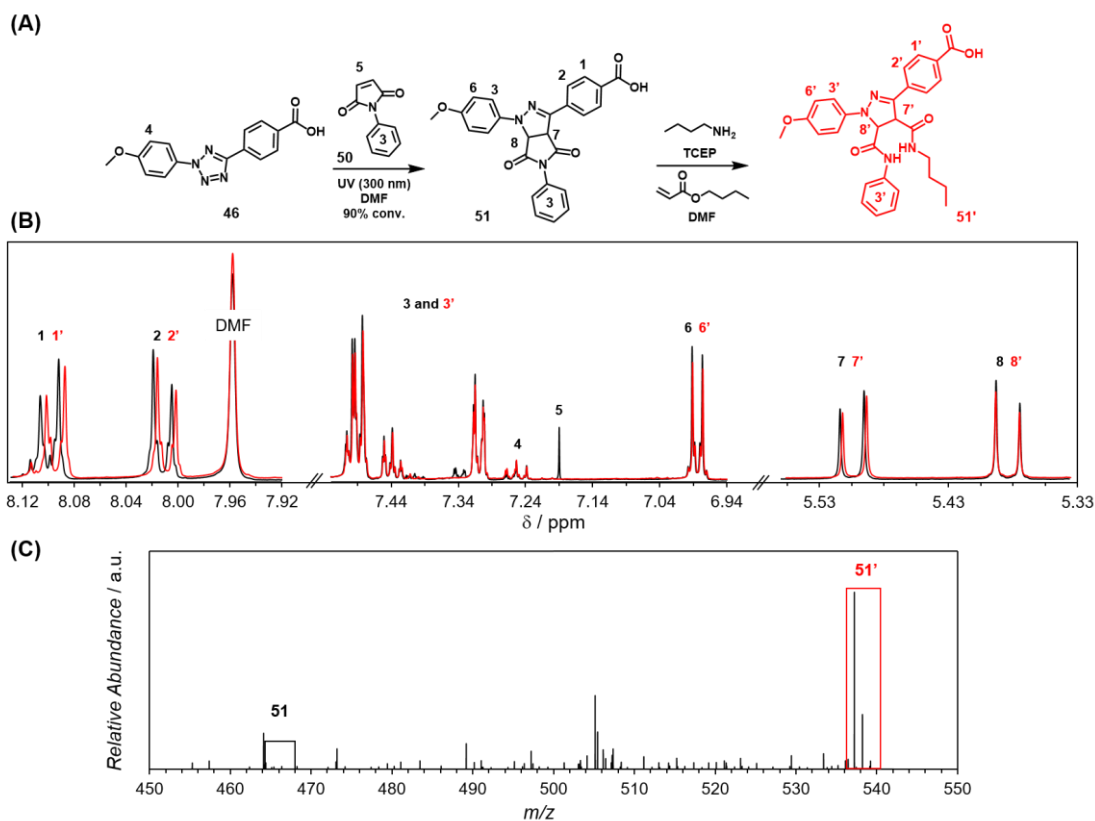


Figure 4.47. (A) Treatment of pyrazoline standard **51** (at 90% conversion) with the reagents used for aminolysis produces the open structure **51'**. (B) ¹H NMR spectra in DMSO-*d*₆ of standard solution **51** before (black) and after (red) aminolysis. (C) ESI-MS spectrum (positive mode) of **51** after aminolysis, confirming the proposed structure ($[\mathbf{51}' + \text{Na}]^+$ *m/z* Calc.: 537.2114, Exp.: 537.2105). Adapted with permission from John Wiley and Sons, Ref 299.

Apart from changing the structure of the pyrazoline fluorophore, the combination of reagents used for aminolysis (TCEP, *n*-butylamine, and butyl acrylate) probably influences the polarity of the medium. Polarity effects also have strong impact in the fluorescence emission properties of fluorophores (refer to Section 2.4.1). Therefore, the emission intensity of the pyrazoline standards **51** was evaluated after systematic removal of each of the aminolysis reagents (Figure 4.48). These experiments demonstrate that the two-fold enhancement of the emission intensity takes place only when all three components of aminolysis are present in the mixture. Removal of TCEP causes lower increase in the fluorescence while only butylamine diminish the intensity, in comparison to control samples **51**. The addition of butyl acrylate has minimum influence in the fluorescence emission of the standards. Importantly, the effect of the medium polarity in the fluorescence emission was, in every case, proportional to the original amount of pyrazoline **51** in the mixture (showed for 38%, 58% and 74% pyrazoline in Figure 4.48).

TOWARDS HOMOGENEOUS ALIGNMENT MEDIA

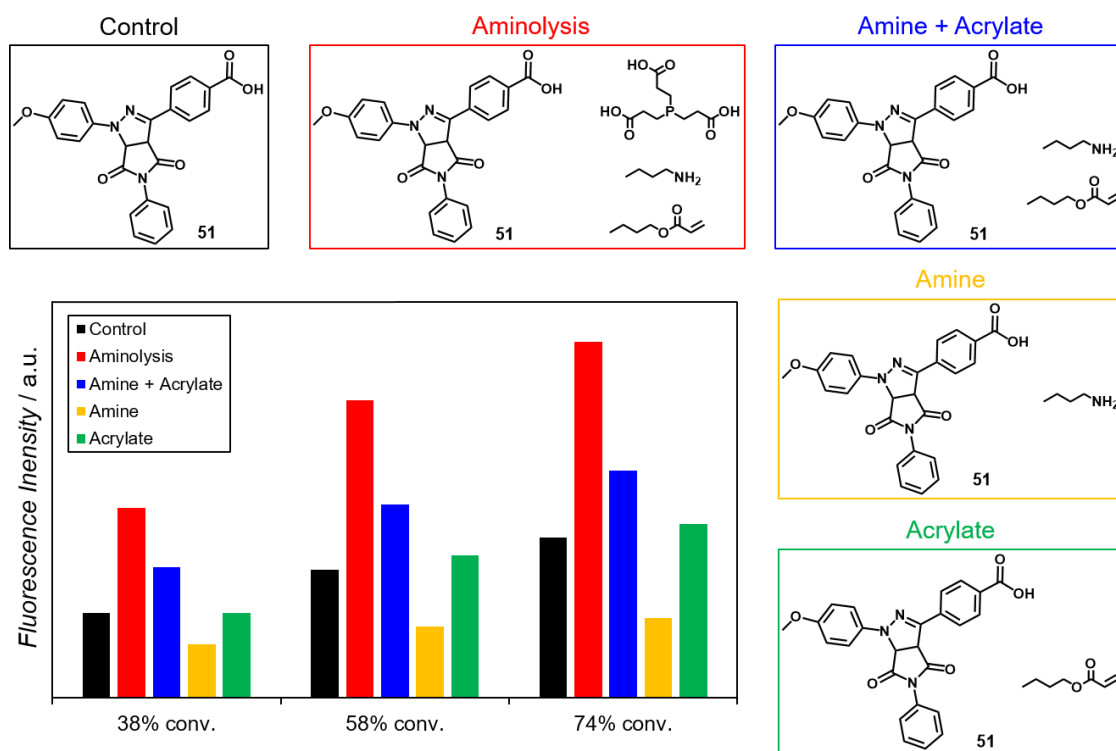


Figure 4.48. Fluorescence emission of pyrazoline standards **51** (38%, 58%, and 74% conversion) before aminolysis (black), after aminolysis (red), after adding only amine and acrylate (blue), after adding amine (yellow), and after adding only acrylate (green). Adapted with permission from John Wiley and Sons, Ref 299.

Lastly, the increase in the fluorescence intensity after aminolysis was evaluated in a polymer model. Tetrazole-functional PS **59** was irradiated with maleimide **50**, producing pyrazoline polymer **64**, at 17%, 48%, 67% and 92% conversion. Subsequently, polymers **64** were subjected to aminolysis to yield samples **64a** (Figure 4.49A). The fluorescence emission of the different samples before and after aminolysis (**64** and **64a**, respectively) was recorded, displaying the approx. two-fold enhancement already observed in the small molecule model (Figure 4.49B). The effective degradation of the trithiocarbonate units in **64** (92% conversion) after aminolysis was characterized by SEC analysis (Figure 4.49C). As expected, the molecular weight distribution of polymer **64a** exhibited lower molecular weight than their parent polymer. Moreover, the opening of the succinimide ring after aminolysis, as observed before in the small molecule model, also took place in the polymer model **64a**, whose structure was confirmed by ESI-MS measurements (see Figure 4.50 and Table 4.5).

TOWARDS HOMOGENEOUS ALIGNMENT MEDIA

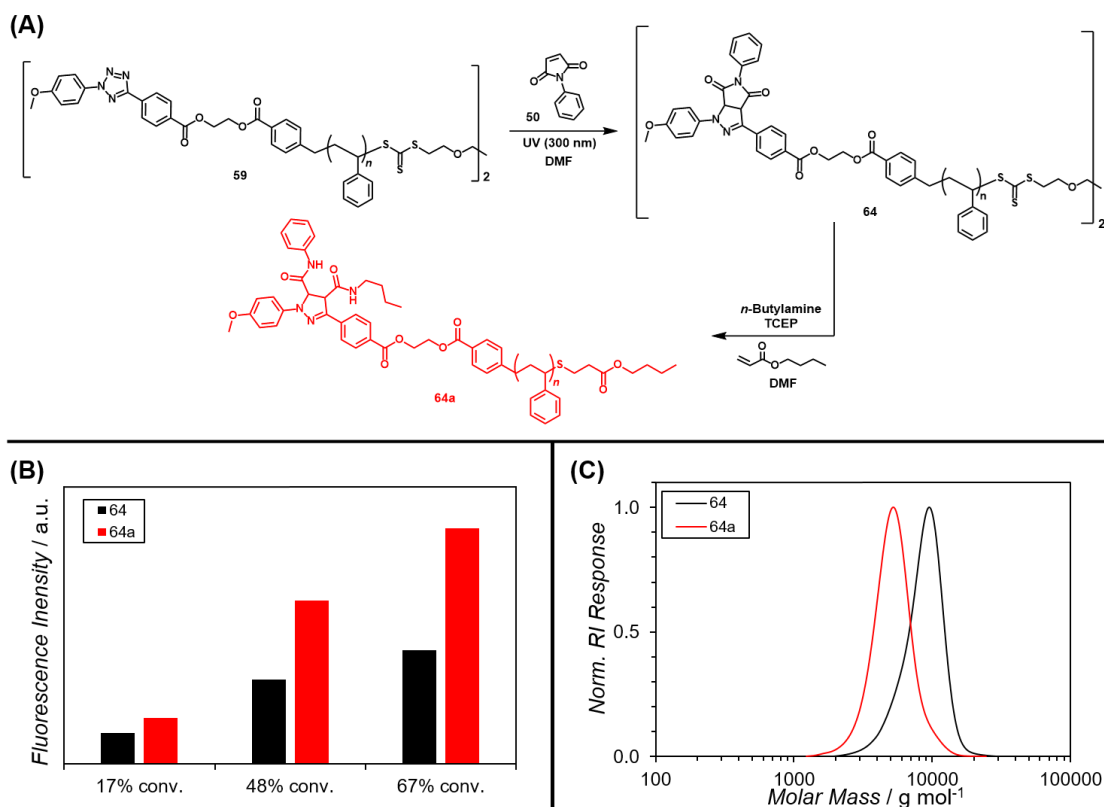


Figure 4.49. (A) Reaction scheme of tetrazole-PS **59** and *N*-phenylmaleimide **50** to produce fluorescent polymer **64**, which was further aminolyzed to **64a**. (B) Fluorescence emission of polymers **64** (black) and **64a** (red) at different conversions. (C) SEC traces of **64** (black) and **64a** (red). Adapted with permission from John Wiley and Sons, Ref 299.

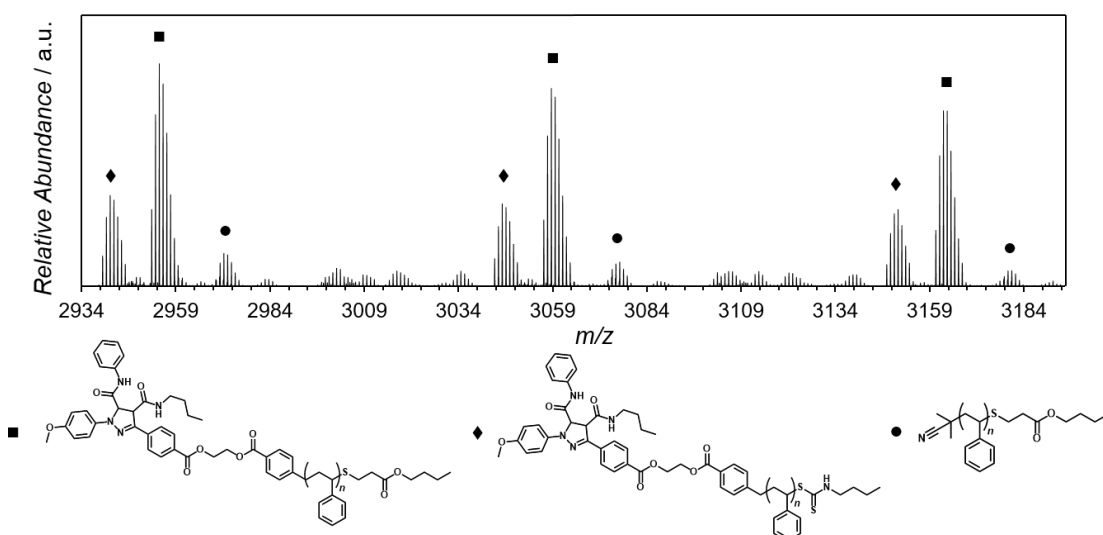


Figure 4.50. ESI-MS spectrum (negative mode) of aminolysis product **64a** showing typical mass and isotopic pattern for the expected structure ■. Secondary structures ♦ (corresponding to incomplete aminolysis) and ● (corresponding to AIBN-initiated polymer after aminolysis), were also found. Reprinted with permission from John Wiley and Sons, Ref 299.

Table 4.5. Structure assignment for the peaks in the MS spectrum in Figure 4.50.

Structure	<i>n</i>	<i>m/z</i> (exp)	<i>m/z</i> (theo)	$\Delta m/z$
[■+Cl] ⁻	20	2952.5593	2952.5669	0.0076
[◆+Cl] ⁻	20	2939.5266	2939.5287	0.0021
[●+Cl] ⁻	26	2969.7035	2969.7101	0.0066

4.2.2.3. Calibration Curve

Once the effect of aminolysis on the fluorescence emission properties of the pyrazoline moieties was evaluated, a calibration curve to determine fluorophore concentration on the aminolyzed networks **60** and **61** was constructed. Small molecule standards **65**, derived from monofunctional tetrazole **46** and trimaleimide **57** (1 : 1 ratio tetrazole : maleimide), synthesized in DMF (see experimental section in Chapter 6), were characterized by ¹H NMR spectroscopy (Figure 4.51).

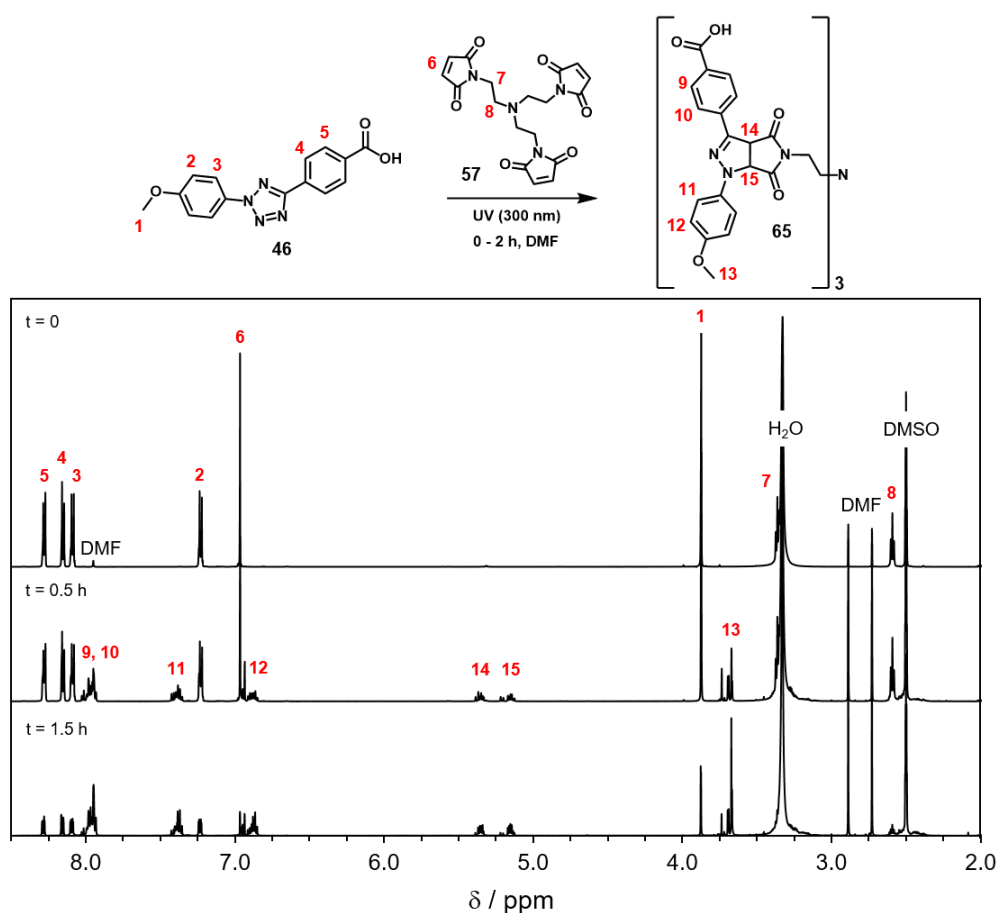


Figure 4.51. ¹H NMR spectra in DMSO-*d*₆ of crude standards **65** obtained after irradiation of tetrazole **46** (3 eq.) and trimaleimide **57** (1 eq.) for 0 h, 0.5 h, and 1.5 h at 300 nm. Adapted with permission from John Wiley and Sons, Ref 299.

TOWARDS HOMOGENEOUS ALIGNMENT MEDIA

The conversion of tetrazole **46** was determined in a similar way as described in Section 4.1 (see Figure 4.9). The area of resonance signals **11** and **12** of product **65** at 7.3 and 6.9 ppm, respectively, was compared with signal **5** of **46** (8.3 ppm), in order to calculate conversion (Equation 4.10). The yield of the pyrazoline adduct was calculated using the areas of the characteristic resonance signals **14** and **15**, in comparison to signal **5** (Equation 4.11). The presence of multiplets in the product signals **9–15** indicates that mixtures of mono-, bi-, and tripyrazoline are obtained in **65**. Nevertheless, this does not prevent the determination of the overall amount of pyrazoline by integration of signals **14** (5.4–5.3 ppm) and **15** (5.2–5.1 ppm), since no other resonances are present in this region. The concentration of pyrazoline in the sample was calculated by Equation 4.12.

$$Conv. = 100 \frac{Area\ 11}{Area\ 11 + Area\ 5} \text{ or } 100 \frac{Area\ 12}{Area\ 12 + Area\ 5} \quad (\text{Eq. 4.10})$$

$$Yield = 100 \frac{2(Area\ 14)}{2(Area\ 14) + Area\ 5} \text{ or } 100 \frac{2(Area\ 15)}{2(Area\ 15) + Area\ 5} \quad (\text{Eq. 4.11})$$

$$[pyrazoline] = \frac{(yield)[tetrazole\ 46]_i}{100} \quad (\text{Eq. 4.12})$$

The standard samples **65** were then treated with the reagents used for aminolysis, namely TCEP, *n*-butylamine, and butyl acrylate. The same experimental conditions as for the small molecule model in Figure 4.46 were employed. Consequently, the succinimide ring opens by nucleophilic attack of the amine, resulting in the open pyrazoline standards **65'** (Figure 4.52A). The fluorescence emission of the different standards before aminolysis (**65**) was recorded and correlated to the yield of pyrazoline retrieved from Equation 4.12, yielding a linear relationship (Figure 4.52B). Analogously, the fluorescence intensity of the aminolyzed standards **65'** was measured, for which the expected two-fold increase in fluorescence intensity in comparison to **65** was observed (Figure 4.52C). As observed before for the small molecule and polymer models, the effect of the aminolysis is systematic and proportional to the concentration of pyrazoline, hence the linearity of the plot is maintained. Critically, the linear relationship between fluorescence of aminolyzed standards **65'** and pyrazoline concentration represents a reliable calibration curve for the NITEC networks degraded by aminolysis.

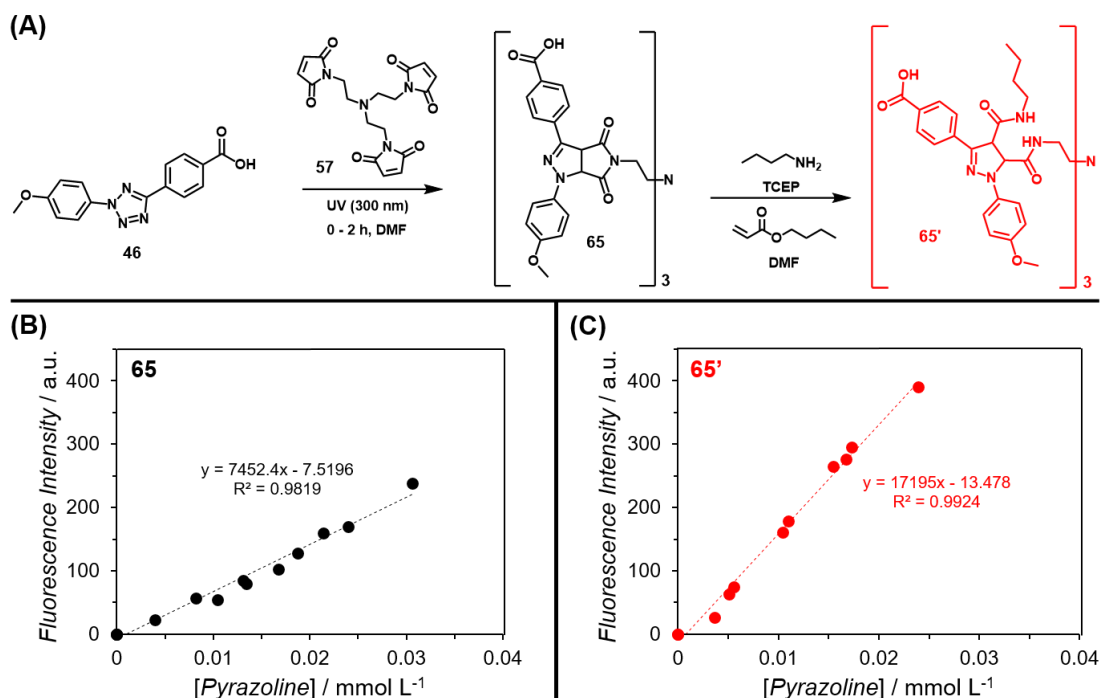


Figure 4.52. (A) Reaction scheme to produce pyrazoline standards **65**, and their corresponding treatment by aminolysis to afford structure **65'**. (B) Fluorescence calibration curve derived from standards **65** before aminolysis. (C) Fluorescence calibration curve derived from standards **65'** after aminolysis. Adapted with permission from John Wiley and Sons, Ref 299.

4.2.3. Quantification of Crosslinking Density

In order to rule out any systematic error coming from the aminolysis procedure, the soluble fractions of networks **61** were analyzed before and after aminolysis by fluorescence spectroscopy (Figure 4.53).

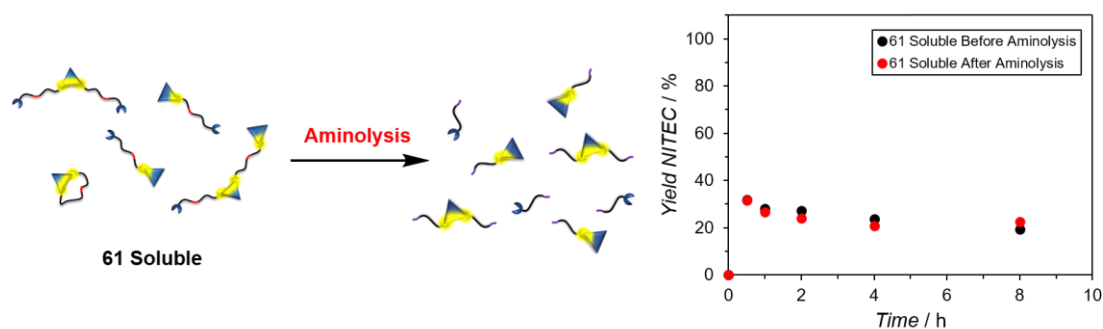


Figure 4.53. Comparison of yield of NITEC reaction in the soluble fractions of networks **61** at different irradiation times. Yields were calculated from fluorescence measurements before (black) and after (red) aminolysis, from suitable calibration curves, giving similar results. Adapted with permission from John Wiley and Sons, Ref 299.

TOWARDS HOMOGENEOUS ALIGNMENT MEDIA

The yield of the NITEC reaction was calculated for different reaction times as the ratio between the amount of pyrazoline groups (from fluorescence measurements) and the initial amount of tetrazole groups in the precursor PS **59**. For the samples before aminolysis, the relation in Figure 4.52B was used to determine pyrazoline concentration, while the curve in Figure 4.52C was employed to estimate the amount of pyrazoline in samples after aminolysis. As depicted in Figure 4.53, the calculated yields are equivalent, regardless of the aminolysis procedure. This observations confirm that after aminolysis the actual number of pyrazoline fluorophores remain constant, but their individual fluorescence intensity changes. Provided that a suitable calibration curve is used, degradation of the networks by aminolysis has no effect in the quantification potential of the fluorescence-based method.

Taking this into account, both soluble and insoluble fractions of networks **60** and **61** (obtained after different irradiation times) were subjected to aminolysis (Figure 4.54A). The fluorescence emission of all crude samples **60** and **61** after aminolysis was employed to determine pyrazoline concentration, using as calibration curve the plot in Figure 4.52C.

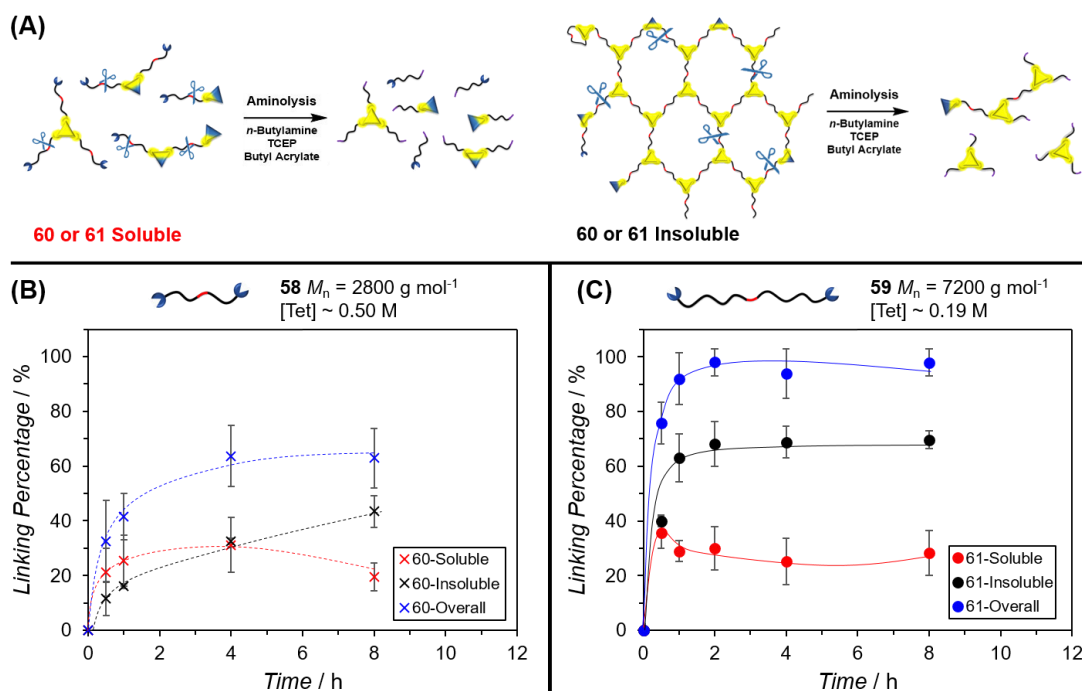


Figure 4.54. (A) Aminolysis of soluble and insoluble fractions of networks **60** and **61**. The linking percentages (NITEC yield) of networks **60** (B) and **61** (C), at different irradiation times, were obtained from fluorescence emission of soluble (red symbols) and insoluble (black symbols) fractions after aminolysis. Blue symbols represent overall yields. Lines are guides for the eye. Error bars represent standard deviation from three independent samples. Adapted with permission from John Wiley and Sons, Ref 299.

TOWARDS HOMOGENEOUS ALIGNMENT MEDIA

The percentage of crosslinks in each sample, i.e. the yield of the NITEC reaction, was calculated from the amount of pyrazoline groups after UV irradiation, and the initial tetrazole groups of precursors **58** or **59**. Yields were determined separately for soluble and insoluble fractions, and added together to obtain the overall NITEC yield. The kinetic plot in Figure 4.54B shows the evolution of the NITEC reaction in networks **60** at different irradiation times. At short reaction times, most of the pyrazoline groups are located in the soluble fraction, indicating that crosslinking is not predominant at the beginning of the reaction. On average, one crosslink junction is obtained after the formation of three pyrazoline groups. Therefore, the longer the samples are irradiated, the more pyrazoline junctions are formed in the insoluble fraction, reaching a value of ca. 44% after 8 h irradiation. The overall yield of pyrazoline groups at 8 h, adding the contributions from soluble and insoluble fractions, is approximately 63%.

Conversely, the linking kinetics for networks **61** (Figure 4.54C) show a markedly faster evolution of the pyrazoline yield. In this case, crosslinking takes place at early stages of the reaction, reaching a constant value of ca. 69% yield in the insoluble fraction already after 2 h irradiation. Moreover, the overall reaction yield shows that the conversion to pyrazoline groups is nearly quantitative. The differences in the overall yields of pyrazoline units for networks **60** (63% yield) and **61** (quantitative yield) indicate that the incidence of dangling ends, stemming from unreacted tetrazole groups, is negligible in samples **61**. However, these networks might present a small fraction of dangling ends derived from AIBN-initiated chains (see Figure 4.27), which are unable to crosslink.

The strong variation of the NITEC kinetics obtained for networks **60** and **61** might be explained by the different initial molar concentration of tetrazole units. Both tetrazole-PS precursors **58** and **59** were dissolved in DMF at the same mass concentration ($710 \text{ mg}\cdot\text{mL}^{-1}$) for network formation. Due to the difference in their molecular weight, the initial molar concentration of these two precursors is different (refer to Figure 4.29). Thus, the initial concentration of tetrazole groups in PS chains **58** and **59** is $\sim 0.50 \text{ M}$ for the former and $\sim 0.19 \text{ M}$ for the latter, accounting for the acceleration of the network formation in samples **61**. The same effect of initial concentration was already observed in the kinetics of NITEC step-growth polymerization described in Section 4.1 (refer to Figures 4.7D and 4.22B). Indeed, control experiments with small molecules corroborate that the more diluted the initial concentration of tetrazole, the faster the kinetics of the NITEC reaction, irrespective of the functionality of the maleimide (see Figures 8.19 and 8.20 in Appendix 8.3).

TOWARDS HOMOGENEOUS ALIGNMENT MEDIA

Additionally, a small molecule control reaction between monofunctional tetrazole **46** and *N*-ethylmaleimide was performed, mimicking the conditions for network formation. The crosslinking of PS **59** with trimaleimide **57** (Figure 4.55A) – performed in ~ 0.19 M DMF solution of tetrazole groups between glass slides – was simulated in the small molecule model mixing **46**, *N*-ethylmaleimide, and RAFT-PS **63** (see Scheme 4.7) as polymer matrix for the monotetrazole (Figure 4.55B). The initial concentration of tetrazole **46** was 0.22 M, and the solid content of **63** was adjusted to 710 mg·mL⁻¹. As depicted in Figure 4.55C, the NITEC kinetics in small molecule and network (overall pyrazoline yield from soluble and insoluble fractions) are roughly equivalent. These results demonstrate that at constant experimental conditions (initial tetrazole concentration, solvent, reaction setup, irradiation wavelength, and irradiation intensity), the NITEC reaction performs identically in small molecule as well as in crosslinked polymer systems.

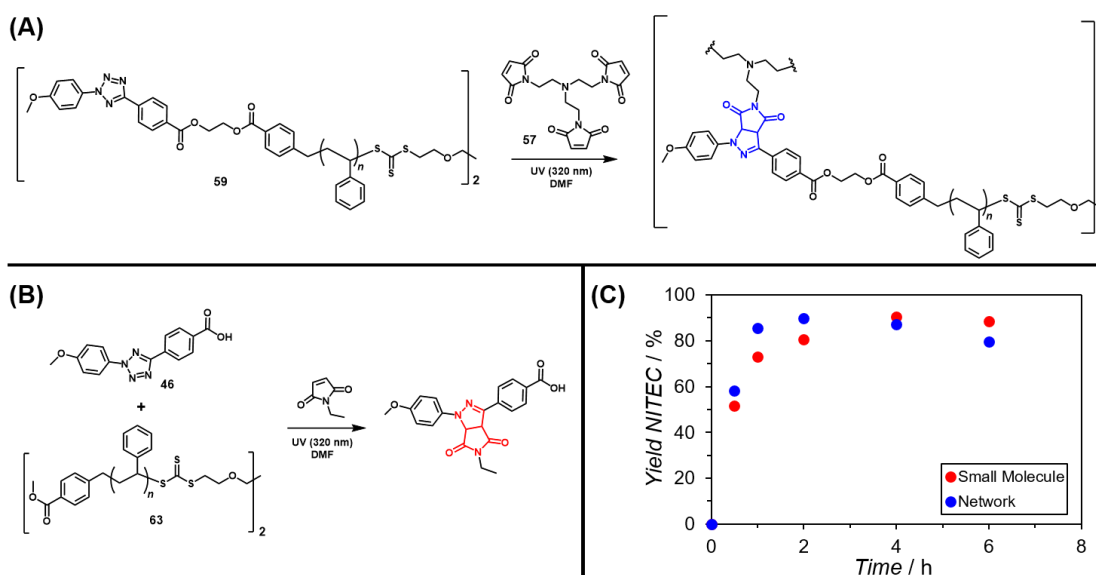


Figure 4.55. (A) Network formation between PS **59** ([tetrazole]_i ≈ 0.19 M) and trimaleimide **57**. (B) NITEC reaction between **46** ([tetrazole]_i = 0.22 M) and *N*-ethylmaleimide, using PS **63** as matrix. (C) Comparison of reaction kinetics for network (blue) and small molecule (red) systems.

Utilizing the kinetic plots in Figures 4.54B and 4.54C and the mass fraction evolution from Figure 4.33D, the quantification of the crosslinking degree of networks **60** and **61** at different irradiation times can be achieved. Critically, the number of pyrazoline units determined in the insoluble fraction of **60** and **61** is directly related to the amount of crosslinks present in the networks (Figure 4.56A). Indeed, a direct correlation between the number of pyrazoline links in the network and the amount of insoluble fraction (in mg) obtained after irradiation was observed (Figure 4.56B). A

TOWARDS HOMOGENEOUS ALIGNMENT MEDIA

higher number of links was determined for networks **60** (derived from the short PS chains **58**) in comparison to networks **61**, at every mass of insoluble fraction. This behavior can be explained by the different number of reactive groups available in precursors **58** and **59** at the same mass concentration (~ 0.50 M vs. ~ 0.19 M tetrazole, respectively). In the same way, the weight fraction of the insoluble fraction of networks **60** and **61** is linearly dependent on the percentage of linking through pyrazoline groups (Figure 4.56C).

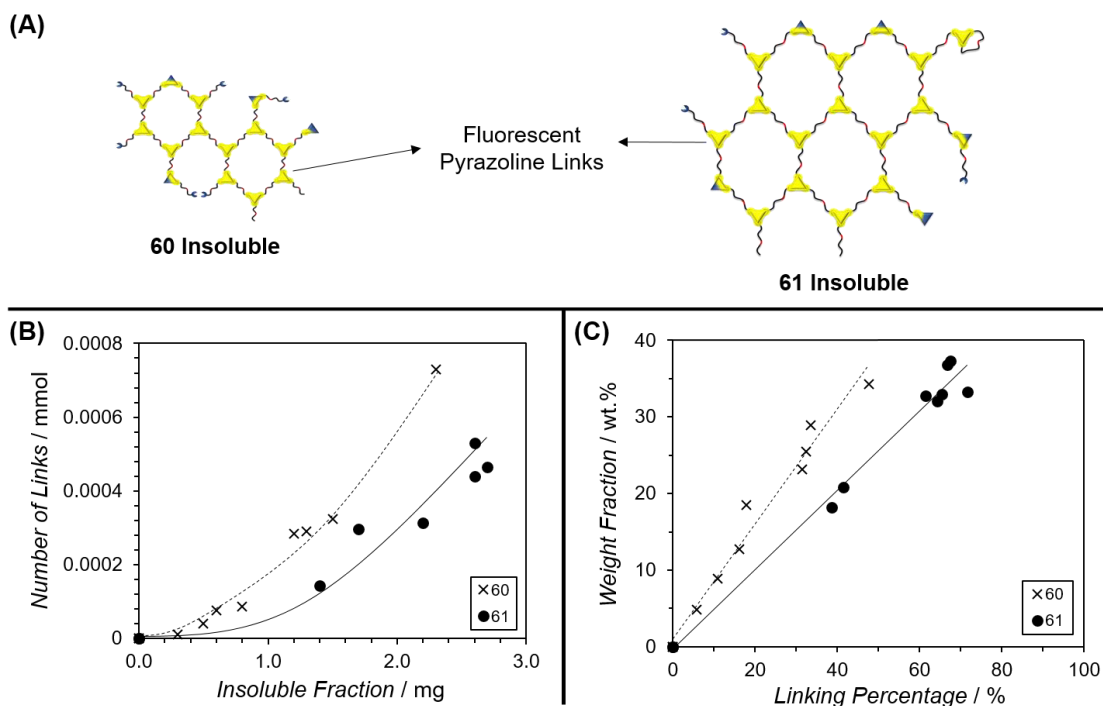


Figure 4.56. (A) Comparison of the number of pyrazoline units (crosslinks) in the insoluble fraction of networks **60** and **61**. (B) Number of pyrazoline links vs. mass of insoluble fraction, and (C) Weight fraction vs. linking percentage of insoluble fraction, determined for networks **60** (crosses) and **61** (dots). Lines are guides for the eye. Adapted with permission from John Wiley and Sons, Ref 299.

Furthermore, the crosslinking density of the networks can be estimated as the number of pyrazoline links per mass unit of insoluble fraction. Figure 4.57A compares networks **60** and **61** in terms of their crosslinking density, obtained at different irradiation times. The temporal evolution of the crosslinking degrees for these two systems showed significant differences. Already after 2 h irradiation, networks **61** (derived from long PS precursor **59**) reach a plateau in the crosslinking density with a maximum value of $\sim 1.8 \times 10^{-4}$ mmol \cdot mg $^{-1}$. Conversely, the crosslinking density of networks **60** (derived from short PS precursor **58**) increases more slowly, but it exceeds that of **61** at irradiation times longer than 4h, reaching $\sim 2.9 \times 10^{-4}$ mmol \cdot mg $^{-1}$ after 8 h. Moreover, a

TOWARDS HOMOGENEOUS ALIGNMENT MEDIA

linear relationship was observed between the crosslinking density of **60** and **61** and the weight fraction of insoluble network (Figure 4.57B). Comparison of the slopes of the curves in Figure 4.57B confirms that networks **60** are more densely crosslinked than networks **61**, at the same weight fraction of insoluble fraction.

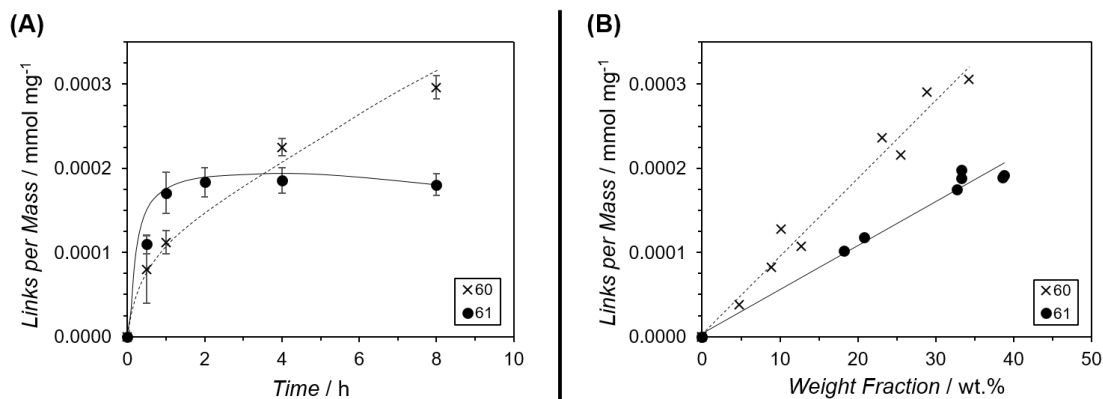


Figure 4.57. Number of pyrazoline links per mass of insoluble fraction (crosslinking density) against (A) Irradiation time, and (B) Weight fraction of insoluble fraction of networks **60** (crosses) and **61** (dots). Error bars represent standard deviation from three independent replicas. Solid and dashed lines are guides for the eye. Adapted with permission from John Wiley and Sons, Ref 299.

As discussed above, the differences in the crosslinking density of networks **60** and **61** stem from the unequal concentration of reactive tetrazole units in the PS precursors **58** and **59**. This difference not only affects the kinetics of the NITEC process (see Figures 4.54B and 4.54C), but also the maximum number of crosslinks attained per mass of polymer. The maximum amount of pyrazoline units that can be obtained from PS **58** and **59** depends on the mass of the repeating unit after NITEC reaction with trimaleimide **57** (Figure 4.58).

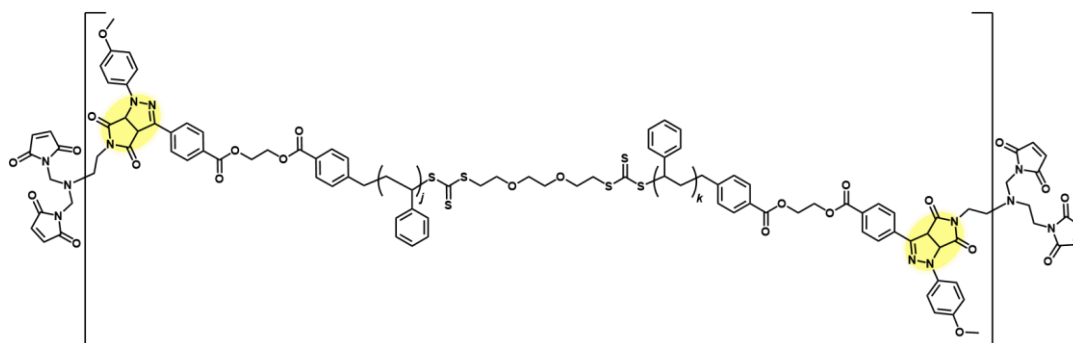


Figure 4.58. Structure of the linking motif in networks **60** or **61**.

According to this, the maximum number of pyrazoline links per mass of polymer can be calculated as follows,

TOWARDS HOMOGENEOUS ALIGNMENT MEDIA

$$Pyrazoline_{\max} = 2 \times \frac{1}{(58 \text{ or } 59) + 2/3(57)} \quad (\text{Eq. 4.13})$$

where **58** and **59** represent the molecular weight of PS precursors, 2800 g·mol⁻¹ and 7200 g·mol⁻¹, respectively (neglecting the mass change after nitrogen gas expulsion), and **57** the molecular weight of the trimaleimide linker (386.4 g·mol⁻¹). It can be seen from Figure 4.58 that two pyrazoline groups are obtained per PS chain, after reaction with – on average – 2/3 of maleimide linker. Hence, Equation 4.13 provides maximum linking values of 6.5 × 10⁻⁴ mmol·mg⁻¹ for network **60** and 2.7 × 10⁻⁴ mmol·mg⁻¹ for network **61**. The experimental values for crosslinking density of **60** and **61** after 8 h irradiation (see Figure 4.57A) represent 45% and 68%, respectively, of the maximum crosslinking density predicted from Equation 4.13. These values are in agreement with the linking percentage in the insoluble fraction determined from Figures 4.54B and 4.54C, namely 44% for network **60** and 69% for network **61**, after 8 h irradiation.

The results obtained from the quantification of crosslinks in the different networks underpin the strong dependence of NITEC network formation on the molecular weight of the polymer precursor. Short PS chains **58** take longer to crosslink than PS chains **59**, as depicted in Figure 4.33D, due to their higher concentration of reactive tetrazole groups per mass of polymer. Nevertheless, this indicates that networks **60** are more compact and more densely crosslinked than networks **61** at the same conversion, as shown in Figure 4.57B. The lower overall conversions reached in the synthesis of **60** generate a higher number of dangling ends, coming from unreacted tetrazole groups, in comparison to networks **61**. The incidence of dangling ends on networks **60** and **61** was confirmed by ESI-MS analysis (refer to Figures 8.21 and 8.22 in Appendix 8.3). On the other hand, close inspection of the crosslinking densities in Figure 4.57A suggests that full network formation is achieved for **61** after 2 h irradiation, while more than 8 h reaction time are needed for networks **60**. Although the NITEC reaction in samples **60** only reaches 63% overall yield after 8 h, longer irradiation times will be deleterious for the network formation due to trithiocarbonate degradation³¹¹ (refer to Figure 4.34). Therefore, under the studied conditions it is not possible to further increase the crosslinking density of networks **60** derived from short PS precursors.

As final remark, possible scenarios that could affect the quantification of crosslink points by fluorescence spectroscopy were investigated. First, aromatization of the pyrazoline ring after long irradiation times, leading to loss of fluorescence intensity, was considered. Such phenomena was observed in the NITEC step-growth polymers presented in Section 4.1 (see Figures 4.15 and 4.21, as well as Figures 8.12 and 8.13 in Appendix 8.2). Therefore, samples **61** were irradiated up to 16 h and the yield of

TOWARDS HOMOGENEOUS ALIGNMENT MEDIA

pyrazoline in the insoluble fraction was determined via fluorescence measurements (Figure 4.59). It can be observed that between 8 h and 16 h irradiation, no change in the NITEC yield takes place, ruling out the degradation of the fluorophore by aromatization. However, the weight fraction of the insoluble networks **61** changes drastically between 8 h and 16 h, from 42% to 24%, due to UV-induced degradation of the trithiocarbonate moieties.

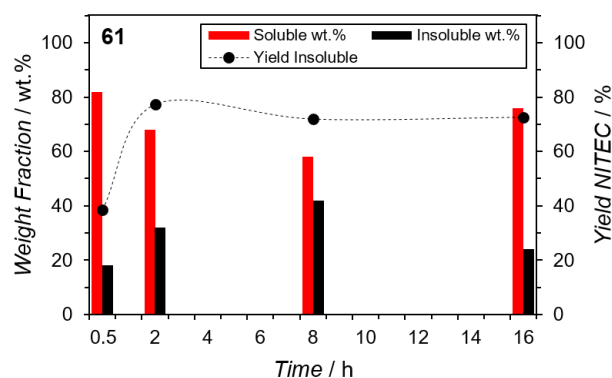


Figure 4.59. (Left axis) Weight fraction of the soluble (red bars) and insoluble (black bars) fractions of networks **61** after different irradiation times. (Right axis) Yield of pyrazoline units (black dots) in the insoluble fraction of networks **61**, achieved after different irradiation times. Dashed line is a guide for the eye. Adapted with permission from John Wiley and Sons, Ref 299.

Furthermore, maleimides are known to produce [2+2] cycloaddition products under UV irradiation^{112,313,314} (refer to Section 2.4.2). In the present case, the formation of maleimide dimers will create non-fluorescent crosslink points, as depicted schematically in Figure 4.60, eventually compromising the quantification of crosslinks in the networks via fluorescence spectroscopy.

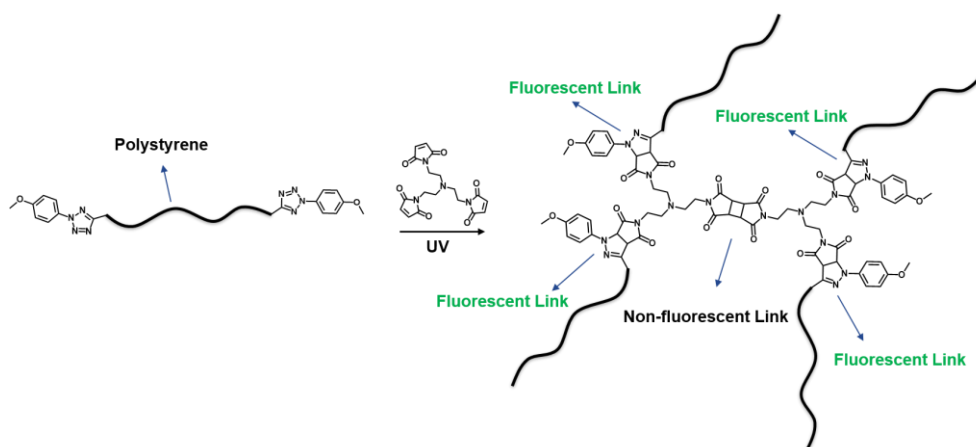


Figure 4.60. Dimerization of maleimide via [2+2] cycloaddition, generating non-fluorescent crosslink points. Reprinted with permission from John Wiley and Sons, Ref 299.

TOWARDS HOMOGENEOUS ALIGNMENT MEDIA

Although no spectral evidence (NMR, ESI-MS) of such dimerization adducts was found in the small molecule models herein presented, additional control experiments at 300 nm irradiation were carried out with trimaleimide **57** and monofunctional tetrazole **41** (refer to the experimental section in Chapter 6). ^1H NMR analyses revealed that in the presence of tetrazole groups, the maleimide reacts as dipolarophile yielding the expected NITEC product **66** (Figure 4.61A). However, when no tetrazole is present in the solution, photopolymerization of trimaleimide takes place, evidenced as white insoluble material **67** in the bottom of the NMR tube (Figure 4.61B). In the remaining solution, only signals corresponding to starting material **57** were detected. Such insoluble precipitate was not obtained in the experiment with tetrazole, evidencing that NITEC cycloaddition is kinetically favored over [2+2] maleimide dimerization.

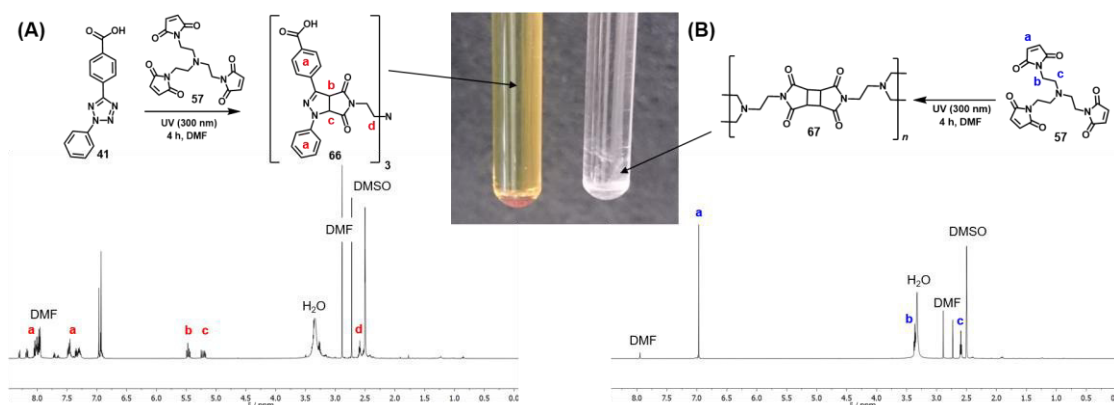


Figure 4.61. ^1H NMR spectra in $\text{DMSO}-d_6$ of (A) Reaction of tetrazole **41** and trimaleimide **57** to produce the expected pyrazoline adduct **66** via NITEC, and (B) Irradiation of **57** in the absence of tetrazole groups, generating insoluble maleimide polymers **67** via [2+2] cycloaddition. Adapted with permission from John Wiley and Sons, Ref 299.

4.2.4. Upscale Experiments

The experimental results presented above highlight the self-reporting properties and spatio-temporal control achieved with NITEC processes on the synthesis of crosslinked networks. By adjusting irradiation time, concentration, and molecular weight of the precursor strands, polymer networks with tunable – and quantifiable – crosslinking densities were obtained. Such characteristics are important for the development of homogeneous gels as alignment media for NMR spectroscopy. As discussed previously in Chapter 3, polymer-based alignment media are obtained primarily by free-radical copolymerization of vinyl monomers and crosslinkers. This procedure leads to gels with highly inhomogeneous internal structure, in contrast to end-linking methods like the NITEC approach (see Figure 4.24A). Critically, polymer

TOWARDS HOMOGENEOUS ALIGNMENT MEDIA

networks with defined topologies will enable the study of systematic relationships between gel structure and alignment properties (Figure 4.62).

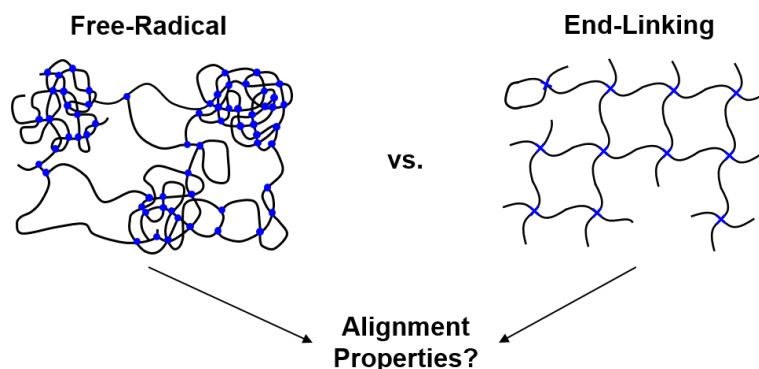


Figure 4.62. Free-radical polymerization and end-linking methods generate networks with different topologies. The structural differences might have a major impact in their application as alignment media.

In this respect, the possibility of obtaining homogeneous alignment media based on NITEC end-linked networks was explored. Bifunctional tetrazole-PS **59** and trimaleimide **57** were irradiated at 320 nm for 7 h – analogous to the process shown in Figure 4.33 – using glass capillaries instead of glass slides as reaction mold, in order to obtain cylindrical sticks (Figure 4.63). Nevertheless, the efficiency of the NITEC crosslinking in cylindrical molds was very low, yielding only 6 wt.% of insoluble fraction, compared to ~ 35 wt.% obtained in glass slides under the same conditions. Adjusting reaction parameters like irradiation time and distance to the lamp did not improve the yield of insoluble fraction. The majority of the insoluble material was obtained at the walls of the capillary, while the bulk of the reaction remained uncrosslinked. Possibly, limitations in the penetration of light into the concentrated precursor solution prevents homogeneous crosslinking of the bulk material.

Next, polydimethylsiloxane (PDMS) molds were employed as reaction vessel instead of glass capillaries (refer to the experimental section). PDMS is an optically transparent silicon polymer, widely applied as mold in UV-induced photoreactions.¹⁶⁴ Thus, PDMS reactors with thin cylindrical cavities were specially designed (Figure 4.64A) and filled with the reaction mixture (Figure 4.64B). In this way, tetrazole-PS **59** and trimaleimide **57** were irradiated at 320 nm for 7 h, and the crude mixture was subsequently washed with several portions of fresh THF. Again, only on the walls of the reactor it was possible to obtain crosslinked material (Figure 4.64C).

TOWARDS HOMOGENEOUS ALIGNMENT MEDIA

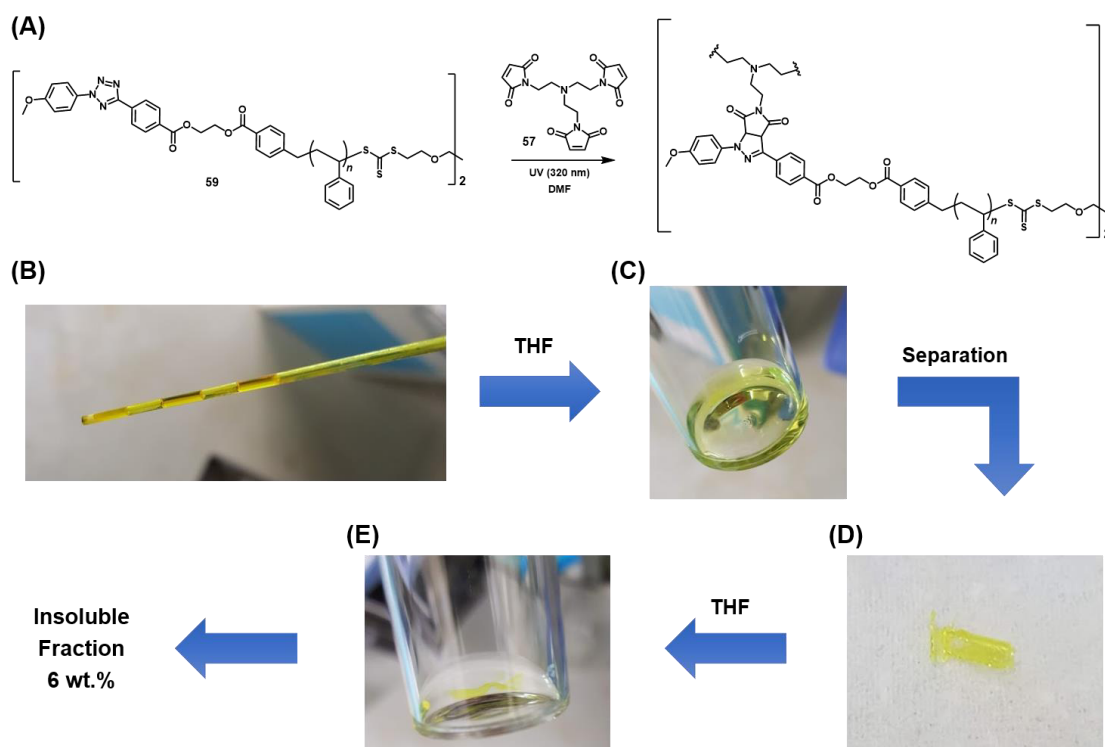


Figure 4.63. (A) Crosslinking of bifunctional tetrazole-PS **59** and trimaleimide **57**, irradiated 7 h at 320 nm in DMF. (B) Reaction was carried out in glass capillaries as cylindrical molds. (C) Solvent was added to remove the soluble fraction. (D) After separation, small amounts of insoluble fraction without defined shape were obtained. (E) Further solvent addition promotes swelling of the insoluble material.

These observations suggest that for an effective NITEC crosslinking, the light penetration path should be kept as small as possible, for instance between glass slides. The formation of cylindrical sticks via NITEC end-linking was thus ruled out.



Figure 4.64. (A) Cylindrical PDMS mold used as reactor. (B) Precursor mixture (in DMF) was filled inside the PDMS mold and irradiated 7 h at 320 nm. (C) After washing with solvent, insoluble material was isolated only at the walls of the reactor.

In general, the experimental results provided in the present section introduce fluorescence spectroscopy as a facile yet powerful technique to access quantitative

TOWARDS HOMOGENEOUS ALIGNMENT MEDIA

information on the crosslinking kinetics of NITEC networks. The reaction conditions for the NITEC crosslinking of α,ω -tetrazole-capped PS chains with a trimaleimide linker were optimized in order to afford high yields and minimize sample degradation. In this respect, irradiation of concentrated precursor mixtures in DMF at 300 nm, sandwiched between thin glass slides, offered the best crosslinking output. Direct analysis of the fluorescence of the NITEC networks in the solid state was not suitable for quantification purposes. Therefore, aminolysis was employed as strategy for network disassembly, by cleavage of the trithiocarbonate groups present in the PS chains. This process generated soluble network fragments and, at the same time, it affected systematically the fluorescence of the pyrazoline fluorophore. An approximately two-fold increase in the fluorescence emission intensity of the aminolyzed samples was observed, keeping constant the original pyrazoline concentration. Nevertheless, the relationship between fluorescence intensity and pyrazoline concentration after aminolysis was found to be linear, allowing the construction of a calibration curve. In this way, simple fluorescence readouts allowed the investigation of the kinetics of NITEC network formation, using PS strands of two different molecular weight as precursors. The molecular weight of the PS precursor strongly affects the crosslinking kinetics, due to the different amount of reactive groups available at per mass unit. Long PS chains crosslink at early stages of the reaction and offer good overall conversions, leading to networks depleted of dangling ends. On the other hand, short PS chains take longer to react, but produce compact networks with higher crosslinking densities than their long-mesh counterparts. Furthermore, the NITEC network synthesis protocol could not be scaled up in order to prepare cylindrical sticks. Most probably, the concentrated precursor solution needed for effective crosslinking limits the light penetration depth that can be reached by the irradiation source, concurring with the Lambert-Beer law (refer to Section 2.4.1). Hence, using as reactor glass capillaries or PDMS molds with thin cylindrical cavities, only low amounts of insoluble material could be obtained, mainly at the walls of the reaction vessel.

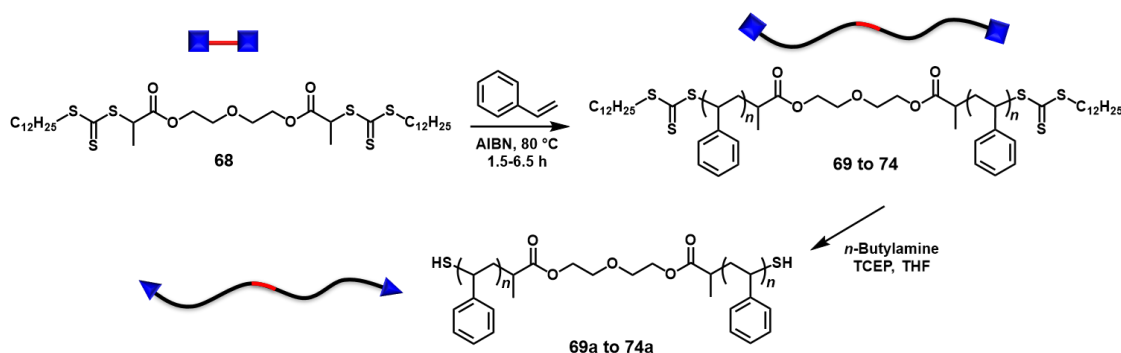
4.3. Network Formation via Thiol-Ene Chemistry

Due to the complications derived from the NITEC upscale experiments, alternative ligation methods were explored for the synthesis of end-linked networks, in particular thiol-ene chemistry. Thiol addition to activated carbon-carbon double bonds has been known since the early 1900's, but only in the last decades the potential of this process for modular synthesis has grown in importance.³¹⁵ Thiol-ene reactions,

mediated either by radical or ionic intermediates, present many characteristics of the so-called click chemistry. For instance, high conversions are normally obtained via thiol-ene chemistry under mild reaction conditions in a chemoselective fashion. The wide range of available thiol-ene combinations has promoted the systematic study of their reactivity patterns and mechanism,^{312,316} and the use of thiol-ene processes for surface modification, biofunctionalization, microfabrication, materials engineering, and polymer functionalization, among others.^{315,316} In the field of polymer chemistry, thiol-ene reactions play a prominent role in side- and end-chain modifications, formation of complex architectures like dendrimers and star polymers, functionalization of polymeric surfaces and particles, and polymer crosslinking.³¹⁷ Formation of polymer networks via thiol-ene chemistry is well documented in the recent literature, including thiol-Michael addition approaches,^{175,202,316,318} as well as photoinduced radical thiol-ene reactions.^{17,102,110,111,164,200,201,319}

4.3.1. Thiol End-Capped PS Chains

A two-step RAFT polymerization/end-linking strategy, similar to the one presented in Figure 4.24A, was adopted for the synthesis of homogeneous networks via thiol-ene chemistry. First, the symmetrical trithiocarbonate-based bifunctional RAFT agent **68** was employed for the controlled radical polymerization of styrene (see experimental section in Chapter 6). Well-defined PS strands of different molecular weight **69–74** were prepared by this method (Scheme 4.8).



Scheme 4.8. RAFT polymerization of styrene, mediated by CTA **68**, yielding PS strands **69–74**. Further aminolysis of the trithiocarbonate groups produces telechelic thiol-functional PS **69a–74a**.

Subsequently, polymers **69–74** were subjected to aminolysis, following a protocol comparable to that described in Section 4.2.2.1. An excess of *n*-butylamine was added to a THF solution of RAFT polymer in the presence of the reducing agent TCEP (see Scheme 4.8). In this case, no coupling agent (e.g. butyl acrylate) was employed, so that α,ω -thiol-capped PS chains **69a–74a** could be afforded after precipitation in cold

TOWARDS HOMOGENEOUS ALIGNMENT MEDIA

methanol (refer to experimental section). The polymers before and after aminolysis were analyzed via SEC, displaying monomodal and narrowly distributed molar masses with low dispersity \mathcal{D} (see Figure 4.65 and Table 4.6). The loss of ca. 500 g·mol⁻¹ observed after aminolysis roughly coincides with scission of two dodecyl-trithiocarbonate groups, as proposed in Scheme 4.8.

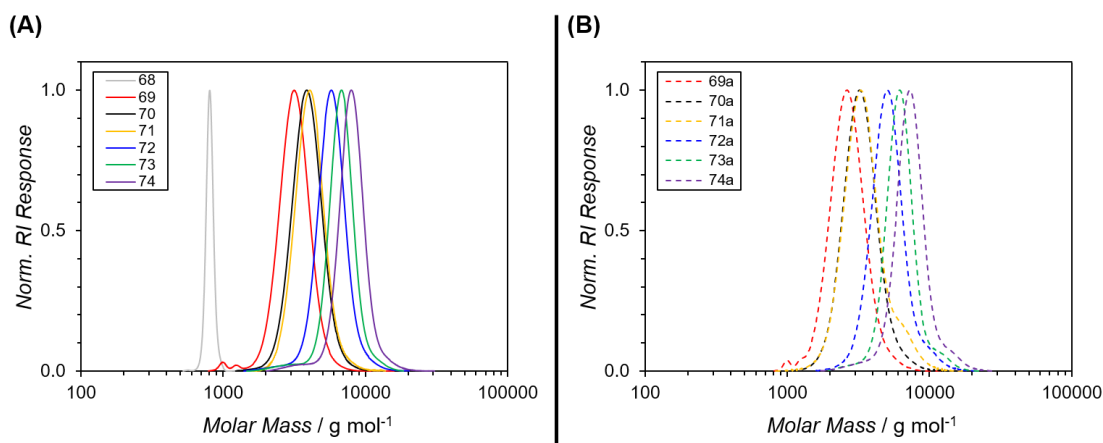


Figure 4.65. SEC traces of (A) RAFT agent **68** and corresponding polymers **69–74** before aminolysis, and (B) RAFT polymers after aminolysis **69a–74a**, showing monomodal distributions in every case.

Table 4.6. Number average molecular weight (\bar{M}_n) and dispersity index (\mathcal{D}) of PS samples before and after aminolysis **69–74** and **69a–74a**, respectively.

Sample	\bar{M}_n ^a	\mathcal{D} ^a	Sample	\bar{M}_n ^a	\mathcal{D} ^a
69	3000 g·mol ⁻¹	1.08	69a	2500 g·mol ⁻¹	1.10
70	3700 g·mol ⁻¹	1.07	70a	3100 g·mol ⁻¹	1.09
71	3900 g·mol ⁻¹	1.06	71a	3200 g·mol ⁻¹	1.12
72	5500 g·mol ⁻¹	1.07	72a	4900 g·mol ⁻¹	1.09
73	6400 g·mol ⁻¹	1.07	73a	6000 g·mol ⁻¹	1.08
74	7600 g·mol ⁻¹	1.07	74a	6900 g·mol ⁻¹	1.09

^a Determined by SEC, calibrated with linear PS standards.

Furthermore, ¹H NMR analysis of the polymers before and after aminolysis confirms the effective removal of the dodecyl-trithiocarbonate groups. As exemplified in Figure 4.66, the RAFT polymerization of styrene mediated by CTA **68** produces PS samples exhibiting the characteristic resonance signals **b**, **c**, **d**, **h**, and **i** at 4.0, 3.4, 3.2, 1.3, and 0.9 ppm, respectively, stemming from the RAFT agent. The typical resonances **k** (6.3–7.2 ppm) and **j** (6.3–7.2 ppm), corresponding to the aromatic side groups and aliphatic backbone of the polymer in **69**, respectively, are also present in the spectrum.

TOWARDS HOMOGENEOUS ALIGNMENT MEDIA

However, after aminolysis, signals **d** and **h** disappear completely, indicating that the dodecyl end-groups are cleaved in PS **69a** (see Figure 4.66).

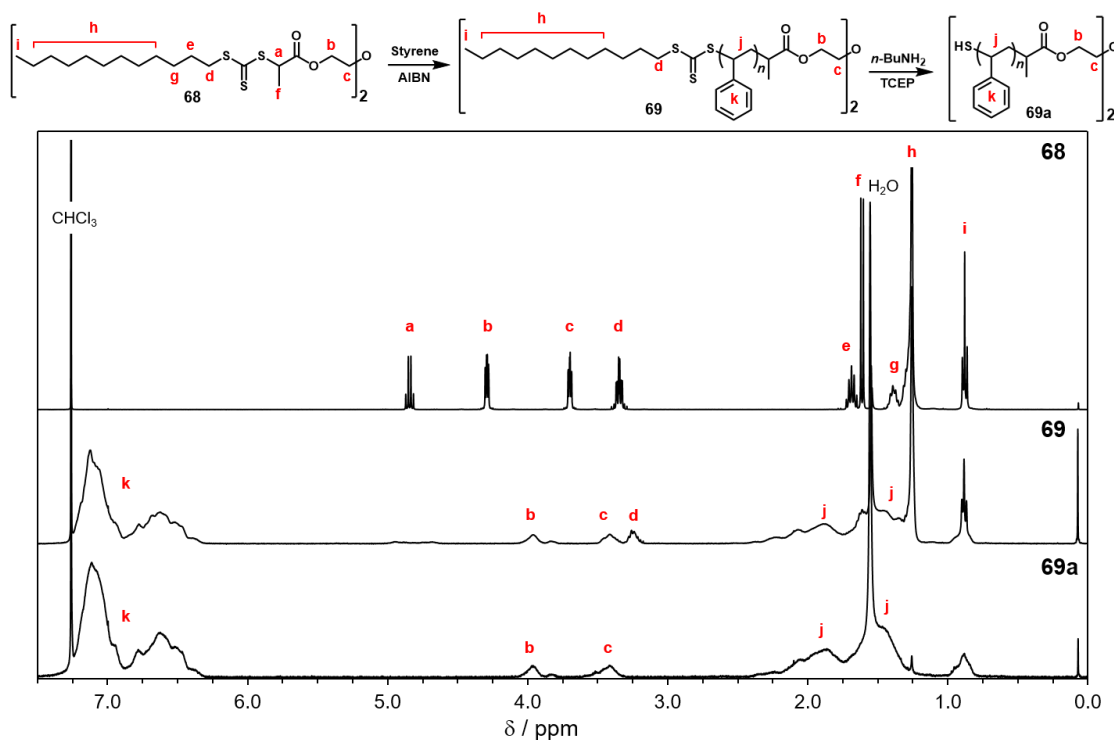


Figure 4.66. ¹H NMR spectra in CDCl₃ of RAFT agent **68**, the corresponding PS **69** and the product of aminolysis **69a**.

SEC-ESI-MS analyses performed on samples **69** and **69a** give insights into the structure of the polymers, corroborating the information retrieved from the NMR spectra. The isotopic *m/z* distribution of PS **69** displays the typical pattern ■, including the functional groups from the RAFT agent **68** into the structure of polystyrene. Moreover, after aminolysis there is a shift in the isotopic distribution in the range of $\Delta m/z = 488.266$, corresponding to the loss of two dodecyl-trithiocarbonate groups in **69a**. Thus, the expected isotopic pattern ♦, associated to α,ω -thiol-capped PS strands, was obtained. An additional isotopic distribution was found in **69a**, corresponding to the secondary PS structure ●, stemming from incomplete aminolysis of the trithiocarbonate groups in the RAFT polymer (see Figure 4.67 and Table 4.7). Such dithiocarbamate species ● were already described in Section 4.2, and are inherent to the aminolysis procedure herein employed. Although the relative abundance of these secondary structures is low, their incidence might negatively impact the formation of homogeneous networks. Since no thiol-ene crosslinking is possible from the dithiocarbamate ends, their presence will lead to the formation of dangling chains in the network structure.

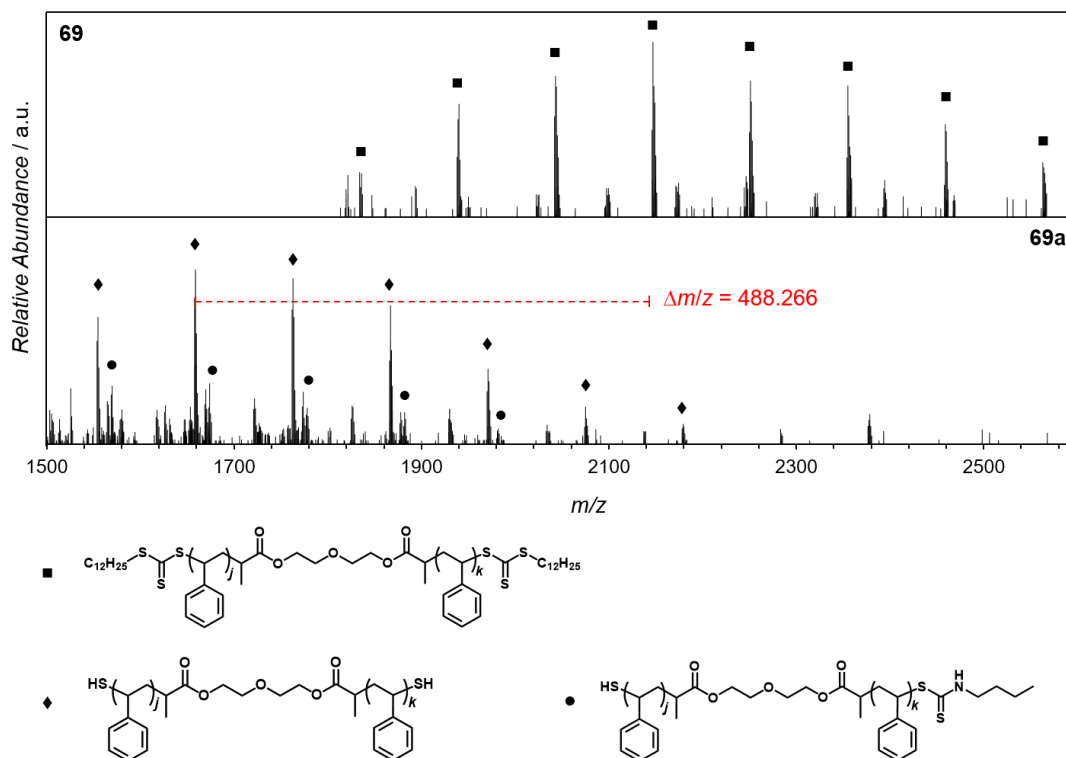


Figure 4.67. SEC-ESI-MS spectra (positive mode) of RAFT PS **69** (top), showing typical mass and isotopic pattern for the expected structure ■, and aminolysis product **69a** (bottom), exhibiting the expected distribution for structure ◆. Secondary structure ● (incomplete aminolysis) was also found. The spectra were recorded at the maxima of the molar mass distribution (retention time 16.2 min and 16.4 min, respectively in SEC chromatograms).

Table 4.7. Structure assignment for the peaks in the MS spectra in Figure 4.67.

Structure	n	m/z (exp)	m/z (theo)	$\Delta m/z$
[■+Na] ⁺	$j + k = 13$	2146.1322	2146.1265	0.0057
[◆+Na] ⁺	$j + k = 13$	1657.8713	1657.8626	0.0087
[●+Na] ⁺	$j + k = 12$	1668.8487	1668.8456	0.0031

4.3.2. Crosslinking of Thiol-PS Chains

Next, the conditions for network formation were screened for thiol-PS **74a**, using as linkers the commercially available trimaleimide **57** and tetraacrylate **75** (Figure 4.68). The polymer precursor (830 mg·mL⁻¹ **74a**) was mixed with the linker in DMF (at equimolar ratio between reactive groups), adding subsequently an appropriate catalyst (refer to the experimental section for detailed synthetic procedures). After overnight

TOWARDS HOMOGENEOUS ALIGNMENT MEDIA

reaction, the material was washed with several portions of THF to extract the soluble and insoluble fractions.

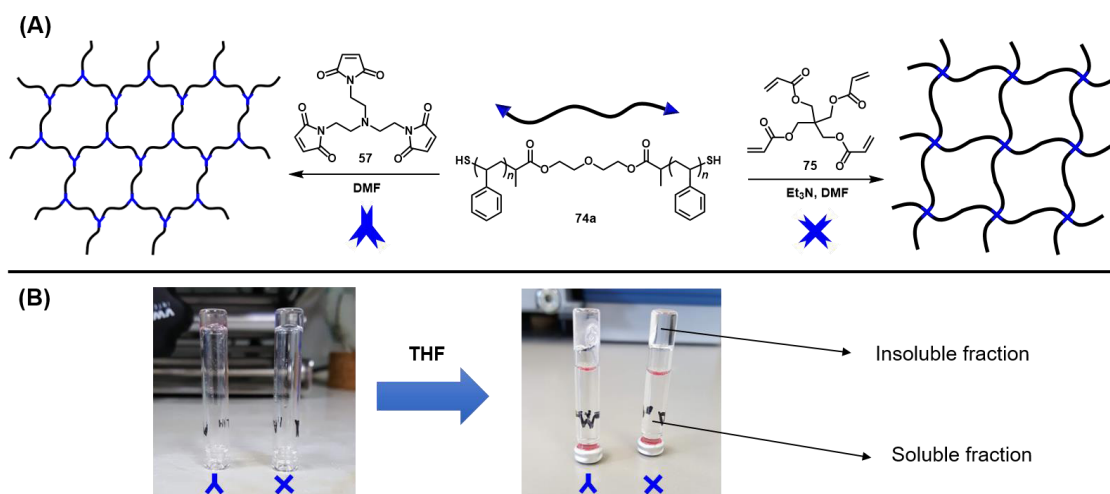


Figure 4.68. (A) Reaction scheme between bifunctional thiol-PS **74a** and linkers trimaleimide **57** (left) or tetraacrylate **75** with triethylamine as catalyst (right) in DMF, producing crosslinked gels. (B) Pictures of gels produced by crosslinking with **57** (left) or **75** (right). After washing with THF, soluble and insoluble fractions are isolated.

According to kinetic studies reported in literature,³¹² thiols readily react in DMF solution with maleimides and acrylates. For the former case no catalyst is required, while for the latter, phosphines or amines can catalyze the thiol-ene addition. Therefore, the conditions reported in Ref 312 were adapted to the ligation of thiol PS **74a**, in order to find optimal reaction parameters for the synthesis of end-linked networks (Table 4.8).

Table 4.8. Screening of the reaction conditions for the crosslinking of thiol-PS **74a**.

Entry	Linker ^a	Catalyst ^b	Gelation Time	Insoluble Fraction
1	Trimaleimide 57	-	< 1 h	64 wt. %
2	Trimaleimide 57	Et ₃ N	< 1 h	54 wt. %
3	Tetraacrylate 75	-	-	0 wt. %
4	Tetraacrylate 75	Et ₃ N	> 8 h	84 wt. %
5	Tetraacrylate 75	Me ₂ PhP	< 1 h	49 wt. %
6	Tetraacrylate 75	PI / UV	> 6 h	8 wt. %

^a 1 : 1 mol ratio thiol : ene, 0.12 M in DMF (thiol-PS **74a**, 830 mg mL⁻¹). Overnight reaction at room temperature.

^b 50 mol% catalyst (Et₃N: triethylamine, Me₂PhP: dimethylphenylphosphine, PI: photoinitiator = 2,2-dimethoxy-2-phenylacetophenone, UV: 320 nm).

TOWARDS HOMOGENEOUS ALIGNMENT MEDIA

All reactions were left to proceed overnight, even though the gelation point (evidenced by the resistance of the mixture to flow) was reached already few hours after addition of the catalyst. The fastest gelation (< 1 h) was observed for trimaleimide **57** with and without catalyst (entries 1 and 2 in Table 4.8), and for the reaction with tetraacrylate **75** catalyzed with phosphine (entry 5 in Table 4.8), in accordance with the kinetic trends reported in literature.³¹² The photoactivated reaction (320 nm) between **74a** and **75** was catalyzed by the photoinitiator 2,2-dimethoxy-2-phenylacetophenone, yielding an insoluble gel after 6 h reaction (entry 6 in Table 4.8). In addition, ligation with **75** could be catalyzed by triethylamine, for which approximately 8 h were necessary to form an insoluble gel (entry 4 in Table 4.8). Conversely, without any catalyst, no gelation was observed in the reaction of **74a** and tetraacrylate **75** (entry 3 in Table 4.8). In every case, after 17 h (overnight) reaction the gels were washed with several portions of THF in order to extract soluble fractions. After evaporation of the solvent, the relative amounts of soluble and insoluble fractions were determined by gravimetry. As shown in Table 4.8, the weight fractions of insoluble fraction are higher than 49 wt.% for almost every experiment, with the exception of the photoinitiated crosslinking (8 wt.%, entry 6). These data suggest that thiol-ene chemistry is more effective than the NITEC end-linking method introduced in Section 4.2 for network formation. The largest amount of insoluble gel was afforded by crosslinking with tetraacrylate **75**, using triethylamine as catalyst in a Michael-type mechanism (84 wt.%, entry 4). Even though under these conditions the gelation takes longer, this reaction was selected as standard for further experiments due to its high network yield.

Next, the influence of the initial concentration of polymer precursor on the yield of the networks was investigated. Since low initial concentrations of precursors favor the incidence of primary and secondary loops,^{175,223} the starting solutions of PS in DMF were prepared as concentrated as possible. Using thiol-PS **73a** as starting material, crosslinking with **75** yielded 85 wt.% insoluble fraction when $[73a]_i = 830 \text{ mg}\cdot\text{mL}^{-1}$. Reducing the initial concentration of **73a** to 530 and 330 $\text{mg}\cdot\text{mL}^{-1}$ resulted in lower yields of insoluble fraction, namely 76 wt.% and 34 wt.%, respectively (refer to Figure 8.24 and Table 8.5 in Appendix 8.4).

Additionally, it was important to determine if – at constant mass concentration – the molecular weight of the precursor polymer has any effect on the yield of insoluble fraction, as was the case for the NITEC networks presented in Section 4.2. Hence, telechelic thiol-PS **69a**, **71a**, and **73a** (2500, 3200, and 6000 $\text{g}\cdot\text{mol}^{-1}$, respectively) were selected as representative starting materials for the end-linking with tetraacrylate **75**, catalyzed with triethylamine, at initial concentration 830 $\text{mg}\cdot\text{mL}^{-1}$ PS in DMF. Reactions

TOWARDS HOMOGENEOUS ALIGNMENT MEDIA

were performed in triplicate to assess the reproducibility of the synthesis method. As depicted in Figure 4.69, the molecular weight of the thiol-PS precursor has little influence in the weight fraction of the insoluble network obtained after thiol-Michael addition end-linking. A constant yield of ca. 85 wt.% was afforded for the three PS samples studied, indicating that the initial amount of reactive groups does not affect the effectiveness of the ligation, contrarily to the photoinduced NITEC reaction (refer to Figure 4.33D).

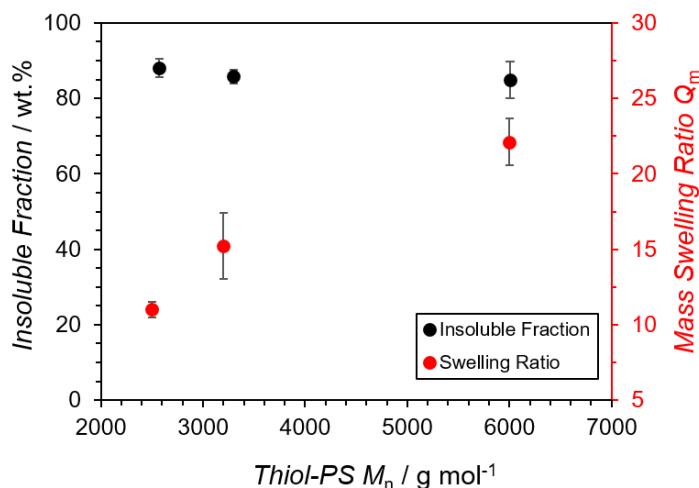


Figure 4.69. Weight fraction of insoluble fraction (black), and equilibrium mass swelling ratio Q_m in chloroform (red) of thiol-ene end-linked gels prepared from PS precursors of different molecular weight **69a**, **71a**, and **73a**. Error bars represent standard deviation from three independent replicas.

Notwithstanding, the mass swelling ratio Q_m of the thiol-ene PS gels in chloroform (determined from Equation 2.55) strongly depends on the molar mass of the PS precursor. Gels produced from short chains **69a** exhibit low swelling ratio ($Q_m = 11.0 \pm 0.5$), which progressively increases with the molecular weight of the polymer precursor, reaching values of $Q_m = 15.2 \pm 2.2$, and 22.1 ± 1.6 for PS precursors **71a** and **73a**, respectively (see Figure 4.69). This behavior agrees with the notion that shorter PS precursors generate more densely crosslinked networks (smaller mesh size), thus displaying smaller swelling ratios. The low standard deviation of the different samples corroborates the reproducibility of this process. Further network formation studies were performed in which addition of a diacrylate linker was combined with tetraacrylate **75** (refer to Figure 8.25 in Appendix 8.4 and experimental section in Chapter 6). The addition of thiol-PS to the diacrylate linker does not produce elastically active chains, directly decreasing the crosslinking density.³²⁰ In this way, it was confirmed that gels with lower crosslinking densities present higher swelling ratios (see Table 8.6 in Appendix 8.4).

4.3.3. Conversion of Thiol Groups

The availability of thiol moieties for thiol-Michael addition end-linking in the PS precursors was estimated using a fluorescent small molecule as model ene substrate. Hence, 9-anthracenylmethyl acrylate **76** was selected as coupling partner for thiol polymers **70a**, **72a**, and **74a**. Mimicking the reaction conditions for network formation (refer to the experimental section), fluorescent polymers **70b**, **72b**, and **74b** were obtained (Figure 4.70A). The corresponding SEC traces are depicted in Figure 4.70B, showing a shift to higher molar mass for polymers **70b**, **72b**, and **74b** after thiol-ene reaction.

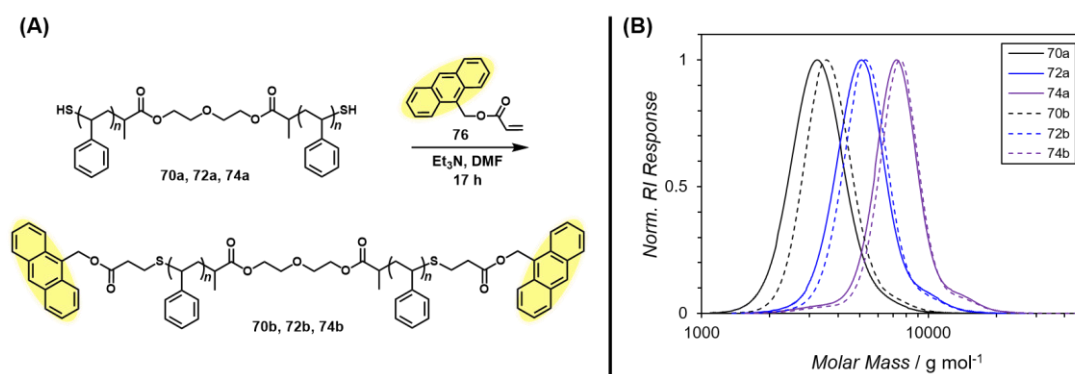


Figure 4.70. (A) Reaction scheme of telechelic thiol-PS **70a**, **72a**, and **74a** with anthracenyl-acrylate **76**, to yield the Michael addition polymers **70b**, **72b**, and **74b**, respectively. (B) SEC traces of polymers before (solid lines) and after (dashed lines) thiol-Michael addition.

The fluorescence emission properties of the anthracene moiety were then exploited to estimate the conversion of thiol groups in the PS chains. First, standard solutions of anthracenyl-acrylate **76** were prepared in DMF and their fluorescence intensity was recorded. It is well known that the fluorescence emission of anthracene solutions depend linearly on the concentration,³²¹ thus a calibration curve could be constructed (Figure 4.71). Monomer **76** shows the typical structured fluorescence spectra of anthracene, with three emission maxima at 393 nm, 416 nm, and 440 nm, along with the expected broad emission around 471 nm corresponding to the excimer fluorescence,³²² as depicted in Figure 4.71A. The fluorescence emission maxima of the monomer were used to construct calibration curves, correlating emission intensity against concentration of **76** at 393 nm, 416 nm, and 440 nm (black, red and blue curves, respectively, in Figure 4.71B).

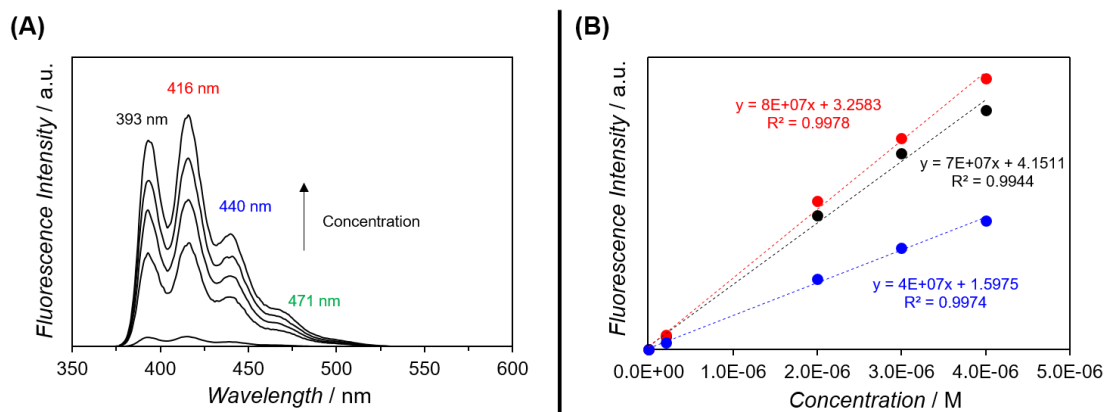


Figure 4.71. (A) Fluorescence emission spectra of solutions of **76** in DMF at different concentrations. Emission maxima for monomer (393 nm, 416 nm, and 440 nm) are clearly visible, in addition to the broad excimer fluorescence emission at 471 nm. (B) Calibration curves of fluorescence intensity vs. concentration of **76**, using the emission maxima at 393 nm (black), 416 nm (red) and 440 nm (blue).

Afterwards, standard solutions of anthracene polymers **70b**, **72b**, and **74b** at $1 \text{ mg}\cdot\text{mL}^{-1}$ mass concentration in DMF were prepared (refer to the experimental section). The solutions were diluted and their fluorescence intensity was recorded under the same conditions as for monomer **76**. It can be observed from Figure 4.72 that the fluorescence emission of the polymers resemble the structured spectrum of **76**. This feature confirms the effective functionalization of **70b**, **72b**, and **74b** with anthracene end-groups, as reported in literature for different polymeric systems.^{117,322}

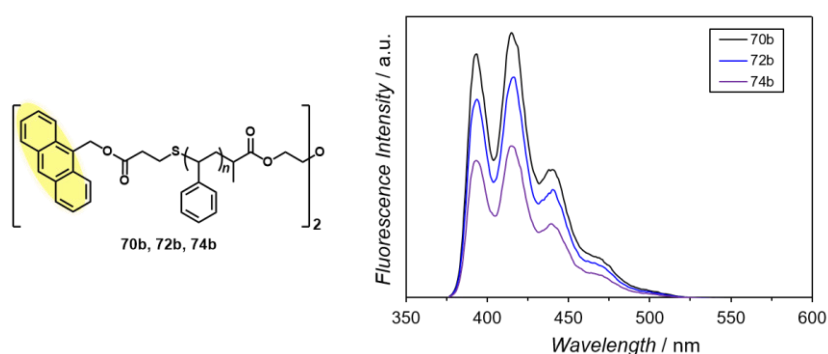


Figure 4.72. Fluorescence emission spectra of polymers **70b** (black), **72b** (blue), and **74b** (purple) in DMF. Emission maxima at 393 nm, 416 nm, and 440 nm were used to determine concentration of anthracene moieties.

Since the polymers were dissolved at the same mass concentration, the intensity of the emission bands follow the trend of relative number of functional groups per mass of polymer. In principle, shorter chains present more functional groups than larger ones per mass unit, as observed in Figure 4.72. Moreover, the emission maxima in the

TOWARDS HOMOGENEOUS ALIGNMENT MEDIA

fluorescence spectra of polymers **70b**, **72b**, and **74b** correspond to the maxima observed for **76** (393 nm, 416 nm, and 440 nm). Therefore, determination of anthracene concentration was performed with the calibration curves depicted in Figure 4.71B. Each calibration curve was used for its respective emission maxima, thus yielding three different values of [anthracene] for each polymer, which were averaged. The theoretical concentration of anthracene in **70b**, **72b**, and **74b**, assuming quantitative conversion, was calculated based on the number average molecular weight \bar{M}_n of the polymers (determined by SEC analyses). Table 4.9 displays the actual percentage of anthracene groups in each polymer, estimated from the fluorescence measurements.

Table 4.9. Percentage of anthracene groups in PS **70b**, **72b**, and **74a**, as determined by fluorescence spectroscopy.

Sample	\bar{M}_n ^a	D^a	Anthracene ^b
70b	3600 g·mol ⁻¹	1.08	75%
72b	5200 g·mol ⁻¹	1.08	90%
74b	7200 g·mol ⁻¹	1.09	85%

^a Determined by SEC, calibrated with linear PS standards.

^b Determined by fluorescence spectroscopy. Average of the values obtained for the emission maxima at 393 nm, 416 nm and 440 nm, from the calibration curves in Figure 4.71B.

An average value of 83% thiol conversion was calculated from the results of anthracene functionalization in samples **70b**, **72b**, and **74b**. This value is in excellent agreement with the mean weight fraction of insoluble fraction (85 wt.%), obtained in the network formation experiments (see Figure 4.69). Even though thiol-ene reactions afford near to quantitative yields in small molecule systems,³¹² diffusional limitations in concentrated solutions of polymeric thiols can reduce the effectiveness of this process. In addition, incomplete aminolysis of the trithiocarbonate groups in the original polymers (see Figure 4.67) decreases the amount of thiol units available for Michael addition reactions, leading to lower yields. Furthermore, possible disulfide bond formation after addition of the base needs to be considered,³²³ since this phenomenon will also decrease the number of available thiol groups.

4.3.4. Thiol-Ene vs. Free-Radical Networks

Using the optimized conditions for network formation, PS precursors **69a–74a** (830 mg·mL⁻¹ in DMF, ca. 46 wt.%) were crosslinked with tetraacrylate **75**, using triethylamine as catalyst, to yield end-linked gels **77–82** (Table 4.10). The mean

TOWARDS HOMOGENEOUS ALIGNMENT MEDIA

molecular weight of the elastically active chains between crosslink points, M_c , was estimated according to the following equation,^{175,319}

$$M_c = 2 \left(\frac{M_{PS}}{f_{PS}} + \frac{M_{75}}{f_{75}} \right) \quad (\text{Eq. 4.14})$$

where M_{PS} represent the molecular weight of thiol-PS (\bar{M}_n determined by SEC, refer to Table 4.6), M_{75} the molecular weight of linker **75** ($352.34 \text{ g}\cdot\text{mol}^{-1}$), and f_{PS} and f_{75} their corresponding functionality ($f_{PS} = 2$, $f_{75} = 4$). Similarly, the average number of styrene units between junctions (n) and the average crosslinking percentage can be calculated using Equations 4.15 and 4.16, respectively.

$$n = \frac{M_{PS}}{104.15} \quad (\text{Eq. 4.15})$$

$$\text{Crosslinking}(\%) = \frac{1}{n} \times 100\% \quad (\text{Eq. 4.16})$$

Table 4.10. Network fraction and swelling ratio of thiol-ene gels prepared from PS precursors of single (**77–82**) and mixed (**82–86**) molecular weights.

Sample	Precursor	M_c^a	n^b	Crosslinking percentage ^c	Insoluble Fraction	Q_m^d
77	69a	$2700 \text{ g}\cdot\text{mol}^{-1}$	25	4.1%	88 wt.%	11.0
78	70a	$3300 \text{ g}\cdot\text{mol}^{-1}$	30	3.4%	79 wt.%	14.4
79	71a	$3400 \text{ g}\cdot\text{mol}^{-1}$	32	3.2%	86 wt.%	15.2
80	72a	$5100 \text{ g}\cdot\text{mol}^{-1}$	47	2.1%	81 wt.%	17.8
81	73a	$6200 \text{ g}\cdot\text{mol}^{-1}$	58	1.7%	85 wt.%	22.1
82	74a	$7100 \text{ g}\cdot\text{mol}^{-1}$	67	1.5%	84 wt.%	22.7
83	69a (88%) + 73a (12%)	$3100 \text{ g}\cdot\text{mol}^{-1}$	29	3.5%	78 wt.%	14.2
84	69a (70%) + 73a (30%)	$3700 \text{ g}\cdot\text{mol}^{-1}$	35	2.9%	67 wt.%	17.8
85	69a (44%) + 73a (56%)	$4600 \text{ g}\cdot\text{mol}^{-1}$	43	2.3%	71 wt.%	18.4
86	69a (54%) + 73a (46%)	$5100 \text{ g}\cdot\text{mol}^{-1}$	47	2.1%	83 wt.%	17.3

^a Average molecular weight between crosslinks, calculated from Eq. 4.14.

^b Average number of styrene units between crosslinks, calculated from Eq. 4.15.

^c Average crosslinking percentage, calculated from Eq. 4.16.

^d Mass swelling ratio, calculated from Eq. 2.55 after free swelling of the sticks in CHCl_3 for 24 h.

TOWARDS HOMOGENEOUS ALIGNMENT MEDIA

In addition to networks **77–82**, prepared by single PS precursors, mixtures of thiol-PS chains of two different molecular weights were employed to synthesize mixed gels **83–86** (refer to experimental section in Chapter 6). In this case, an average molecular weight was calculated

$$\bar{M}_n = \frac{(\text{mol}\%_A \times \bar{M}_{nA}) + (\text{mol}\%_B \times \bar{M}_{nB})}{100} \quad (\text{Eq. 4.17})$$

where the molar masses of both PS precursors (A and B), and their relative amounts (in mol%), were used for the calculation. The average \bar{M}_n values were subsequently used as M_{PS} to calculate M_c as in Equation 4.14. For example, a precursor mixture of 88 mol% of **69a** ($\bar{M}_n = 2500 \text{ g}\cdot\text{mol}^{-1}$) and 12 mol% of **73a** ($\bar{M}_n = 6000 \text{ g}\cdot\text{mol}^{-1}$) was used to prepare network **83**, resulting in average $\bar{M}_n = 2900 \text{ g}\cdot\text{mol}^{-1}$, thus $M_c = 3100 \text{ g}\cdot\text{mol}^{-1}$ according to Eq. 4.14 (see Table 4.10).

In accordance with the observations described in Section 4.3.2, it can be seen from Table 4.10 that the yield of insoluble fraction remains roughly unchanged, irrespective of the molecular weight of the precursor (or mixture of precursors) used for the synthesis. Weight fractions over 80 wt.% were obtained in almost every case, except for the mixed networks **84** (67 wt.%) and **85** (71 wt.%). The inconsistencies observed in those samples probably stem from experimental errors, rather than from the mixing of different PS precursors. On the other hand, the swelling properties of the gels strongly depend on the average molecular weight of the chains between crosslinking points. Larger mass swelling ratios are obtained when PS precursors of high molar mass are utilized, in agreement with the previous observations (refer to Figure 4.69).

Furthermore, the experimental swelling ratio of the mixed networks **83–86** roughly correspond to the swelling expected for single networks of equivalent molar mass (for example, compare Q_m of samples **78** and **83**, and samples **80** and **86** in Table 4.10). In Figure 4.73, the mass swelling ratio of the different gels is plotted against their average M_c . Identical trends were obtained, within experimental error, regardless of the identity of the PS precursors employed, either single or mixed molecular weights. Such behavior coincides with previous findings reported in literature. For instance, Sakai et al. studied the mechanical properties of gels with bimodal M_c distributions^{324,325} demonstrating that, at a macroscopic level, networks prepared from mixed strand lengths behave in a similar way to those obtained from single strand precursors of equivalent molar mass. Plausibly, the macroscopic observables (elastic modulus, fracture energy, elongation ratio) are less sensitive to differences in the microstructure of the gel, but rather dependent on the global macroscopic ($\sim\mu\text{m}$) heterogeneity.³²⁶

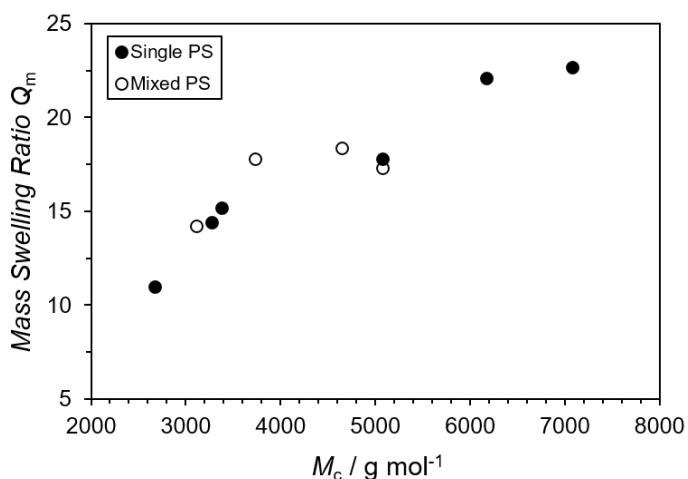


Figure 4.73. Equilibrium mass swelling ratio Q_m in chloroform vs. M_c of thiol-ene gels **77–86** prepared from PS precursors of single (solid symbols) and mixed (open symbols) molecular weight.

Next, free-radical copolymerization techniques were used to synthesize heterogeneous PS gels with crosslinking percentages similar to the end-linked networks **77–86**. For this, DVB amounts of 1.5–4.1 mol% (respect to styrene) were employed for the synthesis of samples **87–94** (Table 4.11). Moreover, DMF was added to the copolymerization mixture, fixing the styrene concentration to 46 wt.%, in order to have comparable conditions as those used for the thiol-Michael addition networks (see experimental section).

Table 4.11. Swelling ratio of free-radical-based PS gels prepared with different amounts of DVB.

Sample ^a	DVB	M_c^b	n^c	Q_m^d
87	4.1 mol%	2500 g·mol ⁻¹	24	6.8
88	3.4 mol%	3100 g·mol ⁻¹	29	7.5
89	3.2 mol%	3300 g·mol ⁻¹	31	7.0
90	2.5 mol%	4100 g·mol ⁻¹	40	9.3
91	2.1 mol%	5000 g·mol ⁻¹	48	9.4
92	1.7 mol%	6100 g·mol ⁻¹	59	10.0
93	1.5 mol%	6900 g·mol ⁻¹	67	11.6
94	0.6 mol%	17100 g·mol ⁻¹	164	23.9

^a Styrene (46 wt.% in DMF) + DVB + 0.1 mol% AIBN. 80 °C, 64 h.

^b Average molecular weight between crosslinks, calculated from Eq. 4.18.

^c Average number of styrene units between crosslinks, calculated from Eq. 4.15.

^d Mass swelling ratio, calculated from Eq. 2.55 after free swelling of the sticks in CHCl₃ for 24 h.

TOWARDS HOMOGENEOUS ALIGNMENT MEDIA

The mean molecular weight of chains between crosslinks in free-radical-based PS networks can be calculated from the molar ratio of DVB, as follows

$$M_c = \left(\frac{100\%}{\text{mol\% DVB}} \right) \times 104.15 \quad (\text{Eq. 4.18})$$

while the average number of styrene units in the chain, n , can be determined as in Equation 4.15. In free-radical-based networks, DVB can be considered as a tetrafunctional crosslinker, allowing a direct comparison with the thiol-ene networks end-linked with tetraacrylate **75** introduced above (Figure 4.74).

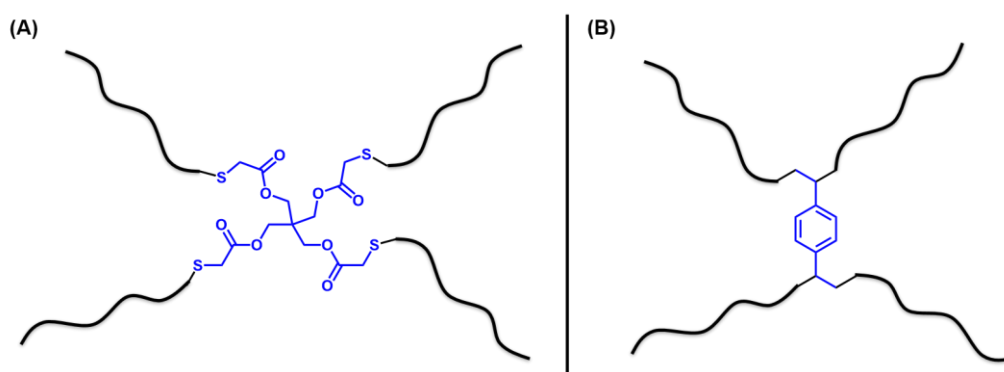


Figure 4.74. Schematic representation of crosslinking junctions of (A) thiol-ene networks ligated by tetraacrylate **75**, and (B) free-radical-based networks crosslinked with DVB. Black lines represent in both cases elastically active PS chains.

Close inspection of the swelling data in Tables 4.10 and 4.11 reveals that, at similar crosslinking percentage, thiol-ene networks exhibit larger swelling ratios than their free-radical-based counterparts. Such differences plausibly arise from the disparate internal microstructures that are obtained from these two methods, as represented schematically in Figure 4.62. Thiol-ene end-linked networks display open structures with a high content of flexible thioether bonds,³¹⁶ in contrast to the more compact structures obtained via free-radical polymerization at high crosslinking degrees. Moreover, the different crosslinking mechanisms that take place during network formation generate structural heterogeneity at different length scales.^{225,327} Free-radical copolymerization follows a chain-addition mechanism (see Section 2.3), producing dense nanogel clusters embedded in a loose gel matrix.^{173,185} These features cause strong spatial fluctuations in the crosslinking degree at the nanometer scale.^{16,225} Contrarily, thiol-ene end-linking can be considered as a step-growth polymerization (refer to Section 2.3), leading to fewer heterogeneities at all length scales,³²⁷ chiefly primary and secondary loops, as well as dangling ends. Consequently, polymer gels

TOWARDS HOMOGENEOUS ALIGNMENT MEDIA

prepared by these two types of crosslinking exhibit unequal properties,^{108,316,327} mainly due to the different length scale of their intrinsic heterogeneities.

Figure 4.75 compares the swelling ratio of the PS gels prepared by thiol-ene (77–86) and free-radical (87–94) crosslinking, along with the theoretical swelling for the polystyrene-chloroform system predicted by the Flory–Rehner equation (refer to Section 2.5.1 and Appendix 8.1). In addition, data corresponding to free-radical-based networks prepared in bulk (see experimental section), analogous to those presented in Section 3.1.1, is included.

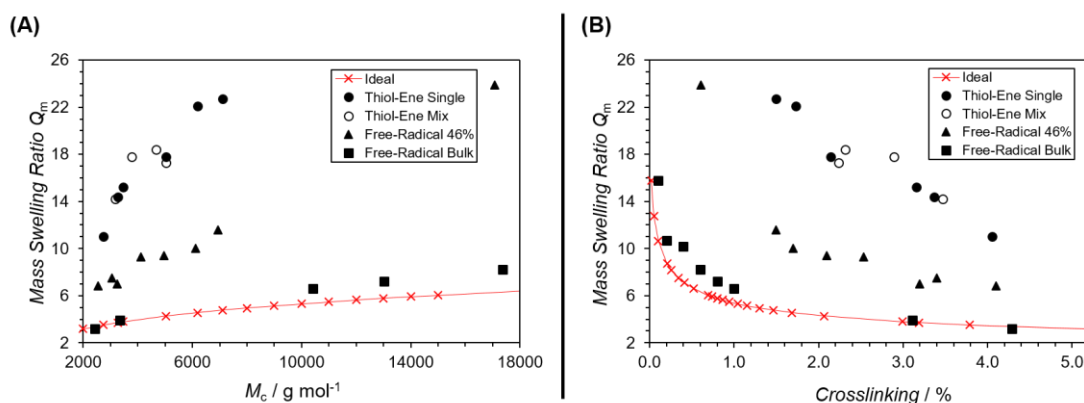


Figure 4.75. Mass swelling ratio Q_m (in chloroform) of PS gels prepared via thiol-ene with single precursors (solid dots), thiol-ene with mixed precursors (open dots), free-radical polymerization 46 wt.% in DMF (triangles), and free-radical polymerization in bulk (squares), against (A) Average molecular weight of chains between crosslinks M_c , and (B) Crosslinking percentage, calculated from Eq. 4.16 for thiol-ene gels, and from the amount of DVB for free-radical gels. Red line with crosses represents in both cases the theoretical Q_m from Flory–Rehner equation.

In general, the mass swelling ratio of the gels increases with higher M_c of the elastic chains (Figure 4.75A) and it decreases with increasing crosslinking percentage (Figure 4.75B). As expected, at higher crosslinking densities Q_m approaches to the theoretical swelling predicted by the Flory–Rehner equation. Moreover, it can be seen that reducing the initial concentration of precursors increases the equilibrium swelling, e.g. networks prepared in bulk (100 wt.%) vs. networks prepared in DMF (46 wt.%), displaying higher deviations from the theoretical values. This behavior has been reported in recent literature^{111,175,201,319} and can be ascribed to increasing cyclization events (loop formation) in diluted precursor solutions, which reduce the actual crosslinking degree (increasing the effective M_c).³²⁸

Additionally, the herein presented experimental results show that the synthesis method has a profound effect in the swelling behavior of the networks. At every

TOWARDS HOMOGENEOUS ALIGNMENT MEDIA

crosslinking degree, higher Q_m values were found for thiol-ene gels (single and mixed) compared to free-radical gels, at comparable precursor concentration (46 wt.% in DMF). In principle, it is expected that end-linking methods generate networks with regular (close to ideal) structures, which would swell less than their heterogeneous free-radical-based counterparts.^{225,327} Notwithstanding, for meaningful comparisons the effect of entanglements, loops and dangling ends on the effective crosslinking percentage of the gels should be taken into account. On the one hand, theoretical simulation studies³²⁹ indicate that end-linked networks display a higher number of trapped entanglements than statistically crosslinked networks with similar number of monomer units between junctions, n . However, in the same study it was found that for end-linked networks, the effect of such entanglements on the swelling of the gel is negligible for $n < 80$. In fact, the simulations predict lower Q_m values for statistical networks in comparison to end-linked ones, when mutual interpenetration of the chains is forbidden.³²⁹ Free-radical polymerization generates highly crosslinked clustered nanogels connected by a loose polymer matrix,^{173,185} as described in Section 2.5.2. Hence, such nanogels do not contribute to the global swelling as strongly as the loose meshes between them. Therefore, lower Q_m ratios at a given degree of crosslinking are expected for statistically crosslinked networks. However, the free-radical-based gels can exhibit higher swelling ratios than end-linked networks when chain interpenetration is permitted.³²⁹

On the other hand, the control experiments described in Section 4.3.3 suggest that the conversion of functional groups in the thiol-ene end-linking method herein presented is not quantitative, thus producing an important amount of dangling chains. Assuming an overall yield of ca. 80% (see Table 4.9), at least 20% of the chains will form dangling ends. In this way, the actual crosslinking percentage of the thiol-ene gels is overestimated by Equation 4.16. Moreover, it is possible that under the applied synthesis conditions, thiol PS precursors are prone to disulfide bond formation.³²³ The incidence of disulfide bonds in the network structure not only diminishes the amount of reactive groups available, but also increases the effective M_c between crosslinks. Indeed, control experiments with thiol-PS **69** and butyl acrylate as monofunctional ene (refer to the experimental section in Chapter 6) suggest that disulfide dimers are obtained at certain extent (Figure 4.76A). The SEC traces of the polymer **69c** after thiol-Michael addition display a shoulder at high molecular weight that might correspond to the disulfide by-product **69c'** (Figure 4.76B). Although no evidence of such dimeric structures was found in the polymers functionalized with anthracenyl-acrylate **70b**, **72**,

TOWARDS HOMOGENEOUS ALIGNMENT MEDIA

and **74b** (refer to Figure 4.70), it cannot be completely ruled out that disulfide bond formation occurs during network formation in samples **77–86**.

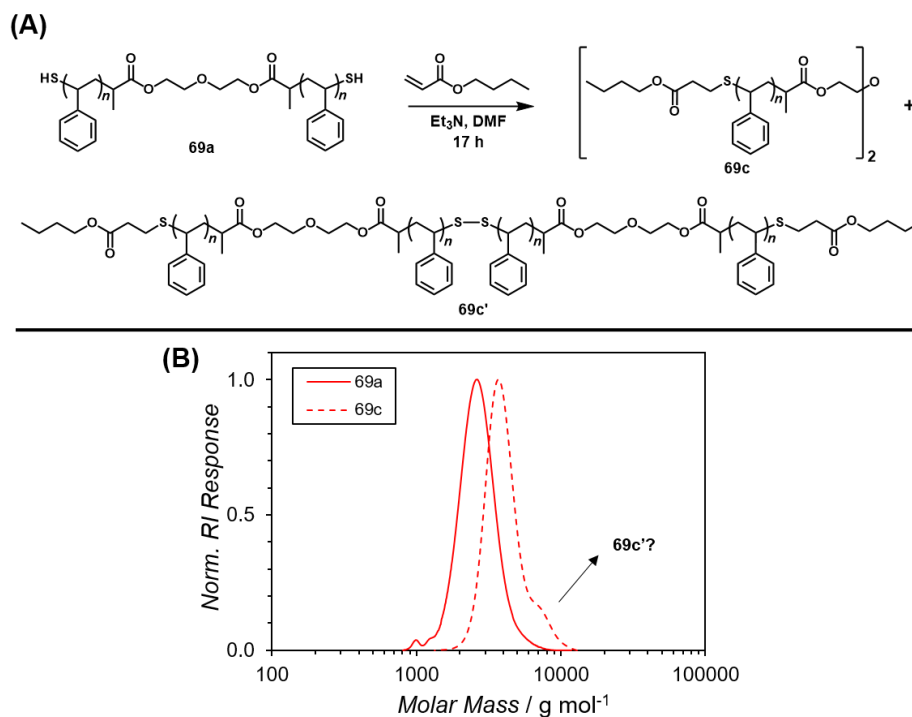


Figure 4.76. (A) Reaction scheme of thiol-PS **69a** with monofunctional butyl acrylate, yielding the expected addition product **69c**, and possible disulfide dimers **69c'**. (B) SEC traces of polymers before (**69a** solid line) and after (**69c** dashed line) thiol-Michael addition. The shoulder in the SEC curve of **69c** might correspond to dimeric structure **69c'**.

In addition to the swelling experiments, the chain mobility in networks composed of short, medium and long segments (different M_c) was investigated by NMR relaxation experiments. As described previously in Section 2.6.2, chain segments adjacent to junctions and entanglements exhibit reduced mobility, therefore their spin-spin relaxation decays (T_2) are shorter than those associated with chain segments with higher conformational freedom.^{250,251} In this respect, T_2 relaxation times were determined for samples **77**, **79**, and **81**, prepared by thiol-ene end-linking, as well as for samples **87**, **89**, and **92**, prepared by free-radical polymerization in DMF (refer to the experimental section for details on the measurement conditions of T_2 decay times). Figure 4.77 displays the relaxation decays of the different gels, in addition to their experimental mass swelling ratios Q_m (inset). The relaxometry experiments confirm the trends previously observed for the swelling behavior of the gels. Samples prepared by free-radical polymerization present the shortest decay times, thus less mobility of chain segments. The mobility increases from sample **87** (short, green symbols) to **89**

TOWARDS HOMOGENEOUS ALIGNMENT MEDIA

(medium, lavender symbols) to **92** (long, yellow symbols), concomitantly with increasing average M_c (see Figure 4.77 and Table 4.11). In the same way, the chains in end-linked sample **81** (blue symbols) are more mobile than the ones in samples **79** (red symbols) and **77** (black symbols) – long, medium, and short chains, respectively – in clear agreement with the swelling data. In general, the results obtained from the relaxometry experiments support the notion that the polymer chains in the thiol-ene gels are more loosely interconnected than those in the free-radical networks, which exhibit a rather rigid structure. Moreover, the long T_2 decays of the end-linked gels suggest that the influence of trapped entanglements on the mobility of their chain segments is negligible.

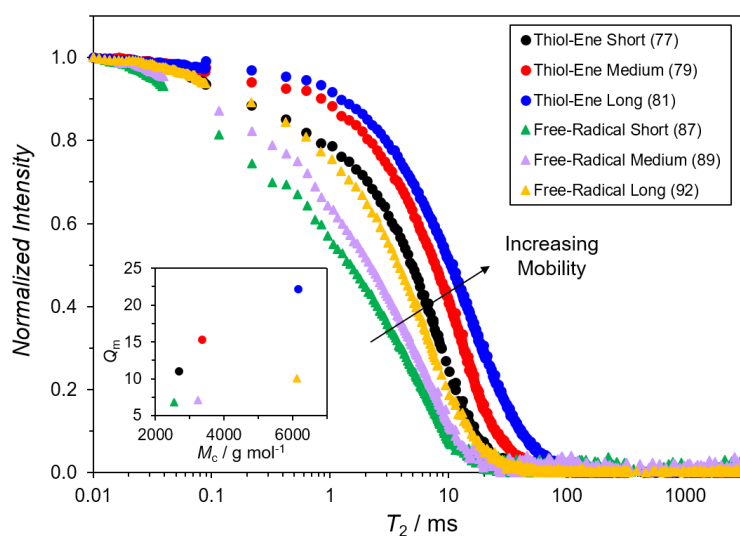


Figure 4.77. T_2 relaxation curves for networks prepared by thiol-ene (dots) and free-radical (triangles) crosslinking, presenting different M_c (short, medium, and long). The inset displays the corresponding swelling (Q_m) vs. M_c data for the different gels.

4.3.5. Thiol-Ene-Based Gels as Alignment Media

Despite the potential issues associated with thiol-ene chemistry as end-linking method to obtain homogeneous polymer gels, this strategy presents several advantages for the synthesis of polymer-based alignment media. First, by simply varying the molecular weight of the thiol-PS precursor, networks with predefined mesh sizes are obtained. In addition, mixtures of PS precursors of disparate molecular weight can be employed for network formation (Figure 4.78A), introducing microstructural heterogeneity in a controlled fashion. In this way, the influence of the mesh size and mesh size distribution on the alignment properties of the gels can be systematically investigated. Furthermore, direct evaluation of structure-property relationships can be

TOWARDS HOMOGENEOUS ALIGNMENT MEDIA

attained by comparison of the alignment behavior with free-radical-based gels (Figure 4.78B) of similar crosslinking densities (or similar swelling ratios).

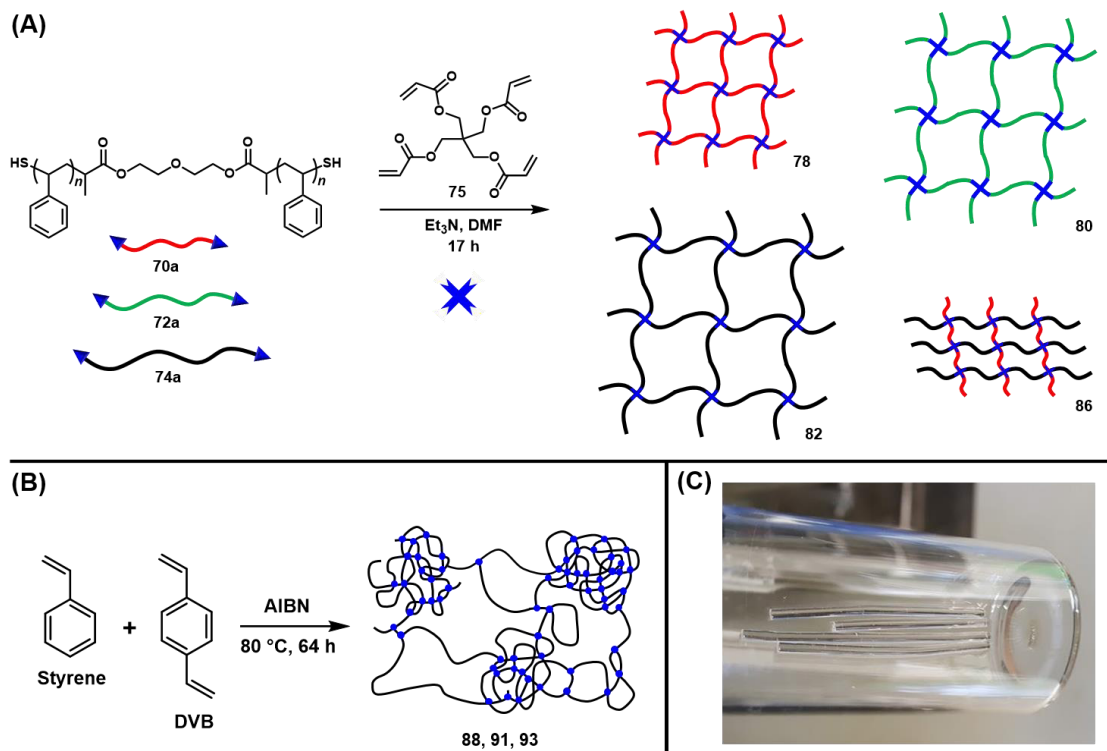


Figure 4.78. (A) Thiol-ene end-linking methods allow the preparation of alignment media with homogeneous (**78**, **80**, **82**) and mixed (**86**) distribution of meshes, starting from PS precursors of different molecular weight (**70a**, **72a**, **74a**), or mixtures of them. (B) Comparison of alignment behavior with free-radical-based gels (**88**, **91**, **93**) allows investigation of structure-property relationships. (C) Cylindrical thiol-ene-based PS sticks can be obtained using appropriate reaction molds.

Second, the extended time needed to reach the gel point in thiol-Michael addition end-linked networks permits shaping them into sticks. Thus, the precursor mixture can be conveniently prepared in common glass vials and then transferred to cylindrical molds such as Teflon[®] tubes (refer to experimental section). In this way, cylindrical PS sticks based on thiol-ene chemistry were afforded (Figure 4.78C). In principle, the thiol-ene end-linking method allows the geometry optimization of the sticks, as described for the free-radical system in Section 3.1.3, with the advantage that no heat transfer or oxygen permeation issues in the reactor need to be considered.

Lastly, the thiol-Michael networks exhibited systematically lower T_g values than their free-radical counterparts, plausibly derived from the open structures attained by the step-growth crosslinking mechanism.³¹⁶ Figure 4.79 displays the glass transition temperature of the different gels, prepared either by free-radical polymerization in DMF (**87–93**), or by thiol-ene end-linking of either single PS precursors (**77–82**) or mixtures

TOWARDS HOMOGENEOUS ALIGNMENT MEDIA

of them (**83–86**). It can be seen that the molecular weight of the elastically active chains between crosslinks, M_c , has little effect on the T_g of the samples, as expected for slightly crosslinked PS networks ($< 5\%$).²⁷¹ The end-linked gels, regardless of single or mixed molecular weight, exhibited T_g values of ca. 41 °C, in contrast to the ca. 57 °C obtained for the free-radical-based networks (see Figure 4.79). Since the plasticizing effect of the DFM can be considered equivalent in both cases, the difference in the glass transition temperature stems more likely from the different structures obtained by both methods. The higher T_g values afforded via free-radical crosslinking are probably a consequence of rigid chains with decreased mobility,²⁰ concurring with the results obtained from NMR relaxometry. In any case, the low T_g values obtained for the different thiol-ene gels will be beneficial for their application as alignment media. Previously in Section 3.1.2 it was determined that PS gels exhibiting $T_g \leq 42$ °C do not present cracks upon swelling in chloroform. Therefore, the thiol-Michael PS networks can be utilized as soft alignment media, avoiding cracking without further addition of plasticizers.

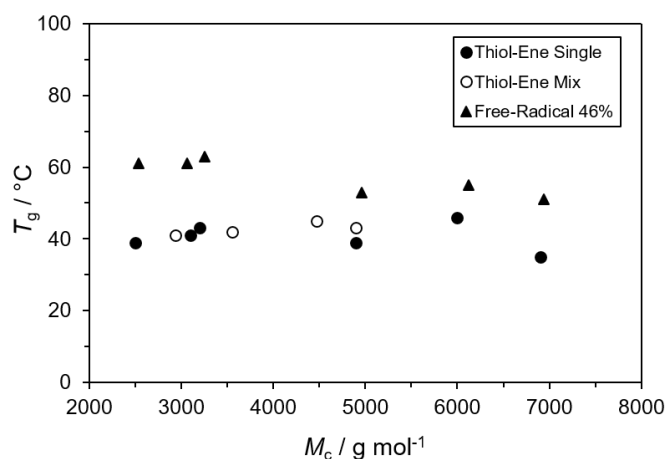


Figure 4.79. Glass transition temperature T_g of thiol-ene end-linked gels (dots), prepared from PS precursor of single (solid symbols) and mixed (open symbols) molecular weight, and free-radical crosslinked gels prepared in DMF (triangles).

Taking this into account, thiol-ene samples **78**, **80**, **82**, and **86**, as well as free-radical-based gels **88**, **91**, and **93** were selected for initial screening of the alignment properties (refer to Figure 4.78 and Tables 4.10 and 4.11). Firstly, it is interesting to know whether the internal structure of the gels has any effect on the linewidth of the quadrupolar splittings of the chloroform signal, since to date no end-linked gels have been employed as alignment media. Second, the influence of the mesh size (samples **70**, **80**, and **82**) on the alignment of various analytes can be assessed. In addition, the

effect of different microstructures in the alignment can be directly evaluated using samples **80** and **86**. Since swelling and crosslinking are kept constant for those samples, the sole influence of regular mesh distribution vs. mixed distribution can be investigated. On the other hand, comparisons of end-linking and free-radical networks in terms of crosslinking degree (e.g. **78** vs. **88**, **80** vs. **91** or **82** vs. **93**) and swelling ratio (e.g. **78** vs. **93**), can be used to determine the role of the network synthesis method in the alignment process. The corresponding NMR analyses using the different anisotropic media are currently ongoing.

4.4. Summary and Outlook

The first two sections of the present chapter describe the use of the pro-fluorescent characteristics of the NITEC reaction as strategy to retrieve quantitative information on polymer systems. First, step-growth polymerization of AA–BB monomers via NITEC chemistry was achieved. For this purpose, a bifunctional tetrazole-RAFT agent was specially designed, combining two orthogonally addressable functional groups, namely tetrazole and trithiocarbonate moieties. On the one hand, intrinsically fluorescent step-growth polymers were prepared in combination with a bifunctional maleimide under UV irradiation (320 nm), and subsequently characterized by NMR and fluorescence spectroscopy. Using a calibration curve to correlate fluorescence intensity and fluorophore concentration, the conversion kinetics of the step-growth process could be monitored by facile fluorescence readouts. Importantly, the results obtained from fluorescence measurements coincided with the information obtained via NMR analysis, confirming that the self-reporting attributes of the NITEC reaction can be applied for quantitative purposes. Nonetheless, in order to ensure accurate results from fluorescence, it is crucial to determine the incidence of secondary processes such as aromatization of the pyrazoline fluorophore. It was found that some reaction parameters like solvent (THF), irradiation time (> 12 h), and initial monomer concentration (< 40 mmol·L⁻¹) favor the onset of aromatization, diminishing the fluorescence emission of the samples. However, the extent of aromatization can be determined straightforwardly by ¹H NMR and used as correction factor. Furthermore, good agreement between the obtained fluorescent polymers and the theoretical Carothers plot (\bar{M}_w vs. conversion) was found only at low conversions (< 75%), probably result of inexact stoichiometry of the reactive tetrazole and maleimide groups. In fact, when a slight excess of the bifunctional tetrazole was used in respect to the bismaleimide (1.05 : 1 and 1.01 : 1 mol ratio), better agreement was achieved. On the

TOWARDS HOMOGENEOUS ALIGNMENT MEDIA

other hand, the bifunctional tetrazole-RAFT agent was utilized as CTA in the controlled radical polymerization of styrene. Thus, well-defined α,ω -tetrazole-functional PS chains of two different molecular weights were obtained and characterized via SEC and ESI-MS analyses. These PS strands were subsequently used as bifunctional monomer for photoligation with bismaleimide. Once more, conversion could be determined by fluorescence and NMR spectroscopy, yielding equivalent values (after correcting the extent of aromatization), demonstrating the application of fluorescence spectroscopy as quantitative characterization method for NITEC-based systems.

Afterwards, NITEC chemistry was employed as end-linking strategy for the preparation of fluorescent polymer networks. RAFT polymerization techniques were used to afford α,ω -tetrazole-functional PS chains of two different molar mass (short and long), which were subsequently crosslinked with a trifunctional maleimide under UV irradiation. In order to maximize the yield of insoluble material and minimize the impact of secondary processes (trithiocarbonate degradation, pyrazoline aromatization), it was necessary to optimize the reaction conditions. Hence, a maximum of 40 wt.% (long PS) and 29 wt.% (short PS) insoluble fraction could be obtained after 8 h UV irradiation (300 nm) of the precursors in DMF solution ($710 \text{ mg}\cdot\text{mL}^{-1}$), pressed between glass slides. Longer irradiation times promoted excessive degradation of the trithiocarbonate groups, diminishing the yield of insoluble material. Next, the fluorescence emission properties of the pyrazoline links between the PS chains were exploited to quantify the number of crosslink points in the networks. Direct determination of fluorescence in the solid state was not feasible, thus network disassembly via aminolysis was investigated. Treatment of RAFT polymers with an excess of *n*-butylamine, followed by coupling to butyl acrylate, generates stable adducts that were characterized via SEC, ESI-MS and ^1H NMR techniques. In this way, the initially insoluble networks were transformed into soluble fragments after aminolysis, without changing the number of pyrazoline bonds originally present in the network. Hence, the fluorescence emission properties of the networks could be analyzed after aminolysis via conventional fluorescence measurements in solution. The effect of aminolysis in the fluorescence emission of the pyrazoline fluorophore was carefully evaluated. A systematic increase (approx. two-fold) in the emission intensity of the fluorophore was observed after aminolysis, in both small molecule and polymeric models. Changes in the chemical structure of the fluorophore, as well as variation of the polarity of the medium, are probably responsible for the enhancement of the fluorescence emission after aminolysis. In any case, it was determined that the effect of aminolysis is linearly dependent on the concentration of fluorophore. Therefore, a new calibration curve relating fluorescence emission and

TOWARDS HOMOGENEOUS ALIGNMENT MEDIA

pyrazoline concentration, after aminolysis, was constructed and validated for quantification purposes. Consequently, quantitative information on the crosslinking kinetics of the different NITEC networks could be obtained. For the short PS precursor, crosslinking proceeds slowly with increasing irradiation times. Most of the pyrazoline groups are found in the soluble fraction at the beginning of the reaction, and crosslinking becomes important only after 4 h irradiation. A maximum linking percentage of 44% was obtained in the insoluble fraction after 8 h (63% overall yield of NITEC reaction). Contrarily, the networks derived from the long PS precursor reached a maximum linking percentage of 69% in the insoluble fraction, already after 2 h irradiation (quantitative overall yield of NITEC reaction). The markedly differences in the crosslinking kinetics were ascribed to the different initial molar concentration of tetrazole groups per mass unit of polymer (ca. 0.50 M for the short and ca. 0.19 M for the long PS precursor), at the same mass concentration. In this way, the crosslinking density of networks derived from long PS chains reached a constant value of ca. 1.8×10^{-4} mmol·mg⁻¹ (68% of the maximum amount possible) after 2 h irradiation. Conversely, the crosslinking density of networks derived from short PS strands constantly increased, exceeding the crosslinking of long PS networks at irradiation times > 4 h. An upper limit in the crosslinking density of ca. 2.9×10^{-4} mmol·mg⁻¹ was reached for the short PS networks after 8 h irradiation (45% of the maximum amount possible). In general, short PS chains take longer to crosslink due to their higher concentration of tetrazole groups per mass of polymer, but generate more compact and more densely crosslinked networks. In this way, by adjusting irradiation time, concentration, and molecular weight of the precursor strands, polymer networks with quantifiable crosslinking densities and tunable properties were obtained.

Although a high level of control and unprecedented network characterization was achieved via NITEC end-linking, this strategy could not be applied for the synthesis of polymer-based alignment media. In order to obtain cylindrical sticks, glass or PDMS capillaries were used as reaction molds, affording very low yields (ca. 6 wt.%) of insoluble fraction. The bulk of the reaction mixture could not be crosslinked, possibly due to limitations in the penetration of light into the concentrated precursor solution. Therefore, in the last section of this chapter thiol-ene chemistry was explored as alternative end-linking method for the synthesis of homogeneous polymer-based alignment media. Firstly, a symmetrical trithiocarbonate-based bifunctional RAFT agent was used to mediate the radical polymerization of styrene. Subsequently, the polymers were subjected to aminolysis affording telechelic α,ω -thiol-capped PS chains that were characterized by NMR, SEC and ESI-MS analyses. Next, the conditions for end-linking

TOWARDS HOMOGENEOUS ALIGNMENT MEDIA

of the thiol-PS chains with a tetrafunctional acrylate were screened. As optimal system, Michael-type crosslinking catalyzed by triethylamine was selected, employing a PS precursor concentration of $830 \text{ mg} \cdot \text{mL}^{-1}$ (46 wt.%) in DMF. A maximum thiol conversion of ca. 83% was estimated under these conditions, using a fluorescent acrylate as marker and thiol-PS precursors of different molar mass. Contrarily to the NITEC system, the molecular weight of the thiol-PS do not influence the yield of insoluble fraction obtained after thiol-Michael addition (ca. 85 wt.% insoluble fraction). However, with increasing molecular weight of the PS precursor, higher mass swelling ratios Q_m are obtained for the respective thiol-ene gels. In general, the chain length of the PS precursors determine the average mesh size of the corresponding gels, which in turn display different swelling ratios. Moreover, mixtures of thiol-PS precursors of disparate molecular weight were used for network formation. The resulting mixed-mesh networks displayed Q_m values corresponding to homogeneous gels made of single PS precursors of average molar mass. Possibly, the swelling behavior of the thiol-ene gels is determined by their global macrostructure, thus insensitive to the small differences in the microstructure introduced by this approach. Afterwards, the Q_m values of the different thiol-ene networks were compared with free-radical-based networks of similar crosslinking percentage (or similar M_c), prepared from 46 wt.% styrene solutions in DMF. In every case, the thiol-ene networks exhibited larger swelling ratios ($Q_m = 11.0\text{--}22.7$) than their free-radical-based counterparts ($Q_m = 6.8\text{--}11.6$). Possible explanations to such differences lie in the different structural heterogeneity generated by these crosslinking methods. Free-radical copolymerization (chain-addition crosslinking) generates dense nanogel clusters embedded in a loose gel matrix, while end-linking methods (step-growth crosslinking) lead to regular meshes, interrupted by primary and secondary loops, as well as dangling ends. Since the thiol-ene end-linking method herein presented is not quantitative, an important amount of dangling chains is expected to be present in the networks, thus diminishing the crosslinking density and increasing Q_m . Additionally, the incidence of disulfide bonds in the network structure cannot be completely ruled out, a phenomenon that will increase the effective M_c between crosslinks, thus increasing Q_m . Furthermore, the chain mobility in thiol-ene and free-radical-based gels was investigated by NMR relaxometry. The differences in the T_2 relaxation times observed for the different samples suggest that the free-radical networks are rather rigid, in contrast to the more mobile chains of the thiol-ene gels. The T_2 analysis confirmed the trends observed in the swelling behavior. Lastly, thiol-ene and free-radical networks of different molecular weight were shaped into sticks, in order to determine their applicability as alignment media for anisotropic NMR experiments. In general, the differences in the microstructure of the samples can be

TOWARDS HOMOGENEOUS ALIGNMENT MEDIA

used to derive structure-property relationships, providing hints to understand alignment processes in polymer gels. The influence of the gel synthesis method on the alignment properties, comparing swelling and crosslinking effects, is currently under investigation. In addition, the use of PS precursors of single and mixed molecular weight for thiol-ene end-linking will be systematically studied. This feature permits the deliberate introduction of topological heterogeneities in the structure of the networks, whose effect on the gel performance as alignment media will be assessed. The results of these investigations will certainly pave the way for the rational design of the next generation of polymer-based alignment media.

CHAPTER 5:

CONCLUDING REMARKS

Anisotropic NMR interactions (e.g. dipolar and quadrupolar couplings) contain important spatial information,^{1-3,252,266} useful for structural elucidation of biological compounds, natural products, and other molecules of interest. However, access to anisotropic parameters via NMR spectroscopy requires the application of a so-called alignment medium. From the media currently known in the literature, polymer gels stand out due to their wide availability, synthetic versatility, solvent compatibility and tunable alignment strength.^{9,11,13} Nevertheless, optimization of their mechanical attributes, functionality, and internal structure is necessary to improve and broaden their application. Therefore, in the present doctoral thesis the synthesis conditions of polymer gels were investigated, with the aim of enhancing the performance of the state-of-the-art systems and developing the next generation of polymer-based alignment media.

In Section 3.1, optimization of the mechanical properties of free-radical-based PS gels, crosslinked with divinylbenzene, was presented. Although conventional free-radical polymerization techniques permit facile adjustment of crosslinking degree (thus alignment strength) and sample geometry (through wide choice of reactor molds), the obtained PS networks display poor resistance to strain forces (e.g. swelling and mechanical deformation). Hence, the use of plasticizers, in particular bis(2-ethylhexyl) adipate, proved to be a simple but effective approach to diminish the mechanical failure of the gels and improve their reusability. In this way, flexible and robust networks with excellent strain-induced alignment properties were afforded. Moreover, precise tuning of their alignment strength was possible by small variation of the mechanical strain applied to the samples, a feature not achieved to date with PS gels. These characteristics – mechanical stability and tunable alignment strength – underpin the development of reusable alignment media for the sequential anisotropic NMR analysis of molecules in one single gel, as depicted schematically in Figure 5.1.

CONCLUDING REMARKS

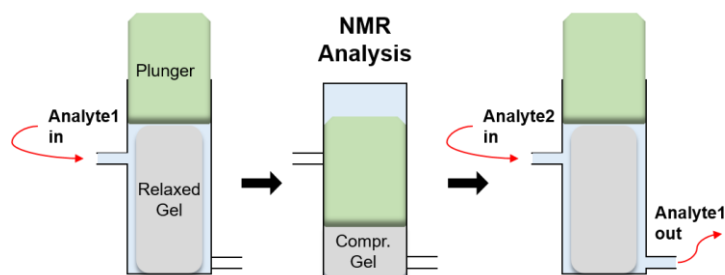


Figure 5.1. Robust PS gels as reusable alignment media, in which analyte molecules are sequentially pumped in, analyzed at a desired alignment strength, and pumped out to repeat the cycle with new molecules.

Even though the addition of plasticizers is clearly beneficial for the flexibility and resistance of the gels, relative high amounts are needed in order to achieve acceptable mechanical properties. This can be detrimental for the resolution of the NMR spectra, since overlap of the resonance signals of the plasticizer with the signals of the analyte cannot be completely avoided. In this respect, it was investigated whether styrene derivatives can be used for the network synthesis, in order to modulate the mechanical behavior without further additives. Preliminary results showed that gels prepared from styrenic monomers with long alkyl chains in *para* position represent promising systems for the development of flexible and robust plasticizer-free PS alignment media. Nonetheless, the networks obtained so far by this approach are brittle, thus further studies are still required to afford networks with optimum mechanical characteristics. Alternatively, the synthesis of interpenetrating^{212,330} and double^{213,214} networks can be explored as strategy to obtain mechanically tough yet soft PS-based gels.

Further on in Section 3.2, functionalization of the networks via conventional free-radical copolymerization was investigated. On the one hand, chiral units were introduced into the PS gels in form of (-)- or (+)-menthol-styrene derivatives. Hence, PS networks with chiral unit content of ca. 25 mol% were prepared and tested as enantiodifferentiating alignment media. Indeed, two pairs of optically active model compounds – the enantiomers (-)-IPC and (+)-IPC, and the diastereomers altenuene and isoaltenuene – could be successfully differentiated via RDC analysis in the chiral PS alignment media, with excellent resolution. These results provide the first example of enantiodifferentiating polymer-based alignment media compatible with apolar solvents. Notwithstanding, the specific interactions between chiral analyte and chiral PS media, ultimately leading to enantiodiscrimination, are not yet understood. In this respect, further experiments using gels with different amounts of chiral moieties (e.g. 5 mol%) are currently ongoing. Moreover, it is possible that the spatial arrangement of

CONCLUDING REMARKS

the chiral units within the network plays an important role in the enantiodifferentiating ability. Hence, the use of reversible-deactivation radical polymerization techniques (e.g. RAFT polymerization) for the controlled placement of chiral units into the network meshes could be implemented. Preliminary experiments confirmed that the model RAFT agent **62** (see Section 4.2.1) lends itself to the preparation of statistical (Figure 5.2A) and block (Figure 5.2B) copolymers of styrene and menthol-styrene.

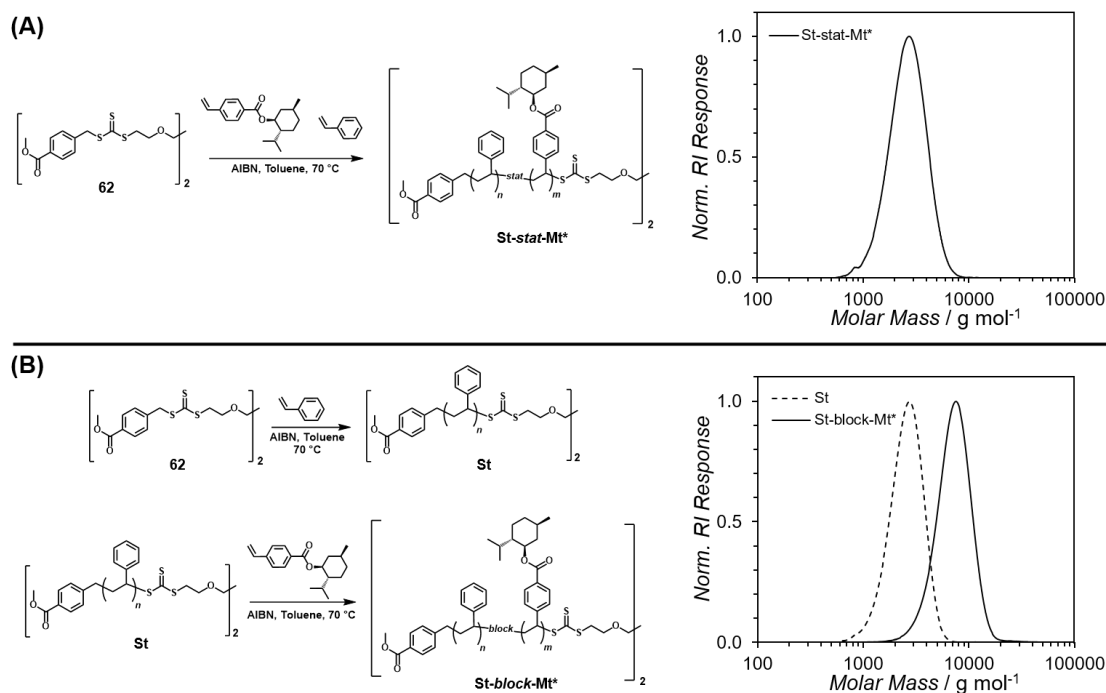


Figure 5.2. Synthesis of (A) Statistical copolymers and (B) Block copolymers of styrene (St) and menthol-styrene (Mt*), mediated by RAFT agent **62**.

On the other hand, conventional free-radical copolymerization was further employed for the functionalization of PS gels with paramagnetic binding tags. In this case, the ligand 1,10-phenanthroline was selected as functional motif and incorporated into the network meshes at 0.8 mol% respect to styrene. Coordination of phenanthroline ligands with lanthanide ions (e.g. europium) generates strongly fluorescent complexes.²⁹⁶ Thus, the effective complexation of europium ions into the phenanthroline-functional gels could be easily confirmed by visual inspection of their fluorescence emission. These results serve as proof of principle and starting point to achieve optimum functionalization of PS gels with paramagnetic ions. The paramagnetic effects exerted by the lanthanide ion (i.e. paramagnetic relaxation enhancement and pseudocontact shifts)²⁹⁰ can be in turn exploited to analyze in detail the alignment process of analytes inside the gels. To accomplish this, precise placement of the lanthanide ions at certain positions of the polymer strands is

CONCLUDING REMARKS

necessary. Specifically, the utilization of reversible-deactivation radical polymerization techniques (see Figure 5.2) or sequence-defined^{331,332} network precursors will be of utmost importance.

The second part of the present thesis was devoted to the synthesis of homogeneous polymer-based alignment media. Networks prepared by conventional free-radical polymerization crosslinking unavoidably exhibit heterogeneous topology.^{16,173,225} It is not yet clear to which extent the structural heterogeneity of the free-radical-based gels affects their application as alignment media. Plausibly, the broad mesh size distribution characteristic of gels prepared by FRP impacts negatively the resolution of the NMR resonance signals. Therefore, a two-step polymerization/end-linking strategy was investigated as potential methodology for the synthesis of alignment media with homogeneous topologies. It is accepted that end-linking of well-defined polymer precursors results in networks with regular mesh distributions.^{197,327} Thus, telechelic PS strands were prepared by RAFT polymerization and subsequently crosslinked using NITEC or thiol-ene protocols.

As first approach, the NITEC reaction was selected as end-linking method due to its pro-fluorescent behavior. In Section 4.1, a novel bifunctional tetrazole-RAFT agent was designed and, first, reacted with a bismaleimide to produce of AA–BB step-growth polymers. It was demonstrated that the kinetics of NITEC step-growth polymerization can be accurately monitored by fluorescence spectroscopy.²⁹⁸ Second, the bifunctional RAFT tetrazole-RAFT agent was employed in the synthesis of α,ω -tetrazole-capped PS chains of different molecular weight. These bifunctional PS strands were further ligated with the bismaleimide in a step-growth photopolymerization process. Once again, it could be proven that fluorescence measurements serve as quantitative characterization method for NITEC-based systems.

These findings led in Section 4.2 to the development of a fluorescence-based method for the determination of crosslinking densities in polymer gels. In this case, the α,ω -tetrazole-capped PS chains were end-linked via NITEC reaction with a trifunctional maleimide, generating insoluble networks. Since each link formed between the tetrazole polymer and the maleimide linker produces a fluorescent unit, the fluorescence intensity of the insoluble fraction gives an estimation of the number of crosslinks.²⁹⁹ Critically, the NITEC strategy positions fluorescence spectroscopy as analytical method to directly quantify the crosslinking degree in end-linked networks, an approach not explored before in the literature. In order to adequately measure fluorescence emission, the initially insoluble networks were disassembled into soluble fragments by aminolysis of the trithiocarbonate groups stemming from the RAFT agent.

CONCLUDING REMARKS

Importantly, such disassembly process do not change the amount of fluorescent links originally present in the network. However, the aminolysis causes an approximately two-fold systematic increase of the emission intensity of the fluorophore, probably due to changes in its structure and in the polarity of the medium. Notwithstanding, since this effect was systematic and linearly dependent on the concentration of fluorophore, the quantification accuracy of the fluorescence-based method was not compromised.

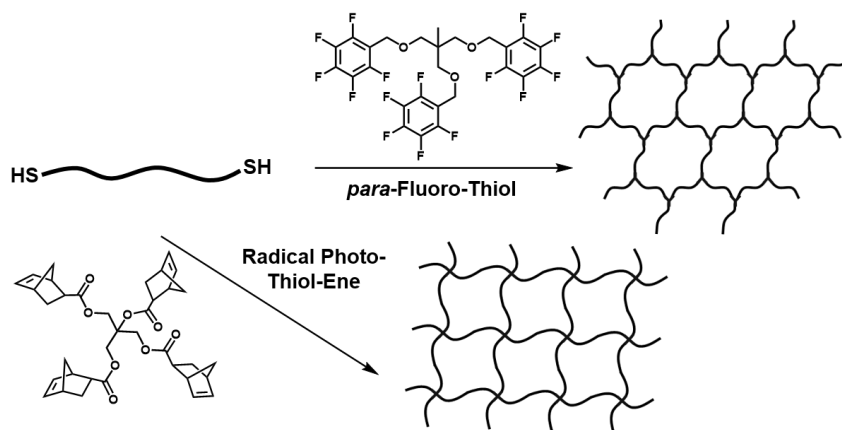
Thus, by means of facile fluorescence readouts, important information on the kinetics of NITEC end-linking was retrieved. It was determined that the molecular weight of the PS precursor has a strong impact in the network formation process. Long PS chains crosslink at early stages of the reaction and offer good overall conversions, hence producing networks depleted of unreacted dangling ends. On the other hand, short PS chains take longer to crosslink due to their higher concentration of tetrazole groups per mass of polymer, but generate more compact and more densely crosslinked networks than their long-mesh counterparts. By adjusting reaction parameters such as irradiation time, concentration, and molecular weight of the precursor, PS networks with tunable crosslinking densities were obtained. Certainly, variations in the crosslinking degree of the networks affect their mechanical properties. Nevertheless, the low amounts of network obtained by the NITEC end-linking method prevented the mechanical characterization of the gels by classical rheological analysis. In this respect, nanomechanical mapping – i.e. spatially resolved force maps obtained from AFM measurements²²⁵ – could be exploited as characterization technique. In fact, recent advances in this field have shown that it is feasible to map the mechanical properties (elastic and dissipative parameters) of polymers, with nanoscale spatial resolution.^{333,334}

Although the NITEC end-linking strategy offered a remarkable control over the synthesis of PS networks, due to limitations in light penetration depth it was not possible to scale up the process for the preparation of alignment media. Consequently, in Section 4.3 Michael-type thiol-ene chemistry was adopted as end-linking strategy. In this case, telechelic α,ω -thiol-capped PS chains (obtained after aminolysis of RAFT polymers) were crosslinked with a tetrafunctional acrylate. High yields of insoluble fraction were obtained by this approach (ca. 85 wt.%), irrespective of the molecular weight of the PS precursor. Variation of the molar mass of the initial thiol-PS strands permitted however the adjustment of the mesh size (thus swelling ratio) of the resulting networks. Moreover, by employing mixtures of thiol-PS of different molecular weights, mixed-mesh networks were obtained. The swelling behavior of the mixed gels corresponded to that expected for gels made of single PS precursors of average molar

CONCLUDING REMARKS

mass. Thus, heterogeneity in the microstructure of the gels could be deliberately introduced.

Subsequently, the properties of the different thiol-ene networks (single and mixed) were compared with free-radical-generated PS gels of comparable crosslinking degree. In every case, the thiol-ene networks exhibited larger swelling ratios than their free-radical counterparts, possibly due to the different structural heterogeneity generated by both methods. In general, free-radical copolymerization generates densely crosslinked nanogels embedded in a loose gel matrix, while end-linking lead to more regular meshes, mainly disturbed by loops and dangling ends.¹⁷³ Indeed, the increased incidence of dangling ends in the herein presented thiol-ene networks might be responsible for the high swelling ratios observed. In this respect, alternative thiol-based linking methods can be explored to maximize the conversion of functional groups, thus diminishing the amount of dangling chains. For instance, *para*-fluoro-thiol ligation^{203,323} or photoactivated radical thiol-ene protocols^{111,200} (Scheme 5.1) have demonstrated good applicability in the synthesis of end-linked polymer networks. In fact, some studies suggest that photoactivated radical thiol-norbornene ligation affords gels with higher crosslinking densities and less structural defects in comparison to thiol-Michael addition.³¹⁹



Scheme 5.1. Synthesis of end-linked polymer networks via *para*-fluoro-thiol or photoactivated radical thiol-norbornene ligation protocols.

In any case, the trends observed in the swelling experiments were corroborated by NMR T_2 relaxometry measurements. Analysis of the T_2 relaxation times suggested that the free-radical networks are rather rigid, in contrast to the more mobile thiol-ene gels. As final remark, the applicability of the different thiol-ene and free-radical networks as alignment media is currently under investigation. The markedly different microstructure of these samples, along with the possibility of introducing structural

CONCLUDING REMARKS

defects in a controlled fashion, will provide insights into the alignment process in polymer gels.

The results presented in this doctoral thesis contribute to the advancement of polymer gels as orientation media for NMR spectroscopy, improving their mechanical, functional, and alignment properties. In addition, the first steps towards the synthesis of homogeneous polymer-based alignment media were taken. With the advent of sequence-defined polymerization techniques^{331,332} and selective disassembly methods for the characterization of defects,^{15,174,223} polymer networks with precisely defined structures will be accessible in the near future. Such systems will allow the development of structure-property relationships and lead to the rational design of the next generation of polymer gels for anisotropic NMR techniques.

CHAPTER 6:

EXPERIMENTAL SECTION

6.1. Materials

2,2'-Azobis(2-methylpropionitrile) (AIBN, >98%, Sigma) was recrystallized from methanol prior to use. Divinylbenzene (stabilized, mixture of isomers, 80%, Alfa), 4-ethoxystyrene (stabilized, 97%, Alfa), 2-fluorostyrene (stabilized, 98%, Alfa), 4-methoxystyrene (stabilized, 98%, Alfa), 3-methylstyrene (stabilized, 98%, Alfa), and styrene (stabilized, >99.0%, Merck), were passed through a column loaded with basic alumina prior to use. *p*-Anisidine (>99%, Sigma), 9-anthracenylmethyl acrylate (98%, Sigma), benzoic acid (ACS reagent, >99%, Alfa), bis(2-ethylhexyl)adipate (>99%, Sigma), 4-(bromomethyl)benzoic acid (97%, Sigma), 1,3-butanediol diacrylate (98%, Sigma), butyl acrylate (stabilized, >98%, Alfa) *n*-butylamine (>99%, Alfa), carbon disulfide (CS₂, for spectroscopy, 99.9%, Acros), 4-carboxybenzaldehyde (98%, Alfa), *N,N*-dicyclohexylcarbodiimide (DCC, 99%, Alfa), diethylene glycol dimethyl ether (diglyme, anhydrous, 99.5%, Sigma), 2,2-dimethoxy-2-phenylacetophenone (>99%, Acros), 4-(dimethylamino)pyridine (DMAP, >99%, Sigma), dimethylphenylphosphine (>97%, Alfa), 1-dodecanol (for synthesis, Sigma), 1-dodecanethiol (>98%, Sigma) *N*-ethylmaleimide (99+%, Alfa), ethylene glycol (anhydrous, 99.8%, Sigma), 2,2'-(ethylenedioxy)diethanethiol (95%, Sigma), (-)-menthol (ReagentPlus, 99%, Sigma), (+)-menthol (99%, Sigma), methyl 4-(bromomethyl)benzoate (98%, Sigma), 4,4'-methylenebis(*N*-phenylmaleimide) (95%, Alfa), *N*-methylmaleimide (97%, Sigma), methyltriocylammonium chloride (Aliquat® 336, >97%, Sigma), pentaerythritol tetraacrylate (inhibited, Sigma) 1-pentanol (98+%, Alfa), *N*-phenylmaleimide (97%, Sigma), pyridine (ACS reagent, >99%, Sigma), sodium nitrite (>98%, Alfa) *p*-toluenesulfonyl hydrazide (98%, Alfa), triethylamine (>99%, Alfa), tris(2-carboxyethyl)phosphine hydrochloride (TCEP, >98%, Sigma), tris(2-maleimidoethyl)amine (trimaleimide, ThermoFisher), and 4-vinylbenzoic acid (98%, Alfa), were used as received. The solvents dichloromethane (DCM, AnalR

EXPERIMENTAL SECTION

NORMAPUR, stabilized with 0.2% ethanol, VWR), dichloromethane (extra dry, 99.8%, stabilized, Acros), *N,N*-dimethylformamide (DMF, extra pure, 99+%, Acros), *N,N*-dimethylformamide (extra dry, 99.8%, Acros), and tetrahydrofuran (THF, extra dry, 99.5%, stabilized, Acros) were used as received. For ESI-MS and SEC measurements, tetrahydrofuran (Multisolvent, stabilized with BHT, Scharlau), and tetrahydrofuran (HiPerSolv CHROMANORM, stabilized with BHT, VWR) were used as solvents, respectively. Deuterated solvents chloroform-*d* (CDCl_3 , >99.8%), *N,N*-dimethylformamide-*d*₇ (DMF-*d*₇, >99.5%), dimethylsulfoxide-*d*₆ (DMSO-*d*₆, >99.8%) and tetrahydrofuran-*d*₈ (THF-*d*₈, >99.5%) were purchased from Euriso-Top and used as received. All other standard chemicals, salts, and solvents were purchased from Acros Organics, Alfa Aesar, Carl Roth or Sigma-Aldrich, and were used without further purification. Thin-layer chromatography was performed on aluminum plates coated with silica gel 60 F₂₅₄ (Merck). 3 mm O.D. high-throughput 7 in NMR tubes (Norell) used as reactor molds, and 5 mm O.D. high-throughput 8 in NMR tubes (Norell), were purchased from Euriso-Top. Borosilicate glass precision cover slips (22 × 22 mm, thickness 170 ± 5 μm, Marienfeld), used as glass slides for NITEC network formation, were purchased from Carl Roth. Soda lime glass capillaries (1.2 mm and 1.5 mm I.D.) were purchased from Hilgenberg. PTFE (Teflon®) tubes (1.5 mm and 1.6 mm I.D., BOLA) were purchased from Häberle.

6.2. Analytical Methods and Instrumentation

6.2.1. Nuclear Magnetic Resonance Spectroscopy

¹H and ¹³C NMR spectra were recorded on a Bruker Avance III 400 spectrometer (¹H: 400 MHz, ¹³C: 101 MHz) or a Bruker Avance III 500 (¹H: 500 MHz, ¹³C: 125 MHz). Samples were dissolved in CDCl_3 , DMSO-*d*₆, THF-*d*₈ or DMF-*d*₇, and the chemical shift scale (δ) was normalized relative to the solvent signal. Abbreviations used in the compound description include singlet (s), doublet (d), doublet of doublets (dd), triplet (t), triplet of doublets (td), and multiplet (m).

For the determination of anisotropic NMR parameters,^a the following conditions were employed. Spectra were recorded on a Bruker Avance II 600 spectrometer equipped with a 5 mm BBI inversely detected ¹H,¹³C double resonance probehead with actively shielded z-gradient, or a Bruker Avance III 600 with a 5 mm CPTCI inversely detected ¹H,¹³C,¹⁵N triple resonance cryogenically cooled probehead (¹H: 600 MHz, ²H: 92 MHz,

^a Anisotropic NMR experiments and data evaluation performed by P. Tzvetkova.

^{13}C : 151 MHz). The temperature was controlled by a Bruker VT-unit and set to 27 °C in all cases. Identical NMR spectra were recorded for all samples in isotropic and aligned phase: ^1H and $^{13}\text{C}\{^1\text{H}\}$ 1D experiments, and CLIP-HSQC³³⁵ and P.E.HSQC²⁹⁵ 2D experiments for the measurement of $^1T_{\text{CH}}$ coupling constants. In addition, ^2H spectra was recorded for the aligned samples to measure quadrupolar splittings as well as a ^2H -imaging experiment for evaluation of the homogeneity of alignment. The typical 1D proton spectral widths are 6 kHz for the isotropic and 12 kHz for the aligned samples, while the carbon spectral widths varied between 28–36 kHz, recording free induction decays with 32k time domain points. The deuterium monitoring experiments were recorded with spectral widths of 28 kHz and 32k time domain points. The CLIP-HSQC and P.E.HSQC experiments were recorded with typical spectral width of 6–12 kHz and 16k time domain points in the direct dimension, while in the indirect dimension the spectral widths were varied between 20–24 kHz with 512 increments to 1k. Zero filling to typically twice the number of points was applied in both dimensions.

For the determination of RDCs,^b coupling constants in isotropic and aligned phase were measured by extracting spectral rows from CLIP-HSQC and P.E.HSQC at corresponding carbon frequencies, following a procedure described before.³³⁶ The values were measured by superimposing the left side of the split signals with the right side of the same signal from a second copy of the same row. The difference between the two sides of the signal in Hz is equivalent to the size of the scalar or total residual dipolar coupling. Maximum error estimates were determined by the outermost imaginable deviations.

For the ^1H NMR T_2 relaxation measurements,^c 40–50 mg of dry sample were swollen in tetrachloroethane- d_2 (1 : 9 ratio). Experiments were conducted on a Bruker minispec NF bench top spectrometer (^1H : 20 MHz). The sample temperature was kept at 30 °C with a BVT3000 unit (Bruker). Before each measurement, the magnetic field was matched and the pulse lengths were determined. Relaxation curves were obtained by a combined set of MSE and CPMG (XX4 and XY16) based pulse sequences. For each measurement 100 data points were recorded and 1024 scans averaged. The MSE was recoded for 40 μs , followed by a XX4 sequence, with a pulse separation of $\tau = 50 \mu\text{s}$. Subsequently, three XY16 pulse sequences were employed with $\tau = 0.04\text{--}100 \mu\text{s}$ to cover the long tailing of the relaxation curve. A recycle delay of 1 s was used.

^b Extraction of RDCs was performed by P. Tzvetkova.

^c Relaxometry measurements were carried out by C. Pfeifer.

EXPERIMENTAL SECTION

6.2.2. Size-Exclusion Chromatography

Molecular weight and molecular weight distributions of polymers were determined on a PSS SECurity² system consisting of PSS SECurity Degasser, PSS SECurity TCC6000 Column Oven (35 °C), PSS SDV Column Set (8 × 150 mm 5 μm precolumn, 8 × 300 mm 5 μm analytical columns, 100 Å, 1000 Å and, 10⁵ Å), Agilent 1260 Infinity Isocratic Pump, Agilent 1260 Infinity Standard Autosampler, Agilent 1260 Infinity Diode Array and Multiple Wavelength Detector (A: 254 nm, B: 360 nm), and Agilent 1260 Infinity Refractive Index Detector (35 °C), or on a TOSOH Eco-SEC HLC-8320 GPC System, comprising autosampler, SDV 5 μm bead-size precolumn (50 × 8 mm, PSS), three SDV 5 μm columns (300 × 7.5 mm, 100 Å, 1000 Å, and 10⁵ Å pore size, PSS), differential refractive index (DRI) detector, and UV detector (set up at 300 nm). Tetrahydrofuran was used as eluent (30 °C) with a flow rate of 1 mL·min⁻¹. The SEC system was calibrated using linear polystyrene standards (PSS ReadyCal) ranging from 266 g·mol⁻¹ to 2.52 × 10⁶ g·mol⁻¹. Calculation of molecular weight and dispersity index proceeded via Mark-Houwink-Sakurada (MHS) parameters in THF at 30 °C ($K = 13.63 \times 10^{-3} \text{ mL}\cdot\text{g}^{-1}$, $\alpha = 0.714$, for PS), using the PSS WinGPC UniChrom software (version 8.2).

6.2.3. Electrospray Ionization Mass Spectrometry

ESI-MS spectra were recorded on a Q Exactive Plus (Orbitrap) mass spectrometer (ThermoFisher Scientific, San Jose, CA, USA) equipped with an HESI II probe. The instrument was calibrated in the m/z range 74–1822 using premixed calibration solutions (ThermoFischer Scientific), and for the high mass mode in the m/z range 600–8000 using ammonium hexafluorophosphate solution. A constant spray voltage of 3.5 kV and dimensionless sheath gas and auxiliary gas flow rate of 10 and 0, respectively, were applied. The capillary temperature was set to 320 °C, the S-lens RF level was set to 150, and the auxiliary gas heater temperature was set to 125 °C. For direct injection, samples were dissolved at 0.03 mg·mL⁻¹ in a THF/methanol mixture (3/2 v/v) containing 100 μmol sodium trifluoroacetate, and injected at 10 μL·min⁻¹ flow rate.

For SEC-ESI-MS measurements, the Q Exactive was coupled to an UltiMate 3000 UHPLC System (Dionex, Sunnyvale, CA, USA) consisting of a pump (LPG 3400SD), autosampler (WPS 3000TSL), and a temperature controlled column department (TCC 3000). Separation was performed on two mixed bead-size exclusion chromatography columns (Agilent, Mesopore 250 × 4.6 mm, particle diameter 3 μm) with a precolumn (Mesopore 50 × 7.5 mm) operating at 30 °C. THF at a flow rate of 0.30 mL·min⁻¹ was

used as eluent. The mass spectrometer was coupled to the column in parallel to an UV detector (VWD 3400, Dionex), and a RI-detector (RefractoMax520, ERC, Japan), in a setup described earlier.³³⁷ A flow of 0.27 mL·min⁻¹ of the eluent was directed through the UV and RI-detectors and 30 μL·min⁻¹ were infused into the electrospray source, after post-column addition of a 50 μM solution of sodium iodide in methanol at 20 μL·min⁻¹ by a micro-flow HPLC syringe pump (Teledyne ISCO, Model 100DM). A 100 μL aliquot of a polymer solution with a concentration of 1 mg·mL⁻¹ was injected into the SEC system.

6.2.4. Fluorescence and UV-vis Spectroscopy

Fluorescence emission spectra were recorded on a Varian Cary Eclipse fluorescence spectrophotometer. Unless otherwise stated, 3.4×10^{-2} mmol·L⁻¹ sample solutions were prepared in an appropriate solvent and measured at ambient temperature in quartz glass high-performance cells (10 mm optical path length, 200–2500 nm wavelength range, Hellma) or far UV-quartz fluorimeter cells (10 mm path length, 170–2700 nm wavelength range, Starna). Fluorescence emission values (in solution) are reported as the average of three independent measurements.

For fluorescence measurements in the solid state, a far UV-quartz cuvette holder for 11 × 22 mm microscope coverslips (10 mm path length, 170–2700 nm wavelength range, Starna) was employed (see Figure 4.35B). The slides were placed at a 45° angle relative to the output beam of the spectrometer, reaching the center of the optical beam (15 mm above the cuvette bottom).

UV-vis spectra were recorded on a Varian Cary 100 at ambient temperature, using analyte concentrations of 2.5×10^{-2} mmol·L⁻¹ in an appropriate solvent. Absorption was measured between 200–800 nm in quartz glass high-performance cells (10 mm optical path length, 200–2500 nm wavelength range, Hellma).

6.2.5. Differential Scanning Calorimetry

Differential scanning calorimetry (DSC) measurements were performed on a DSC 30 calorimeter (Mettler Toledo), equipped with a cooling system of liquid nitrogen. Approx. 10 mg of solid sample was weighted in aluminum pans and heated from 25–150 °C, at a heating rate of 20 °C·min⁻¹. Subsequently, the samples were cooled down to -150 °C (rate 20 °C·min⁻¹) before being subjected to a second heating run (-150–150°C, rate 20 °C·min⁻¹), in order to remove thermal history effects. Values for glass transition temperature were taken at the midpoints (ASTM method) of the heat flow curves, for the second heating run.

EXPERIMENTAL SECTION

6.2.6. Rheology

Oscillatory shear measurements were carried out on the strain controlled rotational rheometer AresG2 (TA Instruments, Eschborn, Germany).^d Aluminum cone-plate geometries (0.02 rad) of 25 mm diameter with a solvent trap were used. The axial force was kept constant at 0.25 ± 0.025 N. The temperature (20 °C) was controlled by a Peltier element (Advanced Peltier System, TA Instruments). Measurements were performed on PS gel disks fully swollen in toluene, after punching out specimens of 25 mm diameter. Additional toluene was added to the solvent trap to minimize evaporation. First, an amplitude sweep was carried out (0.01–100%) at a constant frequency of 1 Hz, in order to determine the linear viscoelastic regime for every new sample. Then, frequency sweeps were performed (0.01–100 Hz) at 1% strain for three independent specimens of the same gel sample. From these measurements, the mean values of storage and loss moduli (G' and G'' , respectively) at 1 Hz were regarded as representative for the sample.

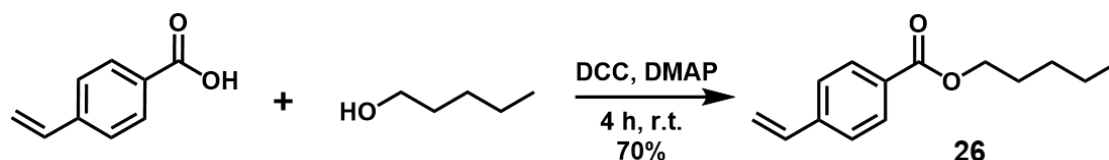
6.2.7. Photoreactors

UV-induced reactions were carried out in a custom-built photoreactor (see Figure 8.8 in Appendix 8.2) with a compact low-pressure fluorescent lamp (Arimed B6), 36 W, $\lambda_{\max} = 320 \pm 30$ nm (Cosmedico GmbH, Stuttgart, Germany), or in a Luzchem LZC-4V photoreactor (see Figure 8.15 in Appendix 8.3) using LZC-UVB lamps, emitting at 300 nm, with a peak of 313 nm. In either case, the internal chamber was ventilated to maintain ambient temperature during the entire experiment. Homogeneous irradiation was ensured by rotating the sample inside the reactors using specially designed carousels (see Figure 4.32 in Section 4.2).

6.3. Experimental Procedures

6.3.1. Synthesis of Small Molecules

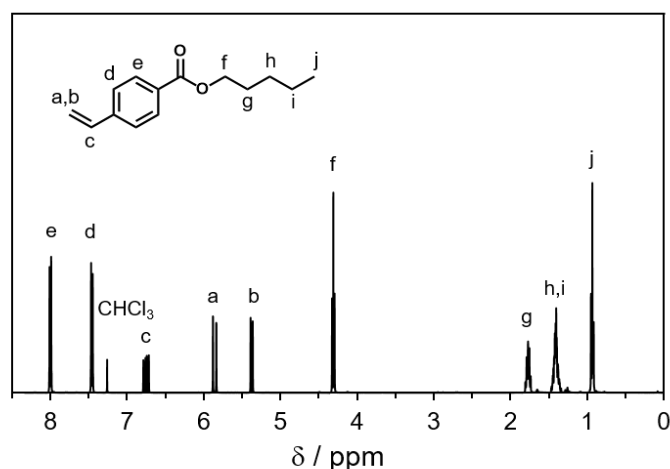
Pentyl 4-vinylbenzoate (26)



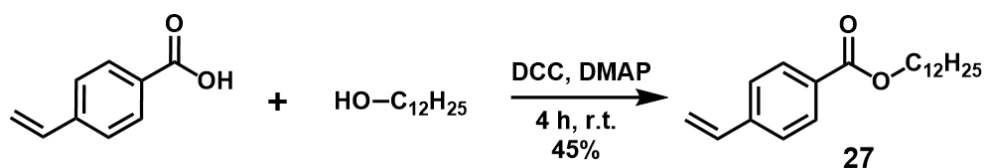
^d Rheology measurements were performed by L. Arens.

EXPERIMENTAL SECTION

4-vinylbenzoic acid (10.0 mmol, 1 eq.), 1-pentanol (10.5 mmol, 1.05 eq.), DMAP (3.19 mmol, 0.32 eq.), and DCC (17.2 mmol, 1.72 eq.) were mixed in a round bottom flask and dissolved in 50 mL dry DCM, under argon atmosphere, and stirred 4 h at room temperature. A solid precipitate was formed, which was filtered out, and the filtrate was washed successively with 1 M HCl, a saturated aqueous solution of NaHCO₃, and brine. Afterwards, the combined organic layers were dried over Na₂SO₄ and the solvent was removed at reduced pressure. The crude product was purified by column chromatography (silica gel), using cyclohexane/ethyl acetate 20/1 (v/v) as eluent ($R_f = 0.48$). Product **26** was obtained as a colorless oil in 70% yield. ¹H NMR (CDCl₃, 400 MHz) δ /ppm: 8.00 (d, $J = 8.4$ Hz, 2H, Ar.H, *ortho* to ester), 7.46 (d, $J = 8.3$ Hz, 2H, Ar.H, *meta* to ester), 6.75 (dd, $J = 17.6, 10.9$ Hz, 1H, CH=CH₂), 5.86 (d, $J = 17.6$ Hz, 1H, CH=CH₂), 5.38 (d, $J = 10.9$ Hz, 1H, CH=CH₂), 4.31 (t, $J = 6.7$ Hz, 2H, OCH₂C₄H₉), 1.77 (m, 2H, OCH₂CH₂C₃H₇), 1.40 (m, 4H, OC₂H₄C₂H₄CH₃), 0.93 (t, $J = 7.1$ Hz, 3H, OC₄H₈CH₃). ¹³C NMR (CDCl₃, 101 MHz) δ /ppm: 166.6 (C(O)O), 141.9 (Ar.C), 136.2 (CH=CH₂), 130.0 (Ar.C), 129.8 (Ar.C), 126.2 (Ar.C), 116.5 (CH=CH₂), 65.2 (OCH₂C₄H₉), 28.6 (OCH₂CH₂C₃H₇), 28.3 (OC₂H₄CH₂C₂H₅), 22.5 (OC₃H₆CH₂CH₃), 14.1 (OC₄H₈CH₃).



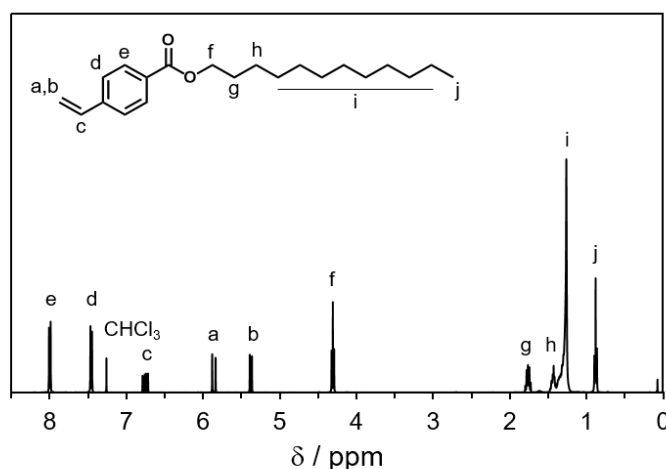
Dodecyl 4-vinylbenzoate (**27**)



The same synthesis procedure as for compound **26** was employed, replacing 1-pentanol by 1-dodecanol (10.5 mmol, 1.05 eq.). Product **27** ($R_f = 0.56$) was obtained

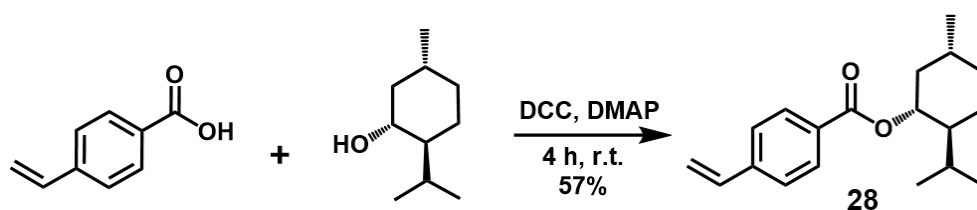
EXPERIMENTAL SECTION

as a colorless oil in 45% yield. ^1H NMR (CDCl_3 , 400 MHz) δ /ppm: 8.00 (d, $J = 8.4$ Hz, 2H, Ar.H, *ortho* to ester), 7.46 (d, $J = 8.3$ Hz, 2H, Ar.H, *meta* to ester), 6.75 (dd, $J = 17.6, 10.9$ Hz, 1H, $\text{CH}=\text{CH}_2$), 5.86 (d, $J = 17.6$ Hz, 1H, $\text{CH}=\text{CH}_2$), 5.38 (d, $J = 10.9$ Hz, 1H, $\text{CH}=\text{CH}_2$), 4.31 (t, $J = 6.7$ Hz, 2H, $\text{OCH}_2\text{C}_{11}\text{H}_{23}$), 1.76 (m, 2H, $\text{OCH}_2\text{CH}_2\text{C}_{10}\text{H}_{21}$), 1.43 (m, 2H, $\text{OC}_2\text{H}_4\text{CH}_2\text{C}_9\text{H}_{19}$), 1.26 (m, 16H, $\text{OC}_3\text{H}_6\text{C}_8\text{H}_{16}\text{CH}_3$), 0.88 (t, $J = 7.0$ Hz, 3H, $\text{OC}_{11}\text{H}_{22}\text{CH}_3$). ^{13}C NMR (CDCl_3 , 101 MHz) δ /ppm: 166.6 (C(O)O), 141.9 (Ar.C), 136.2 ($\text{CH}=\text{CH}_2$), 130.0 (Ar.C), 129.8 (Ar.C), 126.2 (Ar.C), 116.5 ($\text{CH}=\text{CH}_2$), 65.3 ($\text{OCH}_2\text{C}_{11}\text{H}_{23}$), 32.1 (Al.C), 29.8 (Al.C), 29.7 (Al.C), 29.5 (Al.C), 29.4 (Al.C), 28.9 (Al.C), 26.2 (Al.C), 22.8 (Al.C), 14.3 ($\text{OC}_{11}\text{H}_{22}\text{CH}_3$).



(1*R*,2*S*,5*R*)-2-Isopropyl-5-methylcyclohexyl 4-vinylbenzoate (**28**),

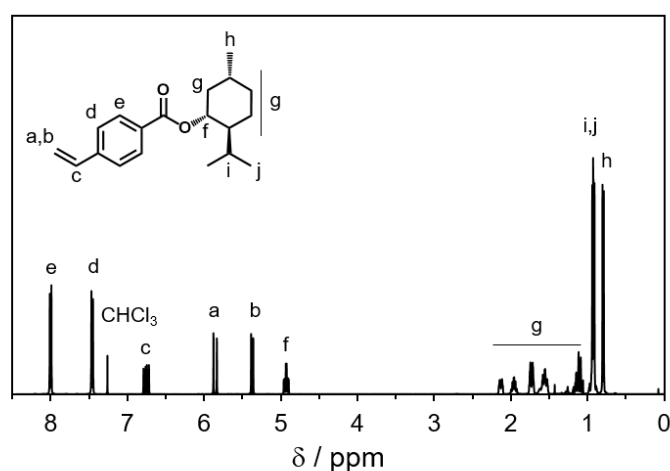
(-)-4-(menthoxy carbonyl)styrene (**28**)



The synthesis of the (-)-menthol-styrene derivative **28** was carried out adapting a literature procedure.²⁹¹ Briefly, 4-vinylbenzoic acid (10.0 mmol, 1 eq.), (-)-menthol (10.5 mmol, 1.05 eq.), DMAP (3.19 mmol, 0.32 eq.), and DCC (17.2 mmol, 1.72 eq.) were dissolved in 50 mL dry DCM under argon atmosphere. The mixture was stirred 4 h at room temperature, after which the precipitate was filtered out. The filtrate was washed successively with 1 M HCl, saturated aqueous NaHCO_3 , and brine. The organic phase was dried over Na_2SO_4 and the solvent evaporated at reduced pressure. The crude product was purified by column chromatography (silica gel), using

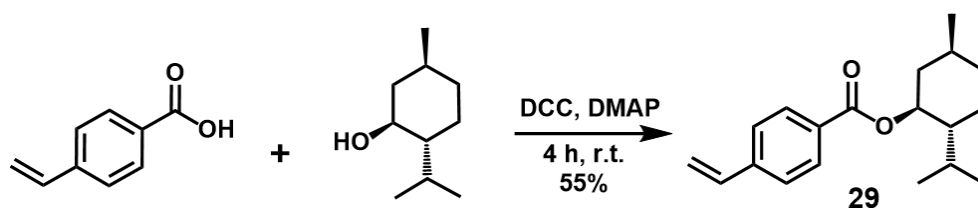
EXPERIMENTAL SECTION

cyclohexane/ethyl acetate 20/1 (v/v) as eluent ($R_f = 0.65$). Product **28** was obtained as a colorless oil in 57% yield. ^1H NMR (CDCl_3 , 400 MHz) δ /ppm: 8.00 (d, $J = 8.4$ Hz, 2H, Ar.H, *ortho* to ester), 7.46 (d, $J = 8.3$ Hz, 2H, Ar.H, *meta* to ester), 6.76 (dd, $J = 17.6$, 10.9 Hz, 1H, $\text{CH}=\text{CH}_2$), 5.86 (d, $J = 17.6$ Hz, 1H, $\text{CH}=\text{CH}_2$), 5.37 (d, $J = 10.9$ Hz, 1H, $\text{CH}=\text{CH}_2$), 4.92 (td, $J = 10.9$, 4.4 Hz, 1H, OCHAl.), 2.13 (m, 1H, Al.H), 1.96 (m, 1H, Al.H), 1.73 (m, 2H, Al.H), 1.55 (m, 2H, Al.H), 1.12 (m, 2H, Al.H), 0.92 (m, 7H, $(\text{CH}_3)_2\text{CHAl.}$), 0.80 (d, $J = 7.0$ Hz, 3H, $\text{CH}_3\text{Al.}$). ^{13}C NMR (CDCl_3 , 101 MHz) δ /ppm: 165.9 (C(O)O), 141.7 (Ar.C), 136.1 ($\text{CH}=\text{CH}_2$), 130.0 (Ar.C), 129.9 (Ar.C), 126.0 (Ar.C), 116.3 ($\text{CH}=\text{CH}_2$), 74.8 (OCHAl.), 47.3 (Al.C), 41.0 (Al.C), 34.4 (Al.C), 26.4 (Al.C), 23.7 (Al.C), 22.1 ($(\text{CH}_3)_2\text{CHAl.}$), 20.8 ($(\text{CH}_3)_2\text{CHAl.}$), 16.6 ($\text{CH}_3\text{Al.}$).



(1*S*,2*R*,5*S*)-2-Isopropyl-5-methylcyclohexyl 4-vinylbenzoate (**29**),

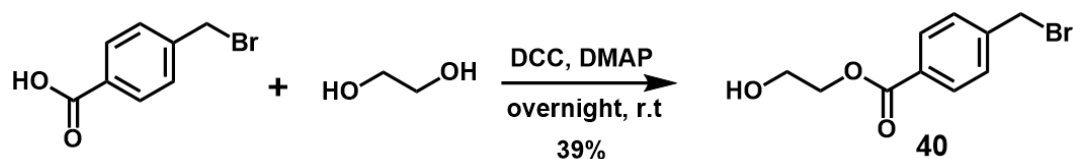
(+)-4-(menthoxycarbonyl)styrene (**29**)



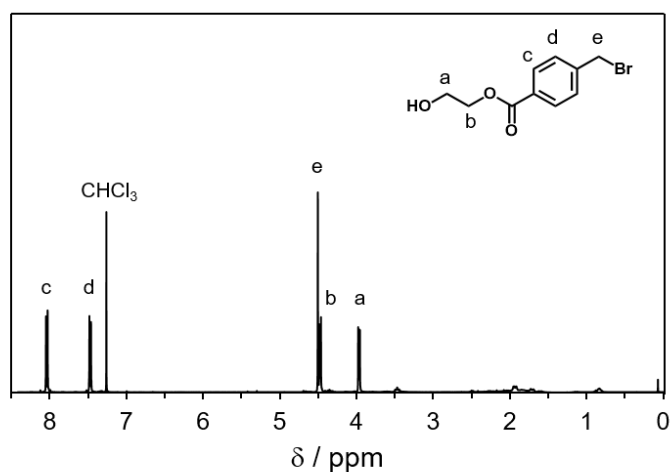
The synthesis of the (+)-menthol-styrene derivative **29** was carried out using the same procedure as for compound **28**, replacing (-)-menthol by (+)-menthol (10.5 mmol, 1.05 eq.). Product **29** ($R_f = 0.65$) was obtained as a colorless oil in 55% yield. NMR characterization showed virtually the same spectra as compound **28**.

EXPERIMENTAL SECTION

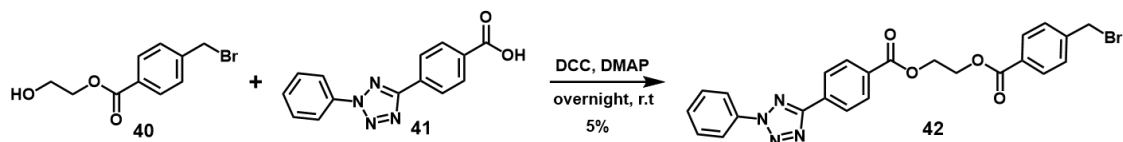
2-Hydroxyethyl 4-(bromomethyl)benzoate (**40**)



Compound **40** was synthesized according to standard literature procedures.⁵⁵ 4-(Bromomethyl)benzoic acid (14.0 mmol, 1 eq.), ethylene glycol (42.0 mmol, 3 eq.), and DMAP (2.8 mmol, 0.2 eq.) were dissolved in 50 mL dry THF under argon atmosphere. Apart, DCC (15.4 mmol, 1.1 eq.) was dissolved in 15 mL dry THF and added dropwise to the previous solution via cannula. The mixture was stirred overnight at room temperature. Afterwards, the precipitate was filtered out and the solvent was removed at reduced pressure. The crude product was then purified by column chromatography (silica gel), using hexane/ethyl acetate 1/1 (v/v) as eluent ($R_f = 0.50$). Product **40** was obtained as a white solid in 39% yield. $^1\text{H NMR}$ (CDCl_3 , 500 MHz) δ /ppm: 8.04 (d, $J = 8.4$ Hz, 2H, Ar.H, *ortho* to ester), 7.47 (d, $J = 8.4$ Hz, 2H, Ar.H, *meta* to ester), 4.50 (s, 2H, CH_2Br), 4.47 (m, 2H, $\text{HOCH}_2\text{CH}_2\text{O}$), 3.97 (m, 2H, $\text{HOCH}_2\text{CH}_2\text{O}$).



2-((4-(Bromomethyl)benzoyl)oxy)ethyl 4-(2-phenyl-2H-tetrazol-5-yl)benzoate (**42**)

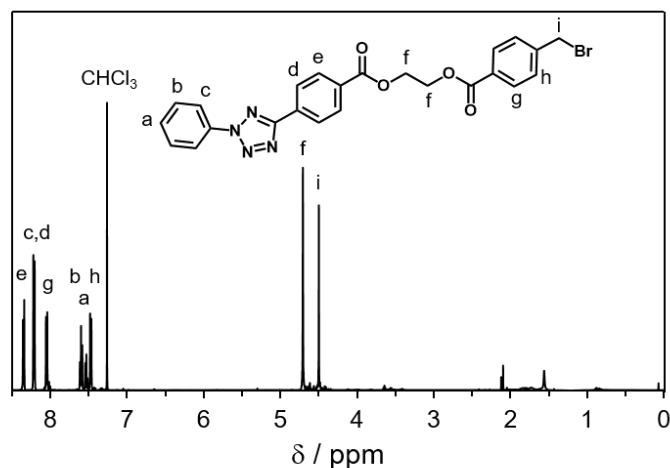


The synthesis of compound **42** was carried out adapting a literature procedure.⁵⁵ Precursor **40** (4.06 mmol, 1 eq.), tetrazole derivative **41**^e (4.06 mmol, 1 eq.), and DMAP

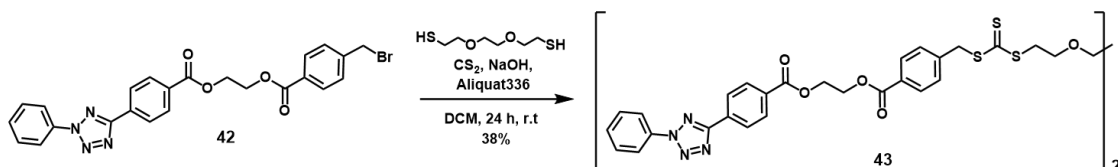
^e Compound **41** was prepared, characterized and kindly provided by K. Hiltbrandt.

EXPERIMENTAL SECTION

(0.41 mmol, 0.1 eq.) were dissolved in 40 mL dry THF under argon atmosphere. Apart, DCC (5.08 mmol, 1.25 eq.) was dissolved in 20 mL dry THF and added dropwise to the previous solution via cannula and the mixture was stirred overnight at room temperature. The solid precipitate was filtered and the solvent was evaporated at reduced pressure. The crude product was purified by column chromatography (silica gel), using hexane/ethyl acetate 4/1 (v/v) as eluent ($R_f = 0.55$). The product **42** was obtained as a slightly red solid in 5% yield. $^1\text{H NMR}$ (CDCl_3 , 500 MHz) δ /ppm: 8.35 (d, $J = 8.6$ Hz, 2H, Ar.H, middle ring *ortho* to ester), 8.21 (d, $J = 8.4$ Hz, 4H, Ar.H, monosubstituted ring *ortho* to tetrazole and middle ring *meta* to ester), 8.05 (d, $J = 8.4$ Hz, 2H, Ar.H, *meta* to CH_2Br), 7.60 (t, $J = 7.3$ Hz, 2H, Ar.H, monosubstituted ring *meta* to tetrazole), 7.53 (t, $J = 7.4$ Hz, 1H, Ar.H, monosubstituted ring *para* to tetrazole), 7.47 (d, $J = 8.3$ Hz, 2H, Ar.H, *ortho* to CH_2Br), 4.71 (s, 4H, $\text{OCH}_2\text{CH}_2\text{O}$), 4.50 (s, 2H, CH_2Br).



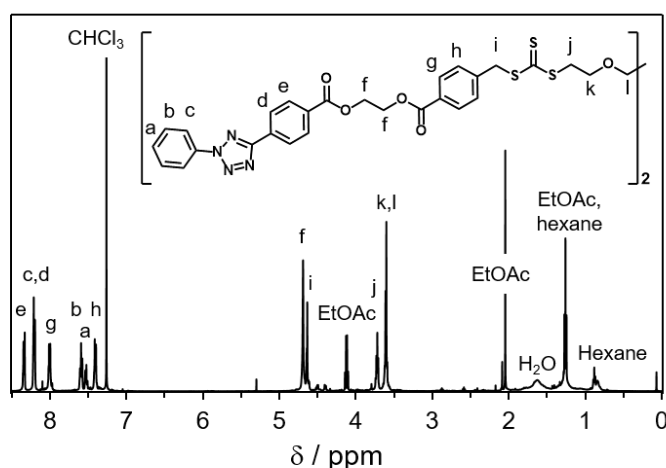
Bis(2-phenyl-2H-tetrazol-5-yl)benzoyl-RAFT agent derivative (**43**)



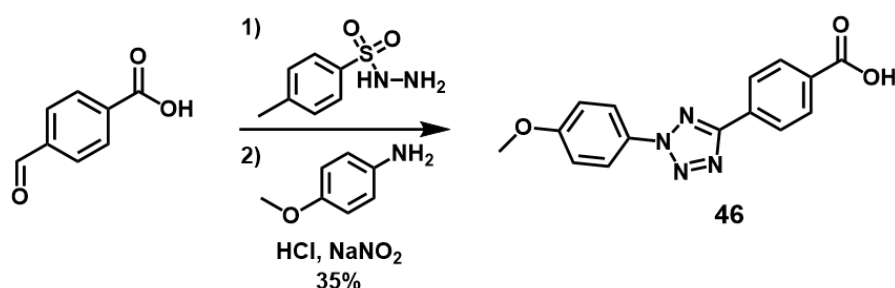
The synthesis of the bifunctional RAFT agent **43** was accomplished adapting a literature procedure.³¹⁰ 2,2'-(ethylenedioxy)diethanethiol (0.08 mmol, 1 eq.), carbon disulfide (CS_2 , 0.24 mmol, 3 eq.), and the phase transfer catalyst Aliquat® 336 (1 mg) were suspended in 1 mL of NaOH aqueous solution (10 mg $\text{NaOH}\cdot\text{mL}^{-1}$). The suspension was stirred 2 h at room temperature. Subsequently, a solution of bromide precursor **42** in DCM (0.24 mmol **42**, 3 eq., in 1 mL DCM) was added and the two phase mixture was

EXPERIMENTAL SECTION

stirred vigorously for further 24 h. Afterwards, the organic phase was washed three times with water and dried over MgSO_4 . Lastly, the solvent was evaporated at reduced pressure and the crude product was purified by column chromatography (silica gel), using hexane/ethyl acetate 3/1 (v/v) as eluent. Once the first red-colored fractions were eluted, the solvent mixture was changed to hexane/ethyl acetate 2/3 (v/v) and elution continued with this mobile phase until the second red-colored fractions (product) were obtained ($R_f = 0.07$). The product **43** was obtained as a red solid in 38% yield. $^1\text{H NMR}$ (CDCl_3 , 500 MHz) δ /ppm: 8.34 (d, $J = 8.4$ Hz, 4H, Ar.H, middle ring *ortho* to ester), 8.20 (d, $J = 8.0$ Hz, 8H, Ar.H, monosubstituted ring *ortho* to tetrazole and middle ring *meta* to ester), 8.00 (d, $J = 8.3$ Hz, 4H, Ar.H, *meta* to $\text{CH}_2\text{SC}(\text{S})\text{S}$), 7.59 (t, $J = 7.3$ Hz, 4H, Ar.H, monosubstituted ring *meta* to tetrazole), 7.52 (t, $J = 7.3$ Hz, 2H, Ar.H, monosubstituted ring *para* to tetrazole), 7.40 (d, $J = 8.2$ Hz, 4H, Ar.H, *ortho* to $\text{CH}_2\text{SC}(\text{S})\text{S}$), 4.69 (s, 8H, $\text{C}(\text{O})\text{OCH}_2\text{CH}_2\text{OC}(\text{O})$), 4.63 (s, 4H, $\text{CH}_2\text{SC}(\text{S})\text{S}$), 3.72 (t, $J = 5.9$ Hz, 4H, $\text{C}(\text{S})\text{SCH}_2\text{CH}_2\text{OCH}_2$), 3.60 (m, 8H, $\text{C}(\text{S})\text{SCH}_2\text{CH}_2\text{OCH}_2$).

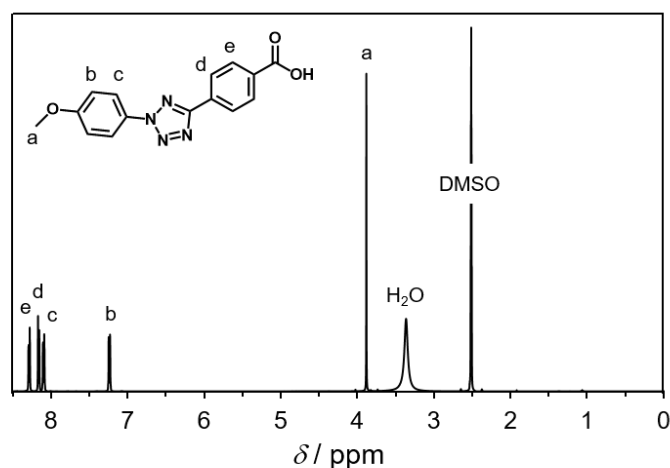


4-(2-(4-methoxyphenyl)-2H-tetrazol-5-yl)benzoic acid (**46**)

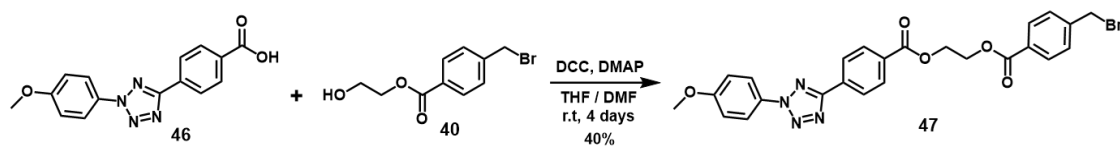


The synthesis of tetrazole derivative **46** was performed following standard literature protocols.¹³⁹ First, 4-carboxybenzaldehyde (4-formylbenzoic acid, 43.7 mmol) and *p*-toluenesulfonyl hydrazide (43.7 mmol) were dissolved in 100 mL ethanol and heated

to reflux for 30 min. After the addition of 100 mL H₂O, the white precipitate was collected by filtration, washed with 100 mL of ethanol/water 1/1 (v/v), and re-dissolved in 200 mL pyridine. Apart *p*-anisidine (32.5 mmol) was dissolved in 8.5 mL concentrated HCl, diluted with 54 mL ethanol/water 1/1 (v/v) and cooled to 0 °C. A solution of sodium nitrite (NaNO₂, 32.5 mmol in 13.5 mL H₂O) was added dropwise to the anisidine solution over 30 min, keeping the temperature at 0 °C. The formed diazonium salt was then slowly added to the hydrazide solution in pyridine prepared in the first step, over a period of 1 h, at room temperature. The mixture was stirred further 2 h, after which it was poured carefully onto 500 mL of aqueous 10% HCl. A red precipitate was hence formed, recovered by filtration and washed with water and ethanol (200 mL each). The solid was heated to reflux in 300 mL ethanol for 20 min, filtered and washed with cold ethanol to afford product **46** as a pale purple solid in 35% yield. ¹H NMR (DMSO-*d*₆, 500 MHz) δ/ppm: 8.28 (d, *J* = 8.1 Hz, 2H, Ar.H, *ortho* to acid), 8.16 (d, *J* = 8.2 Hz, 2H, Ar.H, *meta* to acid), 8.10 (d, *J* = 9.0 Hz, 2H, Ar.H, *meta* to CH₃O), 7.24 (d, *J* = 9.0 Hz, 2H, Ar.H, *ortho* to CH₃O), 3.88 (s, 3H, CH₃O).



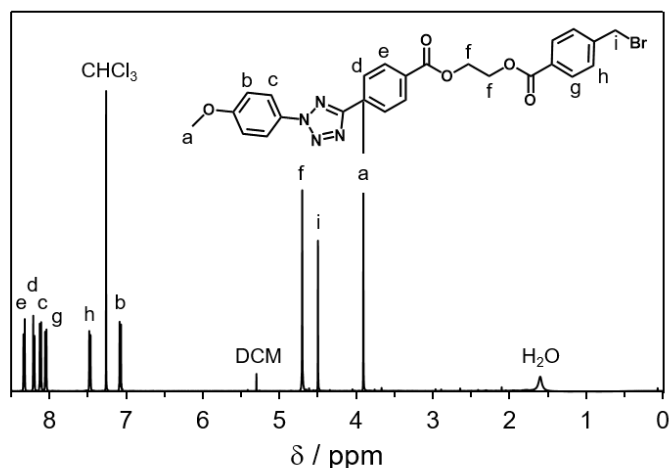
2-((4-(bromomethyl)benzoyl)oxy)ethyl 4-2-(4-methoxyphenyl)-2H-tetrazol-5-yl) benzoate (47)



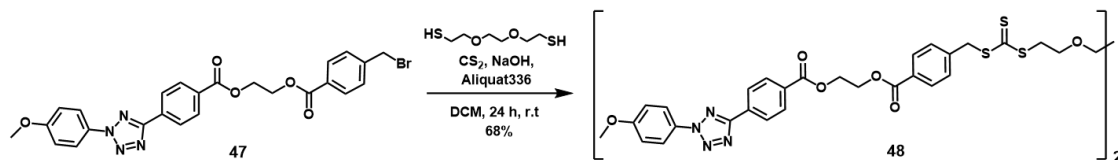
The synthesis of the bromide precursor **47** is reported elsewhere.²⁹⁸ The tetrazole derivative **46** (3.8 mmol, 1 eq.), the bromide **40** (3.8 mmol, 1 eq.), and DMAP (0.76 mmol, 0.2 eq.) were dissolved in a mixture of 60 mL dry THF and 15 mL dry DMF under argon atmosphere. The clear solution was cooled to 0 °C in an ice bath. Apart,

EXPERIMENTAL SECTION

DCC (16.3 mmol, 4.3 Eq.) was dissolved in 40 mL dry THF and added dropwise over 1 h to the previous mixture via cannula. The reaction was left to proceed at room temperature for 4 days. Afterwards, the solid precipitate was filtered out and the solvent evaporated under reduced pressure. The crude product was purified by column chromatography (silica gel), using DCM as eluent ($R_f = 0.30$) to give the precursor **47** as a pale solid (40% yield). ^1H NMR (CDCl_3 , 500 MHz) δ /ppm: 8.33 (d, $J = 8.3$ Hz, 2H, Ar.H, middle ring *ortho* to ester), 8.20 (d, $J = 8.3$ Hz, 2H, Ar.H, middle ring *meta* to ester), 8.12 (d, $J = 9.0$ Hz, 2H, Ar.H, meta to CH_3O), 8.05 (d, $J = 8.3$ Hz, 2H, Ar.H, meta to CH_2Br), 7.47 (d, $J = 8.3$ Hz, 2H, Ar.H, *ortho* to CH_2Br), 7.09 (d, $J = 9.0$ Hz, 2H, Ar.H, *ortho* to CH_3O), 4.70 (s, 4H, $\text{OCH}_2\text{CH}_2\text{O}$), 4.50 (s, 2H, CH_2Br), 3.91 (s, 3H, CH_3O). ^{13}C NMR (CDCl_3 , 125 MHz) δ /ppm: 165.8 ($\text{C}(\text{O})\text{O}$), 164.1 (NCN), 160.7 (COCH_3), 142.6 (CCH_2Br), 131.6 (Ar.C), 131.4 (Ar.C), 130.3 (Ar.C), 130.2 (Ar.C), 129.7 (Ar.C), 129.1 (Ar.C), 128.6 (Ar.C), 127.0 (Ar.C), 121.5 (Ar.C), 114.8 (Ar.C), 63.0 ($\text{OCH}_2\text{CH}_2\text{O}$), 62.8 ($\text{OCH}_2\text{CH}_2\text{O}$), 55.7 (CH_3O), 29.7 (CH_2Br). ESI-MS m/z calculated for $\text{C}_{25}\text{H}_{21}\text{BrN}_4\text{O}_5$ $[\text{M}+\text{Na}]^+$: 559.0593, found 559.0590.



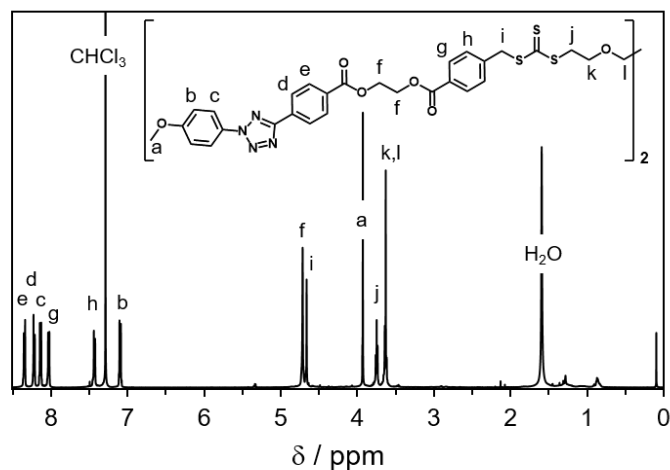
Bis(2-(4-methoxyphenyl)-2H-tetrazol-5-yl)benzoyl-RAFT agent derivative (**48**)



The synthesis of the bifunctional-tetrazole RAFT agent **48** is reported elsewhere.²⁹⁸ Briefly, 2,2'-(ethylenedioxy)diethanethiol (0.064 mmol, 1 eq.), carbon disulfide (CS_2 , 0.19 mmol, 3 eq.), and the phase transfer catalyst Aliquat® 336 (4 mg) were suspended in 7 mL of NaOH aqueous solution ($1.08 \text{ mg NaOH}\cdot\text{mL}^{-1}$) and stirred 2 h at room

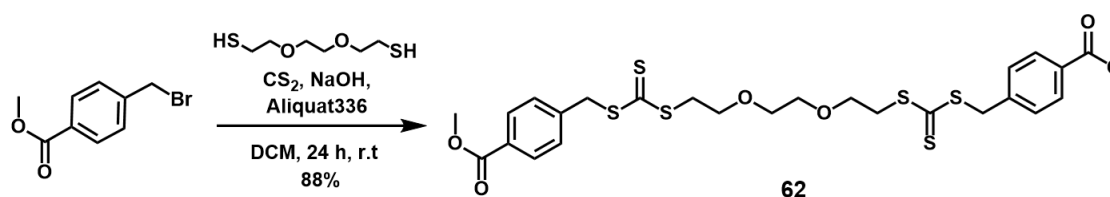
EXPERIMENTAL SECTION

temperature. Subsequently, the bromide precursor **47** (0.19 mmol, 3 eq.) was dissolved in 7 mL of DCM and added to the previous mixture. The two phase system was stirred at room temperature for 24 h. Then, the organic layer was washed with water three times, dried over MgSO₄ and the solvent was evaporated under reduced pressure. The crude product was eluted in a silica gel column with 500 mL of DCM followed by 100 mL of DCM/ethyl acetate 1/1 (v/v). After the change of eluent, the yellow fractions were collected and the solvent evaporated to afford a bright yellow solid. This powder was washed with cold methanol three times and then dried to give the product **48** in 68% yield. ¹H NMR (CDCl₃, 500 MHz) δ/ppm: 8.34 (d, *J* = 8.4 Hz, 4H, Ar.*H*, middle ring *ortho* to ester), 8.22 (d, *J* = 8.4 Hz, 4H, Ar.*H*, middle ring *meta* to ester), 8.14 (d, *J* = 9.0 Hz, 4H, Ar.*H*, *meta* to CH₃O), 8.03 (d, *J* = 8.3 Hz, 4H, Ar.*H*, *meta* to CH₂SC(S)S), 7.43 (d, *J* = 8.3 Hz, 4H, Ar.*H*, *ortho* to CH₂SC(S)S), 7.10 (d, *J* = 9.0 Hz, 4H, Ar.*H*, *ortho* to CH₃O), 4.71 (s, 8H, C(O)OCH₂CH₂OC(O)), 4.66 (s, 4H, CH₂SC(S)S), 3.93 (s, 6H, CH₃O), 3.75 (t, *J* = 6.4 Hz, 4H, C(S)SCH₂CH₂OCH₂), 3.63 (m, 8H, C(S)SCH₂CH₂OCH₂). ¹³C NMR (CDCl₃, 125 MHz) δ/ppm: 222.7 (SC(S)S), 165.9 (C(O)O), 165.8 (C(O)O), 164.1 (NCN), 160.7 (COCH₃), 140.1 (CCH₂S), 131.6 (Ar.*C*), 131.3 (Ar.*C*), 130.3 (Ar.*C*), 130.1 (Ar.*C*), 129.3 (Ar.*C*), 129.1 (Ar.*C*), 127.0 (Ar.*C*), 121.5 (Ar.*C*), 114.8 (Ar.*C*), 70.4, (SCH₂CH₂O), 68.5 (SCH₂CH₂O), 63.0 (OCH₂CH₂O), 62.8 (OCH₂CH₂O), 55.7 (CH₃O), 40.8 (CH₂S), 36.6, (SCH₂CH₂OCH₂). ESI-MS *m/z* calculated for C₅₈H₅₄N₈O₁₂S₆ [M+Na]⁺: 1269.2083, found: 1269.2073.



EXPERIMENTAL SECTION

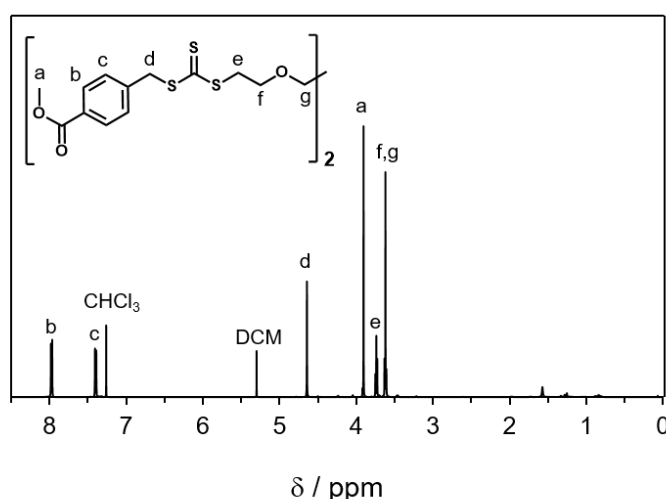
Bis(methyl)benzoyl-RAFT agent derivative (**62**)



The model RAFT agent **62** was prepared adapting a literature procedure.³¹⁰ Briefly, 2,2'-(ethylenedioxy)diethanethiol (3.5 mmol, 1 eq.), carbon disulfide (CS_2 , 10.5 mmol, 3 eq.), and the phase transfer catalyst Aliquat® 336 (30 mg) were suspended in 5 mL of NaOH aqueous solution (88 mg $\text{NaOH}\cdot\text{mL}^{-1}$). The suspension was stirred 2 h at room temperature. Subsequently, a solution methyl 4-(bromomethyl)benzoate in DCM (10.5 mmol, 3 eq., in 5 mL DCM) was added and the two phase mixture was stirred vigorously for further 24 h. Afterwards, the organic phase was washed three times with water and dried over MgSO_4 . Lastly, the solvent was evaporated at reduced pressure and the crude product was purified by column chromatography (silica gel), using DCM as eluent ($R_f = 0.33$). The product **62** was obtained as a bright yellow solid in 88% yield.

^1H NMR (CDCl_3 , 500 MHz) δ /ppm: 7.97 (d, $J = 8.3$ Hz, 4H, Ar.H, *ortho* to ester), 7.40 (d, $J = 8.3$ Hz, 4H, Ar.H, *meta* to ester), 4.64 (s, 4H, $\text{CH}_2\text{SC}(\text{S})\text{S}$), 3.90 (s, 6H, CH_3O), 3.74 (t, $J = 6.5$ Hz, 4H, $\text{C}(\text{S})\text{SCH}_2\text{CH}_2\text{OCH}_2$), 3.62 (m, 8H, $\text{C}(\text{S})\text{SCH}_2\text{CH}_2\text{OCH}_2$).

^{13}C NMR (CDCl_3 , 125 MHz) δ /ppm: 223.0 ($\text{SC}(\text{S})\text{S}$), 166.8 ($\text{C}(\text{O})\text{O}$), 140.6 (CCH_2S), 131.0 (Ar.C), 129.7 (Ar.C), 129.4 (Ar.C), 70.6, ($\text{SCH}_2\text{CH}_2\text{O}$), 68.7 ($\text{OCH}_2\text{CH}_2\text{O}$), 52.3 (CH_3O), 41.0 (CH_2S), 36.7 ($\text{SCH}_2\text{CH}_2\text{O}$). ESI-MS m/z calculated for $\text{C}_{26}\text{H}_{30}\text{O}_6\text{S}_6$ $[\text{M}+\text{Na}]^+$: 653.0264, found: 653.0251.



6.3.2. Polymerizations

Synthesis of crosslinked PS sticks by free-radical polymerization



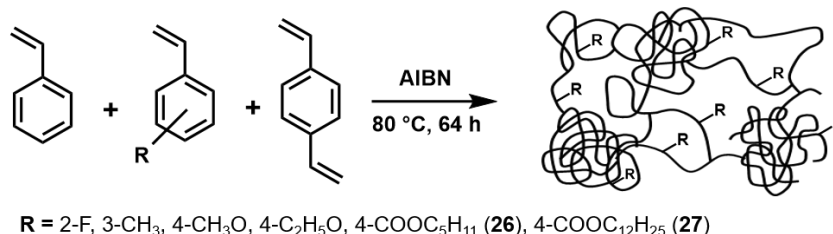
The preparation of crosslinked PS sticks (bulk polymerization) was adapted from previous literature reports.^{9,270} A mixture of styrene (94.5 mmol), AIBN (0.095 mmol, 0.1 mol% in respect to styrene), and DVB (0.1–1.0 mol% in respect to styrene, see Table 3.1), was degassed by bubbling argon during 30 min. Afterwards, the mixture was divided and placed into cylindrical reactors (3 mm O.D. NMR tubes), under argon atmosphere. The reaction mixture was then polymerized for 64 h at 80 °C in an oil bath (see Figure 8.1). After cooling down to ambient temperature, solid translucent sticks **1–6** of 2.2 mm diameter were recovered by breaking the NMR tubes used as mold.

For the samples with plasticizers **7–21**, different amounts of toluene, DMF, and adipate (1–20% v/v in respect to the monomer mixture, see Table 3.2) were added to the mixture of styrene (94.5 mmol), AIBN (0.095 mmol, 0.1 mol%), and DVB (0.378 mmol, 0.4 mol%), and polymerized 64 h at 80 °C as described above.

Networks **87–94** (see Table 4.11) were prepared at a styrene concentration of 46 wt.% in DMF, following the conditions described above.

Sticks with different diameters were obtained by varying the cylindrical reactor used for the polymerization, either PTFE tubes of 1.5 mm or 1.6 mm I.D. (sealed with epoxy glue), or glass capillaries of 1.2 mm or 1.5 mm I.D. (see Tables 3.4 and 3.5).

Synthesis of functional-PS sticks by free-radical polymerization



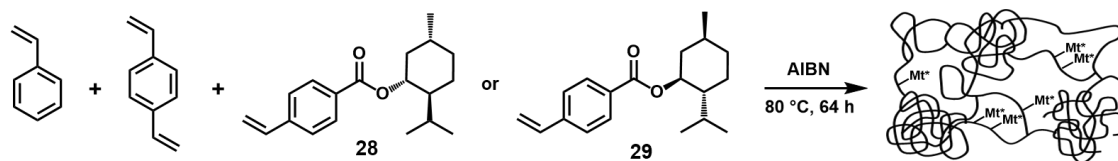
A mixture of monomer (2-fluorostyrene, 3-methylstyrene, 4-methoxystyrene or 4-ethoxystyrene, 45.0 mmol, see Table 3.3), AIBN (0.045 mmol, 0.1 mol% in respect to monomer), and DVB (0.18 mmol, 0.4 mol% in respect to monomer), was degassed by

EXPERIMENTAL SECTION

bubbling argon during 20 min. Afterwards, the mixture was divided and placed into cylindrical reactors (3 mm O.D. NMR tubes), under argon atmosphere. The reaction mixture was polymerized for 64 h at 80 °C in an oil bath (see Figure 8.1). After cooling down to ambient temperature, solid translucent sticks **22–25** were recovered by breaking the NMR tubes used as mold.

For the synthesis of networks with long alkyl chains (see Figure 3.12), mixtures of styrene and pentyl-styrene **26** (70 : 30 to 0 : 100 mol ratio styrene : **26**) or styrene and dodecyl-styrene **27** (95 : 5 to 0 : 100 mol ratio styrene : **27**), 4.4 mmol overall amount of monomer, were prepared. AIBN (0.0044 mmol, 0.1 mol% in respect to monomer mixture) and DVB (0.0176 mmol, 0.4 mol% in respect to monomer mixture) were added, the resulting mixture was degassed by bubbling argon during 5 min and then divided in 3 mm O.D. NMR tubes. Polymerization was carried out at 80 °C in an oil bath (see Figure 8.1) for 64 h. After cooling down to ambient temperature, solid translucent sticks were recovered by breaking the NMR tubes used as mold.

Synthesis of PS networks functionalized with chiral units



Styrene (9.20 mmol) was mixed with (-)-menthol-styrene **28** or (+)-menthol styrene **29** (3.08 mmol) – or a mixture of 1.54 mmol **28** + 1.54 mmol **29** – at a molar ratio 75 : 25 styrene : Mt*. AIBN (0.0123 mmol, 0.1 mol% in respect to monomer mixture) and DVB (0.0246 mmol, 0.2 mol% in respect to monomer mixture) were added and the resulting mixture was degassed by bubbling argon during 10 min and divided in 3 mm O.D. NMR tubes, under inert atmosphere. Polymerization was performed at 80 °C in an oil bath (see Figure 8.1) for 64 h. After cooling down to ambient temperature, solid translucent sticks **30–32** (see Table 3.6) were recovered by breaking the NMR tubes used as mold.

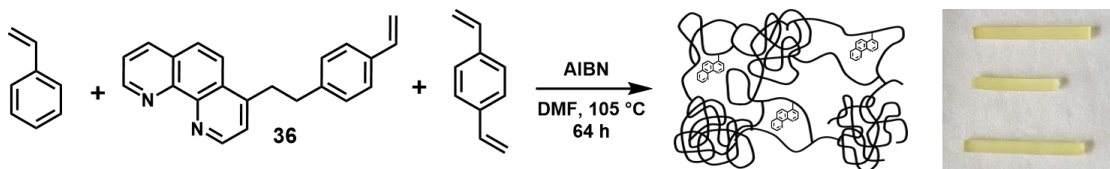
The same procedure was adopted using a molar ratio 95 : 5 styrene : Mt* (18.4 mmol styrene + 0.968 mmol **28** or **29**), 0.0194 mmol AIBN (0.1 mol% in respect to monomer mixture), and 0.0387 mmol DVB (0.2 mol% in respect to monomer mixture), to yield samples **33–35** (see Table 3.6).

The preparation of PS sticks with molar ratio 46 : 52 styrene : **28** (1.80 mmol styrene + 1.93 mmol **28**) required the addition of 3.65×10^{-3} mmol AIBN (0.098 mol% in respect to monomer mixture) and 0.0223 mmol DVB (0.6 mol% in respect to

monomer mixture). Nevertheless, the obtained sticks were too brittle to be used as alignment media.

The determination of reactivity ratios (r_1 and r_2) was carried out for the comonomer pair styrene and (-)-menthol-styrene **28**, adapting previously reported experimental protocols.²⁹² Briefly, feed compositions of styrene and **28** (95 : 5 to 10 : 90 mol ratio styrene : **28**) were prepared in glass vials, keeping 3.0 mmol as overall monomer amount. AIBN (0.003 mmol, 0.1 mol% in respect to monomer mixture) and the internal standard diglyme (0.05 mmol, 1.67 mol% in respect to monomer mixture) were added in each case, and a small aliquot of every sample was taken (before polymerization) for ¹H NMR analysis. Afterwards, the reaction mixture was degassed by bubbling argon during 5 min and polymerized at 70 °C in a heating block for 25 min. Then, the polymerization was quenched by immersing the vials in liquid nitrogen and exposing the reaction to ambient oxygen. A second aliquot (after polymerization) was taken for ¹H NMR analysis, before the polymers were precipitated in cold methanol (three times). The solid precipitate was collected by filtration, dried under reduced pressure and analyzed once more by NMR spectroscopy.

Synthesis of PS networks functionalized with paramagnetic binding tags



Phenanthroline-functional PS sticks were afforded by free-radical copolymerization of styrene and phenanthroline derivative **36**.^f A 99 : 1 mol ratio mixture of styrene (4.465 mmol) and **36** (0.045 mmol) was dissolved in DMF (14% v/v) in a ultrasonic bath. AIBN (0.0045 mmol, 0.1 mol% in respect to monomer mixture) and DVB (0.018 mmol, 0.4 mol% in respect to monomer mixture) were added and the resulting mixture was degassed by bubbling argon during 5 min. The solution was then divided in 3 mm O.D. NMR tubes and polymerized at 105 °C in an oil bath (see Figure 8.1) for 64 h. After cooling down to ambient temperature, solid yellow sticks **37** (see Table 3.12) were recovered by breaking the NMR tubes used as mold. Alternatively comonomer mixtures 99.2 : 0.8 and 99.6 : 0.4 mol ratio styrene : **36** were employed to yield samples **38** and **39**, respectively. In the former case, styrene (5.689 mmol) and **36** (0.025 mmol) were dissolved in 10% v/v DMF in ultrasonic bath before adding AIBN (0.0057 mmol) and

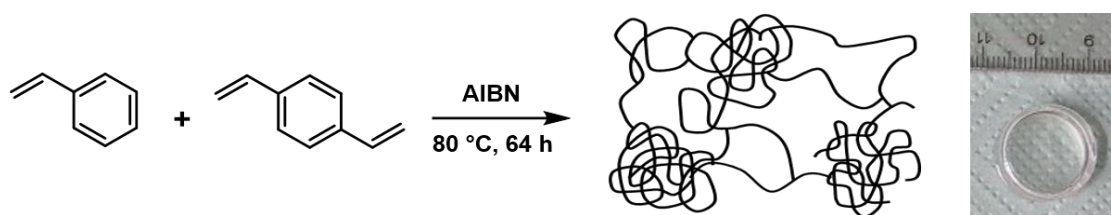
^f Monomer **36** was prepared, characterized and kindly provided by H. Rothfuss and N. Knöfel.

EXPERIMENTAL SECTION

DVB (0.023 mmol). In the latter case, styrene (5.689 mmol) and **36** (0.0225 mmol) were dissolved in 5% v/v DMF in ultrasonic bath before adding AIBN (0.0057 mmol) and DVB (0.023 mmol).

Europium complexation was achieved using the precursor $[\text{Eu}(\text{dbm})_3(\text{H}_2\text{O})_2]$,⁹ as depicted in Scheme 3.4. Sample **38**, having a maximum amount of phenantroline groups of 2.07 wt.%, was chosen for complexation experiments. Sticks of ca. 2 cm long (69.0 mg) containing max. 1.43 mg (0.0046 mmol, 1 eq.) phenanthroline, were swollen in 10 mL of a solution of europium precursor in chloroform ($6.9 \times 10^{-4} \text{ mmol}\cdot\text{mL}^{-1}$, 1.5 eq.) for 24 h. As negative controls, sample **38** swollen in 10 mL chloroform and sample **12** (plain PS) swollen in 10 mL precursor solution, were employed (see Table 3.13). The different samples were re-swollen in fresh chloroform for 24 h (three times), in order to remove the excess of precursor.

Synthesis of crosslinked PS disks for rheology measurements

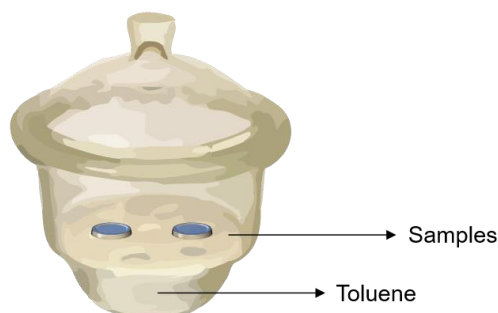


The synthesis conditions of PS sticks described above were adapted for the preparation of disks, as exemplified here for PS networks with 0.1 mol% DVB (**1**). A mixture of styrene (39.42 mmol), AIBN (0.0394 mmol, 0.1 mol% in respect to styrene), and DVB (0.0394 mmol, 0.1 mol% in respect to styrene) was prepared and divided in four 5 mL glass vials. The different samples were degassed by bubbling argon during 30 min and subsequently polymerized in a heating block for 64 h at 80 °C. After cooling down to room temperature, solid translucent disks of 17 mm diameter and 4 mm height were recovered by breaking the glass vials used as mold. The same procedure was employed to afford disks with different amounts of DVB (samples **2**, **3**), plasticizers (sample **20**), and chiral units (samples **30** and **33**).

Free swelling of the disks (without plasticizers) in toluene promoted breaking and formation of cracks, hampering their analysis via rheology (see Figures 3.9 and 8.3). Therefore, a slow swelling procedure was employed as follows: the dry samples were

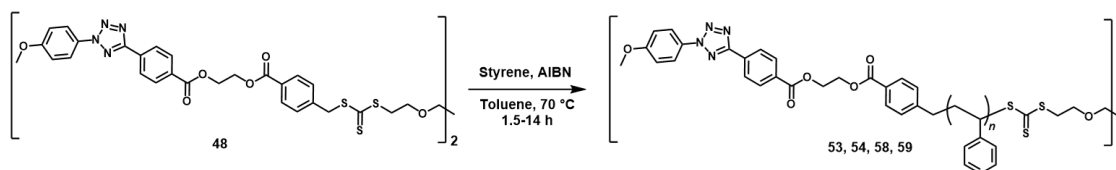
⁹ Europium precursor $[\text{Eu}(\text{dbm})_3(\text{H}_2\text{O})_2]$ was kindly provided by H. Rothfuss and N. Knöfel.

placed inside a desiccator filled with toluene, in a way that the networks were not in direct contact with the solvent.



In this way, the samples were exposed to toluene vapor for 7 days after which significant volume increase (without cracking) was observed. Afterwards, the gels were further swollen in toluene for 24 h, in order to achieve maximum swelling before the characterization by rheology.

RAFT polymerization of styrene using CTA **48**

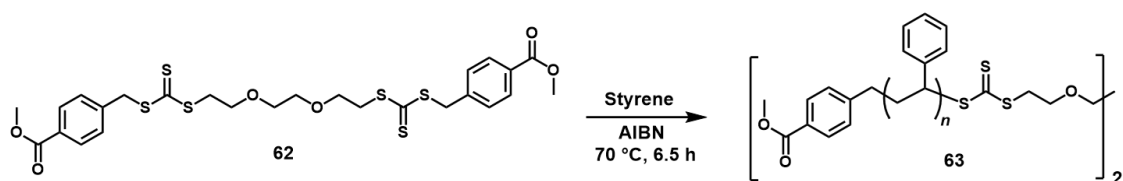


RAFT polymerization of styrene using CTA **48** was performed as described elsewhere.^{298,299} Briefly, RAFT agent **48** (0.036 mmol, 1 eq.), AIBN (0.007 mmol, 0.2 eq.) and styrene (8.1 mmol, 225 eq.) were dissolved in 2 mL of toluene in a Schlenk flask. The reaction mixture was deoxygenated by three consecutive freeze-pump-thaw cycles and the different flasks were placed in an oil bath pre-heated to 70 °C. Samples were polymerized for 1.5 h, 2 h, 5 h, and 14 h, affording PS **53**, **58**, **54**, and **59**, respectively. Polymerizations were stopped by exposing the mixture to oxygen and cooling in an ice bath. The product was isolated by precipitation in cold methanol and subsequently dried under reduced pressure. Determination of molecular weight and dispersity index was performed by SEC in THF (polystyrene calibration).

Sample	\bar{M}_n	\bar{D}
53	1900 g·mol ⁻¹	1.15
58	2800 g·mol ⁻¹	1.15
54	3300 g·mol ⁻¹	1.21
59	7200 g·mol ⁻¹	1.11

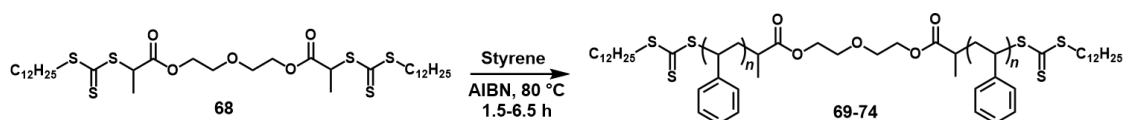
EXPERIMENTAL SECTION

RAFT polymerization of styrene using CTA **62**



RAFT agent **62** (0.0873 mmol, 1 eq.) and AIBN (0.0175 mmol, 0.2 eq.) were dissolved in 2 mL styrene (17.46 mmol, 200 eq.). The mixture was degassed by bubbling argon during 10 min before placing it in an oil bath pre-heated to 70 °C. Polymerization was carried out for 6.5 h, after which the sample was exposed to ambient oxygen and cooled in an ice bath. The crude polymer was dried at reduced pressure to remove the excess of monomer, affording PS **63** ($\bar{M}_n = 4000 \text{ g}\cdot\text{mol}^{-1}$, $\mathcal{D} = 1.15$, determined by SEC).

RAFT polymerization of styrene using CTA **68**

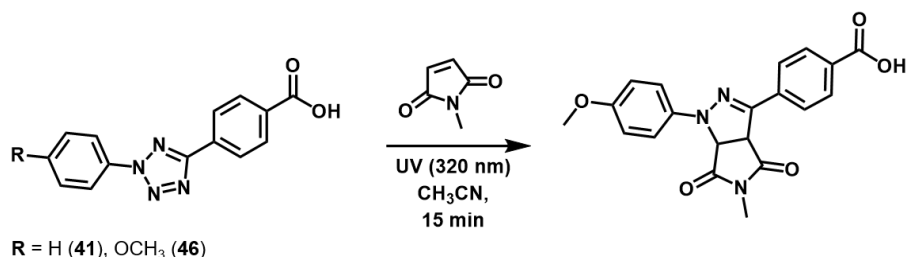


RAFT agent **68**^h was employed to mediate the radical polymerization of styrene. Briefly, **68** (0.20 mmol, 1 eq.) and AIBN (0.02 mmol, 0.1 eq.) were dissolved in 4.6 mL styrene (40 mmol, 200 eq.). The reaction mixture was degassed by bubbling argon during 15 min and then placed in a heating block at 80 °C. Samples were polymerized for 1.5–6.5 h, stopping the reaction by exposing the mixture to oxygen and cooling in an ice bath. The respective products **59–74** were isolated by precipitation in cold methanol (two times) and subsequently dried under reduced pressure. Determination of molecular weight and dispersity index was performed by SEC in THF (polystyrene calibration).

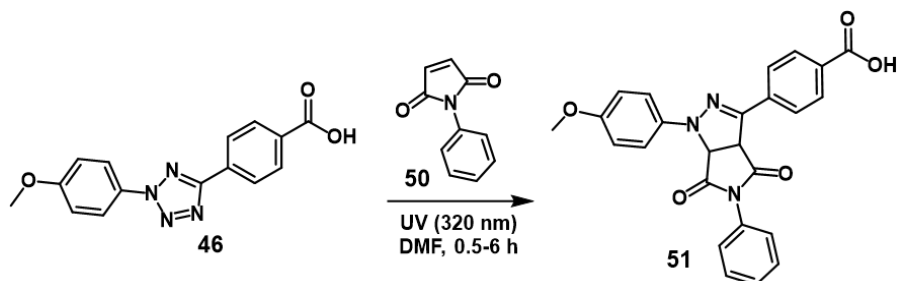
Sample	\bar{M}_n	\mathcal{D}
59	3000 g·mol ⁻¹	1.08
60	3700 g·mol ⁻¹	1.07
61	3900 g·mol ⁻¹	1.06
62	5500 g·mol ⁻¹	1.07
63	6400 g·mol ⁻¹	1.07
64	7600 g·mol ⁻¹	1.07

^h CTA **68** was prepared, characterized and kindly provided by F. Cavalli.

6.3.3. Photoreactions

Reaction of tetrazoles **41** and **46** with *N*-methylmaleimide

Tetrazole **41** or **46** (0.028 mmol, 1 eq) was dissolved in 7 mL degassed acetonitrile in a headspace vial (N20, 23.25 × 75.5 mm, clear glass, flat bottom, Macherey-Nagel). Apart, a solution of *N*-methylmaleimide (0.028 mmol, 1 eq.) in 1 mL acetonitrile was prepared and added to the tetrazole solution via syringe. The resulting mixture ($[\text{tetrazole}]_i = 3.5 \text{ mmol}\cdot\text{L}^{-1}$) was irradiated 15 min at 320 nm in the photoreactor depicted in Figure 8.8. Afterwards, the solvent was evaporated at reduced pressure and the crude product was dissolved in DMSO-*d*₆ for ¹H NMR analysis.

Calibration curve for pyrazoline **51**

The preparation of a calibration curve to correlate concentration of pyrazoline (**51**) and fluorescence emission intensity (see Figure 4.10) is reported elsewhere.²⁹⁸ Briefly, tetrazole **46** (0.29 mmol, 1 eq.) was dissolved in 70 mL DMF. Apart, *N*-phenylmaleimide **50** (0.87 mmol, 3 eq.) was dissolved in 10 mL DMF. The tetrazole stock solution was then divided in 10 headspace vials (N20, 23.25 × 75.5 mm, clear glass, flat bottom, Macherey-Nagel), 7 mL each, crimped airtight. Subsequently, 1 mL of the maleimide solution was added to each vial ($[\text{46}]_i = 3.6 \text{ mmol}\cdot\text{L}^{-1}$), the mixture was degassed with argon for 5 min and placed into the photoreactor (Figure 8.8). The samples were irradiated 0.5–6 h at 320 nm. Following irradiation, a 2 mL aliquot of each standard solution was analyzed by fluorescence spectroscopy after 50-fold dilution ($\lambda_{\text{ex}} = 459 \text{ nm}$, slit 2.5 nm; $\lambda_{\text{em}} = 470\text{--}720 \text{ nm}$, slit 10 nm; photomultiplier voltage: high). The

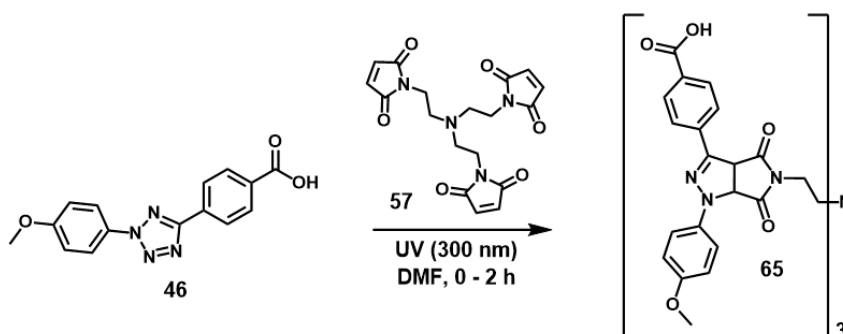
EXPERIMENTAL SECTION

rest of the sample was evaporated under reduced pressure and the crude solid was dissolved in DMSO- d_6 for analysis via ^1H NMR spectroscopy.

For the calibration curve in the solid state (see Figure 4.35), pyrazoline standards **51** were prepared as described above, using THF as solvent. Subsequently, RAFT polymer **63** was dissolved in the different standards at a concentration of $300\text{ mg}\cdot\text{mL}^{-1}$ (25 wt.%). Next, $100\ \mu\text{L}$ of each PS-pyrazoline mixture was casted onto glass slides ($11 \times 22\text{ mm}$, Starna) by spin coating (Spin 150 single wafer spin coater). Thus, thin films of polymer-fluorophore blend were obtained after 75 s coating at 1000 rpm (acceleration $500\text{ rpm}\cdot\text{s}^{-1}$). The different samples were directly analyzed by fluorescence spectroscopy in the solid state ($\lambda_{\text{ex}} = 459\text{ nm}$, slit 5 nm; $\lambda_{\text{em}} = 470\text{--}700\text{ nm}$, slit 10 nm; photomultiplier voltage: medium), using the setup described before in Section 6.2.4. Fluorescence emission curve corresponding to **63** + standard **51** at 0% conversion was taken as blank sample and subtracted from the rest of the emission curves.

For the construction of a calibration curve after aminolysis **51'** (see Figure 4.46), pyrazoline standards **51** were prepared in DMF as described above. Subsequently, 3 mg TCEP were added to each sample, followed by a solution of *n*-butylamine in DMF (50% v/v), 20 eq. amine in respect to the amount of pyrazoline. The resulting mixture was stirred 4 h at room temperature, after which a solution of butyl acrylate in DMF (50% v/v) was added to each sample, 50 eq. in respect to pyrazoline. After overnight stirring at room temperature, fluorescence emission of the different samples was determined after 50-fold dilution ($\lambda_{\text{ex}} = 459\text{ nm}$, slit 2.5 nm; $\lambda_{\text{em}} = 470\text{--}720\text{ nm}$, slit 10 nm; photomultiplier voltage: high).

Calibration curve for pyrazoline **65**



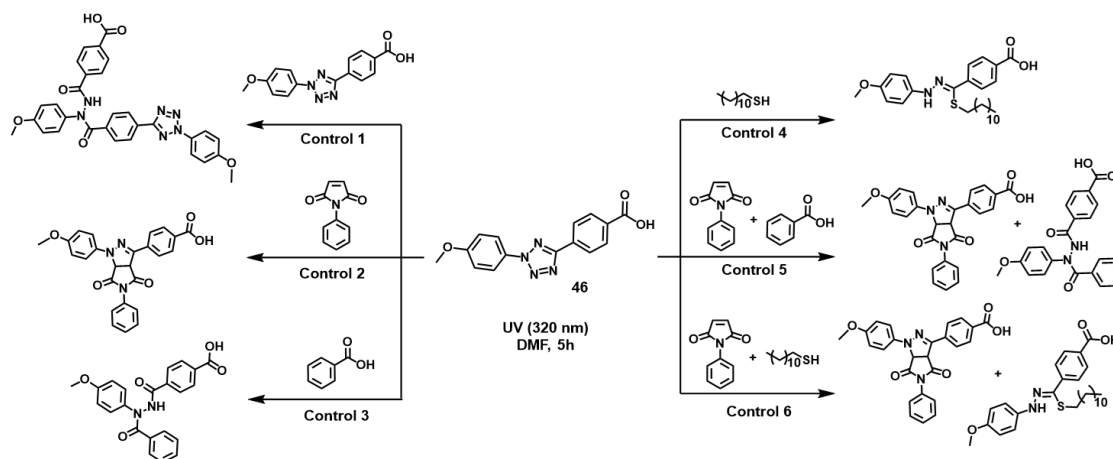
The preparation of a calibration curve to correlate concentration of pyrazoline (**65**) and fluorescence emission intensity (see Figure 4.52) is reported elsewhere.²⁹⁹ Briefly, tetrazole **46** (0.3 mmol, 3 eq.) was dissolved in 78 mL DMF. Apart, a solution of trimaleimide **57** (0.1 mmol, 1 Eq.) in 5 mL of DMF was prepared. The tetrazole stock

EXPERIMENTAL SECTION

solution was divided into headspace vials (N20, 23.25 × 75.5 mm, clear glass, flat bottom, Macherey-Nagel), 7 mL each, and crimped airtight. Subsequently, 1 mL of the trimaleimide solution was added to each vial ($[46]_t = 3.4 \text{ mmol}\cdot\text{L}^{-1}$) and the mixture was degassed with argon for 15 min. The samples were irradiated at 300 nm for a certain amount of time (0–2 h), after which a 4 mL aliquot of each solution was analyzed by fluorescence spectroscopy ($\lambda_{\text{ex}} = 455 \text{ nm}$, slit 10 nm; $\lambda_{\text{em}} = 470\text{--}700 \text{ nm}$, slit 10 nm; photomultiplier voltage: medium) after 100-fold dilution. The rest of the sample was evaporated under reduced pressure and the crude solid was dissolved in DMSO- d_6 for ^1H NMR analyses.

The calibration curve for the samples after aminolysis **65'** was constructed by treating the pyrazoline standards **65** described above with the reagents used for aminolysis.²⁹⁹ Hence, 3 mg of TCEP were added to the standards, followed by *n*-butylamine in DMF (50% v/v, 20 eq. in respect to the amount of pyrazoline) and the mixture was stirred 4 h at ambient temperature. Subsequently, butyl acrylate in DMF (50% v/v) was added (50 eq. in respect to the pyrazoline) and stirred overnight at room temperature. Fluorescence was recorded for the crude samples after 100-fold dilution and correlated to the new pyrazoline concentration.

Control experiments fluorescence photoadducts

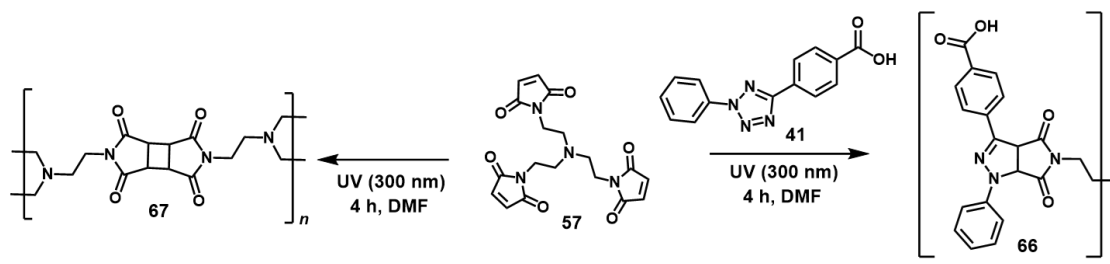


For the control experiments of fluorescence (see Figure 4.13), tetrazole **46** (0.174 mmol) was dissolved in 42 mL DMF and the stock solution was divided in 6 headspace vials (N20, 23.25 × 75.5 mm, clear glass, flat bottom, Macherey-Nagel), 7 mL each, crimped airtight. Subsequently, 1 mL of reaction partner solution in DMF (Control 1: blank, Control 2: *N*-phenylmaleimide, Control 3: benzoic acid, Control 4: 1-dodecanethiol, Control 5: *N*-phenylmaleimide + benzoic acid, Control 6: *N*-phenylmaleimide + 1-dodecanethiol) was added. In every case, equimolar mixtures

EXPERIMENTAL SECTION

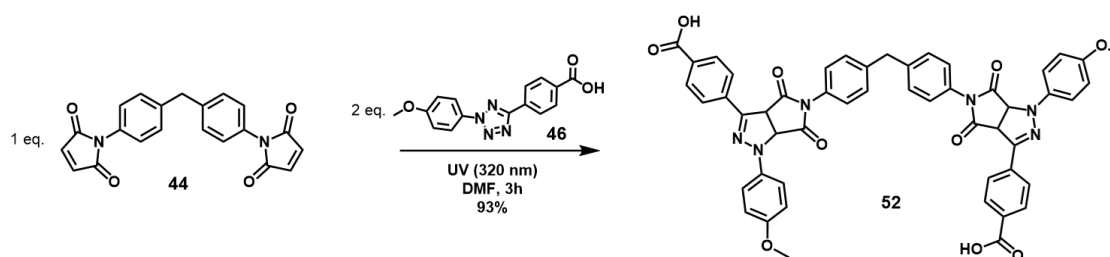
of tetrazole and reaction partner were obtained ($[46]_i = 3.6 \text{ mmol}\cdot\text{L}^{-1}$). The different samples were degassed with argon for 5 min and irradiated 5 h at 320 nm in the photoreaction setup shown in Figure 8.8. After irradiation, a 2 mL aliquot of each solution was analyzed by fluorescence spectroscopy after 50-fold dilution ($\lambda_{\text{ex}} = 459 \text{ nm}$, slit 2.5 nm; $\lambda_{\text{em}} = 470\text{--}720 \text{ nm}$, slit 10 nm; photomultiplier voltage: high).

Control experiments maleimide dimerization



For the control experiments of maleimide dimerization (see Figure 4.61), trimaleimide **57** (0.0034 mmol, 1 eq.) was mixed with tetrazole **41** (0.0102 mmol, 3 eq.) and dissolved in 17 μL DMF- d_7 . An aliquot of 10 mL was sandwiched between glass slides (22 \times 22 mm, thickness $170 \pm 5 \mu\text{m}$, Marienfeld) and irradiated 4 h at 300 nm in the photoreaction setup depicted in Figure 8.15 to produce adduct **66**. The same experiment were performed without tetrazole, resulting in [2+2] adducts **67**. The cure products were diluted with DMF- d_7 and analyzed via ^1H NMR spectroscopy. Only for product **67**, the formation of an insoluble white precipitate was observed.

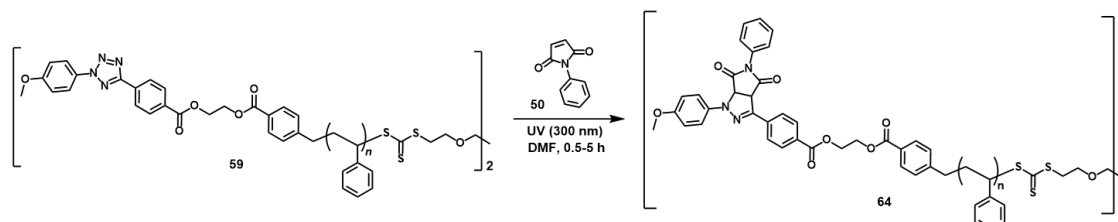
Synthesis of pyrazoline adduct 52



Tetrazole **46** (0.029 mmol, 2 eq) was dissolved in 7 mL degassed DMF in a headspace vial (N20, 23.25 \times 75.5 mm, clear glass, flat bottom, Macherey-Nagel). Apart, a solution of bismaleimide (0.0145 mmol, 1 eq.) in 1 mL DMF was prepared and added to the tetrazole solution via syringe. The resulting mixture ($[46]_i = 3.6 \text{ mmol}\cdot\text{L}^{-1}$) was irradiated 3 h at 320 nm in the photoreactor depicted in Figure 8.8. Afterwards, a 2 mL aliquot was taken for fluorescence analysis after 50-fold dilution ($\lambda_{\text{ex}} = 459 \text{ nm}$, slit 2.5 nm;

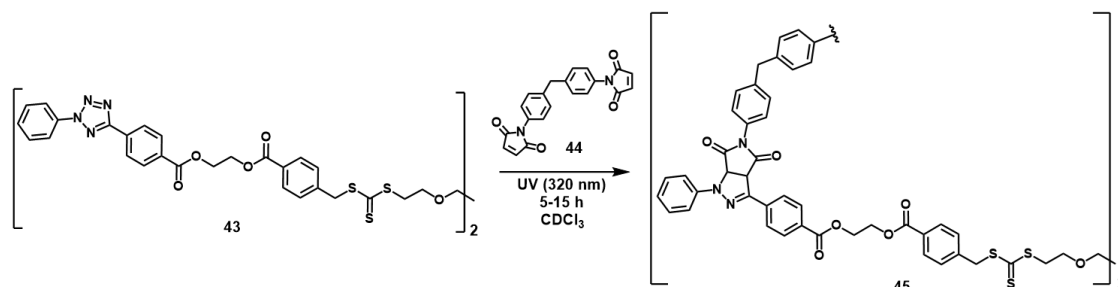
$\lambda_{em} = 470\text{--}720$ nm, slit 10 nm; photomultiplier voltage: high). The rest of the sample was evaporated at reduced pressure and the crude product was dissolved in DMSO- d_6 for ^1H NMR analysis.

Synthesis of pyrazoline-PS **64**



Tetrazole RAFT-PS **59** (0.0145 mmol, 1 eq., 80 $\text{mg}\cdot\text{mL}^{-1}$) and *N*-phenylmaleimide **50** (0.0289 mmol, 2 eq., 19.3 $\text{mmol}\cdot\text{L}^{-1}$) were dissolved in 1.5 mL degassed DMF and the stock solution was divided in crimp neck vials (N8, 7 × 40 mm, clear glass, conical, Macherey-Nagel). The samples were irradiated 0.5–6 h at 300 nm after which a 5 μL aliquot was taken for fluorescence analysis. The rest of the sample was precipitated in cold methanol to recover PS polymers **64**.

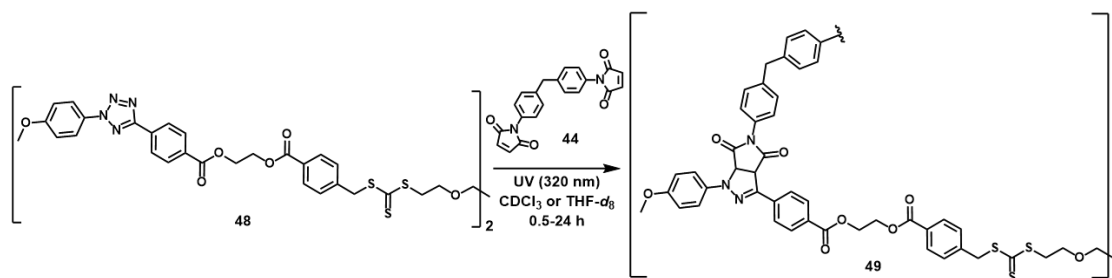
Synthesis of step-growth polymers **45**



CTA **43** (0.0042 mmol, 1 eq., 10.5 $\text{mmol}\cdot\text{L}^{-1}$) and bismaleimide **44** (0.0042 mmol, 1 eq., 10.5 $\text{mmol}\cdot\text{L}^{-1}$) were dissolved in 400 μL degassed CDCl_3 in crimp neck vials (N8, 7 × 40 mm, clear glass, conical, Macherey-Nagel). Samples were irradiated at 320 nm for 5 h and 15 h in the photoreaction setup shown in Figure 8.8. Next, a 5 μL aliquot was taken, evaporated and re-dissolved in 5 mL DMF for fluorescence analysis ($\lambda_{ex} = 400$ nm, slit 2.5 nm; $\lambda_{em} = 410\text{--}720$ nm, slit 10 nm; photomultiplier voltage: medium). The rest of the solution was directly analyzed by ^1H NMR spectroscopy and lastly re-dissolved in HPLC-grade THF for SEC analysis.

EXPERIMENTAL SECTION

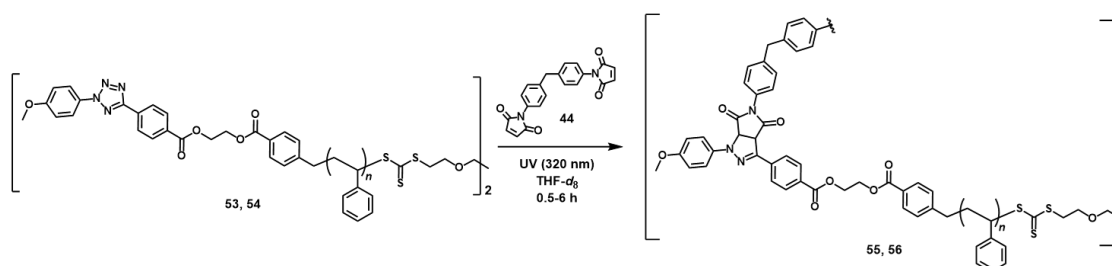
Synthesis of step-growth polymers **49**



The NITEC step-growth polymerization of AA–BB monomers **48** and **44** is reported elsewhere.²⁹⁸ Briefly, RAFT agent **48** (0.05 mmol, 1 eq., 50 mmol·L⁻¹) and bismaleimide **44** (0.05 mmol, 1 eq., 50 mmol·L⁻¹) were dissolved in 1.0 mL degassed CDCl₃ or THF-*d*₈. This stock solution was aliquoted in 10 crimp neck vials (N8, 7 × 40 mm, clear glass, conical, Macherey-Nagel) and irradiated 0.5–24 h at 320 nm in the photoreaction setup depicted in Figure 8.8. Afterwards, aliquots of 5 μL were taken, evaporated and re-dissolved in 5 mL DMF for fluorescence analysis ($\lambda_{\text{ex}} = 459$ nm, slit 2.5 nm; $\lambda_{\text{em}} = 470$ –720 nm, slit 10 nm; photomultiplier voltage: high), or re-dissolved in 10 mL DMF for UV-vis spectroscopy. The rest of the solution was analyzed directly by ¹H NMR in CDCl₃ or THF-*d*₈ and lastly re-dissolved in HPLC-grade THF for SEC analysis.

The same procedure was followed for polymerizations carried out with off-stoichiometric ratios of monomers (from 1.05 : 1 to 1 : 1.05 mol ratio **48** : **44**, see Figure 4.17).

Synthesis of step-growth polymers **55** and **56**

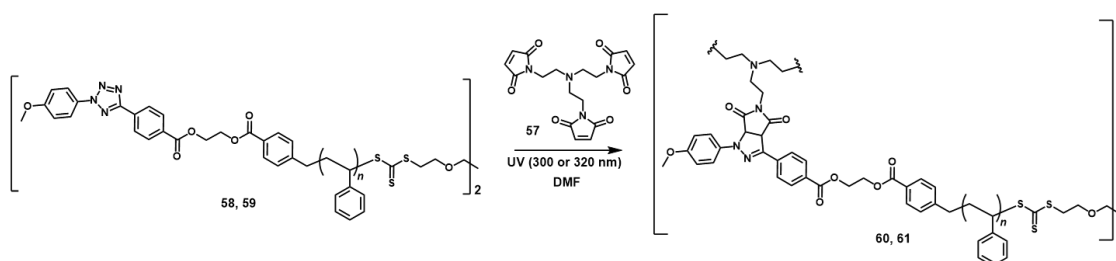


The NITEC step-growth polymerization of bifunctional tetrazole RAFT-PS **53** or **54** with bismaleimide **44** is reported elsewhere.²⁹⁸ Briefly, a stock solution of 14.6 mg of **53**, or 28.4 mg of **54**, and 2.5 mg (0.007 mmol, 1 eq. 20 mmol·L⁻¹) of bismaleimide **44** in 350 μL of THF-*d*₈ was prepared (degassed solvent). The stock was divided in 6 crimp neck vials (N8, 7 × 40 mm, clear glass, conical, Macherey-Nagel) and irradiated 0.5–

6 h at 320 nm in the photoreactor depicted in Figure 8.8. Then, 5 μL of each sample was taken, evaporated and re-dissolved in 2.5 mL DMF for fluorescence analysis. The rest of the solution was analyzed directly by ^1H NMR in $\text{THF-}d_8$ and finally re-dissolved in HPLC-grade THF to record the corresponding SEC traces.

The same procedure was followed for polymerizations carried out with off-stoichiometric ratios of monomers (from 1.01 : 1 to 1 : 1.01 mol ratio **54** : **44**, see Figure 4.23).

Synthesis of crosslinked networks **60** and **61**



For the preliminary experiments on network formation, PS precursors **58** and **59** were dissolved in degassed DMF at a concentration of $470 \text{ mg}\cdot\text{mL}^{-1}$ ($168 \text{ mmol}\cdot\text{mL}^{-1}$ for **58** and $65 \text{ mmol}\cdot\text{mL}^{-1}$ for **59**). Trimaleimide **57** was then added, at equimolar ratio between reactive groups tetrazole and maleimide. The resulting solution was divided either in conical vials (N8, $7 \times 40 \text{ mm}$, clear glass, Macherey-Nagel, $100 \mu\text{L}$ each) or in glass slides ($22 \times 22 \text{ mm}$, thickness $170 \pm 5 \mu\text{m}$, Marienfeld, $10 \mu\text{L}$ each) and irradiated 5–64 h at 320 nm in the photoreaction setup depicted in Figure 8.8. The crude product was washed several times with chloroform and THF to recover the soluble fraction. After evaporation of the solvent at reduced pressure, the relative amounts of soluble and insoluble fraction were determined by gravimetry.

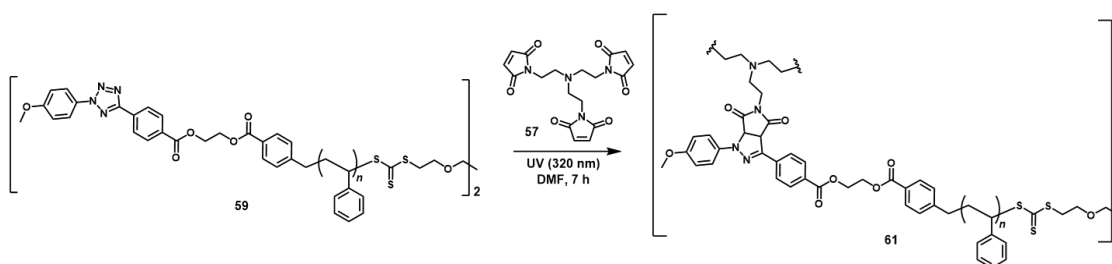
The optimized protocol for NITEC network formation is reported elsewhere.²⁹⁹ Briefly, precursors **58** and **59** were dissolved in degassed DMF at a concentration of $710 \text{ mg}\cdot\text{mL}^{-1}$ (typically 40.5 mg polymer in $57 \mu\text{L}$ DMF, ca. $0.25 \text{ mol}\cdot\text{L}^{-1}$ **58** and ca. $0.09 \text{ mol}\cdot\text{L}^{-1}$ **59**). The trimaleimide linker **57** was added, maintaining 1 : 1 molar ratio tetrazole : maleimide. After complete dissolution of both components, a $10 \mu\text{L}$ aliquot of the stock solution was cast onto a glass slide (Marienfeld) and subsequently pressed with a second glass slide until a thin liquid film was formed. The slides were irradiated 0.5–8 h at 300 nm in the photoreaction setup described in Figure 8.15. In this way, networks **60** and **61**, derived from precursors **58** and **59**, respectively, were afforded. After irradiation, the soluble material was separated from the crosslinked network by

EXPERIMENTAL SECTION

immersion of the slides in THF for 48 h, followed by extensive washing with chloroform and THF. All fractions from washing were recovered and the solvent evaporated at reduced pressure to yield the soluble fraction. The crosslinked network was dried at reduced pressure to afford the insoluble fraction. Gravimetry was employed to determine the amount of the soluble and insoluble fractions (see Figure 4.33).

The same procedure was adopted for network formation with off-stoichiometric ratios of reactive groups (1 : 3 and 1 : 5 mol ratio tetrazole : maleimide, see Figure 8.17).

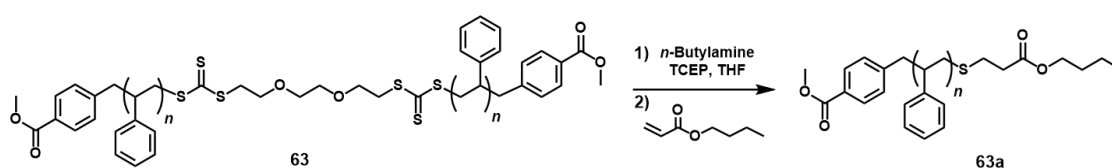
Upscale experiments networks 61



For the upscale experiments on network formation (see Figure 4.63), PS precursor **59** (0.0619 mmol, 3 eq.) and trimaleimide **57** (0.00412 mmol, 2 eq.) were dissolved in degassed DMF at a concentration of 710 mg·mL⁻¹ (**59**). The solution was transferred to 1.5 mm I.D glass capillaries (Hilgenberg) and irradiated 7 h at 320 nm in the photoreaction setup depicted in Figure 8.8. The crude product was washed several times with chloroform and THF to recover the soluble fraction. Determination of weight fractions via gravimetry retrieved 6 wt.% insoluble fraction under the described conditions. The same experiment were performed in PDMS molds (see Figure 4.64). Custom-made PDMS molds were prepared from two component silicone elastomer kit (Sylgard®184, Sigma). A 10/1 (w/w) mixture of elastomer and hardener was poured in 5 mL glass vials and long pieces of steel wire (1.0 mm O.D.) were suspended in the curing mixture. After overnight curing, the pieces of wire were removed, affording PDMS molds with thin cylindrical cavities.

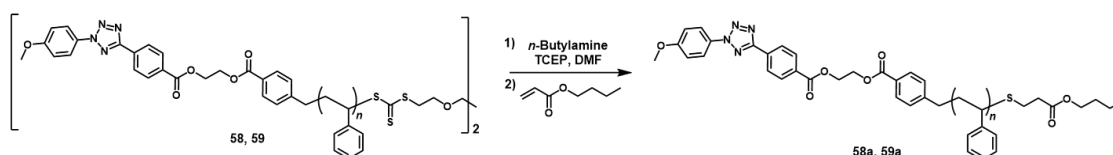
6.3.4. Aminolysis

Aminolysis of RAFT-PS 63



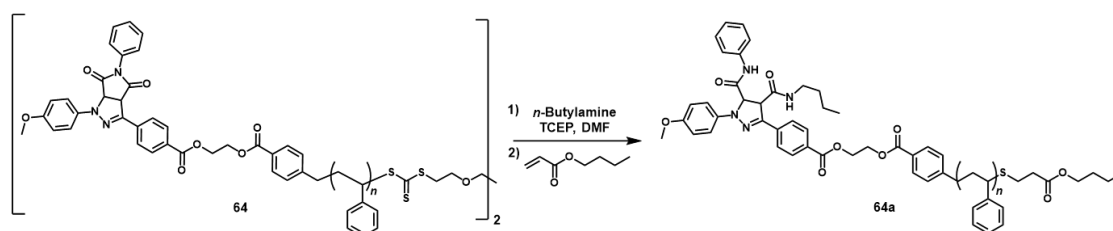
The one-pot aminolysis/Michael addition protocol for RAFT polymers was adapted from previous literature reports.⁶⁹ RAFT-PS **63** (100 mg, 0.025 mmol) and the reducing agent TCEP (3 mg) were dissolved in 1 mL degassed THF. Apart, a 50% v/v solution of *n*-butylamine in THF was prepared and added to the previous solution, in 20-fold molar excess of amine with respect to the theoretical amount of trithiocarbonate groups. The mixture was stirred 4 h at room temperature, after which the yellow coloration of the initial polymer disappeared completely. Then, a 50% v/v solution of butyl acrylate in THF was added, in 50-fold molar excess with respect to the trithiocarbonate groups. The reaction was left to proceed overnight and the modified polymers **63a** were recovered by precipitation in cold methanol.

Aminolysis of tetrazole RAFT-PS precursors **58** and **59**



The aminolysis/Michael addition protocol for RAFT polymers was adapted from previous literature reports.⁶⁹ Tetrazole RAFT-PS **58** or **59** (100 mg) was dissolved in degassed DMF and TCEP (3 mg) was added to the solution. Subsequently, a 50% v/v solution of *n*-butylamine in DMF was added, in 20-fold molar excess of amine with respect to the trithiocarbonate groups. The mixture was stirred 4 h at room temperature before adding a 50% v/v solution of butyl acrylate in DMF, in 50-fold molar excess with respect to the trithiocarbonate groups. The reaction was left to proceed overnight and the modified polymers **58a** and **59a** were recovered by precipitation in cold methanol.

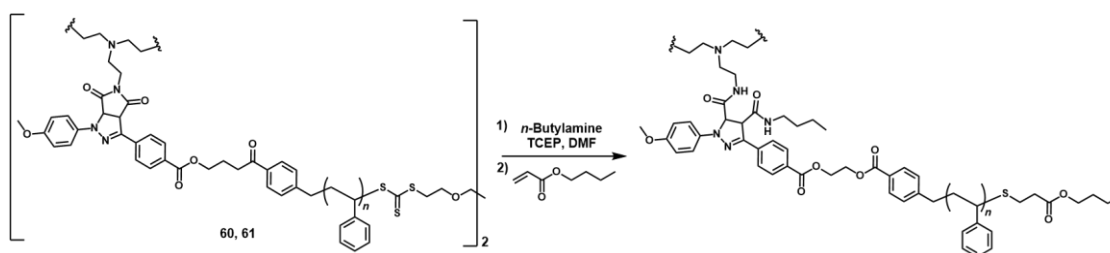
Aminolysis of pyrazoline-PS **64**



The aminolysis of NITEC polymers **64** (see Figure 4.49) was carried out in the same way as described above for sample **59**.

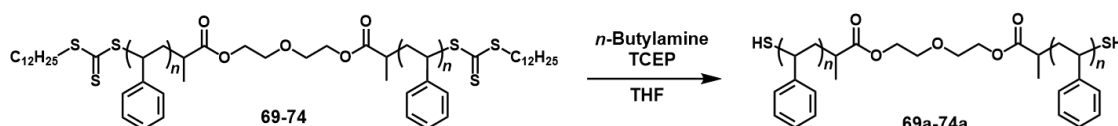
EXPERIMENTAL SECTION

Aminolysis of NITEC networks **60** and **61**



The soluble and insoluble fractions of networks **60** and **61** were subjected to aminolysis as reported elsewhere.²⁹⁹ Degassed DMF and TCEP (3 mg) were added to the dried material, followed by a solution of *n*-butylamine in DMF (50% v/v) at 20-fold molar excess with respect to the theoretical amount of trithiocarbonate groups present in the sample. The mixture was stirred 4 h at room temperature, after which only soluble material was observed. Subsequently, a solution of butyl acrylate in DMF (50% v/v) was added (50 Eq. with respect to the initial trithiocarbonate groups) and the reaction proceeded overnight at ambient temperature. The amount of DMF was adjusted so that the final concentration of the polymer in solution was 4.50 mg·mL⁻¹ for networks **60** (derived from PS **58**), and 11.25 mg·mL⁻¹ for networks **61** (derived from PS **59**). The fluorescence emission of the crude samples was recorded after 200-fold dilution in DMF ($\lambda_{\text{ex}} = 455$ nm, slit 10 nm; $\lambda_{\text{em}} = 470\text{--}700$ nm, slit 10 nm; photomultiplier voltage: medium), and correlated to the calibration curve **65'**.

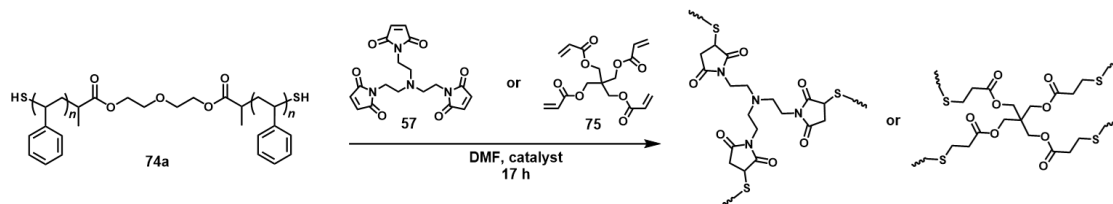
Aminolysis of RAFT-PS precursors **69–74**



The α,ω -thiol-capped PS chains **69a–74a** were afforded after aminolysis of precursors **69–74** (see Figure 4.65 and Table 4.6), adapting literature procedures.⁶⁹ Briefly, RAFT-PS precursors **69–74** (500 mg) were dissolved in 5 mL degassed THF and 15 mg TCEP were added to each solution. Apart, a 50% v/v solution of *n*-butylamine in THF was prepared and added to the previous solutions, in 20-fold molar excess of amine with respect to the theoretical amount of trithiocarbonate groups. The mixture was stirred 4 h at room temperature, after which the yellow coloration of the initial polymer disappeared completely. Subsequently, the thiol-functionalized polymers **69a–74a** were recovered by precipitation in cold methanol.

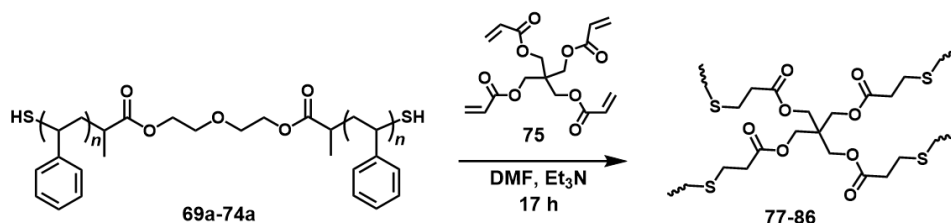
6.3.5. Thiol-Ene Reactions

Screening reactions



The screening of the reaction conditions for thiol-ene ligation (see Table 4.8) was performed adapting literature procedures.³¹² Thiol-capped PS **74a** (30 mg, 0.0043 mmol) was dissolved in DMF and a solution of linker (**57** or **75**) in DMF was added (1 : 1 mol ratio thiol : ene groups). If no catalyst was added (entries 1 and 3 in Table 4.8), the reaction was left to proceed overnight and the gelation point was determined as the moment in which the solution stopped to flow. Otherwise, a solution of catalyst in DMF (triethylamine, dimethylphenylphosphine or 2,2-dimethoxy-2-phenylacetophenone, 50 mol% in respect to the theoretical amount of thiol groups in the polymer) was subsequently added. The amount of DMF was adjusted in every case, so that the final concentration of **74a** in solution was 830 mg·mL⁻¹ (0.12 M). The reactions with triethylamine and dimethylphenylphosphine (entries 2, 4, and 5 in Table 4.8) were left to proceed overnight, while the sample with photoinitiator (2,2-dimethoxy-2-phenylacetophenone, entry 6 in Table 4.8) was irradiated 17 h at 320 nm in the photoreactor shown in Figure 8.8. In every case, the gelation point was determined as the moment in which the solution stopped to flow. Lastly, the samples were washed with several portions of THF in order to extract soluble fractions. After evaporation of the solvent, the relative amounts of soluble and insoluble fractions were determined by gravimetry.

Standard conditions

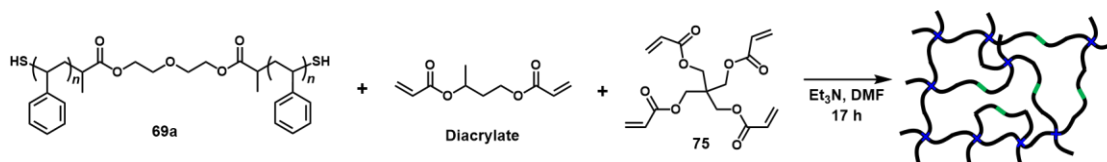


The thiol-Michael addition was selected as standard procedure for network formation. Thiol-capped PS chains **69a-74a** (30 mg) or mixtures of **69a** and **73a** (total mass of polymer 30 mg) were dissolved in DMF in glass vials. Then, a solution of tetraacrylate

EXPERIMENTAL SECTION

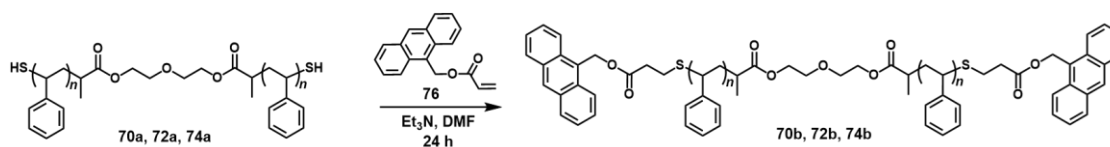
linker **75** in DMF ($180 \text{ mg}\cdot\text{mL}^{-1}$) was added, at equimolar ratio between thiol and acrylate groups. When a homogeneous solution was obtained, triethylamine (50 mol% in respect to the amount of thiol groups) was added and the reaction proceeded at ambient temperature for 17 h. The amount of DMF was adjusted in every case, in order to reach a final concentration of thiol-PS of $830 \text{ mg}\cdot\text{mL}^{-1}$ (46 wt.%). Afterwards, the obtained networks **77–86** (see Table 4.10) were washed with several portions of THF in order to extract soluble fractions. Lastly, the weight fraction of soluble and insoluble fractions was determined by gravimetry after evaporation of the solvent at reduced pressure.

Addition of diacrylate linker



Thiol-PS **69a** (30 mg, 0.012 mmol) was dissolved in DMF in a glass vial. A solution of diacrylate and tetraacrylate **75** in DMF (25 : 75, 50 : 50, and 75 : 25 mol ratio, see Table 8.6) was added, with 0.024 mmol overall amount of acrylate units (equimolar ratio thiol : ene). After complete dissolution, triethylamine (0.012 mmol) was added and the reaction proceeded at room temperature for 17 h. The amount of DMF was adjusted in every case so that the final concentration of **69a** in solution was $830 \text{ mg}\cdot\text{mL}^{-1}$ (0.33 M). Afterwards, the samples were washed with several portions of THF in order to extract soluble fractions. After evaporation of the solvent, the relative amounts of soluble and insoluble fractions were determined by gravimetry.

Functionalization with anthracene groups

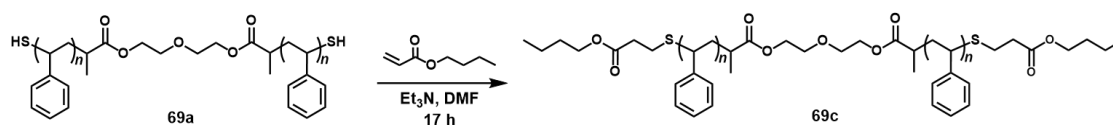


Thiol-PS chains **70a**, **72a** or **74a** (30 mg) were mixed with 9-anthracenylmethyl acrylate **76** (1 : 1 mol ratio thiol : ene) and dissolved in DMF in glass vials. Triethylamine (50 mol% in respect to the amount of thiol groups) was then added and the reaction proceeded at ambient temperature for 24 h. The amount of DMF was adjusted in every case, in order to reach a final concentration of thiol-PS of $830 \text{ mg}\cdot\text{mL}^{-1}$. Afterwards, the fluorescent polymers **70b**, **72b** and **74b** were recovered by precipitation in cold

methanol (see Figure 4.70) and dried at reduced pressure before analysis via SEC and fluorescence spectroscopy. For fluorescence determination, 1.0 mg of product was dissolved in 1.0 mL DMF and the solution was diluted 200 times ($\lambda_{\text{ex}} = 363$ nm, slit 5 nm; $\lambda_{\text{em}} = 375\text{--}600$ nm, slit 5 nm; photomultiplier voltage: medium).

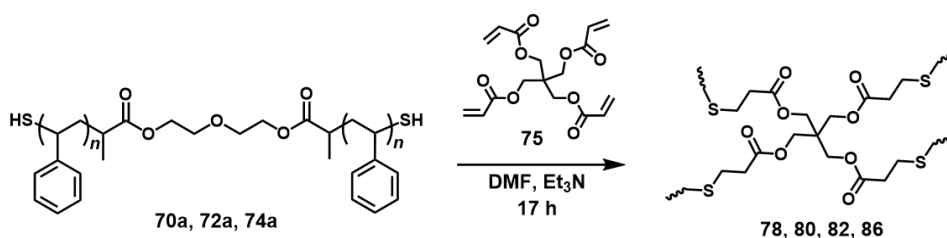
Apart, a calibration curve that correlates fluorescence emission intensity and concentration of anthracene was constructed (see Figure 4.71). A stock solution of **76** in DMF was prepared (4×10^{-6} M) and successively diluted, and the fluorescence emission of the standards was determined ($\lambda_{\text{ex}} = 363$ nm, slit 5 nm; $\lambda_{\text{em}} = 375\text{--}600$ nm, slit 5 nm; photomultiplier voltage: medium).

Functionalization with butyl acrylate



Thiol-PS **69a** (30 mg, 0.012 mmol) was dissolved in 22.6 μL DMF in a glass vial. Then, 11.7 μL of a solution of butyl acrylate in DMF ($262 \text{ mg}\cdot\text{mL}^{-1}$) were added, followed by 1.67 μL triethylamine (50 mol%, 0.012 mmol). After overnight reaction, the product **69c** was precipitated in cold methanol, dried at reduced pressure and analyzed via SEC (see Figure 4.76).

Synthesis of thiol-ene PS sticks



The standard thiol-Michael procedure was adapted for the synthesis of cylindrical sticks. Briefly, thiol-PS precursors **70a**, **72a** or **74a** (300 mg) or a mixture of **69a** (54 mol%) and **73a** (46 mol%) were dissolved in DMF in glass vials. Then, a solution of tetraacrylate linker **75** in DMF ($180 \text{ mg}\cdot\text{mL}^{-1}$) was added, at equimolar ratio between thiol and acrylate groups. After complete dissolution of the precursors, triethylamine (50 mol% in respect to the amount of thiol groups) was added to the mixture. The amount of DMF was adjusted to reach a final polymer concentration of $830 \text{ mg}\cdot\text{mL}^{-1}$ (46 wt.%). When the solution was fully homogeneous, it was transferred to 1.5 mm I.D.

EXPERIMENTAL SECTION

PTFE tubes (sealed with epoxy glue) with a glass pipette. The reaction was left to proceed at room temperature for 17 h, after which PS sticks **78**, **80**, **82**, and **86** were obtained (see Figure 4.78).

CHAPTER 7:

REFERENCES

- [1] G. Kummerlöwe, B. Luy, *Trends Anal. Chem.* **2009**, *28*, 483.
- [2] C. M. Thiele, *Eur. J. Org. Chem.* **2008**, 5673.
- [3] A. Cannales, J. Jiménez-Barbero, M. Martín-Pastor, *Magn. Reson. Chem.* **2012**, *50*, S80.
- [4] M. Di Pietro, C. Aroulanda, D. Merlet, G. Celebre, G. De Luca, *J. Phys. Chem. B* **2014**, *118*, 9007.
- [5] A. Schuetz, J. Junker, A. Leonov, O. Lange, T. Molinski, C. Griesinger, *J. Am. Chem. Soc.* **2007**, *129*, 15144.
- [6] N-C. Meyer, A. Krupp, V. Schmidts, C. M. Thiele, M. Reggelin, *Angew. Chem. Int. Ed.* **2012**, *51*, 8334.
- [7] J. Wöhnert, K. J. Franz, M. Nitz, B. Imperiali, H. Schwalbe, *J. Am. Chem. Soc.* **2003**, *125*, 13338.
- [8] X. Lei, Z. Xu, H. Sun, S. Wang, C. Kobzar, L. Peng, C. Gao, R. X. Tan, *J. Am. Chem. Soc.* **2014**, *136*, 11280.
- [9] B. Luy, K. Kobzar, H. Kessler, *Angew. Chem. Int. Ed.* **2004**, *43*, 1092
- [10] M. E. Di Pietro, G. Celebre, G. De Luca, *J. Magn. Reson.* **2016**, *267*, 63.
- [11] C. Merle, G. Kummerlöwe, J. C. Freudenberger, F. Halbach, W. Stöwer, C. L. von Gostomsky, J. Höpfner, T. Beskers, M. Wilhelm, B. Luy, *Angew. Chem. Int. Ed.* **2013**, *52*, 10309.
- [12] G. Kummerlöwe, J. Auernheimer, A. Lendlein, B. Luy, *J. Am. Chem. Soc.* **2007**, *129*, 6080.
- [13] G. Kummerlöwe, E. McCord, S. Cheatham, S. Niss, R. Schnell, B. Luy, *Chem. Eur. J.* **2010**, *16*, 7087.
- [14] L. F. Gil-Silva, R. Santamaría-Fernández, A. Navarro-Vázquez, R. R. Gil, *Chem. Eur. J.* **2016**, *22*, 472.
- [15] M. Zhong, R. Wang, K. Kawamoto, B. D. Olsen, J. A. Johnson, *Science* **2016**, *353*, 1264.
- [16] F. Di Lorenzo, S. Seiffert, *Polym. Chem.* **2015**, *6*, 5515.
- [17] E. Blasco, M. Wegener, C. Barner-Kowollik, *Adv. Mater.* **2017**, *29*, 1604005.
- [18] S. Yigit, R. Sanyal, A. Sanyal, *Chem. Asian J.* **2011**, *6*, 2648.
- [19] S. Perrier, *Macromolecules* **2017**, *50*, 7433.
- [20] G. Odian, *Principles of Polymerization*, Fourth Edition; John Wiley & Sons Inc.: Hoboken, New Jersey, 2004.

- [21] P. Nesvadba, Radical Polymerization in Industry. In *Encyclopedia of Radicals in Chemistry, Biology and Materials* [Online]; C. Chatgililoglu, A. Studer, Eds.; John Wiley & Sons Ltd., 2012. DOI: 10.1002/9781119953678.
- [22] O. Vogl, M. F. Quin, A. Zilkha, *Prog. Polym. Sci.* **1999**, *24*, 1481.
- [23] C. Barner-Kowollik, P. Vana, T. P. Davis, The Kinetics of Free-Radical Polymerization. In *Handbook of Radical Polymerization*; K. Matyjaszewski, T. P. Davis, Eds.; John Wiley & Sons Inc.: Hoboken, New Jersey, 2002.
- [24] C. Barner-Kowollik, G. T. Russell, *Prog. Polym. Sci.* **2009**, *34*, 1211.
- [25] A. D. Jenkins, K. L. Loening, Nomenclature. In *Comprehensive Polymer Science*; G. Allen, J. C. Bevington, Eds.; Vol 1: Polymer Characterization; Pergamon Press Plc., 1989.
- [26] F. R. Mayo, F. M. Lewis, *J. Am. Chem. Soc.* **1944**, *66*, 1594.
- [27] M. L. Coote, T. P. Davis, Copolymerization Kinetics. In *Handbook of Radical Polymerization*; K. Matyjaszewski, T. P. Davis, Eds.; John Wiley & Sons Inc.: Hoboken, New Jersey, 2002.
- [28] M. L. Coote, T. P. Davis, *Prog. Polym. Sci.* **1999**, *24*, 1217.
- [29] M. L. Coote, T. P. Davis, L. Radom, *J. Mol. Struct. THEOCHEM* **1999**, *461-462*, 91.
- [30] M. L. Coote, T. P. Davis, L. Radom, *Macromolecules* **1999**, *32*, 2935.
- [31] D. A. Shipp, *J. Macromol. Sci. Part C Polym. Rev.* **2005**, *45*, 171.
- [32] D. H. Solomon, *J. Polym. Sci., Part A: Polym. Chem.* **2005**, *43*, 5748.
- [33] G. Moad, E. Rizzardo, S. H. Thang, *Acc. Chem. Res.* **2008**, *41*, 1133.
- [34] K. Matyjaszewski, *Macromolecules* **2012**, *45*, 4015.
- [35] L. Tebben, A. Studer, *Angew. Chem. Int. Ed.* **2011**, *50*, 5034.
- [36] W. A. Braunecker, K. Matyjaszewski, *Prog. Polym. Sci.* **2007**, *32*, 93.
- [37] C. J. Hawker, A. W. Bosman, E. Harth, *Chem. Rev.* **2001**, *101*, 3661..
- [38] S. Shanmugam, K. Matyjaszewski, Reversible Deactivation Radical Polymerization: State-of-the-Art in 2017. In *Reversible Deactivation Radical Polymerization: Mechanisms and Synthetic Methodologies*; K. Matyjaszewski, H. Gao, B. S. Sumerlin, N. T. Tsarevsky, Eds.; ACS Symposium Series 1284; American Chemical Society: Washington, DC, 2018.
- [39] G. Moad, E. Rizzardo, S. H. Thang, *Polymer* **2008**, *49*, 1079.
- [40] G. Moad, C. Barner-Kowollik, The Mechanism and Kinetics of the RAFT Process: Overview, Rates, Stabilities, Side Reactions, Product Spectrum and Outstanding Challenges. In *Handbook of RAFT Polymerization*; C. Barner-Kowollik, Ed.; Wiley-VCH: Weinheim, 2008.
- [41] G. Moad, E. Rizzardo, S. H. Thang, *Aust. J. Chem.* **2005**, *58*, 379.
- [42] D. J. Keddie, G. Moad, E. Rizzardo, S. H. Thang, *Macromolecules* **2012**, *45*, 5321.
- [43] G. Moad, E. Rizzardo, S. H. Thang, *Aust. J. Chem.* **2012**, *65*, 985.
- [44] M. Benaglia, J. Chiefari, Y. K. Chong, G. Moad, E. Rizzardo, S. H. Thang, *J. Am. Chem. Soc.* **2009**, *131*, 6914.
- [45] Sigma-Aldrich, RAFT: Choosing the Right Agent to Achieve Controlled Polymerization [Online]; <https://www.sigmaaldrich.com/technical-documents/articles/materials-science/polymer-science/raft-polymerization.html>
- [46] L. Barner, S. Perrier, Polymers with Well-Defined End Groups via RAFT – Synthesis, Applications and Postmodifications. In *Handbook of RAFT Polymerization*; C. Barner-Kowollik, Ed.; Wiley-VCH: Weinheim, 2008.

REFERENCES

- [47] J. T. Lai, D. Filla, R. Shea, *Macromolecules* **2002**, *35*, 6754.
- [48] A. J. Inglis, M. H. Stenzel, C. Barner-Kowollik, *Macromol. Rapid Commun.* **2009**, *30*, 1792.
- [49] L. Zhang, Y. Chen, *Polymer* **2006**, *47*, 5259.
- [50] A. J. Inglis, P. Pierrat, T. Muller, S. Bräse, C. Barner-Kowollik, *Soft Matter* **2010**, *6*, 82.
- [51] H. W. Ooi, K. S. Jack, H. Peng, A. K. Whittaker, *Polym. Chem.* **2013**, *4*, 4788.
- [52] K. T. Wiss, P. Theato, *J. Polym. Sci., Part A: Polym. Chem.* **2010**, *48*, 4758.
- [53] N. Zhou, Z. Zhang, J. Zhu, Z. Cheng, X. Zhu, *Macromolecules* **2009**, *42*, 3898.
- [54] M. M. Stamenovic, P. Espeel, W. Van Camp, F. E. Du Prez, *Macromolecules* **2011**, *44*, 5619.
- [55] M. Kaupp, K. Hildebrandt, V. Trouillet, P. Mueller, A. S. Quick, M. Wegener, C. Barner-Kowollik, *Chem. Commun.* **2016**, *52*, 1975.
- [56] M. Kaupp, A. S. Quick, C. Rodriguez-Emmenegger, A. Welle, V. Trouillet, O. Pop-Georgievski, M. Wegener, C. Barner-Kowollik, *Adv. Funct. Mater.* **2014**, *24*, 5649.
- [57] M. Li, H. Li, P. De, B. S. Sumerlin, *Macromol. Rapid Commun.* **2011**, *32*, 354.
- [58] M. P. Robin, M. W. Jones, D. M. Haddleton, R. K O'Reilly, *ACS Macro Lett.* **2012**, *1*, 222.
- [59] M. Bejia, M-T. Charreyre, J. M. G. Martinho, *Prog. Polym. Sci.* **2011**, *36*, 568.
- [60] R. J. Mancini, J. Lee, H. D. Maynard, *J. Am. Chem. Soc.* **2012**, *134*, 8474.
- [61] A. Postma, T. P. Davis, R. A. Evans, G. Li, G. Moad, M. S. O'Shea, *Macromolecules* **2006**, *39*, 5293.
- [62] G. N. Grover, J. Lee, N. M. Matsumoto, H. D. Maynard, *Macromolecules* **2012**, *45*, 4958.
- [63] C. Boyer, J. Liu, V. Bulmus, T. P. Davis, C. Barner-Kowollik, M. H. Stenzel, *Macromolecules* **2008**, *41*, 5641.
- [64] M. Glassner, G. Delaitre, M. Kaupp, J. P. Blinco, C. Barner-Kowollik, *J. Am. Chem. Soc.* **2012**, *134*, 7274.
- [65] K. K. Oehlenschlaeger, J. O. Mueller, N. B. Heine, M. Glassner, N. K. Guimard, G. Delaitre, F. G. Schmidt, C. Barner-Kowollik, *Angew. Chem. Int. Ed.* **2013**, *52*, 762.
- [66] D. Varadharajan, G. Delaitre, *Polym. Chem.* **2016**, *7*, 7488.
- [67] S-S. Zhang, K. Cui, J. Huang, Q-L. Zhao, S-K. Cao, Z. Ma, *RCS Adv.* **2015**, *5*, 44571.
- [68] Y-Z. You, D. S. Manickam, Q-H. Zhou, D. Oupicky, *Biomacromolecules* **2007**, *8*, 2038.
- [69] X-P. Qiu, F. M. Winnik, *Macromol. Rapid Commun.* **2006**, *27*, 1648.
- [70] J. M. Spruell, B. A. Levy, A. Sutherland, W. R. Dichtel, J. Y. Cheng, F. Stoddart, A. Nelson, *J. Polym. Sci., Part A: Polym. Chem.* **2009**, *47*, 346.
- [71] M-Q. Zhu, L-Q. Wang, G. L. Exarhos, A. D. Q. Li, *J. Am. Chem. Soc.* **2004**, *126*, 2656.
- [72] Y. K. Chong, G. Moad, E. Rizzardo, S. H. Thang, *Macromolecules* **2007**, *40*, 4446.
- [73] R. N. Carmean, C. A. Figg, G. M. Scheutz, T. Kubo, B. S. Sumerlin, *ACS Macro Lett.* **2017**, *6*, 185.

- [74] C. P. Jesson, C. M. Pearce, H. Simon, A. Werner, V. J. Cunningham, J. R. Lovett, M. J. Smallridge, N. J. Warren, S. P. Armes, *Macromolecules* **2017**, *50*, 182.
- [75] J. Xu, J. He, D. Fan, W. Tang, Y. Yang, *Macromolecules* **2006**, *39*, 3753.
- [76] M. Destarac, *Macromol. React. Eng.* **2010**, *4*, 165.
- [77] S. Oliver, L. Zhao, A. J. Gormley, R. Chapman, C. Boyer, *Macromolecules* **2019**, *52*, 3.
- [78] W. H. Carothers, *Trans. Faraday Soc.* **1936**, *32*, 39.
- [79] V. M. Canuto, J. S. Levine, T. R. Augustsson, C. L. Imhof, M. S. Giampapa, *Nature* **1983**, *305*, 281.
- [80] E. Kohen, R. Santus, J. G. Hirschberg, *Photobiology*; Academic Press, Inc.: San Diego, California, 1995.
- [81] D. Cambié, C. Bottecchia, N. J. W. Straathof, V. Hessel, T. Noël, *Chem. Rev.* **2016**, *116*, 10276.
- [82] H. Meier, *Angew. Chem. Int. Ed. Engl.* **1992**, *31*, 1399.
- [83] S. Takagi, M. Eguchi, D. A. Tryk, H. Inoue, *J. Photochem. Photobiol., C* **2006**, *7*, 104.
- [84] H. D. Roth, *Angew. Chem. Int. Ed. Engl.* **1989**, *28*, 1193.
- [85] N. D. Heindel, M. A. Pfau, *J. Chem. Educ.* **1965**, *42*, 383.
- [86] G. Ciamician, *Science* **1912**, *36*, 385.
- [87] J. C. Maxwell, *Philos. Trans. R. Soc. London* **1865**, *155*, 459.
- [88] M. Planck, *Ann. Phys.* **1901**, *309*, 553.
- [89] A. Einstein, *Ann. Phys.* **1905**, *322*, 132.
- [90] A. Einstein, *Physikalische Zeitschrift* **1909**, *10*, 817.
- [91] K. K. Rohatgi-Mukherjee, *Fundamentals of Photochemistry*, Revised Second Edition; New Age International (P), Ltd.: New Delhi, 1986.
- [92] U. E. Steiner, *Fundamentals of Photophysics, Photochemistry, and Photobiology*. In *Photodynamic Therapy, from Theory to Application*; M. H. Abdel-Kader, Ed.; Springer-Verlag: Berlin, 2014.
- [93] A. Jablonski, *Nature* **1933**, *131*, 839.
- [94] M. G. Evans, N. Uri, *Nature* **1949**, *164*, 404.
- [95] G. Oster, N-L. Yang, *Chem. Rev.* **1968**, *68*, 125.
- [96] Y. Yagci, S. Jockusch, N. J. Turro, *Macromolecules* **2010**, *43*, 6245.
- [97] S. Yamago, S. Nakamura, *Polymer* **2013**, *54*, 981.
- [98] S. Chatani, C. J. Kloxin, C. N. Bowman, *Polym. Chem.* **2014**, *5*, 2187.
- [99] R. W. Peiffer, *Applications of Photopolymer Technology*. In *Photopolymerization Fundamentals and Applications*; A. B. Scranton, C. N. Bowman, R. W. Peiffer, Eds.; ACS Symposium Series 673; American Chemical Society: Washington, DC, 1997.
- [100] M. Hippler, E. Blasco, J. Qu, M. Tanaka, C. Barner-Kowollik, M. Wegener, M. Bastmeyer, *Nat. Commun.* **2019**, *10*, 232.
- [101] D. Gräfe, A. Wickberg, M. M. Zieger, M. Wegener, E. Blasco, C. Barner-Kowollik, *Nat. Commun.* **2018**, *9*, 2788.
- [102] M. M. Zieger, P. Müller, E. Blasco, C. Petit, V. Hahn, L. Michalek, H. Mutlu, M. Wegener, C. Barner-Kowollik, *Adv. Funct. Mater.* **2018**, *28*, 1801405.
- [103] R. Müller, T. J. Feuerstein, V. Trouillet, S. Bestgen, P. W. Roesky, C. Barner-Kowollik, *Chem. Eur. J.* **2018**, *24*, 18933.

REFERENCES

- [104] T. K. Claus, S. Telitel, A. Welle, M. Bastmeyer, A. P. Vogt, G. Delaittre, C. Barner-Kowollik, *Chem. Commun.* **2017**, *53*, 1599.
- [105] T. Tischer, C. Rodriguez-Emmenegger, V. Trouillet, A. Welle, V. Schueler, J. O. Mueller, A. S. Goldmann, E. Brynda, C. Barner-Kowollik, *Adv. Mater.* **2014**, *26*, 4087.
- [106] G. Delaittre, A. S. Goldmann, J. O. Mueller, C. Barner-Kowollik, *Angew. Chem. Int. Ed.* **2015**, *54*, 11388.
- [107] X-H. Qin, K. Labuda, J. Chen, V. Hruschka, A. Khadem, R. Liska, H. Redl, P. Slezak, *Adv. Funct. Mater.* **2015**, *25*, 6606.
- [108] J. J. Roberts, S. J. Bryant, *Biomaterials* **2013**, *34*, 9969.
- [109] D. D. McKinnon, A. M. Kloxin, K. S. Anseth, *Biomater. Sci.* **2013**, *1*, 460.
- [110] A. S. Quick, J. Fischer, B. Richter, T. Pauloehrl, V. Trouillet, M. Wegener, C. Barner-Kowollik, *Macromol. Rapid Commun.* **2013**, *34*, 335.
- [111] H. Shih, C-C. Lin, *Macromol. Rapid Commun.* **2013**, *34*, 269.
- [112] M. Conradi, T. Junkers, *Macromolecules* **2014**, *47*, 5578.
- [113] M. Conradi, T. Junkers, *Macromolecules* **2011**, *44*, 7969
- [114] J. P. Chesterman, T. C. Hughes, B. G. Amsden, *Eur. Polym. J.* **2018**, *105*, 186.
- [115] D. E. Marschner, H. Frisch, J. T. Offenloch, B. T. Tuten, C. R. Becer, A. Walther, A. S. Goldman, P. Tzvetkova, C. Barner-Kowollik, *Macromolecules* **2018**, *51*, 3802.
- [116] H. Frisch, J. P. Menzel, F. R. Bloesser, D. E. Marschner, K. Mundsinger, C. Barner-Kowollik, *J. Am. Chem. Soc.* **2018**, *140*, 9551.
- [117] V. X. Truong, F. Li, J. S. Forsythe, *ACS Macro Lett.* **2017**, *6*, 657.
- [118] B. T. Tuten, J. P. Menzel, K. Pahnke, J. P. Blinco, C. Barner-Kowollik, *Chem. Commun.* **2017**, *53*, 4501.
- [119] T. Pauloehrl, A. Welle, K. K. Oehlenschlaeger, C. Barner-Kowollik, *Chem. Sci.* **2013**, *4*, 3503.
- [120] F. Feist, J. P. Menzel, T. Weil, J. P. Blinco, C. Barner-Kowollik, *J. Am. Chem. Soc.* **2018**, *140*, 11848.
- [121] H. A. Houck, F. E. Du Prez, C. Barner-Kowollik, *Nat. Commun.* **2017**, *8*, 1869.
- [122] A. S. Quick, H. Rothfuss, A. Welle, B. Richter, J. Fischer, M. Wegener, C. Barner-Kowollik, *Adv. Funct. Mater.* **2014**, *24*, 3571.
- [123] J. O. Mueller, F. G. Schmidt, J. P. Blinco, C. Barner-Kowollik, *Angew. Chem. Int. Ed.* **2015**, *54*, 10284.
- [124] J. S. Clovis, A. Eckell, R. Huisgen, R. Sustmann, *Chem. Ber.* **1967**, *100*, 60.
- [125] R. M. Moriarty, J. M. Kliegman, C. Shovlin, *J. Am. Chem. Soc.* **1967**, *89*, 5958.
- [126] F. L. Bach, J. Karliner, G. E. Van Lear, *J. Chem. Soc. D* **1969**, No. 19, 1110b.
- [127] N. H. Toubro, A. Holm, *J. Am. Chem. Soc.* **1980**, *102*, 2093.
- [128] Y. Wang, C. I. Rivera Vera, Q. Lin, *Org. Lett.* **2007**, *9*, 4155.
- [129] S. Li, J. Zhang, C. Deng, F. Meng, L. Yu, Z. Zhong, *ACS Appl. Mater. Interfaces* **2016**, *8*, 21155.
- [130] W. Song, Y. Wang, Z. Yu, C. I. Rivera Vera, J. Qu, Q. Lin, *ACS Chem. Biol.* **2010**, *5*, 875.
- [131] W. Song, Y. Wang, J. Qu, Q. Lin, *J. Am. Chem. Soc.* **2008**, *130*, 9654.
- [132] C. J. Dürr, P. Lederhose, L. Hlalele, D. Abt, A. Kaiser, S. Brandau, C. Barner-Kowollik, *Macromolecules* **2013**, *46*, 5915.
- [133] J. O. Mueller, D. Voll, F. G. Schmidt, G. Delaittre, C. Barner-Kowollik, *Chem. Commun.* **2014**, *50*, 15681.

- [134] J. Willenbacher, K. N. R. Wuest, J. O. Mueller, M. Kaupp, H-A. Wagenknecht, C. Barner-Kowollik, *ACS Macro Lett.* **2014**, *3*, 574.
- [135] J. T. Offenloch, J. Willenbacher, P. Tzvetkova, C. Heiler, H. Mutlu, C. Barner-Kowollik, *Chem. Commun.* **2017**, *53*, 775.
- [136] P. Lederhose, K. N. R. Wüst, C. Barner-Kowollik, J. P. Blinco, *Chem. Commun.* **2016**, *52*, 5928.
- [137] M. Dietrich, G. Delaittre, J. P. Blinco, A. J. Inglis, M. Bruns, C. Barner-Kowollik, *Adv. Funct. Mater.* **2012**, *22*, 304.
- [138] E. Blasco, M. Piñol, L. Oriol, B. V. K. J. Schmidt, A. Welle, V. Trouillet, M. Bruns, C. Barner-Kowollik, *Adv. Funct. Mater.* **2013**, *23*, 4011.
- [139] D. Abt, B. V. K. J. Schmidt, O. Pop-Georgievski, A. S. Quick, D. Danilov, N. Y. Kostina, M. Bruns, W. Wenzel, M. Wegener, C. Rodriguez-Emmeneger, C. Barner-Kowollik, *Chem. Eur. J.* **2015**, *21*, 13186.
- [140] T. Gegenhuber, D. Abt, A. Welle, S. Özbek, A. S. Goldmann, C. Barner-Kowollik, *J. Mater. Chem. B* **2017**, *5*, 4993.
- [141] C. Wang, M. M. Zieger, A. Schenzel, M. Wegener, J. Willenbacher, C. Barner-Kowollik, C. N. Bowman, *Adv. Funct. Mater.* **2017**, *27*, 1605317.
- [142] D. Hoenders, J. Guo, A. S. Goldmann, C. Barner-Kowollik, A. Walther, *Mater. Horiz.* **2018**, *5*, 560.
- [143] S. R. Mane, I-L. Hsiao, M. Takamiya, D. Le, U. Straehle, C. Barner-Kowollik, C. Weiss, G. Delaittre, *Small* **2018**, *14*, 1801571.
- [144] W. Song, Y. Wang, J. Qu, M. M. Madden, Q. Lin, *Angew. Chem. Int. Ed.* **2008**, *47*, 2832.
- [145] W. Siti, A. K. Khan, H-P. M. de Hoog, B. Liedberg, M. Nallani, *Org. Biomol. Chem.* **2015**, *13*, 3202.
- [146] W. Feng, L. Li, C. Yang, A. Welle, O. Trapp, P. A. Levkin, *Angew. Chem. Int. Ed.* **2015**, *54*, 8732.
- [147] Y. Zhang, W. Liu, Z. K. Zhao, *Molecules* **2014**, *19*, 306.
- [148] Z. Li, L. Qian, L. Li, J. C. Bernhammer, H. V. Huynh, J-S. Lee, S. Q. Yao, *Angew. Chem. Int. Ed.* **2016**, *55*, 2002.
- [149] C. Heiler, S. Bastian, P. Lederhose, J. P. Blinco, E. Blasco, C. Barner-Kowollik, *Chem. Commun.* **2018**, *54*, 3476.
- [150] C. Heiler, J. T. Offenloch, E. Blasco, C. Barner-Kowollik, *ACS Macro Lett.* **2017**, *6*, 56.
- [151] L. Delafresnaye, N. Zaquen, R. P. Kuchel, J. P. Blinco, P. B. Zetterlund, C. Barner-Kowollik, *Adv. Funct. Mater.* **2018**, *28*, 1800342.
- [152] Y. Wang, W. J. Hu, W. Song, R. K. V. Lim, Q. Lin, *Org. Lett.* **2008**, *10*, 3725.
- [153] S. Arndt, H-A. Wagenknecht, *Angew. Chem. Int. Ed.* **2014**, *53*, 14580.
- [154] Z. Yu, L. Y. Ho, Z. Wang, Q. Lin, *Bioorg. Med. Chem. Lett.* **2011**, *21*, 5033.
- [155] P. An, Z. Yu, Q. Lin, *Chem. Commun.* **2013**, *49*, 9920.
- [156] E. Blasco, Y. Sugawara, P. Lederhose, J. P. Blinco, A-M. Kelterer, C. Barner-Kowollik, *ChemPhotoChem* **2017**, *1*, 159.
- [157] D. E. Fast, A. Lauer, J. P. Menzel, A-M. Kelterer, G. Gescheidt, C. Barner-Kowollik, *Macromolecules* **2017**, *50*, 1815.
- [158] E. Frick, C. Schweigert, B. B. Noble, H. A. Ernst, A. Lauer, Y. Liang, D. Voll, M. L. Coote, A-N. Unterreiner, C. Barner-Kowollik, *Macromolecules* **2016**, *49*, 80.
- [159] J. P. Menzel, B. B. Noble, A. Lauer, M. L. Coote, J. P. Blinco, C. Barner-Kowollik, *J. Am. Chem. Soc.* **2017**, *139*, 15812.

REFERENCES

- [160] P. Lederhose, D. Abt, A. Welle, R. Müller, C. Barner-Kowollik, J. P. Blinco, *Chem. Eur. J.* **2018**, *24*, 576.
- [161] J. P. Menzel, F. Feist, B. Tuten, T. Weil, J. P. Blinco, C. Barner-Kowollik, *Angew. Chem. Int. Ed.* **2019**, *58*, 7470.
- [162] K. Hildebrandt, M. Kaupp, E. Molle, J. P. Menzel, J. P. Blinco, C. Barner-Kowollik, *Chem. Commun.* **2016**, *52*, 9426.
- [163] K. Hildebrandt, T. Pauloehrl, J. P. Blinco, K. Linkert, H. G. Börner, C. Barner-Kowollik, *Angew. Chem. Int. Ed.* **2015**, *54*, 2838.
- [164] R. R. Batchelor, E. Blasco, K. N. R. Wuest, H. Lu, M. Wegener, C. Barner-Kowollik, M. H. Stenzel, *Chem. Commun.* **2018**, *54*, 2436.
- [165] Y. Tezuka, H. Oike, *Prog. Polym. Sci.* **2002**, *27*, 1069.
- [166] J. Alemán, A. V. Chadwick, J. He, M. Hess, K. Horie, R. G. Jones, P. Kratochvíl, I. Meisel, I. Mita, G. Moad, S. Penczek, R. F. T. Stepto, R. G. Jones, *Pure Appl. Chem.* **2007**, *79*, 1801.
- [167] F. Horkay, G. B. MacKenna, Polymer Networks and Gels. In *Physical Properties of Polymers Handbook*, Second Edition; J. E. Mark, Ed.; Springer Science: New York, 2007.
- [168] W. Kuhn, *J. Polym. Sci.* **1946**, *1*, 380.
- [169] F. T. Wall, P. J. Flory, *J. Chem. Phys.* **1951**, *19*, 1435.
- [170] H. M. James, E. Guth, *J. Chem. Phys.* **1943**, *11*, 455.
- [171] M. Rubinstein, S. Panyukov, *Macromolecules* **2002**, *35*, 6670.
- [172] J. C. Hernández-Ortiz, E. Vivaldo-Lima, Crosslinking. In *Handbook of Polymer Synthesis, Characterization, and Processing*; E. Saldívar-Guerra, E. Vivaldo-Lima, Eds.; John Wiley & Sons Inc.: Hoboken, New Jersey, 2013.
- [173] S. Seiffert, *Polym. Chem.* **2017**, *8*, 4472.
- [174] Y. Gu, K. Kawamoto, M. Zhong, M. Chen, M. J. A. Hore, A. M. Jordan, L. T. J. Korley, B. D. Olsen, J. A. Johnson, *Proc. Natl. Acad. Sci. U.S.A.* **2017**, *114*, 4875.
- [175] A. Metters, J. Hubbell, *Biomacromolecules* **2005**, *6*, 290.
- [176] L. H. Sperling, *Introduction to Polymer Science*, Fourth Edition; John Wiley & Sons Inc.: Hoboken, New Jersey, 2006.
- [177] S. Seiffert, J. Sprakel, *Chem. Soc. Rev.* **2012**, *41*, 909.
- [178] S. Tamesue, Y. Takashima, H. Yamaguchi, S. Shinkai, A. Harada, *Angew. Chem. Int. Ed.* **2010**, *49*, 7461.
- [179] E. A. Appel, X. J. Loh, S. T. Jones, F. Biedermann, C. A. Dreiss, O. A. Scherman, *J. Am. Chem. Soc.* **2012**, *134*, 11767.
- [180] Y-H. Lee, L. He, Y-T. Chan, *Macromol. Rapid Commun.* **2018**, *39*, 1800465.
- [181] Q. Wu, J. Wei, B. Xu, X. Liu, H. Wang, W. Wang, Q. Wang, W. Liu, *Sci. Rep.* **2017**, *7*, 41566.
- [182] Y. Hu, Z. Zhang, Y. Li, X. Ding, D. Li, C. Shen, F-J. Xu, *Macromol. Rapid Commun.* **2018**, *39*, 1800069.
- [183] M. Burnworth, L. Tang, J. R. Kumpfer, A. J. Duncan, F. L. Beyer, G. L. Fiore, S. J. Rowan, C. Weder, *Nature* **2011**, *472*, 334.
- [184] K. Kawamoto, S. C. Grindy, J. Liu, N. Holten-Andersen, J. A. Johnson, *ACS Macro Lett.* **2015**, *4*, 458.
- [185] N. Ide, T. Fukuda, *Macromolecules* **1999**, *32*, 95.
- [186] C. Decker, *Prog. Polym. Sci.* **1996**, *21*, 593.
- [187] O. Okay, *Prog. Polym. Sci.* **2000**, *25*, 771.

- [188] J. Kopecek, *J. Polym. Sci., Part A: Polym. Chem.* **2009**, *47*, 5929.
- [189] K. Ogino, J-S. Chen, C. K. Ober, *Chem. Mater.* **1998**, *10*, 3833.
- [190] X. Feng, K. Zhang, P. Cheng, X. Sui, M. A. Hempenius, B. Liedberg, G. J. Vancso, *Macromol. Rapid Commun.* **2016**, *37*, 1939.
- [191] E. Blasco, B. Yameen, A. S. Quick, P. Krolla-Sidenstein, A. Welle, M. Wegener, C. Barner-Kowollik, *Macromolecules* **2015**, *48*, 8718.
- [192] D. A. Ossipov, J. Hilborn, *Macromolecules* **2006**, *39*, 1709.
- [193] M. Akiba, A. S. Hashim, *Prog. Polym. Sci.* **1997**, *22*, 475.
- [194] T. Krappitz, F. Feist, I. Lamparth, N. Moszner, H. John, J. P. Blinco, T. R. Dargaville, C. Barner-Kowollik, *Mater. Horiz.* **2019**, *6*, 81.
- [195] H. Gao, K. Matyjaszewski, *Prog. Polym. Sci.* **2009**, *34*, 317.
- [196] V. T. G. Tan, D. H. T. Nguyen, R. H. Utama, M. Kahram, F. Ercole, J. F. Quinn, M. R. Whittaker, T. P. Davis, J. J. Gooding, *Polym. Chem.* **2017**, *8*, 6123.
- [197] G. Hild, *Prog. Polym. Sci.* **1998**, *23*, 1019.
- [198] T. Sakai, T. Matsunaga, Y. Yamamoto, C. Ito, R. Yoshida, S. Suzuki, N. Sasaki, M. Shibayama, U. Chung, *Macromolecules* **2008**, *41*, 5379.
- [199] Y. Jiang, J. Chen, C. Deng, E. J. Suuronen, Z. Zhong, *Biomaterials* **2014**, *35*, 4969.
- [200] R. R. Batchelor, G. Kwandou, P. T. Spicer, M. H. Stenzel, *Polym. Chem.* **2017**, *8*, 980.
- [201] A. K. Fraser, C. S. Ki, C-C. Lin, *Macromol. Chem. Phys.* **2014**, *215*, 507.
- [202] L. Zhang, T. Qiu, Z. Zhu, L. Guo, X. Li, *Macromol. Rapid Commun.* **2018**, *39*, 1800121.
- [203] F. Cavalli, H. Mutlu, S. O. Steinmueller, L. Barner, *Polym. Chem.* **2017**, *8*, 3778.
- [204] M. Chen, Y. Gu, A. Singh, M. Zhong, A. M. Jordan, S. Biswas, L. T. J. Korley, A. C. Balazs, J. A. Johnson, *ACS Cent. Sci.* **2017**, *3*, 124.
- [205] K. K. Oehlenschlaeger, J. O. Mueller, J. Brandt, S. Hilf, A. Lederer, M. Wilhelm, R. Graf, M. L. Coote, F. G. Schmidt, C. Barner-Kowollik, *Adv. Mater.* **2014**, *26*, 3561.
- [206] B. J. Adzima, H. A. Aguirre, C. J. Kloxin, T. F. Scott, C. N. Bowman, *Macromolecules* **2008**, *41*, 9112.
- [207] T. A. Plaisted, S. Nemat-Nasser, *Acta Mater.* **2007**, *55*, 5684.
- [208] Y. Fan, C. Deng, R. Cheng, F. Meng, Z. Zhong, *Biomacromolecules* **2013**, *14*, 2814.
- [209] V. X. Truong, F. Li, F. Ercole, J. S. Forsythe, *ACS Macro Lett.* **2018**, *7*, 464.
- [210] Z. Wei, J. H. Yang, J. Zhou, F. Xu, M. Zrínyi, P. H. Dussault, Y. Osada, Y. M. Chen, *Chem. Soc. Rev.* **2014**, *43*, 8114.
- [211] D. E. Apostolides, C. S. Patrickios, *Polym. Int.* **2018**, *67*, 627.
- [212] E. S. Dragan, *Chem. Eng. J.* **2014**, *243*, 572.
- [213] Q. Chen, H. Chen, L. Zhu, J. Zheng, *J. Mater. Chem. B* **2015**, *3*, 3654.
- [214] J. P. Gong, Y. Katsuyama, T. Kurokawa, Y. Osada, *Adv. Mater.* **2013**, *15*, 1155.
- [215] Z. Feng, H. Zuo, W. Gao, N. Ning, M. Tian, L. Zhang, *Macromol. Rapid Commun.* **2018**, *39*, 1800138.
- [216] T. Liu, S. Lu, X. Peng, C. Jiao, J. Zhang, M. Han, H. Wang, *Macromol. Rapid Commun.* **2018**, *39*, 1800474.
- [217] G. J. Berg, T. Gong, C. R. Fenoli, C. N. Bowman, *Macromolecules* **2014**, *47*, 3473.

REFERENCES

- [218] V. X. Truong, M. P. Ablett, S. M. Richardson, J. A. Hoyland, A. P. Dove, *J. Am. Chem. Soc.* **2015**, *137*, 1618.
- [219] J. L. Valentín, J. Carretero-González, I. Mora-Marrantes, W. Chassé, K. Saalwächter, *Macromolecules* **2008**, *41*, 4717.
- [220] C-Y. M. Tung, P. J. Dynes, *J. Appl. Polym. Sci.* **1982**, *27*, 569.
- [221] J. M. Charlesworth, *Polym. Eng. Sci.* **1988**, *28*, 230.
- [222] P. J. Flory, *Chem. Rev.* **1944**, *35*, 51.
- [223] H. Zhou, J. Woo, A. M. Cok, M. Wang, B. D. Olsen, J. A. Johnson, *Proc. Natl. Acad. Sci. U.S.A.* **2012**, *109*, 19119.
- [224] T. Clark, L. Kwisnek, C. E. Hoyle, S. Nazarenko, *J. Polym. Sci., Part A: Polym. Chem.* **2009**, *47*, 14.
- [225] F. Di Lorenzo, J. Hellwig, R. von Klitzing, S. Seiffert, *ACS Macro Lett.* **2015**, *4*, 698.
- [226] S. Naficy, H. R. Brown, J. M. Razal, G. M. Spinks, P. G. Whitten, *Aust. J. Chem.* **2011**, *64*, 1007.
- [227] A. S. Hoffman, *Adv. Drug Delivery Rev.* **2012**, *64*, 18.
- [228] Y. Osada, J. P. Gong, Y. Tanaka, *J. Macromol. Sci. Part C Polym. Rev.* **2004**, *44*, 87.
- [229] D. Buenger, F. Topuz, J. Groll, *Prog. Polym. Sci.* **2012**, *37*, 1678.
- [230] Y. Takashima, S. Hatanaka, M. Otsubo, M. Nakahata, T. Kakuta, A. Hashidzume, H. Yamaguchi, A. Harada, *Nat. Commun.* **2012**, *3*, 1270.
- [231] S. S. Liow, Q. Dou, D. Kai, A. A. Karim, K. Zhang, F. Xu, X. J. Loh, *ACS Biomater. Sci. Eng.* **2016**, *2*, 295.
- [232] D. J. Beebe, J. S. Moore, J. M. Bauer, Q. Yu, R. H. Liu, C. Devadoss, B-H. Jo, *Nature* **2000**, *404*, 588.
- [233] H. Wu, G. Yu, L. Pan, N. Liu, M. T. McDowell, Z. Bao, Y. Cui, *Nat. Commun.* **2013**, *4*, 1943.
- [234] W. Cui, J. Ji, Y-F. Cai, H. Li, R. Ran, *J. Mater. Chem. A* **2015**, *3*, 17445.
- [235] L. Arens, F. Weißfeld, C. O. Klein, K. Schlag, M. Wilhelm, *Adv. Sci.* **2017**, *4*, 1700112.
- [236] H-B. Zhao, Y-Z. Wang, *Macromol. Rapid Commun.* **2017**, *38*, 1700451.
- [237] C. W. Peak, J. J. Wilker, G. Schmidt, *Colloid Polym. Sci.* **2013**, *291*, 2031.
- [238] A. M. Schenzel, C. O. Klein, K. Rist, N. Moszner, C. Barner-Kowollik, *Adv. Sci.* **2016**, *3*, 1500361.
- [239] G. L. Fiore, S. J. Rowan, C. Weder, *Chem. Soc. Rev.* **2013**, *42*, 7278.
- [240] C. Barner-Kowollik, M. Bastmeyer, E. Blasco, G. Delaittre, P. Müller, B. Richter, M. Wegener, *Angew. Chem. Int. Ed.* **2017**, *56*, 15828.
- [241] B. Richter, V. Hahn, S. Bertels, T. K. Claus, M. Wegener, G. Delaittre, C. Barner-Kowollik, M. Bastmeyer, *Adv. Mater.* **2017**, *29*, 1604342.
- [242] E. Blasco, J. Müller, P. Müller, V. Trouillet, M. Schön, T. Scherer, C. Barner-Kowollik, M. Wegener, *Adv. Mater.* **2016**, *28*, 3592.
- [243] R. Tycko, F. J. Blanco, Y. Ishii, *J. Am. Chem. Soc.* **2000**, *122*, 9340.
- [244] Y. Ishii, M. A. Markus, R. Tycko, *J. Biomol. NMR* **2001**, *21*, 141.
- [245] K. Kobzar, H. Kessler, B. Luy, *Angew. Chem. Int. Ed.* **2005**, *44*, 3145.
- [246] R. M. Silverstein, F. X. Webster, D. J. Kiemle, *Spectrometric Identification of Organic Compounds*, Seventh Edition; John Wiley & Sons Inc.: Hoboken, New Jersey, 2005.

- [247] G. de los Santos-Villarreal, L. E. Elizalde, *Polymer Spectroscopy and Compositional Analysis*. In *Handbook of Polymer Synthesis, Characterization, and Processing*; E. Saldívar-Guerra, E. Vivaldo-Lima, Eds.; John Wiley & Sons Inc.: Hoboken, New Jersey, 2013.
- [248] K. Hatada, T. Kitayama, *NMR Spectroscopy of Polymers*, Springer-Verlag: Berlin, 2004.
- [249] K. Saalwächter, D. Reichert, *Magnetic Resonance: Polymer Applications of NMR*. In *Encyclopedia of Spectroscopy & Spectrometry*, Second Edition; J. Lindon, G. Tranter, D. Koppenaal, Eds.; Academic Press: London, 2010.
- [250] D. J. P. Harrison, W. R. Yates, J. F. Johnson, *J. Macromol. Sci., Rev. Macromol. Chem. Phys.* **1985**, *25*, 481.
- [251] A. K. Whittaker, *Annu. Rep. NMR Spectro.* **1997**, *34*, 105.
- [252] G-W. Li, H. Liu, F. Qiu, X-J. Wang, X-X. Lei, *Nat. Prod. Bioprospect.* **2018**, *8*, 279.
- [253] J. R. Tolman, J. M. Flanagan, M. A. Kennedy, J. H. Prestegard, *Proc. Natl. Acad. Sci. U.S.A.* **1995**, *92*, 9279.
- [254] A. Saupe, G. Englert, *Phys. Rev. Lett.* **1963**, *11*, 462.
- [255] N. Tjandra, A. Bax, *Science* **1997**, *278*, 1111.
- [256] G. M. Clore, M. R. Starich, A. M. Gronenborn, *J. Am. Chem. Soc.* **1998**, *120*, 10571.
- [257] T. Montag, C. M. Thiele, *Chem. Eur. J.* **2013**, *19*, 2271.
- [258] G-W. Li, J-M. Cao, W. Zong, L. Hu, M-L. Hu, X. Lei, H. Sun, R. X. Tan, *Chem. Eur. J.* **2017**, *23*, 7653.
- [259] G. Kummerlöwe, S. Knör, A. O. Frank, T. Paululat, H. Kessler, B. Luy, *Chem. Commun.* **2008**, No. 44, 5722.
- [260] R. R. Gil, C. Gayathri, N. V. Tsarevsky, K. Matyjaszewski, *J. Org. Chem.* **2008**, *73*, 840
- [261] Y. E. Moskalenko, V. Bagutski, C. M. Thiele, *Chem. Commun.* **2016**, *53*, 95.
- [262] J. C. Freudenberger, S. Knör, K. Kobzar, D. Heckmann, T. Paululat, H. Kessler, B. Luy, *Angew. Chem. Int. Ed.* **2005**, *44*, 423.
- [263] T. S. Ulmer, B. E. Ramirez, F. Delaglio, A. Bax, *J. Am. Chem. Soc.* **2003**, *125*, 9179.
- [264] A. O. Frank, J. C. Freudenberger, A. K. Shaytan, H. Kessler, B. Luy, *Magn. Res. Chem.* **2015**, *53*, 213.
- [265] T. Niklas, C. Steinmetzger, F. Rüttger, D. Stalke, M. John, *Magn. Res. Chem.* **2017**, *55*, 1084.
- [266] Y. Liu, J. Saurí, E. Mevers, M. W. Peczu, H. Hiemstra, J. Clardy, G. E. Martin, R. T. Williamson, *Science* **2017**, *356*, eaam5349.
- [267] B. Deloche, E. T. Samulski, *Macromolecules* **1981**, *14*, 575.
- [268] H-J. Sass, G. Musco, S. J. Stahl, P. T. Wingfield, S. Grzesiek, *J. Biomol. NMR* **2000**, *18*, 303.
- [269] C. Gayathri, N. V. Tsarevsky, R. R. Gil, *Chem. Eur. J.* **2010**, *16*, 3622.
- [270] C. O. Frank. *Polystyrene-Based Networks as Orientation Media for NMR Spectroscopy*. Bachelor Thesis (unpublished), Karlsruhe Institute of Technology (KIT), July 2015.

REFERENCES

- [271] G. ten Brinke, F. E. Karasz, T. S. Ellis, *Macromolecules* **1983**, *16*, 244.
- [272] J. Rieger, *J. Therm. Anal.* **1996**, *46*, 965.
- [273] W. G. Barb, *J. Polym. Sci.* **1959**, *37*, 515.
- [274] C. G. Overberger, C. Frazier, J. Mandelman, H. F. Smith, *J. Am. Chem. Soc.* **1953**, *75*, 3326.
- [275] K. Koren, L. Hutter, B. Enko, A. Pein, S. M. Borisov, I. Klimant, *Sens. Actuators, B* **2013**, *176*, 344.
- [276] A. Goursoot, T. Mineva, R. Kevorkyants, D. Talbi, *J. Chem. Theory Comput.* **2007**, *3*, 755.
- [277] BOLA, Technical Information BOLA Materials [Online]; http://www.bola.de/fileadmin/media/12_technical_information.pdf
- [278] B. Luy, *J. Indian Inst. Sci.* **2010**, *90*, 119.
- [279] E. Lafontaine, J. P. Bayle, J. Courtieu, *J. Am. Chem. Soc.* **1989**, *111*, 8294.
- [280] D. Merlet, B. Ancian, J. Courtieu, P. Lesot, *J. Am. Chem. Soc.* **1999**, *121*, 5249.
- [281] C. M. Thiele, *J. Org. Chem.* **2004**, *69*, 7403.
- [282] C. Aroulanda, M. Sarfati, J. Courtieu, *Enantiomer* **2001**, *6*, 281.
- [283] S. Hansmann, V. Schmidts, C. M. Thiele, *Chem. Eur. J.* **2017**, *23*, 9114.
- [284] M. Schwab, D. Herold, C. M. Thiele, *Chem. Eur. J.* **2017**, *23*, 14576.
- [285] M. Dama, S. Berger, *Tetrahedron Lett.* **2012**, *53*, 6439.
- [286] U. Eliav, G. Navon, *J. Am. Chem. Soc.* **2006**, *128*, 15956.
- [287] M. Schmidt, H. Sun, A. Leonov, C. Griesinger, U. M. Reinscheid, *Magn. Reson. Chem.* **2012**, *50*, S38.
- [288] P. C. M. van Zijl, B. H. Ruessink, J. Bulthuis, C. MacLean, *Acc. Chem. Res.* **1984**, *17*, 172.
- [289] R. Barbieri, I. Bertini, G. Cavallaro, Y-M. Lee, C. Luchinat, A. Rosato, *J. Am. Chem. Soc.* **2002**, *124*, 5581.
- [290] G. Pintacuda, M. John, X-C. Su, G. Otting, *Acc. Chem. Res.* **2007**, *40*, 206.
- [291] M. Teraguchi, M. Ohtake, H. Inoue, A. Yoshida, T. Aoki, T. Kaneko, K. Yamanaka, *J. Polym. Sci., Part A: Polym. Chem.* **2005**, *43*, 2348.
- [292] C. Pugh, C. N. Tang, M. Paz-Pazos, O. Samtani, A. H. Dao, *Macromolecules* **2007**, *40*, 8178.
- [293] M. Buback, A. Feldermann, C. Barner-Kowollik, I. Lacík, *Macromolecules* **2001**, *34*, 5439.
- [294] L. Barner, C. Barner-Kowollik, T. P. Davis, *J. Polym. Sci., Part A: Polym. Chem.* **2002**, *40*, 1064.
- [295] P. Tzvetkova, S. Simova, B. Luy, *J. Magn. Reson.* **2007**, *186*, 193.

- [296] H. Rothfuss, N. D. Knöfel, P. Tzvetkova, N. C. Michenfelder, S. Baraban, A-N. Unterreiner, P. W. Roesky, C. Barner-Kowollik, *Chem. Eur. J.* **2018**, *24*, 17475.
- [297] G. Accorsi, A. Listorti, K. Yoosaf, N. Armaroli, *Chem. Soc. Rev.* **2009**, *38*, 1690.
- [298] D. Estupiñán, T. Gegenhuber, J. P. Blinco, C. Barner-Kowollik, L. Barner, *ACS Macro Lett.* **2017**, *6*, 229.
- [299] D. Estupiñán, C. Barner-Kowollik, L. Barner, *Angew. Chem. Int. Ed.* **2018**, *57*, 5925.
- [300] J. P. Hooker, L. Delafresnaye, L. Barner, C. Barner-Kowollik, *Mater. Horiz.* **2019**, *6*, 356.
- [301] L. Stolzer, A. Vigovskaya, C. Barner-Kowollik, L. Fruk, *Chem. Eur. J.* **2015**, *21*, 14309.
- [302] H-P. M. de Hoog, M. Nallani, B. Liedberg, *Polym. Chem.* **2012**, *3*, 302.
- [303] J. Hatano, K. Okuro, T. Aida, *Angew. Chem. Int. Ed.* **2016**, *55*, 193.
- [304] J. O. Mueller, N. K. Guimard, K. K. Oehlenschlaeger, F. G. Schmidt, C. Barner-Kowollik, *Polym. Chem.* **2014**, *5*, 1447.
- [305] V. Kumbaraci, N. Talinli, Y. Yagci, *Macromolecules* **2006**, *39*, 6031.
- [306] Y. Nakayama, T. Matsuda, *J. Polym. Sci., Part A: Polym. Chem.* **2005**, *43*, 3324.
- [307] N. B. Cramer, J. P. Scott, C. N. Bowman, *Macromolecules* **2002**, *35*, 5361.
- [308] S. Hurtle, A. S. Goldmann, H. Gliemann, H. Mutlu, C. Barner-Kowollik, *ACS Macro Lett.* **2018**, *7*, 201.
- [309] T. Gegenhuber, L. De Keer, A. S. Goldmann, P. H. M. Van Steenberge, J. O. Mueller, M-F. Reyniers, J. P. Menzel, D. R. D'hooge, C. Barner-Kowollik, *Macromolecules* **2017**, *50*, 6451.
- [310] A. Sugawara, K. Hasegawa, K. Suzuki, Y. Takahashi, *Bull. Chem. Soc. Jpn.* **1987**, *60*, 435.
- [311] L. Lu, H. Zhang, N. Yang, Y. Cai, *Macromolecules* **2006**, *39*, 3770.
- [312] L-T. T. Nguyen, M. T. Gokmen, F. E. Du Prez, *Polym. Chem.* **2013**, *4*, 5527.
- [313] J. von Sonntag, W. Knolle, S. Naumov, R. Mehnert, *Chem. Eur. J.* **2002**, *8*, 4199.
- [314] J. Put, F. C. De Schryver, *J. Am. Chem. Soc.* **1973**, *95*, 137.
- [315] C. E. Hoyle, C. N. Bowman, *Angew. Chem. Int. Ed.* **2010**, *49*, 1540.
- [316] D. P. Nair, M. Podgórski, S. Chatani, T. Gong, W. Xi, C. R. Fenoli, C. N. Bowman, *Chem. Mater.* **2014**, *26*, 724.
- [317] A. B. Lowe, *Polym. Chem.* **2014**, *5*, 4820.
- [318] M. P. Lutolf, J. A. Hubbell, *Biomacromolecules* **2003**, *4*, 713.
- [319] H. Shih, C-C. Lin, *Biomacromolecules* **2012**, *13*, 2003.

REFERENCES

- [320] A. E. Rydholm, S. K. Reddy, K. S. Anseth, C. N. Bowman, *Polymer* **2007**, *48*, 4589.
- [321] F. P. Schwarz, S. P. Wasik, *Anal. Chem.* **1976**, *48*, 524.
- [322] E. C. Buruiana, M. Olaru, B. C. Simionescu, *Eur. Polym. J.* **2007**, *43*, 1359.
- [323] F. Cavalli, L. De Keer, B. Huber, P. H. M. Van Steenberge, D. R. D'hooge, L. Barner, *Polym. Chem.* **2019**, *10*, 2781.
- [324] S. Kondo, H. Sakurai, U. Chung, T. Sakai, *Macromolecules* **2013**, *46*, 7027.
- [325] S. Kondo, U. Chung, T. Sakai, *Polym. J.* **2014**, *46*, 14.
- [326] T. Sakai, Y. Akagi, S. Kondo, U. Chung, *Soft Matter* **2014**, *10*, 6658.
- [327] M. W. Tibbitt, A. M. Kloxin, L. A. Sawicki, K. S. Anseth, *Macromolecules* **2013**, *46*, 2785.
- [328] K. Sivasailam, C. Cohen, *J. Rheol.* **2000**, *44*, 897.
- [329] W. Michalke, M. Lang, S. Kreitmeier, D. Göritz, *J. Chem. Phys.* **2002**, *117*, 6300.
- [330] T. Ghosh, N. Karak, *RSC Adv.* **2018**, *8*, 17044.
- [331] M. Van De Walle, K. De Bruycker, T. Junkers, J. P. Blinco, C. Barner-Kowollik, *ChemPhotoChem* **2019**, *3*, 225.
- [332] W. Konrad, C. Fengler, S. Putwa, C. Barner-Kowollik, *Angew. Chem. Int. Ed.* **2019**, *58*, 7133.
- [333] E. T. Herruzo, A. P. Perrino, R. Garcia, *Nat. Commun.* **2014**, *5*, 3126.
- [334] R. Garcia, R. Proksch, *Eur. Polym. J.* **2013**, *49*, 1897.
- [335] A. Enthart, J. C. Freudenberger, J. Furrer, H. Kessler, B. Luy, *J. Magn. Reson.* **2008**, *192*, 314.
- [336] G. Kummerlöwe, S. Schmitt, B. Luy, *The Open Spectroscopy Journal* **2010**, *4*, 16.
- [337] T. Gruending, M. Guilhaus, C. Barner-Kowollik, *Macromolecules* **2009**, *42*, 6366.

CHAPTER 8:

APPENDIX

8.1. Synthesis of Optimized Polymer-Based Alignment Media

Reactor

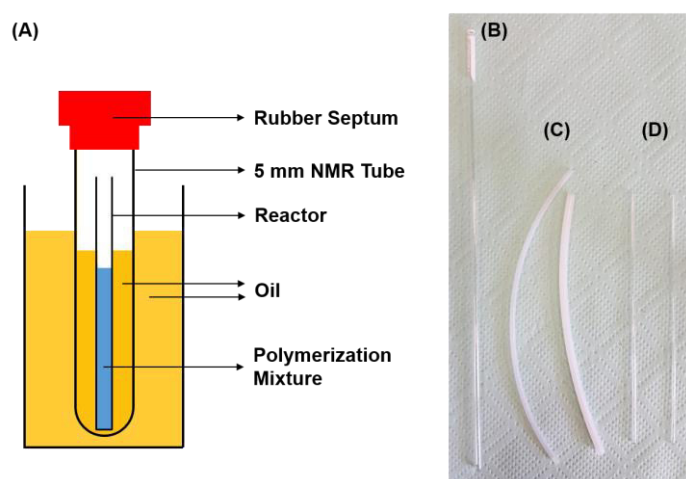


Figure 8.1. (A) Schematic representation of the setup used for the synthesis of polystyrene sticks. The reactor can be: (B) 3 mm outer diameter NMR tubes, (C) PTFE tubes of different diameters (sealed with epoxy glue), or (D) glass capillaries of different diameters.

Flory–Rehner Equation

The ideal degree of swelling can be calculated by the Flory–Rehner equation,

$$v_c = \frac{V_1}{M_c \bar{v}_2} = \frac{-[\ln(1 - v_2) + v_2 + \chi_{12} v_2^2]}{(v_2^{1/3} - 2v_2/f)}$$

here v_c represents the density of elastically active chains, V_1 is the molar volume of chloroform ($80.2 \text{ cm}^3 \cdot \text{mol}^{-1}$), and \bar{v}_2 the specific volume of polystyrene ($0.91 \text{ cm}^3 \cdot \text{g}^{-1}$).¹ M_c , the average molecular weight between crosslinks, is calculated as follows:

¹ D.J. Streeter, R. F. Boyer, *Ind. Eng. Chem.* **1951**, 43, 1790.

$$M_c = M_{styrene} \frac{100}{\%DVB}$$

With these values, the Flory–Huggins interaction parameter ($\chi_{12} = 0.52$ for polystyrene–chloroform),² and the functionality of crosslinks $f = 4$, the polymer volume fraction v_2 can be calculated. Once v_2 is obtained, the ideal mass swelling ratio Q_m can be determined, using the specific volume of chloroform, $\bar{v}_1 = 0.67 \text{ cm}^3 \cdot \text{g}^{-1}$

$$v_2 = \frac{\bar{v}_2}{(Q_m - 1)\bar{v}_1 + \bar{v}_2}$$

Equilibration Time

The equilibration time required for the swollen polymer sticks to achieve constant Δv_Q lineshapes, can reach up to six weeks. As an example, Figure 8.3 displays the evolution of Δv_Q in time, for networks **4** and **6** (sticks pre-swollen in acetone 48 h, then swollen in chloroform inside conventional 5 mm outer diameter NMR tubes).

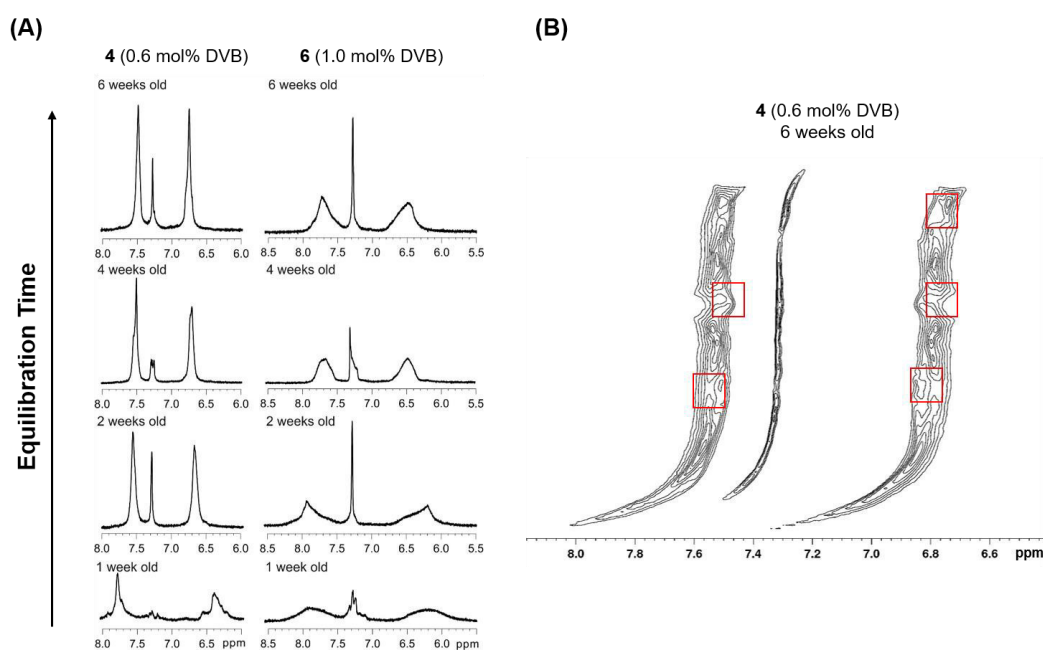


Figure 8.2. (A) Equilibration time for the CDCl_3 quadrupolar splittings determined in sticks **4** and **6**, pre-swollen in acetone and stretched in conventional 5 mm NMR tubes. (B) 2D projection of CDCl_3 Δv_Q values determined along the vertical direction of stick **4**, after 6 weeks equilibration time. The signal in the middle represents isotropic CDCl_3 . Cracks inside the gel leading to inhomogeneities in Δv_Q are highlighted in red.

² R. A. Orwoll, P. A. Arnold, Polymer–Solvent Interaction Parameter χ . In *Physical Properties of Polymers Handbook*, Second Edition; J. E. Mark, Ed.; Springer Science: New York, 2007

Rheology

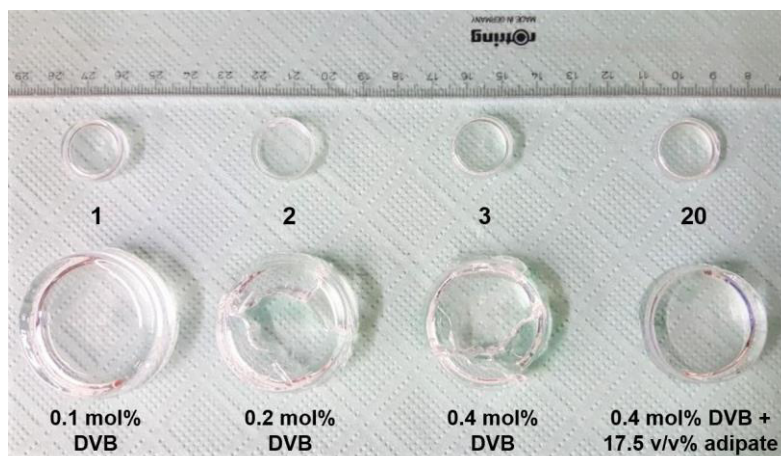


Figure 8.3. Free swelling of PS disks in toluene leads to cracking and breaking of the samples with (DVB > 0.1%) without plasticizer.

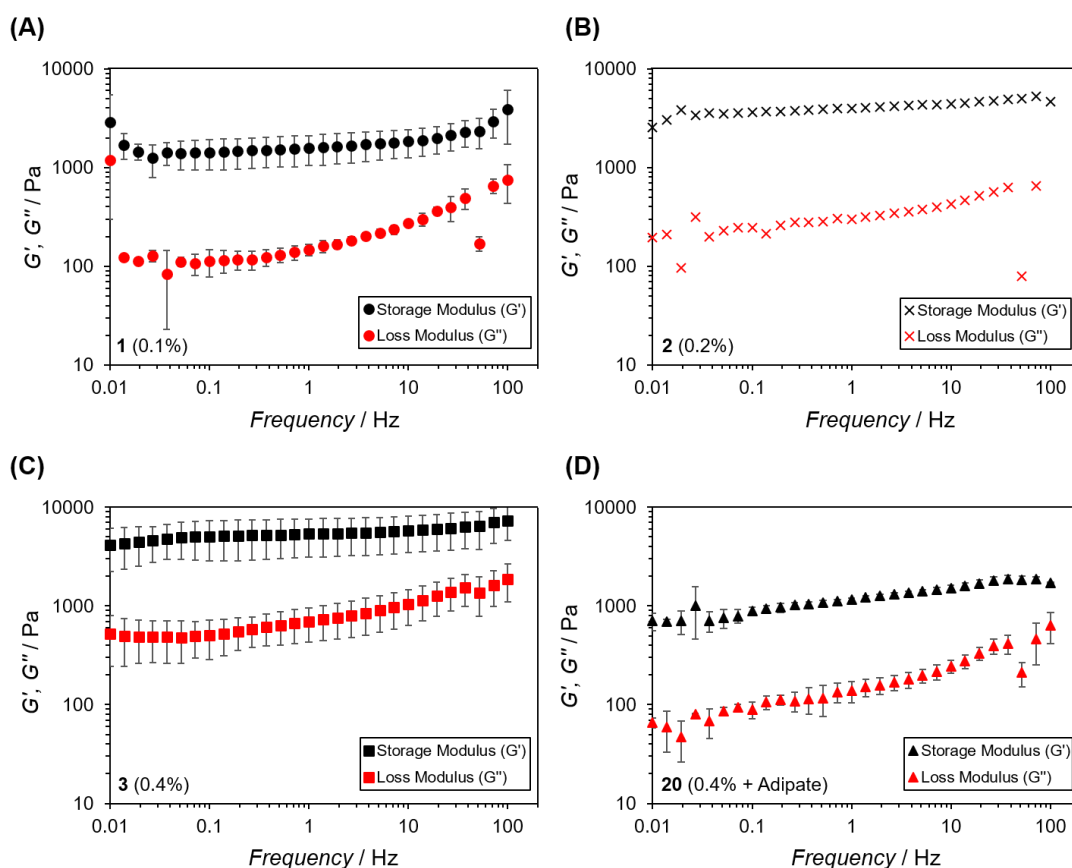


Figure 8.4. Frequency sweep curves displaying storage and loss moduli for (A) **1** DVB 0.1 mol%, (B) **2** DVB 0.2 mol%, (C) **3** DVB 0.4 mol%, and (D) **20** DVB 0.4 mol% + 17.5% v/v adipate. Error bars represent standard deviation from three independent measurements.

Chiral PS Networks

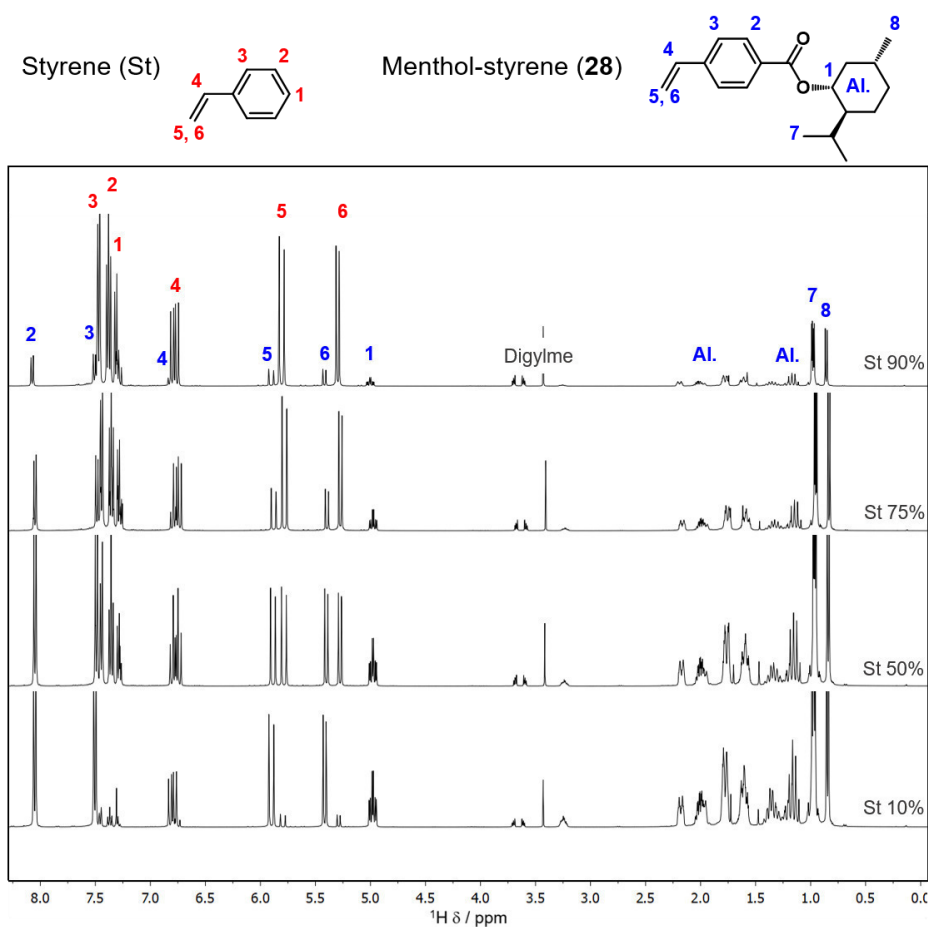


Figure 8.5. ^1H NMR spectra in CDCl_3 of some styrene (St)–monomer (**28**) mixtures (10%, 50%, 75%, and 90% St) before copolymerization.

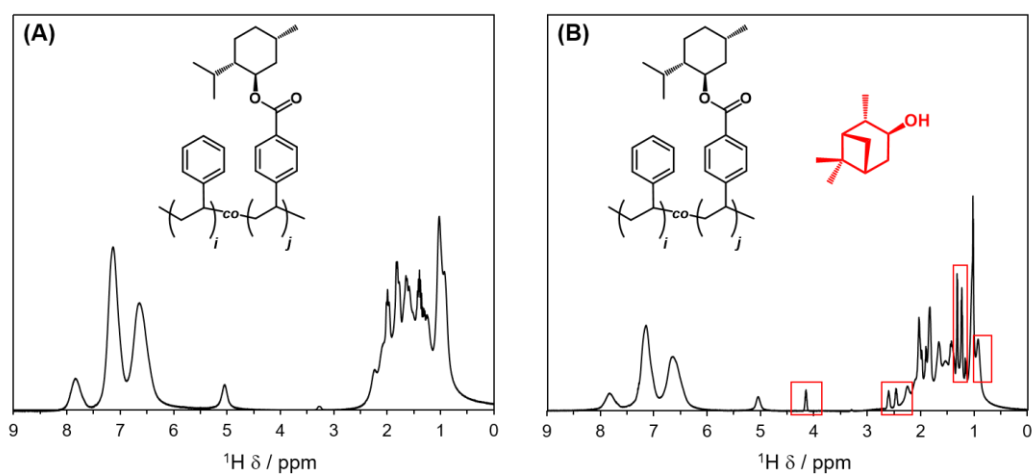


Figure 8.6. ^1H NMR spectra of chiral network **30** (25 mol% (-)-menthol-styrene **28**, DVB 0.2 mol%) without analyte (A) and loaded with (+)-ICP (B). Resonance signals coming from the analyte are marked in red.

APPENDIX

Table 8.1. RDCs of altenuene and isoaltenuene in chiral PS alignment media **30** and **31**.

Analyte Network Assignment ^a	Isoalten.	Isoalten.	Δ_{RDC} (Hz)	Alten.	Alten.	Δ_{RDC} (Hz)
	30 (-)	31 (+)		30 (-)	31 (+)	
	RDC (Hz)	RDC (Hz)		RDC (Hz)	RDC (Hz)	
C13–H13	-5.86	-6.85	0.99	-15.43	-10.90	-4.52
C12–H12	2.51	2.40	0.11	2.45	2.83	-0.37
C10–H10	-3.57	-2.47	-1.10	-0.63	-3.69	3.06
C6–H6	-3.75	-4.14	0.39	-6.46	-5.58	-0.88
C4–H4a	-5.60	-7.68	2.08	-14.49	-11.47	-3.02
C4–H4b	6.49	7.22	-0.73	-9.00	-7.46	-1.54
C3–H3	6.98	7.72	-0.74	2.71	1.38	1.33
C2–H2	9.58	11.68	-2.10	-3.55	-2.63	-0.93
C1–H1	-8.17	-10.36	2.20	-8.63	-4.66	-3.96

^a Atom labels from Figure 8.7. RDCs determined from directly bonded C–H atoms. Carbon atom C4 is bonded to two different protons, here labeled a and b.

Table 8.2. RDCs of altenuene in chiral PS alignment media **30–32**.

Analyte Network Assignment ^a	Alten.	Alten	Δ_{RDC} (Hz)	Alten.	Alten.	Δ_{RDC} (Hz)
	32 (rac)	30 (-)		32 (rac)	31 (+)	
	RDC (Hz)	RDC (Hz)		RDC (Hz)	RDC (Hz)	
C13–H13	-15.27	-15.43	0.16	-15.27	-10.90	-4.37
C12–H12	2.38	2.45	-0.08	2.38	2.83	-0.45
C10–H10	1.54	-0.63	2.17	1.54	-3.69	5.23
C6–H6	-6.88	-6.46	-0.42	-6.88	-5.58	-1.31
C4–H4a	-16.99	-14.49	-2.50	-16.99	-11.47	-5.52
C4–H4b	-12.37	-9.00	-3.38	-12.37	-7.46	-4.92
C3–H3	-0.19	2.71	-2.90	-0.19	1.38	-1.57
C2–H2	-6.64	-3.55	-3.09	-6.64	-2.63	-4.02
C1–H1	-10.14	-8.63	-1.52	-10.14	-4.66	-5.48

^a Atom labels from Figure 8.7. RDCs determined from directly bonded C–H atoms. Carbon atom C4 is bonded to two different protons, here labeled a and b.

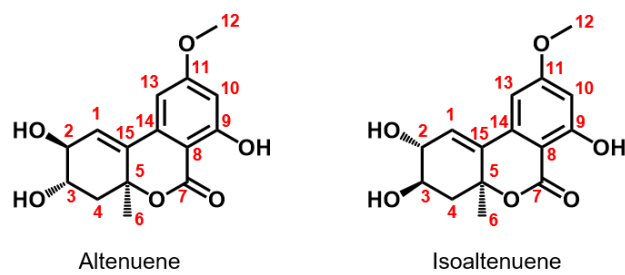


Figure 8.7. Chemical structures of diastereomers altenuene and isoaltenuene, used as optically active analytes for chiral PS networks.

8.2. NITEC Chemistry Applied to Step-Growth Polymers

Photoreactor

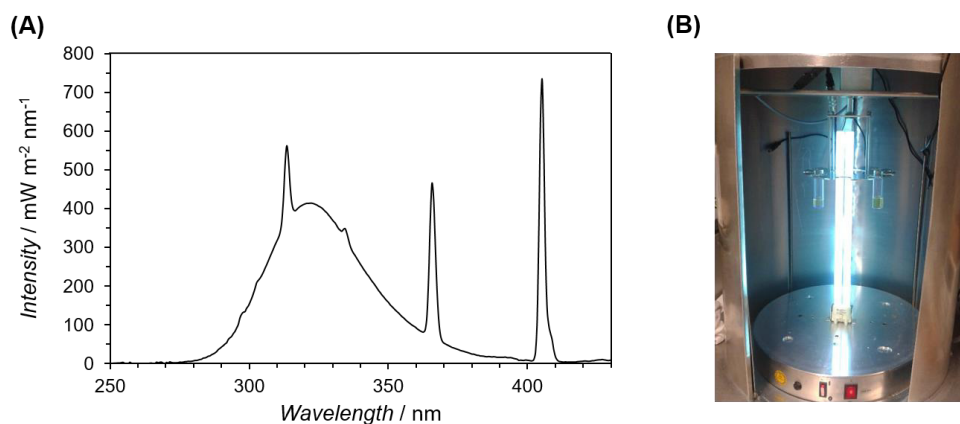


Figure 8.8. (A) Emission spectrum of the UV lamp (Arimed B6, $\lambda_{\max} = 320 \pm 30$ nm) used as irradiation source. (B) Photoreactor. The lamp stands in the middle of the setup and the samples revolve around it in a carousel.

NITEC Step-Growth Polymers

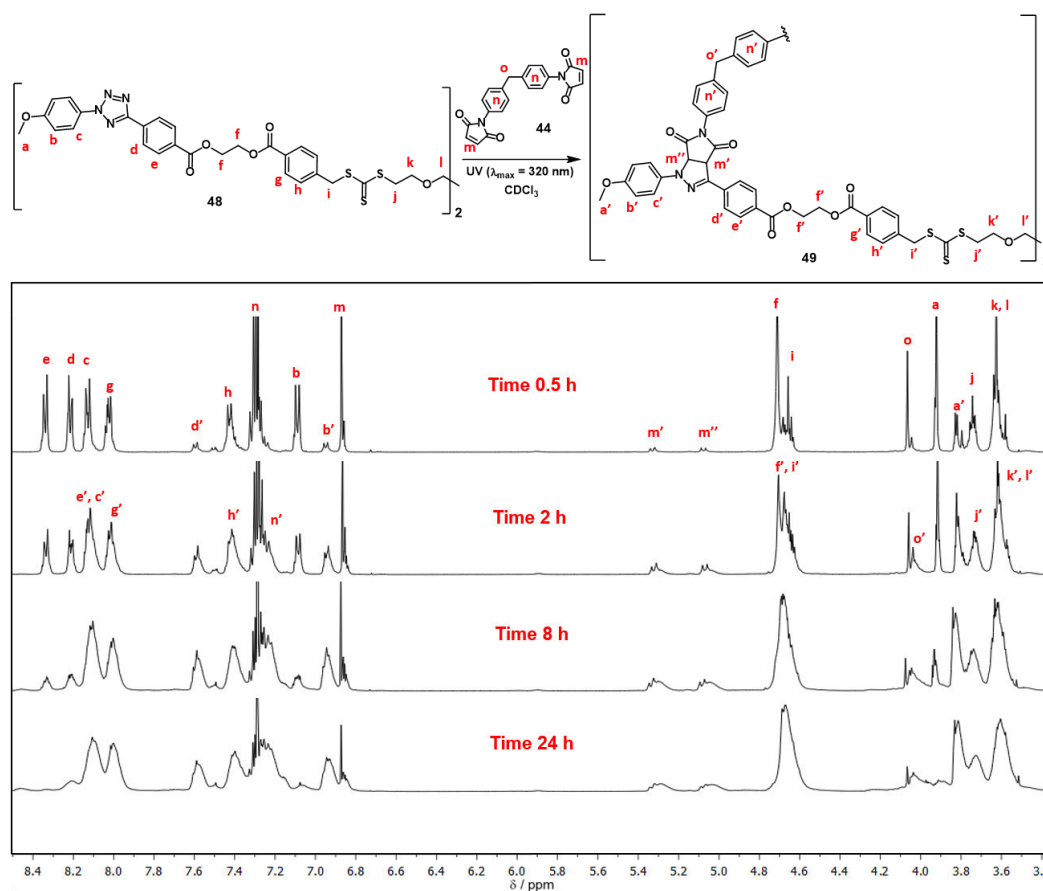


Figure 8.9. $^1\text{H NMR}$ spectra in CDCl_3 of polymers **49** analyzed after several irradiation times.

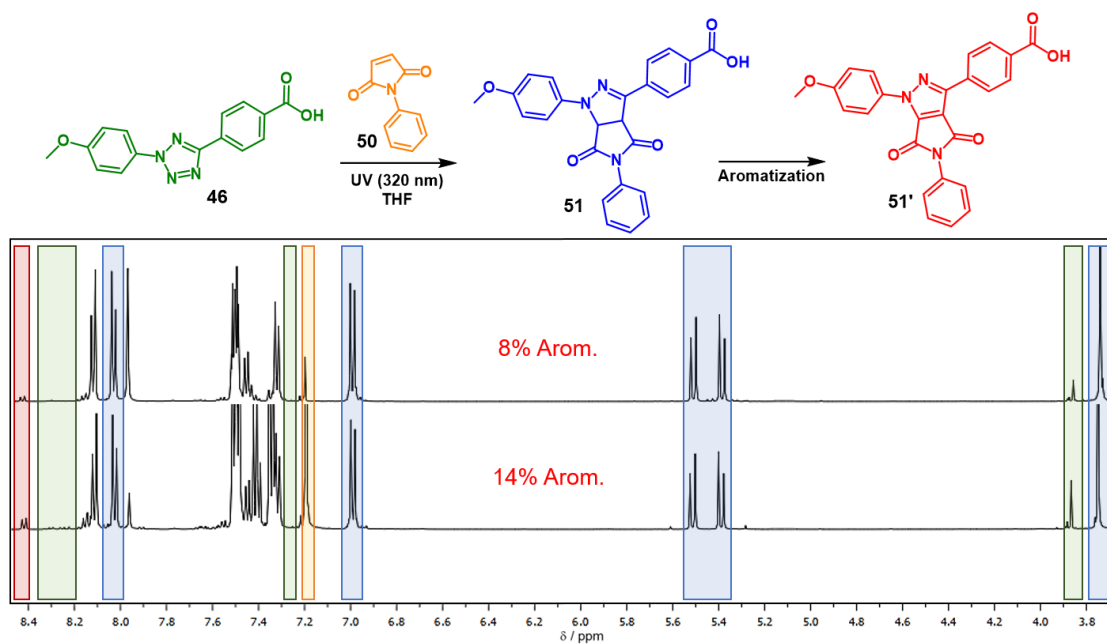


Figure 8.10. ^1H NMR spectra in $\text{THF}-d_8$ of the reaction between tetrazole **46** and maleimide **50**, producing pyrazoline **51** and different amounts of by-product **51'** (aromatization).

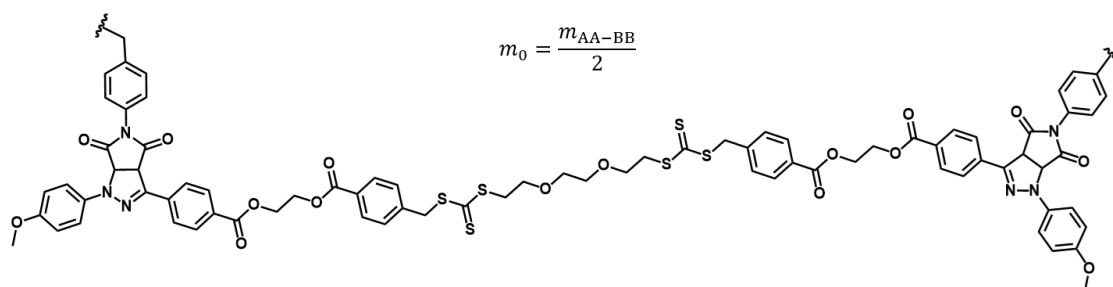


Figure 8.11. Structure of the repeating unit AA-BB in polymers **49**, with $m_{\text{AA-BB}} = 1549.8 \text{ g}\cdot\text{mol}^{-1}$.

APPENDIX

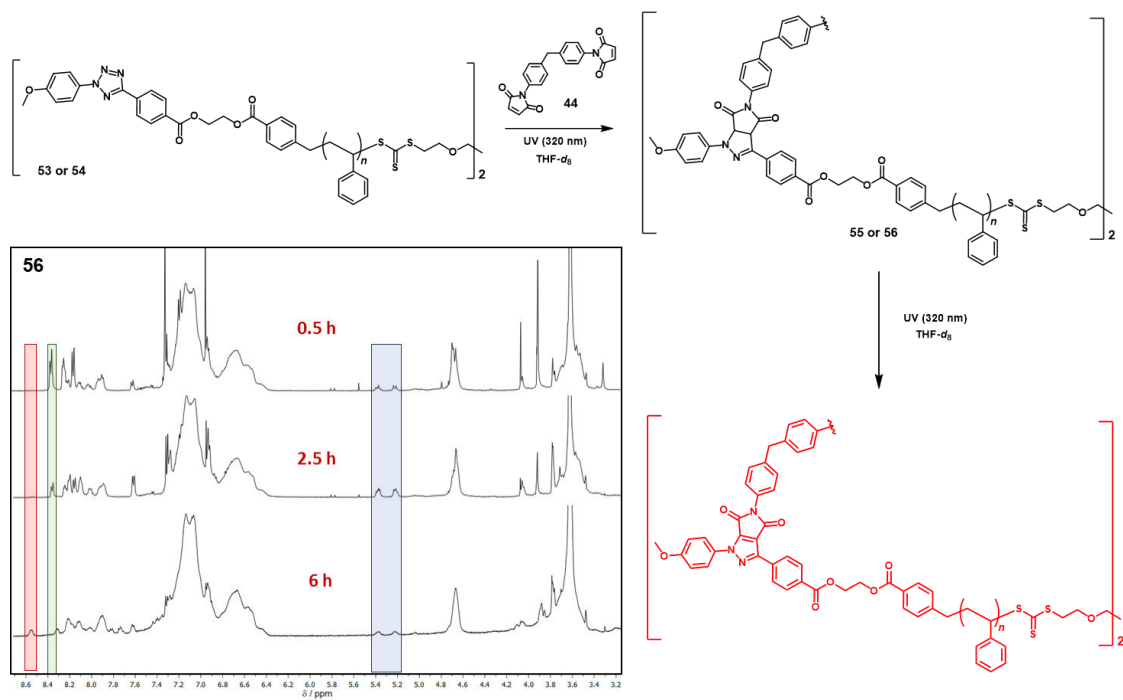


Figure 8.12. ^1H NMR spectra in $\text{THF-}d_8$ of polymers **56**, obtained from PS **54** and bismaleimide **44**. Resonance signals of starting material and product are highlighted in green and blue, respectively. Signals of the aromatization by-product are depicted in red.

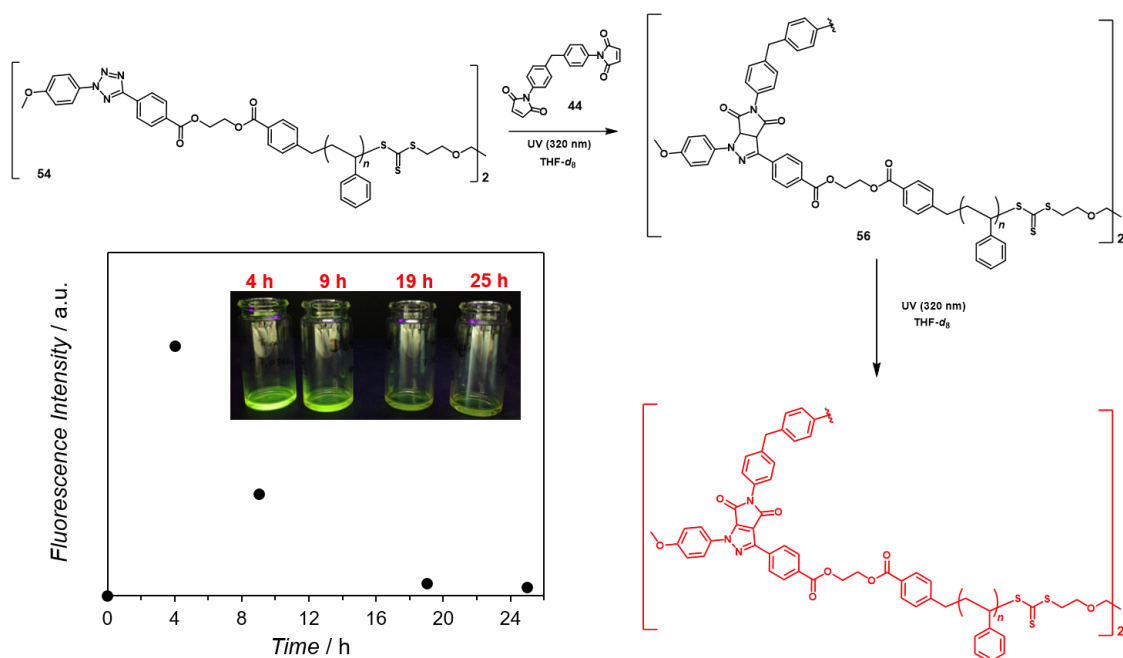


Figure 8.13. The fluorescence emission intensity of poly(pyrazolines) **56** prepared in $\text{THF-}d_8$ strongly decreases due to aromatization, if the samples are irradiated well beyond the completion of the NITEC reaction (< 4 h). Polymers obtained after 25 h irradiation are almost non-fluorescent.

8.3. Network Formation via NITEC

RAFT Polymerization

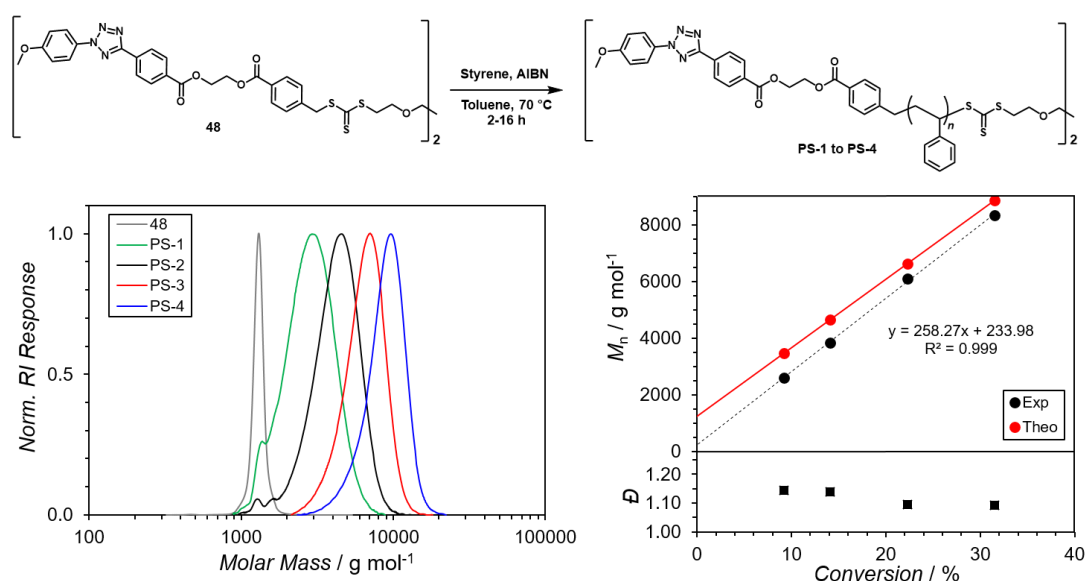


Figure 8.14. RAFT polymerization of styrene mediated by agent **48** yields tetrazole-bifunctional PS chains of different molecular weight (**PS-1** to **PS-4**). The corresponding SEC traces are plotted on the left graph. The right plot displays experimental molecular weight vs conversion data (black), showing a linear tendency, close to the expected theoretical values (red, calculated from Equation 2.23). Black squares represent experimental dispersity values D determined by SEC.

Photoreactor

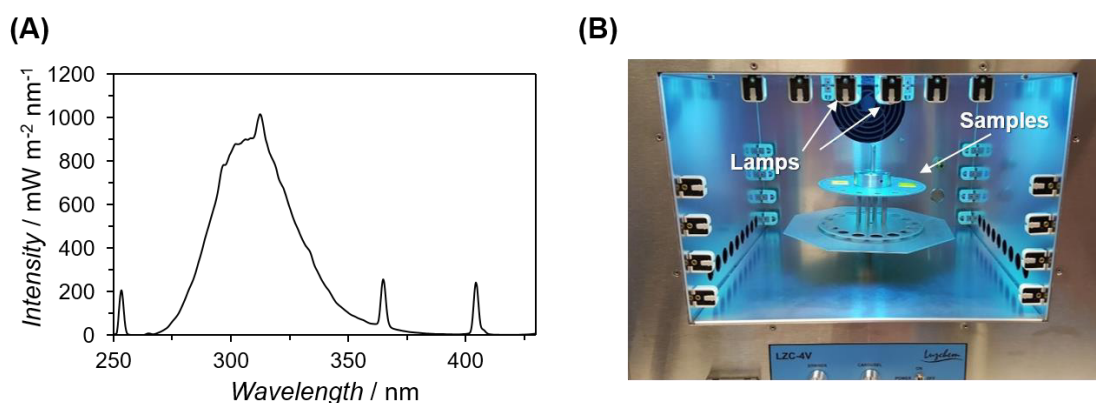


Figure 8.15. (A) Emission spectrum of the UV lamp used for network formation LZC-UVB ($\lambda_{\max} = 300$ nm), showing the absolute light intensity reaching the sample. (B) Setup employed for the photoreactions, using two LZC-UVB (300 nm) lamps that irradiate the samples from the top.

APPENDIX

Aminolysis of NITEC Networks

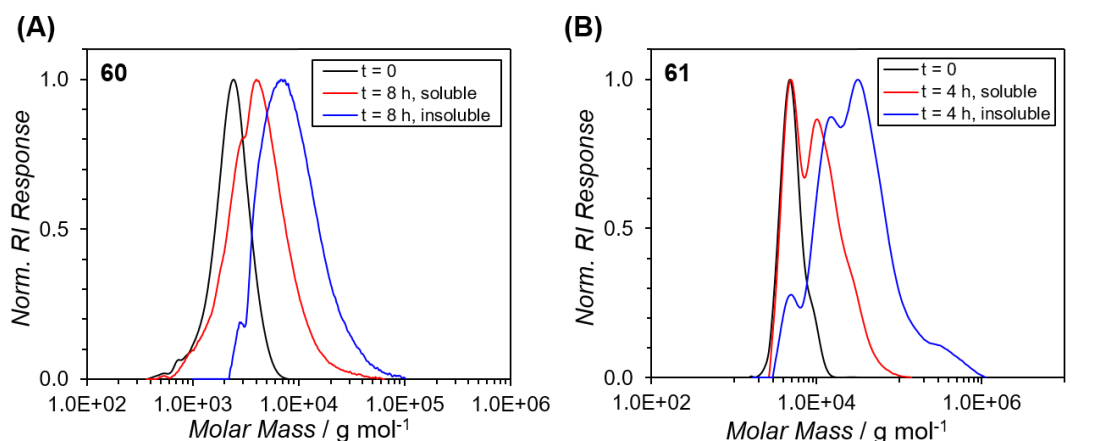


Figure 8.16. (A) SEC traces of networks **60** at $t = 0$ (black) and $t = 8$ h irradiation (red, soluble fraction; blue, insoluble fraction) after aminolysis. (B) SEC traces of networks **61** at $t = 0$ (black) and $t = 4$ h irradiation (red, soluble fraction; blue, insoluble fraction) after aminolysis.

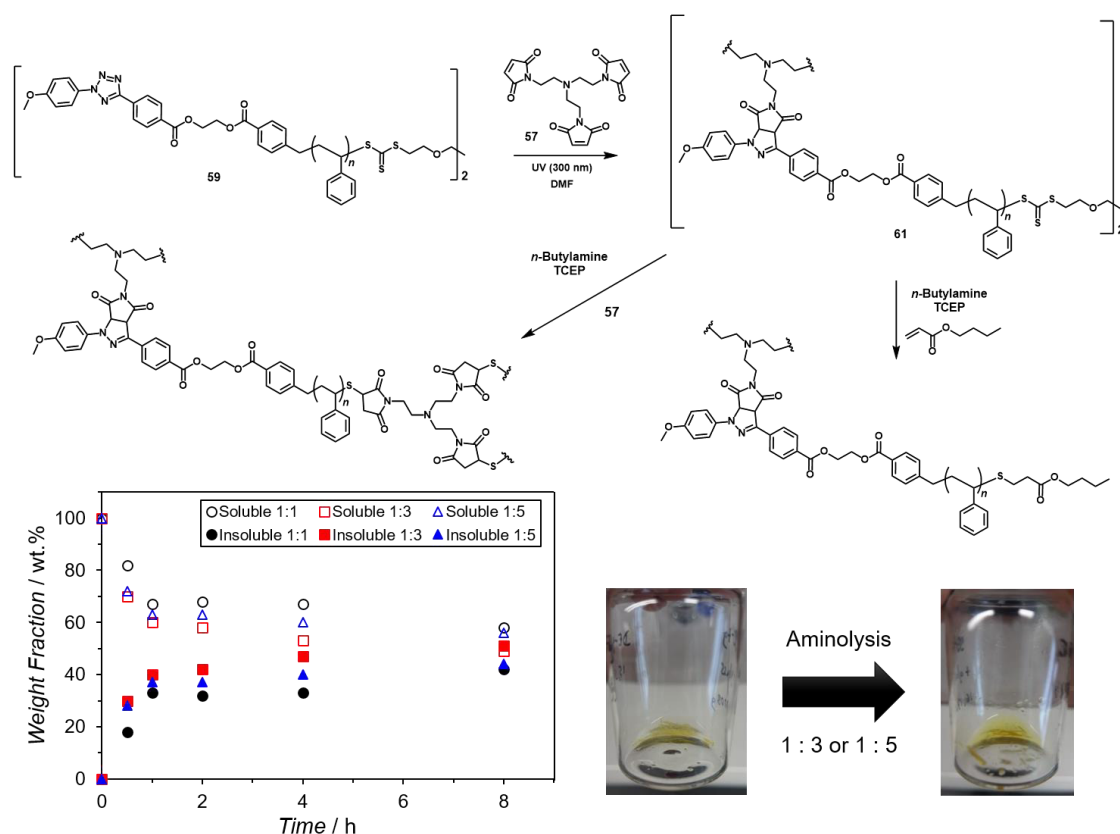


Figure 8.17. Network formation from **59** and **57** using different molar ratios tetrazole : maleimide (1 : 1, black dots; 1 : 3, red squares; 1 : 5, blue triangles). When excess of maleimide is used, higher amounts of insoluble fraction are obtained (bottom left plot), but aminolysis does not produce soluble material (bottom right pictures). The available maleimide groups act as crosslinker in the Michael addition of the thiol polymers yielded after aminolysis.

Effect of Aminolysis on Fluorescence

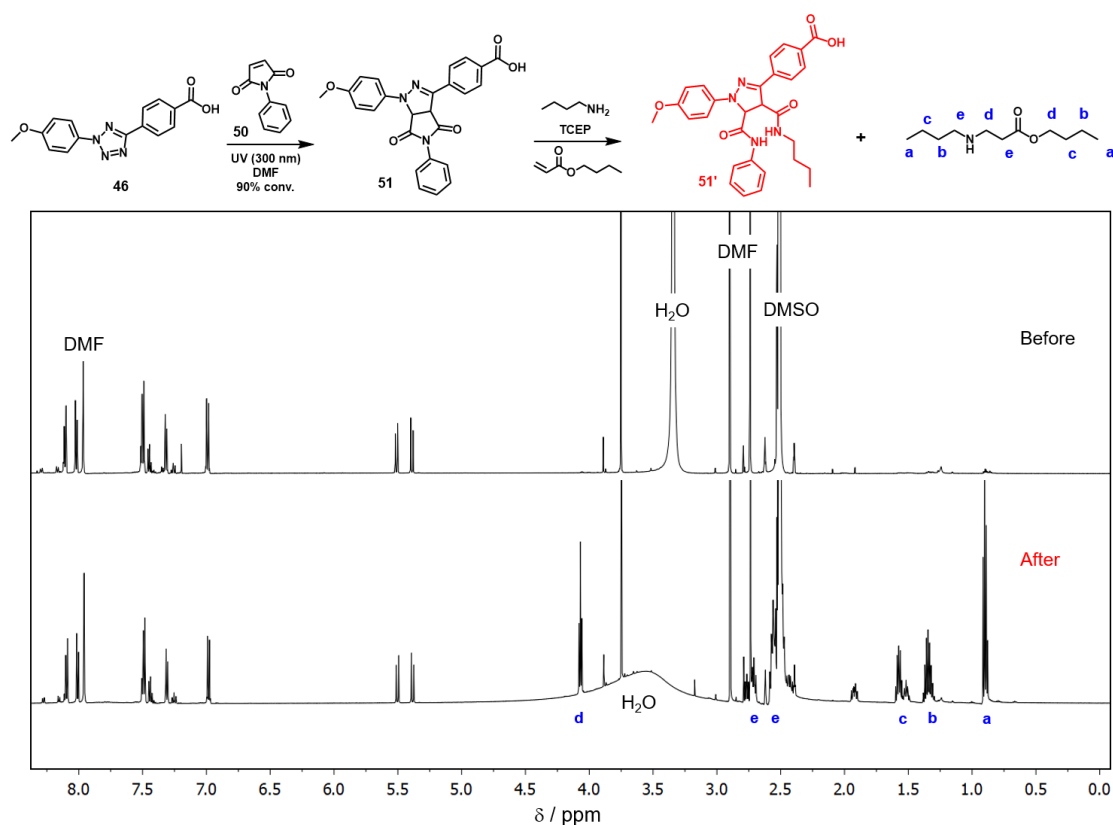


Figure 8.18. ¹H NMR spectra in DMSO-*d*₆ of standard solution **51** (at 90% conversion) before and after aminolysis.

Kinetics of Network Formation

The initial concentration of tetrazole has a strong impact on the kinetics of NITEC processes. Equimolar reaction of tetrazole **46** and *N*-ethylmaleimide at 320 nm in DMF solution was performed as a small molecule model for network formation (Figure 8.19). Increasing the initial concentration of **46** decelerates the tetrazole conversion (determined by NMR). By plotting $-\ln([\mathbf{46}])$ at different irradiation times, linear correlations are obtained, indicating pseudo-first order kinetics of the reaction rate. Keeping constant $[\mathbf{46}]_i$ at 3.62 mM, and changing the monomaleimide by the trimaleimide linker **57** (1 : 1 mol ratio tetrazole : maleimide) does not have significant influence in the kinetics of the NITEC reaction (Figure 8.20).

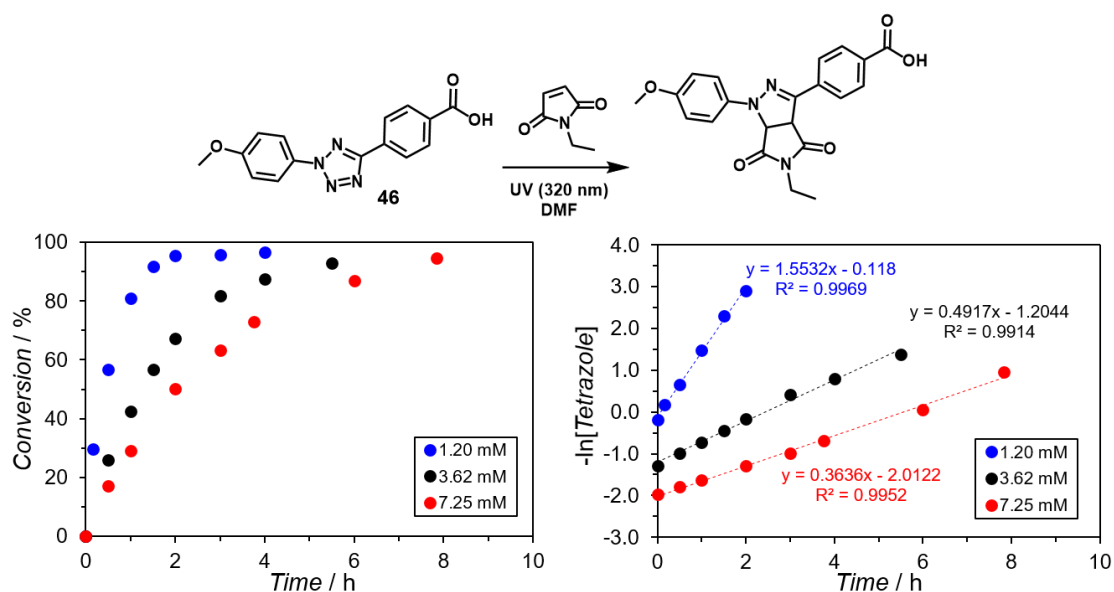


Figure 8.19. NITEC reaction between tetrazole **46** and *N*-ethylmaleimide (1 : 1 mol ratio) under irradiation at 320 nm. The initial concentration of **46** was set to 1.20 mM (blue), 3.62 mM (black), and 7.25 mM (red). Left plot display tetrazole conversion vs irradiation time, right plot shows $-\ln([\mathbf{46}])$ against reaction time. Dashed lines represent linear fits.

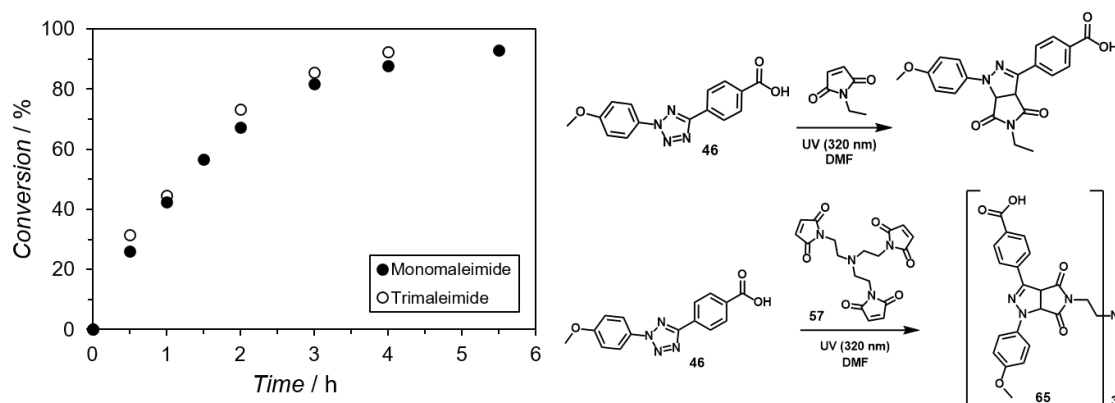


Figure 8.20. NITEC reaction (320 nm) between tetrazole **46** and *N*-ethylmaleimide (solid symbols), or trimaleimide **57** (open symbols), at 1 : 1 mol ratio tetrazole : maleimide. In both cases the initial concentration of **46** was kept at 3.62 mM.

Dangling Ends

The soluble and insoluble fractions of networks **60** and **61**, after aminolysis, were analyzed by SEC-ESI-MS. Due to the high molecular weights of the samples analyzed (see Figure 8.16), poor ionization of the species of interest was obtained. Nonetheless, ESI-MS spectra could be recorded for the region of low molecular weight of the SEC mass distribution.

Figure 8.21 display ESI-MS spectra for networks **61** at $t = 0$ and $t = 4$ h irradiation (soluble and insoluble fractions), after aminolysis. The most intense peaks could be assigned to the expected aminolysis products of unreacted tetrazole-PS chain ends. Species corresponding to thiol addition to butylamine (■), AIBN-initiated polymers (◆), and thiol addition to trimaleimide (▲) were found (Table 8.3). The relative abundance of unreacted tetrazole species in the insoluble fraction is lower than in the soluble fraction, indicating less incidence of dangling ends in the networks. However, the presence of dangling ends stemming from AIBN-initiated chains (unable to crosslink) was confirmed.

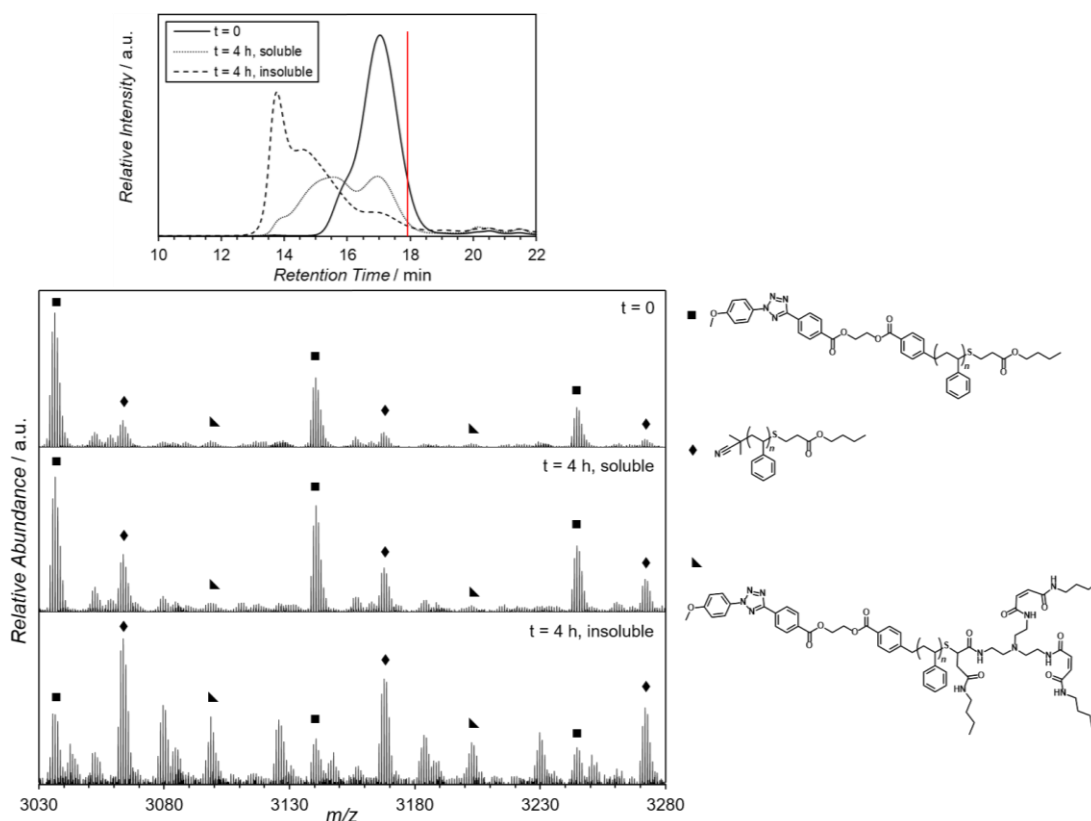


Figure 8.21. Comparison of ESI-MS spectra of samples **61** at $t = 0$ and $t = 4$ h irradiation (soluble and insoluble fractions), after aminolysis. Mass spectra were recorded at 17.8 min retention time (red line in SEC chromatogram).

Table 8.3. Structure assignment for the peaks in the MS spectrum in Figure 8.21.

Structure	n	m/z (exp)	m/z (theo)	$\Delta m/z$
■+I ⁻	22	3034.4936	3034.4970	0.0034
◆+I ⁻	26	3061.6533	3061.6457	0.0076
▲+I ⁻	18	3095.5515	3095.5530	0.0015

APPENDIX

On the other hand, Figure 8.22 compares ESI-MS spectra of soluble and insoluble fractions of networks **60**, obtained after 8 h irradiation (after aminolysis). In this case, the relative abundance of unreacted tetrazole species (■) is still high in the insoluble fraction, indicating a stronger incidence of dangling ends.

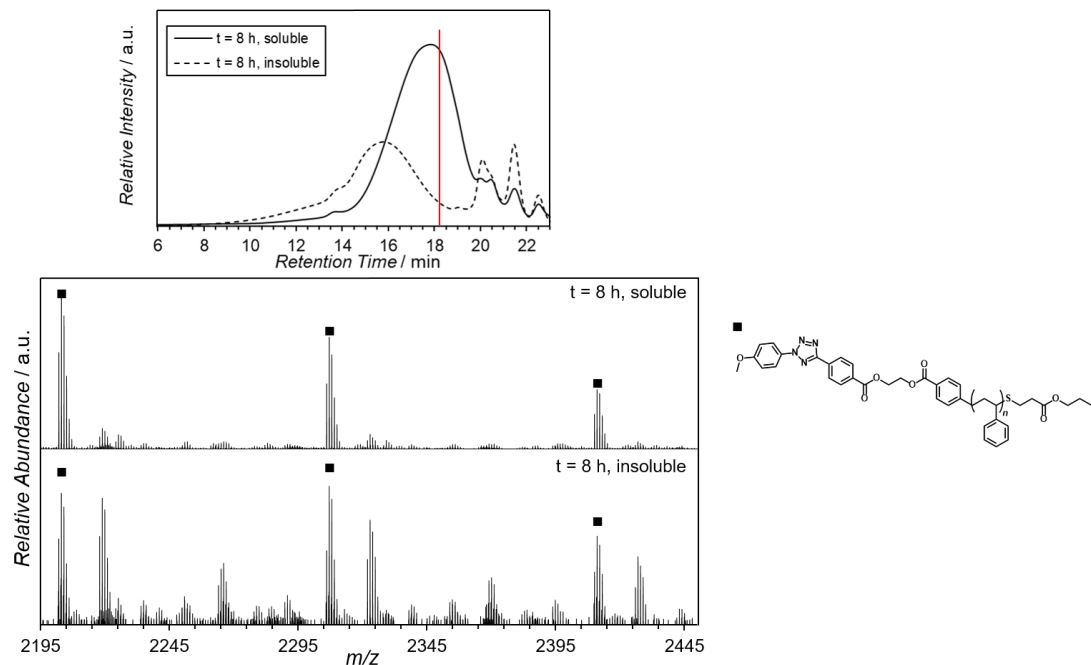


Figure 8.22. Comparison of ESI-MS spectra of samples **60** at $t = 8$ h irradiation (soluble and insoluble fractions), after aminolysis. Mass spectra were recorded at 18.2 min retention time (red line in SEC chromatogram).

Table 8.4. Structure assignment for the peaks in the MS spectrum in Figure 8.22.

Structure	n	m/z (exp)	m/z (theo)	$\Delta m/z$
[■+] ⁺	14	2202.0078	2201.9962	0.0116

8.4. Network Formation via Thiol-Ene Chemistry

Thiol-Ene Crosslinking

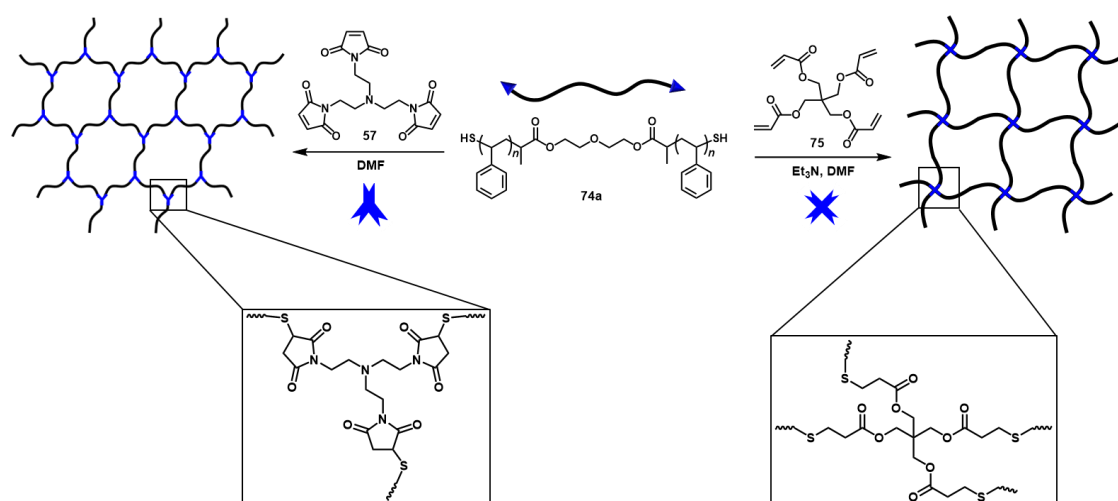


Figure 8.23. Crosslinking motifs of thiol-PS strands **74a** with trimaleimide **57** (left) or tetraacrylate **75** (right).

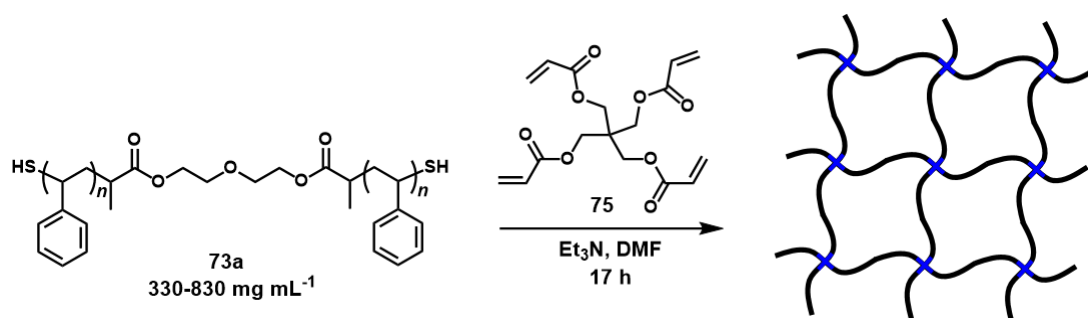


Figure 8.24. Crosslinking of thiol-PS strands **73a** (330–830 mg·mL⁻¹ in DMF) with tetraacrylate **75** (1 : 1 mol ratio thiol : ene), using triethylamine as catalyst.

Table 8.5. Yields of insoluble fraction for the crosslinking reaction depicted in Figure 8.24.

Entry	Concentration 73a	Insoluble Fraction
1	830 mg·mL ⁻¹	85 wt. %
2	530 mg·mL ⁻¹	76 wt. %
3	330 mg·mL ⁻¹	34 wt. %

APPENDIX

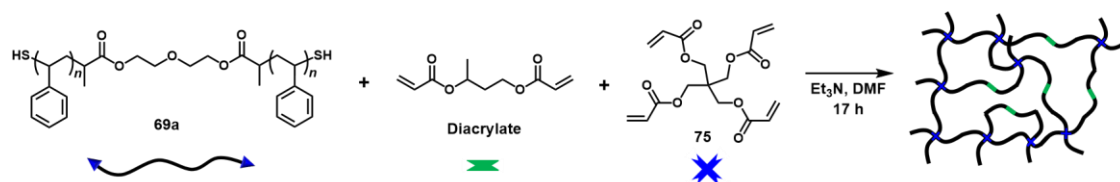


Figure 8.25. Crosslinking of thiol-PS **69a** with tetraacrylate **75** and 1,3-butanediol diacrylate (1 : 1 mol ratio thiol : ene), using triethylamine as catalyst.

Table 8.6. Yields of insoluble fraction and mass swelling ratio Q_m for the crosslinking reaction depicted in Figure 8.25, using different amounts of diacrylate.

Entry	Ratio tetra- : di-linker	Insoluble Fraction	Q_m^a
1	100 : 0	88 wt. %	11.0
2	75 : 25	78 wt. %	15.4
3	50 : 50	39 wt. %	23.5
4	25 : 75	3 wt. %	-

^a Mass swelling ratio, calculated from Eq. 2.55 after free swelling of the sticks in CHCl_3 for 24 h.

8.5. List of Abbreviations

2D	Two-Dimensional
Adipate	Bis(2-ethylhexyl) adipate
AFM	Atomic Force Microscopy
AIBN	Azobisisobutyronitrile
Al.	Aliphatic
AO	Atomic Orbital
Ar.	Aromatic
ARGET	Activators Regenerated by Electron Transfer
ATRP	Atom Transfer Radical Polymerization
BHT	Butylated Hydroxytoluene
CDCl ₃	Deuterated Chloroform
COSY	Correlated Spectroscopy
CTA	Chain Transfer Agent
\bar{D}	Dispersity Index
DA	Diels–Alder
dbm	Dibenzoylmethane
DCC	<i>N,N</i> -Dicyclohexylcarbodiimide
DCM	Dichloromethane
DFT	Density Functional Theory
DLW	Direct Laser Writing
DMAP	4-(Dimethylamino)pyridine
DMF	<i>N,N</i> -Dimethylformamide
DMSO	Dimethylsulfoxide
DMSO- <i>d</i> ₆	Deuterated Dimethylsulfoxide
DN	Double Networks
DOSY	Diffusion-Ordered Spectroscopy
<i>DP</i>	Degree of Polymerization

APPENDIX

DSC	Differential Scanning Calorimetry
DVB	Divinylbenzene
eq.	Equivalent
Eq.	Equation
ESI-MS	Electrospray Ionization Mass Spectrometry
Et ₃ N	Triethylamine
EtOAc	Ethyl acetate
FRP	Free-Radical Polymerization
G'	Storage Modulus
G''	Loss Modulus
H-H	Head-to-Head
HMBC	Heteronuclear Multiple-Bond Correlation Spectroscopy
HMQC	Heteronuclear Multiple-Quantum Correlation Spectroscopy
HSQC	Heteronuclear Simple-Quantum Correlation Spectroscopy
H-T	Head-to-Tail
ICAR	Initiators for Continuous Activator Regeneration
I.D.	Internal Diameter
IPC	Isopinocampheol
IPN	Interpenetrating Networks
IR	Infrared
ISC	Intersystem Crossing
IUPAC	International Union of Pure and Applied Chemistry
k_{act}	Activation Rate Coefficient
k_{add}	Addition Rate Coefficient
k_d	Initiator Dissociation Rate Coefficient
k_{deact}	Deactivation Rate Coefficient
k_{fragm}	Fragmentation Rate Coefficient
k_p	Propagation Rate Coefficient

k_t	Termination Rate Coefficient
k_{tr}	Chain Transfer Rate Coefficient
LAMs	Less-Activated Monomers
LC	Liquid Crystalline
MADIX	Macromolecular Design by Interchange of Xanthates
MAMs	More-Activated Monomers
M_c	Average Molecular Weight of Elastically Active Chains
Me ₂ PhP	Dimethylphenylphosphine
\bar{M}_n	Number Average Molecular Weight
MO	Molecular Orbital
MS	Mass Spectrometry
Mt*	Menthol-Styrene
\bar{M}_w	Weight Average Molecular Weight
m/z	Mass to Charge Ratio
NICAL	Nitrile Imine-Mediated Carboxylic Acid Ligation
NITEC	Nitrile Imine-Mediated Tetrazole-Ene Cycloaddition
NMP	Nitroxide-Mediated Polymerization
NMR	Nuclear Magnetic Resonance
NOE	Nuclear Overhauser Effect
NOESY	Nuclear Overhauser Effect Spectroscopy
Norm.	Normalized
O.D.	Outer Diameter
PBDG	Poly(γ -benzyl-D-glutamate)
PBLG	Poly(γ -benzyl-L-glutamate)
PCBDL	Poly(ϵ -carbobenzyloxy-D-lysine)
PCBL	Poly(ϵ -carbobenzyloxy-L-lysine)
PDMS	Polydimethylsiloxane
PEDG	Poly(γ -ethyl-D-glutamate)

APPENDIX

PELG	Poly(γ -ethyl-L-glutamate)
PTFE	Polytetrafluoroethylene (Teflon [®])
Phen-St	Phenanthroline-Styrene
PI	Photoinitiator
PS	Polystyrene
RAFT	Reversible Addition-Fragmentation Chain Transfer
RDC	Residual Dipolar Coupling
RDRP	Reversible-Deactivation Radical Polymerization
rf	Radiofrequency
RI	Refractive Index
R_f	Retardation Factor
R_i	Rate of Initiation
R_p	Rate of Polymerization
R_t	Rate of Termination
RT-FTIR	Real-Time Fourier-Transform Infrared Spectroscopy
R_{tr}	Rate of Chain Transfer
SEC	Size-Exclusion Chromatography
St	Styrene
TCEP	Tris(2-carboxyethyl)phosphine
TEMPO	2,2,6,6-tetramethyl-1-piperidynyl- <i>N</i> -oxyl
T_g	Glass Transition Temperature
THF	Tetrahydrofuran
THF- d_8	Deuterated Tetrahydrofuran
TLC	Thin-Layer Chromatography
TMS	Tetramethylsilane
TOCSY	Total Correlation Spectroscopy
UV	Ultraviolet
Vis	Visible

8.6. List of Figures, Schemes, and Tables

- Figure 1.1.** Schematic representation of the projects presented in the current thesis. Heterogeneous PS networks were prepared via free-radical polymerization, their mechanical properties and functionalization features were optimized for their application as alignment media (left panel). Homogeneous networks were obtained by RAFT polymerization followed by crosslinking via NITEC or thiol-ene protocols (right panel).....4
- Figure 2.1.** Possible structures obtained by copolymerization of two different monomers M_1 and M_210
- Figure 2.2.** During FRP macroradicals propagate (a), but are also susceptible to chain-braking scenarios like back-biting transfer (b), intermolecular transfer to polymer (c), transfer to monomer (d), termination by recombination (e), and others. These events heavily influence molecular weight distribution, branching, and end-group fidelity of the final polymer.....13
- Figure 2.3.** (A) Simplified mechanism of nitroxide-mediated polymerization, showing the equilibrium between dormant alkoxyamines and activated propagating radicals. (B) Structures of nitroxides typically employed in NMP.....14
- Figure 2.4.** Addition and fragmentation reactions in a RAFT polymerization pre-equilibrium, and selection of available Z and R groups. Figure adapted from Ref 42.....19
- Figure 2.5.** Stepwise growing of monomers into dimers, trimers, tetramers... characteristic of polycondensations.....22
- Figure 2.6.** Comparison of molecular weight evolution in living (or controlled) chain-addition polymerization (solid line), and step-growth polymerization (dashed line).....23
- Figure 2.7.** Combination of atomic orbitals (AOs) to form bonding (σ , π) and antibonding (π^* , σ^*) molecular orbitals (MOs), as well as non-bonding (n) orbitals. The possible electronic transitions are shown as vertical arrows and can be classified with the labels of the involved orbitals (e.g. $\sigma \rightarrow \sigma^*$ or $n \rightarrow \pi^*$ transitions). Figure adapted from Ref 91.....28
- Figure 2.8.** Jablonski diagram displaying singlet ground (S_0) and singlet or triplet excited (S_1 , S_2 , T_1 , T_2) electronic states, with their respective vibrational states.

APPENDIX

- Different radiative (straight arrows) or non-radiative (wavy arrows) photophysical processes can take place upon photon absorption. Figure adapted from Ref 92.....29
- Figure 2.9.** *N*-Substitution of aryltetrazoles changes the activation wavelength necessary for nitrile imine formation.....33
- Figure 2.10.** Structural representation of some polymer architectures. Depending on the connectivity of the constituting chains, polymers can be classified as linear, branched, cyclic or crosslinked topologies.....34
- Figure 2.11.** Schematic representation of an ideal network with $\nu_{el} = 10$ elastically active chains (each one of molecular weight M_c), $\mu_{el} = 8$ active junctions with functionality $f = 4$, and $\xi = 3$ cycles. Figure adapted from Ref 167.....36
- Figure 2.12.** The concentration of elastically active chains (A) in real networks decreases by the presence of structural defects like loops (B), dangling ends (C), and entanglements (D).....37
- Figure 2.13.** Synthesis of statistically crosslinked networks (A) by chain or step copolymerization, or by ligation of randomly functionalized polymer strands. Contrarily, end-linked networks (B) are obtained from end-group reaction of telechelic polymer precursors.....39
- Figure 2.14.** The onset of gelation for a crosslinking polymerization can be determined by rheology as the crossing point (red dashed line) between storage and loss moduli (G' and G'' , respectively).....41
- Figure 2.15.** (A) Splitting of nuclear level energies for $I = 1/2$ in an external magnetic field of magnitude B_0 , parallel to the z -axis. (B) Precession cone of the nuclear levels around the direction of B_0 . The higher population of N_0 confers the system an overall macroscopic magnetization M_0 . Figure adapted from Ref 246.....45
- Figure 2.16.** (A) Deflection of the macroscopic magnetization vector M_0 into the horizontal plane by applying a perpendicular rf oscillating field B_1 . (B) The generated in-plane magnetization M is detected as a signal. (C) Relaxation of M returns the system to the initial lower energy state M_0 . Figure adapted from Ref 246.....46
- Figure 2.17.** Schematic representation of dipolar coupling interaction between two spins (i and j) in an external magnetic field B_0 . Figure adapted from Ref 252.....50

- Figure 3.1.** Upon mechanical strain, network strands (black) orient anisotropically by stretching (right) or compressing (left) the gel. Initially isotropic analyte molecules (yellow), interacting with the polymer surface, adopt the same orientation of the gel strands, thus partially aligning in respect to the external magnetic field B_056
- Figure 3.2.** Representation of deuterium quadrupolar splittings ($\Delta\nu_Q$) for the determination of alignment strength in ^2H NMR spectra. In isotropic media $\Delta\nu_Q = 0$, while in anisotropic media $\Delta\nu_Q > 0$56
- Figure 3.3.** (A) Synthetic pathway for free-radical-based PS network sticks. (B) Free swelling of the dry PS sticks leads to volume increase in all directions, while swelling inside NMR tubes restrict the volume increase in the longitudinal direction (stretching).....57
- Figure 3.4.** (A) Stretched gel in a conventional 5 mm NMR tube. (B) Stretching apparatus. (C) Compressing apparatus.....58
- Figure 3.5.** (A) ^1H NMR spectrum of crosslinked PS stick swollen in CDCl_3 . (B) 2D projection of ^2H quadrupolar splittings ($\Delta\nu_Q$) of the CDCl_3 resonance signal, determined along the vertical direction of the stick (single $\Delta\nu_Q$ slice depicted in the ^2H NMR spectrum in C).....59
- Figure 3.6.** Quadrupolar splitting $\Delta\nu_Q$ of the CDCl_3 resonance signal (black), and equilibrium mass swelling ratio Q_m (red) of PS gels prepared with different amounts of DVB. Dashed black line is a guide for the eye, red solid line represents Q_m predicted from Flory–Rehner equation.....61
- Figure 3.7.** CDCl_3 ^2H NMR spectrum (left) and 2D projection of quadrupolar splittings $\Delta\nu_Q$ (right), determined in (A) stick **2** (0.2 mol% DVB, $\Delta\nu_Q \sim 27$ Hz), and (B) stick **3** (0.4 mol% DVB), for which no $\Delta\nu_Q$ could be determined. Cracking and breaking of the gels hinders $\Delta\nu_Q$ determination. The sharp resonance signal in the ^2H NMR spectra corresponds to isotropic CDCl_3 ($\Delta\nu_Q = 0$).....62
- Figure 3.8.** (A) PS sticks develop cracks upon free swelling in chloroform (left), which can be avoided by the use of plasticizers (right). (B) Variation of mass swelling ratio Q_m with increasing amounts of additives, toluene (blue), adipate (red), and DMF (black). (C) Decrease of T_g with increasing amounts of additives. No cracks were observed for samples with $T_g \leq 42$ °C. (D) Comparison of heat flow curves (right axis) and their corresponding first derivate (left axis) for networks **13** (black, DMF 15% v/v) and **20** (red, adipate 17.5% v/v), revealing broader transition temperature for **13**.....64

APPENDIX

Figure 3.9. (A) Comparison of fast free swelling (left) and slow swelling (right) procedures for PS disks **3** (DVB 0.4 mol%) in toluene. (B) Frequency sweep curves displaying storage (G' , black) and loss (G'' , red) moduli for samples **1** (DVB 0.1 mol%, dots), **3** (DVB 0.4 mol%, squares), and **20** (DVB 0.4 mol% + 17.5% v/v adipate, triangles) fully swollen in toluene.....65

Figure 3.10. (A) Schematic representation of a fully compressed PS gel that is allowed to relax in small decompression steps. (B) Variation of CDCl_3 quadrupolar splitting in network **20** (DVB 0.4 mol%, 17.5% v/v adipate). Fully compressed state is depicted in black ($\Delta\nu_Q$ max.) and intermediate steps in grey. ^2H δ values were artificially fixed at 6.85 ppm (right signal) to facilitate comparison. (C) Variation of CDCl_3 $\Delta\nu_Q$ in network **20** between fully compressed (black) and fully relaxed (red) samples. In the relaxed state, two isotropic CDCl_3 signals can be seen, corresponding to the solvent inside ($\delta = 7.14$ ppm) and outside the gel ($\delta = 7.26$ ppm).....66

Figure 3.11. ^1H NMR spectrum of PS network **20** (DVB 0.4 mol% + 17.5% v/v adipate) showing the characteristic signals of PS (red) and plasticizer (blue).....67

Figure 3.12. Variation of T_g (dots, left axis) and mass swelling ratio (crosses, right axis) of 0.4 mol% DVB crosslinked networks prepared from styrene and different amounts of (A) pentyl-styrene **26**, and (B) dodecyl-styrene **27**. No cracks observed upon swelling for samples with $T_g \leq 42$ °C. Networks prepared with > 55 mol% **26** (or 10–35 mol% **27**) were too brittle in the dry state. Samples obtained from > 35 mol% **27** were very soft and difficult to handle.....69

Figure 3.13. CDCl_3 ^2H NMR spectra depicting the quadrupolar splittings $\Delta\nu_Q$ obtained in (A) sample **33** (5% (-)-M* **28**, $\Delta\nu_Q = 40$ Hz), (B) sample **34** (5% (+)-M* **29**, $\Delta\nu_Q = 37$ Hz), and (C) sample **35** (5% racemic mixture **28** + **29**, $\Delta\nu_Q = 41$ Hz)....75

Figure 3.14. Frequency sweep curves displaying storage (G' , black) and loss (G'' , red) moduli for gels **2** (0 mol% **28**, dots), **33** (5 mol% **28**, squares), and **30** (25 mol% **28**, triangles). Measurements were performed on disks fully swollen in toluene.....76

Figure 3.15. ^1H NMR spectra in CDCl_3 of 50% St–**28** reaction mixture before (top) and after (middle) polymerization, and resulting copolymer after precipitation in cold methanol (bottom). Signals of the residual monomer **28** in the precipitated polymer are marked with asterisks.....77

- Figure 3.16.** ^1H NMR spectra in CDCl_3 of some copolymers (10%, 50%, and 95% St) after precipitation in cold methanol. Signals of the residual monomer **28** used in the calculations are denoted by an asterisk (m^*).....78
- Figure 3.17.** Fineman-Ross (A) and Fineman-Ross inverted (B) methods for the determination of reactivity ratios. From the slope and intercept of the linear fits, values of $r_1 = 0.42$, $r_2 = 1.39$ (Fineman-Ross) and $r_1 = 0.36$, $r_2 = 1.14$ (Fineman-Ross inverted) are obtained.....80
- Figure 3.18.** Kelen-Tüdös method for the determination of reactivity ratios: $r_1 = 0.39$, $r_2 = 1.19$81
- Figure 3.19.** Mayo-Lewis method for the determination of reactivity ratios. Non-linear least-squares fit of the Mayo-Lewis plot gives $r_1 = 0.36$, $r_2 = 1.16$81
- Figure 3.20.** Molecular structures of the model chiral analytes: (A) (+)- vs (-)-IPC (isopinocampheol), (B) Altenuene vs isoaltenuene.....83
- Figure 3.21.** (A) P.E.HSQC spectrum of (+)-IPC in isotropic CDCl_3 solution. $^1J(\text{C,H})$ values of signals C4–H4a (126.89 Hz) and C4–H4s (126.63 Hz), highlighted in blue, are given. (B) P.E.HSQC spectrum of (+)-IPC inside swollen gel **31**. The total couplings are obtained in this case, C4–H4a (128.36 Hz) and C4–H4s (129.49 Hz). The difference between T and J couplings yields the RDCs for C4–H4a (1.47 Hz) and C4–H4s (2.86 Hz).....84
- Figure 3.22.** (A) Determination of RDCs of (+)-IPC in mirror gels **30** and **31**. The difference between these RDC values (Δ_{RDC}) is used to evaluate enantiodifferentiation. (B) Determination of RDCs of enantiomers (+)-IPC and (-)-IPC in PS gel **30**. The corresponding Δ_{RDC} values are used to evaluate enantiodifferentiation.....84
- Figure 3.23.** (A) P.E.HSQC spectrum of altenuene in isotropic CDCl_3 solution. $^1J(\text{C,H})$ values of signals C4–H4a (133.68 Hz) and C4–H4b (129.94 Hz), highlighted in blue, are given. (B) P.E.HSQC spectrum of altenuene inside swollen gel **31**. The total couplings are obtained in this case, C4–H4a (122.21 Hz) and C4–H4b (122.48 Hz). The difference between T and J couplings yields the RDCs for C4–H4a (-11.47 Hz) and C4–H4b (-7.46 Hz).....87
- Figure 3.24.** (A) Determination of RDCs of the diastereomers altenuene and isoaltenuene in (-)-PS gel **30**. The difference between these RDC values (Δ_{RDC}) is used to evaluate enantiodifferentiation. (B) Determination of RDCs of altenuene

APPENDIX

- and isolatenuene in (+)-PS gel **31**. The corresponding Δ_{RDC} values are used to evaluate enantiodifferentiation.....87
- Figure 3.25.** Functionalization of PS networks with lanthanide ions. Phenanthroline-PS networks **38** were swollen in a CHCl_3 solution of $[\text{Eu}(\text{dbm})_3(\text{H}_2\text{O})_2]$ to afford europium-coordinated gels **38-Eu**, characterized by strong red fluorescence emission. After washing the samples to remove excess of lanthanide precursor, the fluorescence emission of **38-Eu** does not disappear, as it is the case for the negative control **12** (plain PS gels).....92
- Figure 4.1.** NITEC approach to fluorescent AA–BB step-growth polymers by reaction of a bifunctional tetrazole and a bifunctional maleimide.....100
- Figure 4.2.** (A) Synthesis of fluorescent step-growth polymers **45** from AA–BB monomers **43** and **44**, under UV irradiation. (B) SEC traces of crude samples obtained after 0 h (red), 5 h (grey), and 15 h (black) irradiation. Signals of starting monomers **43** and **44** are marked by arrows, as well as signals corresponding to degradation products. (C) Fluorescence emission ($\lambda_{\text{max}} = 494 \text{ nm}$) of crude samples **45** after 0 h (red), 5 h (grey), and 15 h (black) irradiation.....101
- Figure 4.3.** ^1H NMR spectra in $\text{DMSO}-d_6$ of crude NITEC reaction between tetrazole **41** and *N*-methylmaleimide after 0 min (red) and 15 min (black) irradiation at 320 nm. Resonance signals marked in blue correspond to side products, while signals in yellow correspond to the expected pyrazoline protons (1% yield).....102
- Figure 4.4.** ^1H NMR spectra in $\text{DMSO}-d_6$ of crude NITEC reaction between tetrazole **46** and *N*-methylmaleimide after 0 min (red) and 15 min (black) irradiation at 320 nm. Resonance signals marked in blue correspond to side products, while signals in yellow correspond to the expected pyrazoline protons (5% yield).....103
- Figure 4.5.** Left axis: UV-vis absorption spectra of monomers **43** (red) and **48** (black), showing a bathochromic shift in the absorption maximum for the methoxy-substituted derivative **48**. Right axis: Emission spectrum of the UV lamp (Arimed B6, $\lambda_{\text{max}} = 320 \pm 30 \text{ nm}$) used as irradiation source (dashed black line).....103
- Figure 4.6.** Synthesis of step-growth polymers **49** from monomers **48** and **44** under UV irradiation, $\lambda = 320 \text{ nm}$. The ^1H NMR resonance signals of monomer (1) and polymer (2, 3, 4, and 5) can be used to determine monomer conversion and polymer yield. Adapted with permission from Ref 299. Copyright 2017, American Chemical Society.....104

- Figure 4.7.** (A) Correlation of conversion of **48** and yield of poly(pyrazoline) **49** in CDCl_3 , calculated by NMR using Equations 4.1–4.4. (B) Kinetic plot displaying conversion of monomer **48** with increasing irradiation time. (C) Decrease in the concentration of **48** during the course of the reaction. (D) Plot of the inverse of monomer concentration ($1 / [\mathbf{48}]$) against reaction time, showing a linear relationship.....105
- Figure 4.8.** (A) SEC traces of step-growth polymers **49** obtained after different irradiation times. Signals of starting materials **44** and **48** are marked by arrows, as well as signals corresponding to dimers, trimers and tetramers. (B) UV-vis absorption spectra of samples **49** after different irradiation times. Broad absorption bands centered at 400 nm are characteristic of the poly(pyrazoline) products. (C) Fluorescence intensity of samples **49** after different irradiation times. The maximum emission increases as polymerization proceeds. Adapted with permission from Ref 298. Copyright 2017, American Chemical Society.... 106
- Figure 4.9.** ^1H NMR spectra in $\text{DMSO}-d_6$ of crude pyrazoline standards **51** obtained after irradiation of tetrazole **46** and maleimide **50** for 0 h, 0.5 h, and 6 h at 320 nm. Adapted with permission from Ref 298. Copyright 2017, American Chemical Society.....107
- Figure 4.10.** (A) Fluorescence emission spectra of crude standards **51** in DMF. (B) Calibration curve for the correlation of fluorescence intensity and pyrazoline concentration. Adapted with permission from Ref 298. Copyright 2017, American Chemical Society.....108
- Figure 4.11.** ^1H NMR spectra in $\text{DMSO}-d_6$ of initial mixture of **44** and **46** at $t = 0$, and crude sample **52** obtained after 3 h irradiation (93% yield = 3.3 mM pyrazoline).....109
- Figure 4.12.** Fluorescence emission spectrum of crude sample **52** obtained after 3 h irradiation (left). Interpolation in the calibration curve (right) gives a concentration of 3.5 mM pyrazoline..... 109
- Figure 4.13.** Control experiments performed with **46** and different nucleophiles. Fluorescence emission intensity of each adduct (in DMF) was recorded and compared with the expected emission of the pyrazoline standard (Control 2). Adapted with permission from Ref 298. Copyright 2017, American Chemical Society.....110

APPENDIX

- Figure 4.14.** Conversion of monomer **48** in CDCl_3 with increasing irradiation time determined via NMR (solid symbols) and fluorescence spectroscopy (open symbols).....111
- Figure 4.15.** (A) Yield of pyrazoline in polymers **49**, determined by NMR (black solid symbols) and fluorescence spectroscopy (open symbols). Red solid symbols represent the percentage of aromatization, calculated by integration of the NMR resonance signals around 8.5 ppm. (B) Exemplary NMR spectra in $\text{THF-}d_8$ of samples **49** after 0 h, 2.5 h, and 14 h irradiation.....111
- Figure 4.16.** (A) Conversion kinetics for the step-growth polymers **49**, determined by NMR (solid symbols) and fluorescence spectroscopy (open symbols) in CDCl_3 (black dots) and $\text{THF-}d_8$ (red squares). (B) Corresponding plot of weight average molecular weight vs. conversion. Dashed line represents the theoretical Carothers curve. Adapted with permission from Ref 298. Copyright 2017, American Chemical Society.....112
- Figure 4.17.** (A) Conversion vs. reaction time for step-growth polymers prepared with different ratios of monomers **48** and **44** (determined by NMR) in CDCl_3 . (B) Corresponding \bar{M}_w vs. conversion plot. Dashed line represents the Carothers curve. (C) SEC traces of polymers prepared from 1.01 : 1 ratio **48** : **44** after 0 h, 8 h, 16 h, and 24 h irradiation. Adapted with permission from Ref 298. Copyright 2017, American Chemical Society.....113
- Figure 4.18.** (A) RAFT polymerization of styrene mediated by **48** to yield bifunctional tetrazole-PS **53** and **54**. (B) SEC traces (RI detector) of PS strands **53** and **54**. Adapted with permission from Ref 298. Copyright 2017, American Chemical Society.....114
- Figure 4.19.** ESI-MS spectrum (positive mode) of bifunctional tetrazole-PS **53**, showing typical mass and isotopic pattern for the expected structure \blacktriangleright (simulated pattern depicted in blue in the inset). A secondary PS structure corresponding to AIBN-initiated polymer (\blacktriangle), inherent to the RAFT process, was also found.....114
- Figure 4.20.** (A) Step-growth polymerization of PS samples **53** or **54** with bismaleimide **44** to yield poly(pyrazolines) **55** and **56**, respectively. (C) SEC traces (UV detector) of NITEC step-growth polymers **55** at different irradiation times. (D) Corresponding SEC traces of polymers **56**. Insets display conversion determined by NMR (solid symbols) and fluorescence (open symbols) spectroscopy. Adapted with permission from Ref 298. Copyright 2017, American Chemical Society....115

- Figure 4.21.** Yield of pyrazoline adducts in polymers **55** (A) and **56** (B), determined by NMR (black solid symbols) and fluorescence (open symbols). The yield of the aromatization by-product is represented in each case by red solid symbols..... 116
- Figure 4.22.** (A) Conversion vs. reaction time for step-growth polymers **55** (black) and **56** (red), determined by NMR (solid symbols) and fluorescence (open symbols) spectroscopy. (B) Plot of the inverse of precursor concentration (average of **53** and **54** determined by NMR) against reaction time..... 117
- Figure 4.23.** (A) Left axis: Conversion vs. reaction time for step-growth polymers **56**, prepared with different molar ratios of precursors **54** and **44** (solid symbols). The open symbols (right axis) represent the extent of aromatization of the different samples with irradiation time. (B) UV-vis absorption spectra of **56** (1 : 1 ratio **54** : **44**) at different irradiation times. (C) Plot of weight average molecular weight vs. conversion for polymers **56** prepared with different **54** : **44** molar ratios. Dashed line represents the theoretical Carothers curve. Adapted with permission from Ref 298. Copyright 2017, American Chemical Society..... 118
- Figure 4.24.** (A) General reaction scheme of network formation. Well-defined end-capped tetrazole PS chains are obtained via RAFT polymerization and subsequently end-linked with a trifunctional maleimide via NITEC chemistry. (B) Structure of tetrazole-RAFT agent **48**. (C) Structure of trimaleimide linker **57**. (D) Structure of fluorescent pyrazoline crosslink motifs obtained after NITEC ligation. Adapted with permission from John Wiley and Sons, Ref 299..... 119
- Figure 4.25.** ^1H NMR spectrum in CDCl_3 of RAFT PS **58**. Ratio of repeat unit resonance integrals (i, 7.2–6.3 ppm) to end group resonance integrals (a, 3.9–3.8 ppm; e, 8.4–8.3 ppm) results in $\bar{M}_{\text{n(NMR)}} = 2700 \text{ g}\cdot\text{mol}^{-1}$. Adapted with permission from John Wiley and Sons, Ref 299..... 121
- Figure 4.26.** ^1H NMR spectrum in CDCl_3 of RAFT PS **59**. Ratio of repeat unit resonance integrals (i, 7.2–6.3 ppm) to end group resonance integrals (a, 3.9–3.8 ppm; e, 8.4–8.3 ppm) results in $\bar{M}_{\text{n(NMR)}} = 7300 \text{ g}\cdot\text{mol}^{-1}$. Adapted with permission from John Wiley and Sons, Ref 299..... 121
- Figure 4.27.** SEC-ESI-MS spectrum (negative mode) of RAFT PS **59** showing typical mass and isotopic pattern for the expected structure \blacksquare . Secondary PS structure \blacklozenge (AIBN-initiated polymer) was also found. The spectrum was recorded at the maximum of the molar mass distribution (retention time 15.9 min in SEC chromatogram). Adapted with permission from John Wiley and Sons, Ref 299..... 122

APPENDIX

- Figure 4.28.** NITEC network formation from PS precursor **59** and crosslinker **57**, irradiated 15 h, 24 h, and 48 h at 320 nm.....123
- Figure 4.29.** Comparison of network formation at different initial concentrations of PS precursors **58** and **59**. Samples were irradiated at 320 nm for 64 h.....124
- Figure 4.30.** NITEC network formation from PS precursor **59** and crosslinker **57**, irradiated 48 h at 320 nm, either inside glass vials or between two glass slides.....124
- Figure 4.31.** (A) SEC traces of soluble fractions obtained from the NITEC reaction of **59** and **57** (in glass slides), after several irradiation times. (B) Comparison of SEC traces of soluble fractions after 48 h irradiation, obtained in glass slides (solid line) and conical vials (dashed line).....126
- Figure 4.32.** Schematic representation of the photoreactors used for network formation. (A) One lamp ($\lambda_{\text{max}} = 320$ nm) in the middle and samples revolving around it at 5 cm distance. (B) Two lamps ($\lambda_{\text{max}} = 300$ nm) irradiating the samples from the top, at 11 cm distance. (C) Comparison of the absolute light intensity reaching the samples in each of the photoreactors: 320 nm (red line) and 300 nm (black line).....126
- Figure 4.33.** (A) PS precursors **58** or **59** and trimaleimide **57** were mixed in DMF and sandwiched between two glass slides. Initial concentration of tetrazole groups is ca. 0.50 M for **58** and ca. 0.19 M for **59**. (B) Irradiation at 300 nm produces yellow solids. (C) From the crude solid, soluble and insoluble fractions are isolated by extensive washing with THF and chloroform. Insoluble networks **60** (from short PS **58**) and **61** (from long PS **59**) are thus obtained. (D) Evolution of soluble (red) and insoluble (black) fractions of networks **60** (crosses) and **61** (dots), at different irradiation times. Error bars represent standard deviation from three independent replicas. Solid and dashed lines are guides for the eye. Adapted with permission from John Wiley and Sons, Ref 299.....127
- Figure 4.34.** (A) ^1H NMR spectra in CDCl_3 of mixtures of **62** and **57**, irradiated at 300 nm for different times. Ratios of resonance signals d/b , d/c , e/b , e/c , d/a , and e/a , were used to determine degradation of trithiocarbonate groups. (B) Plot of percentage of trithiocarbonate groups vs. irradiation time. Ratios from NMR signals were averaged (error bars represent standard deviation) and normalized to 100% for $t = 0$. Adapted with permission from John Wiley and Sons, Ref 299.....129

- Figure 4.35.** (A) Solutions of RAFT-PS **63** and pyrazoline standards **51** in THF were casted onto glass slides by spin coating, obtaining homogeneous fluorescent films. (B) Fluorescence cuvette with special holder for glass slides. The films were thus analyzed in the solid state to construct a calibration curve. Error bars represent standard deviation from eight independent samples..... 130
- Figure 4.36.** (A) Preparation of step-growth polymers from tetrazole-functional PS **59** and bismaleimide **44** in solution, at 320 nm irradiation for 0–7 h. (B) The different samples were dissolved in THF, casted onto glass slides by spin coating and fluorescence intensity measured in the solid state. (C) The yield of poly(pyrazoline) was calculated either by NMR (solid black dots), fluorescence in solution (open black dots), or fluorescence in solid state (open red squares), giving similar results..... 131
- Figure 4.37.** (A) Photographs of samples **61** after $t = 0$ (left) and $t = 8$ h irradiation at 300 nm. (B) Insoluble fraction of **61** ($t = 8$ h) remaining in the glass slide after extensive washing with solvents. (C) Both soluble (left) and insoluble (right) fractions of **61** exhibit strong fluorescence emission..... 132
- Figure 4.38.** (A) One-pot aminolysis/Michael addition of RAFT polymer **63** to produce butyl acrylate-capped chains **63a**. (B) SEC traces (RI detector) of polymer samples before (**63**, solid line) and after (**63a**, dashed line) aminolysis. (B) SEC traces (UV detector at 320 nm) of **63** (solid line) and **63a** (dashed line), showing strong decrease in the signal intensity after aminolysis..... 132
- Figure 4.39.** (A) Aminolysis of RAFT tetrazole-PS precursors **58** or **59**. Treatment with *n*-butylamine in the presence of TCEP generates thiol-capped polymers **58-SH** or **59-SH** which react in situ with butyl acrylate in a Michael-type addition. Polymer strands **58a** or **59a**, with half the molecular weight of their parent polymers, are thus obtained. (B) SEC traces of PS samples before (**58** and **59**, solid blue and black lines, respectively) and after aminolysis (**58a** and **59a**, dashed blue and black lines, respectively). Adapted with permission from John Wiley and Sons, Ref 299..... 133
- Figure 4.40.** ^1H NMR spectra in CDCl_3 of RAFT PS before and after aminolysis, **58** and **58a**, respectively. Disappearance of resonance signals j and k, and appearance of new signals l and m confirm the structure of the expected product. Adapted with permission from John Wiley and Sons, Ref 299..... 134
- Figure 4.41.** SEC-ESI-MS spectrum (negative mode) of aminolysis product **59a** showing typical mass and isotopic pattern for the expected structure ■.

APPENDIX

- Secondary structure **◆**, corresponding to incomplete aminolysis, was also found. The spectrum was recorded at the maximum of the molar mass distribution (retention time 17.1 min in SEC chromatogram). Reprinted with permission from John Wiley and Sons, Ref 299.....135
- Figure 4.42.** Comparison of SEC traces, after aminolysis, of (A) samples **61**, soluble fraction, and (B) samples **61**, insoluble fraction, at different irradiation times. Adapted with permission from John Wiley and Sons, Ref 299.....135
- Figure 4.43.** Aminolysis of insoluble networks **60** and **61** to produce soluble network fragments. These can be analyzed by fluorescence spectroscopy in solution to retrieve the original number of pyrazoline groups. Adapted with permission from John Wiley and Sons, Ref 299.....136
- Figure 4.44.** (A) Aminolysis of RAFT tetrazole-PS **59** followed by Michael addition to butyl acrylate to yield **59a**, or trimaleimide **57**, producing adduct **59b**. (B) SEC traces of PS samples before aminolysis (**59**, black line), and after coupling with butyl acrylate (**59a**, red line) or trimaleimide (**59b**, blue line). (C) SEC-ESI-MS spectra of adducts **59a** (top) and **59b** (bottom). Adapted with permission from John Wiley and Sons, Ref 299.....137
- Figure 4.45.** SEC-ESI-MS spectrum (negative mode) of aminolysis product **59b** showing typical mass and isotopic pattern for the expected structure **■**. Secondary structure **◆**, corresponding to thiol-capped polymer, was also found. The spectrum was recorded at 18.9 min retention time in the SEC chromatogram.....138
- Figure 4.46.** Correlation of fluorescence intensity and concentration of pyrazoline **51** before (black) and after (red) aminolysis. Adapted with permission from John Wiley and Sons, Ref 299.....139
- Figure 4.47.** (A) Treatment of pyrazoline standard **51** (at 90% conversion) with the reagents used for aminolysis produces the open structure **51'**. (A) ¹H NMR spectra in DMSO-*d*₆ of standard solution **51** before (black) and after (red) aminolysis. (B) ESI-MS spectrum (positive mode) of **51** after aminolysis, confirming the proposed structure (**[51'+Na]⁺** *m/z* Calc.: 537.21139, Exp.: 537.21051). Adapted with permission from John Wiley and Sons, Ref 299.....140
- Figure 4.48.** Fluorescence emission of pyrazoline standards **51** (38%, 58%, and 74% conversion) before aminolysis (black), after aminolysis (red), after adding only

- amine and acrylate (blue), after adding amine (yellow), and after adding only acrylate (green). Adapted with permission from John Wiley and Sons, Ref 299.....141
- Figure 4.49.** (A) Reaction scheme of tetrazole-PS **59** and *N*-phenylmaleimide **50** to produce fluorescent polymer **64**, which was further aminolyzed to **64a**. (B) Fluorescence emission of polymers **64** (black) and **64a** (red) at different conversions. (C) SEC traces of **64** (black) and **64a** (red). Adapted with permission from John Wiley and Sons, Ref 299.....142
- Figure 4.50.** ESI-MS spectrum (negative mode) of aminolysis product **64a** showing typical mass and isotopic pattern for the expected structure ■. Secondary structures ♦ (corresponding to incomplete aminolysis) and ● (corresponding to AIBN-initiated polymer after aminolysis), were also found. Reprinted with permission from John Wiley and Sons, Ref 299.....142
- Figure 4.51.** ¹H NMR spectra in DMSO-*d*₆ of crude standards **65** obtained after irradiation of tetrazole **46** (3 eq.) and trimaleimide **57** (1 eq.) for 0 h, 0.5 h, and 1.5 h at 300 nm. Adapted with permission from John Wiley and Sons, Ref 299.....143
- Figure 4.52.** (A) Reaction scheme to produce pyrazoline standards **65**, and their corresponding treatment by aminolysis to afford structure **65'**. (B) Fluorescence calibration curve derived from standards **65** before aminolysis. (C) Fluorescence calibration curve derived from standards **65'** after aminolysis. Adapted with permission from John Wiley and Sons, Ref 299.....145
- Figure 4.53.** Comparison of yield of NITEC reaction in the soluble fractions of networks **61** at different irradiation times. Yields were calculated from fluorescence measurements before (black) and after (red) aminolysis, from suitable calibration curves, giving similar results. Adapted with permission from John Wiley and Sons, Ref 299.....145
- Figure 4.54.** (A) Aminolysis of soluble and insoluble fractions of networks **60** and **61**. The linking percentages (NITEC yield) of networks **60** (B) and **61** (C), at different irradiation times, were obtained from fluorescence emission of soluble (red symbols) and insoluble (black symbols) fractions after aminolysis. Blue symbols represent overall yields. Lines are guides for the eye. Error bars represent standard deviation from three independent samples. Adapted with permission from John Wiley and Sons, Ref 299.....146

APPENDIX

- Figure 4.55.** (A) Network formation between PS **59** ([tetrazole]_i ≈ 0.19 M) and trimaleimide **57**. (B) NITEC reaction between **46** ([tetrazole]_i = 0.22 M) and *N*-ethylmaleimide, using PS **63** as matrix. (C) Comparison of reaction kinetics for network (blue) and small molecule (red) systems.....148
- Figure 4.56.** (A) Comparison of the number of pyrazoline units (crosslinks) in the insoluble fraction of networks **60** and **61**. (B) Number of pyrazoline links vs. mass of insoluble fraction, and (C) Weight fraction vs. linking percentage of insoluble fraction, determined for networks **60** (crosses) and **61** (dots). Lines are guides for the eye. Adapted with permission from John Wiley and Sons, Ref 299.....149
- Figure 4.57.** Number of pyrazoline links per mass of insoluble fraction (crosslinking density) against (A) Irradiation time, and (B) Weight fraction of insoluble fraction of networks **60** (crosses) and **61** (dots). Error bars represent standard deviation from three independent replicas. Solid and dashed lines are guides for the eye. Adapted with permission from John Wiley and Sons, Ref 299.....150
- Figure 4.58.** Structure of the linking motif in networks **60** or **61**.....150
- Figure 4.59.** (Left axis) Weight fraction of the soluble (red bars) and insoluble (black bars) fractions of networks **61** after different irradiation times. (Right axis) Yield of pyrazoline units (black dots) in the insoluble fraction of networks **61**, achieved after different irradiation times. Dashed line is a guide for the eye. Adapted with permission from John Wiley and Sons, Ref 299.....152
- Figure 4.60.** Dimerization of maleimide via [2+2] cycloaddition, generating non-fluorescent crosslink points. Reprinted with permission from John Wiley and Sons, Ref 299.....152
- Figure 4.61.** ¹H NMR spectra in DMSO-*d*₆ of (A) Reaction of tetrazole **41** and trimaleimide **57** to produce the expected pyrazoline adduct **66** via NITEC, and (B) Irradiation of **57** in the absence of tetrazole groups, generating insoluble maleimide polymers **67** via [2+2] cycloaddition. Adapted with permission from John Wiley and Sons, Ref 299.....153
- Figure 4.62.** Free-radical polymerization and end-linking methods generate networks with different topologies. The structural differences might have a major impact in their application as alignment media.....154
- Figure 4.63.** (A) Crosslinking of bifunctional tetrazole-PS **59** and trimaleimide **57**, irradiated 7 h at 320 nm in DMF. (B) Reaction was carried out in glass capillaries as cylindrical molds. (C) Solvent was added to remove the soluble fraction. (D)

- After separation, small amounts of insoluble fraction without defined shape were obtained. (E) Further solvent addition promotes swelling of the insoluble material.....155
- Figure 4.64.** (A) Cylindrical PDMS mold used as reactor. (B) Precursor mixture (in DMF) was filled inside the PDSM mold and irradiated 7 h at 320 nm. (C) After washing with solvent, insoluble material was isolated only at the walls of the reactor.....155
- Figure 4.65.** SEC traces of (A) RAFT agent **68** and corresponding polymers **69–74** before aminolysis, and (B) RAFT polymers after aminolysis **69a–74a**, showing monomodal distributions in every case.....158
- Figure 4.66.** ^1H NMR spectra in CDCl_3 of RAFT agent **68**, the corresponding PS **69** and the product of aminolysis **69a**.....159
- Figure 4.67.** SEC-ESI-MS spectra (positive mode) of RAFT PS **69** (top), showing typical mass and isotopic pattern for the expected structure \blacksquare , and aminolysis product **69a** (bottom), exhibiting the expected distribution for structure \blacklozenge . Secondary structure \bullet (incomplete aminolysis) was also found. The spectra were recorded at the maxima of the molar mass distribution (retention time 16.2 min and 16.4 min, respectively in SEC chromatograms).....160
- Figure 4.68.** (A) Reaction scheme between bifunctional thiol-PS **74a** and linkers trimaleimide **57** (left) or tetraacrylate **75** with triethylamine as catalyst (right) in DMF, producing crosslinked gels. (B) Pictures of gels produced by crosslinking with **57** (left) or **75** (right). After washing with THF, soluble and insoluble fractions are isolated.....161
- Figure 4.69.** Weight fraction of insoluble fraction (black), and equilibrium mass swelling ratio Q_m in chloroform (red) of thiol-ene end-linked gels prepared from PS precursors of different molecular weight **69a**, **71a**, and **73a**. Error bars represent standard deviation from three independent replicas.....163
- Figure 4.70.** (A) Reaction scheme of telechelic thiol-PS **70a**, **72a**, and **74a** with anthracenyl-acrylate **76**, to yield the Michael addition polymers **70b**, **72b**, and **74b**, respectively. (B) SEC traces of polymers before (solid lines) and after (dashed lines) thiol-Michael addition.....164
- Figure 4.71.** (A) Fluorescence emission spectra of solutions of **76** in DMF at different concentrations. Emission maxima for monomer (393 nm, 416 nm, and 440 nm) are clearly visible, in addition to the broad excimer fluorescence emission at

APPENDIX

- 471 nm. (B) Calibration curves of fluorescence intensity vs. concentration of **76**, using the emission maxima at 393 nm (black), 416 nm (red) and 440 nm (blue).....165
- Figure 4.72.** Fluorescence emission spectra of polymers **70b** (black), **72b** (blue), and **74b** (purple) in DMF. Emission maxima at 393 nm, 416 nm, and 440 nm were used to determine concentration of anthracene moieties.....165
- Figure 4.73.** Equilibrium mass swelling ratio Q_m in chloroform vs. M_c of thiol-ene gels **77–86** prepared from PS precursors of single (solid symbols) and mixed (open symbols) molecular weight.....169
- Figure 4.74.** Schematic representation of crosslinking junctions of (A) thiol-ene networks ligated by tetraacrylate **75**, and (B) free-radical-based networks crosslinked with DVB. Black lines represent in both cases elastically active PS chains.....170
- Figure 4.75.** Mass swelling ratio Q_m (in chloroform) of PS gels prepared via thiol-ene with single precursors (solid dots), thiol-ene with mixed precursors (open dots), free-radical polymerization 46 wt.% in DMF (triangles), and free-radical polymerization in bulk (squares), against (A) Average molecular weight of chains between crosslinks M_c , and (B) Crosslinking percentage, calculated from Eq. 4.16 for thiol-ene gels, and from the amount of DVB for free-radical gels. Red line with crosses represents in both cases the theoretical Q_m from Flory–Rehner swelling theory.....171
- Figure 4.76.** (A) Reaction scheme of thiol-PS **69a** with monofunctional butyl acrylate, yielding the expected addition product **69c**, and possible disulfide dimers **69c'**. (B) SEC traces of polymers before (**69a** solid line) and after (**69c** dashed line) thiol-Michael addition. The shoulder in the SEC curve of **69c** might correspond to dimeric structure **69c'**.....173
- Figure 4.77.** T_2 relaxation curves for networks prepared by thiol-ene (dots) and free-radical (triangles) crosslinking, presenting different M_c (short, medium, and long). The inset displays the corresponding swelling (Q_m) vs. M_c data for the different gels.....174
- Figure 4.78.** (A) Thiol-ene end-linking methods allow the preparation of alignment media with homogeneous (**78**, **80**, **82**) and mixed (**86**) distribution of meshes, starting from PS precursors of different molecular weight (**70a**, **72a**, **74a**), or mixtures of them. (B) Comparison of alignment behavior with free-radical-based

- gels (**88**, **91**, **93**) allows investigation of structure-property relationships. (C) Cylindrical thiol-ene-based PS sticks can be obtained using appropriate reaction molds.....175
- Figure 4.79.** Glass transition temperature T_g of thiol-ene end-linked gels (dots), prepared from PS precursor of single (solid symbols) and mixed (open symbols) molecular weight, and free-radical crosslinked gels prepared in DMF (triangles).....176
- Figure 5.1.** Robust PS gels as reusable alignment media, in which analyte molecules are sequentially pumped in, analyzed at a desired alignment strength, and pumped out to repeat the cycle with new molecules.....184
- Figure 5.2.** Synthesis of (A) Statistical copolymers and (B) Block copolymers of styrene (St) and menthol-styrene (Mt*), mediated by RAFT agent **62**.....185
- Figure 8.1.** (A) Schematic representation of the setup used for the synthesis of polystyrene sticks. The reactor can be: (B) 3 mm outer diameter NMR tubes, (C) PTFE tubes of different diameters (sealed with epoxy glue), or (D) glass capillaries of different diameters.....242
- Figure 8.2.** (A) Equilibration time for the CDCl_3 quadrupolar splittings determined in sticks **4** and **6**, pre-swollen in acetone and stretched in conventional 5 mm NMR tubes. (B) 2D projection of CDCl_3 $\Delta\nu_Q$ values determined along the vertical direction of stick **4**, after 6 weeks equilibration time. The signal in the middle represents isotropic CDCl_3 . Cracks inside the gel leading to inhomogeneities in $\Delta\nu_Q$ are highlighted in red.....243
- Figure 8.3.** Free swelling of PS disks in toluene leads to cracking and breaking of the samples with (DVB > 0.1%) without plasticizer.....244
- Figure 8.4.** Frequency sweep curves displaying storage and loss moduli for (A) **1** DVB 0.1 mol%, (B) **2** DVB 0.2 mol%, (C) **3** DVB 0.4 mol%, and (D) **20** DVB 0.4 mol% + 17.5% v/v adipate. Error bars represent standard deviation from three independent measurements.....244
- Figure 8.5.** ^1H NMR spectra in CDCl_3 of some styrene (St)–monomer (**28**) mixtures (10%, 50%, 75%, and 90% St) before copolymerization.....245
- Figure 8.6.** ^1H NMR spectra of chiral network **30** (25 mol% (-)-menthol-styrene **28**, DVB 0.2 mol%) without analyte (A) and loaded with (+)-ICP (B). Resonance signals coming from the analyte are marked in red.....245

APPENDIX

- Figure 8.7.** Chemical structures of diastereomers altenuene and isoaltenuene, used as optically active analytes for chiral PS networks.....247
- Figure 8.8.** (A) Emission spectrum of the UV lamp (Arimed B6, $\lambda_{\text{max}} = 320 \pm 30$ nm) used as irradiation source. (B) Photoreactor. The lamp stands in the middle of the setup and the samples revolve around it in a carousel.....248
- Figure 8.9.** ^1H NMR spectra in CDCl_3 of polymers **49** analyzed after several irradiation times.....248
- Figure 8.10.** ^1H NMR spectra in $\text{THF-}d_8$ of the reaction between tetrazole **46** and maleimide **50**, producing pyrazoline **51** and different amounts of by-product **51'** (aromatization).....249
- Figure 8.11.** Structure of the repeating unit AA–BB in polymers **49**, with $m_{\text{AA–BB}} = 1549.8 \text{ g}\cdot\text{mol}^{-1}$249
- Figure 8.12.** ^1H NMR spectra in $\text{THF-}d_8$ of polymers **56**, obtained from PS **54** and bismaleimide **44**. Resonance signals of starting material and product are highlighted in green and blue, respectively. Signals of the aromatization by-product are depicted in red.....250
- Figure 8.13.** The fluorescence emission intensity of poly(pyrazolines) **56** prepared in $\text{THF-}d_8$ strongly decreases due to aromatization, if the samples are irradiated well beyond the completion of the NITEC reaction (< 4 h). Polymers obtained after 25 h irradiation are almost non-fluorescent.....250
- Figure 8.14.** RAFT polymerization of styrene mediated by agent **48** yields tetrazole-bifunctional PS chains of different molecular weight (**PS-1** to **PS-4**). The corresponding SEC traces are plotted on the left graph. The right plot displays experimental molecular weight vs conversion data (black), showing a linear tendency, close to the expected theoretical values (red, calculated from Equation 2.23). Black squares represent experimental dispersity values \bar{D} determined by SEC.....251
- Figure 8.15.** (A) Emission spectrum of the UV lamp used for network formation LZC-UVB ($\lambda_{\text{max}} = 300$ nm), showing the absolute light intensity reaching the sample. (B) Setup employed for the photoreactions, using two LZC-UVB (300 nm) lamps that irradiate the samples from the top.....251
- Figure 8.16.** (A) SEC traces of networks **60** at $t = 0$ (black) and $t = 8$ h irradiation (red, soluble fraction; blue, insoluble fraction) after aminolysis. (B) SEC traces of

- networks **61** at $t = 0$ (black) and $t = 4$ h irradiation (red, soluble fraction; blue, insoluble fraction) after aminolysis.....252
- Figure 8.17.** Network formation from **59** and **57** using different molar ratios tetrazole : maleimide (1 : 1, black dots; 1 : 3, red squares; 1 : 5, blue triangles). When excess of maleimide is used, higher amounts of insoluble fraction are obtained (bottom left plot), but aminolysis does not produce soluble material (bottom right pictures). The available maleimide groups act as crosslinker in the Michael addition of the thiol polymers yielded after aminolysis.....252
- Figure 8.18.** ^1H NMR spectra in $\text{DMSO-}d_6$ of standard solution **51** (at 90% conversion) before and after aminolysis.....253
- Figure 8.19.** NITEC reaction between tetrazole **46** and *N*-ethylmaleimide (1 : 1 mol ratio) under irradiation at 320 nm. The initial concentration of **46** was set to 1.20 mM (blue), 3.62 mM (black), and 7.25 mM (red). Left plot display tetrazole conversion vs irradiation time, right plot shows $-\ln([\mathbf{46}])$ against reaction time. Dashed lines represent linear fits.....254
- Figure 8.20.** NITEC reaction (320 nm) between tetrazole **46** and *N*-ethylmaleimide (solid symbols), or trimaleimide **57** (open symbols), at 1 : 1 mol ratio tetrazole : maleimide. In both cases the initial concentration of **46** was kept at 3.62 mM.....254
- Figure 8.21.** Comparison of ESI-MS spectra of samples **61** at $t = 0$ and $t = 4$ h irradiation (soluble and insoluble fractions), after aminolysis. Mass spectra were recorded at 17.8 min retention time (red line in SEC chromatogram).....255
- Figure 8.22.** Comparison of ESI-MS spectra of samples **60** at $t = 8$ h irradiation (soluble and insoluble fractions), after aminolysis. Mass spectra were recorded at 18.2 min retention time (red line in SEC chromatogram).....256
- Figure 8.23.** Crosslinking motifs of thiol-PS strands **74a** with trimaleimide **57** (left) or tetraacrylate **75** (right).....257
- Figure 8.24.** Crosslinking of thiol-PS strands **73a** ($330\text{--}830\text{ mg}\cdot\text{mL}^{-1}$ in DMF) with tetraacrylate **75** (1 : 1 mol ratio thiol : ene), using triethylamine as catalyst.....257
- Figure 8.25.** Crosslinking of thiol-PS **69a** with tetraacrylate **75** and 1,3-butanediol diacrylate (1 : 1 mol ratio thiol : ene), using triethylamine as catalyst.....258

APPENDIX

- Scheme 2.1.** Generally accepted mechanism of free-radical polymerization (FRP) of vinyl C=C–R monomers, where I represents an initiator and X a chain transfer species.....6
- Scheme 2.2.** Head-to-tail (H-T) vs. head-to-head (H-H) addition of monomers during propagation.....7
- Scheme 2.3.** Fundamental mechanism of atom transfer radical polymerization, ATRP.....15
- Scheme 2.4.** General mechanism of degenerative transfer radical polymerization.....15
- Scheme 2.5.** The mechanism of RAFT polymerization consist in five different steps, namely initiation, pre-equilibrium, reinitiation, main equilibrium (degenerative transfer), and termination.....16
- Scheme 2.6.** Functionalization approaches of polymers via RAFT. The monomer units are inserted between the R and the thiocarbonylthio groups of the CTA (I), giving an R-group end-functional polymer (II). Eventually, Z can bear also a functional group in (II), or it can be removed via postmodification to afford telechelic polymers (III). Scheme adapted from Ref 46.....21
- Scheme 2.7.** End-group postmodification of RAFT polymers either by [2+4] hetero-Diels–Alder cycloaddition to the thiocarbonylthio group (left), or by its removal via various methodologies (right).....21
- Scheme 2.8.** Step-growth polymerization of (I) AA–BB monomers, in this case a diol and a diacid to produce a polyester, and (II) AB monomers, here an amino acid that forms a polyamide (nylon).....23
- Scheme 2.9.** Selection of photoreactions currently used in polymer modification: UV-induced alkene-enone [2+2] cycloaddition¹¹² (UV light), photogeneration of thioaldehydes from phenacyl¹¹⁹ (UV light) or pyrenacyl¹¹⁷ (visible light) sulfides, and Diels–Alder [4+2] cycloaddition of photo-enols¹²⁰⁻¹²² (UV light X = O, visible light X = S).....31
- Scheme 2.10.** Light-induced degradation of diaryltetrazoles yields a nitrile imine intermediate, which readily reacts with activated alkenes (NITEC), carboxylic acids (NICAL), water, thiols, and imidazole.....32
- Scheme 3.1.** Synthesis route for styrene derivatives **26** and **27**, functionalized with *n*-pentyl and *n*-dodecyl residues, respectively.....69

Scheme 3.2. Synthesis route for monomers (-)-menthol-styrene 28 and (+)-menthol-styrene 29	74
Scheme 3.3. Synthesis of PS networks functionalized with 1,10-phenanthroline units by free-radical copolymerization of styrene, phenanthroline-styrene 36 , and DVB.....	90
Scheme 3.4. Complexation of europium ions by phenanthroline ligands present in polystyrene chains.....	91
Scheme 4.1. Formation of pyrazolines through UV-induced nitrile imine-mediated tetrazole-ene cycloaddition (NITEC) reaction.....	99
Scheme 4.2. Synthesis route for the bifunctional tetrazole-chain transfer agent 43 ...100	
Scheme 4.3. Synthesis route for methoxy-tetrazole 46 and corresponding bifunctional tetrazole-chain transfer agent 48	102
Scheme 4.4. NITEC reaction between bismaleimide 44 and tetrazole 46 to obtain pyrazoline 52	108
Scheme 4.5. RAFT polymerization of styrene mediated by bifunctional-tetrazole CTA 48	120
Scheme 4.6. Synthesis of trithiocarbonate-based symmetrical RAFT agent 62	128
Scheme 4.7. Synthesis of PS strands 63 via RAFT polymerization mediated by CTA 62	130
Scheme 4.8. RAFT polymerization of styrene, mediated by CTA 68 , yielding PS strands 69–74 . Further aminolysis of the trithiocarbonate groups produces telechelic thiol-functional PS 69a–74a	157
Scheme 5.1. Synthesis of end-linked polymer networks via <i>para</i> -fluoro-thiol or photoactivated radical thiol-norbornene ligation protocols.....	188
Table 2.1. Selection of RAFT agents and their compatibility with different monomer classes. MAMs: styrenes, acrylates, methacrylates; LAMs: vinyl esters. (+: compatible, -: incompatible).....	20
Table 3.1. Swelling, thermal, and alignment properties of PS networks prepared with different amounts of crosslinker (DVB).....	60

APPENDIX

Table 3.2. Swelling ratio and crack formation of PS sticks prepared with different amounts of plasticizers: Toluene, <i>N,N</i> -dimethylformamide, and bis(2-ethylhexyl) adipate.....	63
Table 3.3. Swelling and thermal properties of networks prepared with different styrene derivatives.....	68
Table 3.4. Swelling and thermal properties of networks prepared in different mold reactors.....	71
Table 3.5. Swelling and thermal properties of networks prepared in glass reactors of different diameter.....	72
Table 3.6. Swelling and thermal properties of chiral PS networks, prepared with different amounts of (-)- and (+)-menthol-styrene derivatives.....	75
Table 3.7. Initial feed and conversion of monomers 28 and styrene (St), as well as the corresponding copolymer composition.....	79
Table 3.8. Data used to determine reactivity ratios.....	80
Table 3.9. Comonomer reactivity ratios r_1 and r_2 for the copolymerization of styrene (St) and 28	82
Table 3.10. RDCs of (+)- and (-)-IPC in chiral PS alignment media 30 and 31	85
Table 3.11. RDCs of altenuene and isoaltenuene in chiral PS alignment media 30 and 31	88
Table 3.12. Swelling and thermal properties of phenanthroline-functional PS networks, prepared with different amounts of monomer 36 and diluent (DMF).....	90
Table 3.13. Swelling and thermal properties of europium-coordinated PS networks....	91
Table 4.1. Structure assignment for the peaks in the MS spectrum in Figure 4.27.....	122
Table 4.2. Soluble and insoluble fractions of NITEC networks prepared from tetrazole-PS 59 and trimaleimide 57 , irradiated at 320 nm.....	125
Table 4.3. Structure assignment for the peaks in the MS spectrum in Figure 4.41.....	135
Table 4.4. Structure assignment for the peaks in the MS spectrum in Figure 4.45.....	138
Table 4.5. Structure assignment for the peaks in the MS spectrum in Figure 4.50.....	143
Table 4.6. Number average molecular weight (\bar{M}_n) and dispersity index (\mathcal{D}) of PS samples before and after aminolysis 69–74 and 69a–74a , respectively.....	158
Table 4.7. Structure assignment for the peaks in the MS spectra in Figure 4.67.....	160

Table 4.8. Screening of the reaction conditions for the crosslinking of thiol-PS 74a ...	161
Table 4.9. Percentage of anthracene groups in PS 70b , 72b , and 74a , as determined by fluorescence spectroscopy.....	166
Table 4.10. Network fraction and swelling ratio of thiol-ene gels prepared from PS precursors of single (77–82) and mixed (82–86) molecular weights.....	167
Table 4.11. Swelling ratio of free-radical-based PS gels prepared with different amounts of DVB.....	169
Table 8.1. RDCs of altenuene and isoaltenuene in chiral PS alignment media 30 and 31	246
Table 8.2. RDCs of altenuene in chiral PS alignment media 30–32	246
Table 8.3. Structure assignment for the peaks in the MS spectrum in Figure 8.21....	255
Table 8.4. Structure assignment for the peaks in the MS spectrum in Figure 8.22.....	256
Table 8.5. Yields of insoluble fraction for the crosslinking reaction depicted in Figure 8.24.....	257
Table 8.6. Yields of insoluble fraction and mass swelling ratio Q_m for the crosslinking reaction depicted in Figure 8.25, using different amounts of diacrylate.....	258

COMPLETE LIST OF PUBLICATIONS AND CONFERENCE CONTRIBUTIONS

Publications Arising from this Thesis

- [1a] Counting the clicks in fluorescent polymer networks.
D. Estupiñán, C. Barner-Kowollik, L. Barner, *Angew. Chem. Int. Ed.* **2018**, *57*, 5925.
- [1b] Bestimmung der Verknüpfungspunkte in fluoreszenten Polymernetzwerke.
D. Estupiñán, C. Barner-Kowollik, L. Barner, *Angew. Chem.* **2018**, *130*, 6028.
- [2] Self-reporting fluorescent step-growth RAFT polymers based on nitrile-imine mediated tetrazole-ene cycloaddition chemistry.
D. Estupiñán, T. Gegenhuber, J. P. Blinco, C. Barner-Kowollik, L. Barner, *ACS Macro Lett.* **2017**, *6*, 229.

Additional Publications

- [1] Pre-adsorption of antibodies enables targeting of nanocarriers despite a biomolecular corona.
M. Tonigold,[‡] J. Simon,[‡] D. Estupiñán, M. Kokkinopoulou, J. Reinholz, U. Kintzel, A. Kaltbeitzel, P. Renz, M. P. Domogalla, K. Steinbrink, I. Lieberwirth, D. Crespy, K. Landfester, V. Mailänder, *Nat. Nanotechnol.* **2018**, *13*, 862.
- [2] 6-(Aryldiazenyl)pyrazolo[1,5-*a*]pyrimidines as strategic intermediates for the synthesis of pyrazolo[5,1-*b*]purines.
J-C. Castillo,[‡] D. Estupiñán,[‡] M. Nogueras, J. Cobo, J. Portilla, *J. Org. Chem.* **2016**, *81*, 12364.
- [3] The pro-active payload strategy significantly increases selective release from mesoporous nanocapsules.
S. Behzadi, M. Steinmann, D. Estupiñán, K. Landfester, D. Crespy, *J. Controlled Release* **2016**, *242*, 119.

[‡] These authors contributed equally.

- [4] Multifunctional clickable and protein-repellent magnetic silica nanoparticles.
D. Estupiñán, M. B. Bannwarth, S. E. Mylon, K. Landfester, R. Muñoz-Espí, D. Crespy, *Nanoscale* **2016**, *8*, 3019.
- [5] Size-dependent self-assembly of anisotropic silica-coated hybrid nanoparticles.
D. Estupiñán, M. B. Bannwarth, K. Landfester, D. Crespy, *Macromol. Chem. Phys.* **2015**, *216*, 2070.
- [6] 7-Amino-5-methyl-2-phenyl-6-(phenyldiazenyl)pyrazolo[1,5-*a*]pyrimidine crystallizes with $Z = 2$: pseudo-symmetry and the formation of complex sheets built from N–H \cdots N and C–H \cdots π (arene) hydrogen bonds.
 J. Portilla, D. Estupiñán, J. Cobo, C. Glidewell, *Acta Crystallogr., Sect. C: Cryst. Struct. Commun.* **2010**, *66*, o133.

Conference Contributions

- [1] Control and quantification of crosslinking degree in fluorescent polymer networks.
D. Estupiñán, C. Barner-Kowollik, L. Barner. *Dimensional Control of Polymer Materials – From Synthesis to Function. Biennial Meeting of the GDCh-Division of Macromolecular Chemistry*. Karlsruhe, Germany. **September 2018**. Poster presentation.
- [2] Quantification of ligation points in photochemically linked polymer networks.
D. Estupiñán, C. Barner-Kowollik, L. Barner. *Polymer Networks and Gels – 82nd Prague Meeting on Macromolecules, 24th Polymer Networks Group Meeting*. Prague, Czech Republic. **June 2018**. Oral presentation.
- [3] Advanced synthetic avenues to fluorescent polymer-based networks for NMR spectroscopy.
D. Estupiñán, P. Tzvetkova, B. Luy, C. Barner-Kowollik, L. Barner. *International Conference on BioNano Innovation*. Brisbane, Australia. **September 2017**. Poster presentation.
- [4] Accessing polymerization kinetics via self-reporting NITEC strategy.
D. Estupiñán, T. Gegenhuber, J. P. Blinco, C. Barner-Kowollik, L. Barner. *16th European Polymer Federation (EPF) Polymer Congress*. Lyon, France. **July 2017**. Poster presentation.

CURRICULUM VITAE

The curriculum vitae is not included in the electronic version of this thesis.

ACKNOWLEDGEMENTS

“Individually, we are one drop. Together we are an ocean” – Ryunosuke Satoro. The completion of my Ph.D. thesis would not have been possible without the support of many people around me. Therefore, I dedicate the next lines to express my deepest gratitude to the persons that accompanied me in the last years. In the first place I would like to acknowledge the excellent guidance of Dr. Leonie Barner. For her trust in me since the beginning, the humanistic nature of her supervision, and constant support through all the challenges that appeared (even while working in parallel in two different continents), I am very grateful. At the same time, my heartiest gratitude goes to Prof. Christopher Barner-Kowollik for his encouragement and his inspiring and helpful manner. Words cannot express my thankfulness to both of you.

Special thanks also to my collaboration partners from the NMR spectroscopy group, Prof. Burkhard Luy, Dr. Pavleta Tzvetkova and Thomas Gloge. For the very interesting insights into the alignment media, their helpful suggestions and feedback, I will be always thankful. Without their commitment and teamwork spirit it would not have been possible to carry out the fascinating interdisciplinary projects we did.

I want also to thank my “fume-hood-mate” and friend Federica Cavalli. Throughout the everyday research-life I could find in her a perfect buddy for productive scientific discussions, creative brainstorming, and clever decision-making. Likewise, I would like to acknowledge my friends and colleagues from the Macroarc group for the nice working atmosphere, their helpfulness and cooperativeness. In the same line, I am grateful to the members of the QUT node for making my stay in Australia an unforgettable experience.

A big thank you goes to the members of the Soft Matter Lab team at Campus North, especially Dr. Hatice Mutlu for her constant advice and able support, Dr. Sylvain Grosjean for sharing his broad experience in organic synthesis, and Dr. Nicolas Zydziak for introduce me to novel experimental methods and techniques. Here I also want to express my especial appreciation to Birgit Huber for her patience, perseverance and support through scientific as well as administrative issues. Without her taking care of every detail, research could not be done. Similarly, I am deeply indebted to Katharina

Elies who, with engagement and hard work, makes that everything at Campus South runs smoothly.

I also would like to thank Maja Dobrowolska, who I had the pleasure to supervise during her summer internship, within the frame of the DAAD-RISE program 2017. Thanks to her motivation, good grasp, quick understanding, and solid experimental abilities, it was possible for me to easily shape up one of my subprojects and gain first experiences in leadership.

Furthermore, I am grateful to Dr. James Blinco (QUT) for his advices and suggestions, Dr. Lukas Arens for his help with rheology measurements, Christoph Pfeifer for helping me with NMR relaxometry measurements, Dr. Jan Steinkönig for his support with some ESI-MS spectra, Dr. Kai Hildebrandt for providing precursor compounds, as well as to Hannah Rothfuß and Nicolai Knöfel for compound exchange and their know-how in metal complexation.

I also would like to thank my close friends outside the KIT, Cesare Benedetti, Alice Antonello, Inderjeet Singh, Nicolás Moreno, Mariana Alarcón, and Alejandro Posada, for always being there for me.

At the end of my list are the persons to whom I am most thankful, for without them I certainly would have never made it this far. To my parents, my brother, my sister, and my partner Eli, for their unconditional love and support in every aspect of my life, for guiding me through the difficult situations, and for sharing with me the moments of joy and happiness. For all of this and much more, you have always my eternal gratitude.

“¡Gracias... totales!”

